

On the potential of multi-spectral x-ray
and photoacoustic imaging to facilitate
gold nanoparticle mediated
dose-enhanced radiotherapy

A thesis submitted to the University of London for the degree of

Doctor of Philosophy in

The Physics of Biomedical Imaging

By

Oliver Len Paul Pickford Scienti

Joint Department of Physics,

Institute of Cancer Research and Royal Marsden NHS Foundation Trust,

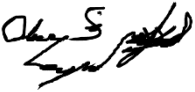
Downs Road, Sutton, Surrey, SM2 5NG, United Kingdom

March 2021

Author's Declaration

I declare that the work reported in this thesis was produced by the author whilst employed to complete a PhD at the Joint Department of Physics, Institute of Cancer Research and Royal Marsden Hospital NHS Trust, beginning on the 5th of October 2015. Where the work or assistance of others was used, this has been acknowledged and referenced appropriately in the text.

Name: Oliver Len Paul Pickford Scienti

Signed: 

Date: 14/07/2021

Abstract

To increase the effectiveness of radiotherapy for treating tumours whilst sparing normal tissues, researchers are investigating gold nanoparticles (AuNPs). AuNPs may be targeted to cancers and are known to produce radiotherapy dose enhancing effects (RDEEs) via physical (increased x-ray absorption), chemical (catalytic for free radical production) and biological (DNA repair inhibition) mechanisms. This thesis asserts that maximising their clinical benefit requires quantitative, AuNP-sensitive, medical imaging to predict the distribution of RDEEs, and assesses the potential of two candidate imaging methods: photon-counting multispectral x-ray imaging (x-CSI) and photoacoustic spectral imaging (PASI).

As physical x-CSI system availability is limited, a simulation framework (CoGI) was developed and experimentally validated, combining Monte Carlo and finite element methods with custom scripts to model a full x-CSI system, including charge sharing correction algorithms (CSCAs). CoGI was then used to investigate the effects of various parameters (pixel pitch, sensor thickness and CSCA choice) on a range of detector metrics. The simulations identified previously undescribed mechanisms by which CSCAs can be differentiated and allowed the listed parameters to be optimised for AuNP detection.

A literature review revealed significant achievements in AuNP detection using PASI, such that PASI is arguably the current gold standard for non-invasive AuNP detection. The AuNPs used are often coated or shaped to improve their PASI suitability, resulting in AuNP types that differ markedly from those used in AuNP-mediated RDEE research. The effect of optimising for PASI on RDEE is not currently considered in the literature, so work was undertaken to assess whether PASI and RDEE optimisations are compatible. Results suggest a previously unexploited synergy between PASI and RDEE optimisations regarding AuNP shape, but also highlight a conflict with regards AuNP coating.

Literature, simulation, and wet-lab results were then pooled to allow the potential of PASI and x-CSI for *in vivo* AuNP imaging to be discussed.

Statement of Covid Impact

The Covid-19 pandemic occurred towards the end of my PhD, and it impacted my work in the following ways:

- 1.) As a result of the outbreak and first lockdown I was initially unable to access the wet-labs for a period of several months. During this time I planned to work on my thesis instead, and to then return to the lab to finish the cell experiments detailed in Chapter 8 of this thesis.
- 2.) Shortly after the first lockdown began (March 2020) I became ill with a cough, hot flushes, lethargy, headache and reduced focus, and was told by a doctor that this was a suspected case of Covid-19. This resulted in me being bed bound for over 2 weeks. I was placed back on an inhaler (which I had not needed since childhood) and advised to discontinue the pain killers and anti-inflammatory medication that I was on for an unrelated chest condition.
- 3.) In addition to not being allowed to use my medications, I was also unable to receive the hospital treatment for my chest condition that I had been scheduled for (due to non-emergency procedures being cancelled) and unable to access the pain management services I had previously been using (due to them being closed out of concern for increasing transmission). This led to a worsening of my chest condition and limited me to no more than a few hours of work per day for a period of 8 months (until November 2020). The time lost was calculated and added to the end date for my thesis as an unpaid extension.
- 4.) Despite lockdown easing and my chest pain becoming manageable, I was advised to avoid going into the labs due to the higher risk that the pain medication and chest condition might have put me at. As such, it was decided that the best approach would be for me to not complete further runs of the lab work and instead to focus on analysing the data gathered already as best as I could.
- 5.) The result of the above disruptions was that Chapter 8 could only make tentative conclusions due to the lack of repeats, and the planned experiments to measure the photoacoustic signal strength of the various gold nanoparticles had to be dropped from the thesis plan entirely.

Signed by Student:



Name: Oliver Len Paul Pickford Scienti

Date: 28/03/2021

Signed by Supervisor:



Name: Dr. Dimitra Darambara

Date: 28/03/2021

Acknowledgements

A research PhD thesis is the culmination of an extended period of scientific study and its content and quality largely depend on the hard work, skill, and perseverance of the author. But in turn, the author and their capabilities depend on those people and events that have shaped them. With that in mind, I would like to extend my thanks to those who have made me who I am.

Firstly, to my mother, Rita Pickford, for her support, encouragement, and love which I am in no doubt has helped shape me into the kind-hearted, thoughtful individual that I am today. From pre-school through secondary school and into university, you have always encouraged me to believe in myself and seen my potential even when I did not, so thank you. Secondly, to my father, Len Pickford, who is my role model as a man and as a father. Our weekly TV nights watching Star Trek and then Stargate helped to stoke my love and passion for science, and your science questions whilst waiting for an Indian takeaway kept me on my toes. Despite what you say now about getting them, I would also like to thank you for my 'Predators of the Wild' VHS series, which helped my scientific interests stay varied. So thank you both. Next, to my wife, Rosie, who supported my decision to return to university after first dropping out (twice actually) and who is always there to hold me up or glue me back together when I struggle, thank you for your continued support. You are always the cheerleader in my corner, and it benefits me greatly to know I can count on you. Without these three people I would not be the man I am today, and as such you have my eternal gratitude. In particular, thank you for the meals, emotional support, financial assistance, and patience that you have all shown me over the Covid-19 pandemic in particular: my working from home for long and unsociable hours cannot have been easy at times I know.

I also thank my supervisors, Dr Dimitra Darambara and Prof Jeffery Bamber. Together you have guided me through my PhD and taught me what it means to be a scientist at a professional level. I am grateful for your insights, support, encouragement, and compassion, which has kept me going through my PhD. In particular, I would like to thank Dimitra for pushing me to present and publish in the face of my doubts about my own abilities, and for giving me the space, opportunities and encouragement to develop my knowledge and skills. Similarly, I would like to thank Jeff for his guidance and support in navigating various issues whilst studying, and for his meticulous feedback on drafts of my papers and thesis chapters: you routinely pushed me to think more by asking awkward questions and picked up more grammar errors than I would care to admit! Additionally, I would like to thank Carol Box for sharing her experience, knowledge, and skills in tissue culture, without which I would not have completed the work in Chapter 8. My biological skills have improved greatly due to her supervision.

To my closest friends, Alistair Biggins, James Harverson, Michael Mulholland, and Kevin McDermott, thank you for your emotional support and level-headed ridicule which has kept me

balanced and jovial throughout a stressful period. Thank you for always being there to let me vent, relax or work out, and for just generally being amazing in my life: my mental health would have suffered, and my world been all the poorer, had I not had you all to share this journey with. You are family to me.

To my colleague and friend, Timothy Eales, a huge thank you and no small debt of gratitude: without your support with note taking and lesson catchup I would not have been able to complete my Physics MPhys when I did (given my simultaneous night work) and consequently could not have completed this PhD. Thank you, my friend, for being a role model in seeking the truth over being right. I look forward to many more philosophical and political discussions in our future (and a few more bottles to mark down).

Last, and though they never knew me, I would like to thank the authors of stories and discussions that have shaped my thinking, hopes and ambitions since my childhood. Thanks in this vein go to Gene Roddenberry, Isaac Asimov, Richard Dawkins, Brian Greene, and Christopher Hitchens.

There is a quote, oft attributed to Isaac Newton in describing his scientific insights: “If I have seen further, it is by standing on the shoulders of Giants”. There are of course more scientific giants than I might cite in this acknowledgment, without whom my studies and conclusions would not have been possible. The people thanked here are more than giants on whose shoulders I stand however: they are those who have loomed largest in my life and credit for my achievements belongs also, in no small part, to their presence in the world. My heart-felt thanks goes out to all of you.

Finally, whilst not a thanks *per se*, I would like to acknowledge that one of the reasons that I chose to pursue this PhD at the Institute of Cancer Research was the heart-breaking loss of my grandad to mesothelioma whilst at university. I love you Grandad: you are missed. I know you always believed in me, and I hope that this thesis would have made you proud.

Table of Contents

LIST OF ABBREVIATIONS	X
THESIS OVERVIEW	1
ORIGINAL WORK AND CONTRIBUTIONS TO THE FIELD	4
CHAPTER 1. BACKGROUND AND THESIS MOTIVATION: RADIOTHERAPY	6
1.1 HISTORY	7
1.1.1 <i>Inception</i>	7
1.1.2 <i>X-ray sources</i>	8
1.1.3 <i>Treatment protocols</i>	9
1.2 PRINCIPLES OF RADIATION INDUCED CELL DAMAGE	11
1.2.1 <i>Physical deposition of energy</i>	11
1.2.2 <i>Chemical conversion of energy to damage</i>	17
1.2.3 <i>Damage fixation and cell fate</i>	19
1.2.4 <i>Summary</i>	21
1.3 MAXIMISING RADIOTHERAPY BENEFITS: TRENDS AND FUTURE OUTLOOK	21
1.3.1 <i>Tumour tracking</i>	22
1.3.2 <i>Normal tissue protection</i>	24
1.3.3 <i>Improved dose effectiveness</i>	26
1.3.4 <i>Conclusion</i>	28
CHAPTER 2. GOLD NANOPARTICLES FOR RADIOTHERAPY DOSE ENHANCEMENT	30
2.1 DEFINITION AND LIMITATIONS OF DOSE ENHANCEMENT	31
2.1.1 <i>Physical parameters measured</i>	31
2.1.2 <i>Calculated dose enhancement metrics</i>	35
2.2 ADVANTAGES OF GOLD NANOPARTICLES AS RDEE DELIVERY AGENTS	39
2.2.1 <i>Radiotherapy dose enhancement</i>	39
2.2.2 <i>Ease of synthesis</i>	48
2.2.3 <i>Versatility of functionalisation</i>	48
2.2.4 <i>Selective tumour accumulation</i>	48
2.2.5 <i>Tailorable uptake kinetics</i>	50
2.2.6 <i>Multi-modality Imaging potential</i>	51
2.3 AN IMPORTANT OUTSTANDING CONSIDERATION IN USING AuNPs FOR PRODUCING RDEES	52
2.4 CONCLUSION	53
CHAPTER 3. PHOTOACOUSTIC SPECTRAL IMAGING (PASI)	55
3.1 THE ROLE OF PASI IN THIS THESIS	56
3.2 FUNDAMENTALS OF PASI	56
3.2.1 <i>History</i>	56
3.2.2 <i>Imaging process</i>	57
3.2.3 <i>Spectral separation of contrast agents</i>	62
3.2.4 <i>Advantages of PASI</i>	64
3.3 AuNPs AS EXOGENOUS PASI CONTRAST AGENTS	65
3.3.1 <i>Principles and mechanism of AuNP detection</i>	65
3.3.2 <i>Advantages of AuNPs for PASI</i>	68
3.3.3 <i>Achievements and potential of PASI in AuNP imaging</i>	69
3.4 LIMITATIONS OF PASI	72
3.5 RELEVANCE OF THIS WORK TO PASI FOR RDEE PREDICTION	74

CHAPTER 4. X-RAY PHOTON-COUNTING SPECTRAL IMAGING (X-CSI)	76
4.1 THE ROLE OF X-CSI IN THIS THESIS	77
4.2 FUNDAMENTALS OF TRANSMISSION X-RAY IMAGING	78
4.2.1 Dimensionality.....	79
4.2.2 Detection mechanisms	82
4.2.3 Detection chromaticity.....	83
4.2.4 Transmission assessment scheme	88
4.2.5 Spectral separation of contrast agents	92
4.2.6 Advantages of x-CSI.....	94
4.3 AuNPs AS EXOGENOUS X-CSI CONTRAST AGENTS	96
4.3.1 Principles and mechanism of AuNP detection.....	96
4.3.2 Achievements and potential of x-CSI in AuNP imaging.....	99
4.4 LIMITATIONS OF X-CSI	104
4.5 RELEVANCE OF THIS WORK TO X-CSI FOR RDEE PREDICTION.	106
CHAPTER 5. SIMULATING AN X-CSI FRAMEWORK: COGI	108
5.1 INTRODUCTION AND MOTIVATION	109
5.2 PROCESSES TO SIMULATE.....	111
5.2.1 Photon generation	112
5.2.2 Photon scattering (Rayleigh and Compton).....	116
5.2.3 Photoelectric absorption.....	116
5.2.4 Atomic deexcitation (x-ray fluorescence and Auger electron production)	116
5.2.5 Charge carrier production.....	116
5.2.6 Charge carrier drift.....	117
5.2.7 Electrode charge induction.....	117
5.2.8 Charge cloud expansion (diffusion and repulsion).....	119
5.2.9 Fate of charge carriers (trapping, recombination, and collection).....	120
5.2.10 Charge sharing correction algorithm.....	120
5.2.11 Conversion from collected charge to incident photon keV.....	121
5.3 OVERVIEW OF COGI	121
5.3.1 Component one (C1).....	123
5.3.2 Component two (C2).....	123
5.3.3 Component three (C3)	126
5.4 METHODOLOGY FOR VALIDATION STUDIES WITH COGI.....	132
5.4.1 Validation experiment outlines	132
5.4.2 Method for validating the basic physics	133
5.4.3 Method for validating CSCA implementation in CoGI	135
5.5 RESULTS OF VALIDATION	138
5.6 DISCUSSION	140
5.7 CONCLUSIONS.....	143
5.8 DISCLAIMER.....	144
CHAPTER 6. OPTIMAL X-CSI SYSTEM PARAMETERS FOR AU K-EDGE IMAGING: PIXEL PITCH AND THICKNESS	145
6.1 INTRODUCTION	147
6.2 SIMULATION SETUP AND METHODOLOGY	149
6.2.1 C1 Parameters	149
6.2.2 C2 Parameters.....	151
6.2.3 C3 Parameters.....	151
6.2.4 Metrics used for comparing simulated detectors.....	153
6.3 RESULTS	154
6.4 DISCUSSION	159
6.4.1 Absolute detection efficiency.....	159
6.4.2 Absolute photopeak efficiency.....	160

6.4.3	<i>Relative coincidence counts</i>	161
6.4.4	<i>Binned spectral efficiency</i>	162
6.4.5	<i>Conclusion</i>	164
6.5	DISCLAIMER.....	164
CHAPTER 7. OPTIMAL X-CSI SYSTEM PARAMETERS FOR AU K-EDGE IMAGING: CHOICE OF CHARGE SHARING CORRECTION ALGORITHM		165
7.1	INTRODUCTION	166
7.2	SIMULATION SETUP AND METHODOLOGY.....	167
7.2.1	<i>Charge sharing correction algorithms considered</i>	168
7.2.2	<i>Metrics assessed</i>	171
7.2.3	<i>Theoretical ADE model</i>	171
7.3	RESULTS	173
7.3.1	<i>Absolute detection efficiency</i>	174
7.3.2	<i>Absolute photopeak efficiency</i>	177
7.3.3	<i>Relative coincidence counts</i>	179
7.3.4	<i>Binned spectral efficiency</i>	179
7.3.5	<i>Other figures</i>	180
7.4	DISCUSSION	182
7.4.1	<i>Absolute detection efficiency</i>	182
7.4.2	<i>Absolute photopeak efficiency</i>	187
7.4.3	<i>Relative coincidence counts</i>	189
7.4.4	<i>Binned spectral efficiency</i>	189
7.5	CONCLUSIONS.....	191
7.6	DISCLAIMER.....	192
CHAPTER 8. WORK TOWARDS IDENTIFYING WHETHER RDEE IS AFFECTED BY AUNP OPTIMISATION FOR PASI		194
8.1	INTRODUCTION	195
8.2	MATERIALS AND METHODS.....	196
8.2.1	<i>AuNP design</i>	196
8.2.2	<i>AuNP synthesis and selection</i>	198
8.2.3	<i>Calibration of the irradiation equipment</i>	198
8.2.4	<i>Dose response curve determination</i>	200
8.2.5	<i>Determination of AuNP-mediated RDEEs</i>	201
8.3	RESULTS	202
8.3.1	<i>AuNP synthesis and selection</i>	202
8.3.2	<i>Calibration of the irradiation equipment</i>	204
8.3.3	<i>Dose response curve determination</i>	207
8.3.4	<i>Determination of AuNP-mediated DEEs</i>	209
8.4	DISCUSSION	211
8.4.1	<i>AuNP synthesis and selection</i>	211
8.4.2	<i>Calibration of the irradiation equipment</i>	212
8.4.3	<i>Dose response curve determination</i>	214
8.4.4	<i>Declaration</i>	216
8.4.5	<i>Determination of AuNP-mediated DEEs</i>	217
8.5	CONCLUSION	221
CHAPTER 9. OVERALL DISCUSSION.....		223
9.1	SYSTEM RESOLUTIONS	224
9.1.1	<i>Spatial resolution</i>	224
9.1.2	<i>Temporal resolution</i>	227
9.2	OTHER IMAGING FACTORS	228
9.3	AUNP DETECTION AND QUANTIFICATION	229

9.4	AUNP PARAMETER SENSITIVITIES.....	233
9.5	AUTHOR’S OPINIONS ON THE CONTRIBUTIONS OF THIS THESIS	234
CHAPTER 10. CONCLUDING THOUGHTS AND FUTURE WORK		235
10.1	AUTHOR’S VIEW ON THE BROADER FUTURE OF THE FIELD	238
REFERENCES		241
APPENDIX 1: PUBLICATIONS, PRESENTATIONS AND AWARDS		267
APPENDIX 2: AUNR SYNTHESIS PROTOCOL.....		269
APPENDIX 3: PROTOCOL FOR DETERMINING DOSE RESPONSE CURVES.....		270
APPENDIX 4: PROTOCOL FOR MEASURING RDEE		273
APPENDIX 5: LIST OF TABLES		275
APPENDIX 6: LIST OF FIGURES		277

List of abbreviations

ADE: Absolute Detection Efficiency	DNA: Deoxyribonucleic Acid
AO: Acridine Orange	DSB: Double Strand Break
APE: Absolute Photopeak Efficiency	EI: Energy Integrating
ASIC: Application Specific Integrated Circuit	EM: Electromagnetic
AuNP: Gold Nanoparticle	EPR: Enhanced Permeability and Retention
AuNPr: Gold Nanoprism	FEM: Finite Element Model
AuNR: Gold Nanorod	FRET: Förster Resonance Energy Transfer
AuNS: Gold Nanosphere	FWHM: Full Width at Half-Maximum
AuNSh: Gold Nanoshell	Hb: deoxy-haemoglobin
AuNSt: Gold Nanostar	HbO2: oxy-haemoglobin
BSA: Bovine Serum Albumin	HEJ: Homologous End Joining
BSE: Binned Spectral Efficiency	HIF-1: Hypoxia Inducible Factor 1
C1: Component 1 (of COGI)	HU: Hounsfield Units
C2: Component 2 (of COGI)	ICP-MS: Inductively Coupled Plasma Mass Spectrometry
C3: Component 3 (of COGI)	ICP-OES: Inductively Coupled Plasma Optical Emission Spectroscopy
CAD: Computer Aided Design	IR: Incident Radiation
CeNP: Ceria Nanoparticle	LOT: Localisation Optoacoustic Tomography
CFU: Colony Forming Unit	LPR: Longitudinal Plasmon Resonance
CIE: Charge Induction Efficiency	MRI: Magnetic Resonance Imaging
CM: Correction Mechanism	MTT: 3-(4,5-dimethylthiazol-2-yl)-2,5-diphenyltetrazolium Bromide
COGI: COMSOL-Gate Interlocutor	NADH: Nicotinamide Adenine Dinucleotide
CPP: Cell Penetrating Peptide	NHEJ: Non-Homologous End Joining
CSCA: Charge Sharing Correction Algorithm	NL: Neighbourhood Localisation
CSE: Charge Sharing Effect	NLS: Nuclear Localisation Sequence
CT: Computed Tomography	NS: Neighbourhood Size
CTAB: Hexadecyl(trimethyl)ammonium Bromide	PA: Photoacoustic
CTG-3D: Cell Titre Glo 3D	PAI: Photoacoustic Imaging
CZT: Cadmium Zinc Telluride	PASI: Photoacoustic Spectral Imaging
DDR: Deposited Dose Ratio	PBS: Phosphate Buffered Saline
DE: Dual Energy	PC: Photon-Counting
DEA: Dose Enhancing Agent	
DEE: Dose Enhancement Effects	
DEF: Dose Enhancement Factor	
DMSO: Dimethyl Sulfoxide	

PDE: Partial Differential Equation
PEG: Polyethylene Glycol
PET: Positron Emission Tomography
PI: Propidium Iodide
PSS: Poly(styrene) Sulfonate
qPCR: Quantitative Polymerase Chain Reaction
RCC: Relative Coincidence Counts
RDEE: Radiotherapy Dose Enhancing Effect
RPMI: Roswell Park Memorial Institute
ROS: Reactive Oxygen Species
SCEP: Single Cell Electrophoresis
SDS: Sodium Dodecyl Sulfate
SEM: Standard Error in the Mean
SER: Sensitivity Enhancement Ratio
SNR: Signal-to-Noise Ratio
SPECT: Single Photon Emission Computed
Tomography
SSB: Single Stand Break
TEM: Transmission Electron Microscopy
TPR: Transverse Plasmon Resonance
UV: Ultraviolet
Vis-IR: Visible and Infrared
x-CSI: x-ray Photon-Counting Spectral Imaging

Thesis overview

For more than 100 years radiotherapy has formed an integral part of oncology treatments, along with chemotherapy and surgery. Modern external beam radiotherapies can combine the non-invasiveness of chemotherapy treatments with some of the precision of surgical interventions, however not without significant drawbacks. Whilst being able to focus dose to a target volume within the body, external photon beam therapies inevitably deposit some radiation dose into healthy tissues along the beam's path to and from the target region. This results in some level of damage outside the desired target volume, which may cause complications such as organ damage, burns or instigation of secondary cancers. Much progress has been made in shaping the spatiotemporal profile of external radiation beams to minimise the damage done to healthy tissues, however all such approaches are constrained by the requirement to deliver a sufficient dose to the target volume to kill/inactivate tumour volumes and prevent cancer disease progression. One way to overcome this limitation is to introduce an agent that can selectively enhance the clinical effectiveness of radiation delivered to the cancerous tissue. Chapter 1 of this thesis explains the rise of radiotherapy as a treatment option, explores the mechanisms by which it works and the limitations it has, before looking at some research directions for addressing its shortfalls, including gold nanoparticles (AuNPs).

AuNPs can be targeted to tumour sites via both active and passive accumulation mechanisms and can be functionalised to accumulate preferentially in cancer cells. Once localised, AuNPs are able to enhance the effects of radiotherapy via a range of physical, chemical, and biological mechanisms, meaning that lower doses of radiation are needed to produce the same disease control. Chapter 2 expounds how AuNPs can intervene at the various stages of radiobiological damage discussed in Chapter 1 and provides the necessary background understanding of how these interactions are measured and defined to allow the cell work in this thesis (Chapter 8) to be understood in context. It is also noted in Chapter 2 that, for AuNPs to realise their full potential in clinical settings, it will be necessary to quantitatively assess their distribution *in vivo*. This information could then be used in clinical studies to relate AuNP concentration to disease control, so that radiotherapy enhancement can be predicted from a measured AuNP distribution. This information could then be used to adjust the treatment plan for each patient, for example to reduce damage to organs at risk. If the AuNP-mediated dose enhancement were large enough, and if the AuNPs could be predictably localised only within cancerous cells, it would substantially reduce the need for motion correction. At the inception of this PhD, neither *in vivo* quantitative imaging of AuNPs nor a consistent relation between their concentration and observed dose enhancement were available clinically. Whilst pre-clinical data existed regarding the use of AuNPs for radiotherapy dose enhancement, these data were limited and often involved concentrations significantly below the detectable limits of conventional medical imaging modalities. For this reason, this work set out to assess the potential of two emerging imaging modalities to quantify AuNPs *in vivo*. The

modalities to be assessed are photoacoustic spectral imaging (PASI) and photon-counting multispectral x-ray imaging (x-CSI).

Chapters 3 and 4 give the reader a background in PASI and x-CSI, respectively. The underlying physics of each imaging approach are explained, and current techniques explored to show where they are deficient. The AuNP properties that PASI and x-CSI are uniquely placed to exploit (plasmon resonance and medically relevant K-edge energy respectively) are then introduced and explained. Chapter 4 also converts the various ways that AuNP concentrations are reported in the literature into a unit (mg/ml) more suitable for comparing with the x-CSI literature to assess the required detection limits needed. Both chapters then conclude with a consideration of the advantages and disadvantages of the relevant approach, along with outstanding issues that need to be addressed to develop the technique. For PASI, the major issue is the lack of information available regarding what effect, if any, optimising AuNPs for PASI has on the suitability of those AuNPs for delivering radiotherapy dose enhancements. For x-CSI, the issues identified are the lack of wide-spread availability of pre-clinical scanners, a lack of x-CSI scanners optimised for the task of AuNP imaging specifically and a general lack of comparability between the various prototype x-CSI systems due to their differing pixel pitches and charge sharing correction algorithms (CSCAs). Steps to complete some of this work then forms the basis of Chapters 5 to 8.

Chapter 5 details the development and validation of a simulation framework (CoGI) for modelling x-CSI systems. The system is validated using a pixelated, photon-counting detector utilising a known CSCA and running in energy binning mode. To my knowledge, this is the first validated simulation framework to include CSCAs in this way. CoGI was used to compare ~3000 x-CSI system designs with respect to a range of detector metrics. Chapter 6 uses these simulations to identify an optimal sensor thickness for further investigation. Chapter 7 focuses on the identified thickness and compares a range of different CSCAs with respect to the same metrics, identifying both the CSCA and pixel pitch trade-off that provides the best performance at the K-edge of Au, and new mechanisms that should be considered in designing future CSCAs.

Chapter 8 then details an extensive piece of wet-lab work that was undertaken to assess the effect of two AuNP parameters (shape and coating) on the AuNP's ability to enhance radiotherapy. These parameters were chosen as they are the ones most commonly manipulated to make AuNPs suitable for PASI. Conclusions from this chapter inform the likely feasibility of using PASI as the imaging modality for predicting AuNP-mediated radiotherapy dose enhancements.

Chapter 9 constitutes a treatise comparing PASI and x-CSI for their potential as imaging modalities for predicting AuNP-mediated radiotherapy dose enhancement. The chapter draws together the results of the previous literature reviews, simulations, and wet-lab work to construct a systematic and informed discussion on the relative merits of each modality, both with respect to minimum

requirements and to each other. Finally, Chapter 10 summarises the main results from the work presented in this thesis and identifies future directions for research in this area, as I see them.

Original work and contributions to the field

Due to the multidisciplinary nature of this thesis, background information is needed from a wide range of disciplines including Physics, Chemistry and Biology. This has resulted in the need for a broad and extensive literature review to allow the reader to contextualise the work, forming the basis of Chapters 1 – 4.

For the x-CSI side of the project, a computational framework, known as CoGI, was developed which extended previous work in this area by including both the contribution of holes to the signal and modelling the application of a charge sharing correction algorithm (CSCA). CoGI was then validated against a CSCA utilising prototype x-CSI detector, provided on loan by an industrial contact. This work formed the basis of Chapter 5. To our knowledge this is the first time this has been achieved and provides the information necessary for groups to compare the effect of various CSCA designs, or of various geometric parameters, on x-CSI detector output.

CoGI was then used in Chapters 6 and 7 to investigate how x-CSI performance, according to a range of both spectral and absolute metrics, varied with changing pixel pitch, sensor thickness, x-ray flux and CSCA. The characterisation of CSCAs based on the parameters of neighbourhood size, localisation and correction mechanism formalised the process of CSCA design so that previously unsuggested CSCAs could be constructed and tested. The resulting trends were explained mechanistically, and importantly the behaviour of various CSCAs were shown to result from the interaction of several previously unelucidated mechanisms. This work puts CSCA design on a firm footing and allows for more informed CSCA design to be conducted in the future.

In summary then, to the field of x-CSI the work behind this thesis contributed both the mechanisms and associated terminology for advancing CSCA design and a flexible simulation framework capable of testing and comparing new CSCAs rapidly, cheaply and comprehensively, as well as data which can be used by x-CSI chip designers to determine optimal pixel dimensions according to a selection of metrics.

For the PASI side of the project, the literature review identified an unmet need to assess if/how AuNP optimisation for PASI interferes with the ability of AuNPs to deliver a radiotherapy dose enhancing effect (RDEE). This question was taken up in the experimental work forming Chapter 8. Whilst the results are currently only preliminary, the work is novel and the results should be of interest to the wider community. The findings of most relevance to the rest of the field are: 1) that optimising AuNP shape for PASI detection appeared to increase the RDEE, 2) coatings favoured for PASI may inhibit RDEE and 3) gold nanorods (AuNRs) were not found to be more toxic than gold nanospheres (AuNSs).

Finding 1 makes clear that the AuNP-mediated RDEE achieved in work currently in the literature is suboptimal due to its use of AuNSs rather than AuNRs or more exotic shapes, and the reasoning I proposed to explain this further supports the role of chemical and biological enhancement mechanisms, too often overlooked in other studies. Finding 2 has implications for theranostic AuNP design, as it shows there can be competition between imaging and treatment requirements that had not previously been explored in this context. Finally, finding 3 is relevant to the discussion in the wider AuNP community regarding whether AuNRs are intrinsically more toxic than AuNSs, or only appear so due to residual CTAB left over from synthesis. The preliminary evidence from this thesis implies it is residual CTAB, not shape, which mediates the toxicity, increasing the number of applications for which AuNRs can be considered appropriate.

This thesis also contains critical reviews of the literature (Chapters 1-4), including identification of a need to standardise the RDEE measurement literature and a need for more cross disciplinary work so that RDEE, PASI and x-CFI fields do not diverge in the AuNPs they use too much, and keep in mind that, for clinical use, AuNP designs will need to allow for both imaging and therapy. Chapters 9 and 10 conclude by providing a critical perspective on the current capabilities for AuNP detection as part of delivering RDEEs. Pathways towards clinical utility, including experimental outlines and major outstanding hurdles as I see them, are then offered up for the reader, or wider community, to take forward.

Chapter 1.

Background and thesis motivation: Radiotherapy

This thesis is motivated by the desire to use gold nanoparticles (AuNPs) for improving radiotherapy outcomes, either by increasing remission rates or reducing the incidence of side effects. To help understand where AuNPs fit in this picture, an overview of radiotherapy as a field, its mechanisms of action and the current trends in its development are given here.

1.1 History

It should be noted that x-rays were discovered in a time before antibiotics, in which bacterial infections could prove not only lethal but also debilitating, even if survived, and were not guaranteed to resolve quickly. Under these circumstances the balance between risk and reward required in medicine was significantly skewed towards higher risks by the lack of therapeutic options. Further, the basic structure of the atom and the existence of electrons had yet to be established when x-rays were first used, meaning their nature was not well understood. The early work on x-rays needs to be seen in this light: as humans searching for applications for their new discoveries to reduce the widespread suffering caused by diseases of all sorts. This explains why control studies, ethical concerns and patient comfort were not priorities in the early story of radiotherapy. With this in mind, and with the realisation that a subset of cancer patients face the same poor prognosis today, we proceed to discuss the history of radiotherapy.

1.1.1 Inception

The first recorded instance of x-rays being used therapeutically to treat cancer dates back to January 29th of 1896, when a second-year medical student, Emil Grubbé, used the open end of an x-ray tube to irradiate a female patient presenting with carcinoma of the breast[1]. Grubbé noted a dermatitis had formed on the hand he routinely used to test that x-ray tubes were working. Suspecting this was caused by the x-rays, he surrounded the patient's lesion with lead to protect her during the hour-long exposure. This case illustrates that risk-benefit trade-offs in radiation therapy were realised even in this earliest case. Unfortunately, the potential biological impacts of x-rays was not appreciated by all, with a variety of other sources for the side effects being suggested until as late as 1900 when the argument was finally settled by experiments on rats. With the ability of x-rays to cause biological changes established, it was not long before x-rays were being used to treat ailments ranging from bacterial infections to cancers, though the high variability in tube design and quality, along with a lack of understanding regarding mechanisms behind x-ray effects, meant that results varied widely.

It is around this same time that, following the discovery of radium by the Curies in 1898[2], multiple experiments demonstrated the biological effects of the radiation emanating from radioisotopes on plants and animals, leading to the advent of implantable, inhalable and injectable radium and radon preparations for treating bacterial, inflammatory and oncological conditions[3]. These included the development of implantable radon containing tubes which could be left in the patient for several days

before removal, with surprising success in treating both cancerous and non-cancerous maladies[4]. These advances represent the founding of what is now known as brachytherapy. Whilst there is no reason that gold nanoparticle mediated dose enhancement cannot be utilised for brachytherapy treatments, and indeed some work has already been done looking into this[5][6][7], this thesis considers the dose enhancement associated with external beam radiotherapy primarily. Arguably external beam radiotherapy has undergone a more rigorous and well documented development than brachytherapy and so the remainder of this chapter will focus on external beam radiotherapy.

1.1.2 X-ray sources

Medical x-ray sources work on the principle that electrons that are rapidly decelerated give off x-rays in the form of Bremsstrahlung. The mechanism is looked at in more detail in Section 5.2.1.2. For now, suffice it to say that the energy of the emitted x-rays covers a continuum of values, with the maximum energy equal to that of the kinetic energy carried by the electrons.

In the early 1900s, as an attempt to standardise the x-ray energies provided by the various tubes, a range of metrics were considered, the most popular of which being the semi-qualitative classification of tubes into ‘very soft’, ‘soft’, ‘medium’, ‘hard’ and ‘very hard’ tubes[3], indicating their penetrating power. These early x-ray tubes increased the ‘hardness’ of the x-ray beam by varying the size of the spark gap. By doing this, tubes from this period were able to produce a range of x-ray energies from ~50 - 200 keV peak[8]. These energies resulted in most of the x-ray energy being deposited at superficial depths, making these tubes suitable primarily for treatment of superficial conditions and shallow carcinomas. For the treatment of deeper tumours radioisotopes were preferred, either interstitially (as the case in gold-radon seeds) or via external irradiation from the sources, referred to as telecurie therapy[9]. Telecurie therapy uses gamma ray sources, (primarily radon in the early years of its development), to deliver photons of higher energy, and thus greater mean free path, to irradiate deeper targets. These could be sub-divided into external applicators and internal applicators, such as the radium bomb[10]. These devices were often designed with little concern for the safety of the technician using them, and suffered from scalability, as radium was a rare commodity.

In the decades between 1920 and 1940, the drive to increase the penetration depth of x-ray sources led to developments in both existing[11] and novel techniques for producing x-rays. By 1940 the first electrostatic devices capable of delivering 1-MeV x-ray beams were being used in clinical practice[12]. These electrostatic systems had several limitations, notably their one-to-one relation between operating voltage and x-ray beam energy. As would become increasingly common with time, technology first developed for application in high energy particle physics[13] was adapted for medical applications, and the medical linear accelerator (linac) was born. In these machines each electron in the beam passes through a series of accelerating regions with the same voltage difference. This means that the final kinetic energy of an electron can be N times the applied voltage difference, where N is the

number of accelerating regions, resulting in x-ray beams with much higher peak energies. In 1953 the first patient was treated in Hammersmith, London using 8-MeV x-rays produced by a clinical linac[14]. These advantages led to linacs replacing the older electrostatic systems over time, with linacs now being the standard for multi-MeV external beam radiotherapies.

Telecurie therapy experienced a revolution of its own during the 1930s to 1950s as well, with the growing research into nuclear reactors and weapons leading to the availability of significant quantities of new, high energy radioisotopes such as ^{137}Cs and ^{60}Co , known at the time as “artificial radium”[15]. The shielding and beam shaping of the telecurie machines also advanced during this era, particularly with units containing ^{60}Co [16]. This was significant as most provincial clinics used telecurie therapy rather than linacs, as the MeV x-ray tubes available at the time were large, expensive, and technically complex machines, suitable mainly for metropolitan hubs.

From the 1970s onwards rapid technological advances led to efficient and controllable access to electricity, as well as a reduction in the cost and size of electronics. The widespread availability of antibiotics, development of steroids, implementation of national vaccination programs and general improvements in lifestyle meant that bacterial, viral, and autoimmune diseases had less dangerous, more efficacious treatments than radiation, leaving oncology as the last major field to utilise radiotherapy. Consequently, the number of radiotherapy clinics decreased, and the arguments against linacs became less compelling. Indeed, with environmental and safety concerns becoming more commonplace, the telecurie therapy machines proved less and less favourable due to their radioactive waste, potential for contamination and constant radiation production. Whilst telecurie therapy machines remain in use today, they are increasingly being replaced by the more common, compact, and controllable linacs. This has the added benefit of separating the radiotherapy and nuclear power industries, allowing both to develop in their own ways.

1.1.3 Treatment protocols

As noted above, there was an early clinical awareness that the energy of the x-rays, their ‘penetrating power’, could impact clinical outcomes and so attempts were made to standardise x-rays based on their ‘hardness’. Similarly the fluxes for treatments to have a given effect were defined, with respect to the imaging speed of the tubes, as exemplified by the 1904 observation that hair could be removed by irradiation with a tube with “an intensity that would take a Rontgen photograph of a man’s hand at 15cm distance in a one minute exposure.”[1]. Modern physicists can appreciate that neither the x-ray energy nor the flux alone can determine biological effect however, but rather that some measure of the energy absorbed is required: the concept of dose. Such an observation was made early in the story of radiotherapy by the physicist Major Phillips, who worked at The Royal Marsden Hospital in London (then called The Royal Cancer Hospital). In 1907 Maj. Phillips laid out the need for standardising the measure of radioactivity, proposing several mechanisms for measuring the level of radiation induced

air ionisation in a sealed chamber[17]. Whilst it would not be until 1928 that the first widely accepted unit of dose, the roentgen, would be adopted, we can see that by 1907 the need for patient dosimetry was being mooted. Once adopted, protocols for calibrating the dose rates of x-ray beams were developed by national metrology labs[18] and circulated widely.

The benefits of fractionating treatment, that is dividing the dose over several treatments spaced out in time, were also noted relatively early in the history of radiotherapy (1920s[19]). The mechanisms responsible for this were investigated and by the mid-1950s the now familiar dose response curves for cancerous cells were being obtained[20] (see Section 2.1.2.1 for more details). The differences in radiosensitivity between healthy and cancerous cells was known, and the theory of selecting an appropriate dose for each treatment such that the optimal ratio of tumour control to tissue damage could be obtained was established in this period as well[21]. With the advent of linacs, the development of telecurie units, and the implementation inter-centre standardisations overseen by national metrology labs, radiotherapy treatments were becoming more quantitative procedures. These advances combined to allow for the development of the first stereotactic radiotherapy systems, which used multiple overlapping beams to maximise the ratio of dose delivered to the tumour and the healthy tissue, minimising side effects for a given level of tumour control[22].

The following decades, from the 1970s to present, saw trends towards maximising the difference between radiation dose delivered to the tumour and that delivered to healthy tissue, utilising advances in both hardware and imaging. The advent of computed tomography (CT) led to high resolution 3D images of the regions to be irradiated[23], with subsequent hybrid-CT systems and dual energy CT advances allowing tumours to be located more precisely than previously possible[24]. The many advances in imaging that have happened in the almost 50 years since CT was developed, in terms of both hardware and reconstruction software, are too numerous for this short historical section, however. Suffice it to say that imaging-based improvements in patient outcome over this period stemmed largely from the improved ability to delineate tumours and other organs at risk. Parallel advances have taken place in terms of the hardware used for delivering the radiation, with multileaf collimators making it possible to cover complex 3D target regions with narrower margins[25]. Modern radiotherapy, with the availability of treatment simulations, beam shapers, and rapidly adjustable tube parameters (voltages and current), allows for prediction and control of the radiation profile the patient receives. Combined with an understanding of radiobiological mechanisms by which radiotherapy works, the result is improved patient outcomes both in terms of disease control and side effect avoidance[26]. As an ancillary benefit, these advances also improved the safety of those who administer the treatments.

The next section will look in detail at the mechanisms by which we now believe that x-rays can lead to cell death. Before closing this section however, it is interesting to think back to those first

radiotherapy treatments by Grubbé and others and realise just how far we have come in so short a time. Using a radioactive source to kill diseased tissue, whilst shielding the healthy tissue from as much radiation as possible to minimise side effects, these early treatments had the same aims as modern therapies, but a century less technology to achieve it with, and no working knowledge of what x-rays or atoms were, nor of the structure and role of DNA. Walking on the frontiers of human knowledge, it is perhaps inevitable that the mechanisms at play were beyond their horizons, yet still they strove to help humanity with the tools they had at their disposal and for that they should be commended.

1.2 Principles of radiation induced cell damage

Radiotherapy involves the damage of tissue by exposing it to ionising radiation, primarily electromagnetic in nature. It is therefore prudent to begin this chapter with a brief review of the ways in which x-rays and γ -rays interact with matter to deposit their energy in matter, before looking at the sequence of chemical and biological steps that convert this deposited energy into tissue damage, and finally the biological mechanisms that determine the response of the irradiated cell to this damage.

1.2.1 Physical deposition of energy

The transfer of energy in a photon-matter interaction is relevant to both the radiotherapy induced tissue damage and x-ray imaging themes of this thesis. Whilst x-ray imaging is not discussed until Chapter 4, the current discussion of the mechanisms is sufficiently detailed to provide the reader with the requisite background to both topics.

The average energy of an incident x/ γ photon in radiotherapy (of the order of several MeV) is several orders of magnitude above the energies associated with chemical bonds (of the order 1 - 10 eV) so for the purposes of energy deposition in radiotherapy only atomic structures are considered and the molecule the atom is bound in is irrelevant. Given the context of radiotherapy, this chapter ignores elastic photon-matter interactions such as Rayleigh and Thomson scattering and instead only considers those processes that result in a non-negligible net transfer of energy to the tissue. At the energies employed in clinical radiotherapy practice the three main mechanisms by which x/ γ -ray photons interact with matter are through Compton scattering, pair production and photoelectric absorption. The probability of each of these mechanisms occurring is dependent on the atomic number of the atom involved (Z) and the energy of the incident x-ray photon (E_x). Figure 1.1 shows an example of the interaction profile for Cd which can be used to illustrate the relation between the various mechanisms. Cd was chosen here out of convenience as this data was used for other parts of this thesis, however the general trends will be the same for other elements, though the specific cross-sections will differ. Plots for other elements can be constructed by using data from a suitable reference[27]. As can be seen, at lower energies (<100 keV) the photoelectric effect dominates, between ~100 keV and ~10 MeV Compton scattering dominates and above ~10 MeV pair production is the primary mechanism of energy

deposition. The relative contributions of the different mechanisms have importance for both radiotherapy dose enhancement and x-ray-based imaging systems.

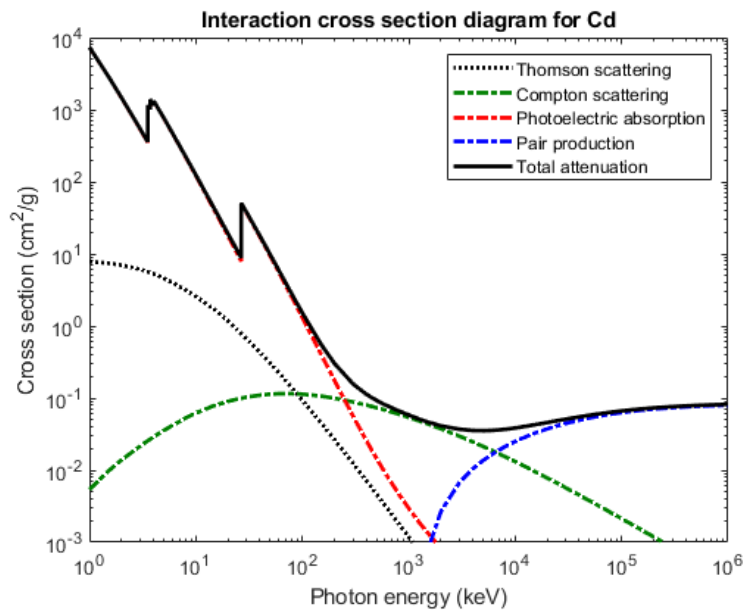


Figure 1.1. Interaction cross-section diagram for photons with Cd. The lines represent the cross-sections for the photon to interact with the atom via the various physical processes. It can be seen that photoelectric absorption is favoured at lower energies whilst pair production dominates at higher energies. At energies relevant to internal organ radiotherapy (MeV) Compton scattering can be seen to dominate. As photons are Compton scattered however, they will lose energy and thus become increasingly likely to be photoelectrically absorbed. Figure plotted using data from NIST[27].

The mechanisms described can all result in the formation of subsequent photons and energetic electrons, which will themselves be able to interact with the tissue via the listed mechanisms. As these secondary particles will be of lower energy than the initial interacting photon, they will have a shorter mean free path in the tissue. This process can repeat many times, resulting in a shower of progressively lower energy particles, causing a significant amplification in local energy deposition.

1.2.1.1 Photoelectric effect

The probability of photoelectric interaction (P_p) is related to the x/ γ -ray photon energy (E_γ) and atomic number (Z) of the target atom by the equation

$$P_p \propto \frac{Z^n}{E_\gamma^{3.5}} \quad \text{eq. 1.1}$$

where n varies between 4 and 5, depending on the value of E_γ . The high-power inverse relation to E_γ explains why the photoelectric effect is only significant at relatively low x/ γ -ray photon energies. The photoelectric effect involves the complete absorption of the incident photon by an atomically bound electron. In principle any atomically bound electron could be involved, however at the energies employed in radiotherapy it is usually the most tightly bound, K-edge electrons that interact as their binding energy most closely matches that of the incident photons[28]. Upon absorption of an x/ γ -ray

photon, the electron receives enough energy to become fully ionised from its host atom, becoming a photoelectron with kinetic energy, E_P , given by the equation

$$E_P = E_\gamma - E_B - E_R \quad \text{eq. 1.2}$$

where E_γ is the energy of the incident photon, E_B is the binding energy of the electron and E_R is the kinetic energy of the ions recoil. Whilst recoil of the resulting ion is required to conserve momentum upon photoelectron emission, the energy associated with the recoil is negligible so E_R is often omitted in calculations. As a result of the photoelectron's ejection from the atom a vacancy is left in the atomic orbital of the host atom, leaving it in an excited state with an excess of energy equal to E_B . The atom then deexcites through one of two mechanisms: x-ray fluorescence or Auger electron production, as illustrated in Figure 1.2.

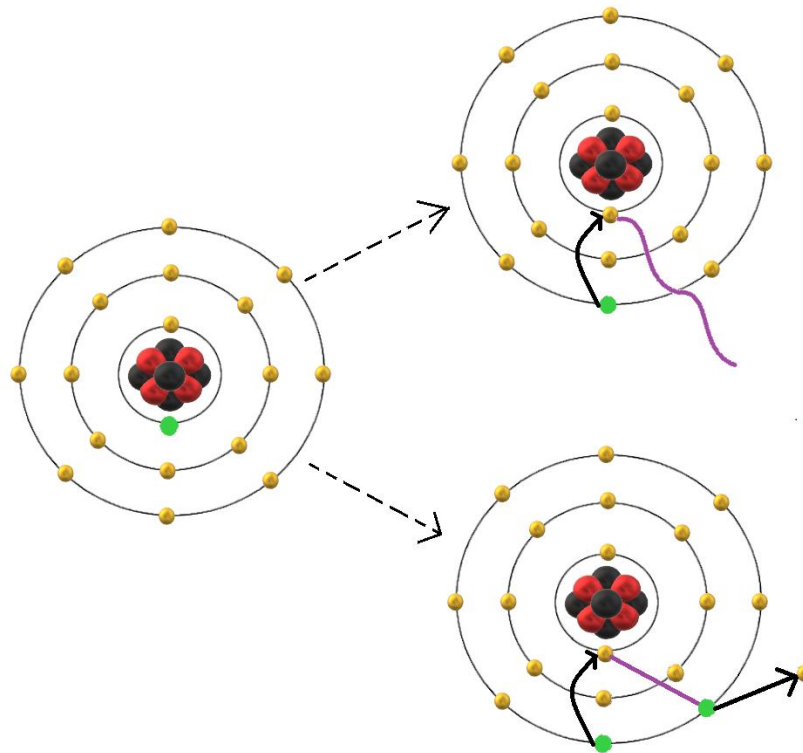


Figure 1.2. Diagram showing the alternative deexcitation pathways of x-ray fluorescence and Auger electron production. On the left is an atom with a vacancy in its inner most electron shell (green circle) which has two possible routes to deexcite (dotted arrows). In fluorescence x-ray production (upper path) an electron from a higher orbital falls directly into the lower energy vacancy, emitting the difference in energy between its starting and final orbitals as a photon of set energy (purple wave). In Auger electron production the transition of the outer electron to the inner orbital is coupled (purple line) to the promotion of an electron outwards to infinity (ionisation). The result of this process is an Auger electron of set energy. If, after Auger electron emission, the ion is not in its lowest energy state then further x-ray/Auger electron deexcitations may occur.

- 1) x-ray fluorescence involves a quantum leap of an outer shell electron to fill the vacancy, resulting in the emission of an x-ray with characteristic energy equal to the difference in energy of the two atomic orbitals involved.

- 2) Auger electron production also involves the deexcitation of an electron from a higher orbital to fill the vacancy produced by photoelectron production, but in this mechanism the energy transfer associated with the deexcitation is coupled to the promotion of another electron[29][30]. As a result of this energy transfer, the second electron can also escape the atom, leaving a second atomic vacancy. For the majority of atoms comprising human tissue this represents the end of the process, however for higher Z -number atoms, present in contrast agents and in smaller quantities in human tissue, the process of x-ray fluorescence or Auger electron production can repeat as the newer orbital vacancies are filled, until the ion reaches its lowest energy configuration.

1.2.1.2 Compton scattering

Compton scattering involves the inelastic scattering of a photon by a charged particle, with a consequent transfer of energy to that charged particle. In human tissue this usually involves the scattering of an incident photon by an electron, as illustrated in Figure 1.3.

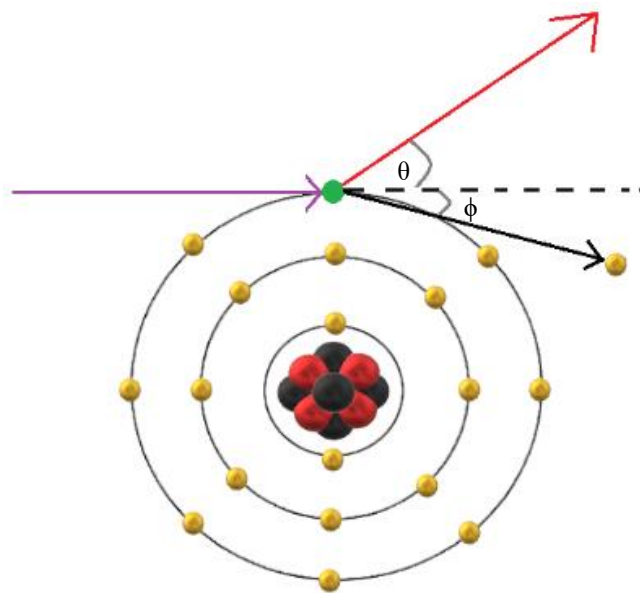


Figure 1.3. Diagrammatic model of Compton scattering. An incident photon (purple arrow) interacts with an atomically bound electron, transferring to it enough energy to liberate it from the atom, leaving a vacant orbital (green circle). The photon is scattered through an angle θ and is shifted into a lower energy photon (red arrow). The electron (yellow ball) is ejected at an angle of ϕ from the path of the original photon (black dashed line). The angles θ and ϕ , as well as the kinetic energy of the ejected electron and the final wavelength of the scattered photon, are derived from the laws of conservation of momentum and energy.

As a result of the interaction, some energy, dE , is transferred from the photon to the electron. The energy of x/ γ -ray photons is significantly greater than the binding energy of the electron (by several orders of magnitude), so the energy used for ionisation is often neglected in energy transfer calculations and the electron is treated as a free electron. Using this approximation, along with the conservation of momentum, it can be shown that the energies of the electron and x-ray photon after scattering are

$$E_{C'} = E_{\gamma} - \frac{E_{\gamma}}{1 + \left(\frac{E_{\gamma}(1 - \cos\theta)}{m_e c^2}\right)} \quad \text{eq. 1.3}$$

and

$$E_{\gamma'} = E_{\gamma} - E_{C'} \quad \text{eq. 1.4}$$

where $E_{C'}$ is the energy of the Compton scattered electron, E_{γ} is the energy of the incident photon prior to scattering, $E_{\gamma'}$ is the energy of the photon after scattering, m_e is the rest mass of the electron, c is the speed of light and θ is the angle the photon is deflected by, as per Figure 1.3. It can be seen from Equation 1.3 that the energy transferred depends on the angle of deflection, ranging from a maximum when the photon is backscattered ($\theta = \pi$) to a minimum of zero (as θ approaches 0). For all values of θ between 0 and π the energy transferred is intermediate, resulting in a continuum of possible residual photon energies, as shown in Figure 1.4. This figure was constructed by calculating the residual photon energy for deflection angles ranging from 0 to π and binning the results into 1 keV wide energy bins. The angular density for a given energy bin is then defined as the number of angles that yield a photon energy within said bin, divided by the number of angles considered.

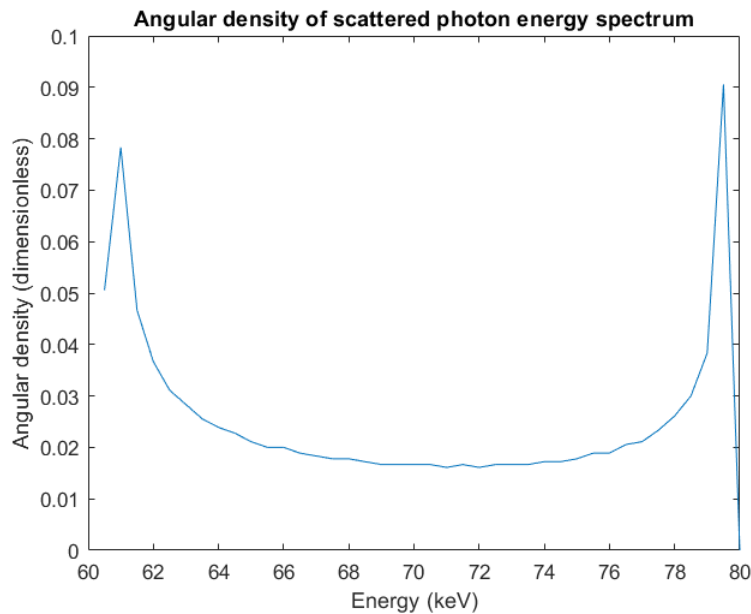


Figure 1.4. A plot showing the distribution of energies with which an 80 keV photon could scatter during Compton scattering. The angular distribution was calculated as described in the text. Figure based on information from 'Practical Gamma-ray Spectrometry'[28]

Whilst the probability of a Compton scattered photon having a given energy is related to the angular density distribution shown in Figure 1.4, it is not directly proportional to it, as the scattering process is not isotropic. The probability of scattering at a given angle can be calculated from the Klein-Nishina formula, however this is beyond the scope of this work. Suffice it to say that the distribution of likely scatter angles tends to smaller angles (and thus lower energy transfers) as the

incident photon's energy increases, resulting in a strong forward scatter bias for photons of MeV energy and above.

For the purposes of this thesis however, the important point to note is that the process of Compton scattering leads to a continuum of energies, with a sharp rise around the backscatter peak. The sharpness of this peak is partly due to the theoretical assumption that the electron being scattered from is a free electron (binding energy neglected), and correction for the binding energy leads to a slightly lower, more rounded back scatter peak, though it still sits above the continuum.

1.2.1.3 Pair production

Pair production involves conversion of an incident x/ γ -ray photon into an electron-positron (e^+e^-) pair, in the presence of the intense electric field of either an atomic nucleus or an electron. The process thus requires that $E_\gamma > 1.022$ MeV, which is twice the rest mass of an electron ($M_e = 511$ keV). Any energy in E_γ in excess of the required e^+e^- pair's rest mass will be converted to kinetic energy of the e^+e^- pair. At values of E_γ just above this minimum the e^+e^- pair will be produced in close proximity with little kinetic energy and so will likely annihilate with each other to produce another photon of energy E_γ . The probability of the e^+e^- pair forming and surviving long enough to diverge is low between energies of 1.022 MeV and 1.5 MeV. The probability of e^+e^- pair production increases with increasing energy however, and this mechanism of energy deposition becomes the dominant form of photon-matter interaction at multi-MeV energy levels. Provided the photon is of sufficient energy, the probability of pair production increases proportionally to Z , as pair production occurs only in the presence of a strong electric field such as is found in the proximity of a proton or an electron. The positron will go on to lose kinetic energy through repeated scattering events with other electrons in the tissue, until its energy is low enough for capture by an electron to form positronium[31]. Positronium oniums formed from radiotherapy are unstable and thus rapidly ($< 1 \mu\text{s}$) self-annihilate to produce two 511 keV γ -ray photons[32].

1.2.1.4 Electron scattering

Energetic electrons that are produced by the above mechanisms initially act as β particles, scattering inelastically either from electrons in the tissue (leaving a trail of ionisation events in their wake) or via coulombic interactions with the nuclei of atoms they pass close to (resulting in the emission of Bremsstrahlung). Sufficient interactions result in the electron's deexcitation to an energy level comparable to that of chemical bonds (a few eV). At this energy level the electrons are better thought of as free radicals: an unstable chemical species possessing an unpaired electron that rapidly forms a bond so as to stabilise itself. The fate of free radicals will be considered in the next section.

1.2.2 Chemical conversion of energy to damage

Regardless of the physical mechanism employed, the result of the radiation's interaction with the tissue is the formation of a localised concentration of ionised molecules and free radicals. Whilst ionisation of a range of metabolically crucial molecules, such as DNA, can be disastrous for a cell, the mechanisms involved are more properly treated as biological in nature, and so will be discussed in the next section. This section will instead focus on the chemical mechanisms involved in converting ionised H₂O molecules and free radicals into cellular damage, as H₂O makes up far more of the cellular mass than does DNA. It should be noted that cells possess a range of antioxidant molecules designed to scavenge and inactivate free radicals from the cellular environment, as well as enzymes designed to detoxify dangerous chemical species such as hydrogen peroxide (H₂O₂) in a controlled manner to minimise their impact on cellular metabolism. These mechanisms operate to oppose the chemical routes outlined in this section, resulting in a complex web of chemical interactions, however as the details of these mechanisms are beyond the scope of this work, this section will focus only on the forward reactions moving in the direction of converting cellular free radicals and ions into DNA damage.

1.2.2.1 Hydrogen peroxide production

The ionisation of a water molecule (H₂O) by incident radiation (IR) to produce a free electron (e⁻) and a singly ionised water molecule is shown in Equation 1.5.



H₂O⁺ is unstable in the presence of water and will react via a multi-step mechanism to yield the hydroxyl radical (HO[·]) and a hydrogen ion (H⁺)[33]. The net reaction is shown in Equation 1.6.



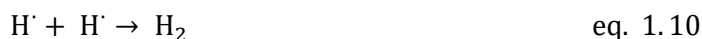
For the reader unfamiliar with chemical symbology, please note that free radicals are designated with a dot, so that for example the free radical version of compound *X* is denoted *X*[·]. The electron emitted from Equation 1.5 can subsequently be captured by a second water molecule, as shown in Equation 1.7, yielding hydroxyl ions (OH⁻) and hydrogen radicals (H[·]).



The net result of these reactions can be summarised as



In principle, these two free radicals could recombine to form water, however the need for the electron mediated reaction means that the two radicals are produced a significant distance apart, resulting in a lower probability of this occurring[34]. Where large numbers of these reactions are occurring in a small region, such as during radiotherapy treatment of a cell, there are three possible reactions that can occur:



The last of these equations can be seen to result in the formation of hydrogen peroxide, a known toxic substance to cells. Whilst there are a variety of mechanisms by which H_2O_2 can initiate cell toxicity[35], in the context of radiotherapy we focus on H_2O_2 induced DNA damage. It is therefore important to note that, as H_2O_2 is much more chemically stable than either free radicals or non-solvated ions, H_2O_2 can travel significant distances from its site of production. This longevity is associated with an amplification in radiotherapy associated DNA damage as it provides a mechanism whereby even irradiation of sites distant from the nucleus can result in DNA damage.

1.2.2.2 Fe mobilisation

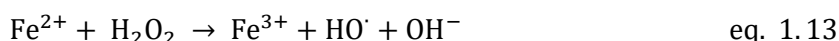
The next free radical of relevance to DNA damage is the superoxide free radical, $\text{O}_2^{\cdot-}$. Superoxide is present naturally in cells where it is produced by occasional mistakes in the electron transport chain. Additionally, and more relevant to radiotherapy applications, superoxide can be produced by the reaction of molecular oxygen with a free electron, as shown in Equation 1.12



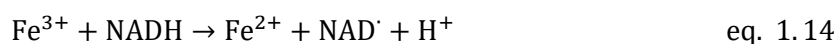
Superoxide is a species of high thermodynamic potential as an oxidising agent, however due to its tight coordination to 4 water molecules in solution and the requirement for H^+ or a transitional metal to stabilise its intermediate state, its reaction with cellular components under *in vivo* conditions is kinetically unfavourable, making it relatively unreactive with DNA[36]. Despite this, superoxide plays an important role in mediating H_2O_2 induced DNA damage by reacting with iron containing enzymes to liberate their iron atoms into solution, making them available as reaction sites for H_2O_2 decomposition, as discussed in the next section[37].

1.2.2.3 Radical regeneration

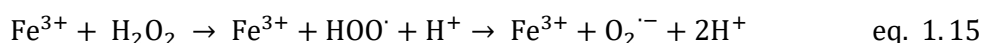
When H_2O_2 enters the nucleus of the cell, it can undergo a redox reaction with free iron to produce free radicals[38] according to the equation



As the nucleus contains iron both coordinated to DNA and as a cofactor in many DNA repair and replication enzymes[39], the radicals produced in Equation 1.13 are in close proximity to the DNA and thus able to react with it prior to being scavenged. As the oxidation state of iron is important to its role as a cofactor, biological mechanisms exist to regenerate the 2+ oxidation state from the 3+ state, using ascorbic acid or NADH for example. NADH can do so with the net reaction



At higher H_2O_2 concentrations where the levels of Fe^{3+} become higher than the biological mechanisms can quickly reverse, H_2O_2 can also facilitate the conversion of Fe^{3+} to Fe^{2+} via the reaction



further increasing the number of radical species present in proximity of the DNA.

1.2.2.4 DNA damage

Damage to DNA from ionising radiation can be either direct or indirect. Direct DNA damage occurs when the atom involved in one of the physical energy deposition mechanisms detailed above (photoelectric absorption, Compton scattering, positron annihilation and electron collision) is situated within the DNA strand. In contrast, indirect DNA damage occurs when the energy is deposited elsewhere in the cell but yields free radicals or free radical precursors which can travel to the DNA and interact with it. Regardless of the route taken, DNA lesions can broadly be classified into double strand breaks (DSBs), single strand breaks (SSBs), base modification and base deletion (resulting in an abasic site). Direct DNA damage by radiation will likely result in a mixture of DSBs and SSBs, whereas indirect DNA damage is more likely to form SSBs and base modifications/deletions.

1.2.3 Damage fixation and cell fate

DNA lesions produced by radiotherapy are not unique to radiation damage, with more than 78000 lesions $\text{cell}^{-1} \text{day}^{-1}$ in humans due to endogenous stresses (e.g. reactive oxygen species, ROS) and replication errors[40]. Maintenance of genomic integrity is of significant importance to cells, no doubt as genes conferring genomic stability produce a self-selecting pressure in evolutionary terms. As such, it is unsurprising that eukaryotic cells have evolved a wide variety of repair pathways for repairing DNA lesions, as well as cellular fail-safes for when the damage is clearly beyond repair[41]. Base modifications/deletions and SSBs offer the chance for highest fidelity repair in all cells, as the complimentary strand of DNA can be used as a template for determining the correct base that should be used to repair the error[42]. In contrast, DSB repair can be a low fidelity process, as for most of a cell's life cycle there is no template available to the cell for repairing such damage. DSBs are thus the more significant determiner of cell fate after irradiation, so we will focus on them here. DSBs can be repaired by one of two mechanisms: homologous end-joining repair (HEJ) and non-homologous end-joining repair (NHEJ). The difference between the two processes is illustrated in Figure 1.5. HEJ is possible when an undamaged homologous DNA strand is available nearby, and so occurs after DNA replication, in the late S and early G2 phases of the cell cycle. This process is of high fidelity, allowing cells to survive otherwise fatal DNA insults. In contrast, NHEJ is of much lower fidelity, prone to significant loss of bases with each repair. The fate of cells that resort to NHEJ is thus that they will contain many more mutations, with potential for either increased tumorigenicity or decreased viability

as a result. The difference in fidelity between HEJ and NHEJ can explain why cells in the S phase of the cell cycle appear more resistant to radiotherapy.

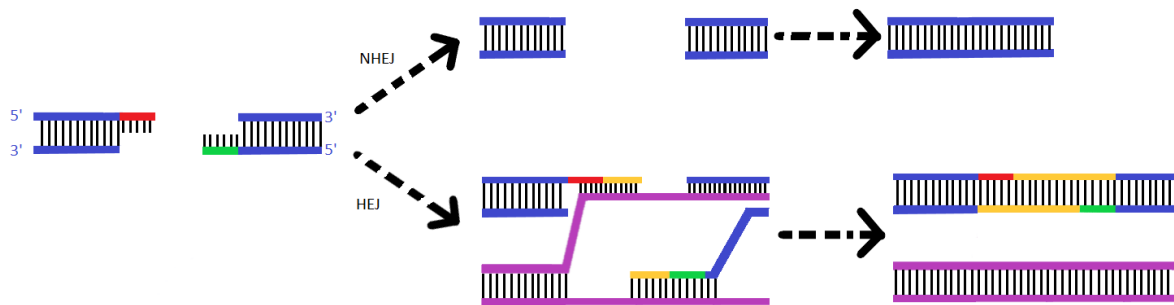


Figure 1.5. Schematic representation of alternative pathways for DNA double strand break repairs. Enzymes responsible for the various stages have been omitted for clarity. A double strand break (DSB) results in the two strands of a DNA helix being completely separated from each other, with trailing ends (red and green highlighted regions) that are prone to rapid deterioration (left). In non-homologous end joining (NHEJ) repair (upper path), the trailing ends of the two strands are cut back to leave a level end (upper middle), which can then be joined together to reproduce a double stranded structure (upper right). In homologous end joining (HEJ) repair (lower path), a sister length of DNA is available, either from a sister chromosome or an identical strand present after DNA replication. This sister helix of DNA (purple strands) is used as a template to ensure accurate DNA replication (lower middle). In this process, the 3' ends in the DSB region associate with their complimentary sequences in the sister strands, allowing the replication of replacement DNA (yellow highlighted regions). The end result (lower right) is that the repaired double strand of DNA contains a complete copy of the information that had been destroyed by the DSB originally. This is in contrast with the final strand from the NHEJ process, which is shortened as a result of the missing bases and may now contain a range of mutations from frame shifts to sequence deletions.

If DNA damage is still present as a cell approaches certain cell cycle checkpoints then progress through the cell cycle can be halted temporarily, to allow additional time for the DNA repair machinery to operate before the cell attempts to divide[43]. If DNA damage is successfully repaired the cell can continue through the cell cycle as before and the net effect of the radiation induced damage will be a delay to division and possibly mutations in the cell's genome, which may or may not express phenotypically. Some cells may become senescent (cease dividing) as a result of the stress induced by the DNA damage. Despite a plethora of sophisticated repair pathways however, some DNA damage is irreparable, either due to the quantity of breaks (which may lead to extensive genome fragmentation) or the interaction of lesions in such a way that repair mechanisms are confounded[44][45]. Direct DNA damage mechanisms in radiotherapy tend to induce more complex DNA lesions, with local clusters of intense damage[46], whereas indirect methods tend to distribute DNA lesions more homogenously throughout the genome. Due to their increased complexity, direct DNA damage mechanisms are associated with higher rates of incomplete DNA damage repair[47]. In such situations, cellular fail-safe mechanisms may be activated to maintain the genomic integrity of the organism as a whole. Details of these fail-safe mechanisms are again beyond the scope of this thesis, however suffice it to say that if triggered the cell will be committed to a path of cell death either slowly (necrosis) or rapidly (via apoptosis). Apoptosis is favoured where the checkpoint failure is at the G2/M stage of the cell cycle

whilst necrosis is favoured by checkpoint failure at the G1/S phase of the cell cycle, adding to the apparent radiosensitivity of cells in the G2 and M phase of the cell cycle[43]. The radiosensitivity of the various cell cycle stages will be returned to later. There are thus 5 possible fates for a cell irradiated during radiotherapy: full DNA repair and cell proliferation, DNA repair and proliferation with mutations, DNA repair and cellular senescence with mutations, cell death by apoptosis or cell death by necrosis.

The case of H₂O₂ is used here as an example of the processes by which radiation induced free radicals may cause DNA damage at sites distant from the point of irradiation, however it should be noted that there are many more chemical species that can act as intermediates in free radical mediated damage, as well as many other targets for radiation damage such as the mitochondria. Whilst evidence has accumulated that damage to these other organelles correlates well with cell viability [48], it seems likely that the effect of damage to such structures is at least partly responsible for an increase in intracellular ROS[49], which lead indirectly to DNA damage and sensitisation of the apoptotic machinery that can be triggered by DNA damage. Indeed, it has been fairly conclusively established for a long time that unrepaired DNA damage is the primary determinant of cell fate in response to ionising radiation exposure[50]. That is not to say that recent advances haven't cast doubt on this DNA centric approach[51] by noting anomalies in cell-kill factors such as in bystander effects[52] [53], however the exact mechanisms behind these effects are yet to be elucidated. As these effects appear to depend on an element of genetic instability or disruption to signalling pathways, these anomalies may yet be traced back to changes resulting from aberrant 'fixing' of the DNA, and so still to DNA damage.

1.2.4 Summary

Radiotherapy involves exposing cells to ionising radiation in order to kill or arrest the growth of a target cell population. This is achieved by inducing DNA lesions in the target cells, either through direct interaction with ionising radiation or indirectly through the creation of free radicals in the cellular environment. Cells possess multiple mechanisms for repairing DNA damage, with an efficiency which varies with the phase of the cell cycle. When the DNA lesions are too complex or too numerous for repair, cells commit to a fate of either cell death or cellular senescence, resulting in tumour volume reduction or growth arrest respectively. These mechanisms are not unique to cancerous cells however, and healthy cells may also suffer DNA damage from radiotherapy.

1.3 Maximising radiotherapy benefits: Trends and future outlook

Radiotherapy is a staple of modern cancer treatment and will remain so for the foreseeable future due to its ability to act both locally for tumours that cannot be safely accessed surgically (e.g. some brain cancers) and broadly over an organ to minimise the chances of recurrence, without introducing whole body toxicity as chemotherapy would (e.g. in localised breast cancers).

Consequently, significant research efforts go towards developing methods to minimise side effects whilst maximising therapeutic efficacy. The proposed techniques can be broadly divided into tumour tracking, normal tissue protective and improved dose effectiveness approaches. A brief discussion of these is given below, with emphasis on techniques for improving dose effectiveness, as that is the technique of primary interest to this thesis. Note that this section will not consider intensity modulated or 3D conformal approaches as, whilst they are still the focus of development work, they are sufficiently integrated into clinical practice as to count as current treatment standards, whilst this section is focussed on future trends.

1.3.1 Tumour tracking

Tumour tracking approaches are most applicable to tumours that move significantly during treatment, such as those on the lungs. These techniques aim to track the tumour in real time, using either fiducial markers[54] or direct tumour imaging and machine learning techniques[55], and then adjust the radiation beams during the treatment. Approaches proposed can be divided into gating and beam steering[56]. To help explain them, consider Figure 1.6. In the first row a non-tracking approach is being implemented, with the beam being defined so as to encompass the tumour at all times, regardless of where in its movement it is (A and B). This results in a large amount of healthy tissue receiving the same radiation dose as the tumour (C).

Temporal gating approaches involve tracking the tumour and switching the radiation beams on and off as the tumour enters and exits the irradiating field respectively[D-F]. In doing this the total size of the irradiated area can be made smaller as it does not need to encompass the whole of the tumour's path. The amount of healthy tissue irradiated is thus reduced. This improved spatial distribution results in a dramatically reduced radiation dose to healthy tissue, though comes at the expense of time as the beam is now on intermittently rather than continuously, so a longer real time is required to deliver the same radiation dose to the tumour.

Beam steering approaches involve tracking the tumour and steering the radiation beams to maintain focus on the tumour as it moves[G-I]. This means that the same total amount of healthy tissue may be irradiated, however as the average radiation dose delivered to this healthy tissue is lower due to the radiation beam sweeping across it rather than running through it continuously. This produces a sharper contrast in the dose experienced by the tumour compared to the healthy tissue, and lower healthy tissue doses even though the same volume is irradiated and the treatment takes the same period of time.

Whichever approach is used, the aim is to reduce the amount of radiation deposited in healthy tissue, so as to minimise the side effects experienced by the patient. There are several drawbacks to tumour tracking approaches however, which stem from the fact that the physical tumour is not what is actually being tracked. Rather, the user of the system specifies a target volume for irradiation, and it is this volume which is tracked through the treatment. The region is specified based on the image obtained,

and therefore is limited to tracking objects which are delineable on the imaging system. Tumours may be visible in one modality and not another, may involve projections too small to detect or may look sufficiently like healthy tissue in the scan that the technician is forced to delineate an amorphous blob, resulting in either under or over coverage of the tumour. Even if a fiducial marker is placed by the surgeon at the desired target site, these markers may shift over time relative to the underlying physiology as the radiotherapy takes effect[57].

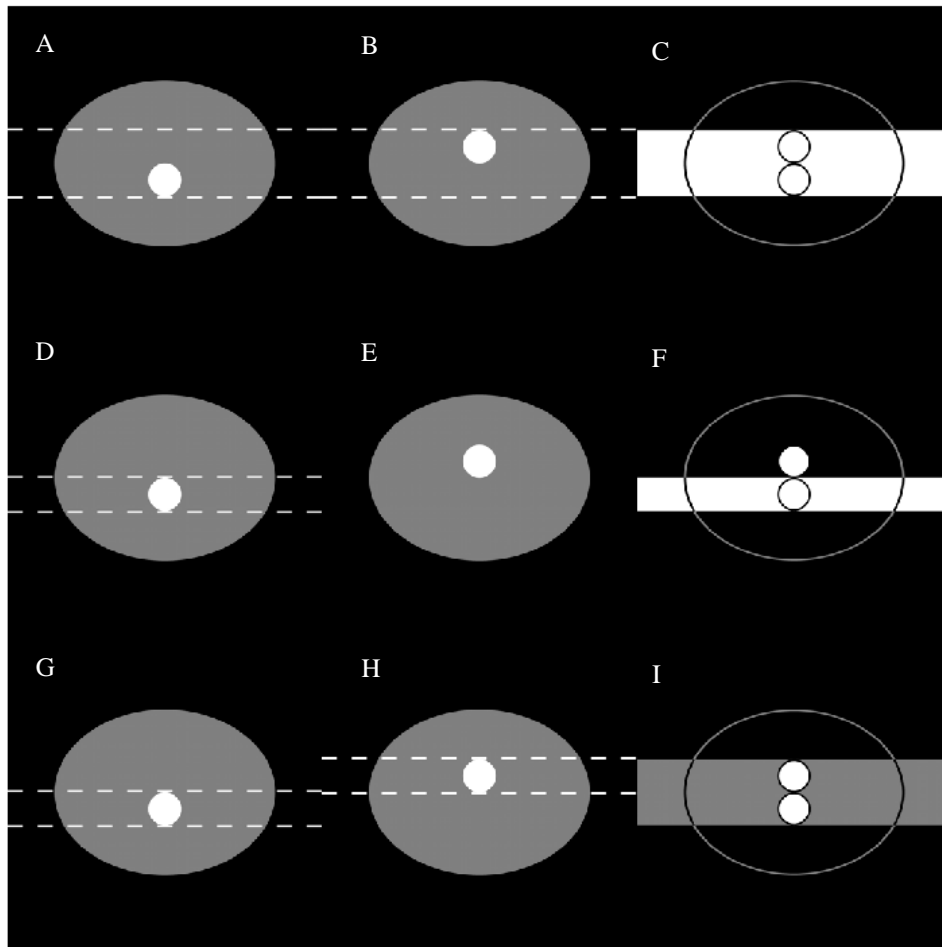


Figure 1.6. Illustration for explaining the various approaches to tumour tracking discussed in the text. For the first two columns (A, B, D, E, G, H) the larger ellipsoid in each image represents the patient body and the lighter, smaller circle represents the tumour. The tumour rises and falls during the treatment, and the images in the first and second columns represent the lowest and highest it moves to respectively. In these columns, the dashed white lines represent the limits of the irradiating beam at that moment in time. The third column represents the radiation dose deposited by the beam, with brighter regions corresponding to a higher dose. Outlines of the extreme tumour locations and the simulated patient body are included for reference. The sizes of the tumours and their motions are exaggerated for visibility. This illustration is considering the case of a single beam. Modern radiotherapy usually involves a range of different beams at different angles and intensities, so the dose to the tumour will be much higher than that to the healthy tissue overall. This diagram considers a single beam for illustrative purposes only.

Even if the tracking in the image space is accurate and the markers fixed, the use of a ‘live’ image from one system to guide the radiation beams produced by another opens the possibility for spatial misalignments or delays in signalling between the imaging and irradiating systems[58]. Such systematic errors are hard to detect on the fly and may result in the tumour being at least partially out of sync with the temporospatial field of irradiation. The risks of this can be partially mitigated by defining regions with larger margins, however this bakes some healthy damage into the equation at the planning stage and so is not the ideal solution.

1.3.2 Normal tissue protection

Tissue protection strategies are applicable to any radiotherapy treatment but are of most interest to treatments that have a higher risk of side effects (e.g. close to organs at risk) or secondary cancer initiation (e.g. younger patient populations). A variety of such approaches have been proposed, though the quantity and quality of the research in this field varies greatly.

Nutritional interventions, such as fasting (>12 hours without calorie intake), calorie restriction (reduced calories compared to baseline over a period >12 hours) and diet modification have all been proposed and studied[52][58]. It is proposed that the fasting and calorie restriction schemes work by upregulating antioxidant production, increasing DNA repair mechanisms and/or increasing the sensitivity of cells to apoptotic signals via inhibition of molecules in their nutrient sensing pathways, such as mTOR. As these pathways are often dysregulated in cancers, it is proposed that the fasting does not increase the resistance of tumour cells to ionising radiation. Some diet modifications are also hypothesised to work along these lines (e.g. protein starvation), whilst others aim to exploit the changes in metabolism associated with cancers (notably the Warburg effect[59][60]) to selectively reduce the energy available to them (e.g. ketogenic diets[62]). These approaches are low cost and easy to implement, though they require a higher level of compliance from the patient as they may be unpleasant. Due to their vulnerable nature, and the high degree of variability in confounding factors, studies of these effects in human radiotherapy groups tend to involve small cohorts. Most of the studies in this field involve non-human animals, and the applicability of these findings to humans is still being established.

Another low cost method for protecting healthy tissue in patients involves varying the time of day at which radiotherapy is administered to maximise the body’s tolerance for it, referred to as chronoradiotherapy[63]. The effects of the circadian rhythm on cancer treatment have been established for chemotherapy since at least the 1980s when it was shown that the time of day can significantly increase the chemotherapy dose that patients can tolerate (up to a 45% increase)[64]. The primary driver of this is hypothesised to be the variations in DNA repair, antioxidant levels and immune function that occur over the course of the day[63][65][66]. These effects could also confer protection to normal tissues during radiotherapy treatments, and indeed chronoradiotherapy has been shown to reduce patient side effects when used to treat a range of cancer types[67]. Chronoradiotherapy is arguably not yet as

well established as chronochemotherapy, though it is moving towards a similar level of acceptance. Despite this, much work remains to establish how time of day affects the wide range of cancer types, as well as how a person’s personal chronotype may result in a shift to the optimal treatment times.

A range of other chemicals are also available that offer radioprotection to healthy tissue[68], however many of these are associated with their own toxicity, leading to an ongoing search for safer alternatives including both synthetic and naturally occurring compounds[69][70]. The mechanisms proposed for explaining the radioprotective effects range from the antioxidant nature of the compounds (reducing ROS induced stress) to their effects on gene expression (e.g. upregulation of heat shock proteins). More research is currently needed to evaluate the efficacy and potential toxicity of new radioprotective compounds, as well as to establish that they offer preferential protection to healthy rather than cancerous tissues.

Finally in this section, though it seems trivial, one way of reducing radiation induced healthy tissue damage is to replace photon-based radiotherapy with ion-based radiotherapies. Photons are attenuated exponentially with material thickness, whereas ions have a much more sharply defined maximum range. As the ions travel, they lose kinetic energy through coulombic scattering with other atoms, slowing slightly. The energy transferred by a scattering ion, dE_i , is inversely proportional to the square of the ion’s velocity, v_i [71]:

$$dE_i \propto \frac{1}{v_i^2} \quad \text{eq. 1.16}$$

The physical consequences of this are that energy transfer rates are highest when the ion is travelling slowest, resulting in a significant spike in energy deposition in the area immediately surrounding the point where the ion comes “to rest” (is thermalised), resulting in a feature referred to as the Bragg peak[72] (see Figure 1.7). This contrasts with photons which decrease energy deposition exponentially with increasing depth. Clinically, this means that dose can more accurately be targeted to a region of interest, without concerns for irradiating tissue behind the target region and whilst minimising the dose deposited in tissue on the way to the target region. Large scale adoption of these therapies is still fraught with problems including the high cost and large size of the facilities required and the uncertainty associated with targeting the beam[73][74]. The latter stems from the higher dependence of energy deposition depth on atomic density in ions compared with photons. Whilst dual energy x-rays can solve this issue to an extent, and emerging technologies such as photon-counting spectral imaging (see Chapter 4) promise to refine these estimates still further, the fact remains that a larger localisation of energy deposition leads to a larger impact on treatment of uncertainties in imaging data and patient positioning. Combined, the above mean that ion-based radiotherapy is unlikely to surpass photon based radiotherapy completely in the near term, though it will still have a place in certain conditions and patient populations (e.g. younger patients with inoperable brain tumours).

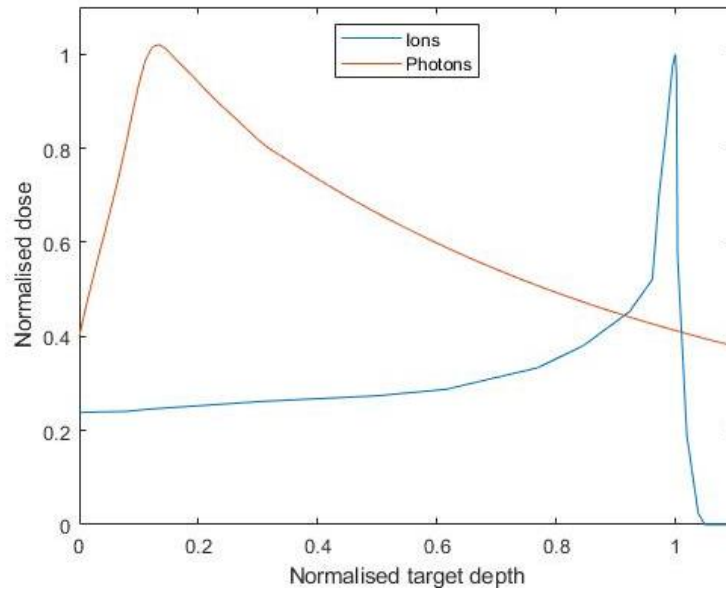


Figure 1.7. A sketch (based on fictional data) showing how ions and x-ray photons differ in their energy deposition profiles as a function of depth. Doses are normalised to the same maximum for both particle types. The target of the irradiation is at a normalised depth of 1. x-rays deposit their energy in a way that drops off exponentially with depth (after an initial build-up region which is usually very small but varies with energy), with considerable dose deposited both before and after the target depth. In contrast, ions deposit most of their energy at a defined depth (the Bragg peak), with a low level of dose deposition per unit length prior to this point and almost no dose deposition at deeper sites.

1.3.3 Improved dose effectiveness

Improved dose effectiveness techniques are those which increase the effectiveness of radiotherapy by making the tumour more susceptible to radiation damage, thus eliciting a response in the tumour that would normally be associated with a higher dose of ionising radiation than is actually used, as is discussed further in Chapter 2. Whilst applicable to all cancers, improving dose effectiveness is of particular interest where cancers are radioresistant. Radioresistant phenotypes can result from environmental factors (such as hypoxia) as well as genetic variations (such as Prp4K upregulation[75]). In general, hypoxia itself means a reduction in ROS stress as a result of ionising radiation, whilst adaptations to hypoxia stem from genetic changes in the cells triggered by hypoxia, largely mediated by hypoxic inducible factor 1 (HIF-1) expression[76]. The reader is reminded that the basic process of tumour cell-kill using ionising radiation involves energy deposition in the cells, production of ROS, damage of DNA, failure to repair the DNA sufficiently and then cell death. There are thus multiple steps at which intervention can improve dose effectiveness, including physically increasing the energy deposited in the tumour, selectively increasing ROS stresses in tumour cells, inhibiting antioxidant production, and inhibiting DNA repair.

One mechanism for improving dose effectiveness involves administering a high Z-numbered material to the tumour such as iodine or gadolinium[77][78]. This higher Z material will attenuate more of the photons in the radiotherapy treatment than the tissue would alone, leading to a

larger fraction of the patient dose being deposited in the tumour. This energy is then transferred to the tumour cells by a combination of thermal energy, Auger electrons, photoelectrons, and short ranged fluorescence x-rays, all of which can result in disruption to the cellular environment and an increase in free radical production. The higher Z material may be dissolved in solution or dispersed as nanoparticles. These approaches are limited by the toxicity of the agents used and, depending on the preparation, either tumour selectivity or tumour penetration, particularly in the case of poorly vascularised tumours. Current research in this area focuses on the use of nanoparticles, as these particles can be designed to actively accumulate in tumours. Whilst competing factors make this task far from trivial, advances in this area are being made[79].

Hypoxia is one of the best-known causes of radio resistance in tumours, with the reduced levels of oxygen available meaning that ROS are less likely to form. This can also have consequences for how DNA damage is mediated, with lower levels of molecular oxygen meaning potentially lower levels of superoxide free radicals (see Equation 1.12), with a consequent reduction in free Fe^{2+} ions available to catalyse H_2O_2 decomposition. Tumour cells are more resistant to hypoxia than their normal tissue counterparts due to a range of adaptations that they develop including upregulation of antioxidants, changes to cell cycle progression and activation of DNA repair proteins[80][81]. Alleviation of hypoxic conditions by reintroducing oxygen to the tissue has been studied using various delivery systems[82] including hyperbaric oxygen chambers (with limited success)[83], non-cell bound haemoglobin[84], hydrogen peroxide gel[85] and oxygen containing microbubbles/nanobubbles[86][87]. Whilst it is self-evident that additional molecular oxygen will lead to a greater potential for ROS production, it is not as obvious that the presence of oxygen will necessarily reverse the other adaptations adopted by hypoxic tumour cells, such as upregulation of DNA repair pathways. Work in this area has shown that the production of HIF-1, a major cellular regulator of hypoxia adaptations in hypoxic tumour cells, can be inhibited by returning the cells to normoxic conditions, with a subsequent increase in radiosensitivity[88]. Importantly, the cells were returned to hypoxic conditions prior to irradiation and yet still showed enhanced radiosensitivity, indicating that it was not the increase in ROS that was responsible for this response, and showing that the hypoxic adaptations can indeed be reversed, or at least mitigated. A major drawback of some of these approaches is that they can also radiosensitise normal tissues, and selective approaches for tumour oxygenation are under investigation. It is important to note here however that the work showing HIF-1 could be inhibited by pre-radiotherapy oxygenation also showed that this approach does not lead to an increase in the radiosensitivity of normal tissues. This offers a potential loophole in the use of oxygen to alleviate hypoxia that could mitigate some of the associated side effects and should be explored in more detail in future.

The final approach discussed here for increasing the effective dose experienced by tumours involves agents designed to directly radiosensitise the tumour cells. These agents encompass a wide range of molecular sizes and target cellular components ranging from small mRNA strands[89] up to

large organelles[90]. These agents act via a variety of mechanisms, inhibiting DNA repair pathways, increasing the sensitivity of apoptotic pathways or delaying progression through certain cell cycle checkpoints to increase the proportion of cells in their most radiosensitive phases. Whatever mechanism is employed however, these approaches differ from the previous ones in that they directly reduce the tolerance of the target cells for radiation induced damage. These agents thus have the potential to affect both healthy and diseased tissues. Strategies have been demonstrated to facilitate deployment of the agents only under hypoxic conditions[91], however their active targeting to tumours initially before activation or organelle sub-localisation is an area in need of further research.

1.3.4 Conclusion

A range of different approaches are available or in development for improving the effectiveness of radiotherapy and minimising its side effects by increasing the ratio of damage done to tumour cells versus healthy cells. External hardware-based approaches such as tumour tracking may be limited in their effectiveness by the need to define treatments in the imaging space of the tracking modality rather than the biological space of the tumour itself. In contrast, biological interventions aimed at healthy tissue protection (such as chronoradiotherapy or fasting) or improving dose effectiveness (such as transiently reversing hypoxia) have the advantage of selecting between healthy and cancerous cells at the molecular level, resulting in better compartmentalisation of the damage induced. These techniques are less well understood and less widely practiced however, with a lot of research still to be done.

AuNPs have a range of advantages as agents for inducing tumour specific effective dose enhancements in radiotherapy which combine the attributes from the above three categories whilst minimising their drawbacks, as will be discussed in Chapter 2. AuNPs have two potential mechanisms for accumulating preferentially in tumours rather than healthy tissue: by passively accumulating there through the leaky blood vessels associated with tumours and by being functionalised to target receptors that are over expressed in tumour cells. Such selective uptake, if it should work ideally, means that the radiation dose enhancement will move with the tumour based on biological data rather than imaging data, without the potential for misalignments found in beam tracking approaches (Section 1.3.1). The high Z AuNPs could also be used as a fiducial marker to allow for better tumour tracking using the approaches detailed in Section 1.3.1. In principle AuNPs could also be used with any of the tissue protective measures discussed in Section 1.3.2, and additionally may allow for lower patient doses to achieve the same level of tumour control, due to the increased physical absorption of the high Z -number of Au. Finally, AuNPs are able to enhance dose effectiveness via a variety of the mechanisms detailed in Section 1.3.3 simultaneously. AuNPs increase physical energy deposition in the tumour due to their high Z -number, can catalyse the production of ROS and other free radicals, inhibit DNA repair pathways, and can lower cellular antioxidant levels by scavenging antioxidants from their environment. There are still limitations to AuNP use for this purpose which will require multidisciplinary approaches

to resolve. Nonetheless, the varied mechanisms by which AuNPs could act to enhance radiotherapy treatments provide the primary motivation for their inclusion in this thesis.

Chapter 2.

Gold nanoparticles for radiotherapy dose enhancement

When selecting an agent to deliver a radiotherapy dose enhancing effect (RDEE) there are a variety of reasons that gold is favoured by researchers. The relatively high biocompatibility[92], relatively high Z-number (compared to human tissues) and long history as a therapeutic agent[93] provide good medical grounds for investigating gold, whilst the extensive literature on gold nanoparticle (AuNP) synthesis[94] allows for size and shape selectivity[95], providing the possibility of tailoring particles for a range of specific requirements. Due to their combination of properties, AuNPs can contribute to all three approaches identified in the previous chapter for reducing radiotherapy side effects (tumour tracking, normal tissue protective and improved dose effectiveness) by accumulating preferentially in cancerous tissues rather than healthy ones, delivering RDEE by physical, chemical and biological mechanisms[96] and acting as a contrast agent [97][98] to allow radiotherapy treatment planning that takes AuNP distribution into account. This chapter will investigate the many advantages of AuNPs as RDEE agents, including their role in a range of different RDEE mechanisms and their suitability for targeted delivery.

2.1 Definition and limitations of dose enhancement

Before discussing the specific benefits of Au as a dose enhancing agent, it is prudent to introduce the ways in which RDEEs are defined in the literature. Whilst an RDEE is broadly definable as “an increase in the effectiveness of a given radiotherapy treatment”, it is not obvious how this should be quantified. As a complex and relatively new field, agreement has not yet been reached regarding how dose enhancement should be measured and calculated. A wide range of physical parameters have been measured, and a variety of metrics calculated, to assess a quantity often labelled as the “dose enhancement factor”. This section will look at the more common ways in which AuNP-mediated dose enhancement has been assessed.

2.1.1 Physical parameters measured

A range of different physical parameters have been assessed as proxies for radiation induced damage including proliferative viability, metabolic viability, DNA damage and absorbed dose. These metrics are all *in vitro* assays, however *in vivo* studies have also been performed in animal models using parameters more directly relevant to medical radiotherapy applications such as tumour volume and mean survival period. These studies vary far more significantly in their design and assessment than the literature on *in vitro* studies however, and introduce the possibility for even more confounding factors that are not examined or explicitly controlled for, such as changes in immune stimulation or differences in irradiation timing. For that reason, this thesis will focus explicitly on the *in vitro* studies and results so far.

2.1.1.1 Proliferative viability

The proliferative viability of a cell is a measure of its ability to continue to produce living copies of itself. It is often measured using a clonogenic assay[99], which involves five steps performed separately for cells in both control and intervention groups simultaneously.

1. N cells are seeded onto a dish very sparsely such that they are effectively isolated from each other.
2. The cells are incubated for long enough that multiple division cycles can occur.
3. The cells are then fixed and stained using methanol and crystal violet respectively.
4. The dishes are examined under a microscope and the number of colonies, n , consisting of at least b cells (b is usually equal to 50 individuals) are counted.
5. The surviving fraction, SF , is then calculated

$$SF = \frac{n}{N} \quad \text{eq. 2.1}$$

Clonogenic assays are widely considered the gold standard for assessing the *in vitro* effectiveness of radiation treatment on cancer cells. This is because choice of a suitable value for n means that SF is equal to the fraction of cancer cells still capable of dividing indefinitely. From a medical perspective, the concern with cancer cells is their ability to divide indefinitely, so cancer cells that no longer meet this criterion can be considered as successfully “treated”, whether they die or simply cease dividing.

2.1.1.2 Metabolic viability

Metabolic viability refers to the ability of cells to drive the metabolic processes necessary for them to live and proliferate. In particular, these assays tend to assess the ability of cells to reduce some tetrazolium salt to a differently coloured compound. A range of tetrazolium salts are available such as XTT and WST-1, though the most used is 3-(4,5-dimethylthiazol-2-yl)-2,5-diphenyltetrazolium bromide (MTT, Figure 2.1). Reduction of these salts can be correlated to availability of NADH[100], and consequently to the metabolic activity of the cell. The MTT assay is performed in seven steps, performed separately but simultaneously for control, intervention and blank groups (blanks contain everything in the dish apart from the cells and serve to provide a background signal against which the signal from the cells can be compared)[101]:

1. A monolayer of cells is plated in wells and allowed time to adhere
2. The cells are then treated with the experimental condition (or left untreated for the same amount of time if they are the control group).
3. MTT is then added to the cells and they are left for several hours in the dark or covered in foil (exact timings are dependent on protocol temperature and other parameters). During this time, the MTT should be internalised and reduced by the cells to give purple crystals.

4. Add an agent to solubilise the crystals such as SDS (sodium dodecyl sulfate), isopropanol or DMSO (dimethyl sulfoxide).
5. The plates are then incubated to allow the crystals to fully dissolve (time is protocol dependent and ranges from 15 minutes to 12 hours). The well contents may need gentle agitation during this time to ensure a uniform colour distribution in each well.
6. Measure the absorbance of the control (A_C), intervention (A_I) and blank (A_B) samples at 590 nm.
7. The viability of the treated cells can then be calculated

$$Viability = \frac{(A_I - A_B)}{(A_C - A_B)} \quad \text{eq. 2.2}$$

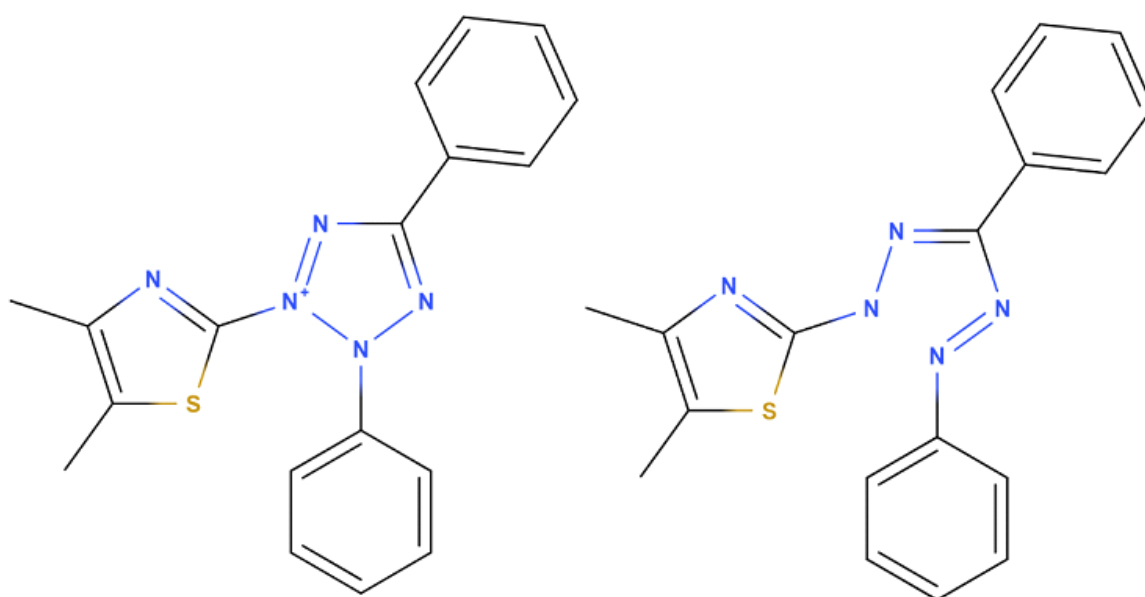


Figure 2.1. The chemical structure of MTT (left) and the molecule that results from its reduction (right). MTT is usually provided in the form of a bromine salt, however the Br^- ion is omitted for clarity. The molecular structures were drawn using the online software MolView, which is open source and provided by The MolView Project[102].

Several caveats with metabolic viability should be noted, including that the viability calculated is not absolute but relative to the same cells when untreated. This is at least partly because the MTT assay measures metabolic activity in the cells, so the same cell could produce different results depending on the stage in the cell cycle it is in. The MTT assay is also limited by the fact that it cannot distinguish what a cell is doing, only how metabolically active it is. For this reason, it cannot distinguish between a cell which is highly metabolically active because it is preparing to divide and one which is highly metabolically active because it is growing to larger than normal sizes but is no longer able to proliferate (a possible effect of radiotherapy). As previously discussed, cancer therapies are primarily aimed at preventing cells from proliferating, so this could result in some cells being scored as “viable” (i.e. not successfully treated) when in fact they are not. Despite these caveats, MTT assays are cheap, quick, and easy to perform in comparison with clonal assays, with a much lower failure rate. Further, the concerns

listed above can be mitigated to some degree by using cancer cells (which spend most of their time actively proliferating), several doubling periods, a larger number of cells and multiple repeats. For these reasons, MTT assays are often used in *in vitro* oncological experiments reported in the literature.

2.1.1.3 DNA damage

As the main mechanism of radiotherapy induced cell death is believed to centre around DNA damage, specifically unrepaired DNA damage[103], it is unsurprising that a number of groups attempt to measure radiotherapy effectiveness using assays for DNA strand breaks such as the comet assay, γ -H2AX staining or 53BP1 staining. Comet assays, also known as single cell electrophoresis (SCEP), measure the amount of DNA that diffuses through an agar gel under an applied electric field. Intact DNA is a large structure, closely bound to histone proteins, which prevents its movement through the gel, whilst strands which have been broken unfurl and can extend out into the gel. Comparison of the DNA that remains in the nucleus to that which extends outwards gives a relative measure of the DNA damage within the cell. This type of assay is not selective for DSBs however, and can also detect single strand breaks, abasic sites and, under appropriate conditions, a range of other DNA lesions through detection of incomplete base excision repair. In contrast, γ -H2AX or 53BP1 staining are considered more selective for DSBs as they detect locations in which specific DNA repair machinery has been activated[104], though they are more labour intensive, expensive and time consuming. Concerns have been raised that γ -H2AX foci can form absent DSBs, unlike 53BP1 which is DSB specific[105]. Literature reports using γ -H2AX staining should thus perhaps more reasonably be considered as a marker of DNA damage in general rather than DSBs specifically. In all these assays, the time after irradiation is a crucial factor that must be maintained, as cells do not simply leave DNA damage resulting from radiotherapy, but rather actively try to repair it. DNA damage assays may therefore be used to assess the damage done to cells by radiotherapy (15 minutes to 1 hour after irradiation) or the long-term effects on the cells by looking at DNA damage the cells could not repair (up to 24 hours after irradiation). In the latter case however, it should be noted that genetic changes resulting from improper repair of the DNA will not be detected by these assays, though they are rightly characterised as damage induced by the irradiation and may be lethal, neutral, or adaptive to the cell treated. A mix of both time points is thus preferred, though not always found in the RDEE literature.

2.1.1.4 Absorbed dose

Absorbed dose is the simplest metric of radiotherapy effect, measuring the energy deposited by physical mechanisms into a given volume of the target. Absorbed dose can be measured either through the use of dosimetric gels/dyes[106][107] or predicted by Monte Carlo simulations[108][109][110]. Absorbed dose is a very crude metric which greatly overlooks the sensitivity of biological systems to nanoscale dose variations, often resulting in an underestimation of the actual radiotherapy dose enhancements that can be achieved *in vitro*[111]. Fortunately work has been done to improve this facet

of the field by moving to simulations measuring nanodosimetry[112][113], with improved Monte Carlo models such as the Geant4-DNA model finding wider use[114][115]. Even these tools are limited in their applicability however, due to their inability to capture the cell’s response to the presence of AuNPs such as potential changes to gene expression or apoptotic machinery sensitivity. Nevertheless, relatively good agreement can be achieved with simulation and cell-work measurements in terms of direct DNA damage and they can be used to highlight the potential impact of variables that may not receive widespread consideration such as cell shape[116].

2.1.2 Calculated dose enhancement metrics

Before we investigate the different metrics used to assess the radiotherapy dose enhancement produced by a given agent, a word of warning. Terminology in this field is not always consistent between publications, with the definition of “dose enhancement” varying between publications[106][117][118][119][120]. Even when the same physical parameter is used, a variety of ways in which dose enhancement is calculated by different authors in the literature means that extreme caution is needed when making comparisons between results from different studies and extrapolating to new applications. It is thus important to check the definitions and methodologies used for calculating dose enhancements in a publication rather than simply relying on the name of the metric used. This has also been noticed by other authors[121], with attempts made to use new labels to separate the various metrics used that would otherwise have the same name. For the benefit of the reader however, a brief overview of some common metrics follows, with a naming convention that will be maintained in this thesis.

2.1.2.1 Dose enhancement factor (DEF)

The *DEF* is a measure of the increase in dose that would need to be given to a control group (cells absent AuNPs) to produce the same change in measured parameter as recorded for the intervention group (cells with AuNPs).

$$DEF = \frac{\text{Radiation dose needed to achieve specific effect when AuNPs are absent}}{\text{Radiation dose needed to achieve specific effect when AuNPs are present}} \text{ eq. 2.3}$$

To calculate the *DEF*, a dose response curve is needed for at least one of the conditions (control or intervention). Such a curve is produced by plotting the measured effect at a range of different irradiating doses and fitting an appropriate model for the metric used: a linear quadratic model for viability metrics[122][123] or a linear model for physical dose or DNA damage[47]. The equation of the curve can then be used to interpolate the dose in one condition that corresponds to the same measured effect in the other. As an example, consider the fictional data in Table 2.1. In this table, IRD represents cells irradiated with D Gy of radiation without AuNPs present, and similarly AuIRD represents cells irradiated with D Gy of radiation in the presence of AuNPs. The first thing to note in this table is that

the presence of AuNPs alone can produce a reduction in the metric being assessed as indicated by the fact that $AuIR0 < IR0$. For this reason, it is important to normalise to the relevant control i.e. IRD should be normalised to $IR0$ (100 in this case) whilst $AuIRD$ should be normalised to $AuIR0$ (80 in this case).

Table 2.1. Fictional data resulting from a series of hypothetical cell irradiations and controls, with and without Au, to assist in explaining how various RDEE metrics are calculated.

Condition	Metric score
IR0	100
IR2	90
IR4	70
IR6	50
IR8	40
IR10	30
AuIR0	80
AuIR2	40

From this data we can see that the effect of 2 Gy of radiation in the presence of AuNPs is a reduction in the metric score of 50% ($40/80 = 0.5$). Considering the case without AuNPs, a dose of 6 Gy is needed to achieve the same 50% reduction ($50/100 = 0.5$). The *DEF* for this example is thus given by

$$DEF_{example} = \frac{6 \text{ Gy}}{2 \text{ Gy}} = 3 \quad \text{eq. 2.4}$$

In other words, a *DEF* score of 3 means that without the AuNPs the dose would have to be increased by 200% to achieve the same response. *DEF* varies as a function of the reference dose used (2Gy in this case), however it can be calculated as a function of dose if a dose response curve for both conditions is available.

2.1.2.2 Dose enhancement effect (DEE)

DEE is defined as the ratio of effects measured in the AuNP group to the AuNP free equivalent, at the same dose.

$$DEE = \frac{\text{Effect measured at specific dose with AuNP}}{\text{Effect measured at specific dose without AuNP}} \quad \text{eq. 2.5}$$

The difference between *DEF* and *DEE* is thus that *DEF* considers an isoeffect between the conditions whereas *DEE* deals with an isodose between the two conditions. Considering again the data from Table 2.1, we can see that whilst 2 Gy of radiation caused a 50% reduction in the metric score for the

AuNP case, it only caused a 10% reduction in the metric score for the non-AuNP case. The *DEE* produced by the AuNPs for this situation is thus

$$DEE_{example} = \frac{50\%}{10\%} = 5 \quad \text{eq. 2.6}$$

In other words, a *DEE* score of 5 means that without AuNPs the measured effect would be 5 times smaller. Whilst in principle the *DEE* can be, and sometimes is, calculated at a single dose, it varies as a function of dose and so again a *DEE* curve, produced by comparing full dose response curves for both conditions, would be preferable.

2.1.2.3 Sensitiser enhancement ratio (*SER*)

SER is a metric normally associated with clonal assays (though in principle it could also be used for metabolic viability assays) which quantifies the shift in shape and position of the entire dose response curve. As an example, consider Figure 2.2 which shows hypothetical dose response curves for clonal assays performed both with and without AuNPs. At extremely low doses, the fraction of cells that survive treatment, *SF*, is close to 1 whilst at extremely high doses it is close to 0. At doses between these two extremes it can be seen that AuNPs lead to fewer surviving cells for a given dose.

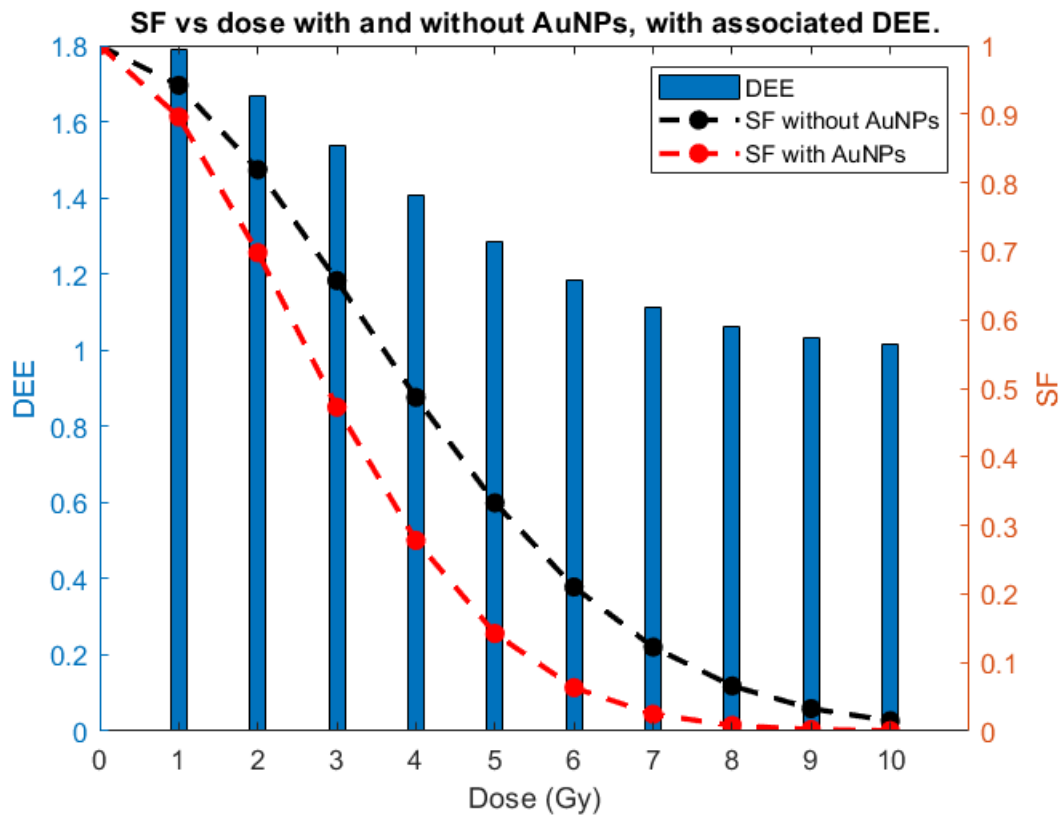


Figure 2.2. Plot of surviving cell fractions found at various radiation doses for both control (without AuNPs) and AuNP incubated cells. The *DEE* that would be calculated for each dose is also shown on the plot, to illustrate that this metric varies depending on the dose selected in its calculation. Data is fictional, for illustrative purposes only.

To get a more representative measure for how AuNPs have increased the effectiveness of the radiation treatment, *SER* evaluates the total area under the dose response curve. This can be done analytically by first fitting the experimentally measured data to a linear quadratic model of the form

$$SF = e^{-\alpha D - \beta D^2} \quad \text{eq. 2.7}$$

where D is the dose and α and β are experimentally measurable parameters, theoretically related to lethal and sublethal DNA lesions respectively[123][124]. The area under the curve, j , is then given by

$$j = \int_{D=0}^{\infty} SF(D) dD \quad \text{eq. 2.8}$$

SER for this setup can then be calculated as

$$SER = \frac{j_{Au}}{j_C} = \frac{\alpha_{Au} \sqrt{\beta_{Au}}}{\alpha_C \sqrt{\beta_C}} \quad \text{eq. 2.9}$$

where the subscripts Au and C represent the values calculated for AuNP and control group curves respectively[121]. This approach has the advantage of being more generalisable based on literature values, as many groups report the α and β values for their fits, even if they do not go on to calculate *SER* or an analogue directly. It has also intriguingly been suggested that the effect of AuNPs on the ratio α/β can be of use in elucidating the mechanisms by which particular AuNPs are enhancing cell radiosensitivity, as they relate to different types of DNA damage[121][124]. This metric does however require the largest amount of data for the AuNP treated cells, necessitating larger amounts of Au and more time than the other metrics.

2.1.2.4 Deposited Dose Ratio (DDR)

DDR refers to the increase in energy deposited within a region due to the presence of the AuNPs. It can be calculated as

$$DDR = \frac{\text{Absorbed dose with AuNPs}}{\text{Absorbed dose without AuNPs}} \quad \text{eq. 2.10}$$

This is a purely physical metric and, as with absorbed dose, is thus of limited use in predicting improvements in treatment outcomes due to a lack of sensitivity to both biological responses of the cell and chemical catalysis caused by the AuNPs. Despite this it has often been used in Monte Carlo studies predicting radiotherapy dose enhancement for high Z -number nanoparticles as it is easily calculable. As previously mentioned, an increase in awareness of the biological and chemical properties of AuNPs, combined with an increase in availability of Monte Carlo software for modelling DNA damage, has led to a decrease in the use of this metric, though it is still used as a first estimate[116][125] due to its ease of calculation and the versatility of simulation based approaches.

2.2 Advantages of gold nanoparticles as RDEE delivery agents.

AuNPs have been extensively studied for use in a variety of medical applications including structural imaging, molecular imaging, biosensing, drug delivery, therapy delivery and as an adjuvant to other therapies[96]. The reasons for their popularity as a probe/vehicle in the field of nanomedicine are due to a combination of their ease of production, synthetic versatility, and perceived low toxicity. Whilst it is true that bulk gold is generally considered to be both biocompatible and non-toxic, the potential toxicity of AuNPs to a range of microorganisms and even humans has been well demonstrated[118][126][127]. In addition to their ability to deliver a RDEE, AuNPs have advantages at each of the stages in their life cycle that make them exceptionally well suited to use in nanomedicine. These include advantages in synthesis, functionalisation, tumour localisation, uptake, and imaging. These advantages are summarised in Figure 2.3.

2.2.1 Radiotherapy dose enhancement

As already noted, the potential of gold to act as a radio-enhancer was demonstrated in 1998 by Regulla *et al*[117] for the case of solid gold films. In their experiment, the mere presence of a thin film of gold beneath the cells being irradiated was sufficient to generate a *DDR* of 53 - 115 in the energy range 40 keV - 120keV. These high *DDR* values translated into *DEE* values ranging from 30 - 48, over the dose range of 50 mGy - 200 mGy. These results produced excitement initially, as gold is known to be biocompatible with a low toxicity and the high *DDR* values achieved could be used to either reduce patient side effects or to improve the chances of producing disease remission. Despite this success with bulk gold, biological uptake and processing would only be possible if the gold was present in a particulate form, and in 2000 Herold *et al* demonstrated the feasibility of this approach by showing that gold microspheres were capable of generating a *DDR* of 1.42 and a *DEE* of 1.43, again as assessed by clonogenic assay[128]. These spheres were still too large to effectively enter living cells however, and it is now widely expected that the best Au-based dose enhancing agents (DEAs) are AuNPs. Multiple groups have since studied AuNPs for their RDEE properties both *in vitro* and *in vivo*, as summarised in several review articles[96][126][129][130][131].

Due to the differing ways in which these groups measured dose enhancement, as well as the variation in study parameters, quantitative comparisons between the experiments reported on are of limited utility. A non-exhaustive list of parameters which can affect the measured RDEE values can be found in Table 2.2. These parameters are not all considered or reported on in literature studies, and the potential consequences of this are overlooked in many review papers. Despite the discrepancies between experimental conditions however, the consensus of the many AuNP RDEE studies is that the presence of AuNPs in a cell often produces a RDEE. Mechanistic studies have been performed which have elucidated the ways in which these effects can be delivered, and these will now be considered.

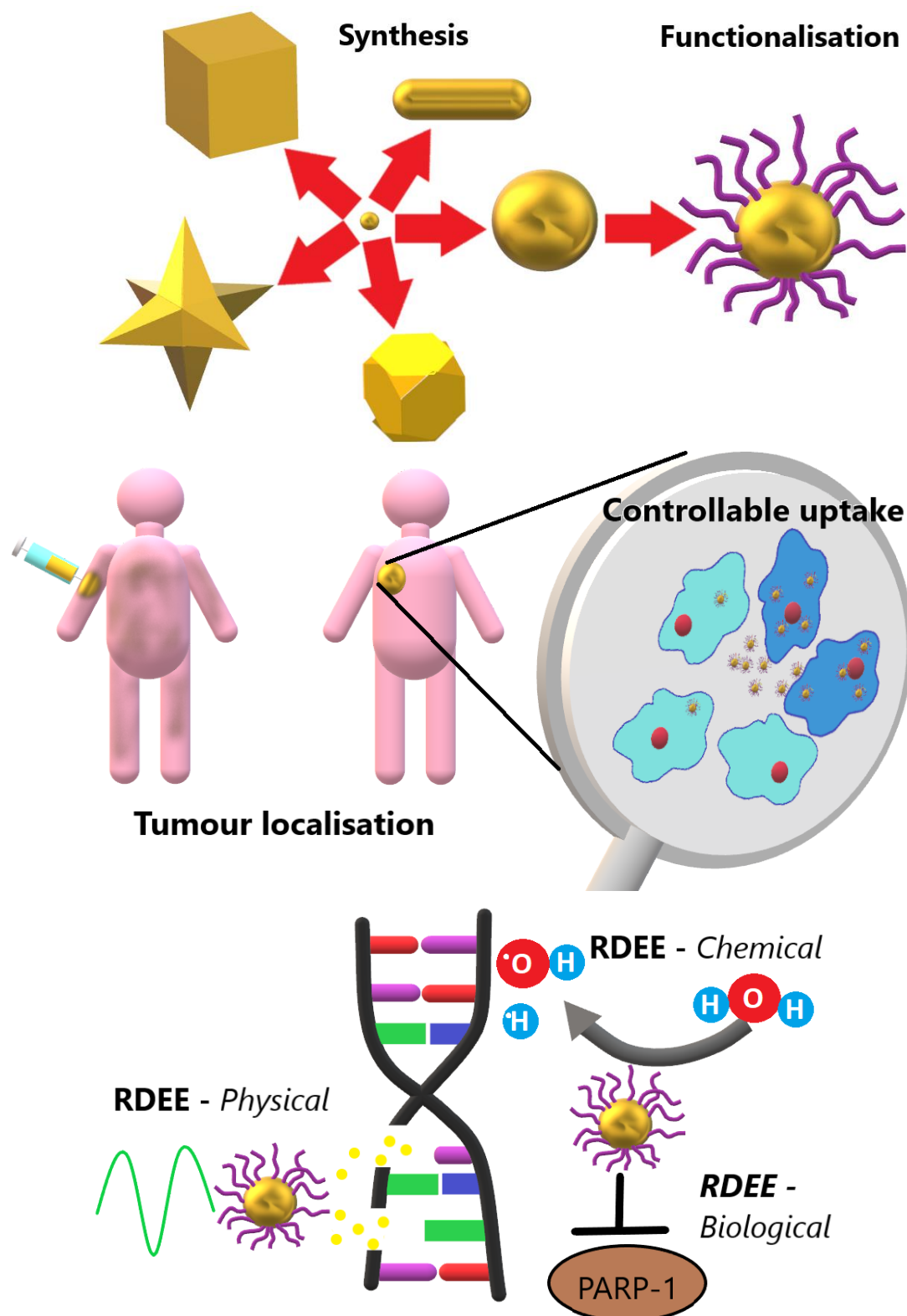


Figure 2.3. Visual summary of the advantages of AuNPs for delivering RDEE therapeutically. **Synthesis:** There are multiple shapes which can be synthesised readily and with rudimentary lab supplies. **Functionalisation:** A range of ligands can be readily attached in combination using click chemistry. **Tumour localisation:** AuNPs administered intravenously can accumulate preferentially at the site of a tumour. **Controllable uptake:** AuNPs can be functionalised to enter cancerous cells (darker blue) preferentially, and even targeted to organelles such as the nucleus (red spheres) once internalised. **RDEE:** Radiotherapy dose enhancement effects can be delivered by physical (secondary electron generation), chemical (catalytic ROS generation) and biological (DNA repair inhibition) mechanisms.

Table 2.2. Parameters that can affect the RDEE delivered by AuNPs, and the major components of each to be considered.

Parameter	Components
Radiation	Energy Type ($\alpha, \beta, \gamma, p, n, e$) Quality
Cells	Line Cell cycle stage AuNP uptake/excretion kinetics AuNP localisation
AuNPs	Shape Size Coating
Dose enhancement measurement	Process scored Reporter used Metric employed

As noted in Section 1.2, radiotherapy effects are effectively delivered across three main stages: energy deposition, conversion of that energy to DNA damage, failure to repair the induced damage. These stages can be considered physical, chemical, and biological domains respectively. AuNPs have advantages over both larger gold structures and over other high Z candidates, such as iodine or gadolinium, when it comes to enhancing radiotherapy treatments. This is because whilst larger gold structures, iodinated compounds and chelated gadolinium agents can all enhance the physical deposition of x-ray energy in a tissue, they do not significantly affect the chemical and biological domains of radiotherapy. In contrast, AuNPs are able to enhance radiotherapy effects in each of these three domains[96].

2.2.1.1 Physical enhancement

Physical enhancement, in the context of this thesis, refers to an increase in the percentage of an incident beam that is deposited in a tissue as a result of AuNP presence. Physical RDEEs are produced by the particularly high Z -number of Au compared with the major elemental components of human tissue, as can be seen in Table 2.3. Whilst a variety of radiation types can and have been shown to produce RDEEs[132], this thesis will focus primarily on photon based radiotherapy. As discussed in Section 1.1, the chances of an x-ray interacting with an atom to deposit energy is proportional to Z^n , where $n = 4 - 5$ for photoelectric interactions (depending on the photon energy) and is roughly equal to 1 for Compton scattering and pair production. As a result, the physical mechanisms of cell damage with

Table 2.3. List of the most common elements in the human body (those comprising >1% of body mass) and their Z-number. Au is included at the end of the list for comparison.

Element	Fraction of body weight (%)	Mole fraction (%)	Z-number
H	9.5	62.0	1
C	18.5	12.0	6
N	3.2	1.1	7
O	65	24.0	8
P	1.0	0.22	15
Ca	1.5	0.22	20
Au	3×10^{-7}	3×10^{-7}	79

the most pronounced increase due to Au are those involving photoelectric effect products (Auger electrons, photoelectrons, and fluorescence x-rays). If we compare Au with O (the most abundant element by mass in the human body) we find that

$$\frac{\text{Photoelectric}(\text{Au})}{\text{Photoelectric}(\text{O})} = \left(\frac{Z(\text{Au})}{Z(\text{O})}\right)^n = 9.88^n \quad \text{eq. 2.11}$$

which corresponds to an increase in photoelectric interactions of between ~9500 and ~94000 fold, depending on the energy of the incident photon. RDEE values are not amplified by anywhere near this amount, however. This is partly because photoelectric interactions are responsible for only a small fraction of the energy depositing interactions at energies relevant to radiotherapy (see Figure 1.1), with the dominant process (Compton scattering) only increasing with Z^n . This is also true however as the location of the AuNP can have a significant impact on the biological effect of the increased energy deposition, making *DDR* across a cell a poor metric for predicting RDEE. This can be seen by comparing the *DDR* predicted by physical dose enhancement with measured RDEE measurements using other metrics determined from cell experiments, as done by Rosa, Connolly, Schettino, Butterworth and Prise in 2017 (Figure 2.4[126]).

DDR on a cellular level can lead to an overestimation of RDEE at lower incident photon energies and an underestimation at higher energies[111][133]. These deviations can be mitigated by considering the linear energy transfer rates of the secondary particles produced by the AuNP-photon interactions, as well as the increase in number of secondary electrons produced. Whilst the presence of AuNPs can lead to increases of secondary electrons in a given volume of between 10 and 2000 fold (depending on incident beam energy and AuNP size[134]), the dose carried by these electrons drops off rapidly with distance from the AuNP surface, especially for higher energy incident photons. Whilst good agreement between simulation and cell work can be shown by taking this or similar approaches, caution needs to be taken as these models are usually fitted using only small number of AuNP sizes and

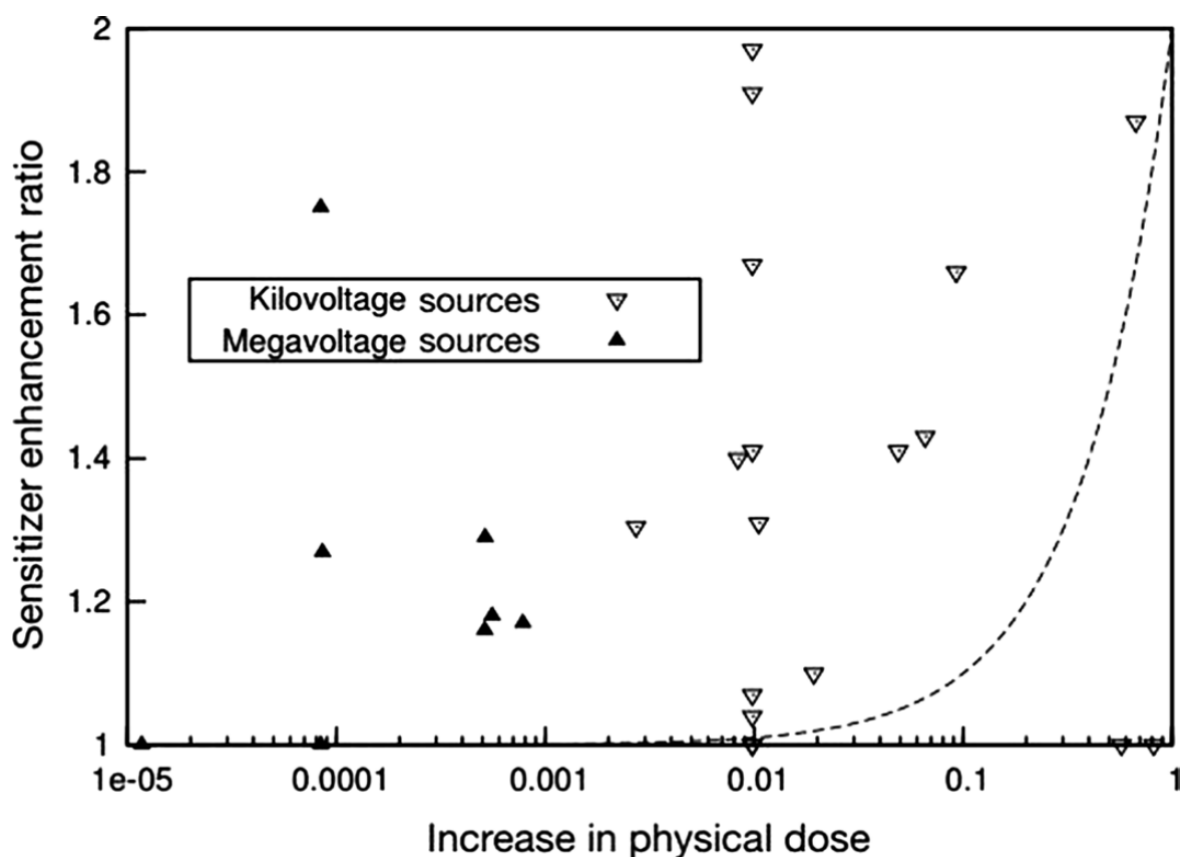


Figure 2.4. Figure comparing the measured RDEE based on cell work (triangles) with that predicted based on physical dose enhancement alone (dashed line). It should be noted that the x-axis measures increase in physical dose whilst the y-axis measures a ratio. An increase in physical dose of 1 is thus equal to a sensitizer enhancement ratio of 2. Figure reproduced, unedited, from Butterworth *et al*'s 2017 review paper[126] under the terms of the Creative Commons Attribution 4.0 International License (<http://creativecommons.org/licenses/by/4.0/>)

incident beam energies. Other approaches focussing on replicating the AuNP location and calculating the dose enhancement on a nanoscale also show good agreement[120], and it has been demonstrated that average cell dose enhancements are not sufficient to predict cell survival[135]. This is because whilst photoelectrons may have long ranges, Auger electrons are more limited in range, though they transfer significant energy over this short range[136]. As a result, AuNPs close to the DNA can massively amplify the number of lethal lesions produced compared with cytosolic counterparts in simulations. The extent of these effects is brought home by carefully performed cell experiments performed by Xiao *et al* involving AuNP-DNA complexes[137]. The AuNPs were separated from the DNA by a spacer coating of 0, 2.5 or 4 nm length, and RDEEs dropped off almost entirely. Whilst the results of this study were likely attributable to a combination of increasing distance and increasing material between the AuNP and the DNA, the results are in keeping with the previously established conclusion that the majority of secondary electrons produced by AuNPs have an energy of <30 eV, and consequently have a very short range in organic material of only up to 10 nm[138].

Despite their success in individual cases, I think it is very unlikely that the current trends in RDEE simulation will ever produce a comprehensive model of AuNP-mediated RDEE, as they include

only physical mechanisms and a short time window, meaning that the cellular response to the AuNPs, both pre- and post-irradiation, are neglected. They are consequently unable to offer insight into how changes in gene expression and cell regulation lead to increasing radio resistance, nor to explain the strong radiosensitising effects associated with AuNPs located distant from the nucleus and absent irradiation[139]. A method to comprehensively predict RDEE for a given AuNP and cell location thus requires an understanding of the chemical and biological role of AuNPs in RDEE.

2.2.1.2 *Chemical enhancement*

In the context of this thesis, chemical enhancement primarily refers to the increase in reactive oxygen species (ROS) produced by ionising radiation in the presence of AuNPs compared with the same radiation treatment when AuNPs are absent. The mechanisms by which these ROS lead to an increase in cell cycle arrest and/or cell death are detailed more in Section 1.2.3. In brief, ROS can cause molecular changes that result in the activation of apoptotic pathways. These changes include DNA DSBs, oxidation of the cell plasma membrane, degradation of compartmentalisation mechanisms, mitochondrial membrane permeability, mitochondrial depolarisation, protein crosslinking or protein misfolding[140].

Unlike physical mechanisms, the RDEE of AuNPs by chemical means is less sensitive to the intracellular location of the AuNPs. This is partly due to the larger number of targets available for their action and partly due to the established equilibrium of ROS that exists in the cell prior to irradiation. Whilst ROS are highly reactive and thus have a limited range within the cell as individual molecules, their increase in one part of the cell can have knock-on effects at more distant targets thanks to the disruption of ROS signalling and control mechanisms. This partly explains why significant RDEEs can be achieved by AuNPs located at significant distances from cellular organelles.

Chemical enhancement also differs from physical enhancement by being dependent on AuNP surface charge and coating in addition to its size and shape. This is because chemical enhancement can result from AuNPs playing a catalytic role in radical production and product formation, so access to surface sites and their relative charge are important factors[141]. It has been shown that AuNPs can form hydrogen bonds with water molecules at a AuNP-liquid interface, reducing the ionisation energy of the water molecule in the process[142]. By lowering the energy required of Auger/Photoelectrons for radical formation, a larger proportion of secondary electrons are thus able to contribute to increasing oxidative stress. Further, the AuNP surface can become activated by superoxides, or charged due to electron emission, allowing for more rapid conversion of intermediates in radical reactions to their end products[96][141]. These processes have been shown to be inversely proportional to AuNP diameter, further supporting a catalytic effect at the AuNP surface[143].

Separate from their catalytic capability, it has been proposed that AuNPs can bind thiol-containing antioxidants[144]. This leads to a reduction in antioxidant levels within the cell,

exacerbating oxidative stress. When thiol-containing antioxidants were added to the AuNPs prior to incubation with the cells, the additional oxidative stress was alleviated, “detoxifying” the AuNPs. This is consistent with a catalytic function of the AuNP surface as the covalent bonding with the thiol groups, which restricts access to the surface, also lowered ROS production rates. An implication of this result is that AuNP-mediated chemical enhancement could be AuNP concentration dependent, with low enough concentrations being “detoxified” by the cells before their antioxidants are depleted.

In addition to their role in increasing intracellular ROS levels, studies have also implicated AuNP interactions with DNA in directly sensitising the DNA to strand breaks[145][146]. Irradiation of AuNP-DNA films with 1-eV electrons produced an increase in single strand breaks (SSBs) in the DNA compared with DNA only films. As this energy is below the threshold at which secondary electrons would be produced by the AuNPs, it was proposed that the SSBs could not be attributed to the increased cross-section of the high Z-number Au atoms, an assumption further supported by the near complete attenuation of the incident electron beam by both types of film[145]. Whilst the exact mechanism responsible for this enhancement is yet to be confirmed experimentally, it is believed to result from the AuNP-DNA bond either weakening the DNA structure or through enhancement of dissociative electron attachment processes[138]. The former may be caused by introduction of steric strain from AuNP-DNA bonding, and the latter caused by AuNP-mediated stabilisation of transient anions involved in dissociative electron attachment.

Whilst not explicitly demonstrated for AuNPs *in vivo*, it has been reported that AuNPs can scavenge radicals to produce negative chemical enhancements[141]. Other nanoparticles have been shown to act as radioprotectors rather than radiosensitisers *in vivo*, due primarily to changes in their chemical interactions with ROS that shift them from net ROS generators to net ROS scavengers. Ceria nanoparticles (CeNPs) for example have been shown to be capable radioprotectors of healthy tissue due to their ready switching between the 4+ and 3+ oxidation state, and consequent ability to function as powerful electron acceptors[48]. Especially interesting is the fact that CeNPs can act as either radioprotector or radiosensitiser, depending on the environmental pH, with the lower pH associated with cancer cells leading to a net increase in ROS production, making their targeting to cancer cells specifically less important. Whilst not directly applicable to AuNPs, this result nonetheless underscores the importance of considering chemical effects of AuNPs and more dynamic metrics when predicting RDEE rather than relying on physical models and DDR alone, as is too common in Monte Carlo studies.

Chemical enhancement has been confirmed for AuNPs using a range of analysis techniques, cell lines, AuNP shapes, AuNP sizes and irradiating photon energies. It has been well argued that physical enhancement alone cannot account for measured RDEEs, and that a combination of physical and chemical enhancement is a better indicator[142], and hopefully this section has equally well convinced the reader of this. These mechanisms still fail to capture cellular responses to AuNP presence

that are not dependent on ROS however, and these responses can be extremely important, as discussed in the next section.

2.2.1.3 Biological enhancement

Several literature reviews of “biological dose enhancement” by AuNPs, as well as several publications on which they are based, include the increases in ROS associated with these particles as biological enhancement[96][126][129][147]. Presumably, the argument is that the presence of these ROS triggers a host of cellular responses and so they are a component of the biological system. In contrast, other reviews consider ROS production, and all downstream cellular responses to them, as physicochemical mechanisms, combining both physical and chemical enhancements[140]. Commonly the various enhancements are either grouped into a ‘two enhancement mechanisms framework’ or else arbitrarily divided into three mechanisms, without justification. This thesis takes a different approach, seeking to define each enhancement mechanism explicitly at the outset. ROS generation is thus classified explicitly as a chemical enhancement, due to its origination in the catalytic effect of the AuNP surface. ROS generation is not deemed a physical process here, as the lower energy threshold to ROS formation produced by the gold does not need any radiation to have an effect, being a chemically catalytic effect. Similarly, ROS generation is not deemed a biological enhancement here as otherwise anything that increases ROS should be considered biological, including the physical enhancement of radiation dose within the cell. Biological enhancement, in this thesis, is thus considered to refer to changes in cell behaviour that predispose the cell to successful treatment with radiotherapy.

Biological enhancements by AuNPs are well demonstrated in the literature, with their existence initially proposed to explain discrepancies between theory and experiment concerning RDEEs associated with AuNPs and MeV x-ray beams. At these energies the photoelectric effect is minor and so physical enhancement alone would result in vastly lower RDEEs than those actually observed[119]. Specific biological enhancement processes have since been recorded which range in scale from whole cell behaviours such as changes in cell migration[148] to localised effects such as DNA repair inhibition[149]. The physical processes by which AuNPs induce these changes are, as yet, not fully understood. Nevertheless, their existence has been widely demonstrated and the associated alterations to metabolic pathways identified in several instances[150]. Details regarding the nature of disruption to individual metabolic pathways is beyond the scope of this thesis, so only general observations on how biological enhancements are achieved will be made.

AuNP presence can alter the levels of proteins associated with cell cycle progression, though the exact nature of the change is governed by variables including cell type and AuNP coating[151]. Changes in checkpoint proteins have been shown by some groups to lead to cells concentrating in the most radiosensitive G2/M phase of the cell cycle, providing a positive biological enhancement to RDEE[152]. AuNPs can have the opposite effect in other cell lines however, concentrating cells in the

most radioresistant S phase, and thus producing a negative biological enhancement, reducing RDEE overall[153]. Yet other groups have shown that AuNPs have no effect on cell cycle progression[154]. These results are not as contradictory as they appear, given that a range of different cell lines, incubation protocols, AuNP shapes/sizes/concentrations and coatings were used. The sheer number of variables makes a systematic investigation unlikely in the short term without expenditure of significant resources.

In addition to cell cycle progression, AuNPs have been shown to be capable of suppressing DNA repair in cells. This has been shown to be the case implicitly by multiple studies working in various cell lines, even when the AuNPs are not close enough to the nucleus to increase the number of DNA lesions initially produced by irradiation. More recent work has identified individual genes in DNA repair pathways that are downregulated in response to AuNP presence. Whilst the group publishing this result did not speculate on a mechanism, it seems at least plausible that it may be related to similar phenomena observed with gold(I) salts. Au atoms have been shown able to bond with cysteine residues in some transcription factors, disrupting transcription of the relevant genes[155]. Despite this work occurring almost 25 years prior to the study in question, this mechanism was not suggested as a possibility, even so it could be discounted. I believe this is symptomatic of the assumption, almost universally made, that AuNPs are chemically stable entities that are not degraded by biological pathways. This belief is no doubt fostered by the long biological lifetimes of large AuNPs *in vivo*. This assumption is a dangerous one given the many unexpected interactions between AuNPs and the cellular machinery already known and is less probable due to the fact that AuNPs are preferred over bulk Au precisely because their size leads to novel properties resulting from quantum effects. This assumption has indeed recently been shown to be invalid[156], and it is now clear that AuNPs can indeed be degraded into atomic Au by cells. This could provide additional biological enhancement mechanisms, such as free Au atoms displacing Zn in the zinc-fingers of PARP-1, an important component of mammalian cell's DNA repair pathway[157]. As far as this literature review could ascertain, no one has yet proposed considering toxicity associated with atomic Au as a factor in AuNP associated cytotoxicity.

The fact that biological enhancements can be radiosensitising or radioprotective, depending not only on the properties of the particles themselves but also on the cell lines in which they are taken up, underscores the importance of designing AuNPs for a particular task. It could even be argued that a fully optimised AuNP could be considered a form of personalised medicine, though likely suboptimal AuNPs will reach the market first as a form of generic radio-enhancer. Now that AuNPs are known to not be biologically inert as once thought they have lost some of the appeal that initially excited researchers. Nevertheless, AuNPs offer a variety of other benefits which still make them a leading candidate for nanoparticle mediated RDEE, as will be discussed in the following sections.

2.2.2 Ease of synthesis

AuNPs can be readily synthesised in a range of shapes (rods, spheres, cubes, diamonds, stars, shells, cages, concave cubes etc.) and sizes spanning 2 orders of magnitude (1-150 nm)[96]. Publications concerning the effects of various parameters in traditional synthesis routes on the resulting AuNPs are abundant and increasing rapidly, along with those proposing newer synthetic routes based on biological or ecologically friendly approaches[158]. The size and shape of the AuNP can drastically alter the optical and electrical properties of the particles, allowing particles to be tailored for specific applications, for example by enhancing electric field gradient for Raman spectroscopy[159] or tuning plasmon resonance to the infrared region for photoacoustic imaging[98]. Chemical synthesis routes for AuNPs that require only commercially available reagents and basic lab supplies (water bath, scales, magnetic stirring bar and glassware) are well documented[94], meaning that AuNPs can be readily synthesised and studied by research groups worldwide. This has led to a wealth of information being produced rapidly on these particles, which provides a strong research base that any other DEA for radiotherapy would have to compete with.

2.2.3 Versatility of functionalisation

Once synthesised, AuNPs are remarkably easy to functionalise with a wide variety of surface ligands, which can be selected based on the intended application to assist in uptake, intracellular localisation, biocompatibility, drug delivery or even signal generation. This versatility is characteristic of the “click chemistry” approach which can be employed with AuNPs, owing to the ready binding of both thiol and amine groups to the AuNP surface. Click chemistry is a term used to refer to reactions that conform to a range of conditions, generalisable as reactions between small biological molecules that occur under mild conditions and with high efficiency[160]. A wide range of ligands can thus be bound onto AuNP surfaces, either in isolation or in combination, depending on the intended application. Some examples are listed in Table 2.4.

2.2.4 Selective tumour accumulation

In 1986 it was noted that the cells lining tumour blood vessels are less tightly packed than in ‘normal’ blood vessels, resulting in gaps which can allow vessel contents to leak out[173]. This increase in vessel leakiness means that circulating AuNPs and other small drug molecules accumulate preferentially at tumour sites as they leak from the circulatory system, an effect dubbed the “enhanced permeation and retention” (EPR) effect. It was later shown however that the size of the AuNPs was crucial to the relative accumulation at the site of tumours, as particles that are too large (~100 nm) would not be able to escape efficiently through the gaps, whilst those that are too small (<10 nm) would escape almost as readily from normal blood vessels[79]. More recently, it has been shown that both nanoparticle shape and charge can also influence the effectiveness of the EPR effect, with nanorods

Table 2.4. Common ligands considered in AuNP designs intended for therapeutic use.

Class of surface ligand	Purposes	Examples
Inorganic atoms	Protection from chemical attack Shifting electric/optical properties Thermal coupling Signal generation Treatment options	Si[161] Pd[162] Gd[163] Radioisotopes[164][165]
Biological molecules	Altering particle charge Improving biocompatibility Facilitating uptake Endosome escape Tissue localisation Cellular penetration Intracellular localisation Triggering immune response Chelator for tracer or treatment option	PEG[166] Bovine serum albumin proteins[167] RALA[168] Antibodies[169] Antigens[170] Nuclear localisation sequences (NLS)[171] Arginine-glycine-aspartic acid(RGD)[171] Endosomal escape molecules[172]

extravasating better than nanospheres and cations extravasating better than either neutrally charged or anionic nanoparticles[174][175]. The picture that has emerged is a complex one in which AuNP accumulation at the tumour site depends on the interplay of a wide range of factors including the hydrodynamic size and charge of the AuNP-ligand complex used, AuNP shape, type of protein corona formed, regional blood flow, extracellular matrix density, intratumoural pressure, the cancer type and stage and the location within the body[127][176][177][178][179]. Indeed, even the growth rate of the cancer appears to play a role, with fast growing carcinomas showing a higher likelihood of displaying EPR effects than slower growing sarcomas[180], presumably due to the more rapid development of blood vessels in the former leading to less time for blood vessel maturation. Despite this complexity, and despite some contentiousness remaining around the issue[181], it is broadly accepted that AuNPs have been shown to accumulate locally around tumours.

It is also commonly proposed that AuNPs can be “actively targeted” by functionalising them with antibodies for cell surface proteins that are overexpressed in tumours compared to their healthy counterparts[169][182]. Whilst active targeting has been extensively demonstrated *in vitro*, the *in vivo* results are mixed[183][184]. Van Haute and Berlin suggested that the variations can be explained by total antibody-target availability[185]. This explains why anti-human targeting sequences used to target human tumours in mouse models show marked targeting, but no such targeting advantage is found when targeting mouse tumours in mouse models. This is because whilst the targeted receptors are

overexpressed on tumours, they are also expressed on healthy cells. As healthy cells significantly outnumber tumour cells, the probability that a given target receptor molecule is located on a tumour cell rather than a healthy cell is small. This result underscores the importance of considering appropriate whole organism models when designing AuNPs, and the limitations of *in vitro* analysis. This result does not however negate the concept of active targeting entirely. Rather it suggests that the AuNPs need first to be localised at the tumour site, by EPR effects or direct intratumoural injection for example.

2.2.5 Tailorable uptake kinetics

Once located at the site of the tumour, AuNPs need to be internalised by tumour cells to maximise their RDEE. Passive diffusion across the cell membrane is impossible for all but the smallest AuNPs, so to facilitate uptake cell penetrating peptides (CPPs) of some description are often attached to the AuNP's surface. CPPs operate via a range of mechanisms, with the dominant mechanism varying based on the CPP employed, however generally the mechanisms can be divided into endosomal and transmembrane, as shown in Figure 2.5.

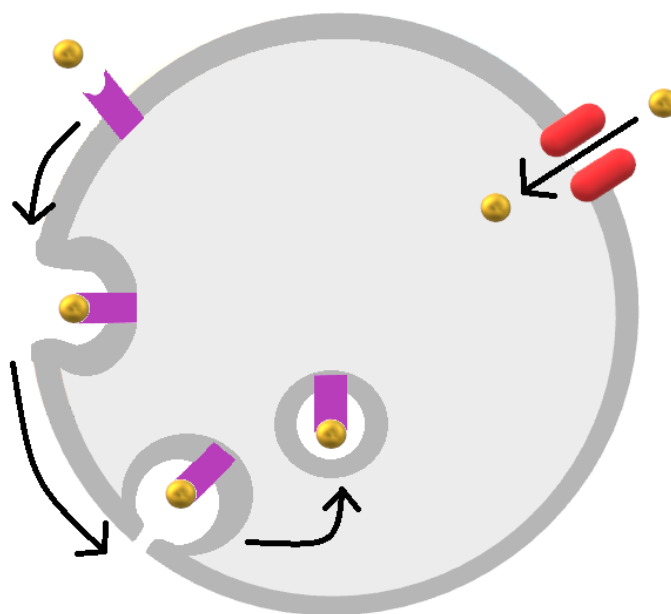


Figure 2.5. Mechanisms of AuNP uptake into a cell (grey circle). Translocation (right side of cell) involves AuNPs (gold balls) interacting with protein channels or transporter proteins (red ovals) to move directly from outside of the cell to the inside. Translocation is rapid and the transporter is not depleted in the process. In contrast, endocytosis (left side of cell) is a complex process which begins when the AuNP binds an external receptor protein (purple cylinder). This binding leads to invagination of the membrane around the receptor. This invagination then pinches and buds off into the cytosol to produce an endosome. This process is slower and more energy intensive than translocation as the external receptors must be regenerated. N.B. the receptors normally attach not to the AuNP surface but rather to ligands attached to it. These ligands have been omitted in this diagram for clarity.

Endosomal uptake is a more energy intensive internalisation route, requiring membrane invagination and budding to form an endosome[186], whilst transmembrane mechanisms tend to directly translocate the AuNP across the membrane[187]. By functionalising AuNPs with ligands for

cell surface receptors that are overexpressed on cancer cells, “active targeting” can bias endosomal uptake to produce a significant increase in the concentration of AuNPs in cancerous cells compared with ‘healthy’ cells[188][189]. ‘Naked’ AuNPs (those without covalent functionalisation) can also use the endosomal uptake route. This is due to the fact that ‘naked’ AuNPs are effective at scavenging free proteins from their environment to form a dual layered protein corona[179][190]. Proteins thus scavenged include growth factors which bind to cell surface receptors, allowing AuNPs to piggyback on the process of endocytosis that would normally recycle the growth factor-receptor complex. The details of the protein corona formed will depend on both the available proteins in the environment and also the AuNP properties of size and shape[191], and the protein corona formed can then affect the uptake mechanism utilised and uptake efficiency[192][193].

Transmembrane uptake mechanisms, whereby the AuNPs bypass the endosomal route of uptake and instead translocate across the cell membrane via transport proteins, have been less well studied and consequently the precise transport proteins involved are not currently known. Despite this, investigations of the dependence of AuNP uptake kinetics on temperature, ATP levels and AuNP concentration have provided convincing evidence of the existence of such a mechanism[187]. Finally it should be noted that AuNPs taken up by the endosomal route will tend to be concentrated and partitioned off from the rest of the cell environment, requiring the use of endosome escape techniques[168][172][194] if the AuNPs are intended for intracellular targeting. Such techniques, whilst ingenious and interesting, are again beyond the scope of this review.

2.2.6 Multi-modality Imaging potential

AuNPs have several physical properties which lend themselves to imaging applications, being detectable by a range of optical and x-ray imaging techniques, as well as being able to carry probes suitable for magnetic or nuclear imaging techniques.

The features of the AuNP that make them suitable for imaging optically and with x-rays are intrinsic to the particles themselves and will be discussed in more detail in the chapters dedicated to photoacoustic spectral imaging (PASI) and x-ray photon-counting spectral imaging (x-CSI) later (Chapters 3 and 4 respectively). Suffice it to say for now that the optical properties can be tuned by selecting the shape and size parameters of the AuNPs, whilst the x-ray interactions are dependent only on Au atom concentration within the imaging volume. As a result, AuNPs can be detected directly by a range of imaging modalities including surface-enhanced Raman spectroscopy, two photon microscopy, PASI, conventional CT and x-CSI. The same intrinsic properties that allow the AuNPs to be detected by these techniques also enhance the detection limits of other optical imaging techniques, allowing for plasmon-enhanced fluorescence microscopy and super-resolution fluorescence microscopy[98].

In addition to these intrinsic AuNP properties, AuNPs can be functionalised to allow for detection by a range of other techniques[195]. These include functionalisation with Gadolinium chelates for magnetic resonance imaging (MRI), ^{111}In for positron emission tomography (PET) and ^{64}Cu for single photon emission computed tomography (SPECT). Functionalisation for detectability by these modalities does not prevent simultaneous functionalisation for other applications such as therapeutic agent delivery or tumour targeting. Where detection is based on conjugation to a reporter moiety, care needs to be taken to ensure that the AuNP and reporter remain attached under the cellular conditions being investigated. This constraint is produced by the fact that functionalisation produces an indirect marker of AuNP presence and concentration rather than the direct measures possible with the optical and x-ray techniques discussed in the previous paragraph.

2.3 An important outstanding consideration in using AuNPs for producing RDEEs

Formulation of gold into nanoparticles brings many advantages as listed above, however it also introduces new mechanisms of enhancement and triggers different cellular responses to bulk gold, meaning that AuNPs should not be considered de facto safe, chemically inert, or biocompatible. Indeed, it has been demonstrated as recently as January 2020 that AuNPs are open to degradation through biological pathways, and may spontaneously form different nanostructures to their original design[156]. Though this process takes several weeks, it highlights the importance of considering long-term clearance of AuNPs if they are to be used clinically. Additionally, AuNPs have been shown across multiple studies to interfere with cell proliferation, spheroid development, cell cycle progression, to reduce cell survival and even to bias stem cell differentiation[196].

This chapter has painted a picture of both the promise and the complexity of using AuNPs for delivering a RDEE. Many of these challenges will require extensive biological and chemical investigations to generate the data necessary to predict a given AuNP's RDEE given its concentration and the cancer being treated. Standardisation in metrics and procedures for measuring RDEE will be needed for these results to be properly compared and replicated, and it is not clear that current procedures and metrics found in the literature appropriately reflect clinical outcomes. This topic will be returned to in Chapter 8.

It should be borne in mind that there are many ways in which modern radiotherapy treatment is currently unoptimized, especially in the case of internal radiotherapy treatments such as brachytherapy and centrally administered radiopharmaceuticals such as yttrium microspheres[197]. As Chapter 1 showed, the history of radiotherapy is not one in which results were carefully and systematically predicted based on fundamental science, but rather one in which lessons were learned and techniques incrementally refined. Whilst as a physicist I appreciate the value of careful design, modelling and optimisation in advance, I am equally cognisant of the lessons from the history of

medicine that benefits are relative, and that imperfect solutions can often be transformative despite their sub-optimality. I am thus not as pessimistic about the timeframe in which AuNPs can be used clinically as DEAs as this chapter might initially imply. Indeed, even regarding the major problem of designing AuNPs that are large enough to utilise EPR effects for targeting yet small enough for intracellular targeting and organism clearance, approaches have been suggested which show great promise. For example, it has been suggested that AuNPs can be encapsulated *en masse* so that small AuNPs act collectively as large enough to effectively target and monitor[198]. Once no longer needed, the encapsulation degrades, releasing the much smaller AuNPs that are then more readily and rapidly cleared from the patient. Assuming therefore that AuNPs suitable for RDEE can be designed, there remains one major prerequisite for their clinical use as radiotherapy DEAs: the distribution of AuNPs within a patient must be measurable prior to treatment commencing.

Imaging AuNP distributions *in vivo* is a precursor to using them clinically for a couple of reasons. Firstly, in developing AuNPs, the accuracy of their targeting will need to be validated in humans, a task which would be considerably easier if the AuNPs could be imaged safely and non-invasively. Such imaging would also allow for quantification of RDEEs to be linked to AuNP concentrations using clinically relevant metrics and with complete human system responses included, e.g. immune responses and body clock variations. Secondly, once in clinical use, imaging is necessary for predicting where RDEEs will occur so that radiation distributions can be modelled appropriately in patient treatment plans. The difficulty of this latter task is compounded by the low concentrations at which RDEEs have been measured in cells *in vitro*, as if these same concentrations are needed to produce RDEEs *in vivo* then extremely sensitive imaging modalities will be required. Detection of AuNPs at these concentrations can be assisted by functionalising the AuNPs for a given imaging modality, though whether the imaging optimisation criteria will align or conflict with the RDEE optimisation criteria needs investigating.

2.4 Conclusion

Ideal DEAs in radiotherapy have a range of design constraints on them, having to accumulate selectively at the site of disease, be capable of penetrating both the dense extracellular matrix and individual cell membranes, as well as potentially being targetable to specific subcellular structures to maximise RDEEs. AuNPs are versatile DEAs, tailorable to target organs in organisms and subcellular components within cells, with techniques for simultaneously doing both being developed. Additionally, they can act to deliver RDEEs via a range of mechanisms, increasing radiation lethality in all three major domains from energy deposition through to cell death pathway activation. There are still limitations to AuNP use as radiotherapy DEAs which will require multidisciplinary approaches to resolve. Nonetheless, their many advantages outweigh their main disadvantages and make them prime candidates for the future in delivering RDEEs, motivating their inclusion in this thesis.

Standardised metrics for measuring RDEE are needed so that the literature results can be better compared with new and emerging models for RDEE. Additionally, better reporting of experimental parameters would facilitate more rapid gains in understanding and validating mathematical and computational models of RDEE. Whilst computer models to exactly predict the RDEE a given AuNP will produce in a given tumour do not yet exist, several approaches have produced approximate results that may be sufficient for some clinical applications.

The outstanding hurdle to the clinical adoption of AuNPs as radiotherapy DEAs that this thesis seeks to address concerns imaging. Specifically, this thesis is assessing the capability of quantitative imaging modalities to detect AuNRs *in vivo*. Such systems would likely need sufficient sensitivity to detect the low concentrations of AuNPs associated with RDEEs, though the exact sensitivity required will vary based on AuNP, tumour and radiation parameters. Two imaging modalities which can potentially exploit unique properties of AuNPs for quantitative *in vivo* imaging are discussed in this work. The first of these is **photoacoustic spectral imaging (PASI)** and the second is **x-ray photon-counting spectral imaging (x-CSI)**.

Whilst only recently emerging into the clinical space, PASI is a more developed technique than x-CSI, with preclinical and clinical systems both available. It is widely researched for both *in vitro* and *in vivo* applications, so will be reviewed primarily based on the literature currently available at the time of writing this thesis. A major feature of PASI is that its ability to detect AuNPs is highly dependent on the AuNPs being optimised for this modality. Whether and to what extent this imaging focussed optimisation will interfere with RDEE focussed optimisation is a key outstanding question. The features of this imaging-based optimisation will be discussed in more detail in Chapter 3 and will be investigated experimentally in Chapter 8.

x-CSI is a bleeding edge medical technique based on adapted particle physics technologies. As a bleeding edge technique, by definition, x-CSI promises to deliver major advances in AuNP quantification compared to existing technologies, however there is a correspondingly large uncertainty as to how best to achieved this. Optimisation of x-CSI systems for AuNP quantification is made more difficult by the lack of clinical scanners currently available and the prohibitive cost (for a PhD project) of a preclinical system. For these reasons, much of the work in this thesis is performed *in silico*, with an aim to expanding our understanding of how these systems can be optimised for AuNP quantification. It is my hope that this work can thus mitigate some of the risks associated with x-CSI development, making its edge more cutting than bleeding.

This concludes the background and motivation section of this thesis. Though long, I hope the reader agrees that the complexity of the subject, and the multidisciplinary nature of its study, justifies its length. The remainder of the thesis will consider these two emerging imaging modalities as they relate to AuNP imaging and RDEE.

Chapter 3.

**Photoacoustic
spectral imaging
(PASI)**

3.1 *The role of PASI in this thesis*

Since this PhD was started in 2015, the use of AuNPs with PASI has grown to the point where PASI can now arguably be regarded as the current gold standard for *in vivo* AuNP imaging. Of particular importance is that PASI has shown a sufficiently high sensitivity to AuNP presence that it is able to detect AuNPs at the lowest concentrations ($\sim 0.1\mu\text{g/ml}$) currently studied for generating AuNP-mediated radiotherapy dose enhancement effects (RDEE)[199]. The limitations that remain to imaging AuNPs with PASI for radiotherapy dose enhancement prediction in clinical applications are now either intrinsic to the technique (e.g. depth of imaging) or application specific and a function of AuNP properties. This thesis therefore does not address PASI system design modifications, but rather focuses on how these limitations could be overcome by either utilising a different imaging technique or utilising specially designed AuNPs. To appreciate why PASI is so well suited to AuNP detection, as well as why alternative solutions need to be investigated, a solid grounding in the basics of PASI is useful. This chapter endeavours to give the reader such a grounding, although it is not intended to be an exhaustive explanation of the technique.

3.2 *Fundamentals of PASI*

3.2.1 History

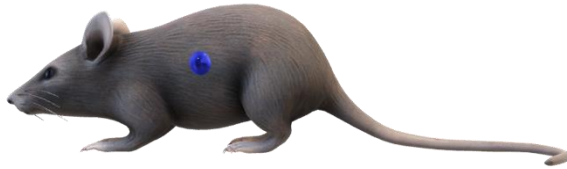
Photoacoustic imaging, also known as optoacoustic imaging, employs a combination of the frequency dependent absorption of a modulated electromagnetic wave and the resulting thermoelastic expansion of the absorber due to non-radiative deexcitation to generate an image. Photoacoustic techniques can use a variety of electromagnetic waves, from radio waves to x-rays, to generate a thermoelastic response, which in turn generates an acoustic pressure wave that can be detected and converted into an image. The intensity of this image relates the spatial coordinates to the relative intensity of absorption of the incident electromagnetic wave. Photoacoustic effects were first reported by A. G. Bell in 1880, when he noticed that optically absorbing materials generated audible sounds when exposed to pulses of sunlight[200]. Despite this early observation, little progress was made in the field of photoacoustics until the 1970s when L. B. Kruezer showed that extremely low levels of contaminants in gas samples (as low as parts per billion) could be detected using photoacoustic techniques[201]. Knowledge of photoacoustic techniques rapidly expanded in the following decades, as illustrated in detail in the wide-scoped literature review paper by C. Tam in 1986[202], and found application in a range of fields including surface analyses, sample quality control and imaging. For the purposes of this thesis however, we focus on the application of photoacoustic techniques to medical imaging. The most widely used form of photoacoustic imaging in the medical field involves the use of photons with a wavelength in the region spanning visible and infrared (Vis-IR) light. The term photoacoustic is thus used here to refer to the absorption of Vis-IR radiation by a sample to generate an

acoustic response. For completeness, the reader should note that the term “photoacoustic” also includes less-common mechanisms for generating acoustic waves such as electrostriction or photochemical change, but these are not relevant to this thesis and so are not considered here. It should also be noted that photoacoustic imaging can be performed either by irradiating with a modulated continuous light source and analysing the acoustic signal in the frequency domain, or by irradiating with short pulses of light and analysing the acoustic signal in the time domain. As is common in medical photoacoustics, however, this work focuses exclusively on pulsed irradiation and time domain analysis of the resulting acoustic signals.

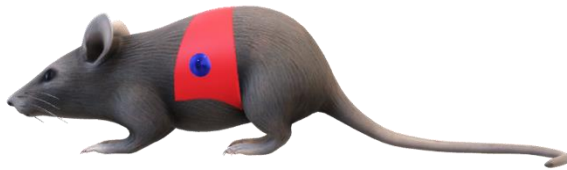
3.2.2 Imaging process

Figure 3.1 shows the stages involved in photoacoustic imaging. The first stage involves the irradiation of the material to be imaged (which may be an *ex-vivo* sample or region of interest within an organism) with a short pulse (dependent on imaging system, though usually in the range of 5 - 10 ns[203]) of Vis-IR photons. Where the region being imaged is not superficial, the Vis-IR wavelengths used are chosen to fall within one of the “optical windows” for body tissues, maximising photon fluence at the desired imaging location. Optical windows refer to the intervals of wavelengths at which penetration depths in body tissue are the greatest. It should be noted that unlike other optical techniques, photoacoustic imaging does not require a low ratio of the scattering to absorbing coefficients, as the light is not collected to form an image. Rather than being a source of degradation to spatial resolution, optical scattering in acoustically focussed photoacoustic imaging is beneficial in that it allows for a more homogenous illumination of the target area, reducing potential artefacts caused by differences in illumination intensity. Consequently, photoacoustic techniques can generally image to greater depths than other optical techniques, as the light only needs to propagate into the sample and not back out again.

The optical windows are located between peaks in the absorption spectra of H₂O, and currently 4 potential optical windows have been identified, as shown in Table 3.1. Which optical window is used will depend on a range of factors including: light attenuation due to endogenous chromophores present; the water content of the tissue; the optical structure of the tissue illuminated tissues; the depth of the region of interest to be imaged; signal generation from the endogenous chromophores and/or any exogenous contrast agents used. As a general principle, the preferred optical window will contain a wavelength, which maximises the fraction of absorption that is due to the chromophore of interest. For medical imaging without the use of exogenous contrast agents, the first optical window is generally preferred, due to the abundance of endogenous chromophores (e.g. deoxy-haemoglobin (Hb) and oxy-haemoglobin (HbO₂)) that have strong absorption peaks in this region. A notable exception to this is in the imaging of bone or where other collagen rich structures are the target of imaging, as the fourth window can potentially provide a higher contrast in these cases[204]. Little work has been done in this



Set up: Mouse or other patient/organic sample contains a target optical absorber (blue sphere), either endogenous or exogenous. Ultrasound transducer and light sources (not shown) are acoustically and optically coupled (respectively) to the patient/sample.



Step 1: Light corresponding to a wavelength from an optical window is shone onto the animal and so penetrates, through scatter and transmission, to a sufficient depth to cover the optically absorbing target.



Step 2: The absorber converts the absorbed light into heat, causing a localised increase in pressure (light blue sphere) which initiates a pressure wave.



Step 3: The transient pressure-increase results in an acoustic wave which propagates outwards throughout the patient/sample. Detection of part of this wave by an ultrasound transducer yields a signal which can be used to construct an image relating spatial coordinates to optical absorption at the wavelength used in Step 1. This is a photoacoustic image. Steps 1-3 can be repeated at a range of wavelengths to generate for each pixel in the image an associated optical absorption spectrum. Such a data set is referred to as a photoacoustic spectral image.

Figure 3.1. Steps involved in acquiring a photoacoustic image. For simplicity, the case of a single optically absorbing structure is shown (blue sphere), and the light source and ultrasound transducer are not shown. The light source is assumed to be placed on the mouse's back, at the top of the figure.

window however, so it is too early to make any definitive statements as to its practical usefulness. This said, it should be noted that were it shown to be possible to achieve higher depths of imaging for collagen using this window, it could be of particular use in oncological applications due to the role collagen structure can play in cancer disease progression[205][206].

Table 3.1. List of optical windows proposed in the literature and their corresponding wavelength ranges. Note that the first and second windows were originally proposed as a single window, before later being reclassified based on the increasing contribution of water to absorption above 950 nm.

Optical Window	Range of wavelengths (nm)
First window	650 - 950[207]
Second window	1000 - 1350[208]
Third window	1600 - 1870[209]
Fourth window	2100 - 2300[204]

A point of clarification regarding terminology is needed here due to the cross disciplinary nature of this field. In biochemistry, chromophore refers to the parts of a molecule where the energy of a change in molecular orbitals corresponds to the energy of a visible photon. Chromophores are thus responsible for the colour of coloured biomolecules. However, in this thesis the term chromophore is used in keeping with its use in the field of bioimaging: to indicate a biomolecule, in its entirety, that can absorb a photon from the ultraviolet to infrared region of the electromagnetic spectrum.

The second stage of imaging involves the chromophore absorbing an irradiating photon and so increasing in energy. The stimulating optical pulse is sufficiently short in duration that the deposited energy can be assumed to remain local to the site of absorption during the irradiation. This additional energy is then dissipated via one of a range of mechanisms, depending on the material involved, as illustrated in Figure 3.2. It should be noted that whilst biological molecules deexcite primarily via direct conversion of absorbed energy to thermal energy, exogenous contrast agents may utilise indirect pathways for this conversion, as shown in Figure 3.2. Where such mechanisms are employed, the generation of heat may present as a delayed impulse, spread out in time, or avoided entirely. This thesis concerns itself primarily with endogenous chromophores and exogenous contrast agents that utilise the direct conversion of light energy to heat however, so for our purposes the generation of heat from absorbed optical energy can be assumed to be rapid, leading to a sharp local rise in temperature. It is important to note that, in the case of AuNPs as exogenous contrast agents, it is not the AuNPs themselves that generate the acoustic signal but rather the medium with which they are in close contact. The AuNPs serve the role of transducing the optical input into a thermal output. This heat is then transferred to the surrounding medium, which undergoes the thermoelastic expansion that drives the photoacoustic (PA) signal.

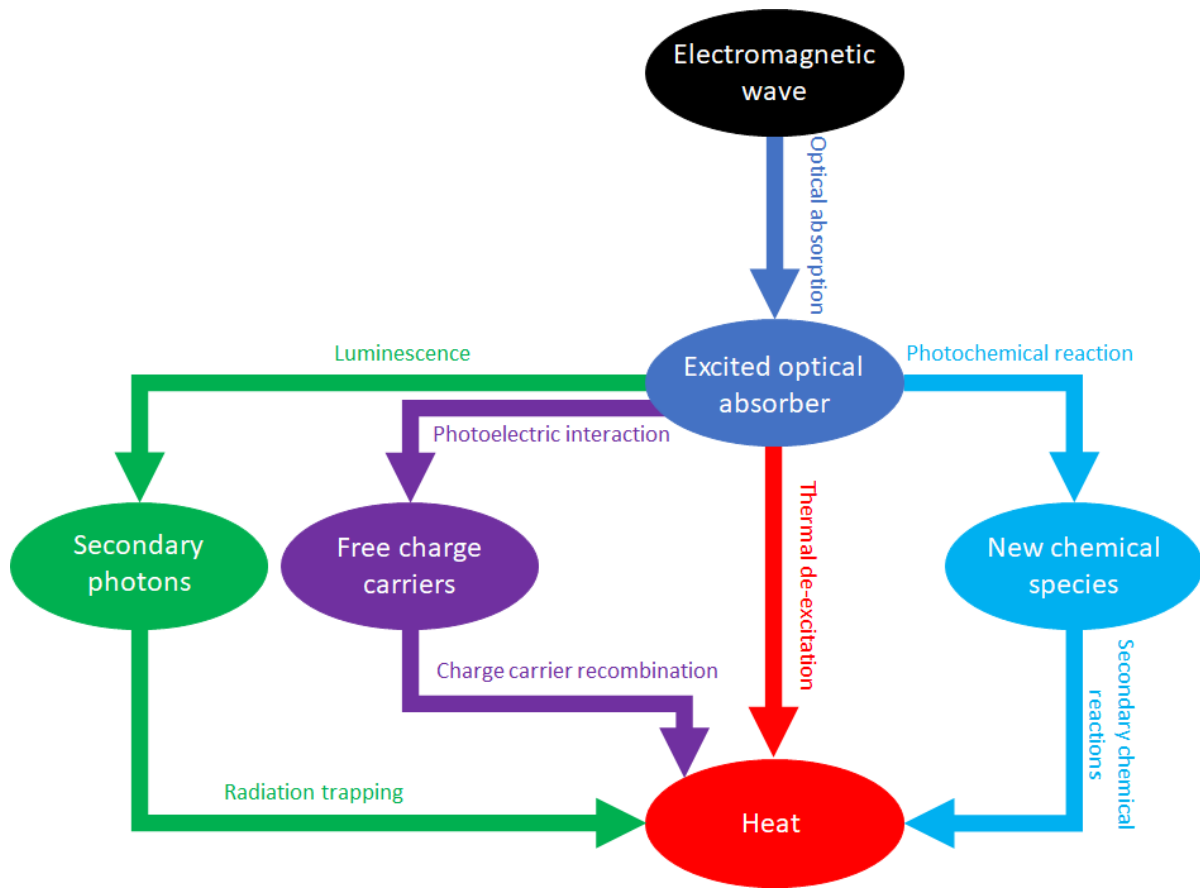


Figure 3.2. Flow diagram of possible energy dissipation mechanisms for optical absorbers relevant to photoacoustic imaging, based on work by A.C. Tam[202]. Ovals represent the form of the excitation energy at each stage whilst arrows indicate the processes which result in the energy changing form. Luminescence (green), photoelectric (purple) and photochemical (light blue) mechanisms may all lead to heat as a product, however their transition through intermediary stages results in a delay to heat production when compared with direct thermal deexcitation (red). Which mechanism dominates will depend on the absorber type and energies involved. For the purposes of this thesis, direct thermal deexcitation is the primary mechanism of interest.

Two conditions are required for effective photoacoustic signal generation: thermal confinement and stress confinement.

Thermal confinement requires that the illuminating pulse duration, t_p , is short compared with the time required for heat to conduct away from the heated region. If this condition is met, then the localised heating will result in a localised increase in pressure around the absorber.

Stress confinement requires that t_p is short compared with the time required for a pressure modulation to escape from the heated region. This condition can be expressed in the equation

$$t_p < \frac{L}{v_s} \quad \text{eq. 3.1}$$

where L is the diameter of the absorbing region and v_s is the speed of sound in the medium being imaged[210]. For medical applications, values of t_p are typically of the order of nanoseconds at most,

to ensure this criterion is met. The rapid rise in temperature of an absorbing target (and, through thermal interaction, molecules in its immediate vicinity) without time for thermoelastic expansion produces a transiently increased pressure in the immediate vicinity of the absorbing target.

In the third step illustrated in Figure 3.1, the transient rise in pressure leads to the dissipation of energy from the absorbing region as an acoustic wave. This wave propagates outwards from the heated region and can be collected by an array of ultrasound transducers to determine the location of the absorber that emitted it, using standard ultrasound imaging techniques (receive-mode only). The deexcitation of the absorber via heat generation causes a rapid relaxation of the absorber back to its ground state, and the dissipation of this absorbed energy by acoustic propagation and thermal diffusion allows for the temperature to return to its original value, ready for the process to be repeated. Acoustic pulses can thus be generated at a high repetition rate, providing photoacoustic imaging with good temporal resolution.

The above procedure allows for the location of an optical absorber, O , to be determined, and the acoustic signal source intensity, I_i , produced can be shown to be a function of the molar optical absorption coefficient of the absorber, e_o , concentration of the absorber, $[O]$, fluence of light at the absorber (F_L) and the efficiency with which the absorbed energy can be converted to acoustic energy, η , as shown in Equation 3.2.

$$I_i = e_o[O]\eta F_L \quad \text{eq. 3.2}$$

e_o varies between absorbers, and η varies depending on the mechanism responsible for acoustic wave generation. As the absorbers considered in this thesis (endogenous chromophores and exogenous AuNPs) utilise direct conversion of optical energy to heat and thermoelastic expansion of the surrounding medium as their mechanism of acoustic signal generation, η can be taken to be a constant with a value in the range of 10^{-12} to 10^{-8} [202]. Note that this value cannot be derived from the thermomechanical properties of either the medium or AuNPs in isolation, as the mechanism for acoustic emission involves transfer of heat from AuNPs to the surrounding medium and the consequent thermoelastic expansion in both (primarily the medium). Due to this extra step of thermal transfer, which depends on the thermal coupling between the AuNP and medium, the thermomechanical properties of the AuNPs and medium alone are insufficient to establish the photoacoustic signal generation efficiency. F_L varies in a depth and wavelength dependent manner, based on the scattering and absorption properties of the tissues both above and below (due to backscatter) the imaged region. The properties of the absorber itself are largely irrelevant to the fluence on the absorber at depth however, so for now we will consider the fluence at a given location to be a constant regardless of the absorber present at that depth. This still leaves the acoustic signal intensity proportional to the variable e_o and $[O]$, so it is not possible in purely photoacoustic imaging to distinguish, for example, a region with $[O] = Y$ and $e_o = X \text{ cm}^{-1}$ from a different region with $[O] = Y/2$ and $e_o = 2X \text{ cm}^{-1}$. This is the case

even before uncertainties associated with F_L and η are considered. To distinguish between different absorbers without the need for *a priori* knowledge of the absorbers involved, photoacoustic imaging requires spectral information, as discussed in the next section.

Before moving on it should be noted that thermal transfer and thermal expansion of the AuNP and surrounding medium are not the only mechanisms by which heat can be dissipated in this process. At sufficiently high laser energies the AuNPs can boil the water in their immediate vicinity, melt, deform or even be partially vapourised themselves[211][212]. These events, referred to as non-linear effects[213], can result in strong photoacoustic signals and show a high sensitivity to laser energy, changing the relation between AuNP concentration and photoacoustic signal strength. Non-linear effects do not occur below a threshold energy however, and for the purposes envisioned in this thesis it is likely that laser energies would be kept below this threshold. There are multiple reasons for keeping the laser energies below the threshold for non-linear effects. Firstly, it is desirable to avoid unpredictability in the relation between RDEE and AuNPs that would occur if their shape/coating/size is altered in the PASI process. Secondly, the increased sensitivity to laser energy would mean that uncertainties in laser energy (due to online fluctuations) would correlate to increased AuNP quantification uncertainties. Thirdly, if vaporisation of the medium the cell is in contact with occurs then the intensity of the photoacoustic signal generated will also depend on the material being vaporised, again compounding the uncertainty.

3.2.3 Spectral separation of contrast agents

The value of the photo-to-acoustic conversion efficiency, η , for a given absorber is constant during the imaging process, assuming heating effects have time to fully dissipate between optical pulses so that the target's temperature just prior to each optical absorption is constant. Whilst $[O]$ can be reasonably approximated as constant for a given voxel during image acquisition, e_o varies as a function of wavelength. This gives a way to differentiate between different absorbers by measuring how the acoustic signal varies as a function of stimulating wavelength, λ . Figure 3.3 shows the optical absorption coefficient profiles of Hb and HbO₂, with the first optical window highlighted in an inset. It should be evident that if two wavelengths are selected, the behaviour of the two absorbers could be distinguished: if the photoacoustic signal intensity is higher at 900 nm than at 700 nm then it is likely to be HbO₂ rather than Hb. Where two absorbers are both present in a voxel, the relative proportions of each can be estimated using spectral unmixing approaches. Spectral unmixing can be performed in a variety of ways, with most involving some form of least squares regression, in which the measured spectrum from the sample, \mathbf{G} , is expressed as a linear superposition of the spectra of absorbers in the sample such that

$$\mathbf{G} = [O_1]\mathbf{A}_1 + [O_2]\mathbf{A}_2 + [O_3]\mathbf{A}_3 + \dots [O_n]\mathbf{A}_n \quad \text{eq. 3.3}$$

where $[O_{1-n}]$ represent the concentrations of the n absorbers and \mathbf{A}_{1-n} represent the product of η , F_L and e_o of the absorbers, as a function of λ . Generally, these methods share the constraint that where n

absorbers are concerned, n different wavelengths are required to determine a unique solution. A physical constraint is also applied, such that $[O_n] \geq 0 \forall n$, to reflect the reality that absorbers cannot be present in negative concentrations.

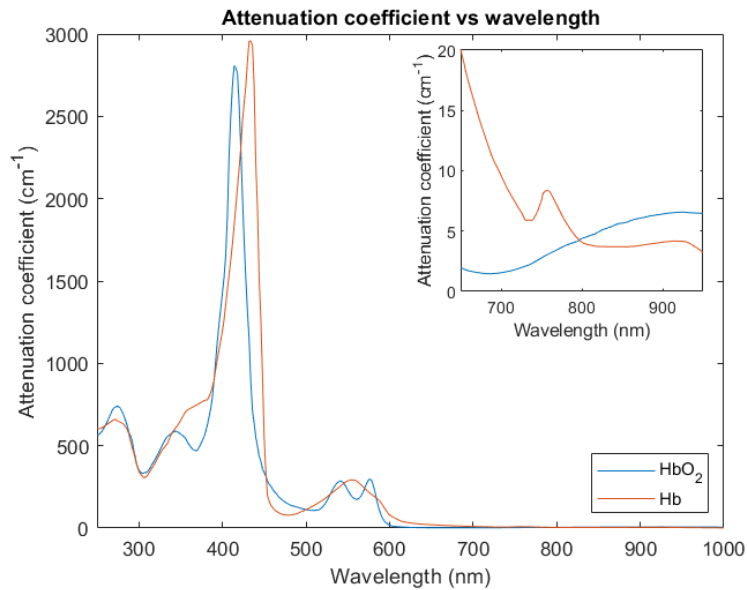


Figure 3.3. Plot of the optical attenuation coefficient versus wavelength for deoxy-haemoglobin (Hb) and oxy-haemoglobin (HbO₂). Whilst attenuation is shown, these complexes are almost non-scattering at these wavelengths and so these curves also represent absorption. Data for the plots was obtained from OMLC.com[216].

A cautionary note should be made concerning spectral unmixing approaches where the concentration of a given absorber being analysed is likely to vary with time. This is due to the finite time required to obtain an image at a given wavelength: the more wavelengths that are scanned, the less valid the approximation that $[O]$ is constant is. Similarly, whilst a variety of approaches to calculate the dependence of F_L on wavelength and depth in a given tissue have been proposed[214], all have narrowly defined applicability based on assumptions regarding the tissue type, measurement geometry, ultrasound frequencies or optical probing wavelengths used. A more generally applicable method has been demonstrated for quantifying metallic nanoparticles in tissue with unknown optical properties[215], by using a series of calculations to replace the unknown F_L in the quantification equations with $\delta A/\delta F$, and two probing fluences for each wavelength to measure the value of $\delta A/\delta F$. This approach requires calibration using AuNPs *in vitro*, and may not be applicable to endogenous chromophores, low AuNP concentrations or wavelengths away from the plasmonic resonance of the AuNPs due to the built-in assumptions that the photoacoustic signal from nanoparticles is substantially larger than the photoacoustic signal from other absorbers in the imaging volume and linear in nature. Additional assumptions include that the nanoparticles do not thermally or optically couple together and that the thermomechanical properties of the material in contact with the AuNPs is known. The implication of these assumptions on the utility of this quantification method as part of predicting AuNP-mediated RDEE will be returned to in the overall discussion section of this thesis.

3.2.4 Advantages of PASI

PASI displays significant strengths as an imaging modality due to its combination of optical stimulation with acoustic signal detection. Optical absorption spectra are known to vary strikingly between endogenous chromophores in the human body[217], allowing for differentiation of materials that would be difficult to differentiate based on their ultrasound echo alone, such as differentiating between Hb and HbO₂. In addition, changes in tissue colouration associated with disease onset are well known (e.g. the appearance of new moles, yellowing of skin, whitening of tongue, blueish hue in cyanosis etc.) since medical professionals, like most humans, see the world through these wavelengths. Traditional lab-based optical techniques are limited by the high optical scattering and attenuation coefficients in human tissue however, with scattering in particular significantly degrading the spatial resolution of optical techniques and limiting their use to thin tissue sections and depths of only a few mm[218].

In contrast, acoustic techniques have comparably good penetration depths, with scatter coefficients several orders of magnitude lower than their optical analogue[219]. Whilst they can use variations in the speed of sound to discern changes associated with a range of physical properties such as density, rigidity, pressure or temperature, acoustic signals do not distinguish structures based on their chemical state *per se* (oxygenated vs deoxygenated) but rather based on how these states affect the above physical properties. This results in a lower sensitivity of acoustic techniques for detecting such changes clearly. This largely limits the utility of ultrasound imaging to the fields of structural and functional imaging, which restricts the ability of purely acoustic techniques to provide information on metabolic changes in the tissues being imaged.

PASI combines the best of both modalities. The inclusion of optical selectivity in stimulating chromophores allows molecular imaging of the microenvironment. For example, the percentage blood oxygen saturation, SO₂, can be calculated from the measurable concentrations of Hb and HbO₂ according to the equation

$$SO_2 = \frac{[HbO_2]}{[HbO_2] + [Hb]} \quad \text{eq. 3.4}$$

(assuming the percentage of carboxy-haemoglobin to be negligible)[220]. In oncological applications this information can then be used to inform treatment planning, as hypoxic tumours are known to be radioresistant compared with their well oxygenated counterparts[221]. In addition to the wide range of biologically relevant endogenous chromophores, the use of optical stimulation allows for many well studied optical dyes to be employed as contrast agents. These can facilitate better functional imaging of small structures in clinical tasks, such as sentinel lymph node identification during surgical resection of a tumour[222][223]. Finally, optical contrast agents that can monitor molecular expression at the cellular level are under development, though their use *in vivo* is only really feasible in many clinical

applications if a non-optical method of optical-signal readout is available, due to the high scattering coefficient of most human tissues.

PASI also has the major advantage of providing quantitative[215] or semi-quantitative[224][225][226] images, with a high timing resolution, without the need for ionising radiation or exogenous contrast agents. Combined, these make PASI a technique of great interest as a potential tool for routine clinical use. Whilst the penetration depth limits its applicability to relatively superficial cancers, it has shown promise in both diagnosing skin cancers[227] and detecting breast cancer lesions[228], with several prototype systems being investigated[229][230].

Finally, it should be noted that there are clinical applications in which *ex vivo* imaging is required rather than *in vivo* imaging, and specialist PASI systems have been designed for these applications where depth of light penetration is no longer a major concern.

The primary focus of this thesis with regards to PASI is the imaging of AuNPs for RDEE prediction, an intrinsically *in vivo* application. Due to the unknown toxicity risks of circulating AuNPs to humans however, a not insignificant amount of PASI research into imaging AuNPs is performed on small animals or in *ex vivo* setups. The following discussion on the uses of PASI for AuNP imaging will thus contain some examples from PASI microscopy or mesoscopy systems for showing the detection limits specifically with respect to AuNPs. Whilst the same sensitivities may not be possible with larger macroscopic PASI systems, they offer a reasonable upper limit for current PASI technology. Further, the development of hybrid systems capable of taking wide angle images to guide focused mesoscopic/microscopic images means that it is theoretically possible to achieve these limits for localised quantitative measurements[231].

3.3 AuNPs as exogenous PASI contrast agents

3.3.1 Principles and mechanism of AuNP detection

AuNPs benefit from advantages in both the optical and acoustic domains of photoacoustic imaging, making them ideal contrast agents for photoacoustic applications. The extent of their advantages depends on several AuNP parameters, as well as on their intended application, and these will be discussed in detail in the next subsection. For now, we will discuss the basic principles by which AuNPs can be synthesised to absorb at specific optical wavelengths, and how this absorption leads to an acoustic signal.

A single AuNP, being a substantially larger system than a single chromophore molecule, does not contain a single molecular orbital transition that corresponds to the energy of an optical photon. Instead, AuNPs interact with incoming electromagnetic radiation via a plasmon resonance. To understand this mechanism, it is instructive to consider the surface layers of Au atoms in the AuNP as comprising a plasma, with a fixed lattice of positive charges and free electrons. Initially, the electrons

are co-located with the positive ions, resulting in an even charge distribution and no net electric field. Figure 3.4 shows this situation for a single spherical AuNP, suspended in some dielectric medium. Now consider the case as an electromagnetic wave passes, where the wavelength of the wave is much greater than the radius of the AuNP. At a given moment, and to a first approximation, we can treat the electric field present as being constant across the volume of the AuNP due to this size disparity between the wavelength (>650 nm) and the AuNP radius (usually <100 nm). The electrons and ions will thus move in opposite directions in response to this applied electric field, generating a net difference in charge across the AuNP. The magnitude of this internal electric field, φ_{int} , is given by the equation[232]

$$\varphi_{int} = \varphi_{ext} \frac{3\varepsilon_m}{\varepsilon_{Au} + 2\varepsilon_m} \quad \text{eq. 3.5}$$

where φ_{ext} is the externally applied electric field, ε_{Au} is the dielectric permittivity of the AuNP and ε_m is the dielectric permittivity of the medium. The presence of this internal field generates a restoring force on the displaced charges, which will act to restore them to their equilibrium position.

As the electromagnetic wave passes the electric field will vary as a function of time, causing a cycling oscillation of the electrons' displacement relative to the ions, and consequently of the direction and magnitude of the restoring force. By applying the approximation that the positive ions do not move (a reasonable approximation considering the considerable difference between their mass and that of the electrons), the movement of the electrons in the AuNP driven by this changing electric field can be modelled to a first approximation as a mass on a spring system. As per any such oscillating system, a resonant frequency exists, which in this instance is given when the Fröhlich condition is satisfied[233]:

$$\text{Re}[\varepsilon] = -\chi\varepsilon_m \quad \text{eq. 3.6}$$

where ε is the dielectric constant of the bulk metal, χ is a geometrical factor, equal to 2 for the spherical case considered here[234]. It is important to note here that ε and ε_m are both functions of frequency. This resonant oscillation in the electron cloud is referred to as a surface plasmon resonance (SPR). Where the frequency of the electromagnetic wave is equal to the resonant frequency of the AuNP, the electron cloud displacement couples most efficiently to the driving force of the light. Energy transfer, to overcome the restoring force acting against electron displacement, is thus maximised.

Before moving on, it is worth noting from the above discussion that the frequency of a AuNP's SPR is evidently dependent upon three variables: ε_m , AuNP shape (χ) and AuNP size (R), as implied both by the requirement that $R \ll \lambda$ and that larger R can support larger mean electron cloud displacements. Unlike chemical chromophores, AuNPs thus offer the ability to tune their absorption spectrum for a given application.

The energy of the oscillating electron cloud is then dissipated in two ways: radiatively (which is negligible for small nanoparticles at about 1.5% of the total dissipation for $R = 20$ nm[235]) or via electron-hole pair production (the dominant effect for small nanoparticles). The electron-hole pairs then

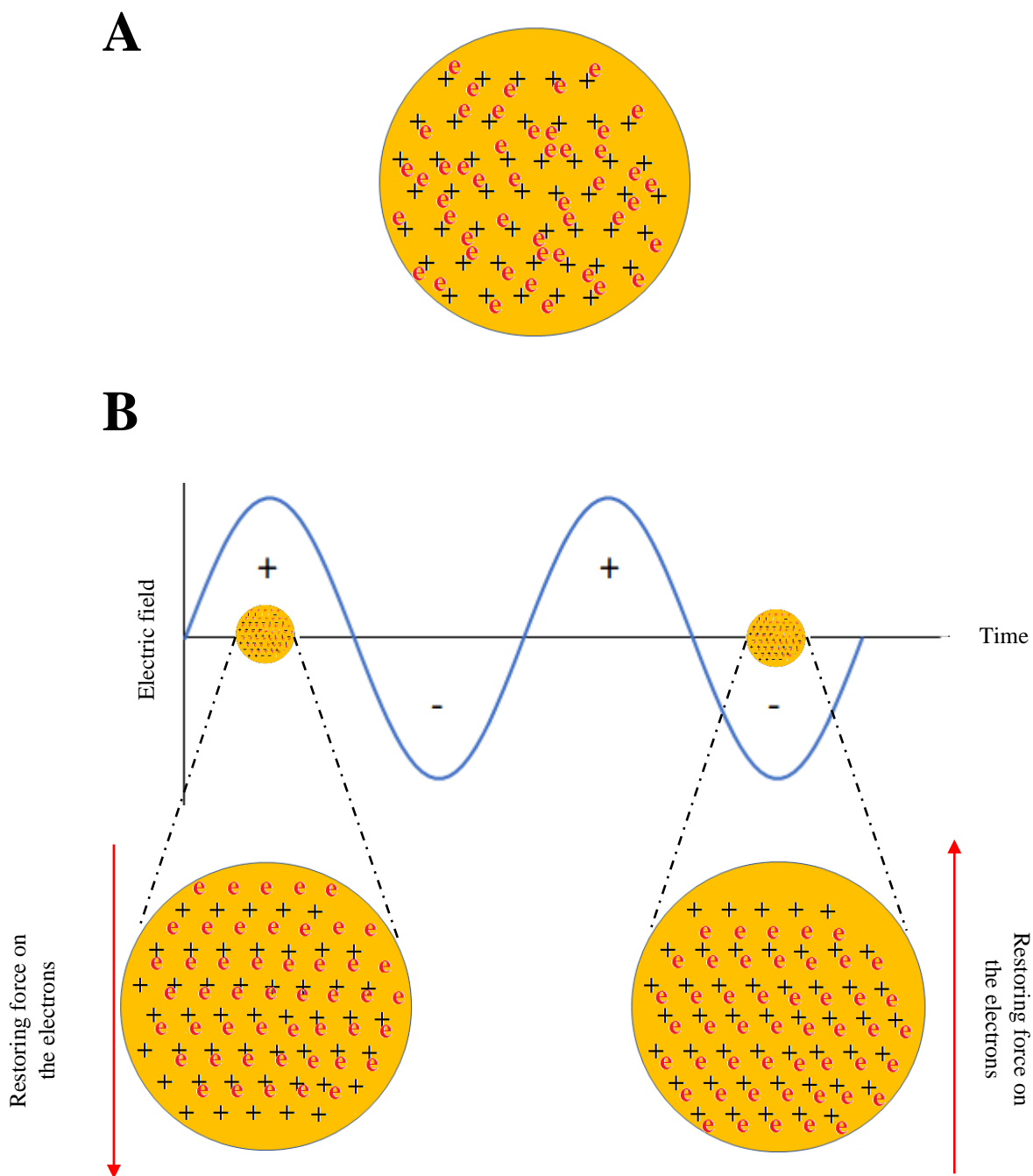


Figure 3.4. (A) Without an external electric field, the electron displacement relative to atomic centres is random and there is no net displacement. (B) In the presence of an external electric field the electrons on the AuNP surface undergo a net displacement to produce an opposing field across the AuNP. A restoring force on the electrons is thus produced to pull them back to equilibrium (as they can be modelled as a mass on a spring).

Since the electric field associated with an electromagnetic wave oscillates with time, the surface electron displacement is also driven in a cyclical manner. When the frequency of the driving wave matches the natural frequency of the surface electron system, resonance is achieved and the restoring force can draw energy from the passing wave most efficiently. Note that the electromagnetic wave and AuNPs are not shown to the same scale as AuNP size has been exaggerated for clarity. For the above mechanism to hold, AuNPs need to be much smaller than the wavelength of the driving electromagnetic wave.

dissipate their energy through interactions with electrons, holes, and lattice phonons, resulting in thermalisation of the particles and an increase in AuNP temperature over the order of about 1-5 ps. Finally, the absorbed energy is dissipated to the surrounding medium via phonon-phonon interactions, over a time scale of tens to hundreds of picoseconds[236].

The result of this process is that an optical photon is converted to a thermal energy increase localised around the AuNP in a roughly sub-nanosecond time frame. This short, localised spike in temperature produces the conditions for a very sharp photoacoustic signal caused by thermoelastic expansion of either the AuNP itself or the water with which it is in contact (N.B. that non-linear effects such as water vaporisation are being omitted in this argument).

3.3.2 Advantages of AuNPs for PASI

The preceding section illustrates how AuNPs possess the prerequisites to serve as photoacoustic contrast agents. This section expands on how a variety of AuNP properties lead to them being well suited specifically for this imaging modality.

AuNPs are particularly good at absorbing optical energy when compared to organic dyes and endogenous chromophores. Indeed, the SPR mechanism of photon interaction employed by AuNPs leads to a molar absorption coefficient approximately 5 orders of magnitude greater than that found in organic dyes[237], though the differences in particle size mean AuNPs are often present at significantly lower molarities. The wavelength of the SPR can be controlled by varying the size and shape of the AuNP so that their absorption can be tailored to a given application, for example to avoid significant spectral overlap with endogenous chromophores in the region of interest. In general, SPR wavelength, λ_{SPR} , can be increased by increasing the AuNP size or by producing a symmetry break in the AuNP design, which results in the production of new resonant frequencies. The simplest example of this is the production of AuNRs, which represent a break in symmetry along one axis, resulting in two SPRs, corresponding to transverse (TPR) and longitudinal (LPR) oscillations of the electron cloud. The λ_{TPR} is centred relatively close to the λ_{SPR} for a AuNS of radius comparable with the narrow dimension of the AuNR, however at a slightly lower energy (higher λ). The value of λ_{LPR} in contrast is usually significantly higher than λ_{TPR} , corresponding to the lower frequency of the resonant oscillation along the longer dimension of the AuNR. More complex shapes such as gold nanoprisms (AuNPr) and gold nanostars (AuNSt) can show even more SPR peaks. The presence of multiple peaks can feasibly be used to differentiate between multiple AuNPs, potentially allowing for the reporting of information on the distribution of a range of biomarkers in a single scan.

As mentioned in Chapter 2, AuNPs can be functionalised with a variety of different biomolecules to allow for targeted binding to receptors or cell types of interest[238], as well as allowing for λ_{SPR} to be adjusted slightly based on chemical interactions between the ligand and the AuNP[233]. This extends the reach of PASI to allow molecular imaging of non-optically absorbing molecules. By

combining this ability with the tunability of the SPR previously discussed, it is feasible to produce a AuNP preparation containing various shapes/sizes of AuNP, with different functionalisation, such that a single injection will facilitate PASI screening for a range of different biomolecules, as well as their quantification. Such multiplexing approaches have been demonstrated in both *ex vivo* and murine models[239][240][241]. In addition to molecular targeting, careful functionalisation of AuNPs can allow for PASI based reporting of the microenvironmental states around them, such as temperature or pH[242][243]. This reporting is usually associated with a change in the AuNP coating that leads to aggregation of AuNPs, resulting in a broadening of the SPR due to plasmon coupling between adjacent particles (see Section 3.4). As tumour microenvironments are known to be more acidic than their normal tissue counterparts, such pH sensing ability could be of use for diagnosing suspicious masses in oncological investigations.

A final synergism worth noting regarding AuNPs and PASI is to do with the nature of the imaging mechanism employed. As PASI relies on the optical absorption of the AuNPs directly, it offers a higher confidence in the localisation of AuNPs than techniques based on the properties of conjugated trackers, such as fluorophores used to assess cell uptake in some AuNP studies. This has added benefit where the imaging is designed to inform treatment, as it ensures peaks in image intensity are collocated with expected peaks in treatment intensity. This is especially true for photothermal therapies, in which the photoacoustic probe beam is of the same wavelength as the photothermal activation beam (though at a lower fluence and for a shorter time) but should also hold true for AuNP-mediated RDEE.

3.3.3 Achievements and potential of PASI in AuNP imaging

The use of AuNPs as contrast agents for photoacoustic measurements is well established, with a consequent plethora of applications conceived and demonstrated in the literature. Indeed, the enhancement associated with AuNPs is so significant that many photoacoustic imaging (PAI) studies employ only a single wavelength, arguing that the strong enhancement of AuNPs results in the AuNP signal dominating the image produced, with background tissues imaged with a standard ultrasound instead and the two images superimposed. This approximation does not hold in situations where tissue with strong photoacoustic contrast is located near to the AuNPs however[244]. Nevertheless, by careful selection of probe wavelength and tissue type, or by subtraction of images before and after AuNP introduction, endogenous contrast can be kept sufficiently low to allow experimental aims to be realised. In assessing the AuNP detection limits using photoacoustic techniques, many studies thus opt to not utilise the spectral advantages of PASI, relying instead on AuNP photoacoustic contrast and single wavelength signal detection. Whilst spectral information is likely to allow the separation of exogenous and endogenous contrast components, information regarding AuNP detection limits in the low endogenous contrast case is likely to give a good indication as to the current detection limits of the technology, sufficient to allow comparisons with x-CSI and RDEE requirements. For this reason, results concerning PAI detection limits will be included alongside similar studies using PASI in this section.

The spatial resolution of PASI systems is known to vary as a function of imaging depth, with lateral resolution, which is diffraction limited, dropping off rapidly from 5 μm at a depth of <0.7 mm to several hundred microns at a depth of several cm[245][246][247][248][249]. This is due to a change in the focussing mechanism from optical at shallow depths to acoustic at greater depths (more than ~ 1 mm). As higher ultrasound frequencies are attenuated more rapidly than lower frequency ones, and as lateral resolution in an acoustically focussed system is proportional to the centre frequency of the detected ultrasound pulse, the resolution thus drops off with increasing imaging depth[203]. Axial resolution, which is dependent on the speed of sound in the medium and the bandwidth of the ultrasound pulse, falls with increasing depth for the same reason, also reaching several hundred microns at an imaging depth of several cm[250]. Within the context of this thesis, namely quantitatively imaging AuNP distributions within a tumour volume and surrounding tissue and at depth, it is likely that spatial resolutions will be of the order of several hundred microns, given the need for acoustic focussing and the results achieved by currently available clinical/preclinical PASI systems[248]. Future developments or optimisations for specific clinical applications may push this limit, however at this point this is only speculative.

Similarly, whilst the upper limit is set by the pulse repetition rate of the optical source, a range of parameters can affect the temporal resolution of a PASI system, including the number of wavelengths being examined, the volume being imaged (as deeper regions require longer for signal propagation to the ultrasound transducer) and the number of optical pulses being averaged over to generate each image frame. Work involving *in vivo* PAI of AuNPs has involved temporal resolutions of the order of tenths of a second to seconds[249]. This high temporal resolution allows not only for the spatial distribution of AuNP labelled cells to be determined, but also the delivery and clearance of AuNPs from the body[225]. Temporal resolutions two orders of magnitude greater are achievable with non-imaging photoacoustic techniques[251], however imaging is a key requirement for the applications envisaged in this thesis and so these techniques are excluded from further analysis here. As an image needs to be obtained separately for each wavelength examined, the temporal resolution deteriorates proportionally with the increase in wavelengths analysed. PASI thus displays slightly lower temporal resolution than PAI techniques, as spectral data is traded against temporal data. As the number of wavelengths probed is usually considerably less than 10 however, the timing resolutions quoted above for PAI systems are likely still the right order of magnitude for PASI techniques. Even were more than 10 wavelengths used, the excellent temporal resolution of PASI would still remain highly relevant to many biological processes. Either way, for the application envisaged for this thesis (quantitative *in vivo* imaging of AuNP distribution within a solid tumour and the surrounding tissue) high temporal resolutions are unlikely to be necessary.

Before further discussing the results achieved involving AuNP imaging with PASI, it should be noted that super-resolution and ultra-fast imaging PASI systems have recently been developed[252].

These systems utilise non-linear photoacoustic effects and the concept of localisation optoacoustic tomography (LOT) to generate images with a spatial resolution down to 0.4 μm [253]. The resolution limits of these systems are likely not applicable to the applications envisaged in this thesis however as the super-resolution imaging techniques require that either the absorbers be quenched (destroyed in the case of AuNPs) or in motion relative to the underlying biological structures between imaging pulses. Either destruction or such relative movement of the AuNPs would invalidate the point of quantifying the AuNP distribution in the first place, which is to predict the AuNP-mediated RDEE. For this reason, despite the impressive resolutions achievable with super-resolution PASI systems, they will not be considered further in this work. With that said, let us now consider some of the demonstrated achievements of *in vivo* AuNP imaging by PASI techniques that are relevant to this thesis.

In assessing PASI sensitivity for AuNP detection, there are many studies that quantify the experimental system's sensitivity *in vivo*[254]. Unfortunately, the majority of these studies assessed sensitivity in terms of the number of AuNP loaded cells that can be detected/imaged, or the number of colony forming units (CFUs) that could be detected. Whilst the sensitivity of these systems in this sense were impressive (down to 0.5 CFU/ml), it is not directly translatable to AuNP quantification as AuNP uptake studies are not routinely performed to quantify the concentration of AuNPs required for detection. Without these data, it is not possible to calculate the sensitivity of these systems in a way that applies to RDEE research. Fortunately, there are a few studies which seek to quantify PASI sensitivity with respect to AuNPs directly. Whilst not all report the equivalent Au concentration (which would be needed for x-CSI and RDEE purposes), sufficient details are available to allow these to be calculated by the interested reader. In general, detection limits for AuNPs vary between 10^{-4} and 10^{-7} g/ml of Au. Sensitivities for gold nanoshells (down to 450 $\mu\text{g/ml}$ [255]), nanospheres (down to 3.1 $\mu\text{g/ml}$ [256]), nanostars (down to 1 $\mu\text{g/ml}$ [257]) and nanorods (down to 0.13 $\mu\text{g/ml}$ [199]) were found. Whilst it is known that different AuNP shapes produce different levels of photoacoustic contrast and thus different detection limits, it is difficult to disentangle this from the various system parameters and experimental setups that will also determine a system's overall sensitivity. This is likely at least partially responsible for the wide range of AuNP detection limits reported (10^{-4} to 10^{-7} g/ml of Au). Importantly, PASI is also able to differentiate between different AuNP types based on their spectral profile[239]. Of particular interest to this thesis, this differentiation of AuNP types has been employed to differentiate between two different cancer cell lines *in vivo* based on the optical absorption peak of differently functionalised AuNPs[244].

Before closing this chapter on the achievements of PASI in quantitatively imaging AuNPs *in vivo*, it is worth considering the advances in AuNP design and development that PASI techniques have facilitated. The effective targeting of AuNPs to specific cell populations *in vivo* based on their cell surface proteins has been demonstrated by several groups[244][258]. Whilst these studies involved the targeting of cells within circulating blood flow rather than stationary within a solid tumour, the principle

of *in vivo* cell surface protein targeting as a mechanism for selectively marking a cell population with AuNPs was nevertheless demonstrated. AuNPs have also been designed which report their immediate cellular environment via PASI without functionalisation, producing a shifted spectral response upon being endocytosed[259]. Similarly, AuNPs have been made that can actively target cancer cells without the need for antibody conjugation[243]. These “smart” nanoparticles are very small (10 nm) and so permeate both healthy and cancerous cells. The acidic environment of the cancer cells results in their aggregation however, preventing their clearance from the cell and shifting their spectral response. As a result, they have been shown to accumulate in cancerous cells at concentrations 17 times greater than healthy cells[260], and with a characteristic shift in spectral profile that can be detected by PASI.

3.4 Limitations of PASI

Despite its clear utility to a range of applications involving both structural and functional imaging, PASI’s utility can be severely restricted for some applications. The application of interest to this thesis is the quantitative imaging of AuNPs for predicting AuNP-mediated RDEEs. The currently known and foreseeable potential limitations of PASI with regards to this application will now be considered.

The primary limitation of PASI that is unlikely to see significant progress in the short term lies in its limited depth of imaging (5 - 7 cm[261]). Whilst transrectal probes[262][263] and endoscopic solutions[264] have been developed or suggested to allow for imaging non-superficial body structures, these will sacrifice one of the biggest advantages of PASI for many applications, namely its non-invasiveness. In the context of cancer surgeries this may be acceptable, as access to the site is readily available and the techniques being employed are inherently invasive to some degree. In the case of AuNP-mediated RDEEs however, the long-term ambition is for the particles to be self-targeting, accumulating selectively at the tumour location. The inability to image deep structures is thus a fundamental limitation to the tumour types that PASI can image in this respect. Further, even if delivery of optical stimulation were somehow overcome, (I would suggest this could perhaps be achieved by chemically induced optical photon generation), deeper imaging depths inherently still suffer from reduced spatial resolution. This is due to the frequency dependent acoustic attenuation, which reduces the centre frequency and bandwidth of the ultrasound pulse as it propagates, reducing axial and lateral spatial resolutions. This will also limit the spatial resolution of any possible AuNP-mediated RDEE predictions, as a function of depth.

The second potential limitation to PASI use for the proposed application involves the change in spectral behaviour associated with AuNP aggregation. As discussed above, the value of λ_{SPR} for a AuNP varies with its size, and secondary SPR peaks can be produced by spatial symmetry breaking of possible collective electron oscillations. The explanation given above considered the case of a single AuNP suspended in a dielectric medium, and at low AuNP concentrations this is a fair approximation.

At higher AuNP concentrations however, such as when the AuNPs are collectively packaged for endosomal uptake into a cell, the distance between AuNPs becomes small enough that their electron oscillations can couple. The strength of the coupling varies with distance, as the electric field enhancement around the surface of a nanoparticle drops off with distance. The result of this coupling is the generation of new modes of oscillation in the AuNP system, which can cause either a red or blue shift in λ_{SPR} . The mechanism for this can be appreciated by again considering the collective electron oscillations to be modelled as a mass on a spring: the collective oscillation can be of higher or lower frequency, depending on whether the springs are connected to the masses in parallel or in series respectively. This is a potential issue if PASI is to be used for quantifying AuNP concentrations in these situations, as the spectral response of the AuNPs will not be constant with concentration. Further, whilst the size of the wavelength shift can be approximated from knowledge of the particle spacing for AuNP dimers[265], the number of possible coupling modes increases rapidly with increasing number of aggregating AuNPs, resulting in a much more unpredictable change to the spectral profile. This change in spectral profile can be mitigated by using molecular spacers to prevent AuNPs getting too close together, for example by encapsulating the AuNPs in silica shells[266]. Silica encapsulation also provides the added benefits of improving thermal stability[161] and photo-to-acoustic conversion efficiency, η , by providing a better thermal coupling between the AuNP and the surrounding medium. Spectral shift can also be reduced by lowering the AuNP concentration, for example by providing a mechanism for endosomal escape[168]. The effect of AuNP aggregation is thus not an absolute bar to using PASI for quantitative imaging in the application considered here, but rather a constraint that needs to be borne in mind.

A potential issue that arises from this constraint on AuNP spacing involves the interplay between this constraint and the various mechanisms of AuNP-mediated RDEE. As alluded to in Chapter 2, AuNP-mediated RDEEs can occur via a variety of mechanisms, which may interfere with each other. The total number of AuNPs delivered to a treatment site is limited by both the difficulties of loading high concentrations of AuNPs selectively into tumour volumes and the potential toxic effects associated with AuNPs at higher concentrations. AuNPs should therefore be designed to optimise the RDEE that they deliver, maximising their utility. Given the mechanisms shown to affect AuNP-mediated RDEE so far, it is a fair assumption that such AuNPs should have the maximum surface area:volume ratio. This is because such a configuration will ensure maximum escape of fluorescence x-rays and Auger electrons from excited Au atoms (by minimising self-attenuation from Au atoms within the same AuNP) and maximise the exposed surface area for catalytic interactions. Whilst the mechanism responsible for AuNP-mediated downregulation of gene expression is not yet known, it seems reasonable, given what is known, that it will be due to a chemical interaction of some description between the AuNP and a cell component, or by an increase in ROS produced by the catalytic properties of the AuNP surface. The potential for conflict here is evident where silica is used as a AuNP coating for example, as this will

inherently reduce access to the AuNP surface for chemical and biological interactions. Selection of shape to tune λ_{SPR} to a desired value in the optical window for imaging may also result in a sub-optimal geometry for AuNP-mediated RDEE.

In addition to affecting the mechanisms of AuNP-mediated RDEE, tailoring AuNP shape and size for PASI detection may also affect the kinetics of circulation time, tissue uptake, cellular uptake, and clearance of AuNPs, as well as their intracellular compartmentalisation, in ways that are incompatible with the aims of AuNP-mediated RDEE therapy. As discussed in Chapter 2, there is ongoing work to optimise AuNPs such that they can exploit the EPR effect (requiring larger size) whilst still being able to access intracellular nuclear compartments (requiring smaller sizes). A current trend appears to be in the delivery of small particles (for nuclear penetration and easier clearance) by larger, temporary structures, such as liposomal delivery[267] or AuNP assemblies that are either biodegradable[198] or can be externally triggered to disassemble[268]. Despite this, it is not yet known whether a solution to AuNP design exists that can satisfy these varied constraints in the context of maximising AuNP-mediated RDEEs, and the addition of PASI signal strength and spectral properties to the list of parameters being optimised for will likely reduce the possible solution space still further.

3.5 Relevance of this work to PASI for RDEE prediction.

PASI detects AuNPs based on their intrinsic optical properties, making it particularly well suited to the task of imaging AuNPs *in vivo*. The swap in signal detection and focussing from optical to acoustic domains significantly reduces signal degradation in PASI, with the probe beam effectively penetrating further than in optical techniques and the response signal suffering less interference from the probing impulse. The ability to tune their plasmon frequency into an optical window, their strong optical absorbance (in this window, compared to the tissues they are in) and the high efficiency of photo-to-acoustic conversion associated with AuNPs makes them excellent contrast agents for PASI based *in vivo* work specifically. The above features result in an exquisite sensitivity for AuNPs, with detection shown down to $\sim 0.1 \mu\text{g/ml}$ of Au with AuNSt. Additionally, the use of optical wavelengths means that AuNP aggregation can be detected, allowing for AuNP designs that report on cellular details such as endocytosis, cell membrane binding or directional cytoplasmic pH deviations, allowing for AuNPs in tumour cells to be identified specifically during radiotherapy treatment planning. Recently, smart photoacoustic probes have even been developed which allow apoptosis to be detected[269], opening the possibility of assessing treatment response and thus validating treatment plans. The excellent temporal resolution of these systems also allows for the tracking of AuNP movements, allowing not just a snapshot of AuNP concentrations at the tumour site but an idea as to their rate of accumulation and clearance as well. Combined, these features show PASI to have great potential for quantitative AuNP imaging in the context of AuNP-mediated RDEE therapy.

Despite these many advantages, PASI is not without its limitations for the intended task, as noted in Section 3.4. The limited penetration depth of PASI is the primary concern, as imaging depths of only several cm severely limits tumour types for which this technique is viable. Whilst the continued development of internal probes (e.g. intravascular[270], intrauterine[264] or transrectal[262][263] probes) since this thesis was started provides hope that an increasing number of sites could be reached for imaging, imaging depths are still limited to several cm, limiting the imaging volume within which AuNP distributions can be mapped. Further, some tumours (such as brain tumours) are not readily accessible to internal probes due either to physical barriers or risk of disturbing sensitive tissues.

Of particular relevance to the quantitative AuNP imaging application envisaged in this thesis is the coupling of plasmon resonances when AuNPs aggregate. As discussed, this coupling produces a spectral shift which, whilst useful for qualitatively reporting on successful targeting, distorts the spectral response of the AuNPs in an unpredictable way, making AuNP quantification much more difficult. This is a fundamental drawback associated with generating a signal proportional to AuNP number rather than Au concentration. Methods have been proposed to prevent this spectral degradation by coating the AuNPs in spacer material[266], however this adds an additional constraint to AuNP design optimisation. Similarly, attempts to maximise PASI sensitivity by selecting the AuNP shape that generates the strongest photoacoustic signal do not consider the effect of such shape changes on RDEEs. To date, studies investigating the effect of AuNP shape on RDEEs consider only physical mechanisms (*in silico* studies) or compare AuNPs with different shapes/coatings in a seemingly random manner, without justification as to why those shapes, coatings and sizes were chosen (largely *in vitro* studies). These studies therefore fail to adequately control for extraneous factors that may also affect the measured RDEEs (such as total Au concentration). In particular, where AuNPs of different shape are used, no attempt is made to match their internal volumes so that the number of AuNPs and concentration of Au can simultaneously be matched. This raises questions regarding whether differences in RDEEs are due to differences in shape or total Au concentration/number of AuNPs.

At the time of this PhD beginning, PASI was already a more mature imaging modality, with a long history in preclinical research, compared with x-CSI. Consequently, it made sense to assign the bulk of the developmental work of the project to x-CSI: to allow time for the added work associated with assessing a technique that was still under development. PASI motivated experimental work was nonetheless undertaken to test the effect of shape and coating on AuNP-mediated RDEEs. The aim of this work, detailed in Chapter 8, was to assess whether AuNP optimisation for PASI detection produced conflicting pressures to AuNP optimisation for RDEE generation. Whilst the work was unable to consider all AuNP shapes and coatings of interest to PASI, it nonetheless provided enough data that the existence of some conflicts could be inferred. It is hoped that this work will form a template which can be followed to allow other AuNP shapes and coatings of interest to be compared so that AuNPs can be designed which maximise either RDEEs or PASI signal as required on a task-by-task basis.

Chapter 4.

x-ray

photon-counting

spectral imaging

(x-CSI)

In this thesis, a distinction is made between the terms ‘sensor’ and ‘detector’: a sensor is a material which transduces x-rays into a measured quantity (charge, optical photons, pigment darkening etc.) whilst a detector refers to the sensor and any additional apparatus needed to measure the generated signal (e.g. associated electronics). These terms are thus not interchangeable within this thesis.

4.1 The role of x-CSI in this thesis

Since this thesis was started in 2015, significant progress has been made regarding the production of both photon-counting and multispectral systems. Major manufacturers have built dual energy photon-counting systems, with Siemens developing a research system based on their SOMATOM Definition Flash hardware[271] and Phillips building a custom scanner as part of the EU funded SPCCT project[272]. Additionally, non-clinical photon-counting detector modules have become commercially available (such as XCounter’s Actaeon series[273]) and preclinical/limited clinical multispectral systems have also been rolled out (such as MARS Bioimaging’s Microlab 5X120[274] and Extremity 5X120[275], respectively). Due to interest in their use as a targetable contrast agent, several teams have looked at the use of AuNPs as a contrast agent within these systems, as will be discussed. The concentrations detected in these studies to date have involved Au concentrations several orders of magnitude above those used in preclinical RDEE work, however there is, as yet, nothing to suggest that this is an intrinsic limit of the technology. This is partly a result of the fact that x-CSI is still an emerging technology and partly a result of the systems used in the studies not being optimised specifically for the task of AuNP imaging. Advances continue in terms of algorithms for image reconstruction, tissue classification and material decomposition based on the energy information produced by x-CSI whilst correcting for the crosstalk in spectral bins specific to this modality. A similar need remains to optimise physical system parameters, though this is understandably more difficult given that physical design and testing of x-CSI systems is a slow and resource intensive process. Considering only pixel pitch, the significant range of size used by x-CSI systems/prototypes during the course of this thesis (50 μm x 50 μm [276] - 756 μm x 800 μm [277]) suggests that a single ‘best’ answer is not obvious, and indeed it may be application specific. This thesis therefore sets out to:

1. Develop and validate a simulation framework for modelling x-CSI detectors that can capture both charge sharing events and the charge sharing correction algorithms (CSCAs) often used to mitigate them.
2. Use the validated framework to estimate the optimal value(s) for the physical parameters of pixel pitch and thickness, for the specific task of AuNP imaging with x-CSI.
3. Assess the impact of CSCAs on the optimal parameters for the task determined above.

To appreciate why x-CSI is well suited to AuNP detection, as well as why it is an interesting alternative to PASI, a solid grounding in the basics of x-ray imaging physics is useful. This chapter

endeavours to give the reader such a grounding, however is not intended to be an exhaustive explanation of the techniques involved.

4.2 Fundamentals of transmission x-ray imaging

Most medical x-ray imaging techniques involve the transmission of x-rays beams through an object of interest and the collection of the transmitted and scattered x-rays, as shown in Figure 4.1. In an analogous way to optical transmission techniques such as confocal microscopy, information is carried in this transmitted beam in the extent to which it has been attenuated. In the simplest forms of x-ray imaging, projection images are formed which convey information regarding the differences in total radiopacity of the material along that projection (neglecting the effects of x-ray scatter in the following discussion for the purpose of clarity). In Figure 4.1, the small blue circle and larger square block in which it is embedded represent bone and soft tissue respectively, the lime-coloured cone represents x-rays emitted from the x-ray source (bottom left) and the light grey block on the right represents the detector. The radiopacity of the materials is ranked as air < soft tissue < bone, and consequently x-ray transmission runs in the order air > soft tissue > bone. This results in the gradient of shadows cast on the detector, allowing for soft tissue to be distinguished from bone in this case.

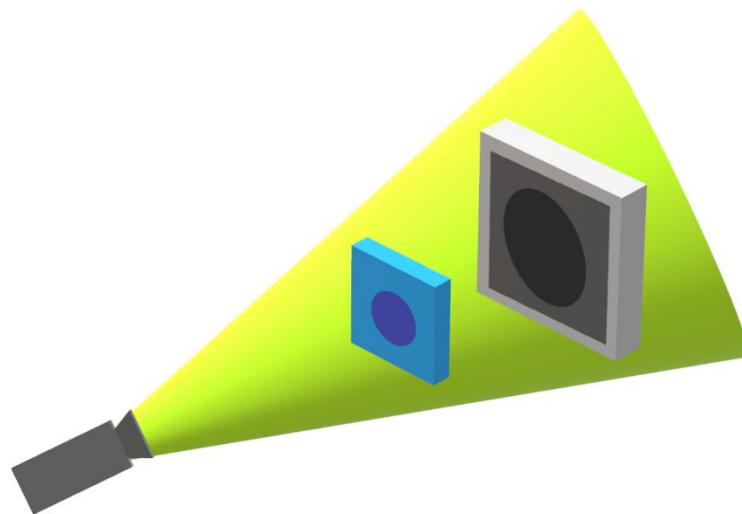


Figure 4.1. The basic principle behind all electromagnetic (EM) transmission imaging techniques. A beam of EM radiation (lime cone) is projected towards an object of interest (central blue square and circle). A pixelated detector (grey rectangle) placed behind the object of interest records the intensity of received EM radiation. Variations in intensity result from variations in beam attenuation, reflecting changes in a material property of the object (such as density or optical transparency). An image of the object is thus formed on the detector. Ideally each pixel in the image is related to the straight line integral between the EM radiation source (grey projector in bottom left) and that pixel. In this case the denser blue circle in the object of interest results in a darker circle in the detected image, corresponding to a lower EM flux at those locations.

This is of course a simplification of the procedure, and a range of different x-ray sources (radioisotope and electron accelerator) and detector technologies may be used in practice, however the general principle involved in transmission x-ray imaging is effectively summarised by Figure 4.1. For the purposes of discussing x-ray imaging techniques in this thesis, the techniques can be classified according to four parameters: dimensionality, detection mechanism, detection chromaticity and transmission assessment scheme.

4.2.1 Dimensionality

Whilst the objects being imaged in medical applications are 3D in nature, a single transmission image such as that acquired from the setup given in Figure 4.1 results in a 2D projection image. x-ray imaging techniques vary in how they handle the mismatch in dimensionality between the object and the image.

4.2.1.1 2D - Planar/projection images

Projection imaging techniques produce 2D images in which the intensity of a given pixel will depend on the radiopacity of all the materials passed through on a straight-line path from the x-ray source to the pixel in question (the transmission path). The signal intensity, S , can thus be related to

$$S \propto \sum_1^n l_n \mu_n \quad \text{eq. 4.1}$$

when μ_n is the linear attenuation coefficient of the n^{th} component material along the transmission path and l_n is the length travelled through that component material. It should be noted that μ_n is a function of incident photon energy, though this will be discussed further in the detection chromaticity section. For example, where the transmission path runs through the chest the component materials could include ribs, skin, air (inside lungs), muscle, fat, and breast tissue. These images can thus give information as to the presence of material along the projection axis as well as localise it in a 2D plane. Projection images are commonly used where a single material of interest is present with a much higher μ than the other materials in the projection and information on its distribution in the 2D plane is sufficient to answer the question of interest, for example in assessing cavities in dental x-rays (where variations in image intensity may indicate the absence of enamel) or assessing bone breaks in A&E departments (where lateral dislocations in images of bones may indicate a break). In these applications the depth of the imaged material is either not needed or easily ascertainable based on a physical exam and knowledge of regular human anatomy.

2D projection imaging does have several limitations that result from the dimensional compression along the axis, however. Firstly, 2D projections cannot determine the depth of a given material component along the line, for example shrapnel embedded in a tissue could be detected, but its depth in the patient could not be determined. Secondly, as l_n and μ_n are both needed to calculate the

contribution of material n to the measured signal, it is not possible to distinguish between a fractional increase in l_n and the same fractional increase in μ_n . Ambiguity will thus exist in the image that precludes easy quantitative analysis of variations between images without external constraining data (e.g. patient thickness). Lastly, the linear superposition of materials along the projection path can also mask the presence of materials that have small l or μ values, especially when these values are small enough that the contribution of them to S is comparable or below that introduced into the system by sources of noise. 3D Computer assisted tomography was developed in part to overcome some of these limitations.

4.2.1.2 3D - Computerised tomographic images

Computed tomography (CT) is the process of taking 2D projection images acquired at a range of different angles with respect to the same central axis (as seen in Figure 4.2) and using them to produce a 3D voxelised map of signal intensity. There are a variety of different reconstruction algorithms that can be used for this purpose, however all aim to reconstruct a 3D data set from a series of 2D projection images. An example of this process can be seen in Figure 4.3, which demonstrates the basic principle of CT reconstructions that the more projection angles available, the better the reconstruction possible. The signal determined for a given reconstructed voxel still represents a sum of the signals from the various component materials present within the equivalent 3D voxel within the patient, however the added spatial information inherent to a 3D data set allows for more detailed questions to be answered, as well as making it more representative of the medical situation of the patient by removing a level of abstraction in the images. The 3D data is not usually viewed as a complete data set but rather is used to construct virtual “slices” through the patient at arbitrary angles, allowing the radiographer to assess structural patterns of interest from the best angles for their application, without having to reposition and rescan the patient.

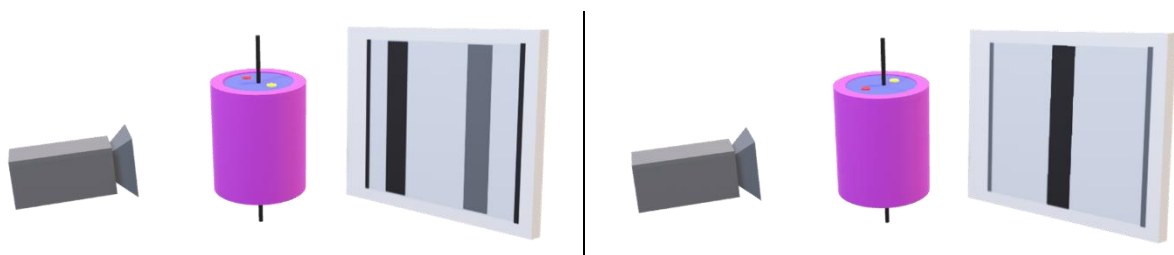


Figure 4.2. The process of CT scanning an object involves the acquisition of multiple projections through the object, taken at different angles. (LEFT) A cylindrical test object (blue) containing two cylindrical inserts (red and yellow) and a jacket (purple) is imaged using a similar setup to that shown in Figure 4.1. The x-ray beams are not shown here for clarity. (RIGHT) The object of interest is then rotated 90 degrees around a central axis (shown in black) and imaged again. This process is repeated for a number of angles ranging from 0 - 180°. In clinical settings it is more common to rotate the source-detector combination rather than the patient.

The first benefit of this approach is that it produces a 3D model that can be resliced to allow for the patient’s anatomy to be viewed from any angle the radiologist wants, including slicing inside of anatomical structures, allowing them to look behind otherwise obstructive features such as the skull or

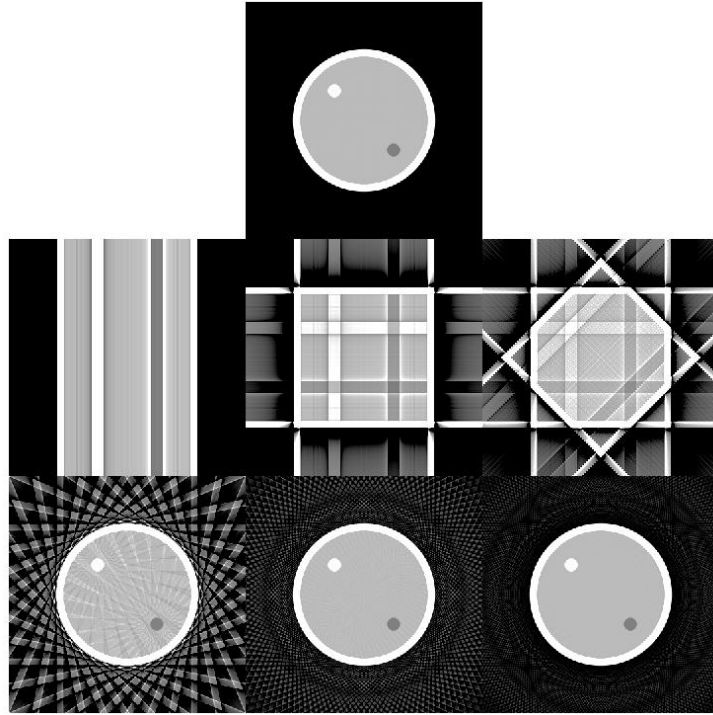


Figure 4.3. Demonstration of how increasing numbers of projections lead to improved image reconstruction. (TOP LINE) A slice through the object being imaged in Figure 4.2. The remaining images show the results of reconstructions based on n equally spaced projection images, where n is, from left to right, (MIDDLE LINE) 1, 2, 4, (BOTTOM LINE) 16, 64 and 128. There is clearly a rapid improvement in image reconstruction as n increases at low values of n , though the benefits show diminishing returns as n increases to larger values.

pelvis. The benefits of this over 2D projection imaging are obvious, saving the patients needing repeat scans if a suspicious structure needs further analysis whilst also allowing for 3D parameters such as organ volume to be compared between scans rather than the area taken up on a projection, which will depend on the orientation of the organ within the patient. There is of course a price to pay for this advantage, namely an increase in patient dose for 3D compared with 2D image acquisition, so the move to 3D is only made when the benefits of gaining additional data outweigh the risk from increased radiation exposure.

The second benefit of producing segmented data in this way is that it leads to a fixed dimension for each voxel, reducing the variability of l_n in comparing different structures. In principle this allows the signal to be made directly proportional to μ_n and so could allow for better material determination based on μ_n , however in practice this is complicated by multiple factors including that the voxels will still contain a variety of different component materials and that the number of photons available to be attenuated by a given voxel (and their energy distribution) will depend on how much the various incoming beams were attenuated before passing through that voxel. A low availability of photons for attenuation in a given voxel, known as photon starvation, can result from highly attenuating materials nearby or a particularly large l_n , such as from a large patient, and can produce artefacts in the image. As a result of the above, most material classification tasks cannot be accurately done in a standard CT.

4.2.2 Detection mechanisms

Detection mechanism refers to the process by which variations in x-ray beam intensity are transduced into a signal that can be viewed and interpreted by a human being or computer directly. This work considers detection mechanisms that involve the three major categories of x-ray sensor: chemical sensors, scintillating sensors and semiconductor sensors.

4.2.2.1 Chemical sensors

The simplest x-ray techniques employ chemical sensors to convert incoming x-rays into a readable signal, producing a projection image. This process often uses a thin film coated in a silver halide (Ag^+X^-) emulsion and a protective coating (radiographic film). Incident x-rays reduce the halide ions to halide atoms, resulting in a free electron which then drifts towards impurities in the film, known as specks. Specks are copious in the film, being introduced as part of the emulsion, meaning the distance between ionisation event and speck is relatively short. The build-up of electrons attracts Ag^+ ions to the speck, where they are reduced to aggregates of Ag metal. The films can then be developed, fixed, and washed to remove unreacted Ag^+X^- , leaving the Ag aggregates attached. Over some limited range (depending on film design), the level of Ag aggregation (and thus film opacity) of each section of film will thus correspond to the radiation dose absorbed. Quantitative conversion of this darkening to radiation dose is possible, however it requires several calibration films to be developed and in practice is not used in most medical imaging applications.

Due to the single use nature of the film, inter-batch variability in film sensitivity, non-digital data format, and the extensive time associated with developing the films, chemical sensors have largely been replaced by scintillating and semiconductor sensors in x-ray imaging. Nevertheless, their lower cost and intrinsic portability make them attractive for some 2D imaging tasks, such as in remote clinics, pop-up hospitals, or smaller clinical practices. Additionally, radiographic film is used for confirming the uniformity of x-ray fields, as done in Chapter 8 of this thesis.

4.2.2.2 Scintillating sensors

Scintillating sensors convert the incoming x-ray photons into photons at a visible (or near UV) wavelength. Such materials should ideally have good stopping power for the x-ray energies being detected, a high conversion efficiency from x-ray photons to visible light photons, and be transparent to the visible wavelength produced. They also require a large band gap, E_g , both to reduce spontaneous promotion across the gap due to thermal excitations and produce higher rates of radiative recombination, which scales with E_g^b , where $b > 1$ [278]. Examples of suitable conversion materials for medical imaging tasks include gadolinium oxysulfide (Gd_2O_2), sodium iodide (NaI), caesium iodide (CsI) and lanthanum bromide (LaBr_3). Electron-hole pairs result from the absorption of x-ray photons by the scintillator. Despite the large band gaps, the direct radiative recombination of these pairs is a low

efficiency process, resulting in most of the energy being transferred by non-radiative mechanisms. The few photons that would be produced from direct transitions would also be of energies above those visible to humans.

To facilitate the production of visible photons then, small quantities of a doping agent are added to these materials (e.g. thallium, Tl, for NaI and CsI scintillators). This results in the production of intermediary energy levels that lie within the band gap of the bulk material, in regions highly localised around the dopant atoms. The holes migrate to the dopant sites where they become trapped, leading to a positive ion. The free electrons, which are free to move across the material, are attracted to the positive charge at these ionisation sites and can make the transition into the dopant's additional energy levels with relative ease due to the significantly reduced energy transition. This results in a neutral dopant site in an excited state, deexcitation of which results in the production of photons of a visible wavelength with a high efficiency. By careful selection of the dopant, the energy of this deexcitation photon can be made to lie below the optical transitions of the bulk material, making the crystal essentially transparent to the photon produced, preventing self-attenuation. The optical photons can then be recorded using conventional optical photodetectors.

4.2.2.3 *Semiconductor sensors*

Semiconductor sensors involve the direct conversion of incident x-rays into electrical currents in a semiconductor material such as silicon (Si), gallium arsenide (GaAs), cadmium telluride (CdTe) or cadmium zinc telluride ($\text{Cd}_{(1-x)}\text{Zn}_x\text{Te}$). In these materials, energy transfer from incident x-rays/charged particles to electrons in the semiconductor results in the promotion of an electron from the valence band to deep in the conduction band (Figure 4.4, left). These promoted electrons can then rapidly deexcite via Auger recombination to produce many electron-hole pairs, forming two localised charge clouds (one of electrons and the other of holes), coincident within the semiconductor (Figure 4.4, middle). These two charge clouds will separate under the influence of a bias voltage applied across the semiconductor (Figure 4.4, right), and their motion within the electric field will induce a measurable build-up of charge at the collecting anode, the intensity of which will be proportional to the energy deposited by the x-rays. By utilising a pixelated array of anodes, the charge built up by an exposure can be read out into an application specific integrated circuit (ASIC) in order to generate an image[279]. More details regarding the various steps in this process can be found in Chapter 5, where an x-ray system based on semiconductor transduction is simulated *in silico*.

4.2.3 *Detection chromaticity*

Detection chromaticity is used here to refer to the ability of the system to differentiate between the energy of incident x-ray beams. I chose this term to draw a parallel to the way that humans perceive

visible photons of different energies: as different colours. I hope that this way of thinking will make the advantages of the various system designs more intuitive.

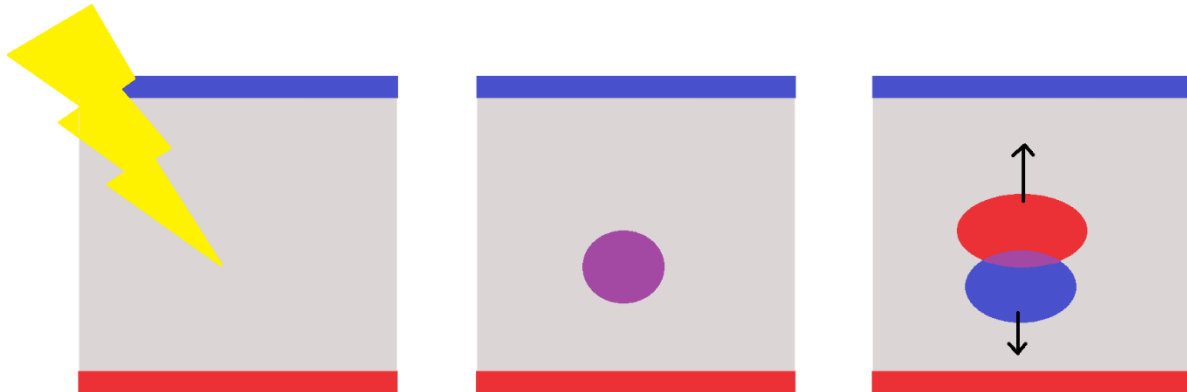


Figure 4.4. The semiconductor material (grey), anode (blue rectangle) and cathode (red rectangle) of a semiconductor-based radiation detector are shown. (LEFT) Initially no significant free charge is present within the semiconductor. An incident photon (yellow bolt) interacts with the semiconductor, producing a highly excited electron. (MIDDLE) The excited electron rapidly deexcites through Auger recombination, producing a cloud (purple) of conduction band electrons and corresponding valence band holes. (RIGHT) Under the influence of an applied electric field, the electron cloud (red oval) and hole cloud (blue oval) drift towards the anode and cathode respectively. The clouds also expand laterally due to diffusion and electrostatic repulsion during this motion. Holes typically have a lower mobility and so will both drift and diffuse at lower rates than the electrons.

4.2.3.1 Monochromatic x-ray detectors

Most medical x-ray images are monochromatic (black and white), meaning they do not attempt to assess how μ varies as a function of energy, but rather just assess μ as it relates to the polychromatic incident x-ray beam as a whole. For monoenergetic CT images, pixels are graded in Hounsfield units (HU)

$$\text{HU} = 1000 \left(\frac{\mu - \mu_w}{\mu_w - \mu_a} \right) \quad \text{eq. 4.2}$$

where μ_w is the linear attenuation of the beam by water and μ_a is the linear attenuation of the beam by air. This scale is thus linearised between these two reference points, making the images semi-quantitative. Comparison of images taken on different systems are complicated however as the HU score for a material can vary significantly based on scanner design parameters (window material, x-ray target, beam angle etc.). Even on the same machine, images can have different HU scales based on the scanning protocol used (tube voltage, filter material and thickness, reconstruction algorithm employed etc.)[280]. When biological variations between patients are factored in, this can result in tissue values varying by up to 200 HU between scans. Such an approach is sufficient for material separation based on radiopacity within a given scan, such as separating bone from soft tissue, but is of limited use in identifying absolute values for radiotherapy planning purposes. Further, as an x-ray beam passes through an object of interest, low energy photons are attenuated at a higher rate than higher energy ones (as μ_n is generally inversely correlated with x-ray energy) resulting in sections deeper in

the object having a higher proportion of high energy photons, referred to as beam hardening. These artefacts can be hard to quantify and correct using only monochromatic images due to the energy insensitivity of the detection scheme. This can have a particularly detrimental effect in material classification tasks, which often depend on spectral differences in absorbance to classify materials. For extracting this data, systems with at least two energies (dual energy) offer an advantage.

4.2.3.2 *Dual energy x-ray detectors*

Dual energy x-ray imaging machines have only relatively recently been developed and put into clinical practice. The main approaches currently employed can be divided into three types, as outlined in Figure 4.5. Voltage switching involves imaging an object at a tube voltage V_1 and then again at a different tube voltage V_2 . This is done for each projection, with the tube voltage switching rapidly between V_1 and V_2 at each projection, resulting in two distinct data sets. This type of imaging thus separates the different energy projections out in time, but spatially they are coincident. Dual source imaging involves the use of two different x-ray sources which differ in the energy spectrum they produce, through variations in tube voltage, target material, filtration, or a combination of these. These systems obtain images simultaneously from each source, with the two sources obtaining different projections, meaning the acquisitions are coincident in time but separated in space. Dual detector imaging involves the use of two x-ray detectors, one placed behind the other, separated by some filtration material. Though only a single source is used, the x-ray beam reaching the second detector will have been attenuated by its journey through the first detector and any associated filtration material, resulting in an x-ray beam that contains a higher proportion of high energy photons. This approach has the advantage of keeping the two energy projections spatially and temporally coincident, though at the cost of fewer photons reaching the high energy detector and an increased complexity in the reconstruction associated with the correlation between the high and low energy readouts.

These approaches all yield two data sets from each object scanned, obtained with two different beam energy spectra, though some overlap of the energy spectra is unavoidable. As noted previously, μ is dependent on the density of the material, its atomic number, and the energy of the incident photon. As the material density and atomic number will not vary between scans, but energy does, the differences in intensity produced from the two different data sets can then be used to establish the materials present. As only two energies are employed, the resulting system of linear equations can be solved for a maximum of two parameters without further constraints. These parameters can be set as two ‘basis materials’ for a semi-quantitative analysis (e.g. material decomposition of a soft tissue voxel into muscle and fat components) or as fitting parameters for determining the electron density, ρ_e , and effective Z-number, Z_{eff} , by determining the ratio of photoelectric and Compton interactions[281]. The details of these processes are beyond the scope of this thesis, though it should be noted that whilst many modern dual energy systems will provide estimates of ρ_e and Z_{eff} , most clinical applications rely on basis material

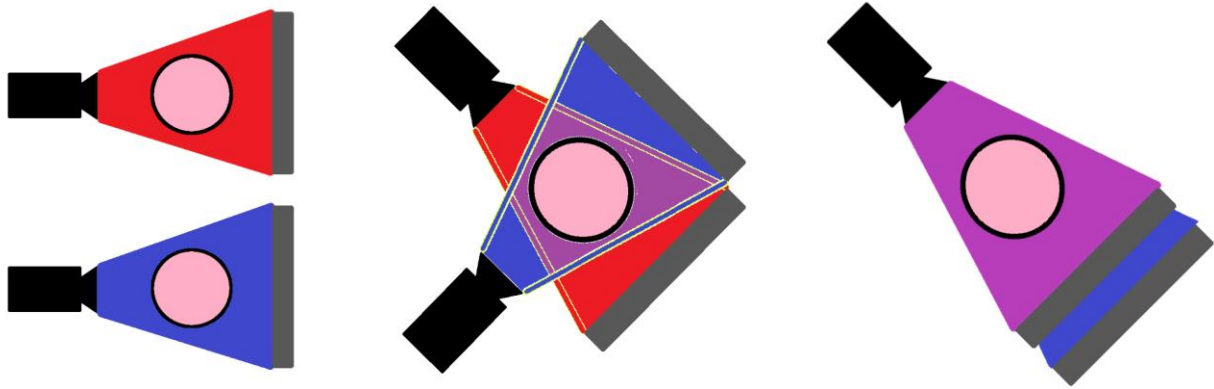


Figure 4.5. Current dual energy approaches can be broadly classified into three categories. In all figures the object being imaged is the pink circle, the x-ray source is in black, the detector is in grey, the high energy x-ray beam is shown in blue and the low energy beam is shown in red. (LEFT) Voltage switching approaches involve imaging the object twice for each projection angle, once at a lower tube voltage and once at a higher tube voltage. This switching can be performed rapidly so that the resulting images are temporally offset, but spatially approximately coincident. (MIDDLE) Dual source approaches involve the simultaneous acquisition of the images using two different x-ray beam-detector pairs. The acquired images are thus temporally synced but spatially offset. (RIGHT) Dual detector approaches involve the use of multiple detectors behind each other. The x-ray beam is attenuated in an energy dependent way as it passes through the first detector such that a beam with a higher average energy spectrum is incident on the second detector. The resulting images are spatially and temporally coincident but show a higher correlation.

decompositions, partly due to the higher mathematical instability associated with determining ρ_e and Z_{eff} using energy integration and only two, significantly overlapping, energy spectra. For a single projection, information regarding the path length can be used to provide a third constraint, allowing three basis material decomposition, however the situation in CT is more complicated due to the variable path lengths contributing to each projection of a voxel. Approaches exist to extend the number of basis materials that CT images can resolve[282], though these require additional image reconstruction algorithms for each task and are thus time and computational resource intensive. Nevertheless, two basis materials are sufficient for many material decomposition tasks, such as separating a contrast agent from the rest of the body or separating two soft tissue types such as fat and muscle. The estimation of ρ_e and Z_{eff} is of primary importance however in the oncological field of proton therapy, as the stopping distance of a proton beam depends on the ρ_e and Z_{eff} of the material that it passes through. Due to the concentrated nature of radiation deposition associated with this form of radiotherapy, uncertainties in ρ_e and Z_{eff} translate into potentially clinically significant misalignment of disease and treatment. To establish the values of ρ_e and Z_{eff} more accurately and stably, or to solve for a larger number of basis materials in a single step, more than two sets of linear equations are needed. This requires truly multispectral systems.

4.2.3.3 Multispectral detectors

Whilst dual energy systems are often colloquially referred to as ‘multispectral’, multispectral imaging is more technically understood to refer to the use of three or more energy channels. Whilst in principle the dual energy techniques could be extended to image three energies, in practice the

approaches used to achieve dual energy imaging offer diminishing returns and increased uncertainty when extended beyond the dual energy case. Table 4.1 lists example complications associated with increasing each dual energy technique to more energy spectra.

Table 4.1. Summary of energy-integrating based dual energy approaches and the complications in generalising them to multispectral systems.

Class of technique	Approach to achieving $n_e > 2$	Potential complications
Voltage switching	Rapid changing of voltage through n_e voltages at each projection	The finite range of x-ray energies useful for medical imaging is divided into n_e segments. The more segments, the harder it is to isolate them by combination of filtration and tube energy, resulting in increased spectral overlap and increased uncertainty in reconstructions. Approaches using $n_e = 2$ already lead to some amount of spectral overlap.
Dual Source	Placing n_e source-detector pairs in a ring around the patient. or adjacent filtration material.	For a fixed ring size, as n_e increases the angle between source-detector pairs decreases. This results in an increasing probability of scattered photons from one source being incident on an unintended detector. This increased interference will result in an increase in reconstruction uncertainty. Approaches using $n_e = 2$ produce a 90 angle between adjacent source-detector pairs, minimising the chance of pair interactions.
Dual Detector	Multiple stacked detectors	Even without added filtration, each additional layer of detector and associated electronics will attenuate the incident x-ray beam further, leading to increasingly low counts in deeper detectors. Increasing counts in these bins will improve statistics and so reduce uncertainty, however such an increase in counts would need to be achieved by increasing either x-ray flux (and thus patient dose) or x-ray tube voltage (and thus reducing soft tissue contrast).

As a result of these difficulties, realisation of multispectral medical imaging requires either monoenergetic irradiation at n_e different energies or a reliable way to divide a single polychromatic beam into non-overlapping, narrower energy range beams. The first of these approaches is achievable given a synchrotron to produce monoenergetic beams, however this is not a readily scalable solution due to the expense and expertise associated with installing synchrotrons in every hospital. The second approach to multispectral imaging can be achieved using photon-counting technologies, and these will be discussed further in Section 4.2.4.2. For now, suffice it to say that the use of photon-counting techniques allows for a polychromatic x-ray beam to be deconstructed by the detector into discrete energy bins.

Multispectral analysis can be used to divide images into a greater number of basis materials, or to find a more stable solution for ρ_e and Z_{eff} with the additional data points. The utility of this in a clinical setting can be transformative beyond the improved accuracy produced by having additional linear equations to constrain the solution space. An example of this is the use of a multispectral system to allow the acquisition and segmentation of images containing multiple contrast agents in a single scan[283]. Such scans could reduce the number of scans a patient is required to have, reducing both their total radiation dose and their use of hospital resources. Whilst additional energy bins lead to improvements in material decomposition and the calculation of ρ_e and Z_{eff} , there is a diminishing return for each additional bin and the optimal number of bins will thus depend on the task at hand.

4.2.4 Transmission assessment scheme

Aside from the number of energies considered, the way in which the photons from the transmitted x-rays are converted into a signal is the other main arbiter of x-ray image quality and quantification uncertainty. In general x-ray transmission can be assessed either by the total energy deposited in the detector (energy-integrating) or by the total number of photons depositing energy in the detector (photon-counting). Each approach has its own advantages and disadvantages.

4.2.4.1 Energy-integrating

Energy-integrating (EI) detectors work by relating the signal intensity in each image pixel/voxel to the energy deposited in the corresponding pixel(s) in the detector. Variations between pixel intensities therefore correspond to differences in energy attenuated from the x-ray beam by material in the path/volume in question. As this approach only assesses the integral of the energy deposited, it is unable to differentiate between one photon at energy E_1 and two photons at energy E_2 , where $E_1 = 2E_2$. This leads to the first problem associated with EI detectors: higher energy photons detected by the system contribute to the signal more than lower energy photons. This statement is true regardless of the energy of the incident photon beam and is a limiting factor in improving soft tissue contrast. This is because soft tissues, by virtue of their lower Z_{eff} values, attenuate higher energy photons less significantly than

harder tissues. One consequence of energy integration therefore is a poorer ability to differentiate between soft tissues at acceptable patient doses.

For monochromatic EI approaches, differences in attenuation indicate variations in radiopacity to the spectrum as a whole and so provides no information regarding how μ varies as a function of energy, E . EI systems that wish to determine how a material's attenuation varies with energy thus require the use of two different incident energy spectra. The introduction of a second beam with differing energy spectra comes at a cost for the system, in terms of a temporal/spatial shift between the two acquisitions or in terms of counts in the second bin. This is the second problem of EI detectors.

The third problem with EI systems is that they produce a signal based on the integral of some physical quantity (chemical converted, light produced, charge deposited etc.) over the acquisition time, so any sources of that quantity outside of the x-ray beam will still contribute to the signal formed, resulting in noise in the image. Examples of such sources include inhomogeneities in chemical deposition for radiographic films, light leakage from the external environment (in scintillating detectors) and electronic noise within electronic circuits. The presence of this noise necessitates higher per-pixel x-ray fluxes to minimise the signal-to-noise ratio (SNR), which can be particularly difficult to achieve in thicker patient projections. This limits the minimum dose required to achieve a given image quality, as well as setting a lower limit on pixel size for these systems.

EI approaches do offer some advantages over photon-counting systems to mitigate these disadvantages. Firstly, due to the fact that they integrate the signal from multiple photons over time, they are not affected by pulse pile-up and do not require electronics operating at high refresh rates. They can even be performed without electronic detectors at all, using instead radiographic film-based approaches. This means that they can be deployed much more cheaply and with lower maintenance than photon-counting systems.

A second advantage of energy integration is the mature state of the field. Whilst not an intrinsic advantage of the technique per se, it is still relevant that as the older and more established technology it has significantly fewer hurdles to use than newer challengers. Many of the problems associated with the development of EI systems have been solved, and mass production has driven down the cost of production. This makes these systems more readily available to a wider community of potential end users. This also extends to the software for image reconstruction for these systems, which have been developed to allow for a range of functions such as artefact reduction and noise suppression to be optimised already. Finally, and importantly, the clinical users of these systems know what they are looking at and looking for when looking at energy integrated images, due to the large amount of research done on them and the wealth of experience they will have gained using them.

4.2.4.2 Photon-counting

Photon-counting (PC) detectors work by relating the signal intensity in each image pixel/voxel to the number of x-ray photons detected by the corresponding pixel(s) in the detector. The basics of this approach are summarised in Figure 4.6 and covered in more detail in Chapter 5. Broadly, the state of a physical quantity (e.g. charge) is measured constantly for each pixel within a PC system by the associated ASIC. When the quantity rises above some pre-set threshold, the counter associated with the threshold for this pixel is incremented by one. Some systems will also short the resistor in the preamplifier at this point to rapidly drain the accumulated charge from the circuit (active reset) whilst others will allow it to bleed off more slowly (exponential decay via the resistor). In either case, when the quantity is again below the triggering threshold the system is ready to count again.

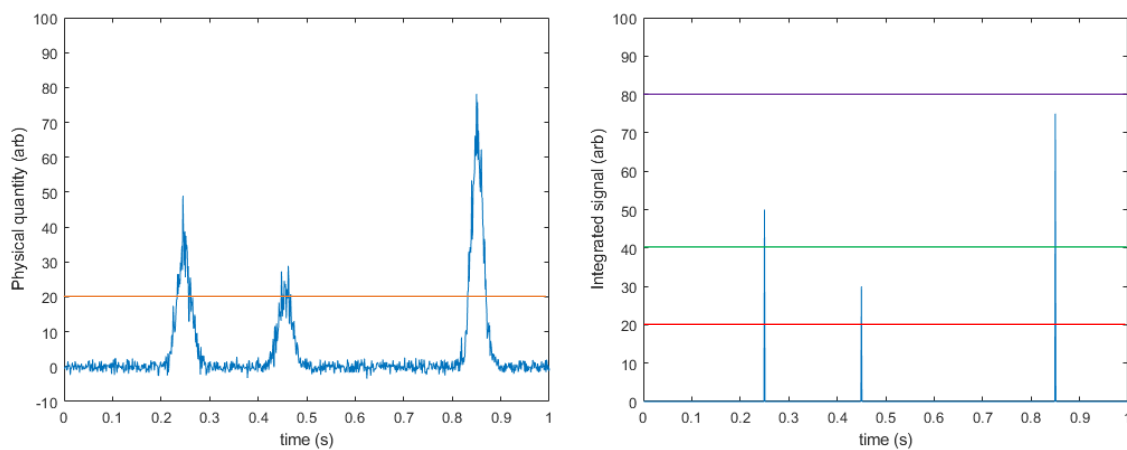


Figure 4.6. Basic principles behind PC approaches. (LEFT) some physical feature of the system such as voltage or current is sampled constantly (blue line). Some level of noise is always present in these measurements, however when a photon interacts with the detector material it causes a sharp and significant change in the measured quantity. A threshold is set (orange line) sufficiently above the noise floor such that any signal rises above this level indicate a photon interaction. Once a signal crosses the threshold, the total signal over some short time interval, Δt , is integrated to produce a value, S . In this figure, the signal rose above threshold on three occasions, and so three counts will be recorded. (RIGHT) For each event detected, S is compared with a series of pre-set thresholds, each associated with a counter. If S is greater than a given threshold then the corresponding counter is incremented by 1. In this example the red counter would be incremented three times, the green counter incremented twice, and the purple counter not incremented at all. The number of events between given thresholds is then determined by subtraction of adjacent counters.

By setting the trigger threshold high enough that variations due to electronic noise in the system are unable to trigger a count (usually at least two standard deviations above the mean of the electronic noise) monoenergetic PC systems can be freed from the deleterious effects of electronic noise. In principle, this allows PC systems to produce lower noise images than EI ones for a given patient dose, or images of the same quality at a lower patient dose. Additionally, by not continually integrating noise into the signal, PC detectors do not need the high per-pixel fluxes required in EI systems, allowing them to operate at lower total doses and smaller pixel sizes, improving the spatial resolution for a given source-detector geometry.

A second advantage associated with PC approaches is how they lend themselves to dual energy and multispectral imaging. As previously alluded to, by using multiple thresholds it is possible to classify incident photons into one of several energy bins based on the size of the change in physical quantity that they induce. Doing so allows for the photons from a single incident beam to be used to generate multispectral data, without the added costs associated with a voltage switching, dual source or dual detector setup. This also has the added advantage of significantly reducing the spectral overlap between energy bins, though imperfect energy deposition and collection, combined with the summation of electronic noise into the determined incident photon energy, will still result in some counts being assigned to the wrong bin even under low flux conditions. Nevertheless, the ability to easily adjust thresholds allows for far more flexible control of energy bin location and width than when filtration materials or similar are used to separate two different incident x-ray tube beams.

The relation of signal to photon number rather than energy deposited eliminates another drawback of EI detectors: the overweighting of high energy photons. This allows for better soft tissue contrast to be achieved for a given exposure. This is a significant advantage of PC systems, as indeed are the others listed above, however PC is not without disadvantages.

As PC systems attempt to assign an energy to each incident photon, they need to be able to differentiate between two different photons interacting with the same pixel during the same image acquisition. This is achieved by utilising extremely fast timing circuits (of the order of nanoseconds) and operating on the assumption that only a single photon interacts with the detector's material over the time interval dt . If photons interactions were uniformly distributed this assumption could be guaranteed by selecting a small enough value for dt . As photon interactions are governed by Poisson statistics however, the probability of two photons being incident on a single pixel at the same time is always non-zero. The number of counts for which this assumption is false can be minimised by selecting a small dt and engineering a low per-pixel x-ray flux, however the minimum value of dt is set by the shaping time of the electronics. This sets an upper limit on per-pixel flux, limiting the x-ray flux, pixel pitch and pixel thickness in a non-trivial way, increasing the complexity of system design. Regardless of the steps taken, some counted events will always be the result of multiple photons interacting with a single pixel within the interval dt , due to the Poisson nature of their distribution. This means that some degree of spectral distortion is inevitable in PC systems. PC techniques are thus less suitable for applications requiring high flux rates, such as cardiac CT imaging.

Another disadvantage associated with PC systems arises from the way in which they assess multiple energies. In contrast to EI systems, the high and low energy bins in a PC system are spatially and temporally coincident on the same pixels, so the ability for cross talk between the different energy bins is greater. The extent of the problem is dependent on pixel size, with smaller pixels making down counting (recording a photon of higher energy in the lower energy bin) more likely, whilst larger pixels

favour up counting (where two lower energy photons combine to produce a count in a higher energy bin).

PC is clearly more complicated than the EI case, however its lower noise profile, better soft tissue contrast and more flexible and extendable multispectral nature means that it is an area of great interest to the scientific community, with significant potential medical advantages. These advantages, and how they relate to AuNP imaging, will be discussed in the next section, whilst work towards solving some of the associated complexities will form a significant part of this thesis.

4.2.5 Spectral separation of contrast agents

This section focuses primarily on x-CSI systems, though some of the approaches are similar to PC dual energy and EI dual energy/multispectral approaches. The general principles behind spectral unmixing were covered in Section 3.2.3 and are expanded on here with an x-CSI focus. As noted in Section 3.2.3, the measured attenuation spectrum as a function of energy, \mathbf{M} , obtained from a mixture containing n materials can be written as

$$\mathbf{G} = [O_1]\mathbf{A}_1 + [O_2]\mathbf{A}_2 + [O_3]\mathbf{A}_3 + \dots [O]\mathbf{A}_n \quad \text{eq. 3.3}$$

where $[O_n]$ is the concentration of the n^{th} material and, in the x-ray case, \mathbf{A}_n is that material's attenuation spectrum as a function of energy. If the attenuation is sampled at N energies then it is possible to use Equation 3.3 to construct a set of N linear equations, which is uniquely solvable so long as the system of equations is critically determined or overdetermined ($N \geq n$). With optical approaches this is a trivial condition to meet, as narrow wavelength optical beams can be constructed relatively easily and optical extinction spectra obtained with $N > 100$ are routinely acquired in labs with desktop equipment. Similarly, in nuclear physics, γ -spectroscopy equipment exists which can measure the incident energy spectrum of a beam, though with significant restrictions compared with optical spectroscopy (significantly lower fluxes, higher susceptibility to pile-up and charge loss, poorer spatial resolution etc.). This approach works because the γ -ray emissions are a finite sum of discrete energy emissions. In contrast, x-ray imaging is not so controllable, with probe beams being polychromatic. In x-CSI, detection equipment often trades spectral resolution against spatial resolution, with spatial resolution providing equally important medically relevant data.

Another major difference between optical and x-ray spectroscopy is the size of n . Whilst optical approaches are sensitive to molecular species (due to the energies involved corresponding to molecular excitation levels), x-ray techniques interrogate samples at the atomic level. Thus, whilst samples scanned optically typically contain only a few chromophores, x-CSI medical samples contain a wide range of elements at markedly differing concentrations, particularly when contrast agents are introduced. The result is that whilst optical problems are often overdetermined, x-CSI problems are often underdetermined, leading to potential instability in the approaches used to solve them.

One common solution to this problem, also employed in dual energy CT material decomposition tasks, is to define a small number of ‘basis materials’ which differ in their atomic composition, and then use these to determine the contribution of broad tissue types such as ‘fats’ and ‘muscle’. With careful selection of appropriate basis materials, this approach is sufficient for many medical applications, and with x-CSI systems is extendable to allow for high Z -number contrast agents to be defined as their own basis materials[284]. Alternatively, the additional bins provided by a multispectral system can be used to extend the dual energy case of determining Z_{eff} and ρ_{eff} to include quantification of high Z -number contrast agents[285]. In both cases, high Z -number contrast agents are preferred due to their sharp discontinuities at the K-edge of their attenuation spectrum.

The process of photoelectric absorption of an x-ray by an atom was described in Section 1.2.1.1 of this thesis as “the complete absorption of the incident photon by an atomically bound electron”. The probability that photoelectric absorption will occur is given in Equation 1.1 of that section and is reproduced below for ease of reference.

$$P_p \propto \frac{Z^n}{E_\gamma^{3.5}} \quad eq. 1.1$$

where P_p is the probability of a photoelectric interaction between an x-ray of energy E_γ and an atom of atomic number Z . n typically takes values ranging from 4 - 5, depending on the value of E_γ . The first thing to note from this is the strong dependence of P_p on Z , which provides the motivation for using high Z -number materials as contrast agents. The second thing to realise is that whilst these atoms possess many candidate electrons, they can be broadly differentiated based on the electron shell to which they belong (Figure 4.7).

K-shell electrons are the most tightly bound to the nucleus due to their proximity and lack of electron screening between them and the nuclear protons, with a binding energy of E_B . K-shell electrons thus require the most energy to ionise, with the exact value varying between elements. P_p is greatest for electrons in the shell with the highest E_B that is still below E_γ . The result of this simple statement is that there is a profound change in attenuation profile for a given element as E_γ increases from below E_B to above E_B , resulting in a discontinuity at $E_\gamma = E_B$, referred to as a K-edge.

K-edges can be used in x-CSI to differentiate materials with differing Z -numbers. Suffice it to say that K-edges provide useful spectral features for contrast separation, provided they lie within the energy range of the probe x-ray beam and that they are sufficiently well separated to allow for the construction of energy bins which can differentiate between them and other attenuators in the image. Many high Z -number materials used as contrast agents for conventional x-ray imaging meet the first of these criteria, including I, Ba, Gd, Hf and Au. These agents have K-edges ranging from ~30 keV to ~81 keV. These agents also meet the second criteria when used individually in human bodies as C, N, O and H (the most abundant elements in the human body) all have $E_B < 1$ keV, and even the relatively

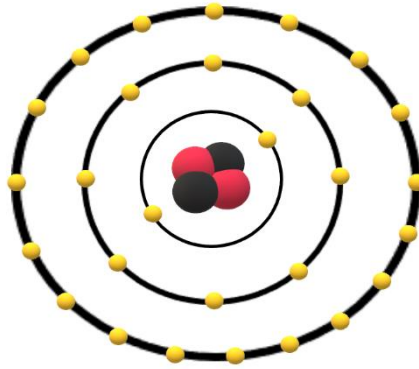


Figure 4.7. Electrons in an atom can be subdivided into a range of shells based on their principal quantum number, n . The inner shell is the K shell, corresponding to $n=1$, and it can hold 2 electrons. The next shell is the L shell, corresponding to $n=2$, and it can hold 8 electrons. The next shell is the M shell, corresponding to $n=3$, and it can hold 18 electrons. Further shells corresponding to $n < 3$ exist but are not shown here for convenience. For a given atom, lower values of n correspond to more tightly bound electrons. Shells greater than $n=1$ show a fine structure, but exploration of this is beyond the scope of this thesis.

high Z -number Ca and Fe have E_B of only ~ 4 keV[286] and ~ 7 keV[287] respectively. The simultaneous imaging of several contrast agents is a unique potential application of multispectral imaging, and it has been shown that high Z -number contrast agents with K-edges as close as 4 keV can be separated[283], provided appropriate bin number and placement.

4.2.6 Advantages of x-CSI

x-ray transmission imaging modalities offer several advantages over other clinically available imaging modalities. In contrast to ultrasound systems, x-ray imaging can rapidly produce whole-body images for the whole patient volume regardless of depth, with less noise, better artefact reduction and less user dependence. In contrast to PET and SPECT, x-ray images can be generated with higher spatial resolution, significantly more quickly, with less patient dose and without the need for specialist nuclear pharmaceuticals. Compared to MRI, x-ray techniques are quicker, less stressful for the patient, cheaper and are suitable for patients with metal implants or cardiac pacemakers.

Traditional x-ray transmission imaging systems suffer from several drawbacks compared to these other modalities however, including the presence of artefacts around metal implants/foreign bodies, the delivery of an ionising radiation dose, poor soft tissue contrast and significantly a lack of molecular imaging which makes traditional x-ray images primarily structural rather than functional in nature. Many of these disadvantages are mitigated, in a significant way, by the development of x-CSI. The use of spectral information can be used to provide significant reduction in metal artefacts during iterative reconstruction[288], allowing for unprecedented detail in assessing the state of metal implants[289]. x-CSI can also produce images of comparable quality to EI CT at a significantly lower dose (67% and 83% for sinus and temporal bone examinations respectively[290]), or produce diagnostically better images at the same x-ray dose due to the reduction in noise associated with PC (12.8% - 40.0% improvement[291][292][293]), though the exact dose savings vary between imaging

tasks. The ability to assess x-ray attenuation as a function of energy also allows for x-CSI to improve the soft tissue contrast of the images that it obtains. Whilst a similar approach is available on current EI scanners using dual energy protocols, x-CSI allows for a more even weighting of high and low energy photons, improving soft tissue contrast[294], whilst the additional energy bins allow for material decomposition with more basis materials, providing more soft tissue categories[295]. In terms of molecular imaging, it is feasible that the additional basis materials provided by the multispectral approach of x-CSI could be used to detect functionalised high Z-number nanoparticles[296] so that the distribution of molecules of interest can be ascertained by proxy[297][298][299].

In addition to overcoming historical disadvantages between x-ray imaging and other medical imaging modalities, x-CSI can further enhance the advantages associated with x-ray imaging. CT is already known for its excellent spatial resolution, however the exclusion of false counts due to electronic noise means that the pixel sizes associated with x-CSI can be significantly smaller than those for EI CT systems for a given noise level. This can equate to an improved spatial resolution in the images resulting from a given scanner geometry. Small pixels are necessary for the detection of diagnostically relevant microcalcifications, a process made still easier by the energy resolving capabilities of x-CSI. It has already been mentioned that the additional energy bins associated with a multispectral approach can produce more basis materials in a single image, however the power of this extends beyond improved soft tissue classification. Having more basis materials can also reduce the number of scans a patient requires by allowing multiple contrast agents to be acquired in a single scan, freeing hospital resources, reducing overall patient doses and removing spatial mismatch between different images caused by patient motion. In a clear indication of the future potential of x-CSI, MARS Bioimaging have been able to simultaneously image three contrast agents along with three common biological basis materials (bone, lipids and water) in a phantom study[300], which was later extended to identify three high Z-number contrast agents in a mouse model. Similar work by Siemens has demonstrated the ability to simultaneously image three high Z-number contrast agents in a time dependent manner, though at the cost of body tissue discrimination and a noisier reconstruction method[301]. It is also worth noting at this point the advantages of using x-CSI for contrast agent quantification over EI dual energy approaches. x-CSI techniques allow for direct quantification of the contrast agents, without the need for complex calibrations and conversions. This is because x-CSI systems produce absolute measures of x-ray transmission as a function of energy, rather than the relative values obtained using HU.

A final point to note in favour of x-CSI as a medical imaging modality lies in the wealth of evidence and experience that already exists in the community concerning the interpretation and clinical relevance of x-ray images. Links between radiopacity and various diseases are well known, such as the link between tumour formation and increased radiopacity. By producing less noisy, higher-resolution images in a modality that already has an extensive clinical infrastructure and evidence base behind it,

x-CSI can prove valuable in the short term even if in an unoptimised form, allowing for the time and funding necessary to develop image reconstruction and material classification algorithms that better realise the potential of the additional spectral data and different noise effects associated with x-CSI.

4.3 AuNPs as exogenous x-CSI contrast agents

4.3.1 Principles and mechanism of AuNP detection

The major elements comprising the human body (defined in Chapter 2 as elements comprising more than 1% of the body by mass) range in Z -number from 1 - 20, which is significantly less than the Z -number of Au (79). At medically relevant x-ray energies there are two physical processes that dominate x-ray beam attenuation: photoelectric absorption and Compton scattering.

As can be seen from Figure 4.8, the human body is most likely to interact with the beam by Compton scattering at mid to high energies (relative to medical x-ray imaging) whereas Au interacts predominantly by photoelectric interaction across this range. This is because the probability of photoelectric interaction between x-ray photons and an element scales with Z^n (with n ranging from 4 - 5, depending on energy), so the significantly higher Z value of Au, combined with the relatively large exponent n , leads to a much more significant photoelectric effect. As can be seen from Figure 4.9, Au is consequently a much stronger attenuator of x-ray beams than the tissue it is in, allowing for significant contrast even at relatively modest concentrations in a monochromatic image of human soft tissue. The high concentrations of Ca in human bones can produce a similar strong absorption in monoenergetic imaging however, limiting the use of Au's monochromatic contrast improvement to soft tissues. The contributions of photoelectric and Compton effects can be separated by using a dual energy approach, providing an alternative way to separate the Au signal from host tissues. As can be seen from the lower two plots in Figure 4.9, this spectral separation can be extensive due to the stark differences in photoelectric and Compton attenuations of the two materials respectively.

As previously mentioned, AuNPs may be used alongside other contrast agents, and under these circumstances the presence of a K-edge in the medical imaging energy range becomes relevant. Consider the change in attenuation associated with crossing the K-edge for Au at ~80 keV in Figure 4.10. The attenuation shows a marked increase associated with the K-edge. Now consider the change in attenuation associated with I and Gd across the same change in energy: they both decrease smoothly. The effect of this sharp rise in attenuation means that Au goes from being the weakest of the three attenuators at ~75 keV to the strongest attenuator at ~85 keV. Away from the K-edge, the attenuation of Au decreases smoothly, along with I and Gd and so this new order of attenuations is maintained. Similar patterns can be seen for I (at ~33 keV) and Gd (at ~50 keV) in which they move from being the worst attenuator to the dominant one. By constructing energy bins above and below each of these K-edges, multispectral imaging can distinguish between the various contrast agents. The

process of energy bin selection is complicated by the need to get sufficient counts in each bin to keep statistical uncertainties reasonable and the width of the optimal energy bin will be affected by the energy response of the detector at that energy, however these details will be returned to in later chapters. For now, suffice it to conclude this section by noting that AuNPs are good x-CSI contrast agents due to their high Z -number and the presence of a K-edge relatively central within the range of medical x-ray tubes (<140 keV).

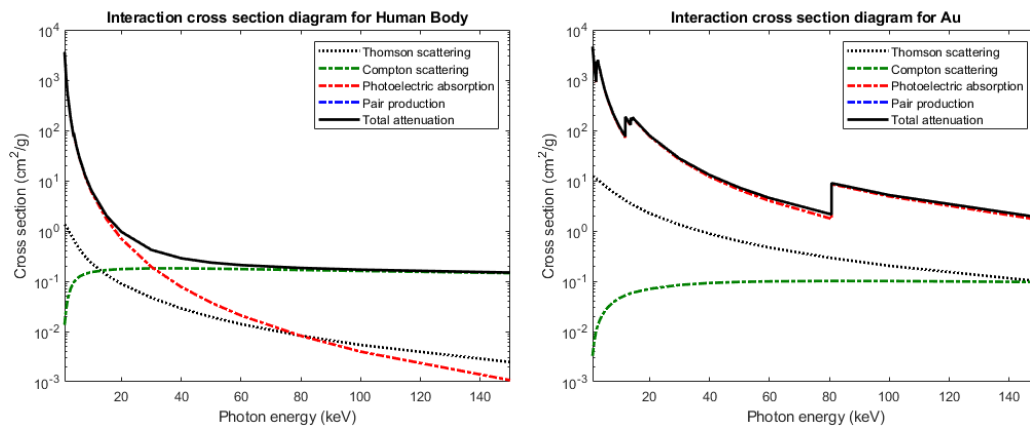


Figure 4.8. Interaction cross-section diagrams for Au and a 'Human Body' representative material across energies relevant to medical imaging (1 - 140 keV). The 'Human Body' material is composed of elements in the same proportions as they make up the human body. This material would not be suitable for imaging simulations due to the gross averaging that is employed, however it is sufficient for illustrating the different physical mechanisms which dominate for Au and human body tissues in general. Photon-Au interactions in this energy range are most likely to be photoelectric in nature, whilst above 20 keV the dominant photon-'Human Body' interactions are Compton scatterings. Figure plotted using data from NIST[27].

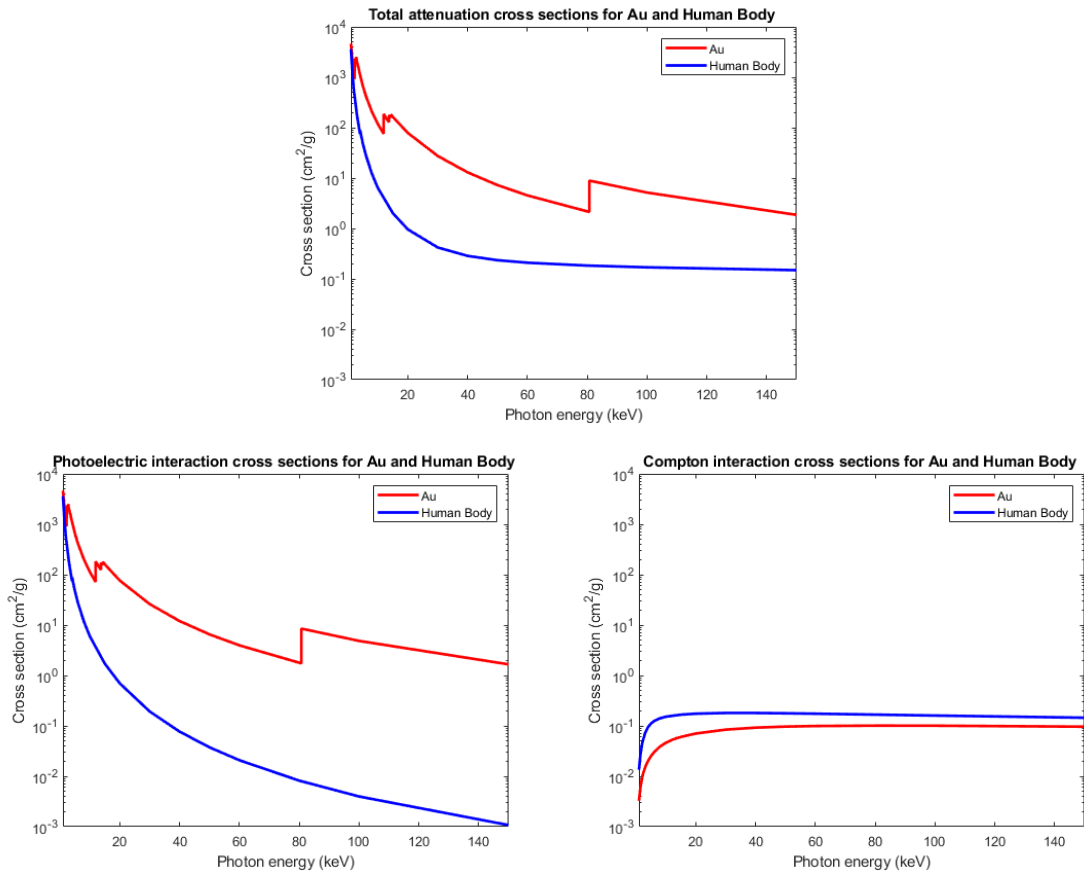


Figure 4.9. Comparisons of attenuation cross-sections for Au and the previously mentioned 'Human Body' representative material (see Figure 4.8) across energies relevant to medical imaging (1 - 140 keV). Monoenergetic imaging systems are only sensitive to differences in total attenuation (TOP), though may still be able to differentiate between these two material types based on their density. In contrast, dual energy systems can decompose images into photoelectric (BOTTOM LEFT) and Compton (BOTTOM RIGHT) interactions. This will allow for better material separation as photoelectric interactions are predominantly associated with photon-Au interactions whilst Compton interactions are predominantly associated with photon-'Human Body' interactions. Figure plotted using data from NIST[27].

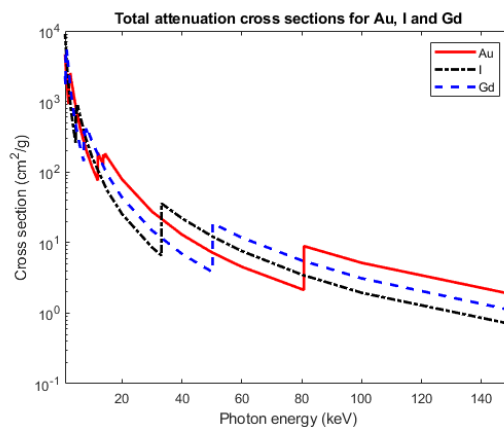


Figure 4.10. Total attenuation cross-section diagram for three contrast agents: Au, I and Gd. K-edges are clearly visible for all three elements, and the L-Edge for Au can also be seen towards the left of the figure. Figure plotted using data from NIST[27].

4.3.2 Achievements and potential of x-CSI in AuNP imaging

Despite the rising number of papers using AuNPs with x-CSI, most of the work concerning AuNP detection limits with transmission x-ray imaging still concerns EI mono/dual energy approaches or PC dual energy systems. It is reasonably expected that the introduction of either PC or multispectral approaches individually would improve the detection limit of a given system, yet whether the introduction of both together results in their benefits summing linearly or synergistically remains to be determined. However, as these approaches are similar to x-CSI in physical principles, and as they are more mature in terms of optimisation, these results can give an indication as to a minimum level of sensitivity that x-CSI systems can hope to achieve in AuNP quantification. Some of these approaches will thus be referred to in this section.

In the context of this thesis the relevant question is whether a technique can image AuNPs at concentrations relevant to AuNP induced RDEEs. A great deal of caution is needed in comparing AuNP concentrations between the imaging and RDEE literature however, as differing conventions for quantifying AuNP concentration can be used, even within one branch of the literature. RDEE studies have reported AuNP concentrations used in terms of mass percentage (mg/kg)[302], mass concentration (mg/ml)[303], particle density (M)[118] and optical density[304] for example. It is important to note that the correct unit of molarity is particles per litre. This means that experiments using the same molarity may actually be using differing numbers of Au atoms if they use AuNPs of differing sizes or shapes. Whilst comparing results based on AuNP molarities may make sense for some biological processes (such as AuNP uptake which is dependent on the number of AuNPs), for x-ray imaging processes it is the density of Au atoms which is of primary concern. Further, a large majority of *in vivo* RDEE studies record the dose injected into the animal rather than the concentration at the site of treatment[302][305][306]. This significantly complicates the process of determining the AuNP dose associated with the observed RDEE, as both tumour factors (location, type, size, perfusion) and AuNP factors (shape, size, and coating) may result in differing levels of AuNP accumulation at the site of interest. A similar problem exists in the imaging literature for *in vivo* AuNP imaging. Many studies show qualitative distributions but do not confirm the distributions quantitatively, nor assess the concentrations of AuNP that can be detected. For these reasons, it was decided to exclude *in vivo* results from analysis.

The detection limit of AuNPs can, in principle, be pushed arbitrarily high by employing progressively higher radiation doses. This is of course not an option clinically as there is an upper limit in dose that is allowable to human patients during diagnostic imaging. For this reasons, whilst work has been done to show that micro CT can resolve AuNP concentrations down as far as 0.5 mg/ml[307] (though with a non-trivial 20% uncertainty), it is not applicable to the imaging tasks relevant to this thesis. However, it is interesting to note that the same study quantified the HU increase associated with various AuNP concentrations, and when the 30 HU increase requirement for clinical CT contrasts[308]

is applied, the detection limit rises significantly, to 4 mg/ml. This result was obtained *in vitro*, and similar work specifically with x-CSI systems and *in vitro* phantoms has shown an improvement in detection limit, down as far as 2 mg/ml[299]. This work also used a series of dilutions of AuNPs in water to test the limits, and 2 mg/ml was simply the lowest concentration they used, so does not represent an absolute limit for x-CSI systems. Indeed, the same study found ~0.15 mg of AuNP (with a fairly small uncertainty) within a cell pellet, though without reporting the size of the pellet a comparison cannot be made in terms of Au atom concentration. It is also unfortunate that the concentration in the pellet was not independently verified by inductively coupled plasma mass spectroscopy (ICP-MS), inductively coupled plasma optical emission spectroscopy (ICP-OES) or similar technique, as given the maximum volume of the pellet was 0.5 ml (the volume of the Eppendorf tube it was contained in) this could have been the lowest reported x-CSI based AuNP detection to date if the pellet took up any more than 1/3 of the tube's volume. At the time of writing, the lowest AuNP concentration detected by an x-CSI system is 1 mg/ml[309], again obtained as part of calibrating the system for AuNP quantification using a phantom and again this was simply the lowest concentration used. This work involved a system with a small field of view and went on to assess AuNP quantification in a mouse model *in vivo*. AuNP concentrations ranging from 5 mg/ml to < 1 mg/ml were observed in the mice, though the uncertainties in the measurements associated with noise were significant (~1 mg/ml). *Ex vivo* analysis of the imaged organs by ICP-OES revealed a systematic underestimation of AuNP concentration by the x-CSI system of ~23%, though overall a good agreement in linearity between x-CSI and ICP-OES was found.

The takeaway from the above is that x-CSI has currently been used to image AuNPs down to a few mg/ml by independent groups using different systems. This has included *in vivo* imaging of animal models to assess AuNP distribution both qualitatively and quantitatively. Again returning to the central motivation for this thesis, we need to ask how this demonstrated sensitivity compares to AuNP concentrations used to deliver RDEE in the literature.

Table 4.2 shows a selection of studies from the literature in which AuNP induced RDEE was shown. The AuNP concentrations were reported in a range of different units and were standardised to units of mass density for this table. The standardisation was performed by first calculating the effective volume for a single Au atom based on the unit cell for bulk gold (Figure 4.11).

The unit cell for bulk gold is face centred cubic, and so contains 6 half Au atoms (Au atoms shared between 2 unit cells) and 8 eighth Au atoms (Au atoms shared between 8 unit cells) for a total of 4 Au atoms. The volume of the unit cell is 0.0679 nm³[310], and so the volume for a single gold atom is

$$\frac{0.0679 \text{ nm}^3}{4} = 0.016975 \text{ nm}^3 \quad \text{eq. 4.3}$$

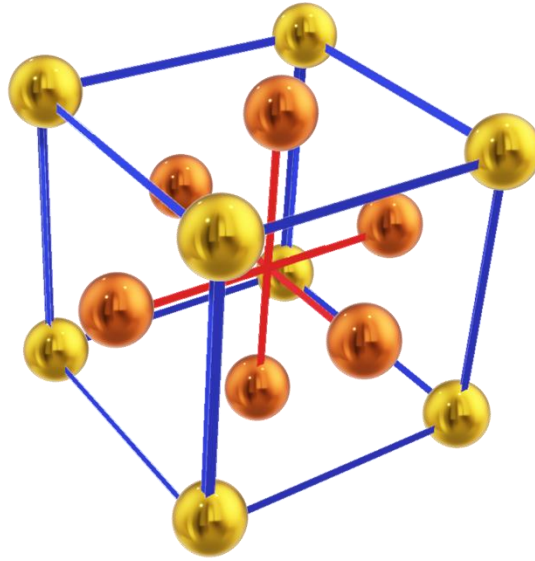


Figure 4.11. The unit cell of Au is face centred cubic, with 8 Au atoms present at the corners of the unit cell (gold spheres on blue frame) and 6 Au atoms present at the faces of the unit cell (orange spheres on red frame). Note that Au atom colours in the diagram are different simply for visualisation clarity, but no unit cell location is materially different from any other.

The unit crystal structure of AuNPs can vary very slightly between particle types, so as a first approximation 0.017 nm^3 is taken here to be equal to the average volume of a Au atom within a AuNP. For a AuNS the volume, V_{NP} , is related to its radius, r_{NP} , according to the equation

$$V_{NP} = \frac{4}{3}\pi r_{NP}^3 \quad \text{eq. 4.4}$$

The number of Au atoms, N_{NP} , in a spherical AuNP with volume V_{NP} is thus given by

$$N_{NP} = \frac{V_{NP}}{0.017} \quad \text{eq. 4.5}$$

assuming that V_{NP} is expressed in units of nm^3 . Next the molarity of the AuNPs, M_{NP} , is used to determine the number of moles of Au atoms per ml, N_{Au}

$$N_{Au} = \frac{N_{NP}M_{NP}}{1000 \frac{[\text{ml}]}{[\text{l}]}} \quad \text{eq. 4.6}$$

where the denominator is a conversion factor needed to convert between Molarity and moles ml^{-1} . Finally, the number of moles is then multiplied by the atomic mass of gold (197) to yield the mass of gold per ml, which is referred to here as the standardised density, ρ_s

$$\rho_s = (197)(N_{Au}) \left(1000 \frac{[\text{mg}]}{[\text{g}]} \right) \quad \text{eq. 4.7}$$

where the final term is a conversion factor from g to mg so that ρ_S can be reported as mg/ml, for easier comparison with the imaging literature. Combining Equations 4.3 - 4.7 yields the direct standardisation used:

$$\rho_S = 197M_{NP} \frac{\frac{4}{3}\pi r_{NP}^3}{0.017} \quad \text{eq. 4.8}$$

This approach involved several assumptions including:

- Unit cell for all AuNPs equal to unit cell for bulk Au.
- AuNPs were perfectly spherical.
- The mean volume of a group of AuNPs can be represented by the volume of a AuNP with diameter equal to the group's mean diameter.

The validity of these assumptions was tested for AuraVist™ AuNPs from the studies reviewed, as these had concentration reported both in molarity and mass density. The calculated mass density was 0.2% smaller than that reported by that study, however the two values round to the same value to 2 significant figures and no description of the rounding applied to the value in the study is provided, so to all intents and purposes the two values agree, validating this approach.

Table 4.2 reveals that AuNP-mediated RDEEs have been found with AuNP concentrations spanning eight orders of magnitude: from tens of g/ml to a few tenths of µg/ml. It should be noted that only a single study reported any RDEE at the lowest concentration reported here and that there are reasons to question whether the concentration stated is a fair reflection of the concentration within the cells at the time of irradiation. The study in question incubated the cells for 24 hours with AuNPs at the stated concentration before replacing the cell culture medium with fresh medium, again at the same concentration. AuNPs taken up from the first medium would thus be present in addition to the AuNPs in the medium added, and this amount may be significant given the ability of cells to concentrate AuNPs within themselves. Even discounting this result however, AuNPs appear to induce RDEEs as concentrations down to a few tens of µg/ml: two orders of magnitude below the currently demonstrated limits of x-CSI detection.

This is not to say that x-CSI cannot be used to quantify AuNP distributions *in vivo* as part of predicting AuNP induced RDEEs: indeed there is significant overlap between Au concentrations used for imaging and RDEE work, with 58% of the RDEE studies listed in Table 4.2 involving Au concentrations above the 1 mg/ml currently detectable with x-CSI. However, it is a concern from a radiotherapy planning perspective if AuNPs are present at concentrations that can induce RDEEs but are not detected due to being below the sensitivity of the imaging system. Again, this is not immediately disqualifying for the technique, especially if the AuNPs are being used to reduce the overall doses used, though it does need to be borne in mind.

Table 4.2. A summary of RDEE studies in the literature. AuNP concentrations reported are given, as well as the calculated standardised density.

AuNP diameter (nm)	Reported AuNP concentration	Standardised density (mg/ml)	Author
1.9	2.4 μ M	1.0E-01	Butterworth <i>et al</i> [118]
1.9	0.24 μ M	1.0E-02	
13	10 nM	1.3E-01	Chang <i>et al</i> [311]
30	2.4 mg/ml	2.4E+00	Chattopadhyay <i>et al</i> [303]
??	36 μ g/ml	3.6E-02	Chen <i>et al</i> [312]
14	7 x 10 ⁹ NPs/ml	1.9E-04	Chithrani <i>et al</i> [313]
50	7 x 10 ⁹ NPs/ml	8.8E-03	
74	7 x 10 ⁹ NPs/ml	2.9E-02	
1.9	12 μ M / 500 μ g/ml	5.0E-01	Coulter <i>et al</i> [314]
2.7	0.5 mg/ml	5.0E-01	Cui <i>et al</i> [315]
14	1.25 nM	2.1E-02	Geng <i>et al</i> [316]
14	2.5 nM	4.2E-02	
14	5 nM	8.3E-02	
1.9	12 μ M / 500 μ g/ml	5.0E-01	Jain <i>et al</i> [317]
1.9	12 μ M / 500 μ g/ml	5.0E-01	Jain <i>et al</i> [119]
12	1 mM	1.0E+04	Joh <i>et al</i> [305]
7	5.5 μ mol /mL	1.1E+04	Kaur <i>et al</i> [318]
47	50 μ M	3.1E+04	Khoshgard <i>et al</i> [319]
10.8	15 μ M	1.1E+02	Kong <i>et al</i> [320]
6.1	0.4 mM	5.5E+02	Liu <i>et al</i> [321]
6.1	1 mM	1.4E+03	
4.7	500 μ M	3.1E+02	Liu <i>et al</i> [322]
14.8	1.5 μ g/mL	1.5E-03	Liu <i>et al</i> [323]
14.8	15 μ g/mL	1.5E-02	
1.9	0.25 mM	1.0E+01	Rahman <i>et al</i> [324]
1.9	0.5 mM	2.1E+01	
1.9	1 mM	4.2E+01	
1.9	12 μ M / 500 μ g/ml	5.0E-01	Taggart <i>et al</i> [139]
13	20 nM	2.7E-01	Wang <i>et al</i> [325]
16	20 nM	5.0E-01	Wang <i>et al</i> [326]
49	20 nM	1.4E+01	
30	15 nM	2.5E+00	Zhang <i>et al</i> [327]
<2	50 μ g/ml	5.0E-02	Zhang <i>et al</i> [302]
10.8	15 nM	1.1E-01	Roa <i>et al</i> [150]
4.8	0.05 mM	3.4E+01	Zhang <i>et al</i> [328]
12.1	0.05 mM	5.4E+02	
27.3	0.05 mM	6.2E+03	
46.6	0.05 mM	3.1E+04	

So what is the limit below which AuNPs do not produce a measurable RDEE? This is a complicated question due to the variety of factors that can affect RDEE for all the reasons outlined in

Chapter 2, and so cannot be answered simply as a concentration of Au. The study by Chithrani *et al* in Table 4.2 for example showed that cellular uptake and consequent RDEE was AuNP size dependent, with an optimal uptake size and reduced uptake either side of this. That study also looked at how changing the initial AuNP concentration affected the measured RDEE for the uptake optimised AuNPs (50 nm). Unfortunately, this data was not statistically analysed as it was provided to illustrate a different point, however examination of the figures indicates that RDEEs were not present at roughly 10^7 NPs/ml ($[Au] = 1.7 \times 10^{-5}$ mg/ml). This indicates that there is a minimum concentration below which RDEEs are not produced (so imaging is not relevant), though this concentration will depend upon AuNP design. It may be that in realising clinical utility of AuNPs with x-CSI, AuNPs need to be optimised such that they do not deliver RDEE below their detection limit.

As a final comment on this section, the reader is reminded that none of the x-CSI studies considered here used machines, protocols or algorithms specifically optimised for AuNP detection and as such there is no reason to suppose at this point that x-CSI, as a technology still very much in development, has reached its detection limits regarding AuNPs. Indications are present in some of the data reviewed[299] that a further order of magnitude improvement in sensitivity may already be achievable based solely on the existing hardware. Optimisation of the hardware and reconstruction software should allow this limit to be further pushed down. Thus, whilst AuNP optimisation so that concentrations below detection limits could not induce RDEEs would present an additional AuNP optimisation constraint compared with PASI, it is too soon to know what these limits would be and so this additional constraint will not be considered in the remainder of this thesis.

4.4 Limitations of x-CSI

x-CSI suffers from a variety of limitations when compared with other imaging techniques and with what is required for predicting AuNP induced RDEEs *in vivo*. The first limitation is related to the use of x-rays in general and it is the safe dose that can be tolerated by a patient. Whilst x-CSI does offer significant advantages in dose when compared with conventional CT systems, it still requires some radiation dose which may limit its use in radiosensitive populations. This limitation is of particular salience given that AuNPs are being used specifically for their ability to enhance radiation damage, and so were they found to have built up in an unintended organ during the x-CSI scan, this would translate to an increased unintended dose to that organ.

In contrast to optical techniques such as PASI, x-CSI is also indifferent to the shape and size of the AuNPs that it is imaging. Whilst this is an advantage in terms of preventing aggregation-based signal degradation and allowing more flexibility in AuNP design, it also means that x-CSI cannot differentiate between AuNPs functionalised for different targets, limiting its ability to probe only a single molecular species in each scan. This limitation could in principle be overcome by using

differently functionalised nanoparticles of different high Z -numbered elements, though such nanoparticles are not considered here as this thesis focuses on AuNPs.

Current x-CSI systems are also limited based on the x-ray fluxes that they can tolerate before pile-up effects begin to degrade the spectral performance of the system[294]. This is a limitation in the count rate of the electronics used, however it translates to a limitation in temporal resolution at a given noise level as the flux cannot be arbitrarily increased to generate an image in a shorter exposure time. This contrasts with EI approaches which measure the total dose delivered, and so perform better with shorter exposures because they minimise electronic noise.

Spectral performance of x-CSI systems can also be degraded by charge sharing effects between pixels[329], which limits the effective pixel sizes used. Despite the trade-off between spatial resolution and energy resolution, x-CSI pixel sizes are typically below their EI equivalents so in principle charge sharing could be mitigated by increasing pixel size whilst still providing adequate spatial resolution. Larger pixels also result in shorter intervals between counts however, increasing the spectral distortion due to pulse pile-up as previously noted. This makes optimisation of pixel size a more complicated process and a more important component of designing an x-CSI system for a given application, potentially reducing the versatility of x-CSI machines compared with their EI counterparts. Nevertheless, the spectral information contained in an x-CSI scan makes them uniquely suited to some tasks.

One approach to reducing spectral distortions without sacrificing spatial resolution that has been employed involves the execution of charge sharing correction algorithms (CSCAs) at the level of the ASIC[330][331]. This approach involves linking pixels together so that charge sharing events can be identified between them and corrected for in the analogue domain before electronic readout. This can result in impressive preservation of spatial and spectral resolutions, however again limits count rates and so limits temporal resolution[332]. This is because in pooling information from N pixels to reconstruct a single event, a CSCA reduces the maximum number of photons the system could report by a factor of N . Such a CSCA would also sum the electronic noise from the N pixels together, increasing the contribution of electronic noise to the calculated photon energy. Alternative approaches have been proposed to overcoming this limitation by shifting the CSCA offline, into the digital domain[333][334]. This approach maintains system temporal resolution whilst providing a more modest reduction in spectral distortions, though it may find utility for some applications.

Remaining spectral distortions complicate the reconstruction of x-CSI scans in a way that is different from optical spectral imaging. This is because, whilst optical photons can be reliably assumed to be completely absorbed and so to register within a relatively narrow energy range, x-ray fluorescence and other charge sharing effects can cause x-ray photons to register as a broad range of different energies[335]. Whilst approaches have been proposed to deconvolve these effects, and indeed

impressive separation and quantification of materials has already been noted in this chapter, it remains the case that offline algorithms to optimise the spectral clean-up and unmix materials are still a matter of research and under development.

A major limitation that should be noted from a research perspective regarding the development and improvement of x-CSI systems is their scarcity and likely cost. As previously noted, to date there is only one supplier of commercially available x-CSI systems for research applications, and even these are designed for small animal rather than human use. This limits the number of research teams that can develop the systems, and unfortunately limits the exploration of clinical applications. A significant amount of work is being done on x-CSI systems *in silico*, and fortunately some research groups with access to physical machines are making data available to the wider community to work with, however it remains the case that time with a physical x-CSI system is a rare commodity and that this can limit development of this new technology. When these systems are eventually released for commercial use, they will likely initially be expensive compared with CT, ultrasound, and a range of other modalities, though likely still cheaper than MRI. This cost is due to a range of factors including material availability, fabrication efficiency and the small scale of the production, and hopefully will reduce in the long term.

When used for clinical analysis, the amount of data an x-CSI system produces is enormous compared with its competitors, with data files for a human whole-body scan predicted to be ~1 TB. For comparison, DICOM files of a CT used in hospitals tend to be tens of MB in size[336], and the most detailed whole body CT data set taken and available for public use clocks in at ~40 GB[337]. Questions surrounding how such large data sets will be preserved, transferred, and curated remain to be answered, though this is largely an issue of logistics and hopefully will be resolved by future improvements in data infrastructures in general.

A final limitation of x-CSI that should be borne in mind when considering its clinical potential is the current understanding of CT held by doctors. The ubiquity of CT scanners in the modern medical setting has led to many doctors understanding the uses and limits of x-ray imaging. They are thus aware of problems associated with conventional CT that simply will not exist with x-CSI systems, such as poor soft tissue contrast, significant radiation doses and a lack of molecular imaging. As it will be the doctors, not the systems engineers, who will ultimately decide which scan is most appropriate for a given patient, work will be needed to remove these engrained assumptions regarding what is possible with CT, and when MRIs would be more appropriate. This problem is less prominent in techniques such as PASI as this technique is so dissimilar from the other tools currently used routinely in a clinical setting that doctors will likely not have a reference point or set of biases that first need displacing.

4.5 Relevance of this work to x-CSI for RDEE prediction.

x-CSI has many advantages for the specific task of quantitatively imaging AuNPs, including the ability to use physical properties (the K-edge) as spectral fingerprints for Au atoms, the low noise

of the system, higher dose efficiency than EI CT and the higher interaction probability between Au and x-rays compared to other components of the body. To date, x-CSI has shown itself capable of accurate quantification of AuNPs down to concentrations of at least 1 mg/ml. For the specific task of imaging AuNPs *in vivo* to predict RDEE, this sensitivity is less than ideal, with 42% of AuNP-mediated RDEE studies considered in this section utilising Au concentrations lower than this threshold. It is hoped that this threshold can be reached through optimisation of the hardware and software used in x-CSI systems specifically for AuNP imaging. Optimising both x-CSI hardware and software, in addition to assessing the feasibility of using PASI for *in vivo* AuNP imaging, constitutes more work than is reasonable for a single PhD placement. For this reason, this thesis will focus specifically on the optimisation of an x-CSI detector's hardware for AuNP detection.

Section 4.4 identified a range of limitations for x-CSI including a scarcity of physical x-CSI systems and the complicated trade-off between spatial and spectral resolution associated with optimising pixel sizes. The optimisation is further complicated by the variable use of CSCAs by different groups, as these algorithms will intrinsically affect effective pixel size.

The work in this thesis sets out to compensate for the scarcity of physical x-CSI systems by developing and validating a simulation framework capable of modelling a range of x-CSI processes and system parameters, including charge sharing effects and the algorithms designed to correct for them. The development of this framework and its validation form the basis of Chapter 5. Using this framework, this thesis then aims to optimise sensor physical parameters such as pixel thickness and pitch for the specific task of Au detection. An investigation of the effect of pixel pitch and sensor thickness on a range of metrics forms the basis of Chapter 6. Due to this thesis focussing on hardware rather than software optimisation, optimising for sensor performance at the K-edge of Au is used as a proxy for Au imaging tasks, so that the optimisation can be reconstruction agnostic. Finally, in Chapter 7, this thesis considers the role of CSCAs in shaping an x-CSI detector's response. This is done by comparing a range of different CSCAs and looking for common patterns in their effects on the metrics considered in Chapter 6. In keeping with the decision to focus on hardware rather than software optimisation, only online, analogue CSCAs are considered in that chapter.

The simulation framework developed can simulate the entire imaging chain from photon production to projection image generation, with and without a range of CSCAs, and at a range of medically relevant fluxes. It is hoped that this work will provide a reproducible tool for simulating x-CSI systems and demonstrate their utility in optimising x-CSI systems for AuNP detection, as well as providing insight into the likely optimal hardware parameters for quantifying AuNPs accurately with x-CSI.

Chapter 5.

Simulating an x-CSI framework: CoGI

The previous chapter constituted a major overview of how x-CSI systems work, including sources of signal degradation and potential noise. This chapter will look at how the physical processes occurring within an x-CSI detector can be modelled to give an estimate of the signals it would likely output in response to a given irradiation condition. The simulation framework that is developed is referred to as CoGI (**COMSOL-Gate Interlocutor**), and both its development, utility and limitations will be considered in this chapter. This chapter will conclude with experimental validation of CoGI using two different detector-source combinations.

5.1 Introduction and Motivation

The many benefits of x-CSI systems proposed in Chapter 4 depend on the ability of an x-CSI system to distinguish incident photons based on their energy. Good energy resolution is essential to photon energy discrimination and thus, for medical applications of x-CSI, materials with a high intrinsic energy resolution that operate at medically relevant fluxes ($10^6 - 10^9$ photons $\text{mm}^{-2} \text{s}^{-1}$) are required. For widest clinical impact, these materials should be able to deliver these properties at or near to room temperature, with little additional cooling. Cadmium telluride (CdTe) and cadmium zinc telluride (CZT) are the most widely studied materials for medical x-CSI applications, owing in part to their higher absorption efficiencies at photon energies relevant to medical imaging (1 - 140 keV) when compared with more commonly used semiconductor materials (~80% for 1 mm CdTe at 100 keV compared with ~35% for 1 mm Ge and ~4% for 1 mm Si at the same energy)[338]. Additionally, CdTe and CZT have relatively high charge carrier mobilities for both electrons and holes, and low pair production energies, producing good intrinsic energy resolutions, as can be seen from Table 5.1.

Table 5.1. List of physical properties at 298.15K for common semiconductors radiation sensors. Data obtained from Ballabriga et al[344]. Z-numbers for compounds are listed in order of appearance in the material's name.

Material	CdTe	CZT	Si	Ge	GaAs
Z-Number	48, 52	48, 30, 52	14	32	31, 33
Density (g cm⁻³)	6.2	5.78	2.33	5.33	5.32
Band gap (eV)	1.44	1.57	1.12	0.67	1.43
Pair creation energy (eV)	4.43	4.6	3.62	2.96	4.2
Resistivity (Ω cm)	1E9	1E10	1E4	50	1E7
μ_e	1.1E3	1.0E3	1.4E3	3.9E3	8.0E3
$\mu_e\tau_e$	3.3E-3	1.0E-3	>1	>1	8E-5
μ_h	1.0E2	1.0E2	4.8E2	1.9E3	4.0E3
$\mu_h\tau_h$	2E-4	3E-4	~1	>1	4E-6

From an imaging standpoint, smaller pixels are generally desirable as they can produce higher resolution images for a given system geometry, however smaller pixel sizes come at the expense of lower SNRs and increased spectral distortions caused by incident photons depositing their energy across multiple pixels (charge sharing effects: CSEs). Application specific integrated circuits (ASICs) designed for x-CSI detectors typically utilize smaller pixel sizes (down to 55 μm pitch[339]) than conventional EI systems. This is because unlike x-CSI ASICs, EI ASICs integrate electronic noise in addition to the signal contributed by collected photons. This means that, for a given flux, smaller pixels on an EI ASIC result in an increasing fraction of the output signal originating from noise (decreasing SNR), as a smaller number of photons are intercepted per pixel. x-CSI ASICs can bypass this constraint however, by employing a trigger threshold, set above the electronic noise floor, so that false counts due to electronic noise can be entirely excluded from the system, preserving SNR[340]. Further, x-CSI ASICs can actually benefit from smaller pixels because they mean lower per-pixel count rates for a given flux, reducing the necessary reset speed of the counting electronics. CSEs are more of a problem for x-CSI ASICs however, as x-CSI systems rely on information about incident photon energy to perform material classification and quantification tasks[295][341][342]. The effect of CSEs on spectral metrics is arguably the single strongest limiter of x-CSI ASIC pixel sizes[343].

Charge sharing correction algorithms (CSCAs), employed at the level of the ASIC and usually operating pre-thresholding, have been shown to reduce CSEs and improve multiple imaging metrics[345] [335]. A variety of different CSCA implementations have been proposed, however they all operate according to similar principles. CSCAs operate by identifying temporally close events in adjacent pixels and using them to correct the recorded energy spectrum in some way, either by reconstructing a likely incident photon energy or suppressing counts identified as being the result of CSEs. CSCAs have been shown to improve spectral response at pixel sizes down as far as 55 μm [346], however always at the expense of some other metric e.g. lowering the x-ray flux at which pile-up becomes a problem[332] or falsely flagging unrelated events in adjacent pixels as being from a single incident photon[347].

The optimal pixel size for an x-CSI ASIC is thus determined by a variety of competing pressures on pixel size and will likely vary based on the CSCA employed (if any), the application of interest and the x-ray flux regime it is operating in. Currently there is no way to determine optimal pixel size based on these many parameters *a priori*. Where the costs of ASIC prototyping are prohibitively high or technologically difficult, comparisons of different ASIC designs are often performed using simulations[348][349][350]. Such simulations allow ASIC geometric parameters to be optimised rapidly, facilitating prototype development and allowing x-CSI systems still in development to be compared with more mature imaging systems such as EI detectors in dual energy CT[351]. Many of these simulations model photon-detector interactions using Monte Carlo techniques and either directly convert these interactions into output signals based on experimental data from similar systems (e.g. by

introducing a measured blurring to match energy resolution[352]) or reconstruct the estimated signals based on simulation of some ASIC electronics[353], again including free parameters fitted to experimental reference data (e.g. by allowing the simulated voltage to differ from that used experimentally[354]).

The work presented in this chapter aims to advance on these simulations in three main ways:

1. by incorporating more physical processes involved in CSEs than comparable previous work from our group[355] such as Auger electrons
2. by incorporating the signal contribution from holes into a full simulation for the first time
3. by simulating CSCAs into the signal processing chain, allowing for CSCA corrected energy resolutions to be simulated rather than intrinsic ones.

As a result of these changes, CoGI will be able to model the widest range of system designs to date, allowing for new applications such as the *in silico* optimisation of pixel dimensions for a given CSCA, or the reverse problem of selecting which of a range of CSCAs provides the best performance for a given pixel dimension, with respect to a task relevant spectral metric.

5.2 Processes to simulate

The processes simulated to model an x-CSI system can be broken down as shown in Table 5.2. In the context of an x-CSI detector, photon-matter interactions concern all events from photon production to either total energy deposition in a material (after any fluorescence) or escape from the simulated volume. Semiconductor charge transport covers the processes by which energy deposited within the sensor can then go on to produce a charge accumulation at the collecting anode of the sensor, producing a signal that can be read out from a charge sensitive preamplifier. Finally, the resulting signal from a given pixel is then processed, first by combing signals from adjacent pixels in accordance with some charge sharing correction algorithm (CSCA), and then by calibrating the output of the detector so that signal intensities can be correlated to incident photon energies.

5.2.1 Photon generation

Photons can be generated in one of four ways in CoGI: radioactive decay, Bremsstrahlung, primary source, and x-ray fluorescence.

Table 5.2. List of the physical effects and electronic processes modelled in CoGI to represent an x-CSI scanner.

Category	Effects
Photon-matter interactions	Photon generation, Compton scattering, Rayleigh scattering, photoelectric absorption, x-ray fluorescence, Auger /photoelectron production and Auger /photoelectron energy dissipation (pair production and radioisotope decay chains are also useful for other medical imaging processes, however they are not relevant to this thesis and so whilst they are part of the simulation framework, they will not be discussed further here).
Semiconductor charge transport	Charge carrier production, charge carrier drift, charge carrier diffusion, electrode charge induction, charge carrier trapping.
Signal post-processing	Charge sharing correction, conversion of collected charge to incident photon keV.

5.2.1.1 Radioactive decay

Radioactive decay concerns the rearrangement of the nucleus of a radioisotope from a higher energy configuration to a lower energy one. An example of this process can be seen in Figure 5.1. The reconfiguration of the nucleus can involve transformation of protons to neutrons or vice versa, or simply a shift in nuclear orbitals occupied by either nucleon. Where nucleon transformation occurs, a massed particle is ejected from the nucleus, whilst in purely nucleon orbital transitions only a γ -ray is required.

Regardless of the mechanism, conservation of energy requires that the energy differential of these two states be emitted from the nucleus in the form of α , β or γ radiation (where the increase in kinetic energy of the recoiling nucleus is negligible). α -radiation is equivalent to the nucleus of ${}^4\text{He}$ (two protons and two neutrons), without any orbiting electrons. β -radiation comes in two varieties: β^- and β^+ , which are equivalent to a high energy electron or positron respectively. γ -radiation in contrast is an electromagnetic photon. Technically a distinction is made between x-rays and γ -rays based on their origin, with γ -rays being specifically due to nuclear rearrangements in radioisotopes whilst x-rays result from all other sources. In all other respects however, x-rays and γ -rays can be treated as identical where their energies coincide. As CoGI is concerned with the interaction of photons with matter, their origin is not relevant and so the term x-ray shall be used in this chapter to cover both x-rays and γ -rays.

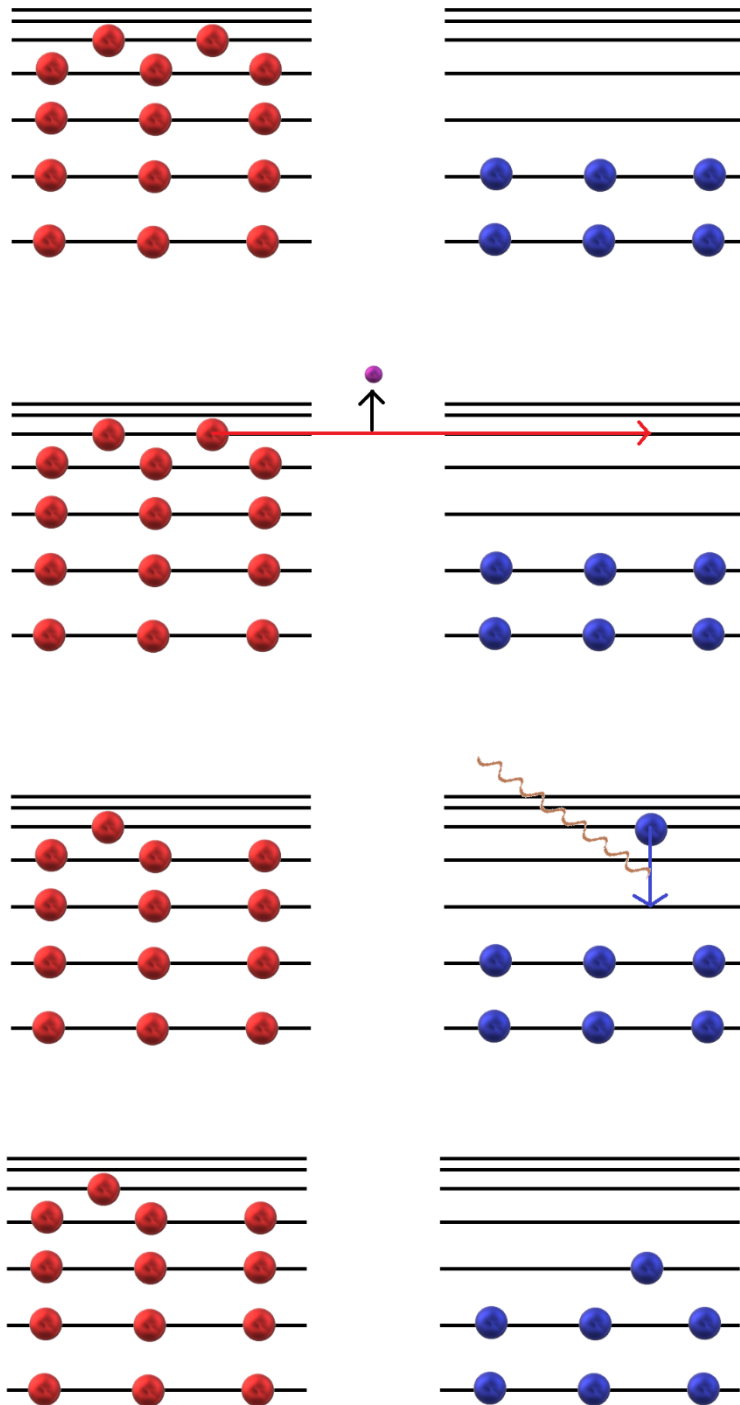


Figure 5.1. Schematic representation of the process of radioactive nuclear decay. This diagram is designed to illustrate the general principles of nuclear decay and is not designed to be reflective of a particular isotope or atomic decay. Energy levels are shown separately for the protons (red) and neutrons (blue). (TOP) In the initial configuration shown here the most energetic protons occupy a significantly higher energy level than the most energetic neutrons. (SECOND LINE) A proton can spontaneously transition into a neutron, with the emission of an electron (purple) to conserve charge. (THIRD LINE) The new neutron occupies an energy level with vacant levels beneath it. This neutron thus spontaneously deexcites via emission of a gamma ray (orange wave) to fill this vacancy. (BOTTOM) The resulting configuration is in a lower total energy state than it was previously, resulting in a consequent increase in atomic stability. The change in Z-number means that the final atom is now a different element to the one it was before it decayed. Note that there may be a significant delay between the second and third lines of this diagram, and the deexcitation may proceed via a variety of routes if more than one lower energy level vacancy is available to it.

5.2.1.2 Bremsstrahlung

Bremsstrahlung, or braking radiation as it is also known, is produced by the deceleration of a charged particle within a magnetic field. According to Maxwell's equations, an accelerating charge will emit electromagnetic waves, and from the conservation of energy the energy of the wave will be equal to the change in kinetic energy of the deflecting particle. In the context of medical x-CSI, the charged particles in question are likely to be Auger electrons or photoelectrons, ejected from atoms after interaction with an incident photon. As they travel through matter, these particles are deflected by the

charge of other nuclei and consequently decelerated, resulting in the emission of electromagnetic energy (x-rays). The energy lost by such electrons per unit length is given by the equation

$$-\langle \frac{dE}{dx} \rangle \approx \ln \left(\frac{183}{Z^{\frac{1}{3}}} \right) \frac{4N_{\alpha}Z^2\alpha^3(\hbar c)^2}{m_e^2c^4} E_F \quad \text{eq. 5.1}$$

where N_{α} is the number of atoms per unit volume, Z is the atomic number of the material the electron is passing through, α is the fine structure constant of that same material, x is the path length through the material, m_e is the mass of the electron, E_F is the energy of the incident free electron, \hbar is Planck's constant, and c is the speed of light in a vacuum. What is evident from Equation 5.1 is that the stopping power of a material is related to its atomic number, Z . For the simulations considered in this project, that means the major sources of Bremsstrahlung radiation will likely be AuNPs, any metal in the detector casing or contacts, and the semiconductor sensor material.

5.2.1.3 Primary source

Primary source photons are assumed to already exist at the start of the simulation. This process is used to save computational resources in simulating the production of x-rays from a linear accelerator, which is otherwise a resource intensive process that is very inefficient due to the large number of Bremsstrahlung photons that are attenuated by the collimator or source casing without being emitted towards the detector. In order to avoid this time intensive process, two approaches are possible in CoGI: spectrum extrapolation or compartmental spectrum generation.

In the spectrum extrapolation process, the photon fluence at a range of discrete energies is given for an x-ray source, determined from experimental measurement, simulation, analytical approaches, or written reference materials. A linear interpolation is then made for the fluences between each discrete energy measurement to generate an energy spectrum, as shown in Figure 5.2. The area under this spectrum is then normalised such that the probability of a photon taken at random from the spectrum having an energy of k is given by the height of the spectrum at k . This approach has the advantage of allowing as many photons as wanted to be calculated from this spectrum and so the solution is easily scalable. The main limitation of this approach is that an x-ray tube's spectrum is inherently non-linear in nature, with sharp discontinuities around the K-edges of the target material used in generating the x-rays. It is therefore necessary to have a large enough number of measurements, particularly around the K-edge fluorescence peaks, to ensure that the linear approximation does not introduce severe artefacts into the energy spectrum such as a particularly broad range of K-edge energies.

In the compartmental spectrum generation approach, a Monte Carlo simulation is performed using the open source Monte Carlo program GATE[353] to simulate an x-ray generator involving the acceleration of electrons towards a solid target. The electrons emit Bremsstrahlung as they decelerate,

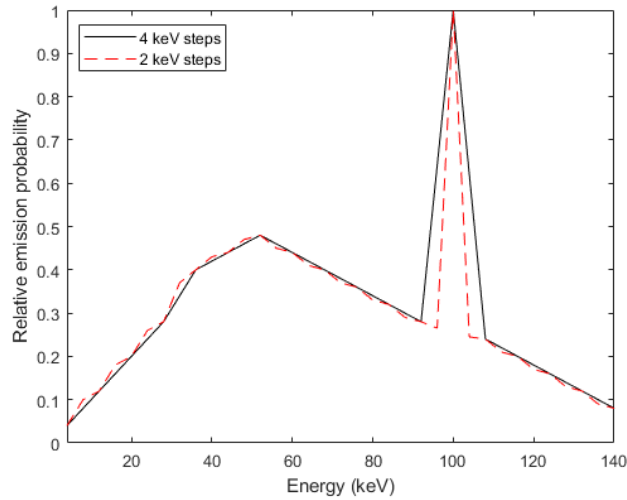


Figure 5.2. A fictional energy spectrum was sampled at two different resolutions: 2 keV or 4 keV. The spectrum was then reconstructed using the process of linear interpolation described in the text. Over most of the spectrum the difference in sampling is small, however around the K-edge of the target (sharp spike at ~100 keV) the 2 keV step size leads to a much narrower peak, more consistent with the K-edge which should ideally be modelled with a δ function.

and an aperture in the generator casing allows a subset of x-rays produced to escape the generator. A simulation tool is placed coincident with that aperture, which records the energy, velocity, time, and type of all particles (including photons) that cross the aperture. This recording can then be placed into full CoGI simulations to allow for the output of an x-ray tube to be simulated without requiring the full calculation to occur within CoGI. The primary advantage of this is that the computational resources needed for simulating the x-ray tube are only needed once, even if CoGI is used to simulate hundreds of different sensor types and phantom arrangements. Another advantage is that by increasing the number of photons in the x-ray generator simulation, the energy spectrum can be determined to arbitrarily fine structure. The major disadvantages of this approach however are that it requires a comparatively long time to determine the energy spectrum of a new x-ray generator, and that when the photons are called in a CoGI simulation their values are read from the file in order rather than randomly assigned. This means that there is an upper limit to the number of unique photons that can be called in the new simulation, and that is equal to the number of photons in the original file.

5.2.1.4 x-ray fluorescence

x-ray fluorescence was discussed in Section 1.2.1.1 and will only be recapped briefly here. As part of the interaction between a photon and an atom, an electron may be ejected from one of the core electron-shells of the atom, leaving a vacant orbital position. Where this vacancy is lower in energy than an occupied orbital within the atom, the electron from the occupied orbital can leap to the lower energy vacancy, resulting in the emission of a photon to carry away the energy difference between the two energy levels. As the energy levels within an atom are well defined and quantised in energy, the

emitted photons are of defined energies, with fluorescence x-ray energies being characteristic for each element.

5.2.2 Photon scattering (Rayleigh and Compton)

Photons can scatter from matter either elastically (Rayleigh scattering) or inelastically (Compton scattering). Rayleigh scattering involves a change in direction of the photon, without a net transfer of energy between the photon and the scattering particle, whereas Compton scattering involves a change of both photon direction and photon energy. In Compton scattering, the scattering particle is a weakly bound electron and by result of Compton scattering it is freed from its bound state (see Section 1.2.1.2). The freed electron recoils from the point of interaction with the energy and momentum equal to that lost by the incident photon (where the binding energy of the electron is considered negligible).

5.2.3 Photoelectric absorption

Photoelectric absorption involves the complete absorption of a photon by an electron in the target material (see Section 1.2.1.1). Due to the much higher energy value of x-rays compared with the binding energies of even the most tightly bound atomic electrons in current materials, x-ray absorption leads to the ejection of the absorbing electron from its bound state, with the electron carrying away a kinetic energy equal to the energy of the incident photon, minus the negligible values of its binding energy and the kinetic energy transferred to the recoiling nucleus it was ejected from, to conserve momentum. Due to the lower energy difference between them, the electrons most likely to photoelectrically absorb a photon are the most tightly bound, K and L shell electrons. The resulting vacancy in a core electron shell leaves the ion in an excited state, requiring deexcitation to the ground state by some mechanism.

5.2.4 Atomic deexcitation (x-ray fluorescence and Auger electron production)

An excited atom relaxes by having an electron from a higher energy orbital transition into the lowest unoccupied orbital. The resulting excess energy is then released from the atom either via x-ray fluorescence or less commonly by the production of an Auger electron (see Chapter 1, Figure 1.2). An Auger electron is an electron from a higher orbital which absorbs the excess energy and is consequently ejected from the atom. Auger electrons are thus produced with discrete energies, much like fluorescence x-rays.

5.2.5 Charge carrier production

Where a photon interaction with a semiconductor results in an excited electron, it is more appropriate to talk in terms of the band structure of the material than the atomic orbitals unless we are near to the surface of the material, due to the significant overlap in atomic orbitals and consequent energy level splitting. Local energy deposition from the above processes can thus lead to an electron

being excited from the valence band to the conduction band. Such an excitation results in both a conduction band electron and a vacancy in the valence band. This vacancy is referred to as a hole and for the purposes of this thesis can be thought of as another type of charge carrier with its own mobility, mass etc.

As x-ray photon energies tend to be several orders of magnitude greater than inter or intraband transition energies (keV for x-rays vs several eV for band gaps), an electron excited by an x-ray tends to be displaced, either directly or after losing energy as a free electron due to multiple scatterings and the production of Bremsstrahlung, towards the very top of the band structure. Once here, the electron rapidly deexcites to the bottom of the conduction band through a combination of coupled phonon and electron excitations. Due to the incredibly high energy of the excited electron compared to the band gap, many electrons are promoted across the band gap, and consequently many holes are produced. Semiconductors used for x-ray detection typically have electron-hole pair production energies orders of magnitude lower than the x-rays detected, meaning that a single x-ray photon can give rise to thousands of electron-hole pairs, resulting in a cloud of charge carriers.

5.2.6 Charge carrier drift

It is again important to remember that holes do not exist as physical entities, but rather are a mathematical tool for simplifying the net behaviour of the remaining electrons in the valence band. As holes are the result of the removal of an electron with charge $-e$ from a neutrally charged site, they have an effective charge of $+e$. We can thus model bulk electron motion in a semiconductor as the drift of two types of charge carriers, with opposite charge, in response to an applied electric field. The drift velocity of the charges will depend on the mobility of the charge carriers and the electric field experienced by the charge carriers. The mobility of the carriers depends on a wide range of material parameters. The field experienced by the mobile charge carriers is determined largely by the applied voltage across the semiconductor. In practice, there will be interaction between the two types of charge carriers, including charge screening. To limit the computational resources required to model them however, the two types of charge carrier are treated as independent in CoGI.

5.2.7 Electrode charge induction

For simplicity, Figure 5.3 shows the case of a single electron approaching an electrode in response to an applied external field. Let us define the weighting potential, φ_k , for the electrode A as the electric field that would exist were A set to 1 volt, all other electrodes set to 0 volts and space charges (such as the free electron) removed.

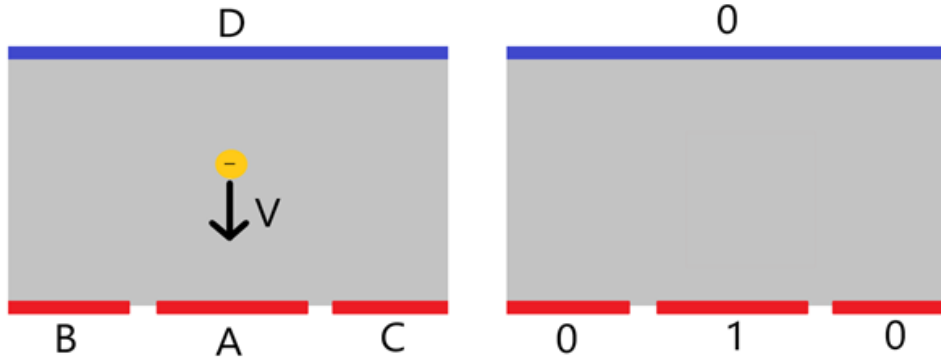


Figure 5.3. (LEFT) The situation within a semiconductor in which an electron (yellow ball) is moving with respect to four fixed electrodes (A-D). Calculation of the induced charge on electrode A by the movement of this electron as a function of time is a time consuming and computationally intensive process to solve directly. The problem can be greatly simplified by approaches such as the one detailed in this section. (RIGHT) These approaches all require the calculation of the weighting potential, which is the electric field that is present within the volume of interest (the semiconductor in this case) when the electrode of interest (A) is set to unit voltage, and all other electrodes are set to zero Volts.

Considering the setup of Figure 5.3, and utilising the concept of a weighting potential as described, Ramo[356] and Shockley[357] were able to independently show that the presence of the electron induces a charge on electrode A as given by the equation

$$Q_A = -e\varphi_e \quad \text{eq. 5.2}$$

where Q_A is the charge induced on electrode A, e is the elementary charge of the electron and φ_e is the potential of φ_k at the point occupied by the electron. The induced charge is thus seen to be opposite in sign to the charge whose movement induces it. This conclusion is reached from a purely electrostatic argument. To consider the case of a moving charge, we differentiate Equation 5.2 with respect to time, giving

$$\frac{dQ_A}{dt} = -e \frac{d\varphi_e}{dt} \quad \text{eq. 5.3}$$

φ_k does not vary in time, however it does vary in space, so the value of φ_e will vary as the electron moves. For this reason, we exchange the differential of φ_e with respect to time with its partial differential with respect to the direction of electron motion. For simplicity, let us consider the case in which the electron's motion is parallel with the electric field of the weighting potential, which we denote as the x -axis. The differential of x with respect to time then needs to be included to balance the equation, giving

$$\frac{dQ_A}{dt} = -e \frac{\partial \varphi_e}{\partial x} \frac{dx}{dt} \quad \text{eq. 5.4}$$

Finally, we note that $\frac{dQ_A}{dt}$ is i (the current induced at A), $\frac{dx}{dt}$ is the electron's velocity (v_e), and $\frac{\partial \varphi_e}{\partial x}$ is the negative of φ_v , where φ_v is the component of the electric field in the direction of electron motion. This gives us

$$i = ev_e\phi_v \quad \text{eq. 5.5}$$

Generalising for the case in which the electron's motion is not directly along the x-axis we find that

$$i = e\phi_v \cdot \mathbf{v}_e \quad \text{eq. 5.6}$$

where ϕ_v is the component of the weighting field in the direction of \mathbf{v}_e .

It should be noted that this method for calculating the induced current on an electrode is independent of the actual electric field experienced by the electron, as well as the presence of any stationary space charges, as demonstrated by He[358]. It is important to note that whilst the current induced for a given movement is not affected by space charges and applied voltages, the rate of movement, v , can indeed be affected by these factors, meaning space charges can still degrade overall detector performance.

The above arguments can be used to determine the current induced by holes by reversing the polarity of the charges in Equation 5.2.

5.2.8 Charge cloud expansion (diffusion and repulsion)

Whilst Ramo and Shockley considered the case of a single electron, Section 5.2.5 explains that the high energy of x-rays compared with the band gap in most semiconductors leads to the production of a cloud comprised of many thousands of charge carriers from a single incident photon. In addition to drift down an electric potential towards a collecting electrode, the motion of a charge carrier will also include components from the pressure to move down its concentration gradient (diffusion) and electrostatic interactions with the other charge carriers in the cloud (repulsion). Both diffusion and repulsion will add a lateral velocity component to the charge carriers, pointed away from the centre of the charge cloud, causing the charge cloud to expand with time. As with drift, charge carrier mobility will determine how fast the charge cloud expands, however unlike drift the extent of the externally applied voltage will not affect the speed of lateral expansion. Lateral expansion does depend on the number of charge carriers in the cloud, however. Consequently, processes which increase (e.g. higher energy photon absorption) or decrease (e.g. charge carrier loss to trapping) the number of charge carriers will result in faster or slower charge cloud expansion respectively. As a result of the interplay between drift and these cloud expansion mechanisms, higher applied voltages tend to result in smaller cloud sizes at the collecting electrodes. A relevant distinction between diffusion and repulsion is that whilst diffusion of a charge carrier is dependent on the concentration of that charge carrier only, the extent of repulsion may be affected by both types of charge carrier, as attraction to opposite charges occurs in parallel with repulsion by the same charges. As noted in Section 5.2.6, CoGI simulates the motion of electrons and holes independently, and consequently calculation of the interplay between them is not possible at this time. CoGI thus models charge cloud expansion as resulting purely from diffusion, with a consequent underestimation of charge cloud size at the time it reaches the anode.

5.2.9 Fate of charge carriers (trapping, recombination, and collection)

Charge carriers that drift towards an electrode can be removed from the bulk of the sensor material in one of three ways: through being trapped in crystal defects, recombination or reaching the electrode and being “collected”.

5.2.9.1 *Trapping*

Defects in the crystal lattice of the semiconductor introduce new energy levels into the band structure localised around the defects. These defects may be due either to the inclusion of unexpected elements into the crystal lattice (contamination) or displacement of the lattice structure at a range of size scales (point, line, or surface defects). As a result of these energy levels being spatially localised around the defects, electrons that deexcite into them also become spatially localised within the semiconductor, arresting their drift towards the electrodes. Such trapped electrons may be able to escape from the trap by acquiring sufficient energy from thermal fluctuations to return to a delocalised energy level (de-trapping), or alternatively they may be lost by deexciting into a vacancy in the valence band (recombination). As before, similar arguments can be used to explain how holes can become trapped at defect sites.

5.2.9.2 *Recombination*

As holes are essentially gaps in an energy level from which an electron has escaped, it is possible for holes in the valence band to recombine with electrons in the conduction band, removing both the hole and electron as charge carriers. Recombination can occur via one of several mechanisms, broadly classified as radiative recombination (with excess energy carried away by a photon) or non-radiative recombination (dissipated by another charge carrier or a phonon). Trapping centres increase the rate of recombination by both concentrating charge carriers into a smaller spatial region and providing a mechanism for momentum matching between electrons and holes attempting to recombine.

5.2.9.3 *Collection*

Finally, electrons may reach the electrode they were drifting towards, at which point they are said to have been collected by that electrode. For the purposes of this thesis, the fate of the charge carriers beyond this point is not relevant.

5.2.10 Charge sharing correction algorithm

Interaction of a single photon with the sensor material may lead to charge being deposited across multiple detector pixels, either because the photon’s energy was initially deposited across several pixels (due to Compton scatter, Auger/photoelectron travel or fluorescence x-rays) or because charge cloud expansion produced a charge cloud that spanned several pixels by the time it reached the

collecting electrode. Charge sharing correction algorithms (CSCAs) try to identify where charge has been shared like this and prevent those events from degrading the spectral information in the image overall, either by removing them or by attempting to combine the energies recorded on the various pixels to reconstruct the original photon's energy. A range of different CSCAs have been proposed and details of any specific ones modelled in this thesis will be provided in the relevant sections.

5.2.11 Conversion from collected charge to incident photon keV

The above processes result in some amount of charge, q' , accumulating on the anodes, which will be read out as a signal that must then be correlated with an incident photon energy. The size of the charge induced by a given photon depends on a variety of material parameters such as the pair production energy, trap density and charge carrier mobility, as well as on the amount of time over which the charge is integrated. To convert between signal out and incident photon energy, a series of sources with known energy may be used to establish reference points in the energy spectrum recorded by the detector. These energies should be chosen to cover the energy range over which the detector is intended to operate. Where calibration is needed in the work described in this chapter, a simple three-point linear calibration is used.

5.3 Overview of CoGI

CoGI is comprised of three different simulation environments that work together to model all of the processes discussed in the previous section: GATE, COMSOL and MATLAB. This section will look at how the physical processes are handled in each of the above environments, as well as how the different environments are linked together into a single framework. Figure 5.4 shows a schematic overview of the major components of CoGI, along with the data that are passed between them. As can be seen, the user of CoGI provides information on the experimental setup to be simulated to GATE, and information on the material properties and physical geometry of the detector to both GATE and COMSOL. GATE and COMSOL then output data that are fed into a custom MATLAB environment, along with information on the detector design and shaping time applied in the electronics. The MATLAB environment is pre-programmed with any CSCAs that are necessary for the simulation, and the user is prompted to specify which if any CSCAs should be considered in constructing the output signals. Where these CSCAs require additional information (e.g. coincidence windows), the user is asked to provide them at the time of running the MATLAB scripts. In reality these parameters are hard wired into ASIC design, but it was decided to keep these parameters as variables to provide more flexibility to optimise for a given application. In addition to a raw data file containing the signals from the various pixels as a function of time, CoGI can output visual plots of the simulated detector results, for quick comparison with experimentally determined results. Each component of the simulation will now be looked at in more detail.

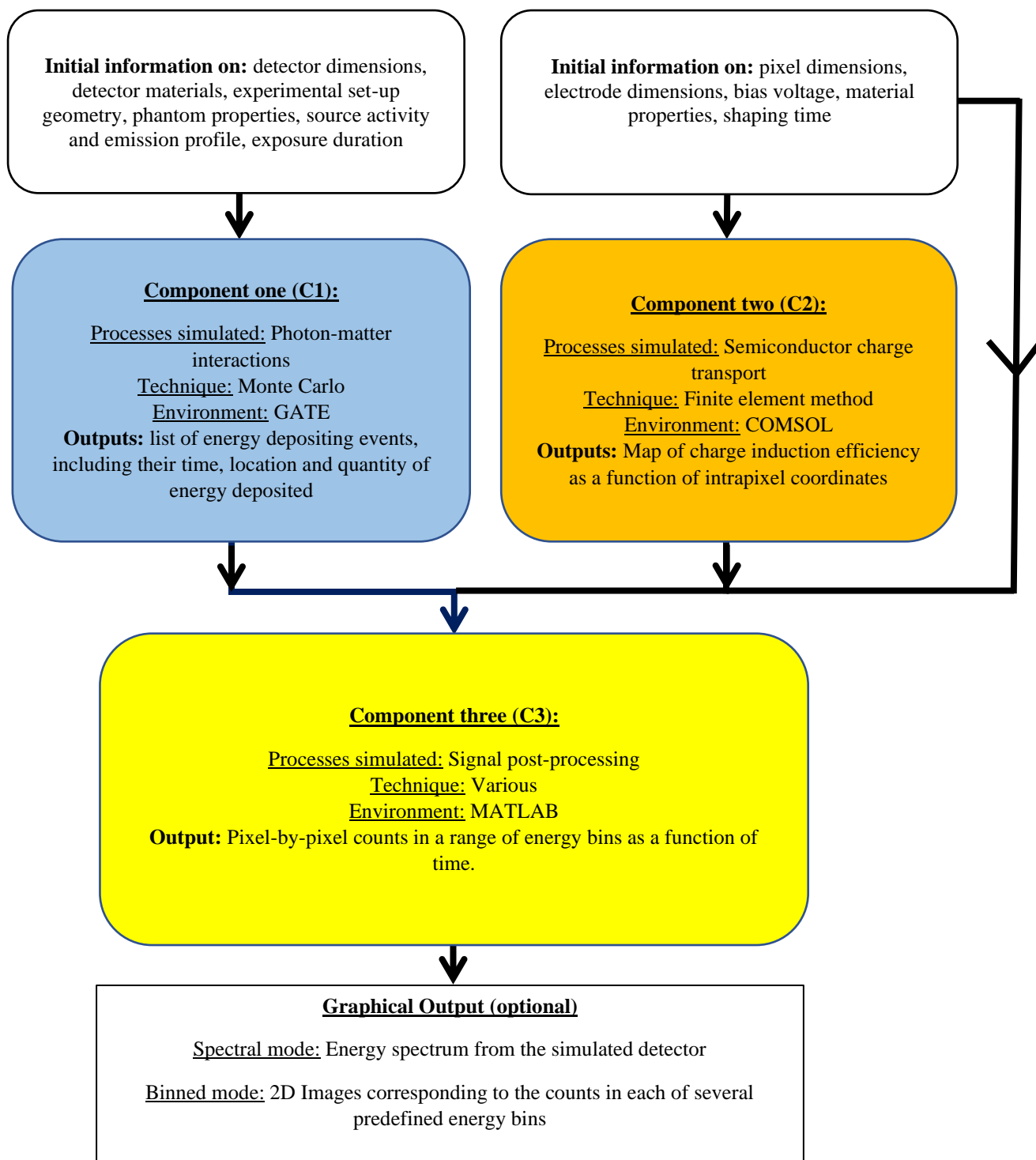


Figure 5.4. Flow chart illustrating how information is fed into and passed between the various components of CoGI. With reference to Table 5.2, C1 handles the Photon-matter interactions, C2 models the effect of semiconductor charge transport. C3 then takes the output from C1 and C2 and implements signal processing to generate the detector output.

5.3.1 Component one (C1)

Component one (C1) is a Monte Carlo simulation which is used to model the physical processes classified in Section 5.2 as photon-matter interactions. Monte Carlo techniques use a combination of random number generation and probabilistic equations to determine probable outcomes to a question where the analytical solution is either too complex to efficiently calculate or is unknown, based on the accumulation of many events calculated using simpler equations. In the example of a photon interaction with matter, we cannot answer the question “At what depth will a photon be absorbed” analytically to give a unique solution, as the process of photon absorption is probabilistic. By simulating a large number of photons however, we can answer statistical questions regarding the mean absorption depth, as well as the range of depths, and other statistical factors.

The Monte Carlo work performed in CoGI uses the open source software known as GATE[353], which is based on the well-known Geant4 framework[359], however with pre-built modules for simulating major components of common medical detector systems and managing their data output. The processes listed in Sections 5.2.1 - 5.2.4 were modelled as discussed, with the ‘Livermore model’ (physics calculations optimised for low energy x/ γ rays) and atomic deexcitation included, and the data extracted in raw form: without utilising any of the internal GATE signal reconstructions. This data file contains information on the spatial and temporal coordinates of energy depositions within the sensor material, along with the quantity of energy deposited by that event. Only final energy depositions are output, after accounting for atomic deexcitation effects.

5.3.2 Component two (C2)

Component two (C2) is a finite element method (FEM) simulation which is used to model the physical processes classified in Section 5.2 as semiconductor charge transport. Finite element methods are applied in solving problems in which a physical quantity varies in both space and time as governed by some system of partial differential equations (PDEs), where an analytical solution cannot be applied. FEM works by approximating the variables in the PDEs that have a spatiotemporal dependence, using a linear combination of more easily calculable basis functions. The selection of appropriate basis functions can be performed easily for small enough spatial domains, so the geometry to be solved for is discretised into smaller geometric regions of simpler shape (usually some combination of squares and triangles in 2D, and 3D volumes with surfaces comprising of these shapes, such as triangular pyramids or cubes). The equations for all the discretised elements are then collected into a large set of equations, which can be solved by numerical techniques for given boundary conditions. Similar discretisation of the problem in time allows for a complete solution to the problem that approximates the solution to the original PDEs. Due to a long history of study, a range of mathematical approaches are available for quantifying (or at least bounding) the error of the solution when compared with the true solution.

The finite element method implemented in CoGI is performed using the commercially available software package COMSOL, version 5.2a[360]. The processes listed in Sections 5.2.5 - 5.2.9 were modelled, by implementation of Prettyman's adjoint continuity equations for determining the current induced in a collecting anode in a semiconductor detector[361], as shown in Equation 5.7

$$\frac{\partial C}{\partial t} = \mu_C \nabla \varphi \cdot \nabla C + \nabla \cdot (D_C \nabla C) - \frac{C}{\tau_C} + \mu_C (\nabla \varphi \cdot \nabla \varphi_k) \quad \text{eq. 5.7}$$

where C is the concentration of the charge carrier in question, t is time, μ_C is the mobility of the charge carrier, D_C is the charge carrier's diffusion coefficient, τ_C is the average lifetime of free charge carriers, φ is the electric field in the pixel during operation and φ_k is the weighting potential within this pixel, as defined in Section 5.2.7. The processes of charge carrier generation ($\mu_C \varphi \cdot \nabla \varphi_k$), diffusion ($D_C \nabla C$), drift ($\mu_C \nabla \varphi \cdot \nabla C$) and loss to trapping (C/τ_C), can be seen represented in this equation. It should be noted that the de-trapping of charge carriers from traps is not captured in this equation. The use of this approximation is justified here on the basis that the high voltage applied across the semiconductor, in combination with the high mobility for the materials modelled (CdTe and CZT), means that the transit and collection times for the charge carriers is sufficiently short compared to the residency time within the traps that the effects of de-trapping on charge collection can be ignored to a first approximation.

It has been shown[358][361][362] that the solution to Equation 5.7 results in a time dependent map of the charge induction efficiency (CIE) for a unit charge deposited at all possible locations. CIE is thus a function of time and is defined in this context as

$$CIE(t) = \frac{Q_A}{q} \quad \text{eq. 5.8}$$

where q is the charge deposited in the detector and Q_A is the charge on anode A due to the presence of this charge at the time t .

In order to model these equations in COMSOL, first the "Semiconductor module" was used to calculate static solutions for the electric field strength in the sensor material as a function of position, both under actual operational voltages (φ) and under weighting potential conditions (φ_k), as shown in Figure 5.3. Next, these values were used in the "Transport of Diluted Species module" to define a time dependent study which solves the equation

$$\frac{\partial C}{\partial t} + \nabla \cdot (-D_C \nabla C) + U \cdot \nabla C = R \quad \text{eq. 5.9}$$

where U is the velocity field for the dilute species and R is a generation term intended for simulating the time evolution of chemical reactions. In CoGI, U is defined as

$$U = -\mu_C \cdot \omega \quad \text{eq. 5.10}$$

and R as

$$R = \mu_c(\omega \cdot \omega_k) - \frac{C}{\tau_c} \quad \text{eq. 5.11}$$

where the symbols ω and ω_k are equal to $\nabla\varphi$ and $\nabla\varphi_k$ respectively. Substituting Equation 5.10 and Equation 5.11 into Equation 5.9 gives

$$\frac{\partial C}{\partial t} + \nabla \cdot (-D_c \nabla C) \pm \mu_c \cdot \omega \cdot \nabla C = \mu_c(\omega \cdot \omega_k) - \frac{C}{\tau_c} \quad \text{eq. 5.12}$$

Rearranging to fit the form of Equation 5.7 gives

$$\frac{\partial C}{\partial t} = \mu_c \cdot \omega \cdot \nabla C + \nabla \cdot (D_c \nabla C) - \frac{C}{\tau_c} + \mu_c(\omega \cdot \omega_k) \quad \text{eq. 5.13}$$

It can thus be seen that Equation 5.13 and Equation 5.7 are equivalent if we accept the notation difference that $\omega = \nabla\varphi$ and $\omega_k = \nabla\varphi_k$.

By solving Equation 5.13 for both electrons and holes, C2 can thus produce a map of the total charge induced in an anode as a function of time. In solving for holes, the drift term needs to be reversed ($-\mu_c \cdot \omega \cdot \nabla C$ rather than $\mu_c \cdot \omega \cdot \nabla C$) to indicate that the direction of drift in an electric field is opposite in direction for holes compared with electrons, due to their opposite charges. Relevant CIE maps are calculated and output for three different pixel types, named according to their position within an array of pixels, as illustrated in Figure 5.5. Central pixels (purple) are entirely surrounded by other pixels, edge pixels (green) are surrounded on three sides by other pixels and corner pixels (red) are surrounded on two sides by other pixels. For computational reasons, the work in this chapter evaluates Equation 5.13 for electrons and holes, for each pixel type, at a single time point, t_s , which corresponds to the time over which charge is integrated in the system being modelled. Justification for this is given in Section 5.3.3.

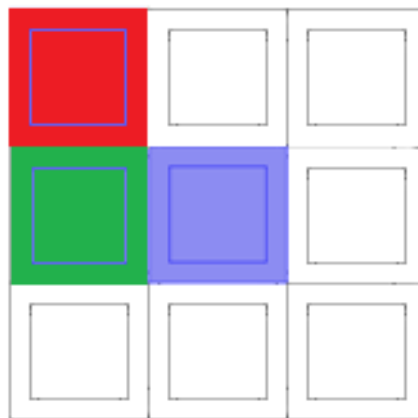


Figure 5.5. 3x3 grids of pixels like the one pictured above were used in calculating the CIE maps in COMSOL. Each pixel is defined as the central collecting anode (smallest squares) plus half of the distance between it and its neighbouring anodes (medium sized squares). 3 different pixel types were simulated in turn: ‘central’ pixels surrounded by 8 others (purple), ‘edge’ pixels surrounded on all but one side (green) and ‘corner’ pixels surrounded on all but 2 sides (red).

5.3.3 Component three (C3)

Component three (C3) is a custom MATLAB script that performs several functions based on the data output by both C1 and C2. The overall aims of these functions are illustrated in Figure 5.6. More detail about each step is helpful in understanding how C3 merges the output data from C1 and C2 to simulate the output from an x-CSI detector.

Step 0: When calling C3 the user supplies (either directly or via a file):

- the address of the folder containing the C2 output
- the address of the file containing the C1 output
- an array containing information on the detector geometry and pixelation
- a variable setting the CSCA to be implemented (if any)
- a variable setting the shaping time being simulated
- a variable setting the non-extendable deadtime being modelled
- a variable setting the desired output (continuous energy spectrum, binned energy spectrum, raw projection images or all of the aforementioned)
- an array containing information on the energy bins desired

Step 1: CoGI has a standard procedure for naming files so that the parameters used in creating them are coded into their file names. C3 first checks that the C1 and C2 output file names provided match expectations based on the array of geometry information. It then checks that the names of all output files it will produce are within the character limit of the system it is working on. If both checks are passed, CoGI proceeds to data processing.

Step 2: C2 generated *CIE* maps are read into the MATLAB workspace. The absolute dimensions of the simulated pixels, along with the spatial sampling rate in each of the three spatial directions, are compared across all maps imported, to ensure that the maps are compatible. Once this is verified, the *CIE* for a given location is calculated as a superposition of the *CIE* contributions from holes and electrons according to the equation

$$CIE(x, y, z) = CIE_e(x, y, z) + CIE_h(x, y, z) \quad \text{eq. 5.14}$$

where CIE_e is the charge induction efficiency of electrons, CIE_h is the charge induction efficiency of holes and CIE is the total charge induction efficiency of all charge carriers.

Step 3: The spatial coordinates used in the output of C1 are absolute with respect to the centre of the simulation space. A translation is applied to convert these ‘within simulation space’ coordinates to a coordinate system defined with respect to the limits of the sensor material: a ‘within sensor’ coordinate system. The sensor is then pixelated, based on a user provided pixelation scheme, and global events assigned a corresponding pixel number. GATE is capable of performing this pixelation itself, however for reasons of computational efficiency it was decided this will be left to C3 instead.

Step 0: Receive data addresses, detector geometry information and list of signal processing parameters from the user.
Step 1: Check all data files are formatted as expected and correspond to user selections for pixel geometry.
Step 2: Superimpose electron and hole <i>CIE</i> maps for a given pixel type to produce a “charge carrier” <i>CIE</i> map. Normalise spatial dimensions of map. Repeat for all pixel types considered. Store in a 3D <i>CIE</i> matrix.
Step 3: Use spatial coordinates to assign pixel numbers to each event.
Step 4: Convert spatial coordinates of events from global reference frame to normalised intrapixel reference frame.
Step 5: Classify pixels as central, edge or corner, based on pixel location within sensor.
Step 6: Sort and convert 3D <i>CIE</i> matrix into a 4D matrix to speed up searching
Step 7: For all events: assign <i>CIE</i> based on trilinear interpolation of the spatially nearest <i>CIE</i> values, using <i>CIE</i> maps selected based on the pixel type and intrapixel event spatial coordinates.
Step 8: Remove events for which <i>CIE</i> is determined to be zero.
Step 9: Calculate protosignals from remaining events
Step 10: Integrate protosignals from pixel volume for each pixel and apply CSCA if indicated by user.
Step 11: Save data to file and free up
Step 12: Apply signal thresholding and energy binning
Step 13: Output energy spectrum or image of distribution of counts in the detector, as requested by user
Step 14: Save binned data to file.

Figure 5.6. Summary of the steps involved in CoGI. The descriptions for each step in this summary are given in terms of the aims the step intends to achieve. In contrast, the step descriptions in the text focus on the operations performed to achieve these results. This summary table thus provides a higher-level overview of the motivations and actions of the various steps in CoGI.

Step 4: Once the pixel numbers are known, the spatial coordinates for events are converted from a ‘within sensor’ frame to a ‘within pixel’ frame and normalised to the pixel extents. The coordinates are converted rather than simply calculated as a new column to reduce the demand on system RAM, however original spatial coordinates can be reconstructed at any point from pixel number, intrapixel coordinates and spatial information from the user input geometry array, should this be required.

Step 5: Pixels are classified as central, edge or corner so that the correct *CIE* maps can be used for each pixel. This is done by adding 1 to a temporary variable if the pixel is at the maximum or minimum of the x range for pixels and adding 1 again if the pixel is at the maximum or minimum of the y range for pixels. 0 for this variable thus indicates a central pixel, 1 an edge pixel and 2 a corner pixel.

Steps 6: This step simply converts the 3D matrix (entry number, variable, map type) of *CIE* maps into a 4D matrix (x position, y position, z position and map type). The reason this reduces search times is not immediately obvious, however a brief explanation is given at the end of Step 7.

Step 7: For each event, the intrapixel coordinates and pixel type are used to determine the 8 nearest points for which *CIE* values are stored in the relevant discretised *CIE* map. A trilinear interpolation can then be performed using these points, as shown in Figure 5.7, to determine the likely value of *CIE* at an arbitrary interaction point, k . This is done by sequentially interpolating along the three spatial dimensions. The method works as follows. Let the coordinates of the 8 surrounding points ($P1$ - $P8$) and the point k be

$$\begin{array}{lll}
 P1 = x1,y1,z1 & P2 = x1,y1,z2 & P3 = x1,y2,z1 \\
 P4 = x1,y2,z2 & P5 = x2,y1,z1 & P6 = x2,y1,z2 \\
 P7 = x2,y2,z1 & P8 = x2,y2,z2 & k = x',y',z'
 \end{array}$$

where, by definition, $x2 > x' > x1$ Further, let $CIE(P)$ stand for the *CIE* value of the point P .

The first step is then to interpolate along the x-axis to collapse the 3D volume defined by eight points ($P1$ - 8) into a 2D surface defined by four points ($P'1$ - 4), with the point k lying on this surface. $P'1$ - 4 can be calculated according to the equations

$$P'1 = CIE(P1) \frac{x2 - x'}{x2 - x1} + CIE(P5) \frac{x' - x1}{x2 - x1} \quad \text{eq. 5.15}$$

$$P'2 = CIE(P2) \frac{x2 - x'}{x2 - x1} + CIE(P6) \frac{x' - x1}{x2 - x1} \quad \text{eq. 5.16}$$

$$P'3 = CIE(P3) \frac{x2 - x'}{x2 - x1} + CIE(P7) \frac{x' - x1}{x2 - x1} \quad \text{eq. 5.17}$$

$$P'4 = CIE(P4) \frac{x2 - x'}{x2 - x1} + CIE(P8) \frac{x' - x1}{x2 - x1} \quad \text{eq. 5.18}$$

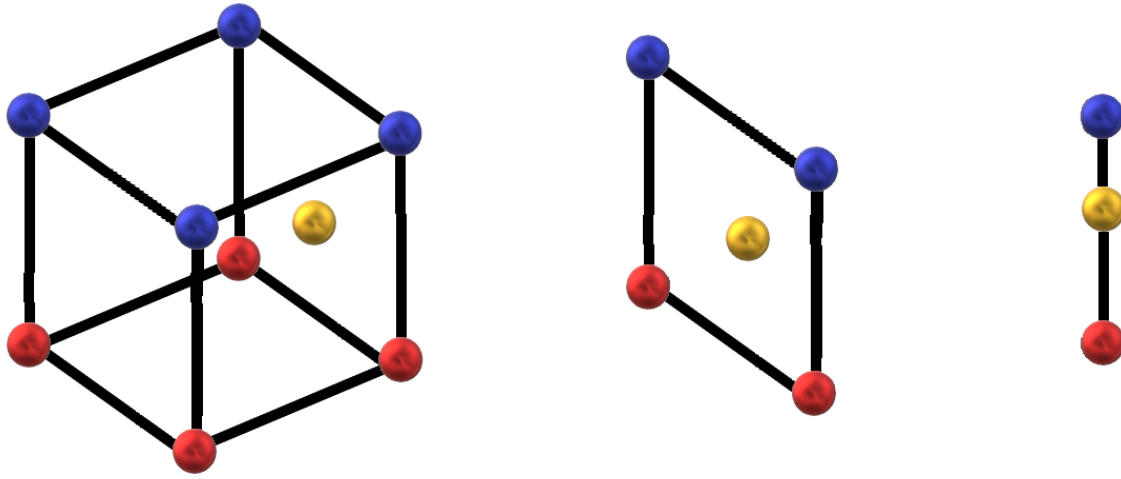


Figure 5.7. The process of trilinear interpolation. (LEFT) The point at which the value is desired (gold ball) is surrounded by 8 points with a known value (red and blue balls), with the 8 points forming the vertices of a cube. (MIDDLE) Interpolation along one spatial axis collapses the 3D cube into a 2D square, with the point of interest imbedded within its surface. (RIGHT) Interpolation along a second spatial axis collapses the 2D square into a 1D line that intersects with the point of interest. The value at this point can now be determined by interpolation along the third spatial dimension.

The next step is to interpolate along the y-axis to collapse the 2D surface defined by four points ($P'1-4$) into a 1D line defined by two points ($P''1-2$), with the point k lying on this line. $P''1-2$ can be calculated according to the equations

$$P''1 = CIE(P'1) \frac{y2 - y'}{y2 - y1} + CIE(P'3) \frac{y' - y1}{y2 - y1} \quad \text{eq. 5.19}$$

$$P''2 = CIE(P'2) \frac{y2 - y'}{y2 - y1} + CIE(P'4) \frac{y' - y1}{y2 - y1} \quad \text{eq. 5.20}$$

The final step is to interpolate along the z-axis to collapse the 1D line to the point S . The CIE value at the point k is thus given by the equation

$$CIE(k) = CIE(P''1) \frac{z2 - z'}{z2 - z1} + CIE(P''2) \frac{z' - z1}{z2 - z1} \quad \text{eq. 5.21}$$

As can be seen from the above, performance of a trilinear interpolation first requires the identification of the location and CIE values of the eight nearest points to the point k . Initially a binary search approach was utilised to locate these values within the CIE maps, however this results in extremely long simulation times, with increasing lookup times as the spatial sampling frequency of the maps is increased. This means that simulation run time and CIE map resolution were traded against each other. To prevent this detrimental trade-off being necessary, a method was devised to produce a pseudo hash table for each spatial direction independently. A custom function was then written to locate, for a given pixel type and an arbitrary intrapixel location, the CIE values of the eight nearest points in the discretised CIE maps, using a combination of these pseudo-tables. The result is a search algorithm whose lookup time does not increase as CIE map resolution is increased. This function requires a 4D matrix however, which is why the conversion of the CIE matrix from 3D to 4D is required in Step 6. This approach requires more RAM than a binary search algorithm, but significantly fewer steps in all relevant applications.

Step 8: Events with a *CIE* of 0 cannot contribute to the signal out from the detector and so are removed from the simulation at this point to both save time and reduce the demands on computational resources.

Step 9: Whilst *CIE* is a function of time, the maps were calculated for a single time, t_s , where t_s is the shaping time of the system. This is because the electronics being modelled in this simulation are active reset pulse processing circuits. Once triggered, these circuits integrate the charge on the preamplifier for a fixed time, t_s , and then read out this charge as the signal before resetting the circuits ready to detect the next event. In practice, the circuit is triggered when the charge on the anode rises above some predetermined threshold, with the threshold set just above the electronic noise floor. To avoid the need to calculate *CIE* at multiple times, and the large increase in both RAM and run time that such a simulation would require, C3 assumes that the circuit is triggered upon charge being deposited at any point in the sensor volume. The implications of this to the overall limitations of CoGI are discussed in the ‘Discussion’ and ‘Conclusion’ sections of this chapter.

As *CIE* is calculated for a unit charge, the *CIE* values from C2 represent the charge on the anode at the time t_s , as a fraction of the deposited charge. Protosignals, κ , are thus calculated as

$$\kappa = CIE_k E_k \quad \text{eq. 5.22}$$

where CIE_k and E_k are the *CIE* and deposited energy at the point k , where k is the interaction location for the current event. This process is performed for all events, to produce a list of protosignal sizes, along with their corresponding locations and times.

Step 10: Where no CSCA is employed, the following algorithm is used to calculate output signals from the system:

- i. Start with $n = 1$.
- ii. Loop starts
- iii. The counter N is set to 0.
- iv. Select the n th event, in chronological order, and record its time, t_n , and pixel ID, p_n .
- v. If the “processed” flag, *Flag*, is equal to 1 for this event, increment n by 1 and return to the “Loop starts” step (N.B. that all events have *Flag* = 0 at initialisation)
- vi. The next event in chronological order is taken and its timestamp, t_i , is compared with t_n . If $t_i \leq t_n + t_s$, the counter N is incremented by 1. This step is repeated until an event is reached for which $t_i > t_n + t_s$.
- vii. The value of the signal for event n , S_n , is then given by the equation

$$S_n = \sum_{i=n}^{n+N} \kappa_i \delta(\text{pix}_n - \text{pix}_i) (1 - \text{Flag}) \quad \text{eq. 5.23}$$

where δ is the Dirac delta function and $\text{pix}_{i/n}$ are the pixel IDs of events i/n respectively. It should be noted that this approximation assumes events occurring in a single pixel volume within the time window t_s are all likely to be from the same event, and so all events summed in this way were deposited in the pixel over a time, $\Delta t \ll t_s$. In

situations where this assumption is violated (pile-up) the calculated signal will likely be an overestimate.

- viii. Finally, the following equation is implemented, to ensure that protosignals that have been summed in this loop are not counted again in later steps,

$$Flag(i) = \sum_{i=n}^{n+N} \delta(pix_n - pix_i) \quad \text{eq. 5.24}$$

- ix. Where the user specified a non-extendable dead time, t_d , the algorithm will then set a new counter, h , equal to 0 and move through events, starting with $j = n+N+1$, assessing whether $t_i \leq t_n + t_s + t_d$. Where this is true, the counter h is increased by 1. Once this inequality is no longer true, the algorithm advances to the next step.
- x. The following equation is then applied, to remove events that occur during the deadtime of a pixel from analysis by setting their “processed” flags to 1.

$$Flag = \sum_{i=j}^{j+h} \delta(pix_n - pix_i) \quad \text{eq. 5.25}$$

- xi. Increment n by 1 and return to the “Loop starts” step

Where a CSCA is employed, a modified version of the above algorithm is employed. The exact modifications will depend on the CSCA being modelled, however all will involve modification to steps vii and viii. Specifically, Step vii is modified to allow for protosignals from adjacent pixels to be combined, subject to them occurring within some temporal coincidence window, and step viii is modified in the same way to again ensure that protosignals cannot contribute to more than one output signal.

Step 11: Two files are produced from this step. The first is the ‘raw C3 output data’ file, containing the full matrix of events with their intrapixel coordinates, pixel number, deposited energy, time of interaction, *CIE*, protosignals, output signals and processed flags. This data is then deleted from the workspace to free up RAM, except for the data on intensity, time, and pixel ID of the output signals. The second file saved is the ‘signals file’, containing the output signals with their intensity, time, and pixel ID.

Step 12: The default behaviour of this step is to bin the output signals from the detector into 1-keV wide bins, beginning with the 0 - 1 keV bin, to generate a ‘continuous spectrum’. If the user instead requested a binned spectral output, the signals are compared to the energy thresholds specified by the user. The counter for the highest energy threshold that a given signal passes is incremented by 1, and then the next signal is considered. In practical systems the counters of each threshold passed are incremented and the spectrum reconstructed later by subtraction. This is done by moving from the highest to the lowest energy threshold, subtracting the counts in the higher threshold counter from the lower threshold counter. The outcome of these two approaches is the same however, and the direct approach simulated is chosen for being quicker to implement.

Step 13: Where an energy spectrum was requested by the user, a plot of said spectrum (binned or continuous) is now output to the screen. Where the user requested projection images, these are produced by incrementing counters for each pixel based on the number of events with that pixel ID in the output signals. These projection images are again passed to the screen.

Step 14: After a pause to allow the user to see the output data, the data behind the generated spectra and/or projection images are saved, along with images of the generated plots and/or projection images.

5.4 Methodology for validation studies with CoGI

CoGI was based on previously published work from our research group, however significant changes have been implemented since these works, as illustrated in Table 5.3. CoGI was constructed to include the additional physics processes, however these led to a significant slowing of the overall process, necessitating the improvements to CoGI's speed and fidelity. A simulation set up was implemented that yielded a 'raw C3 output data' file containing 33 million events. This file was then used as a reference, and each subsequent modification to C3 or C2 was tested to ensure it would reproduce this data for the same simulation set up. This constituted a validation that the speed and fidelity code edits did not influence the core functioning of CoGI, however it left the new physics processes modelled in CoGI to be validated. As the previous simulations performed by the group did not include these processes, comparison between CoGI and previously obtained results was not deemed to be appropriate. Instead, two experiments were designed to validate CoGI. This section reports on these experiments.

5.4.1 Validation experiment outlines

To validate CoGI, two experiments were performed using physical systems, and the results compared with those simulated in CoGI. The two experiments were

1. A validation of the core physics of CoGI, without the need for pixelation or CSCA. This involved a comparison of simulated and experimental measurement for a commercially available γ -ray spectrometer with an ^{241}Am source. Energy resolution, spectral efficiency and total photopeak detection efficiency were used as validation metrics.
2. A validation including sensor pixelation and CSCA. This involved simulating the output of an XCounter Actaeon[273] series detector to a ^{57}Co source. The Actaeon series detector is a pixelated, CdTe based, photon-counting detector with two energy thresholds and a proprietary CSCA.

Table 5.3. Summary of advances in CoGI over previous work in the group.

<u>Features added</u>	<u>Changes to improve speed</u>	<u>Changes to improve fidelity</u>
Contribution of holes to output signal	Pixelation process moved to C3 from GATE	Standardised filename coding to include simulation parameters
Auger electron production	Pseudo hash table search function replaces binary search algorithm	Comparison of data file names with user requested geometries implemented at start
Implementation of CSCA	Non-contributing events removed as they are identified	Consistency checks introduced at <i>CIE</i> map construction point
Non-extendable deadtime option	COMSOL mesh resolution optimised different for region of interest and remote regions	Consistency checks performed post <i>CIE</i> matrix normalisation.
	Connection of data generation, analysis, and output into a single user prompt	Debugging mode added with data output before and after each manipulation.
	Switch from external functions to native functions or hard coded functions, as needed.	Switch from defined volumes to normalised volumes

5.4.2 Method for validating the basic physics

5.4.2.1 Modelling the detector

The first validation experiment used a GR1 photospectrometer (by Kromek[363]) to obtain the energy spectrum of an ^{241}Am source, and compared this to the energy spectrum predicted by a model of the GR1 running in continuous spectrum mode in CoGI. The GR1 uses a crystal of CZT as the sensor material (cube with side length of 1 cm). The material properties required by CoGI to model the CZT used were obtained from the manufacturer and are shown in Table 5.4.

Table 5.4. List of material properties used by CoGI in modelling the GR1 photospectrometer.

Parameter	Symbol	Value	Unit
Mobility, electrons	μ_e	1000	$\text{cm}^2 \text{V}^{-1} \text{s}^{-1}$
Mobility, holes	μ_h	65	$\text{cm}^2 \text{V}^{-1} \text{s}^{-1}$
Lifetime, electrons	τ_e	3.0	μs
Lifetime, holes	τ_h	1	μs
Density of CZT	ρ_{CZT}	5850	kg m^{-3}
Diffusion coefficient, electrons	D_e	2.58×10^{-3}	$\text{m}^2 \text{s}^{-1}$
Diffusion coefficient, holes	D_h	1.68×10^{-4}	$\text{m}^2 \text{s}^{-1}$
Relative permittivity	ε	11.0	-

Based on this information, a model of the GR1 photospectrometer was built in CoGI. There were two main limitations to this model:

1. The beryllium transmission window on the GR1 was omitted from CoGI, as its thickness and purity were unknown. Beryllium is known for being highly transparent to high energy photons such as x/γ -rays, so this approximation is not unreasonable. It should be noted however that this transparency is only partial at energies below ~ 2 keV[364], and consequently CoGI would thus be predicted to overestimate the number of photons detected below this threshold. To prevent this discrepancy affecting our validation, a readout threshold of 2.5 keV was applied to both simulated and experimental data.

2. The GR1 utilises a coplanar electrode configuration, however we were unable to get the details of its arrangement from the manufacturer. As this array could not be modelled accurately, it was decided that a planar electrode arrangement would be modelled instead. The benefit of this approach as opposed to attempting to model a coplanar array is that it led to the clear expectation that CoGI would underestimate the energy resolution of the GR1, due to the increased dependence of simulated signal on holes, compared with the physical case. Previous work by our group using the same photodetector neglected holes entirely and showed an overestimation of energy resolution, so the transition to a slight underestimation supports the claim that the signal contribution from holes was now being incorporated.

5.4.2.2 Experimental setup and metrics assessed

The experimental setup implemented for the validation involved the placement of a sealed ^{241}Am source (0.34 MBq) in contact with, and approximately centred on, the window of a GR1 photospectrometer. The energy spectrum was recorded during a 1-minute exposure and a Gaussian fitted to the primary full-energy photopeak at ~ 60 keV. Several metrics were then used to compare the simulated and physical GR1 spectra: spectral efficiency (S_{eff}), total photopeak detection efficiency (T_{pp}) and the energy resolution (measured at the photopeak). S_{eff} is defined as

$$S_{eff} = \frac{P_c}{T_c} \times 100\% \quad \text{eq. 5.26}$$

where T_c is the total number of counts recorded in the detector and P_c is the number of counts in the spectrum assigned to the photopeak. T_{pp} is defined as

$$T_{pp} = \frac{T_c}{\Gamma_e} \times 100\% \quad \text{eq. 5.27}$$

where Γ_e is the total number of photons output from the source during the acquisition time. The energy resolution of the photopeak is defined in this work by the full width at half-maximum (*FWHM*) of a Gaussian fitted to the photopeak data.

5.4.3 Method for validating CSCA implementation in CoGI

5.4.3.1 Modelling the detector

The second experiment in this chapter was designed to validate the pixelation and CSCA processes of CoGI. This was done by comparing measurements of a ^{57}Co source by both a physical and a CoGI simulated version of an Actaeon series pixelated detector from XCounter. First, a digital model of the detector needed to be built in CoGI. The Actaeon series detector contained two identically configured ASICs, mounted side by side, for a total sensor active area of 2.56 cm x 2.56 cm. The anode was pixelated at a pitch of 100 μm onto the conversion material (CdTe), which had a thickness of 0.75 mm. The manufacturer provided detailed internal and external measurements of the main components comprising the detector. Additionally, the material composition of the transmission window was obtained, along with information on the shaping time, CSCA implementation and operating voltage used, allowing for the Actaeon model in CoGI to be as accurate as possible. The material properties used to model the CdTe in C2 can be seen in Table 5.5. Some of these properties were available under a non-disclosure agreement, whilst others represent approximations based on averaged literature values.

Table 5.5. List of material properties used by CoGI in modelling the GR1 photospectrometer.

Parameter	Symbol	Value	Unit
Mobility, electrons	μ_e	1100	$\text{cm}^2 \text{V}^{-1} \text{s}^{-1}$
Mobility, holes	μ_h	100	$\text{cm}^2 \text{V}^{-1} \text{s}^{-1}$
Lifetime, electrons	τ_e	3.0	μs
Lifetime, holes	τ_h	2.0	μs
Density	ρ_c	5850	kg m^{-3}
Diffusion coefficient, electrons	D_e	2.84×10^{-3}	$\text{m}^2 \text{s}^{-1}$
Diffusion coefficient, holes	D_h	2.58×10^{-4}	$\text{m}^2 \text{s}^{-1}$
Relative permittivity	ϵ	11.0	-

5.4.3.2 Experimental setup and metrics assessed

In order to better capture the functioning of an x-CSI system, it was decided that this validation experiment would look at energy binned data. The Actaeon detector used is composed of two ASICs mounted side by side, with each ASIC containing two independently settable energy thresholds, as well as offering XCounter’s “AntiCoincidence mode” (their proprietary CSCA). The two available energy thresholds were used to define an energy bin containing the 122 keV photopeak, isolating it from the CSEs at lower energies. The thresholds defining the limits of this energy bin were determined using the “sweep” feature of the Actaeon detector to produce a rough energy spectrum of the source. Details of this feature are provided later in this chapter. A Gaussian was fitted to the 122 keV photopeak in the obtained spectrum and its mean, \bar{x} , and standard deviation, σ , determined. The lower energy threshold was then set as $\bar{x} - 2\sigma$ and the upper energy threshold set to $\bar{x} + 2\sigma$. This bin should thus contain 95% of the counts in the modelled Gaussian distribution. The same two energy thresholds were then implemented in the CoGI simulated detector, for comparison.

For the validation experiment, a ^{57}Co point source (1.12 MBq) was placed on the detector’s window, approximately centred on the gap between the two ASICs. This placement was performed by hand, using the live imaging mode of the detector which provides a rapidly refreshing image to show sources in close to real time. This arrangement was then replicated in CoGI, as shown in Figure 5.8. Data was recorded with the detector running in “AntiCoincidence mode” for 1 minute of decay time (in simulation and reality). The number of counts in the predefined energy bin was then used as the metric to compare the simulated CSCA with the physically implemented one. Details concerning the operation

of the “AntiCoincidence” algorithm were provided by the manufacturer under the terms of a non-disclosure agreement, so cannot be disclosed here in full. Suffice it to say that, like all CSCAs, XCounter’s CSCA searches for likely CSEs by identifying events with a high spatiotemporal correlation.

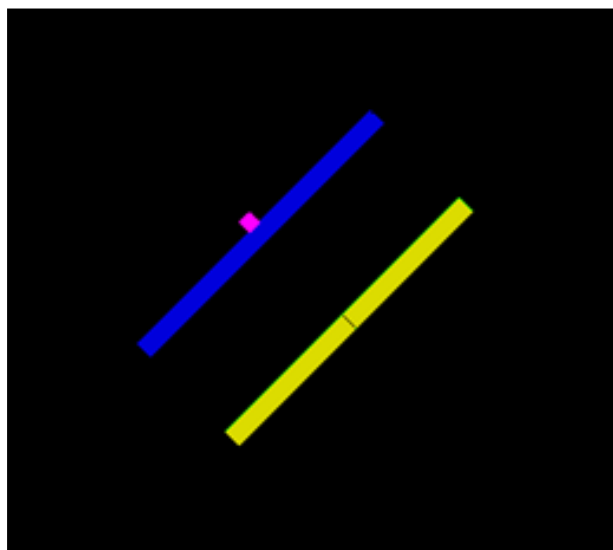


Figure 5.8. Setup for simulation of ^{57}Co on the Actaeon pixelated detector. The ^{57}Co source (small pink square) is placed in contact with the carbon fibre window (blue rectangle) and directly over the gap between the two CdTe crystals (yellow rectangles). The ASICs on which the CdTe crystals are mounted are not simulated, though the cathode and pixelated anodes are.

5.4.3.3 Determination of thresholds for energy bin placement

Placement of the energy thresholds to isolate the 122 keV source from the ^{57}Co source was guided by the building of an approximate energy spectrum of the source in the energy range 105 - 130 keV. To build this spectrum with only two thresholds, a short data run was first acquired with the lower threshold, LT , set to 105 keV and the upper threshold, UT , set to 106 keV. Data was then acquired with $LT = 105$ keV and $UT = 107$ keV. The process was repeated, increasing UT by 1 keV at each step, until an image was acquired with $LT = 105$ keV and $UT = 130$ keV. Data from each acquisition was then processed as follows:

1. The counts above LT were scaled to be equal to the counts above LT in the acquisition with $UT = 106$ keV. This was done to smooth out variations between acquisitions, as LT should return a constant value.
2. The counts above UT were then scaled by the same factor
3. The counts in the n th energy bin were calculated as: the counts above UT when $UT = n$ keV, minus the counts above UT when $UT = (n+1)$ keV.

When this was initially done, it was noticed that two peaks were present from the detector output where only 1 was expected: one centred at ~ 122 keV and the other at ~ 112 keV. Spectra were constructed from each ASIC individually to verify this result, however when this was done it was found that only one peak was visible in each ASIC, implying that the calibration of energy thresholds varied between the two ASICs. Investigations revealed the cause was a mistaken application of the first ASIC’s

calibration file to both ASICs during setup. As the correct calibration file for the second ASIC was not available, and our lab was not equipped to produce one ourselves, it was thus decided to proceed using only the data acquired from the ASIC with an XCounter issued calibration. The simulated data was similarly adjusted, using only the counts output from one ASIC (but leaving the other ASIC in the simulation to allow for x-ray fluorescence effects that could contribute to the counts in the first detector).

The *FWHM* of a Gaussian fitted to the 122 keV photopeak found in this way was measured as 4.6 keV, consistent with expectations based on manufacturer provided information (~4% energy resolution at 120 keV). For a Gaussian, the *FWHM* is related to σ by the equation

$$FWHM \approx 2.355\sigma \quad \text{eq. 5.28}$$

For this detector, $\bar{x} \pm 2\sigma$ corresponded to a *LT* of 118.1 keV and an *UT* of 125.9 keV. The physical system could only be set in whole keV steps, so the energy thresholds chosen for the validation were *LT* = 118 keV and *UT* = 126 keV. Subtraction of the counts above *UT* from those above *LT* will thus determine the counts in this energy bin. Before setting these same thresholds on the CoGI simulated version of the detector, the simulated detector was calibrated using prominent peaks in the simulated ^{57}Co spectrum, as determined by CoGI operating in continuous spectrum mode. The features used for this calibration were the full-energy photopeak, single escape peak and the Cd x-ray fluorescence peak, as shown in Figure 5.10 in the next section.

5.5 Results of validation

Figure 5.9 shows the data and Gaussian fits for the 60 keV photopeak, as measured on both the physical and CoGI simulated GR1 detectors. The measured data points from the physical system are represented by the black circles whilst the CoGI simulated data points are represented by the red dots. Gaussians were plotted for each data set, as is routine in γ -ray spectroscopy, so that relevant metrics could be calculated (see Table 5.6).

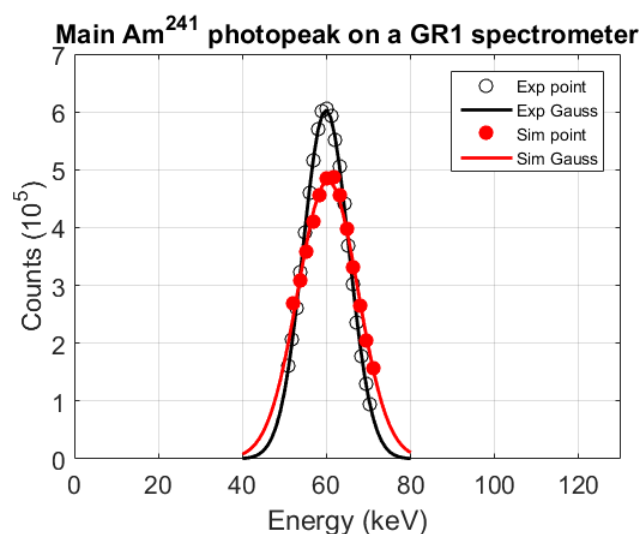


Figure 5.9. Comparison of the main ^{241}Am photopeak as recorded by a GR1 spectrometer (*Exp*) and predicted by CoGI (*Sim*). The data recorded/simulated are shown (circles), along with the Gaussian fits (coloured lines). The widths of the two peaks and areas underneath them are in good agreement.

Table 5.6. Comparison of photopeak metrics found in simulation (CoGI) and experiment (GR1).

	GR1	CoGI
<i>FWHM (keV)</i>	13	16
<i>P_c</i>	8.2E6	8.4E6
<i>T_c</i>	9.9E6	1.0E7
<i>T_{PP} (%)</i>	40.2	41.2
<i>S_{eff} (%)</i>	83	82

The metrics assessed show good agreement between the practical experiment and simulation, however the energy resolution found from CoGI is poorer than the experimentally measured energy resolution from the physical detector. This was expected considering the limitations to the GR1 model in CoGI, listed in Section 5.4.2.1. Discussion of the impacts of these limitations can be found in that section and in Section 5.6. With the caveats in these sections noted, the generally good agreement between simulation and practical experiment for S_{eff} , P_c , T_c and T_{PP} were taken as validating the basic physics of CoGI. The second validation experiment, involving the Actaeon series detector, was then used to assess the other new feature of CoGI: application of a CSCA.

Figure 5.10 shows the spectrum of signals that were produced in the Actaeon detector modelled in CoGI, both where no CSCA is applied and when XCounter’s CSCA was simulated (black and blue dashed lines respectively). As previously mentioned, the conversion from simulated channel number to measured photon energy was performed using a three-point calibration. The spectral features used for this calibration are labelled in the figure. (A = Cd K α line, B = escape peak and C = full-energy photopeak).

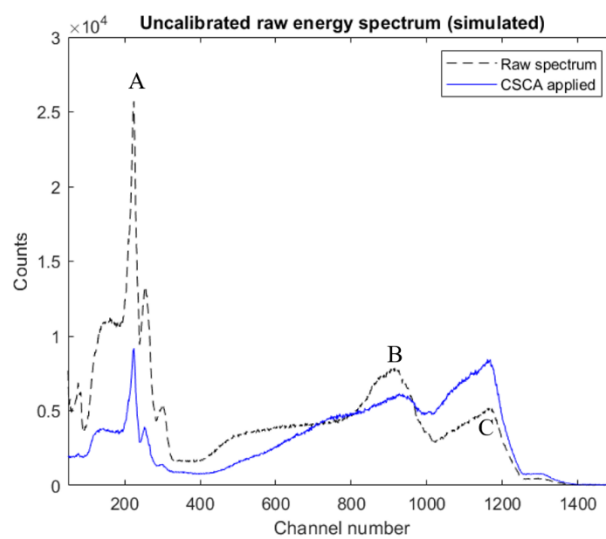


Figure 5.10. Simulated ^{57}Co energy spectrum produced by CoGI with (solid blue line) and without (black dashed line) a CSCA applied. The spectral features corresponding to x-ray fluorescence (A), escape peak (B) and full-energy photopeak (C) from the raw spectrum were used to calibrate the simulated detector using a linear calibration technique.

Table 5.7 shows the number of counts recorded in the energy bin as measured by the physical or simulated detector. A single value is shown, representing the total counts recorded by the detector, summed over all pixels on the ASIC. Detector averaged data was used as opposed to a pixel-by-pixel comparison to minimise discrepancies caused by any discrepancies between the placement of the ^{57}Co source in the simulation and physical setup (where the centre of the ASIC was approximated by hand). In addition to the CoGI simulated data, Table 5.7 also contains results from a simulation referred to as CoGI (long). This refers to a variation of the CoGI simulation performed with a longer value of t_s in C2, and the justification for this can be found in the next section.

Table 5.7. Comparison of the counts assigned to the photopeak energy bin in experiment (Actaeon) and simulations (CoGI). Differences between CoGI and CoGI(Long) are explained in the text.

	Counts in photopeak bin	Discrepancy with experiment
Actaeon (Physical)	3.11e5	N/A
CoGI	2.96e5	4.9%
CoGI (Long)	3.10e5	0.2%

5.6 Discussion

Comparing the simulated and experimental results for the validation experiment involving the GR1 detector shown in Table 5.6 shows that CoGI can produce a reasonable approximation of many of the metrics assessed. The deviations between CoGI and experiment for total detection efficiency and spectral efficiency are $\sim 2.4\%$ and $\sim 1\%$ respectively. Superficially these results reassure that the core physics of CoGI are correctly modelled, however the much larger deviation in simulated and experimental energy resolution (~ 3 keV) requires some explanation. It was predicted in Section 5.4.2.1 that CoGI would underestimate the energy resolution, due to its approximation of the coplanar array as a simple planar array. This approximation proved necessary due to the lack of information available on the coplanar array (geometry and associated voltage differences between strips), and its implications can now be discussed and explained. The following discussion assumes that the detector is designed such that the anode signal is read as the output signal.

In a non-pixelated detector with a planar array, the signal at the anode contains contributions from both electrons and holes regardless of where the charge carriers are generated. Complete collection of holes and electrons results in the maximum possible signal, however due to their lower mobility holes take longer to drift towards their collecting electrode and are more likely to become trapped. The extent of this trapping is reduced when photons are deposited close to the cathode, as the holes have a shorter distance to travel, resulting in a depth dependent signal profile and consequently a reduced energy resolution compared to what would be possible if the holes did not contribute to the signal. This represents the situation modelled in CoGI.

In a detector with a coplanar array, the anode is fragmented into alternating sections with slightly differing voltages (see Figure 5.11). The result of this arrangement is that the weighting

potential is much steeper close to the collecting anodes, as would be the case in a pixelated detector, and consequently charges contribute to the signal on the anode only when relatively close to the anode. As holes tend to drift away from the anode, only those that are formed within the steep weighting signal region will contribute to the signal. In contrast, the electrons drift towards the anode so, thanks to their much greater mobility, contribute relatively consistently to the output signal, regardless of their point of formation within the crystal. This screening of charges based on their location thus largely prevents the signal degradation caused by holes. Holes trapped close to the anode may still degrade energy resolution, however the effect will be suppressed compared with the planar anode arrangement.

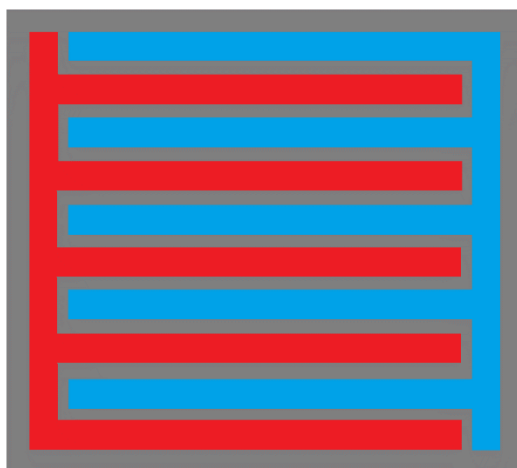


Figure 5.11. Example of how a coplanar arrangement can be implemented in an anode. The anode is divided into two interlaced strips (red and blue). Both anode strips are of a negative voltage with respect to the cathode, but there is an additional voltage difference between the red and blue strips. This results in a steep gradient in field strength in proximity to the anodes, similar to the small pixel effect in a pixelated anode.

The poorer energy resolution predicted by CoGI is thus explainable as being a result of the simulation limitations, rather than as a fundamental failure of the framework. Indeed, the reason that whole photopeak efficiencies (spectral and total) were assessed (as opposed to a channel-by-channel count comparison) is that these variables allow the physical factors determining energy deposition to be assessed, without reference to energy resolution. The energy resolution was included however to assess whether hole contributions to signal were now being included. Previous work within this group considered only the contribution of electrons to the signal in the GR1 detector, and consistently overestimated the energy resolution of the detector, despite again simulating a planar arrangement. The switch to an underestimation of energy resolution using a comparable experimental setup can thus be viewed as a confirmation that the signal contribution of holes is now being modelled in CoGI.

The results from this first experiment thus validate that the core physics processes are being modelled accurately in CoGI. Work thus proceeded to validate the situation of a pixelated detector operating using the CSCA modelling feature of CoGI.

Figure 5.10 shows spectra of signals produced by the Actaeon series detector, as simulated in CoGI, when exposed to the ^{57}Co source. The signals produced both before and after application of the simulated CSCA are displayed. The CSCA modelled results in a marked suppression of counts associated with x-ray fluorescence (A) and the corresponding escape peak (B), whilst simultaneously

increasing counts in the full-energy photopeak (C). For a mono-energetic irradiation as simulated here, an ideal detector would record only one prominent photopeak, corresponding to the energy of the photons. In non-ideal detectors however, CSEs lead to the formation of the x-ray fluorescence and escape peaks seen in Figure 5.10. As the CSCA suppresses these two features and increases counts in the photopeak, this clearly supports the assertion that XCounter’s CSCA can identify instances of charge sharing and recombine these counts into a single peak of corrected energy. It should be noted that where a full-energy event splits into escape-energy and fluorescent-energy events, the escape-energy event must remain in the detector, but the fluorescent x-ray may leave the detector and not be recorded. For this reason, it is more difficult to suppress the escape peak than the x-ray fluorescence peak, as seen here.

Comparison between signals prior and post CSCA application is not possible on the physical Actaeon series detector, due to the CSCA being applied pre-thresholding at the ASIC level, prior to signal readout. Instead, an energy bin was defined which should contain 95% of the counts deriving from the photopeak, as detailed in Section 5.4.3, and the counts in this energy bin compared between simulation and experiment. Table 5.7 shows good agreement between simulation and experiment for this energy bin, with a discrepancy of less than 5%. This is a more complicated case than the earlier validation involving the GR1, as the counts in the full-energy bin will contain a mixture of counts recorded directly and after CSCA summing of lower energy events. Further, using the measured *FWHM* of the physical system to define the energy bin meant that any underestimation of energy resolution in the simulation would result in more counts being excluded from the energy bin: a sub 5% disagreement is thus all the more impressive.

Table 5.7 also contains an entry for a simulation labelled “CoGI Long”, which will now be discussed. By selecting only a single time point at which the *CIE* maps are extracted, it is intended that the effects of signal loss from charge trapping, charge diffusion to adjacent pixels and ballistic deficit can all be represented in a single map. Ballistic deficit, being the loss of output signal amplitude due to incomplete charge collection, depends intimately on the time available to charges to drift and be collected before a signal is read out. In the physical system the relevant time is the shaping time, whilst in CoGI it is the time used to calculate the *CIE* map in C2, t_s . The results presented so far examined the case where t_s is equal to the shaping time of the system, as this work set out to provide a framework that could simulate the results of a physical system without requiring experimental data to calibrate a free parameter. During discussions on simulation setup however it was noted that as some material properties used were based on literature averages, they might lead to a difference in rise time between simulation and physical system. In devising a way to compensate for this the following things were noted:

1. Where t_s is excessively short, the full-energy photopeak will be shifted to a lower channel number, compared to what the ideal value of t_s would produce, due to ballistic deficit.
2. Where t_s is slightly too long, the full-energy photopeak will not be shifted with respect to the ideal value of t_s as there will be negligible ballistic deficit.

3. The manufacturers selected a value of t_s to minimise ballistic deficit.
4. As de-trapping was not modelled in CoGI and the operational voltage was not changed, charge lost to trapping or cross-pixel diffusion should not be altered by this greater value of t_c , allowing the ballistic deficit to be corrected for in isolation.

A suitable value of t_s was thus estimated by simulating a range of t_s values in CoGI: starting with t_s equal to the shaping time and increasing t_s until further increasing it resulted in no detectable change in the full-energy photopeak's channel number, as measured when no CSCA was applied. The results of the simulation in which t_s was equal to this optimised value (approximately 60% greater than the physical system's shaping time) are referred to as the "CoGI Long" results. As can be seen in Table 5.7, adjusting the value of t_s as described significantly improved the agreement between simulation and experiment, with the discrepancy reduced to a mere 0.2%.

Taken together, the results of these experiments constitute a validation of CoGI as a simulation framework capable of modelling pixelated x/ γ -ray detectors based on CdTe or CZT, including in situations where CSCAs are applied. There is however a limitation that stems from the approximations used in constructing CoGI that should be borne in mind when using CoGI in future applications. The *CIE* maps generated by C2 represent the charge that would be produced on the anode at the time t_s seconds after the charge was first generated in the detector. The use of this single map for all events thus means that all events are given the same amount of time to drift within the detector before the signal is read out. The spatiotemporal distribution of events caused by the same incident photon is sufficiently narrow that this approximation is reasonable, provided that the value of t_s is sufficient that charges can be collected from all depths within the pixel. In this work, the average time between incident photons interacting with a given pixel, t_p , is significantly greater than t_s , and so each incident photon can be treated independently. At much higher fluxes however, t_p becomes comparable to t_s , leading to a significant number of cases where more than one photon interacts with a pixel during the same counting window. This is referred to as pile-up, and due to the stochastic nature of the interactions can occur even if t_p is slightly above t_s as t_p is only an average separation time. As the integrating time on the pixel is initiated with the first photon's interaction, the time available for charges from the second photon to induce a signal will be reduced. Application of the same *CIE* map to the two photons would thus result in an over estimation of the signal contribution by the second photon. Care should thus be taken when simulating high flux regimes with CoGI, with the possible requirement that multiple *CIE* maps would be needed, depending on the question that CoGI is being used to answer. As noted in Step 9 of Section 5.3.3, this will result in a significant increase in the RAM and/or computational time required to simulate a given setup in CoGI.

5.7 Conclusions

The work detailed in this chapter constitutes the development and validation of CoGI: a simulation framework combining Monte Carlo and finite element modelling techniques to simulate the response of x-CSI detectors to irradiation. In an advance over previous work in the field, CoGI includes

the signal contributions of holes and CSCAs, allowing for the comparisons of a wider range of systems and the optimisation of CSCAs for specific pixel geometries or vice versa. Two validation experiments were devised: the first to test the core physics modelling in CoGI using a GR1 γ -ray spectrometer and the second to test the CSCA implementation using a pixelated, energy binning Actaeon series detector, running XCounter’s proprietary “AntiCoincidence” CSCA.

As a result of these validations CoGI was established as a simulation framework capable of predicting (with a deviation from reality of $< 5\%$) the signals output from a defined energy bin in a pixelated x-CSI detector running a CSCA. The pixel pitch was sufficiently small ($100\ \mu\text{m}$) that CSEs would be significant, meaning the correct application of the CSCA was essential in achieving this good agreement between simulation and reality. This achievement was possible when information on pixel geometry, source emission profile, operating voltages, signal shaping time, CSCA scheme and material properties of any intervening windows were provided by the manufacturer, with material properties of the sensor material reasonably approximated from literature values. It was further shown that calibration of the simulated detector’s signal shaping time to compensate for the uncertainty in sensor material properties could reduce this discrepancy to $\sim 0.2\%$. The main limitation of CoGI, as derived from the approximations used in its construction, were highlighted and explained as being that pile-up effects may be overestimated at higher fluxes using the current approach.

The inclusion of CSCAs directly into the signal reconstruction (at the pre-thresholding level) makes CoGI especially useful for determining the response in small pixel detectors ($< 200\ \mu\text{m}$) in spectral applications such as x-CSI, as these detectors rely most strongly on CSCAs to preserve spectral response. Whilst XCounter’s CSCA was modelled in this work, CoGI is capable of modelling a wide range of CSCAs provided enough details on their operation. CoGI is thus demonstrated as a powerful tool for addressing questions regarding pixel geometry or CSCA based optimisation, as it allows for fully reconstructed signals to be compared for a wide range of different designs without the need for experimental data derived from expensive prototypes.

5.8 Disclaimer

Please note that the results presented in this chapter have since formed the basis of a publication[365]. Figures 5.5, 5.8 - 5.10 and Tables 5.4 - 5.7 were taken directly from this publication with little or no modification, though their captions may have been changed to be consistent with the level of detail in this chapter.

Chapter 6.

Optimal x-CSI system parameters for Au K-edge imaging: pixel pitch and thickness

Chapters 6 and 7 detail work using CoGI to optimise a range of x-CSI system parameters for the specific task of imaging AuNPs. x-CSI systems involve a wide range of parameters that lend themselves to optimisation, ranging from hardware and low-level charge sharing correction algorithms (CSCA) to imaging parameters and reconstruction techniques. In order to reduce the number of parameters to something feasibly addressable within the time frame of a PhD, this work employs an assumption to simplify the problem, namely that, whatever material classification algorithm is used, the K-edge of Au will likely be a region in which changes in system sensitivity will have the greatest impact. The reason for this is that there is a sharp discontinuity in x-ray absorption at this energy in the Au spectrum that would not be present in the absorption spectra of any other major element of human bodies, as can be seen from Figure 4.9. Consequently, changes in the ratio of Au absorption to non-Au absorption will be maximised at this point, allowing for maximum confidence in material classification. The task of optimising an x-CSI system for AuNP detection thus becomes the more readily solvable problem of optimising an x-CSI ASIC for performance around the K-Edge of gold (~80 keV).

This is still far from a trivial task, as there are strong interplays between the parameters being optimised for. The optimal value for one parameter will thus depend upon the employed values of the others. For example, whether a CSCA is needed will depend on the pixel pitch employed, which will itself depend upon the thickness of the sensor material used. Additionally, many non-ASIC system variables will have an impact on ASIC design, such as operational photon fluxes and the energies of interest. No analytical approaches currently exist to simultaneously optimise these parameters. For this reason, these two chapters concern an optimisation study undertaken using CoGI. 715 different x-CSI systems were systematically assessed with respect to a range of commonly used metrics. The 715 systems considered comprise every possible combination of 5 different pixel thicknesses (1 - 3 mm), 11 different pixel pitches (100 - 600 μm) and 13 different CSCA possibilities (including the application of no CSCA). These systems were each tested in 4 different flux regimes, ranging from $\sim 10^6$ - $\sim 10^9$ photons $\text{mm}^{-2} \text{s}^{-1}$, resulting in 2860 unique simulations.

The results of these simulations constitute an extensive study on the impacts of four variables (thickness, pitch, flux, CSCA choice) on a range of x-CSI system metrics. There are thus a considerable number of ways in which the results could be analysed. To prevent the analysis becoming overly cumbersome or convoluted, the analysis will be broken down into two discrete sections. These sections were spread across separate chapters, so that no single chapter becomes too long. This chapter establishes the basic set-up of the work and considers the effects of pixel pitch and thickness on the performance of the simulated detectors, at a single x-ray flux and absent any CSCAs. Chapter 7 then introduces the concept of CSCAs and looks at how the different classes of CSCA considered in this work perform with respect to each other, as well as with respect to the case where no CSCA is applied, as a function of pixel pitch. That chapter considers only a single pixel thickness but presents results from fluxes ranging from 10^6 - 10^8 photons $\text{mm}^{-2} \text{s}^{-1}$ to support the proposed mechanisms responsible for the difference in CSCA behaviour. Division of the analysis across these chapters was designed to allow a more in-depth discussion of the trends identified, including proposal of mechanistic

explanations for them. Where necessary, results from one chapter were brought in to validate a proposed mechanism and ensure it still held explanatory power if the variables held constant were changed. Where this was the case, the data used are clearly identified and their inclusion in the relevant chapter justified.

6.1 Introduction

As mentioned previously, traditional x-ray imaging systems rely on integrating the signal from a pixel over some time interval, t_e . The resulting signal will be a linear integration of the electronic noise in the circuit and the signal due to photon interactions with the sensor material (either signal directly from electrical charge formed in the case of semiconductors or via an optical photon intermediary in the case of scintillating detectors). Even in the absence of photons therefore, traditional energy integrating (EI) systems will produce some level of signal. Consequently, EI systems are designed such that many photons are incident on a given pixel within t_e , so that the electronic noise represents a smaller fraction of the recorded signal. There are three major disadvantages to this approach:

1. In averaging the contribution of all photons together, regardless of their energy, EI systems discard potentially diagnostically useful information, such as how x-ray attenuation of a material varies as a function of incident photon energy. To partially compensate for this loss of information, dual energy (DE) systems were developed, which can assess how x-ray attenuation differs between high and low mean energy x-ray beams, for example to improve soft tissue contrast. Nevertheless, DE systems still average a range of photon energies together, and there is significant spectral overlap between the high and low energy beams[366]. This means DE systems require a higher dose to extract energy dependent attenuation information than if it could be measured on a photon-by-photon basis.
2. As they integrate the contributions of multiple photons together, EI systems are sensitive to the total energy deposited rather than the energy of individual photons. They therefore cannot distinguish between X photons of energy Y , and Y photons of energy X . Consequently, photons of higher energy contribute more strongly to the signal than do lower energy photons[340]. This is particularly detrimental in medical imaging tasks involving soft tissue discrimination, as these tissues are almost equally transparent to higher energy photons, and low energy photons carry much of the information needed to distinguish between them.
3. Where the path between source and detector involves passing through thicker patient body parts or highly x-ray attenuating materials such as those used in metal implants, the resulting x-ray flux impinging on the detector is significantly reduced. Such attenuation induced low fluxes, referred to as photon starvation[367], result in a much higher fraction of the output signal deriving from electronic noise rather than incident photons. If these signals are then used to reconstruct images, significant artefacts may be produced. To prevent this, EI systems can use higher fluxes (and therefore higher

patient doses) or larger pixels (with consequent loss of spatial resolution) to ensure that the per-pixel flux remains high enough to deliver the desired SNR.

A variety of approaches for EI system design and image reconstruction have been developed to mitigate these disadvantages, with various degrees of success[368][369]. Nonetheless, it is becoming increasingly widely accepted that the future of x-ray imaging lies not in mitigating these disadvantages in EI systems but rather in developing new, x-CSI technologies. x-CSI systems are designed to compare the energy of each detected photon, either as a function of signal size[370] or with respect to some predefined set of energy thresholds[339][343], as discussed in Section 4.2.4.2. Because they use a larger number of energy thresholds than dual energy systems (as many as 8 in some ASICs[371]), and because they assess each photon's energy individually rather than the average energies of two different beams, x-CSI systems can perform better in material decomposition[372] and soft tissue contrast tasks, as well as reducing dose for a given image quality[373]. x-CSI system design introduces its own challenges though, with unique constraints that need to be considered when optimising pixel dimensions. These difficulties, and consequent constraints, can be classified into their effects on the temporal and spectral performance of the system.

Temporal constraints refer to the factors that limit the ability of x-CSI systems to distinguish between two incident photons that interact with a given pixel within a short time of each other. The required time interval between successive incident photon interactions, t_i , must be longer than t_s , the time involved in shaping and reading out a signal. As photon interactions with the sensor are stochastic in nature, maximising the probability that two successive incident photons are separable by the x-CSI system requires that $t_i \gg t_s$. Medically relevant x-ray fluxes thus require extremely fast counting from x-CSI ASICs, with values of t_s of the order of 10^{-8} s. One way of reducing the required counting rate for a given x-ray flux is to reduce the pixel volume, reducing the probability of two photons both interacting with the same pixel during a given irradiation.

Spectral constraints refer to the factors that limit the accuracy with which an x-CSI system can classify the energy of an incident photon. Obvious constraints include any factors which affect the collection of deposited charge within an x-CSI pixel, such as trapping frequency, shaping time, electric field distortions at pixel edges, conductivity differences between electrodes and the inter-electrode gap, average charge deposition depth and the ratio between charge cloud drift and expansion (due to diffusion and repulsion). Other constraints need to be considered however, as any factor which affects the total energy deposited within a given pixel by an incident photon can affect the spectral performance of the system. For this reason, the stopping power of the sensor material and the rates of fluorescence x-ray escape also need to be considered as potential sources of spectral constraint. Increasing pixel pitch and pixel volume will reduce the effect of many of these issues, though some degree of spectral degradation will remain for even large pixel sizes.

Many x-CSI ASICs currently in development utilise small pixels (in comparison with those in traditional EI systems) to reduce the required count rates to manageable levels, however this introduces increased spectral distortions as a consequence. One proposed method of compensation for this entails

implementation of a charge sharing correction algorithm (CSCA) into the ASIC. Whilst a variety of CSCAs have been proposed, all work by attempting to identify charge sharing events and then correcting for them in some way to reduce the spectral distortion created. CSCAs cannot perfectly compensate for charge sharing effects however, and inevitably will under compensate where the lost charge escapes the sensor altogether (e.g. x-ray fluorescence escape) and overcompensate where incident photons arrive in adjacent pixels in too short of a time interval. Further, in looking for correlated events across several pixels, CSCAs also have a detrimental effect on temporal resolution, by forming larger pseudo pixels for the purposes of minimising spectral distortions. Nonetheless, the benefits of CSCAs in reducing spectral distortions is well established[345] and their limitations have also been studied[332][347].

It can therefore be seen that optimising x-CSI systems for temporal and spectral performance places competing pressures on pixel size, with the extent of those pressures potentially being modulated by which, if any, CSCA is applied. Determination of optimal pixel geometries for a given application is thus difficult if not impossible to address in a purely analytical approach. Traditionally, Monte Carlo simulations are used for optimising a variety of medical imaging systems[350][374], however CSCAs are not incorporated in these approaches, making them less suitable for x-CSI applications where CSCAs could conceivably have a significant impact on optimal system geometry.

The work presented in this chapter aimed at a systematic evaluation of the effects of various design parameters (pixel pitch and thickness) on a range of spectral metrics. The work aimed to identify general trends that could prove important to x-CSI system design and explain them mechanistically where possible. Results are considered at a range of medically relevant fluxes, and occasionally with CSCA, to justify the conclusions reached.

6.2 *Simulation setup and methodology*

The simulations conducted in this chapter were performed on CoGI, which is detailed in Chapter 5. CoGI requires that a Monte Carlo setup be defined for C1, as well as a range of input variables for constructing finite element method models in C2 and variables to allow simulation of the signal output, including any CSCAs employed, in C3. These parameters are detailed in this section.

6.2.1 C1 Parameters

Monte Carlo simulations for the different geometries were all performed using the same, fixed random seed, producing the exact same incident photon properties and initial interactions, to ensure variations in different simulation results would originate from geometric factors rather than differences in random number generation.

6.2.1.1 *Geometry:*

A rectangular crystal of CdTe, with cross-sectional dimensions of 21 mm x 21 mm was simulated to represent the sensor. The crystal thickness was varied across five different simulations, ranging from 1 to 3 mm, in 0.5 mm increments. These five simulations are referred to as the “geometric

templates”. Each simulation saw the crystal irradiated by a flat field source, slightly larger in cross-section than the CdTe crystal (24 mm x 24 mm). The setup can be seen represented in Figure 6.1.

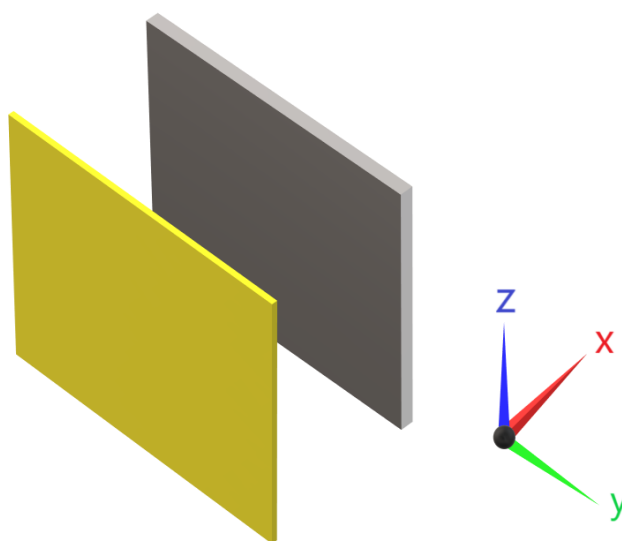


Figure 6.1. Simulation setup (not to scale). The CdTe sensor was modelled by a solid rectangular block (grey) measuring 2.1 cm x 2.1 cm at its face and with a thickness that varied based on the geometric template chosen between 1 mm and 3 mm (see text). A rectangular radiation source was defined (yellow) that was slightly larger than the CdTe in the y- and z-axes and parallel to one of the larger sensor faces. Both radiation source and CdTe sensor were centred with respect to the x-axis. Radiation was emitted from the radiation source from a random location (rectangular distribution) propagating initially with zero y and z components so that it was perpendicularly incident on the sensor (emitted parallel to the x-axis).

6.2.1.2 Irradiation:

The rectangular source shown in Figure 6.1 produced monoenergetic photons which were confined to be perpendicularly incident on the largest area face of the CdTe crystal. The energy of the photons (80 keV) was chosen for three reasons:

1. it is, rounded down to the nearest keV, equal to the K-edge of Au and so is relevant to assessing systems for detecting AuNPs.
2. it is of a sufficiently high energy that the expected prominent spectral features (full-energy photopeak, escape peak and Cd x-ray fluorescence peak) should be spaced tens of keV apart and so be easily separable by most geometries.
3. it lies within the medically relevant range of x-ray energies (< 140 keV).

Each geometric template was simulated four times, once at each of four different x-ray fluxes ($\sim 10^6$, $\sim 10^7$, $\sim 10^8$ and $\sim 10^9$ photons $\text{mm}^{-2} \text{s}^{-1}$). The irradiation duration was adjusted based on the x-ray flux so as to preserve the total number of photons incident on the sensor. The number of incident photons was selected based on preliminary simulations involving the thinnest CdTe crystal, as a thinner material would have the lowest total number of interactions. The number of interactions was chosen to keep the uncertainty originating from the Poisson statistics of a Monte Carlo simulation below 0.1%: the minimum number of photon interactions with the sensor across all simulations was ~ 1.7 million events.

6.2.2 C2 Parameters

The material parameters used for modelling CdTe in Section 5.4.3 were used for the finite element method models again, as they represented our most complete dataset for CdTe material properties. The values of voltage, inter-anode gap and shaping time for a system with which our team has experience were taken as prototype values, denoted as α -values. In simulating a range of pixel geometries for comparison, the anode size and voltage were calculated so that the inter-anode gap and drift time were constant between systems, allowing for the use of a single shaping time across all systems that produces a constant degree of ballistic deficit. For a system with pixel pitch of W_p μm and thickness d μm , the anode width was W_n μm , with W_n given by the equation

$$W_n = W_p - S_\alpha \quad \text{eq. 6.1}$$

where S_α is the anode gap from the prototype system. Similarly, the voltage applied to the pixel in such a system, V_n , was given by the equation

$$V_n = V_\alpha \left(\frac{d}{d_\alpha} \right)^2 \quad \text{eq. 6.2}$$

where d_α is the pixel thickness from the prototype system. This relation was derived from the requirement that the drift time be equal to that of the prototype system.

6.2.3 C3 Parameters

6.2.3.1 Pixelation and signal generation

C3 was used to pixelate the CdTe crystals simulated in C1 at a range of pixel sizes ranging from 100 μm to 600 μm , in 50 μm increments. The total number of pixels thus varied between the various pixelation patterns but concerned the same total area of sensor material. Applying pixelation in C3 rather than C1 has a variety of advantages, reducing the total simulation time and making for a more realistic Monte Carlo simulation. It does this by preventing the assessment of absorption at arbitrary pixel boundaries within a continuous CdTe crystal, eliminating a potential source of error due to rounding issues if continuity constraints across these boundaries are not correctly implemented.

The differently pixelated data sets are then used to convert energy depositions from global to intrapixel coordinate systems, and these intrapixel coordinates in turn used to determine induced protosignals for each pixel, on an event-by-event basis, using the charge induction efficiency (*CIE*) maps from C2. It should be noted at this point that, in contrast to the work done in Chapter 5, the different *CIE* maps for edge, corner and central pixels were not calculated, as this would triple the computational time for the maps and computational time was a valuable commodity. All pixel *CIE* maps were thus treated as central, as this is the modal pixel type by a substantial amount.

Consequently, 220 different data sets (5 geometric templates, pixelated with 11 different pixel pitches and simulated at 4 different x-ray fluxes) are produced. CSCAs can then be applied directly to the data, to simulate pre-threshold charge summing algorithms. The case of no CSCA, as well as 12 different CSCAs, were assessed for each unique set of protosignals, resulting in signal readouts for a

total of 2860 system designs. Finally, the signals from each pixel are compared against the pre-set energy thresholds so that relevant energy counters can be incremented. As explained in Chapter 5, practical systems would normally increment all counters and then subtract counts from successive counters to determine the counts in each energy bin, however CoGI calculates the counts in energy bins directly, for reasons of computational efficiency.

6.2.3.2 CSCAs

CSCAs are not the focus of this chapter and are explained in more detail when they are introduced in Chapter 7. Nonetheless, some results obtained using a CSCA are shown in the results section of this chapter to provide support for the proposed mechanisms. For the purposes of this chapter however, the reader need only be aware that CSCAs work broadly by summing events from adjacent pixels together if they meet some criteria, as described in the introduction above.

6.2.3.3 Selection of pre-set energy bin thresholds

Before defining the energy bin thresholds, the full energy spectra (1 keV binning) for all systems considered were manually checked to ensure the major expected spectral features (photopeak, escape peak, fluorescence peak) were present. An automated process was used to check if energy calibration was required for the various geometries, based on whether Gaussians fitted to the observed peaks were more than 1 keV from their expected energies. This process indicated no need for calibration for any geometry where all three peaks were easily distinguishable. A discovery from this automated calibration check however was that extreme pixel geometries yielded photopeaks for which the single Gaussians model was an extremely poor fit. Three reasons are suggested for this:

- 1). The relatively low x-ray energies used in medical x-ray imaging means there is little separation between a photopeak and its Compton continuum.
- 2). Extremely large ratios of pixel pitch to thickness cause *CIE* values that deviate markedly from unity in a significant part of the pixel volume. This will produce significant low energy tailing from *CIE* alone.
- 3). Extremely small pixel geometries (pitches and thickness) produce sufficiently low probability of full photopeak capture within a single pixel that the full-energy photopeak is comparable in size to the low energy tail.

Collectively, the above factors reduce the validity of the Gaussian approximation at extreme pixel geometries, and the more technically robust Voigt function should be used. The higher uncertainty associated with function fitting where the photopeak height is small in comparison to the height of the low energy tail serves as a caution against using energy resolution and other energy spectrum metrics for system comparison in this work. Fortunately, x-CSI systems do not produce full energy spectra but rather operate in an energy binning mode whereby the counts in several discrete energy bins are reported. Comparing the simulated systems operating in this mode produced the added benefit of ensuring the metrics assessed could be clearly defined and equally valid for all simulated geometries,

as signals are compared based on thresholding, without introducing uncertainty from the quality of a function's fit to a given photopeak.

As there were three major spectral features expected, four energy bins were simulated so that each could be placed into a discrete bin whilst keeping the number of thresholds realistic based on current technological capabilities. Comparisons of the energy spectra from CoGI and the Monte Carlo data they are based on revealed that where the complete energy of a photon with energy E was deposited within a single pixel, the energy registered by the system could be significantly lower due to low CIE values but was never recorded as more than $(E + 1.5)$ keV. Based on this, the energy bins were defined as follows:

i). The noise floor, above which a signal needs to rise to be registered by the detector, was set at 10 keV. Consequently, signals below 10 keV, after any applicable CSCAs were applied, were suppressed.

ii). Signals registering between 10 keV and 30 keV were assigned to energy bin 1: the “fluorescence bin”. Bin 1 should thus contain all the events resulting from Cd fluorescence x-rays (~23 keV and ~26 keV photons) being captured.

iii). Signals registering between 30 keV and 60 keV were assigned to energy bin 2: the “escape bin”. Bin 2 should thus contain almost all the escape photopeak photons.

iv). Signals registering between 60 keV and 83 keV were assigned to bin 3: the “photopeak bin”. Bin 3 should thus contain almost all the full-energy photopeak photons.

v). Signals registering above 83 keV were assigned to bin 4: the “coincidence bin”. As full-energy photons should not register above about 81.5 keV, bin 4 should only contain events resulting from separate photons being summed together as a result of pulse pile-up.

6.2.4 Metrics used for comparing simulated detectors

A range of metrics have been proposed to assess x-CSI system performance, and this work will consider four representative metrics. The different system designs will be compared with respect to their absolute detection efficiency, absolute photopeak bin efficiency, spectral efficiency, and fractional coincidence counts. These metrics will be assessed using signals pooled from all pixels, so that the total sensor area is the same between all systems compared. These metrics are defined below.

Absolute Detection Efficiency (ADE): The number of counts recorded in the detector divided by the number of incident photons.

$$ADE = \sum_{k=1}^4 \frac{B_k}{\Gamma_i} \quad \text{eq. 6.3}$$

where B_k is the number of counts in bin k and Γ is the number of photons impinging upon the sensor (area of sensor multiplied by x-ray flux).

Absolute Photopeak bin Efficiency (APE): The number of counts in the photopeak bin divided by the number of incident photons.

$$APE = \frac{B_3}{\Gamma_i} \quad \text{eq. 6.4}$$

where B_3 is the number of counts in the photopeak bin.

Relative Coincidence Counts (RCC): The number of counts in the coincidence bin divided by the number of counts in all bins. This is a proxy for the extent of pulse pile-up.

$$RCC = \frac{B_4}{\sum_{k=1}^4 B_k} \quad \text{eq. 6.5}$$

where B_4 is the number of counts in the coincidence bin.

Binned Spectral Efficiency (BSE): The number of counts in the photopeak bin divided by the number of counts across all bins.

$$BSE = \frac{B_3}{\sum_{k=1}^4 B_k} \quad \text{eq. 6.6}$$

6.3 Results

The results considered in this subsection were all obtained at a single flux of $\sim 10^7$ photons $\text{mm}^{-2} \text{s}^{-1}$ and represent the signals from the systems without any CSCAs applied, unless otherwise stated.

Figure 6.2 shows the variation in ADE as a function of the pixel pitches and thicknesses considered in this work. The main trends evident are that ADE is positively correlated with pixel thickness and negatively correlated with pixel pitch. It should be noted that neither correlation is linear in nature and that many system geometries have ADE values greater than 100%. Though counterintuitive, ADE values greater than 100% are possible due to the way that ADE is defined, as will be discussed.

Figure 6.3 and Figure 6.4 shows how APE changes with pixel pitch and thickness. Figure 6.3 shows the case without CSCA whilst Figure 6.4 illustrates the effect of applying a CSCA (3x3Dy). It is clear from Figure 6.3 that APE increases with pixel thickness, whilst it has a convex relationship with pixel pitch. Figure 6.4 shows the same convex relation, though with a greater curvature.

Figure 6.6 plots the percentage of recorded counts assigned to energy bin 4 (the coincidence bin) as functions of pixel pitch and thickness. RCC is shown to increase with an increase in either pixel pitch or thickness, however this relation is less evident at the smallest pixel pitches examined. Figure 6.5 and Figure 6.7 show the same trend when the incident flux is $\sim 10^6$ photons $\text{mm}^{-2} \text{s}^{-1}$ and $\sim 10^8$ photons $\text{mm}^{-2} \text{s}^{-1}$ respectively.

Figure 6.8 and Figure 6.9 represent the relation of BSE to pixel thickness and pixel pitch. Figure 6.8 considers the relation when no CSCA is applied, whilst the case of a CSCA (3x3Dy) is

considered in Figure 6.9. The relation between *BSE* and pixel geometry is much less clear than the other metrics, as is discussed in detail in the discussion section.

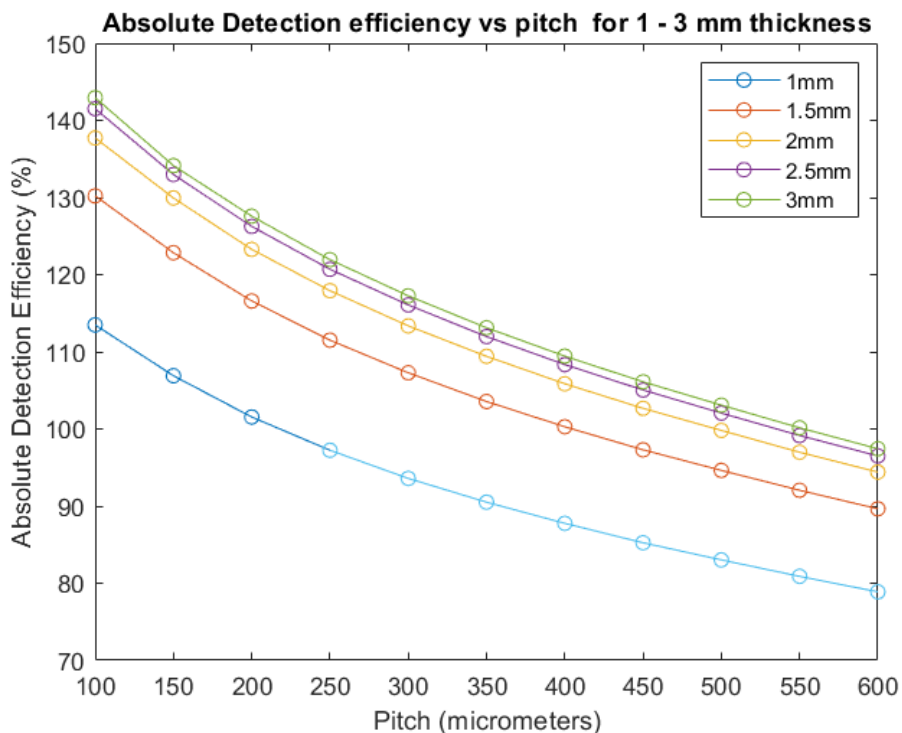


Figure 6.2. Plot of absolute detection efficiency (ADE) as a function of pixel pitch and pixel thickness. ADE is defined as the counts recorded divided by the number of photons incident on the sensor. The data shown concerns a flux of $\sim 10^7$ photons $\text{mm}^{-2} \text{s}^{-1}$.

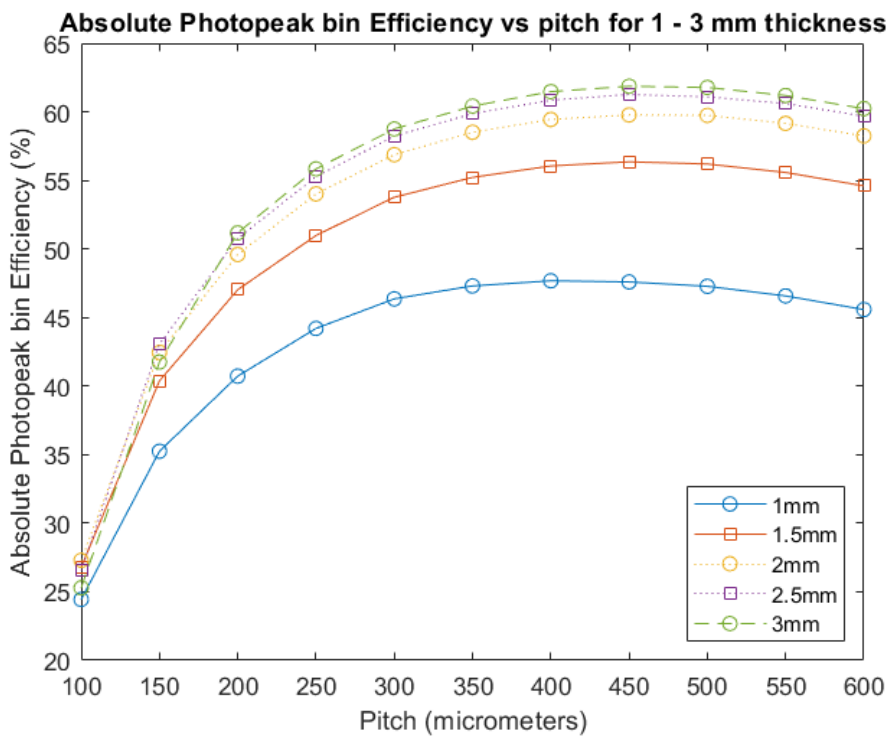


Figure 6.3. Plot of absolute photopeak bin efficiency (APE) as a function of pitch and thickness. APE is defined as the counts recorded in the photopeak bin divided by the number of photons of 80 keV incident on the sensor. The data shown concerns a flux of $\sim 10^7$ photons $\text{mm}^{-2} \text{s}^{-1}$.

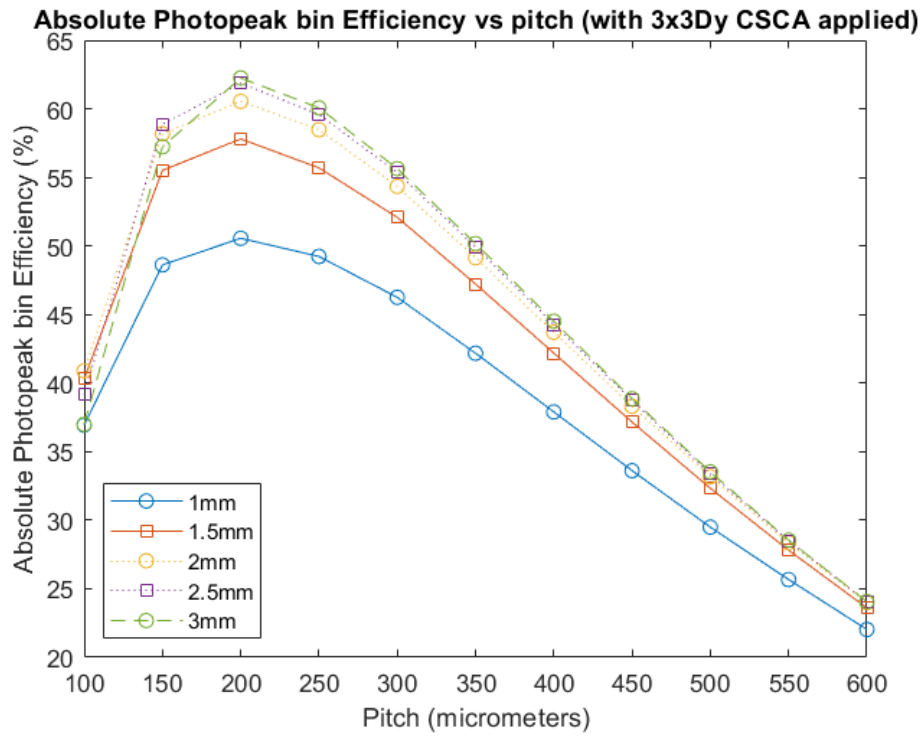


Figure 6.4. Plot of absolute photopeak bin efficiency (APE) as a function of pitch and thickness. APE is defined as the counts recorded in the photopeak bin divided by the number of photons of 80 keV incident on the sensor. In this case, a CSCA (3x3Dy) has been applied. The data shown concerns a flux of $\sim 10^7$ photons $\text{mm}^{-2} \text{s}^{-1}$.

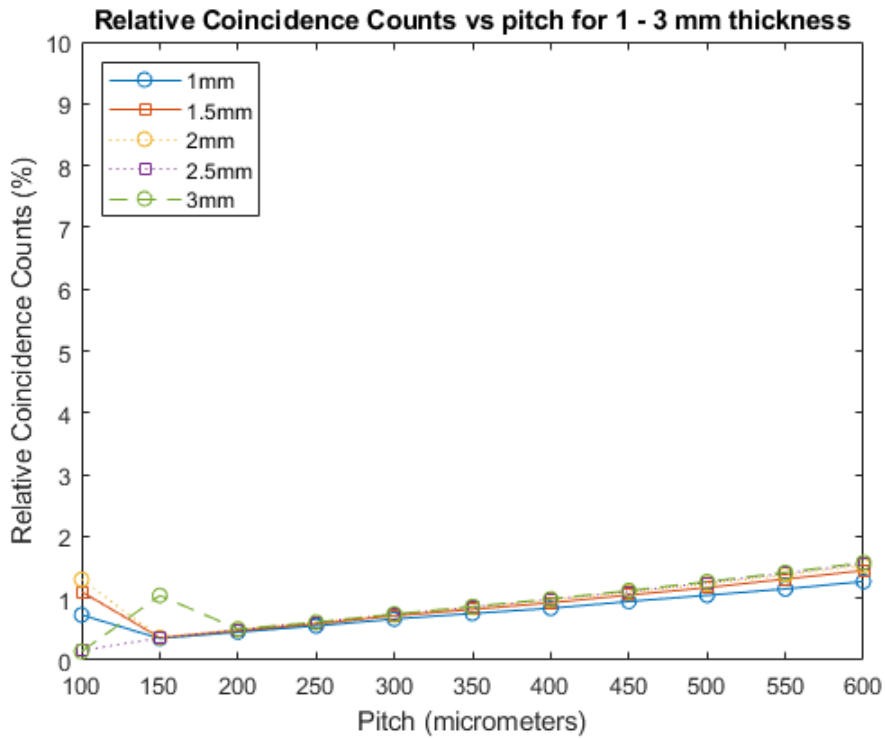


Figure 6.5. Plot of relative coincidence counts (RCC) as a function of pixel pitch and pixel thickness. RCC are defined as the counts recorded in the coincidence bin divided by the sum of counts in all bins. The data shown concerns a flux of $\sim 10^6$ photons $\text{mm}^{-2} \text{s}^{-1}$.

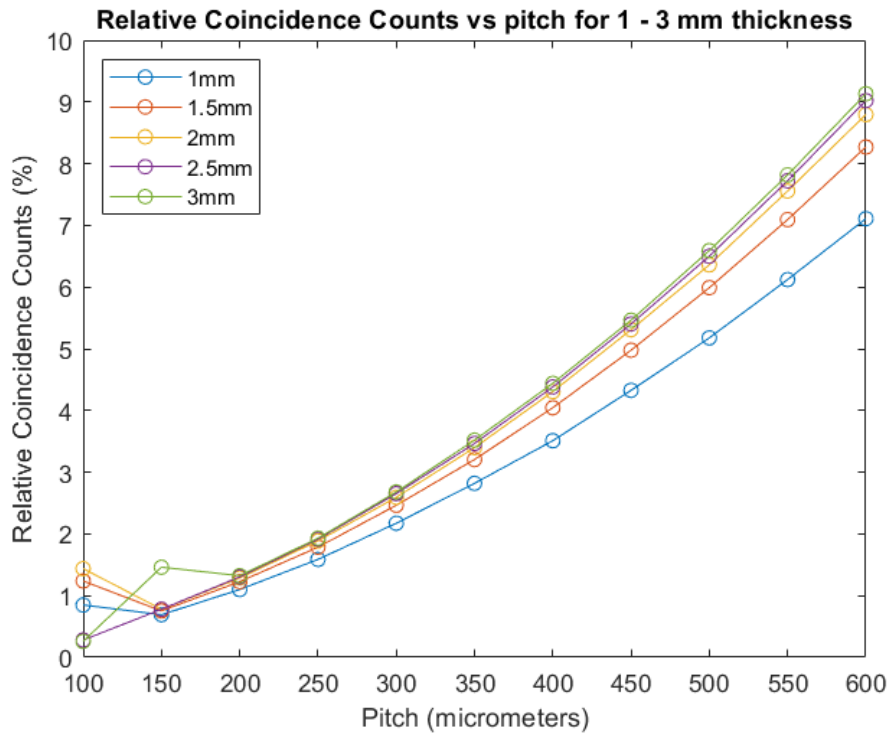


Figure 6.6. Plot of relative coincidence counts (RCC) as a function of pixel pitch and pixel thickness. RCC are defined as the counts recorded in the coincidence bin divided by the sum of counts in all bins. The data shown concerns a flux of $\sim 10^7$ photons $\text{mm}^{-2} \text{s}^{-1}$.

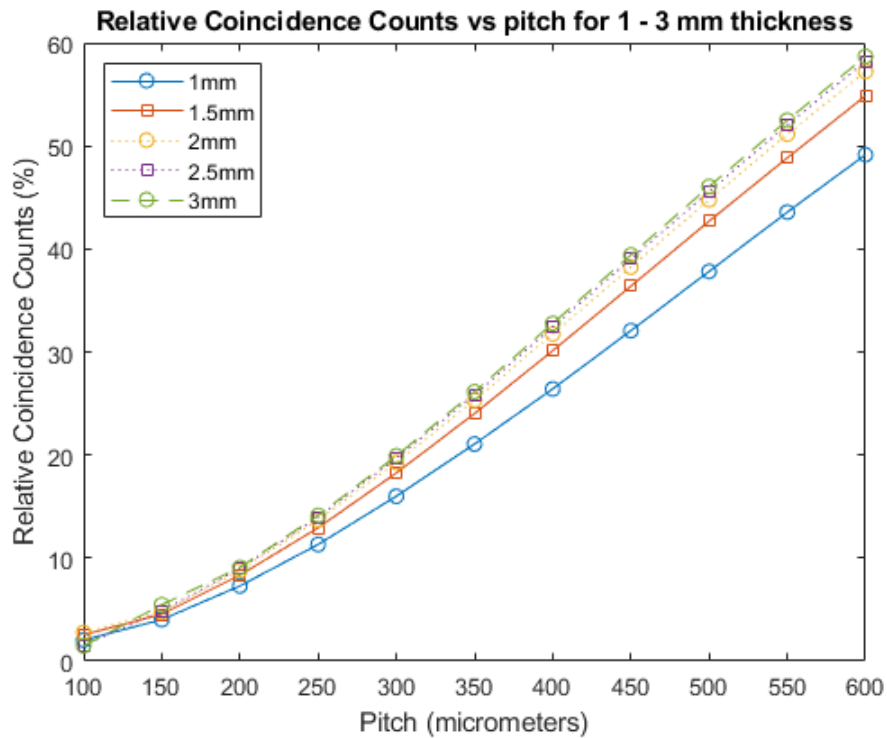


Figure 6.7. Plot of relative coincidence counts (RCC) as a function of pixel pitch and pixel thickness. RCC are defined as the counts recorded in the coincidence bin divided by the sum of counts in all bins. The data shown concerns a flux of $\sim 10^8$ photons $\text{mm}^{-2} \text{s}^{-1}$.

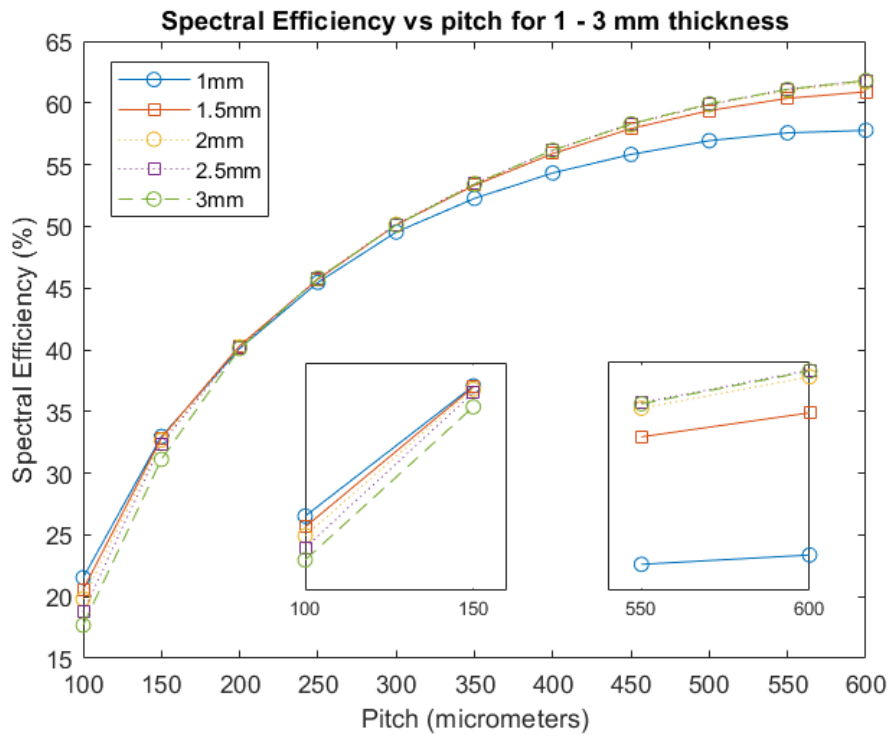


Figure 6.8. Plot of binned spectral efficiency (BSE) as a function of pixel pitch and thickness. BSE is defined as the counts in the photopeak bin divided by the sum of counts in all bins. The relation between efficiency and thickness is reversed between small (left inset) and large (right inset) pixel pitches. The data shown concerns a flux of $\sim 10^7$ photons $\text{mm}^{-2} \text{s}^{-1}$.

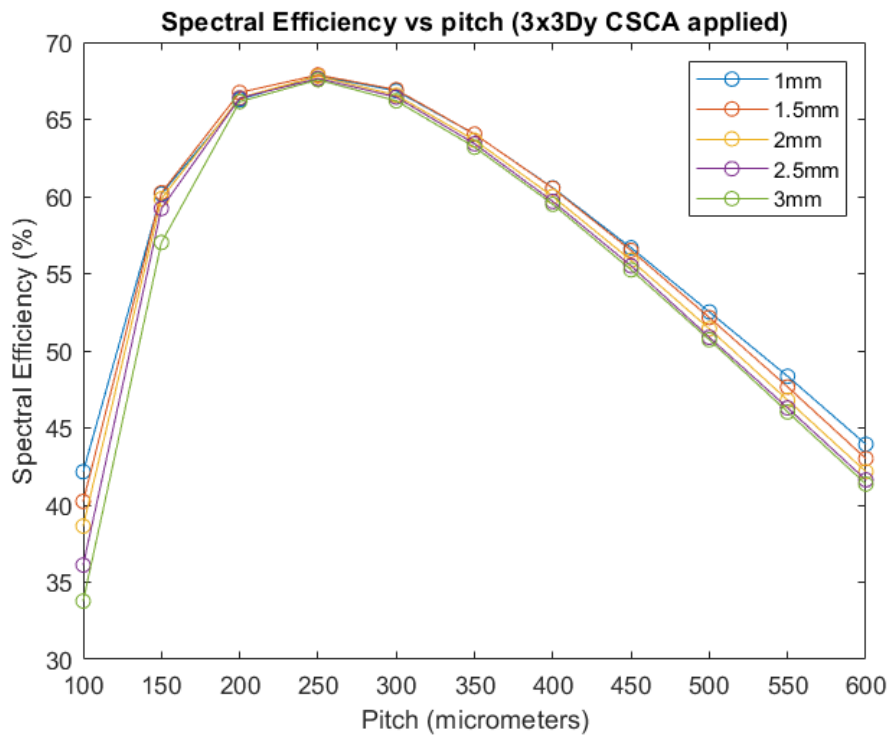


Figure 6.9. Plot of binned spectral efficiency (BSE) as a function of pixel pitch and thickness. BSE is defined as the counts in the photopeak bin divided by the sum of counts in all bins. In this case, a CSCA (3x3Dy) has been applied. The data shown concerns a flux of $\sim 10^7$ photons $\text{mm}^{-2} \text{s}^{-1}$.

6.4 Discussion

It is important to remember in the following discussions that the exact values given by CoGI for any metric are specific to the range of factors not varied in this work, such as the material properties, shaping times, pixel pad spacing, operational bias voltage-thickness ratio, incident photon beam energy etc. These factors were chosen based on the work and experience of our research group, though they could be different for other applications or other sensor materials. It is thus best that the discussion be seen not as aiming for precise quantitative statements regarding what a given *APE* will be for pixels of *X* pitch and *Y* thickness, but rather to elucidate trends in metric response as pixel pitch and thickness vary. In this way, mechanisms and concepts may be discovered and discussed that generalise to any x-CSI system that employs a semiconductor sensor with known x-ray fluorescence.

6.4.1 Absolute detection efficiency

The first thing of note in Figure 6.2 is that *ADE* values go above 100% for a significant number of geometries considered, which seems to imply that a detection efficiency of over 100% is possible. The actual reason for these high *ADE* values lies in the pixelated nature of the systems however, with the consequent possibility that a single photon could deposit energy across multiple pixels, and thus trigger multiple counts. When charge sharing mechanisms such as x-ray fluorescence are taken into account, it is clear that *ADE* values significantly greater than 100% are possible, and that higher *ADE* values are not necessarily an indication of better detection efficiency for pixelated detectors. With this caveat noted, the trends in *ADE* as a function of pixel's pitch and thickness are assessed. There are two trends evident from Figure 6.2 that require addressing:

- The increase in *ADE* with increasing pixel thickness (for a constant pixel pitch).
- The decrease in *ADE* with increasing pixel pitch (for a constant pixel thickness).

With regards the increase in *ADE* with increasing pixel thickness, it can be noted that this increase apparently diminishes exponentially, as indicated by the smaller increase in *ADE* moving from 1.5 - 2 mm compared with the increase from 1 - 1.5 mm. This relation can be explained by the increasing thickness leading to an increased path length for photons crossing through the sensor. Thicker sensors thus stop a higher proportion of photons and register more counts for a given x-ray flux and pixel pitch. As x-ray transmission decreases exponentially with path length, this also explains why the increase in *ADE* for adding an additional 0.5 mm decreases with increasing initial thickness.

With regards the decrease in *ADE* with increasing pixel pitch, this behaviour is likely due to a combination of two factors correlated with larger pixel pitches:

- a higher probability of absorbing multiple incident photons within a given time (due to larger cross-section to the x-ray flux)
- a reduced incidence of Cd fluorescence x-ray escape (due to a larger mean path over which the photon must travel to escape the pixel).

The first factor leads to an increase in the probability that two discrete incident photons are summed into a single event (coincidence events) by the simulated system: so called pulse pile-up. The long-term trend in *ADE* as pixel pitch continues to increase depends on whether the detector is paralyzable or non-paralyzable in nature. Both paralyzable and non-paralyzable models result in *ADE* values that tend to zero with increasing pixel pitch, as *ADE* is a measure of the counts as a fraction of the actual flux. Paralyzable models would be expected to tend to zero more quickly than non-paralyzable models, as paralyzable models produce a count rate that drops off at high fluxes, whereas non-paralyzable models tend to a constant non-zero value.

The second factor, reduced fluorescence x-ray escape from the pixel, reduces the number of occasions on which the fluorescence x-ray escapes the primary pixel and is registered instead in an adjacent pixel, generating two counts in the system, and thus increasing *ADE*. The decrease in *ADE* for a fixed increase in pitch reduces exponentially with increasing initial pitch, again due to x-ray transmission decreasing exponentially with path length. This explains the concave shape of the relation between *ADE* and pixel pitch.

6.4.2 Absolute photopeak efficiency

Figure 6.3 shows the behaviour of the *APE* metric as a function of pixel pitch and thickness. A trend of increasing *APE* with pixel thickness, with gradually diminishing returns at larger thicknesses, is evident. As was the case for this same trend in the metric of *ADE*, this is likely due to the increasing path length associated with increasing thicknesses, as the *APE* is also an absolute metric and so is affected by the total number of photons the pixel stops. The pitch vs *APE* curves in this figure are convex in shape (with respect to the x-axis), having a negative gradient at higher pitches but a positive gradient at lower pixel pitches. Such behaviour is indicative of (at least) two competing effects, with the changing ratio between them causing the inversion in the gradient. The two effects proposed to account for this behaviour are pulse pile-up and charge sharing effects. The effect of pulse pile-up is to reduce *APE*, and whilst pulse pile-up is negligible for small pixel pitches, it rapidly increases with pitch². This is because, for a fixed flux, the pile-up probability increases with the area of the pixel. In contrast, the effect of charge sharing effects is to increase *APE* with increasing pixel pitch. The mechanisms of charge sharing that are modelled in this simulation included x-ray fluorescence, Compton scattering, and charge lost from a pixel due to charge cloud diffusion out of the pixel in which it was formed. For small pixel pitches, these effects lead to a significant reduction in the number of incident photons that register counts at their full energy. With increasing pitch, the fraction of the pixel volume in which charge sharing effects are significant decreases, increasing *APE*. The interplay between these two opposing pressures is proposed to be the cause of the convex shape seen in the curves of Figure 6.3. Figure 6.4, which shows the difference that a CSCA has on the shape of the curves, is included to support this claim. The CSCA causes a significant increase in the rate of curvature seen with pitch, with the peak value occurring at a much lower pitch than when no CSCA was applied. The CSCA used (3x3Dy, see Chapter 7 for further details) identifies events in adjacent pixels that occur within some short time window and sums them together. The assumption behind this is that where two

events are so closely correlated in space and time, they originate from a single photon charge sharing across the pixels. As photon interactions are stochastic however, the CSCA can also result in unrelated photon interactions in adjacent pixels being summed together, where they arrive close in time by chance. The net effect of this CSCA is thus to reduce charge sharing effects whilst simultaneously increasing pulse pile-up. The increased curvature seen in Figure 6.4 thus supports the assertion that the curvature results from the competition between pulse pile-up and charge sharing effects. Application of a CSCA has shifted the peak in *APE* to a lower pitch and allows the longer-term trend in *APE* with pitch to be seen. Examining the *APE* values after the peak reveals that greater pixel thicknesses experience a steeper negative gradient. This supports the assertion that pulse pile-up is responsible for the reducing *APE* with increasing pitch, as thicker pixels absorb more photons and so experience greater increases in pulse pile-up, in absolute terms, for a given increase in pixel pitch.

6.4.3 Relative coincidence counts

Figure 6.6 shows the value of the *RCC* metric (fraction of counts in the coincidence bin) as a function of pixel pitch and thickness. Unsurprisingly considering the preceding discussion, *RCC* increases with both pixel pitch (due to the increased per-pixel flux) and thickness (due to a larger pixel volume and consequent higher probability of two unrelated photons being absorbed at the same time). More interestingly, the data at very low pitches shows a poor fit to expectation, with cases of *RCC* decreasing with both increasing pitch (100 μm to 150 μm) and increasing thickness (2 mm to 2.5 mm) being present. It is initially tempting to speculate that these deviations from expected behaviour are artefacts caused by the low counting statistics for this bin at these pitches ($< 2\%$ of all events), especially given the consistency of the trends observed for data above 150 μm with expectations based on the other metrics. Further support for this explanation is provided by Figure 6.5 and Figure 6.7 which show that the deviations from expected value are more pronounced at lower fluxes and less pronounced at higher fluxes respectively. Whilst this likely plays some role in explaining the varying degree of deviation for the different thicknesses, it is suspicious as by this reasoning the 3mm should be the most reliable (due to its higher number of counts) yet the 3 mm thick pixels at 150 μm pitch show the greatest deviation from the expected trend. Considering these three figures, we can see that this specific deviation is more pronounced at 10^6 photons $\text{mm}^{-2} \text{s}^{-1}$ than at 10^7 photons $\text{mm}^{-2} \text{s}^{-1}$ (2.9 vs 1.9 times the 2.5 mm thickness respectively) and absent entirely at fluxes of 10^8 photons $\text{mm}^{-2} \text{s}^{-1}$. It therefore appears that this result is a statistical effect, however due to the aforementioned suspicious nature of this result, this conclusion is tentative and the existence of an as yet unelucidated mechanism that dominates at low fluxes or large pixel thicknesses cannot be ruled out. Conclusive data to settle this issue could be obtained by repeating the experiment with larger numbers of photons and a different random seed, tracking the change using smaller steps in thickness and pitch around this point. This would take considerable resources however, and is not necessary to answer the questions of primary interest to this thesis. Thus, given the explanatory power of the mechanisms proposed so far, and their consistency with all other data points within this study, the data for 3 mm thick, 150 μm pitch pixels is simply tentatively accepted as anomalous.

6.4.4 Binned spectral efficiency

Arguably Figure 6.8 is the most intriguing figure in this section, though appreciating why may require brief explanation. The trends in *BSE* with increasing pixel pitch and thickness appear superficially similar to those seen for *APE* in Figure 6.4, with the same curved behaviour explained by the competition between charge sharing effects (which increase *APE* and dominate at low pitches) and pulse pile-up (which decreases *APE* and dominates at higher pitches). Application of a CSCA in Figure 6.9 again produces a sharper curvature, with a peak at a lower pixel pitch, and supports the competition argument for *BSE* in Figure 6.8 in an analogous way to how Figure 6.4 supports the arguments for Figure 6.3. Further examination reveals some important and striking distinctions between the trends in Figure 6.8 and Figure 6.3 however. First the effect of increasing pixel thickness is not as significant on *BSE* as it was on *APE*, with little effect evident for most pixel pitches. This is sensible given that *APE* has the number of incident photons as its denominator, whilst *BSE* has all counts in the detector as the denominator. This means that whilst an increase in thickness, and thus in the total number of photons absorbed, will increase *APE*, it is not obvious that the same should be true for *BSE*, as absorbing more photons does not necessarily affect the proportion of photons recorded as full energy events, all else being equal. All else cannot be equal however, as evidenced by the reversal of the relationship between *BSE* and thickness seen when comparing low and high pixel pitches (Figure 6.8 insets). For smaller pixel pitches *BSE* increases with thickness, as expected based on the other metrics, however *BSE* decreases with increasing thickness at the higher pixel pitches. This complicated relation is not seen in the other metrics assessed and requires explanation. It is proposed that this behaviour stems from the subset of charge sharing effects produced by Cd fluorescence. To illustrate how this could work, it is instructive to consider a fluorescence photon being emitted within a pixel, as illustrated in Figure 6.10. Such a photon has three possible fates:

Reabsorbed: The photon is reabsorbed within the same pixel. This would keep the whole charge of the event within the pixel, resulting in an increment in the photopeak bin counter, increasing *BSE*.

Escape: The photon escapes the sensor entirely (without being reabsorbed). This would leave charge in the pixel that would register as an escape peak event, incrementing the escape bin counter and reducing *BSE*.

Displaced: The photon escapes the pixel it is emitted by but is absorbed in another pixel. This would produce two events in the system, one of escape peak energy and one of x-ray fluorescence energy. Escape and fluorescence bin counters would thus be incremented, reducing *BSE*.

(It is worth pausing to note that the above argument does not apply to *APE*, as that metric does not consider any events outside of the photopeak bin, and so escape and displaced photons are indistinguishable to it).

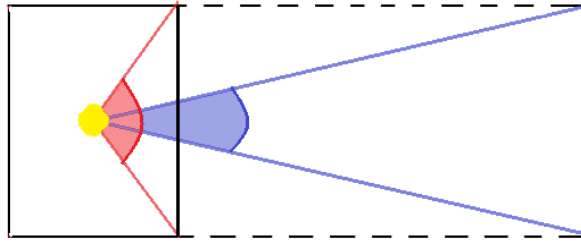


Figure 6.10. When a fluorescence photon is produced (yellow circle) the direction of its emission is random. In thinner pixels (solid lined box) there are more possible angles of escape from the sensor (red angle) than there are angles in a thicker pixel (purple angle and dashed line respectively).

Whilst *escape* and *displaced* outcomes lead to a reduction in *BSE*, *displaced* events lead to a greater reduction in *BSE* than *escape* photons, as *displaced* photons increment the denominator in the *BSE* calculation by 2 whereas *escape* photons only increment it by 1. The complicated behaviour noted in this metric can then be understood by considering first a small pixel pitch and then a much larger one. For low pixel pitches charge sharing effects are significant, and the relative likelihood of *escape* and *displaced* outcomes need to be considered. To a first approximation we can consider *escape* to be possible only where the photon exits from its pixel of formation without crossing into another pixel volume at all. Figure 6.10 shows the widest angles for which this condition is met at two different pixel thicknesses. For a thinner pixel (solid lined box) the paths with the largest angle (with respect to the central axis of the pixel) for which this condition holds are shown as red lines, whilst for the thicker pixel (dashed lined box) the corresponding paths are shown in purple. The angle subtended by these extreme paths in the thinner pixel is much larger than in the case of the thicker pixel, corresponding to a wider range of possible emission angles that favour *escape* over *displaced* outcomes. Assuming isotropic emission of the fluorescence x-ray, this result translates to photons being more likely to be *displaced* and less likely to *escape* as pixel thickness increases. Thicker pixels would thus produce a lower *BSE*, at low pitches where CSEs are still dominant, as is seen in the data.

As pixel pitch increases however, the mean path length from point of fluorescence photon emission to pixel edge increases, resulting in a reducing proportion of photons being *displaced* and an increasing proportion being *reabsorbed* instead. The larger pitches will thus see degradation in *BSE* predominantly from *escape* rather than *displaced* photons. The geometric arguments from Figure 6.10 mean that, for the larger pitches, thicker pixels will produce higher *BSE*s due to their reduction in the solid angle which allows for escape from the sensor without crossing pixel boundaries. Further, with the number of *displaced* photons becoming negligible, an increased pixel thickness will result in a larger probability of a fluorescence photon being *reabsorbed* as it means an increased path length within the sensor material. As discussed, *reabsorbed* photons increase *BSE* by incrementing the numerator in the *BSE* calculation.

Taken together, the above discussion constitutes an explanation of the inversion of the dependence of *BSE* on pixel thickness seen in Figure 6.8. For this explanation to be concordant with the explanations given for the trends observed in the other metrics in this section it is necessary that, for sufficiently large pitches, *BSE* begins to fall as pulse pile-up effects cause a rise in coincidence bin counts. Moreover, the downwards pressure on *BSE* with increasing pitch should be greater for thicker

pixels, as they stop more photons and so are more likely to stop two unrelated photons for a given flux. Larger pixel sizes were not simulated in this work, however the arguments in Section 6.4.2 for Figure 6.4 explain that application of a CSCA can simulate artificially larger pixels in that it increases pulse pile-up whilst reducing charge sharing effects. Figure 6.9 shows the data from Figure 6.8 if a CSCA (3x3Dy) had been applied. The effect of a CSCA reveals that where pulse pile-up effects begin to dominate, (larger pixel pitches) *BSE* drops more rapidly for thicker pixels, as predicted.

6.4.5 Conclusion

The effect on x-CSI system performance of varying x-ray flux, CSCA application, pixel pitch and sensor thickness have been assessed in this work. The systems' performance was assessed using a monoenergetic photon beam at 80 keV, as this is the energy of highest potential impact for our intended applications (AuNP detection). The simulated systems were operated in an energy-binned mode to best reflect real x-CSI systems designs, and four system parameters were considered: absolute detection efficiency (*ADE*), absolute photopeak bin efficiency (*APE*), relative coincidence counts (*RCC*) and binned spectral efficiency (*BSE*). The large range of detection setups simulated in a relatively short time by a single simulation framework demonstrates the versatility of CoGI, and the work in this chapter should be seen firstly as a demonstration of the advantages of such a framework for assisting rapid system prototyping.

Trends were identified for each system parameter with respect to each assessed metric and explanations for the determined trends proposed in terms of competing physical mechanisms and geometric arguments. Where trends appeared counter intuitive, CoGI was used to model different signal processing schemes (e.g. application of a CSCA) or to reproduce the same data under different external conditions (e.g. varying x-ray flux). This additional data was then used to further elucidate the mechanisms responsible and support the proposed explanations of the observed behaviour.

Significant disagreement could be found when considering seemingly similar metrics (e.g. *APE* and *BSE*), and analysis of the trends involved revealed that physical effects indistinguishable to one could be instrumental in determining the value of another. This underscores the importance of metric selection in assessing an x-CSI system, with selection being driven by the intended application and the likely operating flux. Further, the results suggest caution is needed in applying assumptions from other spectroscopic techniques to novel or extreme pixel geometries in x-CSI, as evidenced by the breakdown at extreme thickness/pitch ratios of the assumption that photopeaks can be readily fitted with Gaussians.

6.5 Disclaimer

Please note that the results presented in this chapter have since formed the basis of a publication[375]. Figures 6.2 - 6.10 were taken directly from this publication with little or no modification, though their captions may have been changed to be consistent with the terminology used in this chapter.

Chapter 7.

**Optimal x-CSI
system parameters
for Au K-edge
imaging: choice of
charge sharing
correction algorithm**

7.1 Introduction

x-CSI is attracting a lot of attention in the medical research community due its promised advantages over EI dual energy CT approaches. Such advantages include improved material decomposition[376], lower patient doses[294][377], images free of counts originating from electronic noise[378] and greater energy separation abilities that can be used to get more quantitative data with greater accuracy than dual energy CT[379]. Access to truly multispectral x-ray data offers the possibility of transforming x-ray imaging into a molecular imaging field rather than the largely structural imaging field it is at the moment[284][299]. Realising these possibilities requires that x-CSI detectors possess good detection efficiencies and energy resolution. The semiconductors CdTe and CZT are often favoured as sensor materials in these systems due to their high detection efficiencies (1 mm of CdTe has an absorption efficiency of ~80% at 100 keV, compared with ~35% for Ge and ~4% for Si sensors of the same thickness[338]) and good intrinsic energy resolution. With the significant development of these materials for high flux applications that has happened in recent years[380], the factor determining the upper limit of x-ray flux in x-CSI has shifted to how fast the associated electronics can count and reset. As discussed in Chapter 4, this places pressure on the increase of x-CSI pixel sizes as larger pixels will require higher count rates at a given photon flux[343].

Some groups thus initially moved to smaller pixels[381] as this provides for better spatial resolution and lower per-pixel flux rates. There are problems with moving to ever smaller pixels however, mainly associated with the increasing prevalence of charge sharing effects (CSEs) in which charge produced by a single photon interacting with the semiconductor is spread across multiple pixels. CSEs can result from a fluorescence photon or Compton scattering event meaning that the incident photon deposits its energy as charge clouds in multiple pixels, or it can result from a single charge cloud expanding such that it crosses pixel boundaries. Regardless of the mechanism involved however, CSEs degrade the spectral performance of the detector.

A variety of count correction schemes have been proposed by research groups to preserve some of the spatial resolution and count rate advantages of small pixels whilst mitigating detrimental CSEs[347][382][383][384]. These schemes are broadly referred to as charge sharing correction algorithms (CSCAs) and may be implemented in either the analogue (on chip, prior to signal thresholding) or digital (post digitisation of signals) domains.

Analogue CSCAs involve some form of communication between groups of pixels such that when a CSE is suspected the integrated charge on the relevant pixels can be summed together before thresholding[330][331][385]. This approach aims to reverse CSEs and so by its nature needs to be performed online i.e. simultaneous with image acquisition.

In contrast, digital CSCAs simply record the pixels associated with suspected CSEs and how many charge sharing events were suspected[334]. This information is then used to make a statistical correction to the recorded energy spectrum at some later point, and so can be performed offline i.e. after image acquisition is complete. Due to the reasons mooted in Section 4.5 for restricting the x-CSI

optimisation process to hardware-based parameters, only analogue CSCAs will be considered in this chapter.

In developing CSCAs, groups will often compare the results from a given detector geometry with and without the CSCA, however relatively few publications have been produced which attempt to compare various CSCAs with each other. This makes comparison of the various CSCAs on a purely literature review basis difficult, as they are often tested on very different system geometries. Similarly, the literature investigating the effect of pixel dimensions on PC/x-CSI system performance[386][387][388] often only consider a single x-ray flux, or a single pitch-thickness, and rarely consider the role of CSCAs at all. The potential of CSCAs is generally well demonstrated, however a better understanding of the interplay between CSCA parameters, detector performance and pixel dimensions is needed in order to predict which CSCA will be best for a given x-ray flux, imaging task and pixel geometry. The work presented in this chapter aims to fill this gap in knowledge by identifying relations between different groups of CSCA and associated metrics and explaining them mechanistically.

A subset of the 11 pixel-geometries considered in the previous chapter (100 μm - 600 μm pitch in increments of 50 μm at 1.5 mm sensor thickness) were again evaluated at 4 different medically relevant x-ray fluxes ($\sim 10^6$, $\sim 10^7$, $\sim 10^8$ and $\sim 10^9$ photons $\text{mm}^{-2} \text{s}^{-1}$). This time however, in addition to the normal signal formation process, the protosignals from these 44 simulations were also processed by 6 different analogue additive CSCAs to produce a total of 308 distinct system responses (11 geometries, each at 4 fluxes, each with 7 different CSCA schemes, including the case of no CSCA being applied) that were again compared using the four metrics outlined in the previous chapter. Details of these CSCAs and a reminder of the metric definitions will be provided in the methods section. The many degrees of freedom considered in this study could make discussion unwieldy, so to simplify the analysis it was decided to hold the sensor thickness constant and consider the effect that pixel pitch has on the various CSCAs. Similarly, for ease of discussion, the results presented here focus primarily on an x-ray flux of $\sim 10^7$ photons $\text{mm}^{-2} \text{s}^{-1}$, though results from other fluxes considered are brought in where doing so helps to clarify the mechanisms responsible for observed trends.

7.2 *Simulation setup and methodology*

The work in this chapter was conducted using CoGI and the same geometries and simulation conditions outlined in the previous chapter. Details of the CSCAs considered in this study are given below. All CSCAs tested were employed between the processes of protosignals integration and signal readout and so form a part of Step 10 in CoGI (see Chapter 5).

This chapter concerns exclusively additive CSCAs, though the concept of subtractive CSCAs is also introduced for comparison. To my knowledge there is not a major drive for subtractive CSCAs within the community and there may be good reasons for this in terms of maximising dose efficiency in patients. Nevertheless, I can envisage some applications for which subtractive CSCAs could be

instrumental in achieving clinical utility, and so they are included in the definition here for completeness.

7.2.1 Charge sharing correction algorithms considered

The CSCAs employed in this chapter all follow a similar approach of identifying candidate CSEs based on their proximity in space and time. Generally, these CSCAs compare pixels within a search region (their neighbourhood) after one of them registers an event. If another pixel within the search area also registers an event within a given time window the two events are treated as a candidate CSE and the CSCA applies some form of correction to the signals before incrementing a counter. These CSCAs are thus based on the assumption that detected events that are very closely correlated in space and time likely share an origin in a common photon. The truth of this assumption will vary as a function of photon flux and there is potentially scope to optimise the time window, however within this chapter it is assumed that all systems use the same search time as they should all have the same drift time as described in Section 6.2.2. The way that the CSCA deals with this information is described by the type of correction mechanism they apply: additive or subtractive.

7.2.1.1 Correction mechanism

Correction mechanism (CM) refers to how the CSCA deals with events that have been registered as potential CSE candidates. Additive approaches sum together the charge from the various pixels involved before thresholding the signal and incrementing the appropriate counter. In this way they aim to reconstruct the signal that would have been produced by the original photon had it not been divided across multiple pixels. Subtractive approaches suppress a counter from being incremented at all when they suspect a CSE was detected. In this way they aim to preserve spectral integrity by only counting photons that interacted with a single pixel.

7.2.1.2 Neighbourhood size

This metric refers to the size, in pixels, of the search area used to search for suspected CSEs. For example, CSCAs that groups together 9 pixels into a 3-pixel by 3-pixel square would have a neighbourhood size (NS) of 3x3.

A special class of CSCA included in this work, referred to as Hybrid CSCAs, have a neighbourhood size which changes between 3x3 and 2x2 at different stages of its execution. Their operation is slightly different to the 2x2 or 3x3 CSCAs and so is discussed here separately. CSCAs with an NS value of ‘Hybrid’ initially define a 3x3 neighbourhood based on their neighbourhood locality rules (see next section). Within this neighbourhood, all four possible contiguous-2x2 neighbourhoods are defined and their resulting signals determined in parallel (Figure 7.1). For additive Hybrid CSCAs, the 2x2 neighbourhood which returns the largest signal is then used to determine which counter to increment. For subtractive Hybrid CSCAs, the 2x2 neighbourhood which returns the smallest signal is used instead. In either case, all events within the 3x3 neighbourhood which are not within the chosen

2x2 neighbourhood are discarded, and all pixels within the 3x3 neighbourhood are reset for counting again.

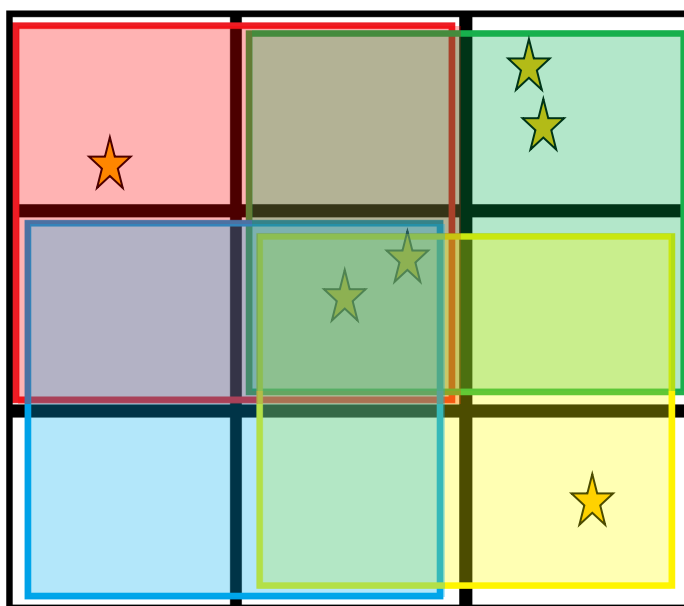


Figure 7.1. Hybrid CSCAs first define a 3x3 neighbourhood based on their neighbourhood locality rules. Secondly 4 overlapping 2x2 neighbourhoods are constructed to cover the 3x3 neighbourhood, as shown. The charge (stars) in each 2x2 neighbourhood is summed and compared, with the winner selected based on the CM of the CSCA. In this example, assuming all stars represent equal amounts of charge, the four neighbourhoods would have charge of: red (top left) = 3, green (top right) = 4, blue (bottom left) = 2 and yellow (bottom right) = 3. The output signal for this pattern of events would thus be 4 (the highest sum) for an additive CSCA or 2 (the lowest sum) for a subtractive CSCA. All pixels would then be reset and any charge not used for the signal generation process discarded.

7.2.1.3 Neighbourhood localisation

The way in which a CSCA's search area is defined is referred to as its neighbourhood localisation (NL) model. The two major categories of NL can be defined as static and dynamic. Static CSCAs define neighbourhoods in a fixed way throughout the acquisition, such that the members of a neighbourhood do not change depending on the counts detected (Figure 7.2, left). In contrast, dynamic CSCAs define neighbourhoods as and when events are detected based on a standard rule, such that at different points in the irradiation a pixel may find itself in neighbourhoods with different members. Neighbourhoods are formed, used to determine the output signal and then disbanded so that the pixels can reset to count again. For the CSCAs used in this work, the dynamic allocation rules were:

2x2 dynamic CSCAs (Figure 7.2, centre): When an event is detected in a pixel, that pixel is linked with all neighbouring pixels that share its top-right corner. Mathematically, if the event is in a pixel with position (x,y) , a neighbourhood is formed containing the pixels (x,y) , $(x+1,y)$, $(x,y+1)$ and $(x+1,y+1)$.

3x3 and Hybrid dynamic CSCAs (Figure 7.2, right): When an event is detected in a pixel, that pixel is linked with all neighbouring pixels that share a corner with it. Mathematically, if the event is in a pixel with position (x,y) , a neighbourhood is formed containing the pixels $(x-1,y-1)$, $(x-1,y)$, $(x-1,y+1)$, $(x,y-1)$, (x,y) , $(x,y+1)$, $(x+1,y-1)$, $(x+1,y)$ and $(x+1,y+1)$.

The on-the-fly allocation of neighbourhoods by dynamic CSCAs can result in a pixel being assigned to a new neighbourhood before its old neighbourhood has disbanded and the pixel has reset. In this situation the pixel will report its full charge to the first neighbourhood it is assigned to, whilst other neighbourhoods will see it as having zero charge until its first neighbourhood has disbanded and it has reset.

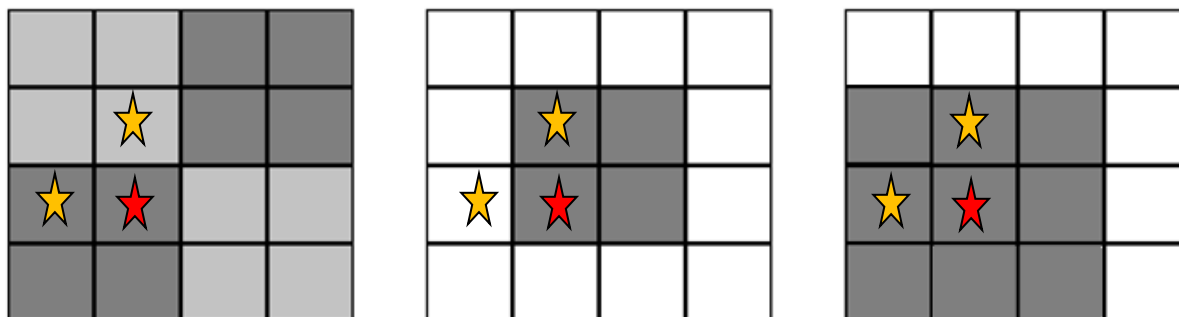


Figure 7.2. A 4-pixel by 4-pixel array of pixels in which three events (stars) are detected within the search time of the CSCA. The red star indicates the first event detected which triggers the CSCA. (LEFT) A static CSCA uses predefined neighbourhoods (grey shaded regions) which remain the same throughout the irradiation. In this example, the bottom left neighbourhood (dark grey) could sum the energy from the 2 events within its neighbourhood, and the top left neighbourhood (light grey) would sum the energy from the upper event into a separate count. (CENTRE) A 2x2 dynamic CSCAs defines a 2x2 neighbourhood such that the pixel with the first detected event is located in the bottom left. In this example, two of the events could be summed and the third would cause a different neighbourhood to be formed. (RIGHT) 3x3 and Hybrid dynamic CSCAs define a 3x3 neighbourhood such that the pixel with the first detected event is located at the centre. In this example, all three events could be summed together to a single count, fully reconstructing the energy of the original photon if all three events were triggered by charge sharing from a single photon.

The CSCAs considered in this chapter are listed in Table 7.1, along with shorthand labels to make discussion easier.

Table 7.1. A list of the different CSCAs used in this work along with their NS, NL, and CM categorisations.

CSCA Label	NS	NL	CM
2x2St	2x2	Static	Additive
2x2Dy	2x2	Dynamic	Additive
3x3St	3x3	Static	Additive
3x3Dy	3x3	Dynamic	Additive
HybridSt	Hybrid (3x3 and 2x2)	Static	Additive
HybridDy	Hybrid (3x3 and 2x2)	Dynamic	Additive

7.2.2 Metrics assessed

The metrics assessed are the same as those outlined in the previous chapter. For ease of reference, their definitions are reproduced here.

Absolute Detection Efficiency (ADE): The number of counts recorded in the detector divided by the number of incident photons.

$$ADE = \sum_{k=1}^4 \frac{B_k}{\Gamma_i} \quad \text{eq. 6.3}$$

where B_k is the number of counts in bin k and Γ_i is the number of photons impinging upon the sensor (area of sensor multiplied by x-ray flux).

Absolute Photopeak bin Efficiency (APE): The number of counts in the photopeak bin divided by the number of incident photons.

$$APE = \frac{B_3}{\Gamma_i} \quad \text{eq. 6.4}$$

where B_3 is the number of counts in the photopeak bin.

Relative Coincidence Counts (RCC): The number of counts in the coincidence bin divided by the number of counts in all bins. This is a proxy for the extent of pulse pile-up.

$$RCC = \frac{B_4}{\sum_{k=1}^4 B_k} \quad \text{eq. 6.5}$$

where B_4 is the number of counts in the coincidence bin.

Binned Spectral Efficiency (BSE): The number of counts in the photopeak bin divided by the number of counts across all bins.

$$BSE = \frac{B_3}{\sum_{k=1}^4 B_k} \quad \text{eq. 6.6}$$

7.2.3 Theoretical ADE model

As noted in the previous chapter, the metric of *ADE* can lead to values above 100% due to charge sharing events. This is in contrast to *APE*, *RCC* and *BSE* which have 100% as a maximum value they can take. Whilst the ‘ideal’ performance for a detector based on *APE*, *RCC* or *BSE* is directional (bigger for *APE* and *BSE*, smaller for *RCC*), a similar statement cannot easily be made by considering an *ADE* value alone, particularly when CSCAs are involved. This is because an *ADE* value above 100% that is reduced by application of a CSCA could be doing so because:

- it is correctly identifying events caused by CSEs and correcting for them or
- it is incorrectly identifying unrelated events and summing them together, making pulse pile-up worse.

To compare CSCAs correctly it is therefore necessary to have a reference level for what *ADE* value an ideal detector would exhibit, absent charge sharing events and charge loss due to trapping or ballistic deficit. This idealized value, referred to as the ‘Theoretical *ADE*’, will vary with pixel pitch, sensor thickness and x-ray flux. The Theoretical *ADE* is calculated analytically using the following approach:

1. First calculate the interaction probability for a given photon passing through the sensor. Consider an incident beam comprising a number of photons, Γ_i , incident on a CdTe crystal with thickness d . After transmission through the detector, the beam has been attenuated to a lower number of photons, Γ_t . This attenuation process can be related to the mass attenuation coefficient, M_A , by the equation[389]

$$M_A = \frac{\ln\left(\frac{\Gamma_t}{\Gamma_i}\right)}{d} \quad \text{eq. 7.1}$$

Values for M_A can be found from standard sources such as those maintained by NIST[27]. In calculating *ADE*, only those interactions which lead to a count in the detector need to be considered, so the M_A value needed is the one corresponding to energy depositing interactions (total attenuation without coherent scattering). The probability of a given photon interacting as it passes through this sensor is then given by the equation

$$P_I = 1 - e^{-M_A d \rho_c} \quad \text{eq. 7.2}$$

where ρ_c is the density of CdTe.

2. The incident photon flux, F_{det} ($\sim 10^7$ photons $\text{mm}^{-2} \text{s}^{-1}$ in this case), is spread uniformly across the sensor. This means that for a pixel of area B , the rate of photon flow through a pixel, f_{pix} , is given by

$$f_{pix} = F_{det} B \quad \text{eq. 7.3}$$

where f_{pix} has units of photons s^{-1} .

3. The rate at which photons interact with the CdTe crystal, R_I , is thus given by

$$R_I = f_{pix} P_I \quad \text{eq. 7.4}$$

4. Next assume that the photon interactions with the pixel can be represented by Poisson statistics. To represent an ideal detector in which no charge sharing occurs, we assume that photons that interact with the sensor do so at a single point in space and time. Combined, these assumptions mean that the probability, P_t , of two photons interacting with the pixel within some time window, t_w , is given by

$$P_t = 1 - e^{-(R_I t_w)} \quad \text{eq. 7.5}$$

5. Φ , the rate of photon interactions with the sensor that are separated by a time greater than t_w is then given by

$$\Phi = R_I (1 - P_t) \quad \text{eq. 7.6}$$

6. Setting t_w equal to the shaping time of the system makes Φ an estimate of the rate at which uniquely identifiable photon interactions occur within the detector. This allows for the counts in a detector over a given time to be estimated. Note that this approximation breaks down for high values of P_t as it does not include a term to account for the forced resetting of the counting electronics after a fixed interval. In this way it better models a paralyzable detector than the non-paralyzable detectors modelled in this work. The values for P_t considered in this chapter vary between 0.3% and 10% however, so should be low enough to provide reasonable estimates. As per the earlier disclaimer, the results of this chapter should be seen as an investigation of the qualitative trends in system response and an exploration of their mechanistic causes rather than as a quantitative prediction for a given system configuration, and in that spirit this approximation of Φ will be sufficient for our present needs.
7. Finally, the *ADE* value for this idealised detecting pixel can be calculated by

$$ADE = \frac{\Phi}{f_{pix}} \quad \text{eq. 7.7}$$

as per the definition given in Equation 6.3. This represents the final approximation made in this model, as Equation 6.3 technically refers only to the counts recorded after thresholding for low energy events and electronic noise (a 10 keV threshold was used in the current work). Electronic noise is not added to the Theoretical *ADE*, and all events are assumed to register at the same energy, so it is likely that the Theoretical *ADE* should be slightly higher than that predicted by the CoGI simulations. Use of a lower threshold (1 keV) led to an increase in *ADE* values of between 1% and 13%, depending on the pixel pitch, but did not alter general trends to be discussed, nor did it change the order at which the various CSCAs cross this theoretically derived ideal *ADE* line.

The above steps can be performed for each pixel pitch, sensor thickness and x-ray flux considered in this chapter to provide Theoretical *ADE* values for each detector. These values then act as points of reference with which to compare the *ADE* produced by a given detector-CSCA combination: to a first approximation, *ADE* values above this point represent imperfect correction of CSEs and *ADE* values below this point represent exacerbation of pulse pile-up effects.

7.3 Results

The results considered in this subsection were all obtained at a single flux ($\sim 10^7$ photons $\text{mm}^{-2} \text{s}^{-1}$) and a single thickness (1.5 mm) unless otherwise stated. Where data from other fluxes is used (to support an argument regarding the role of pile-up in an observed behaviour for example) this will be clearly stated. The results demonstrate the difference that CSCA selection can make to system output when the same physical inputs are presented. To avoid repetition, trends that were observed and explained in the previous chapter will be noted but not discussed again here, except where doing so helps to clarify observed differences in the behaviour of different CSCAs. It should also be noted that, as with the previous chapter, a useful way in which to compare data from different flux

regimes is by the per-pixel flux. This value need not be calculated due to the order of magnitude separation of the different fluxes examined here, so suffice it to say that a higher per-pixel flux is obtained by either increasing the pixel pitch at a given x-ray flux or moving to a higher x-ray flux at the same or greater pixel pitch.

7.3.1 Absolute detection efficiency

Figures 7.3, 7.4 and 7.5 show the variation in *ADE*, at $\sim 10^6$, $\sim 10^7$ and $\sim 10^8$ photons $\text{mm}^{-2} \text{s}^{-1}$ respectively, as a function of pixel pitch for the 6 different additive CSCAs evaluated in this chapter. For comparison, variation in *ADE* with pitch is also included when no CSCA is employed (the ‘No CSCA’ case) and for the Theoretical *ADE* result which represents the case where CSEs are absent, but pulse pile-up effects remain. Note that the ‘No CSCA’ case always produces *ADE* values that are higher than the Theoretical *ADE* values under the fluxes examined here as CSEs will result in a proportion of photons creating multiple counts in the detector in the ‘No CSCA’ case. All CSCAs examined led to a reduction in *ADE* from the ‘No CSCA’ case, implying that CSEs are being corrected for to some extent.

At lower fluxes the 2x2 CSCAs act the same regardless of NL. With increasing flux the static 2x2 CSCAs decrease in *ADE* value more rapidly, though static and dynamic 2x2 CSCAs remain close in performance, forming a distinct band in the middle of the plot between the 3x3 CSCAs and the ‘No CSCA’ case.

3x3 and Hybrid CSCAs, in contrast, show a distinct difference between the static and dynamic NL types but almost identical behaviour based on NS alone. At the lowest per-pixel fluxes (Figure 7.3, 100 μm pitch) the dynamic variety produces lower *ADE* values, whilst at the highest per-pixel fluxes (Figure 7.5, 600 μm pitch) dynamic CSCAs produce higher *ADE* values. Intermediate fluxes show transitory behaviour between these two extremes. Which of these NL choices performs closer to the Theoretical *ADE* value depends on the per-pixel flux in question.

In comparing CSCAs, it will be helpful to compare their effect on the deviation from the Theoretical *ADE* that they produce. Figures 7.6 and 7.7 show how the magnitude of this deviation varies as a function of pitch for the various CSCAs. Lower deviations thus imply a better fit between the CSCA value and the Theoretical *ADE* value. These plots concern photon fluxes of $\sim 10^6$ and $\sim 10^7$ photons $\text{mm}^{-2} \text{s}^{-1}$ respectively. Deviations were calculated directly from Figures 7.3 and 7.4 and so are expressed in percentage points rather than as a percentage. All CSCAs can be seen to display a concave shape (with respect to the x-axis): dropping in value with increasing pitch until some value, after which they rise again. For both considered fluxes, the 3x3 and Hybrid CSCA reach peak performance (lowest deviation) at a lower pitch than the 2x2 CSCAs. 3x3 and Hybrid CSCAs also outperform their 2x2 counterparts at smaller per-pixel fluxes, but due to their earlier peaking underperform both 2x2 CSCAs and even the ‘No CSCA’ case at higher per-pixel fluxes.

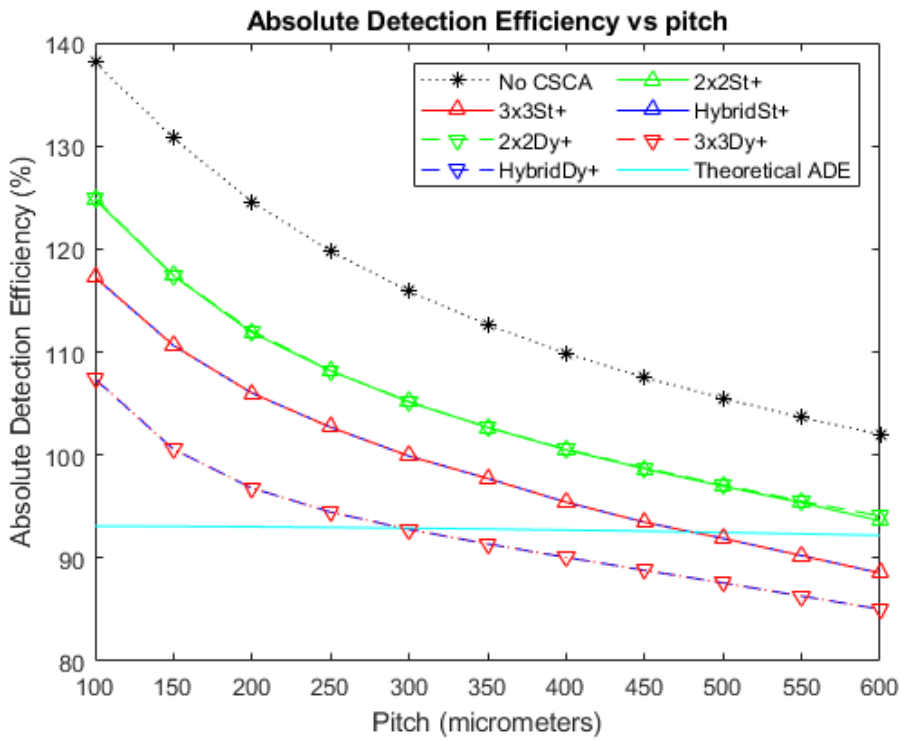


Figure 7.3. A plot of ADE versus pixel pitch at an incident photon flux of $\sim 10^6$ photons $\text{mm}^{-2} \text{s}^{-1}$. The Hybrid and 3x3 CSCAs perform indistinguishably according to this metric, resulting in significant overlap. Similarly, the 2x2 dynamic and static CSCAs overlap almost entirely at this flux level. The case where no CSCA is applied is also shown, along with the Theoretical ADE value proposed earlier, for reference.

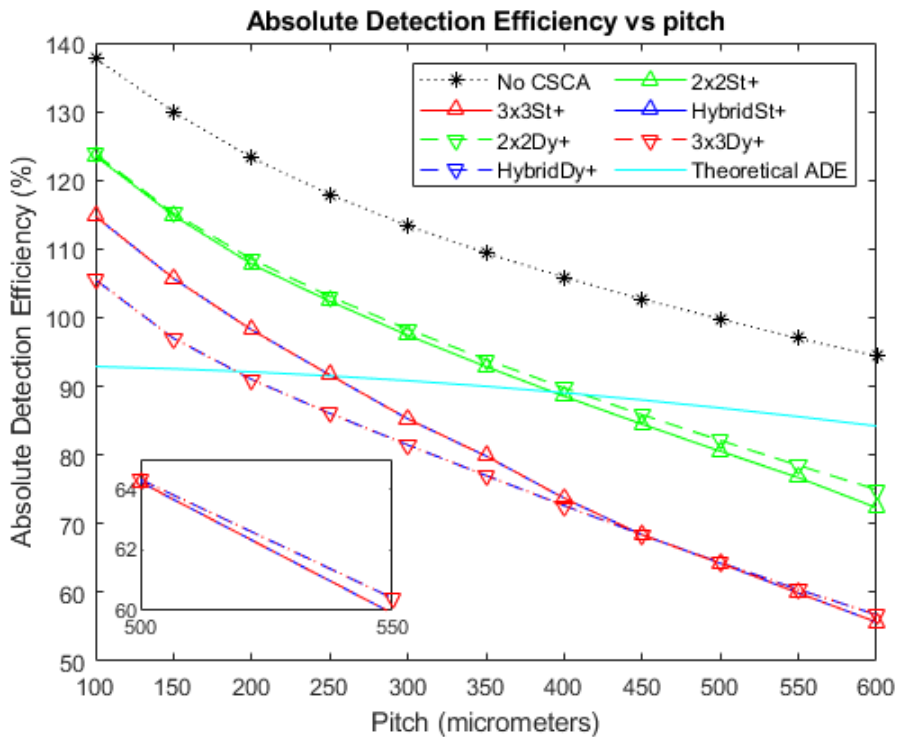


Figure 7.4. A plot of ADE versus pixel pitch at an incident photon flux of $\sim 10^7$ photons $\text{mm}^{-2} \text{s}^{-1}$. The Hybrid and 3x3 CSCAs perform indistinguishably according to this metric, resulting in significant overlap. Figure inset shows that the dynamic and static CSCAs swap order at the highest pitches considered in this figure. The case where no CSCA is applied is also shown, along with the Theoretical ADE value proposed earlier, for reference.

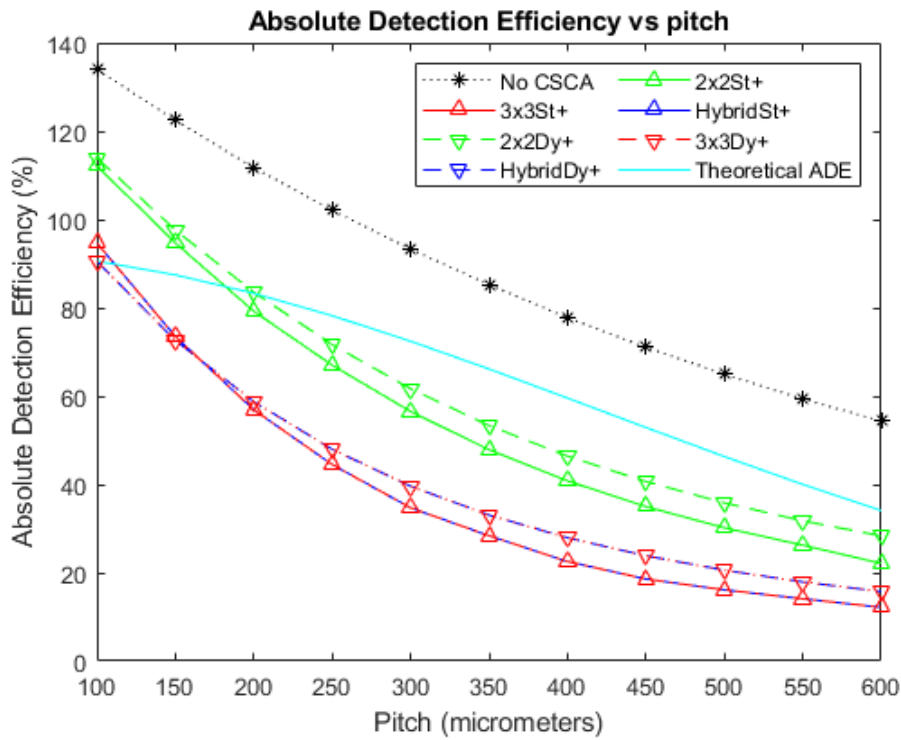


Figure 7.5. A plot of ADE versus pixel pitch at an incident photon flux of $\sim 10^8$ photons $\text{mm}^{-2} \text{s}^{-1}$. The Hybrid and 3x3 CSCAs perform indistinguishably according to this metric, resulting in significant overlap. The case where no CSCA is applied is also shown, along with the Theoretical ADE value proposed earlier, for reference.

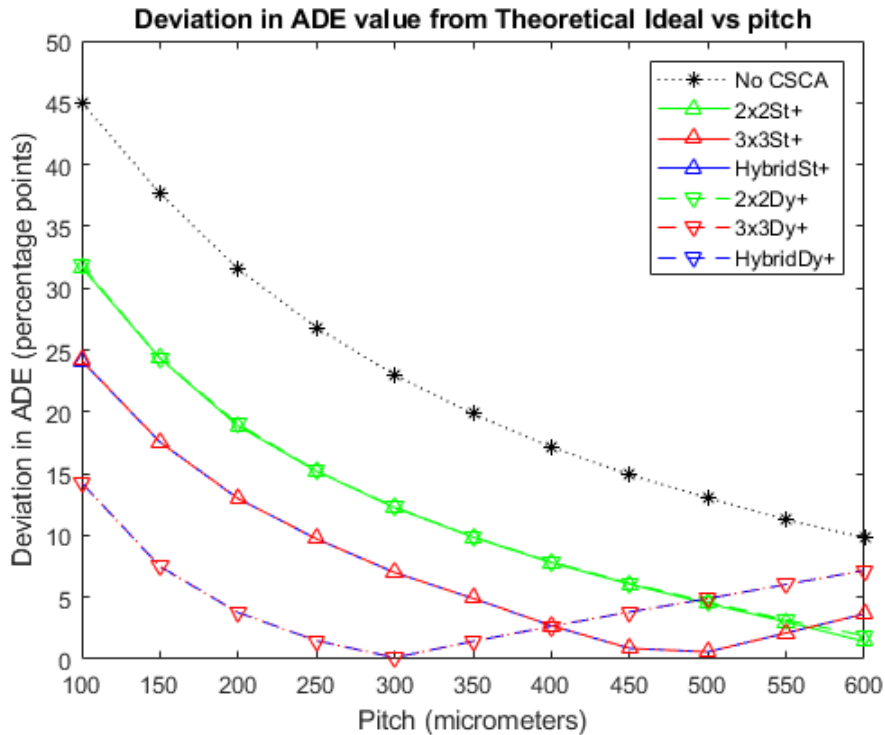


Figure 7.6. A plot of the difference between each CSCA and the Theoretical ADE proposed earlier at an incident photon flux of $\sim 10^6$ photons $\text{mm}^{-2} \text{s}^{-1}$. The difference is taken directly from the data for Figure 7.3 and so is expressed in percentage points. Again, the case where no CSCA is applied is presented for comparison.

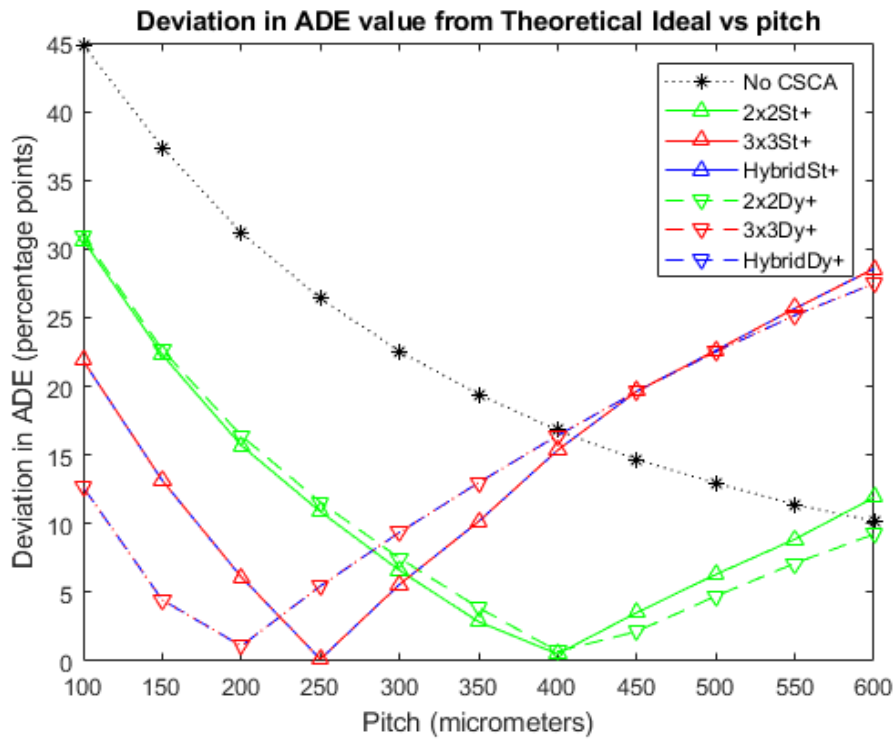


Figure 7.7. A plot of the difference between each CSCA and the Theoretical ADE proposed earlier at an incident photon flux of $\sim 10^7$ photons $\text{mm}^{-2} \text{s}^{-1}$. The difference is taken directly from the data for Figure 7.4 and so is expressed in percentage points. Again, the case where no CSCA is applied is presented for comparison.

7.3.2 Absolute photopeak efficiency

Figures 7.8 and 7.9 show *APE* as a function of pitch for the various CSCAs at photon fluxes of $\sim 10^6$ and $\sim 10^7$ photons $\text{mm}^{-2} \text{s}^{-1}$ respectively. The case where no CSCA is applied is again present for reference. For the metric of *APE*, higher values represent better detector performance. All trend lines show a convex shape (with respect to the x-axis): rising to a peak value before beginning to decline. The CSCAs all reach peak *ADE* value at smaller pixel pitches than the ‘No CSCA’ case, resulting in ‘No CSCA’ outperforming the CSCAs at higher per-pixel fluxes. Similarly, 3x3 and Hybrid CSCAs peak sooner than the 2x2 CSCAs and so underperform them at larger per-pixel fluxes. As was the case with *ADE*, both NL versions of the 2x2 CSCAs behave indistinguishably at all but the highest per-pixel fluxes, where dynamic CSCAs have a slight advantage. Equally unchanged is the fact that dynamic 3x3 and dynamic Hybrid CSCAs perform near identically, however this is not the case for the static CSCAs. In contrast to *ADE*, *APE* values for static Hybrid and static 3x3 CSCAs perform markedly differently. Whilst both rise to their peak performance at around the same rate, the static Hybrid CSCA drops off in performance far more gradually than its 3x3 counterpart. This results in the static Hybrid CSCA underperforming the dynamic Hybrid CSCA at low per-pixel fluxes but outperforming it at higher per-pixel fluxes. In contrast, the dynamic 3x3 CSCA always outperforms the static 3x3 CSCA.

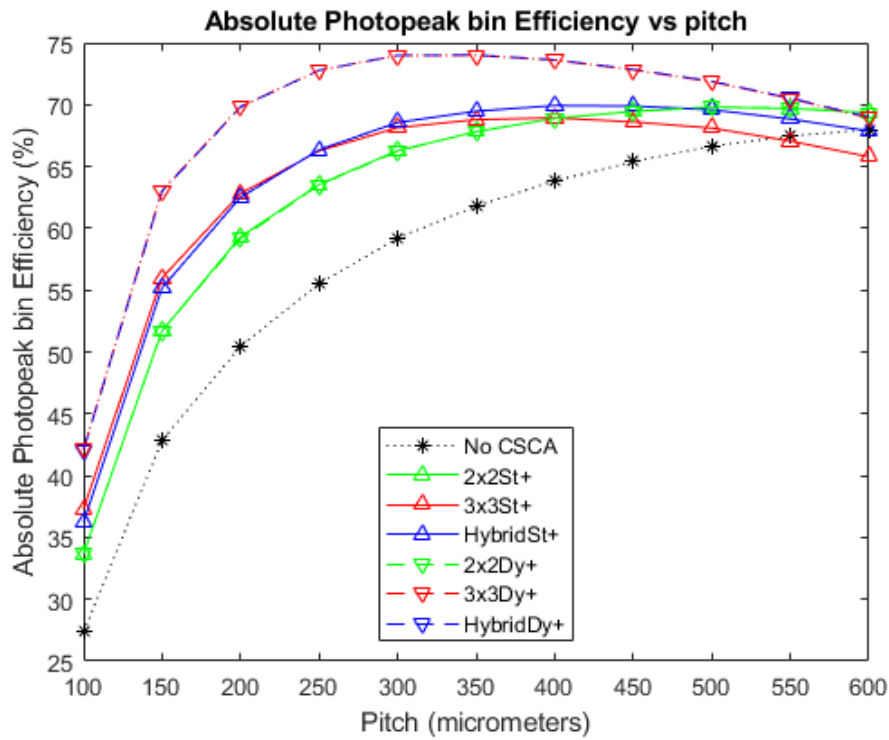


Figure 7.8. A plot of APE versus pixel pitch at an incident photon flux of $\sim 10^6$ photons $\text{mm}^{-2} \text{s}^{-1}$. The dynamic Hybrid and dynamic 3x3 CSCAs perform indistinguishably according to this metric, resulting in significant overlap. Similarly, the 2x2 dynamic and static CSCAs overlap almost entirely at this flux level. The case where no CSCA is applied is also shown as a reference.

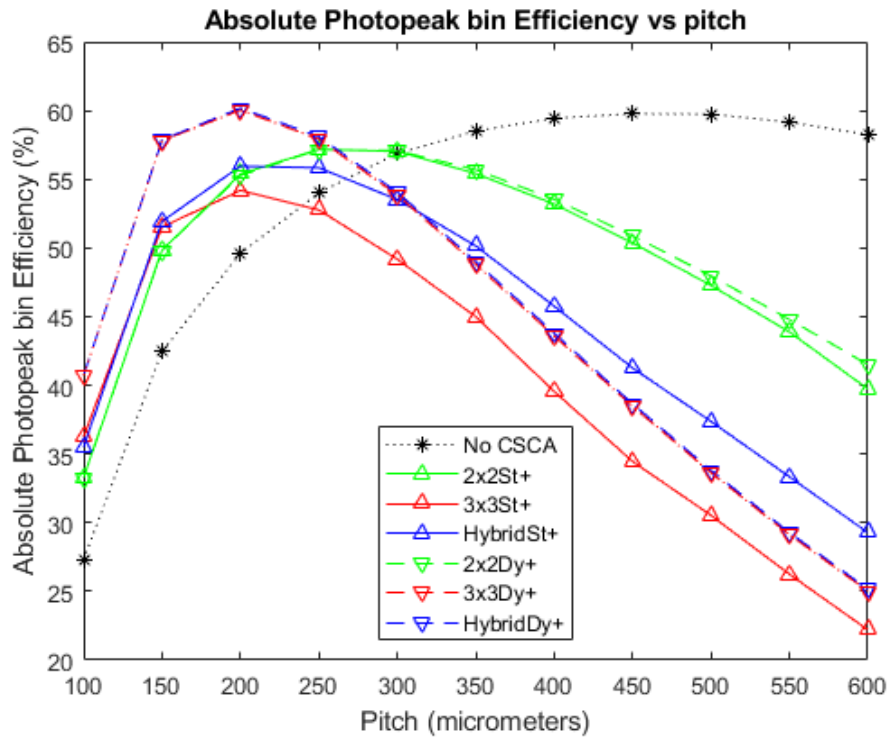


Figure 7.9. A plot of APE versus pixel pitch at an incident photon flux of $\sim 10^7$ photons $\text{mm}^{-2} \text{s}^{-1}$. The dynamic Hybrid and dynamic 3x3 CSCAs perform indistinguishably according to this metric, resulting in significant overlap. Similarly, the 2x2 dynamic and static CSCAs overlap at low pitches (below ~ 350 μm) but begin to become distinguishable at the higher pitches considered here. The case where no CSCA is applied is also shown as a reference.

7.3.3 Relative coincidence counts

Figure 7.10 plots *RCC* for the various CSCAs as a function of pixel pitch at an x-ray flux of $\sim 10^7$ photons $\text{mm}^{-2} \text{s}^{-1}$. Again the ‘No CSCA’ case is shown for comparison. *RCC* registers counts that can only result from two unrelated photons being summed together (either through action of a CSCA or through coincidence in arrival time in the same pixel) and is thus a useful proxy for pulse pile-up. Consequently, lower *RCC* values indicate better detector performance. As can be seen from Figure 7.10, all CSCAs produced *RCC* values greater than the ‘No CSCA’ case, with 3x3 and Hybrid CSCAs producing the largest *RCC* values. Interestingly, whilst dynamic and static CSCAs produce similar results at most pixel pitches for NS of both 2x2 and 3x3, this is not the case with Hybrid CSCAs. Additionally, where the 2x2 and 3x3 NL types diverge it is the dynamic NL type which produces a lower *RCC*, but for the Hybrid CSCAs it is the static NL type which produces the lowest *RCC*, and by a large amount (up to ~ 20 percentage points).

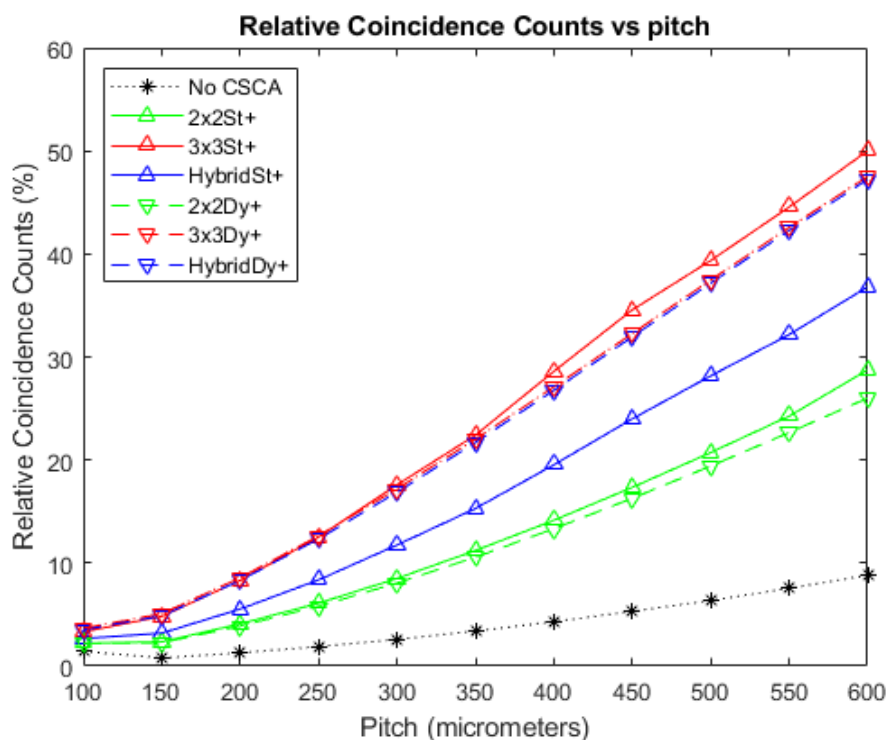


Figure 7.10. A plot of *RCC* versus pixel pitch at an incident photon flux of $\sim 10^7$ photons $\text{mm}^{-2} \text{s}^{-1}$. The dynamic Hybrid and dynamic 3x3 CSCAs overlap significantly with each other at all pitches, and with the static 3x3 CSCA at pitches below $\sim 300 \mu\text{m}$. Similarly, the 2x2 dynamic and static CSCAs overlap at low pitches (below $\sim 300 \mu\text{m}$) but begin to become distinguishable at the higher pitches considered here. The case where no CSCA is applied is also shown, for reference.

7.3.4 Binned spectral efficiency

Figures 7.11, 7.12 and 7.13 plot *BSE* as a function of pixel pitch for the various CSCAs at x-ray fluxes of $\sim 10^6$, $\sim 10^7$ and $\sim 10^8$ photons $\text{mm}^{-2} \text{s}^{-1}$ respectively. Again the ‘No CSCA’ case is included for reference. As for *APE*, a convex trend is seen at each flux considered with increasing pixel pitch. The curvature of this trend increases with increasing x-ray flux. Application of any CSCA results in the peak shifting to a lower pitch than in the ‘No CSCA’ case though the 3x3 and Hybrid CSCAs again appear to peak at lower pixel pitches than their 2x2 counterparts. NL choice makes little if any difference for

2x2 CSCAs, though can be seen to make a stark difference in the case of 3x3 and Hybrid CSCAs. For static NL, the 3x3 and Hybrid CSCAs perform similarly at low per-pixel fluxes, though after peaking the static Hybrid CSCA drops off more gradually than the static 3x3 CSCA, causing them to diverge. For the dynamic NL, 3x3 and Hybrid CSCAs behave similarly across all pixel pitches studied here. These dynamic CSCAs outperform the static 3x3 CSCA in all cases tested, whilst they only outperform static Hybrid at low per-pixel fluxes (Figure 7.11 and below 400 μm in Figure 7.12), after which they underperform it.

7.3.5 Other figures

Figure 7.14 shows data from FEM simulations performed as part of CoGI. This data is included as it is pertinent to discussions regarding the mechanisms behind the observed trends for all metrics. Figure 7.14a shows a cross-section of the 3D charge induction efficiency (*CIE*) maps used for determining signals induced in the anode of a pixel. The cross-section is taken at right angles to the long axis of the pixel and shows data for electrons only. The *CIE* appears highly uniform under the anode (demarcated by the central white square), dropping off rapidly with increasing in-plane distance from the anode. Figure 7.14b plots *CIE* vs distance for a line profile taken across the middle of Figure 7.14a. *CIE* drops from $\sim 87\%$ at the edges of the anode (dotted lines) to $<50\%$ a mere 15 μm away (at the midline of the inter-anode space).

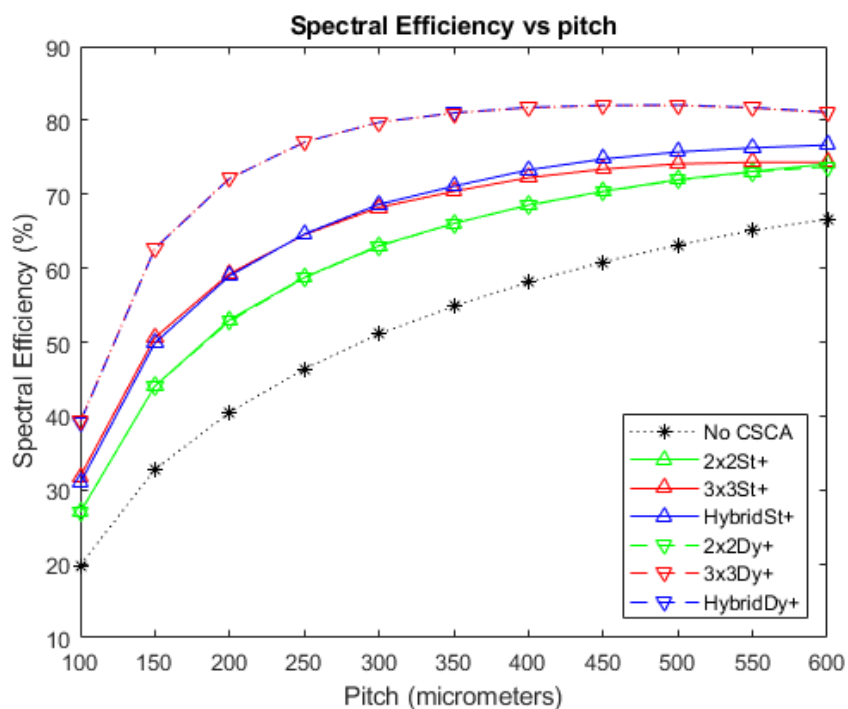


Figure 7.11. A plot of BSE versus pixel pitch at an incident photon flux of $\sim 10^6$ photons $\text{mm}^{-2} \text{s}^{-1}$. The dynamic Hybrid and dynamic 3x3 CSCAs perform indistinguishably according to this metric, resulting in significant overlap. The same is true for the dynamic 2x2 and static 2x2 CSCAs. Similarly, the static Hybrid and static 3x3 CSCAs overlap significantly at lower fluxes but diverge from about ~ 300 μm . The case where no CSCA is applied is also shown, for reference.

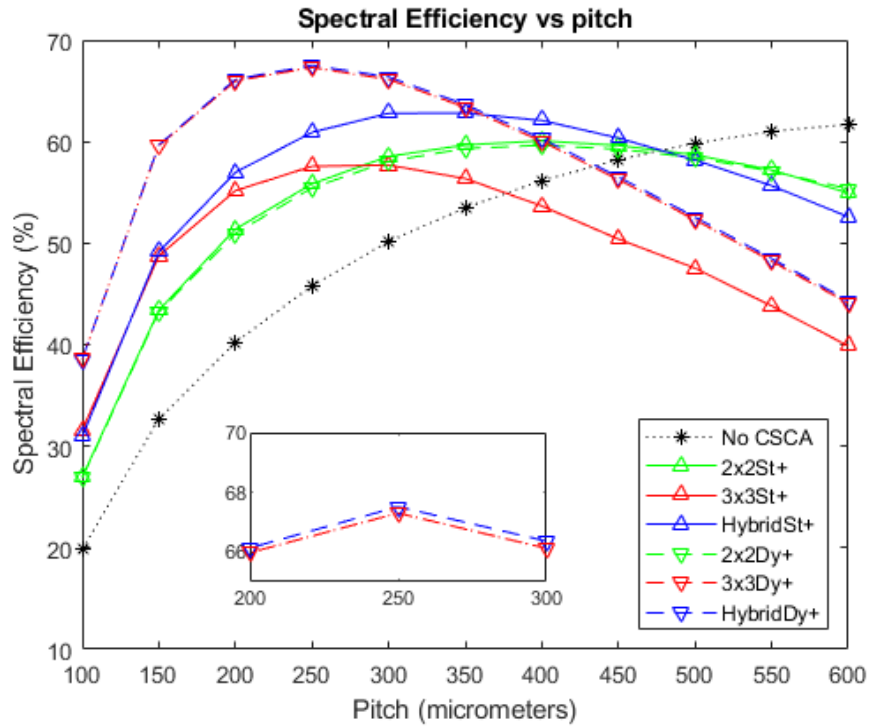


Figure 7.12. A plot of BSE versus pixel pitch at an incident photon flux of $\sim 10^7$ photons $\text{mm}^{-2} \text{s}^{-1}$. The dynamic Hybrid and dynamic 3x3 CSCAs perform exceptionally closely according to this metric (see inset), resulting in significant overlap. The same is true for the dynamic 2x2 and static 2x2 CSCAs. The case where no CSCA is applied is also shown, for reference.

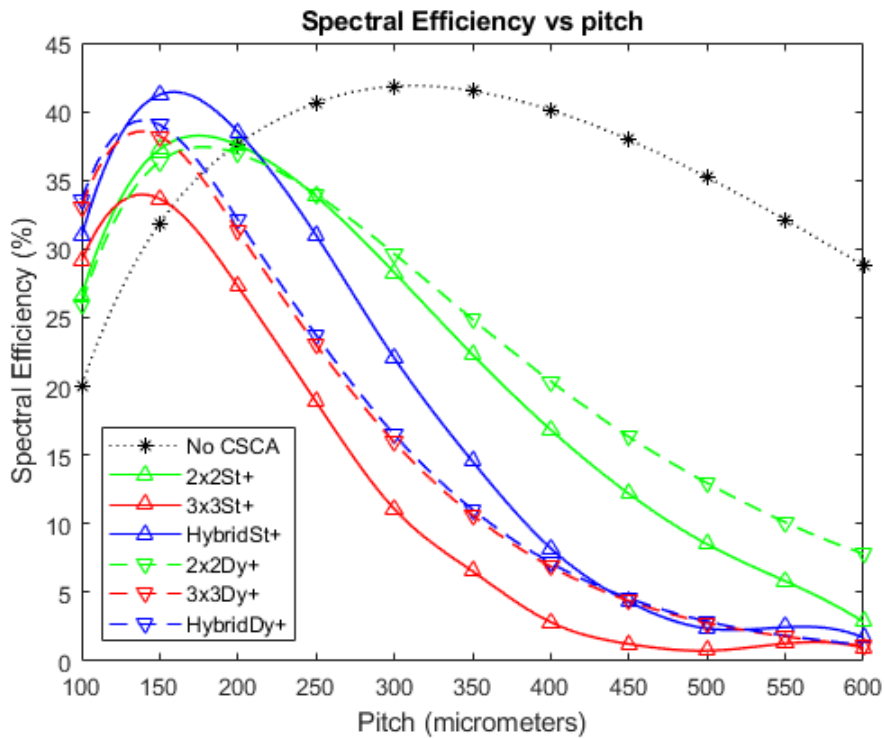


Figure 7.13. A plot of BSE versus pixel pitch at an incident photon flux of $\sim 10^8$ photons $\text{mm}^{-2} \text{s}^{-1}$. The dynamic Hybrid and dynamic 3x3 CSCAs perform exceptionally closely according to this metric, resulting in significant overlap. The case where no CSCA is applied is also shown, for reference.

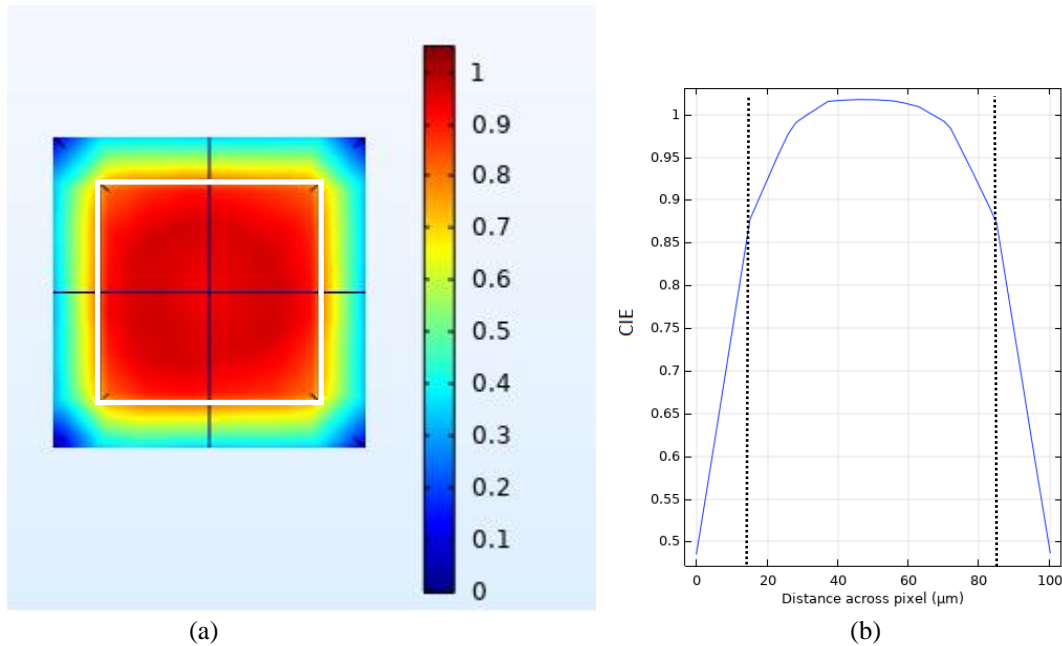


Figure 7.14. (a) Heat map representing CIE across a single pixel as generated and viewed in COMSOL. The plot represents a cut through taken perpendicular to the incident photon flux and at a depth below the anode equal to 10% of the pixel's length. The edges of the anode are marked by the white square superimposed on the image. (b) A plot of CIE vs distance along a path taken across the centre of the pixel (the horizontal black line in a). Other black lines are spatial markers from COMSOL and can be ignored here.

7.4 Discussion

7.4.1 Absolute detection efficiency

As previously noted, the non-linear decline in *ADE* with increasing pixel pitch observed for all CSCAs and the 'No CSCA' case is explained as resulting from the joint downwards pressures on *ADE* of reduced charge sharing and increased pulse pile-up associated with larger pixel pitches (Section 6.4.1). Additionally, as can be seen from Equation 6.3, *ADE* is sensitive only to the total number of counts in the detector and not to which bin they are placed into. Hybrid and 3x3 CSCAs will therefore act identically, as they each convert all events within a single 3x3 search area into a single count, though they may assign that count different energy. For this reason, Hybrid CSCAs will be considered a class of 3x3 CSCA for the rest of the discussion regarding *ADE* values in this chapter.

The trends shown in Figure 7.4 that remain to be explained therefore are the ordering of *ADE* values based on NS ($3 \times 3 < 2 \times 2 < \text{'No CSCA'}$), the ordering of CSCAs crossing the Theoretical *ADE* line ($3 \times 3 \text{Dy} < 3 \times 3 \text{St} < 2 \times 2 \text{St} < 2 \times 2 \text{Dy}$) and why NL choice affects 2x2 and 3x3 CSCAs in opposite ways. These patterns can all be explained in terms of the extent to which the CSCAs reduce CSEs and increase pulse pile-up.

Consider first the order of the CSCAs based on NS classification. The default case of 'No CSCA' causes *ADE* values significantly above 100% to be recorded, as CSEs allow a single photon to trigger counts in multiple pixels. In contrast, the 'Theoretical *ADE*' line shows what a detector would record were CSEs corrected for perfectly, and only pile-up allowed to deteriorate *ADE*. For all pitches looked at in this study, CSCAs produce lower *ADE* values than the 'No CSCA' case, with 3x3 and hybrid CSCAs producing lower *ADE* values than the 2x2. In line with the conclusions from

Section 6.4.1, this could result from either a reduction in CSEs, as is the aim of CSCAs, or from an increase in pile-up effects. Varying x-ray flux allows for a way to increase the contribution of pile-up (which is a blurring over time) without affecting the probability of CSEs (which are blurrings over space), so considering *ADE* plots at different fluxes allows verification that pulse pile-up accounts for some of the observed drop in *ADE* seen from CSCAs compared with the ‘No CSCA’ case. Figure 7.3 and Figure 7.5 show plots of *ADE* vs pitch for fluxes of $\sim 10^6$ and $\sim 10^8$ photons $\text{mm}^{-2} \text{s}^{-1}$ respectively. Comparing these plots reveals that when the flux increases by 2 orders of magnitude it causes a relatively small drop in *ADE* for pixels of 100 μm pitch (3% drop from 138% to 134%) but a much larger drop in *ADE* for pixels of 600 μm (a 47% drop, from 102% to 54%). This is consistent with pile-up leading to the drop in two ways; firstly, by showing a drop in *ADE* for all pitches at a higher flux and secondly, by showing that the extent of the drop is proportional to the pixel’s sensitivity to pile-up (larger pixels being more sensitive to it).

Similarly, comparison of the ‘No CSCA’ case with the Theoretical *ADE* line in the lowest flux case where pile-up is minimal (Figure 7.3) can be used to establish that CSEs also contribute to the perceived improvements of the various CSCAs. The low flux constraint is required in this case to ensure minimal differences between the analytical and numerical approaches used, which model paralyzable and non-paralyzable models respectively. The ‘No CSCA’ *ADE* values calculated by CoGI are significantly higher than those predicted by the analytical model. The extent of this discrepancy drops off exponentially with increasing pixel pitch, consistent with it being due to the result of x-ray fluorescence (with photon transmission probability dropping off exponential with distance through a material). Further, a 2 order of magnitude increase in flux causes little shift in the *ADE* value for the smallest pixels (3% drop at 100 μm as previously noted), indicating that these high *ADE* values are predominantly caused by uncorrected CSEs.

With the above noted, the results shown in Figure 7.4 indicate that all CSCAs reduce the contribution of CSEs to the *ADE* metric, whilst increasing the effect of pulse pile-up. This is not in and of itself surprising as this is what CSCAs are designed to do, however it serves as a useful experimental verification that they work as intended.

It is similarly unsurprising that 3x3 CSCAs result in lower *ADE* values than 2x2 CSCAs as they cover a larger search area and so will find both more true-CSEs to reconstruct but also more random coincidences that will lead to pulse pile-up. It needs to be noted however that these CSCAs will assign their output to a single pixel, in an attempt to preserve spatial resolution gains from having the smaller pixels. The correct point of reference for measuring the performance of a CSCA according to the *ADE* metric is thus the Theoretical *ADE* calculated for a single pixel. Figures 7.6 and 7.7 show the absolute deviations from ideal behaviour for the different CSCAs (and the ‘No CSCA’ case) at fluxes of $\sim 10^6$ and $\sim 10^7$ photons $\text{mm}^{-2} \text{s}^{-1}$ respectively. CSCAs that produce *ADE* values markedly below this line can thus be described as underperforming just as significantly as those producing *ADE* values the same amount above the line.

The first thing to note is that the deviation between CoGI predicted ‘No CSCA’ *ADE* values and the theoretically calculated values decreases exponentially with pitch. This supports the assertion that CSEs are primarily responsible for the deviation seen at these fluxes as pile-up effects are included in the Theoretical *ADE* but CSEs are not.

The second point of note is that the vertical ordering of the CSCAs changes as a function of per-pixel flux. For the lowest flux (Figure 7.6), where pile-up is negligible, the 3x3 CSCAs outperform (have a lower deviation from the ideal) the 2x2 and ‘No CSCA’ approaches in approximating the ideal detector at all but the largest two or three pixel pitches. In contrast, at a flux of $\sim 10^7$ photons $\text{m}^{-2} \text{s}^{-1}$, the increased sensitivity of the 3x3 CSCAs to pile-up (due to their larger NS) mean that they underperform not only the 2x2 CSCAs at a wide range of pitches investigated, but also produce a poorer *ADE* value than the ‘No CSCA’ approach.

Figures 7.3 - 7.7 can also be used to compare CSCAs based on NL. In Figures 7.3 - 7.5 there is little difference between static and dynamic approaches for 2x2 CSCAs at low per-pixel fluxes. Dynamic 2x2 approaches produce higher *ADE* values at higher per-pixel fluxes however, suggesting they are either less susceptible to pulse pile-up or less capable of negating CSEs. We shall determine which of these options is likely to be true in a moment, but first it should be noted that the same pattern is not visible for the 3x3 CSCAs. 3x3 CSCAs show more clear differences between dynamic and static approaches at almost all per-pixel flux levels considered. Further, the order of the 3x3 CSCAs based on NL varies as a function of flux: with static CSCAs producing higher *ADE* values at low per-pixel fluxes but dynamic CSCAs producing higher *ADE* values at higher per-pixel fluxes. The difference between the way that 3x3 and 2x2 CSCAs respond to a shift from static to dynamic NL models can be explained by geometric arguments.

Consider two events registering in two adjacent pixels, A and B, as a result of a CSE. Event A registers first, and B is then searched for within the neighbourhood built by A. With 2x2 CSCAs the probability that A and B are located within the same neighbourhood is independent of which neighbourhood pixel event A is recorded in, assuming the spatial correlation between A and B is isotropic. This is because all pixels in a 2x2 neighbourhood will be linked to 3 of their 8 neighbours, so the odds of the CSCA detecting the CSE is 3/8. In contrast, the 3x3 neighbourhoods contain 3 geometrically distinct pixel types: corners (3 of 8 neighbours linked, detection probability 3/8), edges (5 of 8 neighbours linked, detection probability 5/8) and central (8 of 8 neighbours linked, detection probability 8/8). By building a neighbourhood such that A is always in a central pixel, dynamic 3x3 CSCAs thus experience a significant advantage over their static counterparts. This is referred to as a ‘**geometric advantage**’.

Geometric advantage explains why dynamic 3x3 CSCAs have lower *ADE* values than static 3x3 CSCAs at low per-pixel fluxes, however not why they have higher *ADE* values at high per-pixel fluxes. Nor can it explain why dynamic 2x2 CSCAs experience a slower drop in *ADE* value with increasing per-pixel flux than their static counterparts. The mechanism proposed to explain this is referred to here as ‘**variable pixelation**’. Briefly, this refers to the fact that dynamic CSCAs can support

a higher maximum count rate than static CSCAs, due to the way in which they define neighbourhoods. It is worth exploring this concept in a bit of detail.

The detectors modelled in CoGI are all non-paralysable in nature and so for a detector with a fixed number of pixels, n , the maximum count rate, Ω_{max} , is given by

$$\Omega_{max} = \frac{n}{\tau_r} \quad \text{eq. 7.8}$$

where τ_r is the time between a photon triggering a pixel to record a count and that same pixel resetting to be able to count another photon. For static $N \times N$ CSCAs the pixels linked into a neighbourhood all reset in sync and can only count once between them, so the maximum count rate, Ω_{max}^N is reduced to

$$\Omega_{max}^N = \frac{n}{N^2 \tau_r} \quad \text{eq. 7.9}$$

assuming that n is a square number, the pixels are arranged in a $\sqrt{n} \times \sqrt{n}$ grid and N is a factor of \sqrt{n} . For a dynamic CSCA however this is not the case, as each neighbourhood is defined dynamically and so the order of interactions matters. Consider Figure 7.15 which shows how this can lead to a variable max count rate. Dynamic 2x2 and static 2x2 CSCAs are compared for simplicity, though analogous arguments can be made for 3x3 CSCAs.

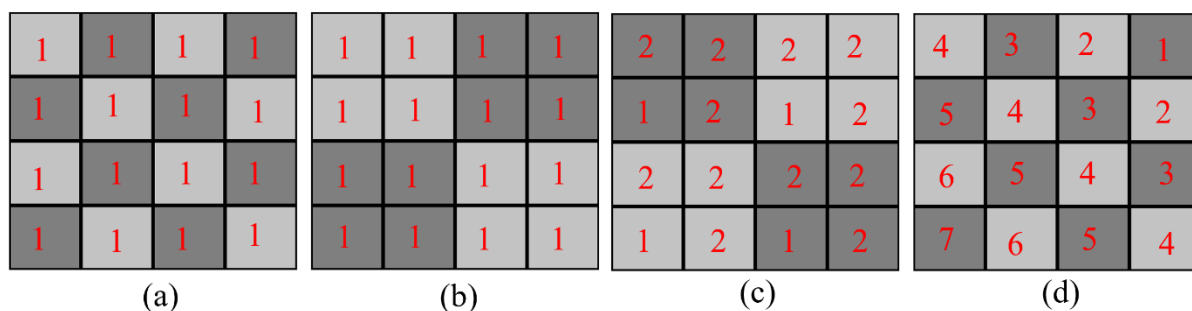


Figure 7.15. A 4x4 pixel array can produce a range of different counts depending on its segmentation. The numbers in pixels refer to the order in which they are triggered. Pixels with the same number can be triggered in any order, so long as they are all triggered before higher numbered pixels. For the case where no CSCA is applied (a) the maximum count rate is equal to the number of pixels: 16. For a static 2x2 CSCA (b) the maximum count rate is equal to the number of neighbourhoods defined: 4. For a dynamic 2x2 CSCA however the maximum count rate depends on the order in which the pixels are triggered and can range from 4 (c) up to 16 (d). The more highly ordered state of the triggering required to produce 16 counts makes it less likely however, so the measured count rate will likely lie somewhere in between 4 and 16.

As dynamically assigned neighbourhoods can overlap, the maximum number of neighbourhoods is greater than would be assumed by simply dividing n by N^2 . In fact, as the only requirement for a new neighbourhood to be plotted is that it has 1 pixel that is not currently in a neighbourhood, the maximum count rate is again equal to Ω_{max} . It is unlikely that the count rate will reach Ω_{max} , though over large numbers of events the count rate will tend to some value, Ω_{max}^{Ndy} , between Ω_{max} and Ω_{max}^N . To verify this, a Monte Carlo simulation was defined in which the pixels had infinite deadtime so could only count once. Irradiation time was variable, stopping when no pixels were left available to count. In this way, the number of neighbourhoods (the effective number of pixels) that would be produced under maximum count rate conditions could be measured. A 21000 $\mu\text{m} \times 21000 \mu\text{m}$ block of CdTe was simulated and pixelated with four different pixel pitches. Each pitch was simulated for 10^4 runs using a dynamic 2x2 CSCA and 10^4 runs using a dynamic 3x3 CSCA. The ratio of Ω_{max}^{Ndy}

to Ω_{max}^N was calculated for each value, and the outcomes can be seen in Table 7.2. As can be seen from these runs, dynamic 2x2 CSCAs and 3x3 CSCAs have maximum count rates roughly 1.6 and 1.7 times larger than their static counter parts respectively. Consequently, for the specific metric of *ADE*, dynamic CSCAs tend to a higher *ADE* value than static CSCAs of the same NS.

Table 7.2. The ratios of maximum count rates for dynamic and static 2x2 and 3x3 CSCAs.

Array size (pixels)	Equivalent pixel pitch (μm)	1x1 max count rate	Static 2x2 max count rate, Ω_{max}^{S2}	Dynamic 2x2 max count rate, Ω_{max}^{D2}	$\Omega_{max}^{D2} / \Omega_{max}^{S2}$	Static 3x3 max count rate, Ω_{max}^{S3}	Dynamic 3x3 max count rate, Ω_{max}^{D3}	$\Omega_{max}^{D3} / \Omega_{max}^{S3}$
210x210	100	44100	11025	17647	1.6	4900	8301	1.7
84x84	250	7056	1764	2840	1.6	784	1342	1.7
60x60	350	3600	900	1455	1.6	400	689	1.7
42x42	500	1764	441	716	1.6	196	341	1.7

The consequences of the above arguments can be seen by considering Figures 7.6 and 7.7. Considering first the 2x2 CSCAs, there is little difference seen between the performance of dynamic and static CSCAs at small per-pixel fluxes. As the per-pixel flux increases however the static CSCAs appear to improve more rapidly than the dynamic CSCA until both 2x2 CSCAs perform as close to the theoretical ideal as possible (around 400 μm). As pitch increases further beyond this point however, the dynamic CSCA is closer to the Theoretical ideal. At sufficiently large pitches (>600 μm at this flux) both 2x2 CSCAs will perform worse than the ‘No CSCA’ case, though static 2x2 CSCAs reach this point sooner. It can now be seen that this is a simple consequence of dynamic CSCAs being able to support a higher count rate. At low fluxes the dominant deviations between theoretically ideal and CoGI simulated *ADE* values are due to CSEs. 2x2 CSCAs increase the effective pixel size, resulting in a reduction to CSEs and thus lower *ADE* values. As neither static nor dynamic CSCAs have a geometric advantage, the two algorithms are comparable where CSEs are the dominant determiner of performance. At higher fluxes and larger pixel sizes the dominant deviations between theoretically ideal and CoGI simulated *ADE* values are due to pulse pile-up. The larger effective pixel size produced by 2x2 CSCAs makes systems employing them more prone to pile-up than the ‘No CSCA’ case, resulting in an increasing deviation between theoretically ideal and CoGI simulated results. In this regime in which pulse pile-up is the dominant factor in deteriorating performance, the dynamic CSCAs outperform static CSCAs due to their higher effective pixel number (and consequent lower sensitivity to pile-up).

The above argument also applies to the 3x3 CSCAs, however there is one notable difference: dynamic 3x3 CSCAs have a geometric advantage over their static counterparts. The difference this makes is significant, as can be seen by considering Figure 7.7. High per-pixel fluxes still lead to static 3x3 CSCAs outperforming dynamic ones due to variable pixelation, however static and dynamic 3x3 CSCAs are not roughly equivalent at low per-pixel fluxes. Instead, at low per-pixel fluxes, where CSEs dominate, dynamic 3x3 CSCAs outperform their static counterparts due to their geometric advantage. This also results in dynamic 3x3 CSCAs reaching optimal performance at smaller pixel

itches. The interplay between geometric advantage and variable pixelation results in two transition points rather than one: dynamic CSCAs outperform at below the first and after the second transition point, but static CSCAs outperform in between them. Comparing Figures 7.6 and 7.7, it is clear the pitches at which these transitions occur, both for 2x2 and 3x3 CSCAs, depend on the operating flux.

7.4.2 Absolute photopeak efficiency

As *APE* is a spectral metric, the energy bin to which a count is assigned is relevant to the *APE* value calculated and so Hybrid and 3x3 CSCAs will be considered separately.

The trend in *APE* displayed by Figure 7.8 is that of a peak in *APE* value at some pixel pitch, with drop offs in *APE* as pitch is either increased or decreased from that value. Section 6.4.2 explained this behaviour as arising from the competition between reducing CSEs (which dominate at smaller pitches) and increasing pulse pile-up (which dominates at larger pitches). It was also noted in that discussion that the effect of a CSCAs is to reduce CSEs and increase pulse pile-up, and this was demonstrated using a 3x3Dy+ CSCA as an example. All CSCAs considered in Figure 7.7 show this same behaviour, and so are consistent with these proposed mechanisms. Full discussion of these trends can be found in that section.

Comparison of the CSCAs considered in Figure 7.8 reveals several interesting trends within CSCA selection, the first of which is that all CSCAs lead to the peak *APE* value being found at a lower pitch than in the ‘No CSCA’. This is because all CSCAs, regardless of their NL or NS, increase the effective pixel size and so result in a shift in peak location to smaller pixel pitches. The role of effective pixel size in reducing the peaking pitch is evidenced by the lower pitch values for peaks in 3x3 CSCAs compared with their 2x2 analogues (200 μm vs 250 μm - 300 μm for 3x3 based and 2x2 based CSCAs respectively). As a result of this earlier peak, 3x3 CSCAs perform better than 2x2 CSCAs at low pixel pitches, but the 2x2 NS CSCAs produce higher *APE* values when pixels are larger, and consequently pulse-up is more of an issue. Dynamic Hybrid CSCAs peak at approximately the same pitch as dynamic 3x3 CSCAs, as they both benefit from the same geometric advantage for finding CSEs described in the *ADE* section above. This geometric advantage also results in higher peak *APE* values associated with the dynamic 3x3 and Hybrid CSCAs when compared with their static counterparts. That geometric advantages explain these differences between static and dynamic CSCAs is further supported by the fact that these differences are absent from the peaks in the 2x2 CSCAs, as all pixels in 2x2 CSCAs are geometrically identical.

The second observation regarding CSCA choice on *APE* values is the change in maximum *APE* value that is obtained. Figure 7.8 shows that only the dynamic 3x3/Hybrid CSCAs result in an *APE* value that is higher than the ‘No CSCA’ case at a flux of 10^7 photons $\text{mm}^{-2} \text{s}^{-1}$, with all other CSCAs producing lower peak *APE* values. The reason for this is that pulse pile-up is more significant with the larger effective pixel sizes produced by the CSCAs, resulting in a stronger downwards pressure on *APE* with increasing pitch, and consequently a lower maximum *APE* value. Confirmation that this is due to pile-up is given in the form of Figure 7.7 which shows that at the lower flux of $\sim 10^6$ photons $\text{mm}^{-2} \text{s}^{-1}$,

where pile-up is negligible and CSEs are the dominant source of *APE* degradation, all CSCAs produce higher peak *APE* values than the ‘No CSCA’ case. The lower flux regime also leads to a more gradual downwards slope after the peak, again supporting the assertion that the decline in *APE* value at higher pitches results from increased pulse pile-up.

Considering next the difference NL choice has on *APE*, it is significant to note that whilst dynamic CSCAs produce higher *APE* values for CSCA with NS of 2x2 and 3x3, the reverse observation is made for Hybrid CSCAs. This is the first instance of Hybrid and 3x3 CSCAs deviating and deserves explanation.

The variable pixelation concept proposed to explain the higher *ADE* values for dynamic CSCAs than static ones at high fluxes can also explain this deviation in *APE* metric. Due to the energy sensitivity of *APE* that is absent in *ADE* however, the role of this mechanism in favouring dynamic CSCAs with regards *APE* needs elucidating. At low per-pixel fluxes, the probability of multiple events defining overlapping neighbourhoods on the detector is small, and consequently variable pixelation effects are negligible. This explains the extensive overlap of 2x2 static and dynamic CSCAs at low per-pixel fluxes. In contrast, as pulse pile-up becomes significant, pixel neighbourhoods may begin to overlap. Consequently, some neighbourhoods will be defined that are smaller than the 2x2/3x3 sizes intended, and these regions will be less prone to pulse pile-up. Dynamic CSCAs thus have a range of neighbourhood sizes at high per-pixel fluxes, leading to a reduction in the average effective pixel size and thus in the pile-up experienced, improving *APE*. For dynamic 2x2 CSCAs for example, the maximum count rate is 1.6 times larger than its static counterpart, implying an average neighbourhood size 1.6 times smaller (2.5 pixels vs 4 pixels). This explains why dynamic CSCAs outperform static CSCAs at high per-pixel fluxes when NS is 3x3 or 2x2. Dynamic Hybrid CSCAs define neighbourhoods in the same way as dynamic 3x3 CSCAs, so should experience this same effect, as indeed was demonstrated when considering *ADE*. The question then becomes why are static Hybrid CSCAs so effective with regards *APE* compared with static 3x3 and dynamic Hybrid CSCAs?

Considering first static 3x3 CSCAs, it can be seen from Figure 7.7 and Figure 7.8 that the advantage of static Hybrid CSCAs is related to pulse pile-up, as evidenced by the advantage growing with increasing per-pixel flux. The major difference between these CSCAs is that whilst the static 3x3 CSCA reads out an event energy based on charge in the whole neighbourhood, the Hybrid CSCA only reads out an event energy based on the charge in a 2x2 sub-neighbourhood. This leads to a lower effective pixel size when reconstructing incident photon energy and so a lower contribution of pulse pile-up.

Comparing static and dynamic CSCAs is more complicated, however the crucial difference can be explained in terms of geometric advantage. Dynamic Hybrid CSCAs define neighbourhoods with the initially detected event in the centre pixel, meaning that this event exists in all sub-neighbourhoods that could be read out. This maximises the chance of correctly matching the event to any related events (correcting CSEs), but also maximises the chance of incorrectly matching this event to an unrelated event (pulse pile-up). At low per-pixel fluxes pulse pile-up is unlikely and so CSEs are the dominant

factor degrading *APE*. Under these circumstances geometric advantage mainly provides better correction of CSEs, and so dynamic Hybrid CSCAs outperform static Hybrid CSCAs. As per-pixel fluxes increase the probability of pulse pile-up also increases, eventually resulting in pulse pile-up being the dominant factor in degrading *APE*. Under these conditions the same geometric advantage means that dynamic Hybrid CSCAs suffer more severely from pulse pile-up, as can be seen in Figure 7.10. This is referred to as the ‘**geometric disadvantage**’ of dynamic Hybrid CSCAs. As a result, static Hybrid CSCAs outperform their dynamic counterparts at high per-pixel fluxes.

7.4.3 Relative coincidence counts

Figure 7.10 shows that the same general trend of increasing *RCC* with increasing pixel pitch noted for the ‘No CSCA’ cases in Section 6.4.3 holds equally well for all CSCAs considered in this work, though the extent of the increase, as well as the *RCC* value at a given pixel pitch and flux, varies significantly between CSCAs. It was proposed in that section that the increase in *RCC* resulted from an increase in the probability of two unrelated photons being absorbed by the same pixel closer in time than the temporal resolution of the system. This increase in probability was purely the result of an increased effective cross-section per pixel presented to the incident x-ray flux. This explains why 3x3 and Hybrid CSCAs produce higher *RCC* values than 2x2 CSCAs, however it does not explain the different behaviour of static and dynamic CSCAs.

Dynamic 2x2 and 3x3 CSCAs produce lower *RCC* values at higher per-pixel fluxes than their static counterparts. Further, the size of the divergence appears to be similar for 2x2 and 3x3 CSCAs, implying that geometric reasons are not responsible. Consistent with the discussion for *APE*, variable pixelation explains this observation as it leads to dynamic CSCAs having a smaller average effective pixel size and higher maximum count rate. The role of variable pixelation in this behaviour can further be inferred from the increasing divergence between static and dynamic CSCAs as pixel pitch increases, and consequently the average distance between random neighbourhoods decreases. The dynamic Hybrid CSCA bucks this trend, instead underperforming when compared with its static counterpart. As with *APE* however, this can be explained by the concept of geometric disadvantage for the dynamic Hybrid CSCA, whereby centring the neighbourhood on a detected event forces all sub-neighbourhoods to contain that event. This increases the probability that coincident events will be detected in at least one subregion, thus making a count in the coincidence bin (an *RCC* count) more probable. Again the increasing advantage of a static Hybrid CSCA over a dynamic one with increasing pixel pitch is consistent with the idea that neighbourhood overlap is a factor in the observed differences.

7.4.4 Binned spectral efficiency

Figure 7.12 shows the relation between *BSE* and pixel pitch for the considered CSCAs. The overall curved shape seen in Section 6.4.4 for the ‘No CSCA’ case is also present for all CSCAs. The reasoning for this is laid out in that section, though briefly it results from CSEs degrading *BSE* as pixel pitch decreases from the peak and pulse pile-up effects degrading it as pixel pitch increases from the peak. As was noted in that section, despite similarities between *APE* and *BSE*, *BSE* is a more sensitive

spectral metric than *APE* as it uses the variable counts in the detector as the denominator in its definition rather than a constant (the incident flux). This means that any CSEs that go uncorrected increment the denominator multiple times, in addition to failing to increment the numerator. The increased sensitivity to CSEs manifests itself in the *BSE* peak occurring at a larger pitch for a given CSCA than *APE* does (e.g. $\sim 400 \mu\text{m}$ vs $\sim 250 \mu\text{m}$ for the 2x2 CSCAs and $250 \mu\text{m}$ vs $200 \mu\text{m}$ for the dynamic 3x3 CSCA at $10^7 \text{ photons mm}^{-2} \text{ s}^{-1}$). This shift in peak position can be understood as originating from a shift in the balance between CSEs and pulse pile-up: with CSEs being more impactful, a higher per-pixel flux can be tolerated before increasing pulse pile-up effects outweigh the CSEs. This shift in balance between CSEs and pulse pile-up for this metric is more impactful on 2x2 CSCAs than 3x3 and Hybrid CSCAs due to their smaller effective pixel size and thus lower susceptibility to pulse pile-up. Indeed, over the flux ranges examined in this work, there is no combination of pixel pitch and x-ray flux for which 2x2 CSCAs offer the best *BSE* of the options available. This conclusion is notable as *BSE* is the metric discussed here that is most closely related to quantitative AuNP imaging with x-CSI, as it concerns the relative weight of one bin with respect to the others: a fundamental feature of K-edge imaging.

The remaining trends evident in Figures 7.11, 7.12 and 7.13 should not be surprising given the thorough discussions in this chapter so far regarding the other metrics. Nevertheless, it is useful to check that the results for this metric are consistent with the mechanisms proposed to explain the observed behaviour of the other metrics.

Considering first the pitch at which peak *BSE* value is reached, we can see from Figure 7.12 that the static CSCAs can be ordered by NL category as $3 \times 3 < \text{Hybrid} < 2 \times 2 < \text{'No CSCA'}$, consistent with the idea that a larger effective pixel size will result in better CSE correction and a more significant effect of pulse pile-up. Hybrid CSCAs search a 3×3 area but only read signal from a 2×2 area, so their effective pixel size for detecting CSEs would be expected to be somewhere between the 3×3 and 2×2 cases, as found. We would also expect, based on the arguments so far, that dynamic 3×3 CSCAs would outperform static 3×3 CSCAs at all pitches due to the geometric advantage they enjoy, and indeed this is seen. Similarly, the presence of both geometric advantage and geometric disadvantage for the dynamic Hybrid CSCA lead us to expect it to outperform the static Hybrid CSCA at low per-pixel fluxes but underperform at high per-pixel fluxes. This is again seen in the results, with static underperforming dynamic in Figure 7.11 and in Figure 7.12 up to $350 \mu\text{m}$ pitch, and then outperforming it from $400 \mu\text{m}$ in Figure 7.12 and throughout all of Figure 7.13. In a marked deviation from earlier metrics, NL has no noticeable effect on the 2×2 CSCAs at fluxes of $\sim 10^6$ and $\sim 10^7 \text{ photons mm}^{-2} \text{ s}^{-1}$. It was shown for all other metrics that NL model plays a role in determining performance for the 2×2 CSCAs, however if this were not shown to still hold for *BSE* then it would bring into question the variable pixelation idea previously mooted as advantaging dynamic CSCAs at high per-pixel fluxes. Fortunately, the divergence does occur, with dynamic 2×2 CSCAs outperforming the static 2×2 CSCAs as expected, at fluxes of $\sim 10^8 \text{ photons mm}^{-2} \text{ s}^{-1}$ (Figure 7.13). The higher flux needed to produce this deviation in *BSE* than *APE* further supports the assertion in this section that *BSE* is more sensitive to CSEs and so comparatively less sensitive to pulse pile-up.

The main takeaway from the results in this chapter so far is that, contrary to common belief, the effects of CSCAs cannot be explained simply by their production of a greater effective pixel size. Were this the case then NS would be sufficient to differentiate CSCAs and NL would not contribute. In stark contrast to this, the three mechanisms identified in this chapter to account for major changes in metric response (geometric advantage, geometric disadvantage and variable pixelation) all arise due to changes in NL rather than NS. Specifically, these mechanisms all arise from the functioning of dynamic CSCAs. Even within static CSCAs however, effective pixel size increases are insufficient to explain the observed effects of CSCAs entirely. If they were then it would be reasonable to expect that the *BSE* for a static 3x3 CSCA running on 200 μm pixels would be the same as a static 2x2 CSCA running on 300 μm pixels and the same as a 600 μm running ‘No CSCA’. This is because these formulations all have an effective pixel size of 600 μm . Comparing the *BSE* values of these CSCAs however, we find that the ‘No CSCA’ produces the highest *BSE* value, followed by the 2x2 and then the 3x3 CSCAs: 62%, 58% and 55% respectively. As these three approaches all present an equal cross-section to the incident x-ray flux, it would at first seem reasonable to expect them to produce the same *BSE* value. However, *BSE*, being an energy dependent metric, is sensitive not just to the presence of charge deposited in the crystal but also to the energy the system assigns to this charge. *BSE* is thus also affected by any underestimation of event energies, such as that caused by non-uniform charge induction efficiency (*CIE*). If the *CIE* was consistent across the whole sensor volume, then it would be reasonable to expect these static CSCA results to be the same as those from ‘No CSCA’ pixels of equivalent size. The variation in *CIE* is significant across a single pixel however, as shown in Figure 7.14. *CIE* values are comparably very high in the area directly under the anode (>87%) but drop rapidly within the inter-anode spacing (from 87% to 45% over a 15 μm distance). This can result in the various charges produced by CSEs being recorded at different energies, such that when they are summed they no longer add to a value that lies within the energy bin used for determining *BSE*. Even a photon that deposits its full energy in a single location will only register within this bin if its location of interaction has a high enough *CIE*. The width of these inter-anode spacings is kept constant across the various systems modelled in this chapter, meaning that the more pixels required to cover a given area, the higher the fractional pixel area comprised of inter-anode spaces. This explains why *BSE* counts in the 600 μm pixels with no CSCA are greater than the *RCC* counts in 300 μm pixels using a 2x2St+ CSCAs, which are greater than the 200 μm pixels using a 3x3St+ CSCA, even though these cases represent the same cross-sectional area to the incident x-ray flux.

7.5 Conclusions

The work presented in this chapter involved the use of our inhouse simulation framework, CoGI, to compare a range of reconstructive charge sharing correction algorithms (CSCAs) running on an x-CSI detector. The CSCAs utilised both static and dynamic neighbourhood localisation (NL) schemes, as well as neighbourhood sizes (NS) of 2x2 and 3x3 pixels. Hybrid algorithms which searched a 3x3 area but only reconstructed over a 2x2 area were also considered. These CSCAs were compared to each other and to the case where no CSCA was applied. Comparisons were made with respect to the

metrics of absolute detection efficiency (*ADE*), absolute photopeak efficiency (*APE*), relative coincident counts (*RCC*) and binned spectral efficiency (*BSE*).

The choice between dynamic and static NL scheme was found to have a significantly larger impact on 3x3 and Hybrid CSCAs than 2x2 CSCAs. This was identified as resulting from the geometric advantage afforded to the 3x3 and Hybrid CSCAs by centring the neighbourhood on the charge sharing events. This centring shifted from advantageous to disadvantageous for the Hybrid CSCAs at higher per-pixel fluxes, however. 2x2 and 3x3 dynamic CSCAs were found to have higher maximum count rates than their static counterparts. It is proposed that this is due to the dynamic CSCAs supporting a larger number of neighbourhoods due to the possibility of partial neighbourhood overlap: an effect called variable pixelation. Evidence to support this was provided in the form of separate Monte Carlo studies that showed approximately 1.6 - 1.7 times higher max count rates for dynamic CSCAs compared with their static counterparts. Variable pixelation leads to improvements in spectral performance at high fluxes where pile-up was significant, as the average effective pixel size is reduced compared to a static scheme at the same pixel pitch.

Metrics which consider absolute count rates of the detector (*ADE* and *APE*) show similar behaviour for Hybrid and 3x3 CSCAs. In contrast, metrics which consider relative counts within the detector to assess spectral parameters (*RCC* and *BSE*) show a significant divergence in behaviour for 3x3 and Hybrid CSCAs. For example, whilst Hybrid CSCAs experience the same geometric advantage as 3x3 CSCAs at low per-pixel fluxes, they experience a much less pronounced drop in performance associated with increasing per-pixel fluxes due to their only summing from a 2x2 subpixel. Further, by spectral metrics, dynamic Hybrid CSCAs perform worse at higher per-pixel fluxes than their static counterparts, rather than better as is the case for 3x3 CSCAs, due to their suffering from geometric disadvantage.

In addition to identifying these mechanisms, which apply to dynamic CSCAs, this work also showed that static CSCAs cannot be accurately treated by a simple model of effective pixel size. This is because fluctuations in charge induction efficiency induced by inter-anode spacing take up a greater proportion of the effective pixel volume. Spectral performance thus decreases for a given effective pixel size as the number of physical pixels comprising it increases.

Collectively, the results of this chapter underscore the importance of using simulations such as CoGI to optimise system parameters, as there is no such thing as a better or worse CSCA that can be determined intuitively, even with respect to a single metric. Rather, the optimal CSCA will depend on the metric being considered and the relative contributions of CSE and pulse pile-up, which will in turn depend on pixel pitch, incident photon energy, incident photon angle and x-ray flux. The intended application will play a crucial role in constraining these parameters.

7.6 Disclaimer

Please note that the results presented in this chapter have since formed the basis of a publication[390]. Figures 7.1 - 7.15 and Table 7.2 were taken directly from this publication with little

or no modification, though their captions may have been changed to be consistent with the terminology used in this chapter.

Chapter 8.

**Work towards
identifying whether
RDEE is affected by
AuNP optimisation
for PASI**

8.1 Introduction

The ability of gold nanoparticles (AuNPs) to deliver a radiotherapy dose enhancement effect (RDEE) has been well studied in the literature[96][126][129][130][131], however to achieve clinical utility the RDEE that the AuNPs will produce in a given patient would need to be known. This information can then be used to modulate the patient's treatment: adjusting the irradiation plan based on which regions will experience AuNP-mediated RDEE and to what extent. Obtaining this information for a given patient will require two things: a quantitative map of AuNP concentrations within the patient and an equation relating AuNP concentration to RDEE.

The relation between AuNP concentration and RDEE is dependent on a variety of parameters both inherent to the AuNPs (e.g. size, cellular uptake, and surface charge) and extrinsic to them (e.g. cell line and oxygen availability). This complicates the development of a precise quantitative relation, with *in vivo* animal model studies usually recording the injected AuNP quantities rather than the collected AuNP concentrations at the site of treatment[96][298]. Nevertheless, these studies do show that significant clinical benefit can be expected by this approach[311][391]. In practice, the second requirement for patient treatment, a quantitative *in vivo* approach to AuNP imaging, could also accelerate efforts to ascertain the relation between RDEE and AuNP concentration. It is for this reason that the imaging aspect was selected as the focus for this PhD. One leading candidate for that application, which is already available in pre-clinical animal imaging systems, is photoacoustic spectral imaging (PASI).

PASI has been shown to possess exquisite sensitivity to the presence of AuNPs in organic samples[199][255][256][257], as well as having demonstrated an ability to track AuNPs in animal models non-invasively over time[266]. These studies use AuNPs that are optimised for PASI detection however, which is needed to overcome issues associated with high attenuation rates of visible light in human tissues and degradation of AuNP photoacoustic spectra upon their aggregation. Whilst both gold nanorods (AuNRs) and gold nanospheres (AuNSs) result in surface plasmon resonances that can be used for PASI, AuNSs produce a peak at ~520 nm which is not within one of the optical windows of human tissues detailed in Chapter 3. In contrast, AuNRs produce two peaks: again, one around 520 nm but also a second peak that is tuneable based on the aspect ratio of the AuNRs. This second peak can be selected so that it is within the optical window of human tissue, and thus useful for *in vivo* imaging. To protect against spectral degradation upon aggregation, PASI optimised AuNPs are often coated in a spacer that prevents the AuNPs from getting too close to each other, such as silica[266][392], or a detoxifying layer such as poly(styrene sulfonate) (PSS)[393].

In contrast, AuNPs used for dose enhancement measurements in the literature are primarily AuNSs, with AuNR investigations much rarer. Where coatings are used, they are usually small (e.g. glucose), easily displaceable (e.g. citrate) and/or fluid (e.g. PEG), rather than the large, rigid spacers used for PASI optimisation. As mentioned in Chapters 2 and 3, AuNP-mediated RDEE studies vary greatly in the way they report RDEE, measure cellular effects, quantify AuNP concentration and deliver

the radiation treatments, making comparison between them complicated. Even where RDEE is measured and compared between AuNS and AuNRs by a single group, studies often concern primarily physical mechanisms of enhancement, using simulations which are unable to account for biological effects such as inhibition to DNA repair.

For these reasons, there is a gap in the literature regarding whether optimisation for PASI affects the RDEE that AuNPs deliver. In particular, there is a significant disconnect between the simulation studies which try to assess the effect of shape and coating on AuNP-mediated RDEE by assessing physical enhancement mechanisms and the abundance of literature which suggests that this mechanism alone cannot capture the full range of RDEE mechanisms. Considering the helpful role PASI could play in answering important questions in the RDEE field, this gap needs to be addressed and that is the aim of the work detailed in this chapter.

In this work, comparisons were made between AuNPs optimised for PASI and those commonly used for RDEE. These comparisons were based on shape (AuNRs vs AuNSs) and coating (PSS/PEG vs citrate). A combination of optimisation routes (shape only, coating only or shape and coating) were considered so that the effects of shape and coating on RDEE could be separated. Efforts were taken to minimise variation in any other physical parameters such as number of Au atoms per particle and AuNP concentration. RDEE was measured using biological cells rather than by simulation, so that physical, chemical, and biological enhancement mechanisms could all be included.

8.2 *Materials and methods*

The study detailed in this chapter required a range of experiments to be performed as part of the calibration and set up. As results from some steps affected the parameters chosen in subsequent ones, some discussion of results is required in this section, though it will be kept to a minimum and all results will then be presented and analysed in full in the subsequent sections. The experiment involved the following steps: AuNP design, AuNP synthesis, calibration of the irradiation equipment, cell dose response curve determination, and determination of AuNP-mediated RDEEs.

8.2.1 *AuNP design*

As mentioned in the introduction, the aim of this experiment was to determine what effect, if any, the choice of coating and shape would have on the RDEE produced by AuNPs. AuNRs and AuNSs were compared, and to maximise the validity of comparisons between the two this study aimed to match as many of the physical parameters as possible between the particles themselves. To minimise the number of confounding variables, it was decided that the same number of AuNPs would be used, regardless of their shape. As physical dose enhancement is proportional to the total number of gold atoms present, and as I did not want to intentionally preference any particular RDEE mechanism, it was decided that the AuNSs and AuNRs should contain the same number of Au atoms. This was achieved by matching the volumes of the two particle types. The particle type with the most constraints on its dimensions was the AuNR, as the dimensions of this particle would determine the wavelength of its

longitudinal plasmon resonance. A formula was thus needed to determine the diameter of a AuNS which would yield the same volume as a AuNR of specified length and width. To see how this was done, consider briefly Figure 8.1. As can be seen, the volume of a AuNR can be thought of as the sum of the volumes of one gold nanocylinder of length $(L - 2R)$ and two gold nanohemispheres with radius R .

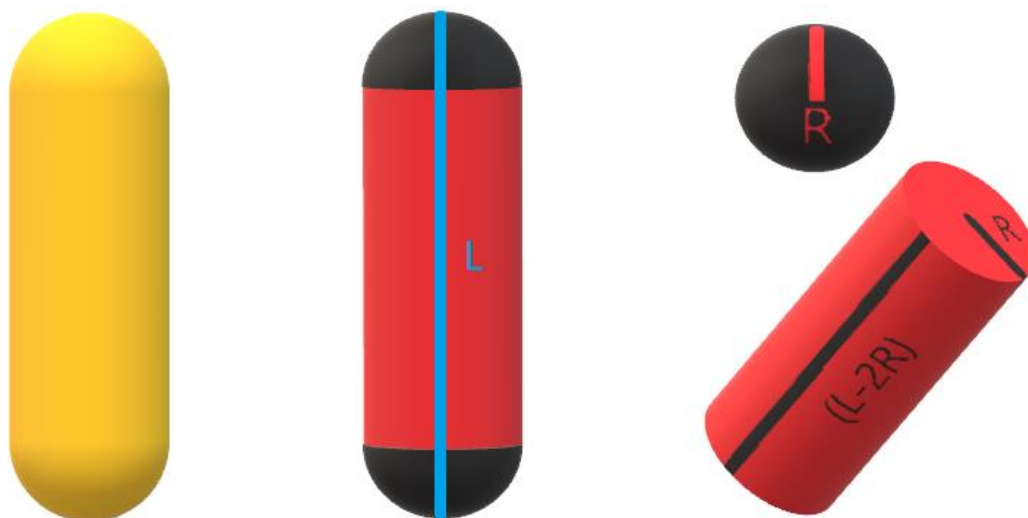


Figure 8.1. A AuNR of length L and diameter $2R$ can be considered as being comprised of two hemispheres of radius R and a connecting cylinder of length $(L - 2R)$ and radius R .

The volume of the hemispheres is given by

$$V_{hemisphere} = \frac{4}{6}\pi R^3 \quad \text{eq. 8.1}$$

the volume of the cylinder is given by

$$V_{cylinder} = \pi R^2(L - 2R) \quad \text{eq. 8.2}$$

and the volume of a AuNR is given by

$$V_{rod} = 2V_{hemisphere} + V_{cylinder} \quad \text{eq. 8.3}$$

For a AuNS we note that the volume of a sphere is given by

$$V_{sphere} = \frac{4}{3}\pi r^3 \quad \text{eq. 8.4}$$

where r is the radius of the AuNS. Setting the two volumes equal, we can derive an equation for r in terms of L and R .

$$V_{sphere} = V_{rod} \quad \text{eq. 8.5}$$

$$\frac{4}{3}\pi r^3 = \frac{4}{3}\pi R^3 + \pi R^2(L - 2R) \quad \text{eq. 8.6}$$

$$r^3 = R^3 + \frac{3}{4}R^2(L - 2R) \quad \text{eq. 8.7}$$

$$r = \sqrt[3]{R^3 + \frac{3}{4}R^2(L - 2R)} \quad \text{eq. 8.8}$$

Once the AuNRs are synthesised, their aspect ratio can be determined (from optical spectroscopy) and their length measured (by transmission electron microscopy). The radius of AuNSs that will result in them containing the same number of Au atoms as the AuNRs can then be determined using Equation 8.8. Note that this is an approximation as volume is a function of radius, so the volume calculated from the mean of the radii will not be exactly the same as the mean of the volumes. The calculated radii are thus the aim of synthesis, though the final distribution of radii will need to be measured experimentally.

8.2.2 AuNP synthesis and selection

Initially, the AuNPs needed were going to be purchased commercially, however the need to match AuNP volumes between shapes meant that they were prohibitively expensive for the budget of this project. It was therefore decided that the AuNPs would be synthesised in house. The AuNRs were synthesised based on a modified version of the Turkevich method, as detailed by Comenge *et al*[266]. The steps involved in this synthesis are listed in Appendix 2.

This process was repeated to yield two batches of AuNRs. However, important factors (the lateral plasmon resonance and its relative height compared with the transverse plasmon resonance) varied markedly between the batches, demonstrating poor reproducibility with the approach used. Potential reasons for this were assessed and equipment needed to rectify it, and to modify the synthesis for AuNSs with various coatings, was going to be purchased. However, whilst this was underway, a fortuitous meeting at an Institute of Physics event with a PhD student from the University of Leeds, who was specialising in AuNP synthesis, led to the potential for outsourcing AuNP synthesis to be revisited. The student in question, Lucien Roach, had recently published an optimisation study regarding a two-surfactant approach to AuNR synthesis that allowed for careful control of AuNR aspect ratio and size[394]. Lucien had the required lab facilities and experience for most of the particles required and was graciously prepared to produce the particles in exchange for the cost of the reagents. It was therefore decided that AuNP synthesis would be left to him and I proceeded to the next step of the project: calibration of the irradiation equipment.

8.2.3 Calibration of the irradiation equipment

It was decided to test the various designs in the same cell line, irradiated at the same time and under as close to the same conditions as possible, to minimise the variability between the various AuNP types being tested. The cells were to be irradiated in an Xstrahl CIX series cell irradiator, so the radiation field in this cabinet was quantitatively measured to understand the systematic and random variations in dose distribution, so that bias could be reduced, and repeatability maximised in the results.

Members of the dosimetry team placed Radiochromic film (Gafchromic EBT3, lot number: 12121702) on the irradiation shelf and its orientation and location were marked using a felt tip pen. The

film was then irradiated (160 kV, 11.3 mA, metal-ceramic target, 0.4 mm beryllium filtration (internal) and 1 mm Al filtration (external)) to deliver a 5 Gy dose to the film, as established by regular QA performed on the machine using an ionisation chamber. The films were left for 24 hours to develop (in the dark and at room temperature) before being digitised using a flattop scanner at a resolution of 150 dpi. This digitised image was then analysed by me using FilmQA Pro 2016 software (Ashland, Covington, KY) to produce a dose map according to the red channel of the scanned image (on the advice of the dosimetry team due to its linear dose response in this dose range). This map was calibrated using a series of irradiated film strips covering the dose range 0 Gy to 10 Gy, obtained by the dosimetry team. The calibrated dose map was then loaded into MATLAB (MathWorks, Natick, MA) and cropped to exclude the felt pen marks used for orientation purposes. The resulting MATLAB matrix was then filtered with a 51x51 pixel median filter, to remove dust, scratches, and grain noise from the image, and normalised based on the reference dose of 5 Gy to give a map of relative dose.

AuNPs and cells were to be irradiated in the wells of five rows of a 96-well plate, so a digital mask was defined in MATLAB that would span an equivalent area (10.7 cm x 7.2 cm). This mask was then used to find the plate location within the irradiator that would be subject to the smallest variation in dose across the plate, and to quantify this variation. This was achieved by considering all possible placements of the mask within the dose map and at each location taking the following steps:

1. The dose map for the area under the mask was extracted and the half-range *Variation* and *MidDose* calculated as defined in Equations 8.9 and 8.10

$$Variation = \frac{(MaxDose - MinDose)}{2} \quad \text{eq. 8.9}$$

$$MidDose = \frac{(MaxDose + MinDose)}{2} \quad \text{eq. 8.10}$$

2. The percentage variation in dose under the plate was then defined as

$$\%Variation = \frac{Variation}{MidDose} \times 100\% \quad \text{eq. 8.11}$$

3. If this *%Variation* was equal to the lowest *%Variation* found so far, the location of this mask was added to a running list of mask locations. If the *%Variation* was lower than the lowest one on record, the previous list was deleted and the coordinates of the mask used to start a new list.

Investigation of the dose maps at the identified locations revealed a directional bias. In order to average out this systemic bias, I proposed rotating the plates by 180° half-way through their irradiation (see Figure 8.2). To simulate the effect that this would have on the dose distribution experienced by the cells, the above optimisation was repeated, but with an additional step added in before Step 1. In this additional step, the dose map from under the mask was copied, rotated 180° and then averaged with the unrotated version. This approach was shown to produce a more uniform dose map, with a narrower variation in dose across the plate (see Table 8.2). The location at which this variation was minimised was etched onto one of the cell irradiator shelves using computer-aided design (CAD) software and a 3D laser cutter so that the cells could be correctly placed during irradiation.

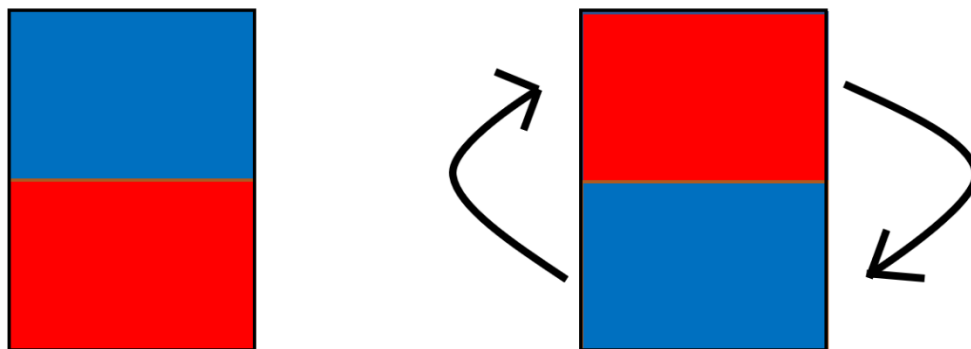


Figure 8.2. (LEFT) The plate is irradiated for 1/2 of the irradiation time in one orientation and then (RIGHT) rotated before being irradiated for the second 1/2 of the time required.

8.2.4 Dose response curve determination

After optimising the plate placement, the next step was to determine a dose response curve for the cells in the absence of any AuNPs. This would allow a subsequent experiment, involving cells and AuNPs at a single dose, to be performed at a dose chosen to maximise the sensitivity of response to any RDEEs, as explained in the next section.

RDEEs have been investigated in many different cancer types in the literature[96], however only a single cell type was used in the work detailed in this chapter, for simplicity. In selecting which cancer type to investigate, I considered factors such as access to tumour site for PASI, use of radiotherapy in the standard of care, the likely proximity of organs at risk and trends in the field towards or number of radiotherapy fractions. Based on these factors (and the development of transrectal PASI probes) I opted to investigate prostate cancer cell lines. Of these, PC-3 was chosen as it was available from a local cell bank (Institute of Cancer Research, London, UK) and was used in multiple RDEE studies in the literature, both *in vitro* and *in vivo*[118][304].

It was desirable that the conditions experienced by the cells and AuNPs used in this experiment were as close to those that would be experienced *in vivo* as possible. For that reason, PC-3 cells were grown into spheroids to give the cells a more clinically realistic 3D interaction. There was little experience in the group with this 3D model of PC-3 beyond the knowledge that it is difficult to grow into spheroids, so a Matrigel[395] based approach was taken, to support the formation of the spheroids, as described below. In addition, due to the large uncertainty associated with the spheroid growth, it was decided that dose response curves should also be obtained with adherent monolayers of PC-3 cells. This would allow confirmatory data to be gathered and experience of the behaviour of this cell line to be gained as a fallback plan should the riskier spheroids prove an issue.

Appendix 3 outlines the procedure followed to produce dose response curves for PC-3 cell lines in monolayer and spheroids. The results from these assays were then used to determine the dose at which RDEEs would produce the largest change in cell viability. The above procedures would normally be repeated at least three times to ensure sufficient statistical confidence in identifying the optimal dose. Due to time restrictions for this work caused by factors beyond my control, there would not have been

time to do this and still complete the primary end point of the study: the assessment of the effect of AuNP properties on RDEE. For that reason, it was decided to treat the work as a preliminary study to investigate the feasibility of the proposed approach for assessing whether factors associated with PASI optimisation contribute to changes in AuNP-mediated RDEEs. Nevertheless, the fact that the dose response curve for these cells was assessed using four different combinations of cell culture (monolayer or spheroid) and viability assay (MTT and CTG-3D), and all four combinations indicated a similar dose at which assay sensitivity was maximised, gives confidence that the identified dose range is indeed one in which changes in RDEE should be most discernible. For that reason, the results were used to set the dose for determining the AuNP-mediated RDEEs.

8.2.5 Determination of AuNP-mediated RDEEs

It was decided to measure RDEE using the metric of dose enhancement effect (*DEE*), defined in Chapter 2 as

$$DEE = \frac{\text{Effect measured at specific dose with AuNP}}{\text{Effect measured at specific dose without AuNP}} \quad \text{eq. 2.5}$$

Experience with the dose response curve experiments had identified two major difficulties with spheroid use: inconsistent spheroid density and evidence of spheroid fragmentation. Evidence of these difficulties can be seen in the results section. Despite several repeats of the spheroid generation process using a range of different seeding numbers and conditions, no solution was found. The decision was therefore made to proceed with measurement of the RDEE produced by the various AuNPs using adherent monolayers of PC-3 cells.

In selecting the AuNP concentration, there were no comparable reference points in the RDEE literature for the shapes and sizes considered here to guide the decision. A study does exist in the AuNP synthesis literature however which considered AuNRs of very similar dimensions to those used here and showed that the toxicity of the AuNRs was greater than for AuNSs[396]. This paper investigated AuNR toxicity down to Au atom concentrations of 8 μM , finding cytotoxicity drops sharply below 16 μM (from ~80% reduction in viability at 31 μM to only ~25% reduction in viability at 16 μM). The AuNRs used in that study were coated with an agent that itself produced slight cytotoxicity, so it is reasonable to expect that the AuNPs used in this chapter will be slightly less toxic. Ideally, the AuNPs used in this work would not be toxic at the concentration used, so that detected changes in cell number between conditions can be related directly to RDEE rather than the presence of toxic AuNPs. To be on the safe side, a nanoparticle concentration of 10 μM of Au atoms (equivalent to 29 pM of AuNPs or 2 $\mu\text{g/ml}$ of Au) was chosen, below this literature indicated toxicity threshold.

In assessing RDEE, it was decided that a viability assay such as that used in determining dose response would not be the most suitable because viability assays would not distinguish between cytotoxic and cytostatic effects. Due to the potential of AuNPs to cause cell cycle arrest by themselves (noted in Chapter 2), the ratio of these two effects could thus vary with AuNP presence and AuNP type. For that reason, it was decided that cell death and living cell number should be counted, using a suitable

dye and cell counting software. The approach chosen employed the fluorescent dyes acridine orange (AO) and propidium iodide (PI). AO/PI analysis works by taking advantage of how AO and PI stain cells: AO is membrane permeable and so can enter both live and dead cells whilst PI is membrane impermeable and so can only enter cells which are dead. Once inside a cell, both dyes bind to nuclear DNA, producing fluorescence (~526 nm for AO, ~617 nm for PI). Crucially, binding shifts the stimulation wavelength of PI to overlap with the emission wavelength of AO. As a result, where both AO and PI bind to the same nucleus, the AO signal is quenched by the PI in a process known as Förster resonance energy transfer (FRET). Given a sufficient level of PI in the cells, the result is that live cells are marked with AO fluorescence only whilst dead cells are marked with PI fluorescence only. If PI concentrations are too low however, AO signal is not fully quenched and so AO fluorescence will mark both dead and live cells.

Based on this, the RDEE was measured according to the procedure laid out in Appendix 4. The layout of the resulting plate is reproduced here for ease of reference as it is relevant to the discussion section.

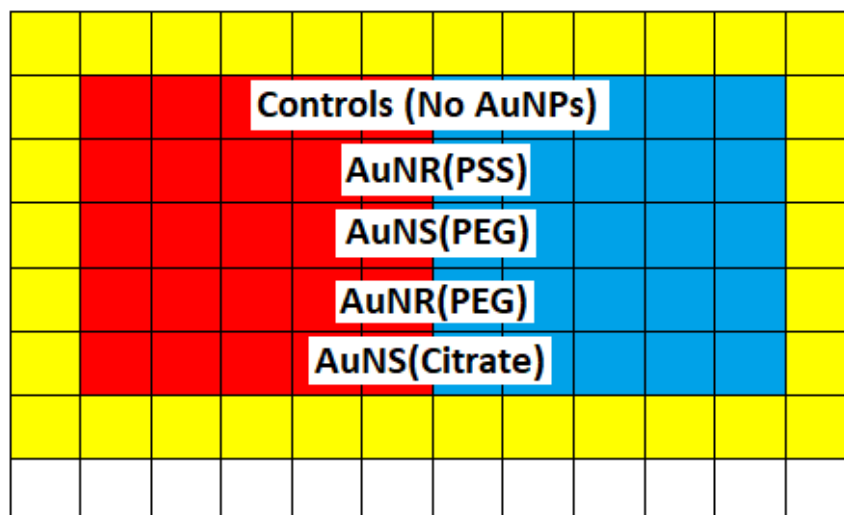


Figure 8.3. Schematic of a 96-well plate showing the division of AuNP conditions and AO/PI mixtures. Wells marked in red or blue were plated with two thousand PC-3 cells to form monolayers. Wells marked in yellow contained 200 μ l of PBS. AuNPs of the types listed were added to each well as described in the text. Mixture A was added to the red well whilst mixture B was added to the blue wells (see Appendix 4 for the composition of the mixtures).

8.3 Results

The results from the various stages of the above work are shown below. Major conclusions from the data are left to the discussion section, with this section discussing only what the data shows at a superficial level.

8.3.1 AuNP synthesis and selection

Figure 8.4 shows the optical absorption spectra, obtained using a spectrophotometer in the range 400 - 900 nm, for samples from my two AuNR syntheses. The samples were not diluted to the same AuNP concentration, instead being normalised at 400 nm, which is the wavelength used to calculate the number of Au atoms in the sample recommended in the literature due to the dominance of

intraband transitions over other effects at this wavelength[397]. In both cases the plotted spectra are shown after ‘blank’ subtraction using a double distilled H₂O filled ‘blank’ cuvette.

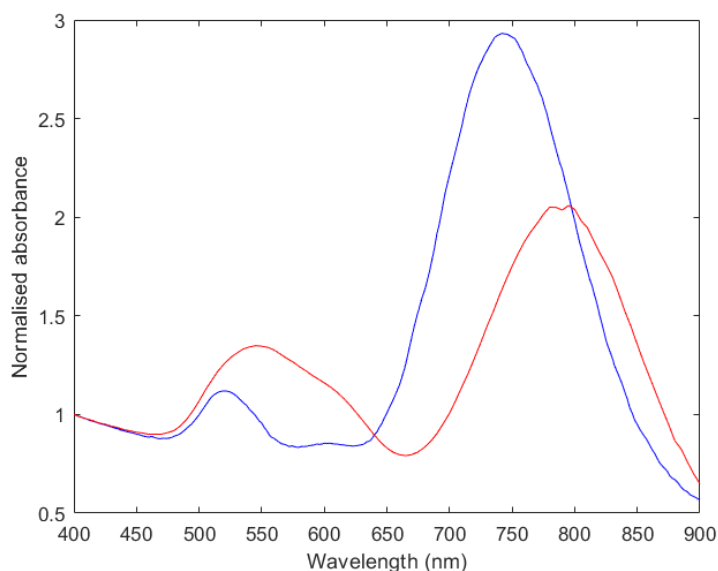


Figure 8.4. Optical absorption spectra for AuNRs produced from the first (blue) and second (red) syntheses. Absorption spectra have been normalised at 400 nm as this wavelength should represent intraband transitions and not plasmon resonances, and so can be used to determine the quantity of Au atoms present.

Table 8.1 summarises the data from characterisation of the various AuNPs provided by my collaborators at Liverpool University. AuNP shape was assessed using Transmission electron microscopy (TEM), zeta potential was measured using a zeta analyser and the UV-Vis peaks were based on optical spectra obtained at 1 nm intervals in the range 400 - 1000 nm. The equivalent spherical diameters were measured directly for AuNSs using TEM and calculated for the AuNRs based on TEM measurements of the AuNRs and Equations 8.4 and 8.5.

Table 8.1. Summary of the physical parameters of the AuNPs provided by collaborators at Liverpool University. Particle sizes were assumed to be normally distributed and the uncertainties shown represent σ for that distribution. Zeta potentials were measured in triplicate and the standard error in the mean presented in the table. UV-Vis data was not obtained for the largest AuNS batch as it was not deemed necessary given that the large uncertainty in size made this batch unsuitable for this project anyway.

Particle Type	Coating	Batch number	Equivalent spherical diameter (nm)	Zeta potential (mV)	UV-Vis peaks (nm)
AuNS	Citrate	1	35.6 ± 7.4	-12.2 ± 1.4	519
AuNR	PSS	1	32.5 ± 5.1	-36.0 ± 2.0	509, 812
AuNR	CarboxyPEG	1	44.0 ± 8.6	-18.5 ± 0.4	510, 857
AuNR	CarboxyPEG	2	34.9 ± 4.3	-24.1 ± 0.5	511, 776
AuNS	CarboxyPEG	1	35.6 ± 5.4	-22.3 ± 0.4	535
AuNS	CarboxyPEG	2	42.1 ± 12.3	-23.1 ± 1.0	Not assessed

8.3.2 Calibration of the irradiation equipment

The dosimetry measurement procedure described in the ‘Materials and methods’ section led to the map of relative radiation dose as a function of location within the cell irradiator shown in Figure 8.5. The dimensions are labelled in terms of pixels, with each pixel being equal to 0.17 mm. The sharp drop to zero dose that forms a straight border at the edge of the figure is deliberate: digitised data were set to zero to exclude artefacts that were due to the scanner bed being larger than the film or to the median filtering. The irregular-shaped artefact in the top right-hand corner is part of the pen mark used for film orientation.

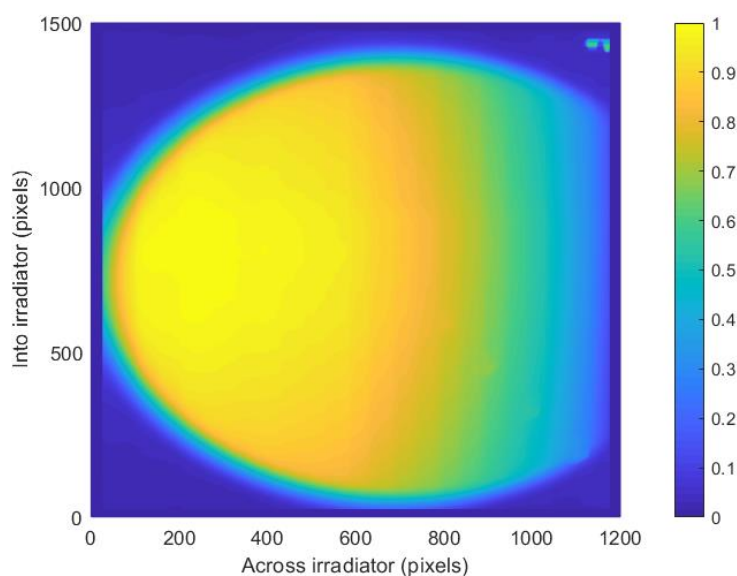


Figure 8.5. Map of relative dose within the cell irradiator, recorded by digitising the dosimetry film and applying a median filter to remove grain noise but preserve the dose gradient. The reported values are normalised to the reference dose delivered (5 Gy).

The search algorithm described in the ‘Materials and methods’ section was then run to identify all regions where the dose delivered to the wells of a cell culture plate would deviate from the *MidDose* to the plate by no more than 5%. As described, for each possible mask position, the case of a static cell culture plate and one rotated half-way through the irradiation was considered, and the location marked accordingly. The area identified where plates would experience an acceptable dose variation is shown in Figure 8.6.

Dose maps for the location corresponding to the lowest dose variation were produced for cases where the cell culture plate was static and rotated mid-irradiation. As it was noted that the dose dropped most sharply at the edge of this region, the effect of excluding the outer wells from the irradiation was also considered. These maps can be seen in Figure 8.7, Figure 8.8 and Figure 8.9 respectively. The maximum deviations from the *MidDose* found for each of these maps is summarised in Table 8.2.

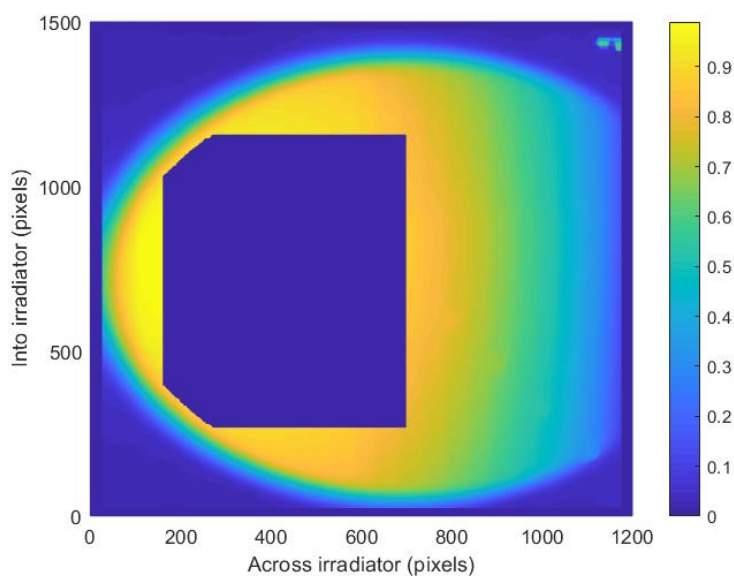


Figure 8.6. Shows the same normalised map of relative dose from Figure 8.5, however with a region of pixels removed (set to 0) in the middle of the high dose region (the blue rectangular shape within the yellow oval).

This region represents the area in which a 96-well cell culture plate can be placed so that the maximum variation in dose across the plate is less than 5% from the MidDose. Note that due to the removal of the highest dose regions in this process, the colour scaling of dose has been shifted slightly compared to Figure 8.5. This map was not used in further calculations but is a useful visual aid for checking the tolerance to plate placement.

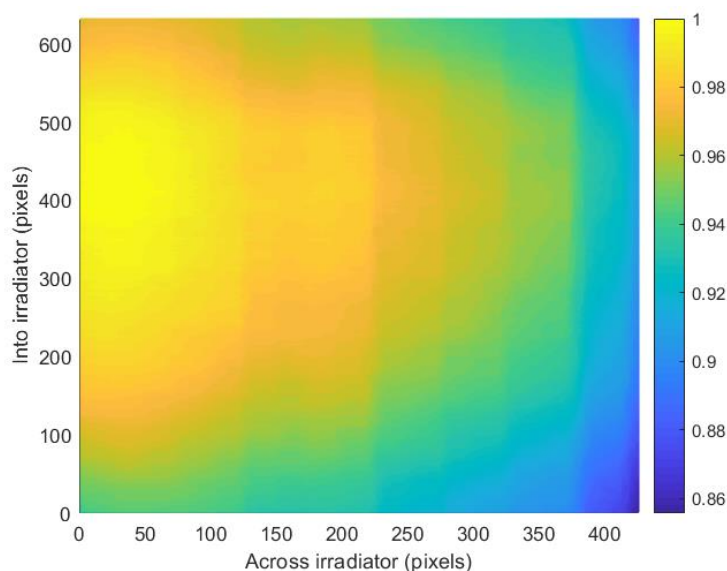


Figure 8.7. Enlarged subsection of Figure 8.5 showing only the cell-culture-plate-sized area identified as having the lowest variation in dose. This map represents the doses that would be produced across the plate if it were left in a single orientation for the full irradiation time.

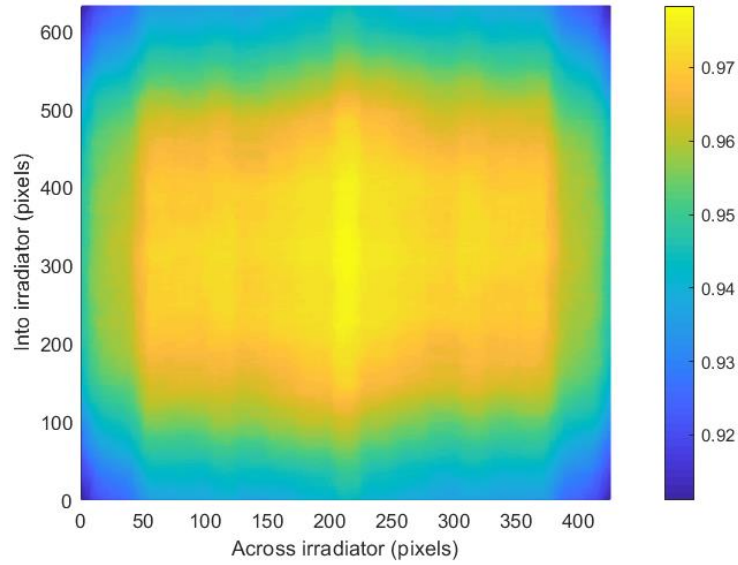


Figure 8.8. Enlarged subsection of Figure 8.5 showing only the cell-culture-plate-sized area identified as having the lowest variation in dose. This map represents the doses that would be produced across the plate if it were rotated by 180° halfway through its irradiation. Repeats of each experimental condition will run in the direction labelled “Into irradiator”, and the different experimental conditions will run in the direction labelled as “Across irradiator”.

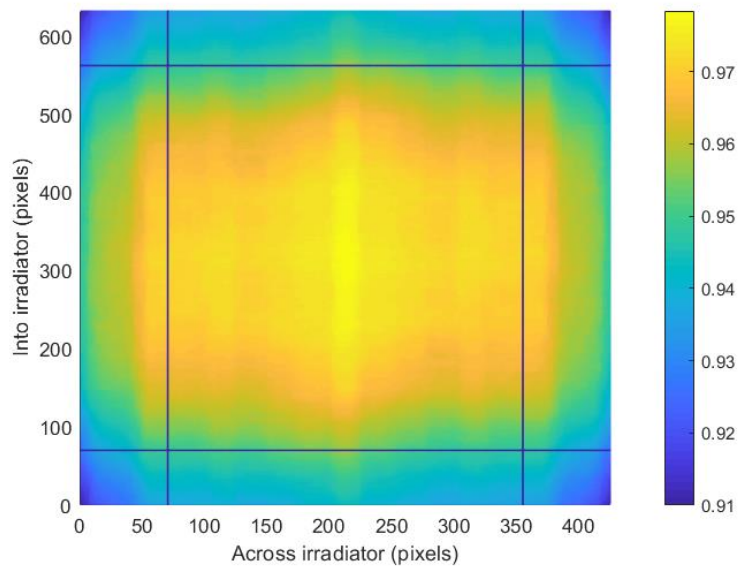


Figure 8.9. Reproduction of Figure 8.8 with lines added to separate the area in which the experimental cells would sit (central region) from those that will be filled with PBS (outer regions). As a result of this arrangement, the dose distribution across experimental conditions will be reduced.

Table 8.2. The variation in dose experienced across the plate is listed for the various configurations considered in Figure 8.7, Figure 8.8 and Figure 8.9. The values reported are the maximum deviations from the MidDose for the plate, as defined in Equation 8.10.

Object	Variation (%)
96-well ULA plate (unflipped)	5.8
96-well ULA plate (flipped)	3.6
96-well ULA plate (flipped, edge wells excluded)	2.0

8.3.3 Dose response curve determination

Figure 8.10 and Figure 8.11 show the dose response curves obtained using Cell Titre Glo 3D (CTG-3D)[398] for PC-3 cells when cultured as a monolayer or as spheroids respectively. Figure 8.12 and Figure 8.13 show the dose response curves obtained using MTT for PC-3 cells when cultured as a monolayer or as spheroids respectively. In all cases the luminescence recorded was after blank subtraction and normalised to the maximum recorded signal across all doses. The blank used was averaged over 3 repeats, each containing the same volume of cell culture medium and either CTG-3D or MTT/DMSO mixture as the wells in the experimental conditions. Error bars represent two standard deviations from the mean over 10 repeats for the monolayer, and 5+ repeats for the spheroid results. Dose response curves were fitted according to Equation 2.7 (reproduced below) using the non-linear method fitting tool in MATLAB 2019a.

$$SF = e^{-\alpha D - \beta D^2} \quad \text{eq. 2.7}$$

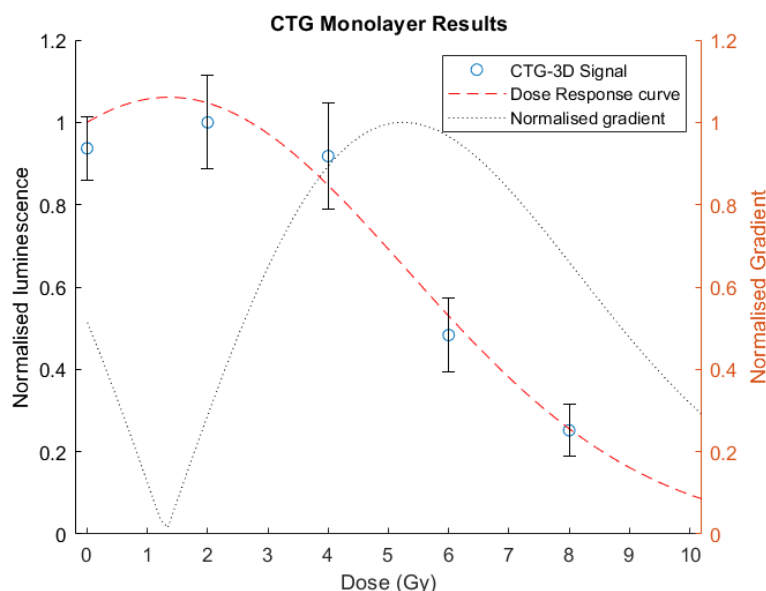


Figure 8.10. Cell viability as measured by the luminescence produced by a monolayer of PC-3 cells irradiated at different doses when assayed with Cell Titre Glo-3D. Experimental data (signal) are plotted as blue circles with error bars representing 2σ derived from a sample size of $n=10$ wells. The dose response curve extrapolated from these points is plotted as a red dashed line. These data sets are plotted against left axis. The absolute gradient for this curve, normalised to its peak, is plotted as a black dotted line, against the right axis.

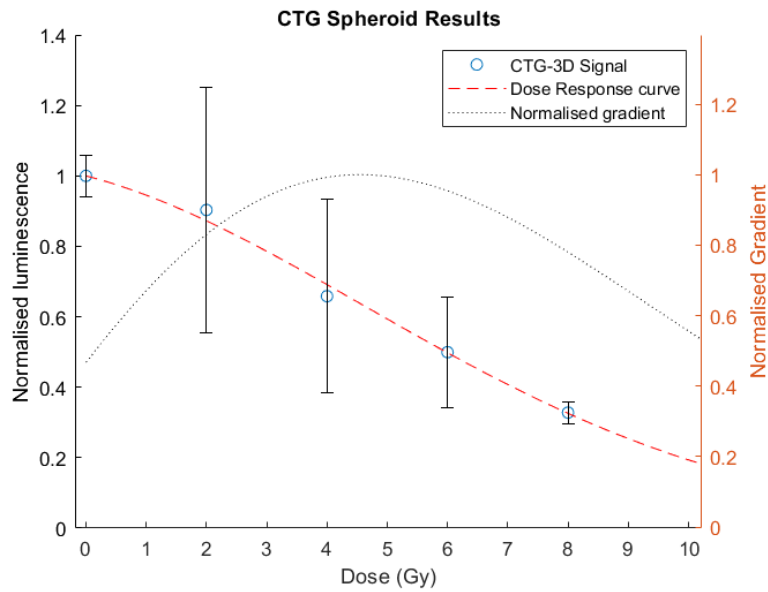


Figure 8.11. Cell viability as measured by the luminescence produced by PC-3 spheroids irradiated at different doses when assayed with Cell Titre Glo-3D. Experimental data (signal) are plotted as blue circles with error bars representing 2σ derived from sample sizes ranging from $n = 5 - 10$ spheroids, depending on dose. The dose response curve extrapolated from these points is plotted as a red dashed line. These data sets are plotted against the left axis. The absolute gradient for this curve, normalised to its peak, is plotted as a black dotted line, against the right axis.

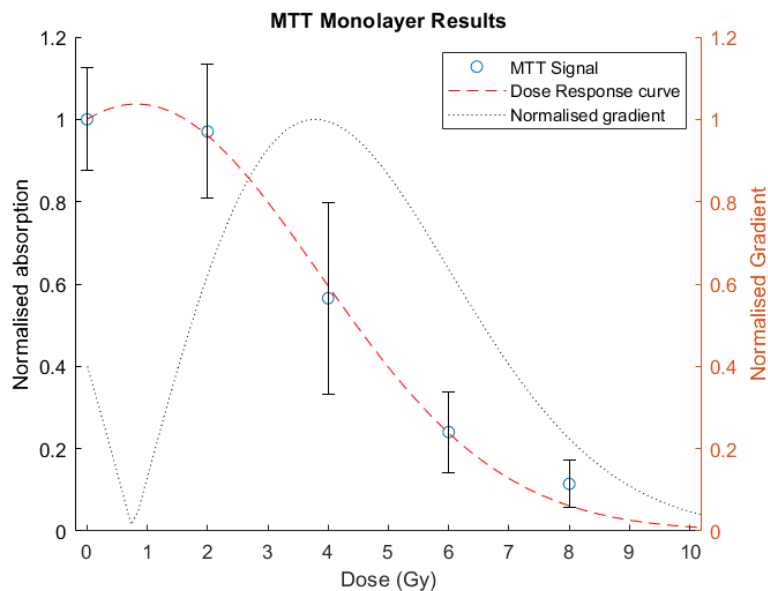


Figure 8.12. Cell viability as measured by the absorption produced by a monolayer of cells irradiated at different doses when assayed with MTT. Experimental data (signal) are plotted as blue circles with error bars representing 2σ as derived from a sample size of $n=10$ wells. The dose response curve extrapolated from these points is plotted as a red dashed line. These data sets are plotted against the left axis. The absolute value of gradient for this curve, normalised to the peak, is plotted as a black dotted line, against the right axis.

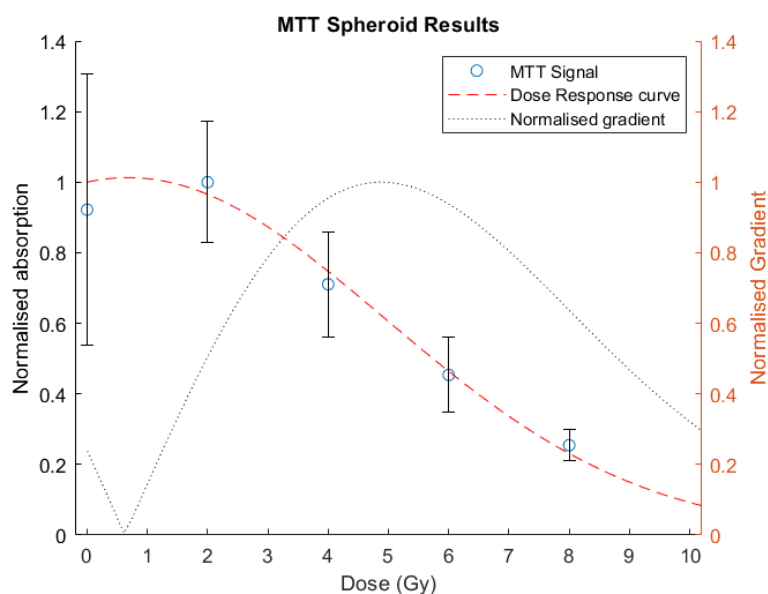


Figure 8.13. Cell viability as measured by the absorption produced by PC-3 spheroids irradiated at different doses when assayed with MTT. Experimental data (signal) are plotted as blue circles with error bars representing 2σ as derived from samples sizes ranging from $n = 7 - 9$ spheroids, depending on dose. The dose response curve extrapolated from these points is plotted as a red dashed line. These data sets are plotted against the left axis. The absolute value of gradient for this curve, normalised to the peak, is plotted as a black dotted line, against the right axis.

The absolute gradient of these fits was then assessed, normalised to peak values, and plotted. The dose with greatest gradient is the one at which a fixed change in dose will produce the largest change in metric response. The doses with the steepest absolute gradient from the above figures are compiled in Table 8.3. From these data, it was decided that *DEE* would be measured at a dose of 5 Gy.

Table 8.3. Summary of the doses corresponding to the steepest gradient in the fitted dose response curves for the various metrics assessed.

Metric	Optimal Dose (Gy)
Cell Titre Glo-3D Monolayer	5.2
Cell Titre Glo-3D Spheroids	4.5
MTT Monolayer	3.8
MTT Spheroids	4.9

8.3.4 Determination of AuNP-mediated DEEs

The lower concentration of PI used in mixture A (see Figure 8.3) was too low for effective quenching of the AO signal in dead cells, meaning that AO counts would not exclusively represent live cells. This caused complications in the counting as it meant that live cells could not be readily differentiated from dead cells under these conditions. The higher concentration of PI used in mixture B was sufficient to cause quenching in dead cells and so produced a more reliable live cell indication. For

this reason, analysis of the data was confined to the 5 wells with mixture B. All measurements were averaged over these 5 wells for each condition and time point.

The results of the live cell counts using AO/PI staining and the image analysis software in a Celigo Image Cytometer[399] are shown in Table 8.4. Proliferation for a given dose, D , was defined as

$$\text{Proliferation at } D \text{ Gy} = \frac{\text{live cell count on day 5}}{\text{live cell count on day 1}} \quad \text{eq. 8.12}$$

Equation 2.5 defines DEE relative to a measured effect, and in this case the measured effect was the inhibition of cell proliferation produced by 5 Gy of radiation. For each condition, Con , the inhibitory effect was defined as

$$\text{Inhibition under condition } Con = 100\% \left(1 - \frac{\text{Proliferation at 5 Gy}}{\text{Proliferation at 0 Gy}} \right) \quad \text{eq. 8.13}$$

The DEE for each condition could then be calculated by combining Equations 2.5 and 8.13 to give

$$\text{DEE for condition } Con = \frac{\text{Inhibition under condition } Con}{\text{Inhibition under control conditions}} \quad \text{eq. 8.14}$$

Table 8.4. Summary of the changes in proliferation associated with 5 Gy irradiation for the various experimental conditions. The DEE was calculated for each condition. Standard errors in the mean (SEM) were calculated for the raw data at each time point and added in quadrature to determine the associated uncertainties in proliferation (presented here in bracket notation, where the figure in brackets represents the uncertainty in the final reported digit). Uncertainties in inhibition and DEE were calculated by adding, in quadrature, the uncertainties in proliferation for the different doses. No uncertainty is associated with the DEE value for the control group as it is 1.00 by definition.

Condition	0 Gy Proliferation	5 Gy Proliferation	Inhibition (%)	DEE	p-value of difference from Control
Control	1.41(7)	0.75(4)	47(3)	1.00	N/A
PSS coated AuNRs	1.04(3)	0.50(2)	52(3)	1.11(5)	0.03
Carboxy-PEG coated AuNRs	1.07(4)	0.46(2)	57(3)	1.22(7)	< 0.01
Carboxy-PEG coated AuNSs	1.20(5)	0.65(3)	46(3)	0.98(6)	0.47
Citrate coated AuNSs	0.49(2)	0.23(1)	52(3)	1.10(7)	< 0.10

8.4 Discussion

8.4.1 AuNP synthesis and selection

Attempts to produce AuNRs were successful, as can be seen from the optical absorption spectra for the synthesis products shown in Figure 8.4. AuNSs have spherical symmetry and so resonances exist at the same frequency along all potential axes. AuNRs in contrast break this spherical symmetry in one direction (along their long axis) and so exhibit resonance at two frequencies: one across the width of the particle (transverse) and another, at a lower frequency, along the long axis of the AuNR (longitudinal). As frequency is inversely proportional to wavelength, a lower frequency oscillation will correspond to a longer wavelength absorbed. AuNSs exhibit resonance at ~520 nm (depending on their size) whilst AuNRs would thus have two resonances: one at ~520 nm and one at a longer wavelength. These properties are shown in Figure 8.4. It should be noted that this synthesis method requires the initial formation of AuNSs which are then selectively extended from two crystal faces. For this reason, it is possible that some AuNSs remain at the end of the synthesis, however the ratio of AuNSs to AuNRs was not measured in this work. Comparing the absorption spectra between syntheses, it is clear that though both produced AuNRs, the second synthesis yielded a relatively larger proportion of non-AuNR shapes, as suggested by the larger, broader peak at the lower wavelengths. It is not possible to tell from optical analysis alone what shape these were, though the wavelength of ~600 nm is unlikely to correspond to AuNSs. These additional shapes could result from impurities in the reagents used[400], contamination of the reaction mixture (perhaps caused by insufficient cleaning of the glassware) or incorrect concentrations of capping agents or reducing agents. The major capping agent used in this case, hexadecyl(trimethyl)ammonium bromide (CTAB), was used in excess and so its concentration is unlikely to be relevant. The facet specific capping agent AgNO_3 was used at low concentration, however as it is only relevant to the early stages of AuNR growth it is unlikely to have a significant role in AuNP shape selection beyond facilitating CTAB mediated AuNR elongation. Regardless of their origin, the dominant AuNP species still appears to be AuNRs, though produced with a lower shape selectivity than in the first synthesis.

Additionally, Figure 8.4 indicates that the AuNRs produced in the second synthesis are of a higher aspect ratio, as indicated by the red shift in their longitudinal plasmon resonance compared with those from the first synthesis (~800 nm vs ~750 nm). Two potential sources of this variation can be proposed that are consistent with this data. First, it is noted that a lower concentration of reducing agent (ascorbic acid) in the second step of the synthesis could result in a slower nucleation process, amplifying the shaping effects of the CTAB and AgNO_3 . Secondly, a higher concentration of AgNO_3 could produce this effect, as it would result in a more rapid capping of the favoured crystal facets, producing narrower AuNRs[401]. These mechanisms are not mutually exclusive either, so both may be in operation. Due to the time constraints for the AuNP synthesis in general, the cost (in time and money) associated with tracking down the variable responsible for the discrepancies in AuNR properties, and the already identified need to update equipment before attempting synthesis of other AuNP shapes (of which our

group had no prior experience) it was decided that the best approach would be to outsource the synthesis of the AuNPs to collaborators at Liverpool University, as noted in the ‘Materials and methods’ section.

Table 8.1 shows the properties of the particles supplied to us for this work. Particle sizes (radii and lengths) were determined by TEM analysis for at least 200 AuNSs/AuNRs in each batch by our collaborators, along with equivalent AuNS radii. I then used these data to calculate the standard deviations.

All AuNPs provided had a significant negative potential and so surface charge would not be expected to directly affect uptake route or protein corona formation, allowing all coating types provided to be considered for inclusion in the cell work. Indeed, it was decided to use carboxy-PEG rather than another PEG formulation specifically so that a negative charge could be induced in these particles to match that of the citrate capped AuNSs. As I was aiming to match the volumes of the AuNPs as much as possible between the different AuNP types, I decided to use the second batch of carboxy-PEG AuNRs and the first batch of carboxy-PEG AuNSs along with the citrate AuNSs and PSS coated AuNRs as these were all of comparable volume (equivalent AuNS diameter ~35 nm).

8.4.2 Calibration of the irradiation equipment

Whilst the oval shape of the radiation field within the cell irradiator shown in Figure 8.5 was expected based on the source geometry, a clear gradient in the radiation field is also evident which was not. This gradient shows the radiation dose decreasing from the left to the right of the unit. The drop in radiation dose across the unit is not insignificant, with the right most edge of the indicated irradiation area (as indicated on the manufacturer provided placement plates) receiving a dose ~80% lower than the left most edge. Enquiries revealed that the machine had been modified for other purposes and the gradient in radiation field introduced as an unintended consequence, however the plates used to guide placement of samples to a uniform region of the field had not been updated. It was therefore required that new plates be manufactured to ensure reproducibility in sample radiation dose and to minimise variation in dose across the 96-well plate in each irradiation.

This was achieved by calculating the range of doses that would be deposited across an area the size of a cell culture plate for all possible placements of the plate within the field. For reasons of computational efficiency, only one orientation of the plate was considered in this work: that in which the long axis of the plate was aligned perpendicular to the gradient in the radiation field. This approach used the *a priori* knowledge of the field shape to minimise dose variation and reduce simulation time. As this work would be beneficial to other users of this equipment, two different approaches to plate placement were considered.

Discussions with biologists in the group revealed a preference for simpler placement procedures and a tolerance for a maximum variation in dose across the plate of $\pm 5\%$. This was deemed suitable for experiments in which the effect of radiation was being compared with that of unirradiated controls as the biological variability in many of their experiments is of this order and they were happy with anything that reduced the variability in radiation dose to a comparable level, as the measurements across wells

would all be aggregated for analysis anyway. A map of places where the plate could be placed whilst still complying with this restriction (the dark blue regions cut out of the oval shaped radiation field) can be seen in Figure 8.6. These locations all required the plate to be rotated, for reasons discussed shortly.

The second approach pursued was to find the single location with the lowest variation in dose and mark it to allow consistent repeatability and more accurate dose quantification. This approach would be more useful for work in which radiosensitisation or radiation dose enhancements were being studied, as otherwise variations in applied dose between conditions could interfere with results. Figure 8.7 shows the relative dose distribution found for this optimal placement. As expected from the known gradient in the radiation field there is a marked increase in radiation dose moving from the right to the left of the plate. The effect of this on experimental results would be to introduce a systematic bias between conditions if they were varied in this direction. The effect of this on comparisons between experimental conditions could be mitigated slightly if experimental conditions were varied in the “Into irradiator” direction and repeats of each condition run in the “Across irradiator” direction, though they would not be removed completely and this approach would limit the number of repeats that could be performed for each condition significantly, from 10 to 6. Further, as *DEE* is a function of dose, variations in dose between repeats of a single condition that this approach would produce would prevent absolute *DEE* values being calculated, though the relative order of the various conditions could still be determined.

To reduce the systematic bias caused by this left-right asymmetry, it was decided that the plates could be rotated half-way through the irradiation, as explained in the ‘Materials and methods’ section. This resulted in a much smaller spatial variation in dose, as seen in Figure 8.8. Comparing this with the previous setup, it can be seen from Table 8.2 that the variation in dose across the plate can be reduced by almost 40%: from 5.8 to 3.6. Further, the directional bias in the left-right direction has been significantly reduced, replaced instead with a central region of high dose uniformity (yellow region, 0.96 - 0.98 of set dose) and a peripheral region of greater dose variability (blue and green edges).

Any further improvements in dose uniformity would require the use of only a subsection of the plate. This was achieved by employing the standard practice, within our tissue culture labs, of excluding the outermost wells on a given plate from experiments due to the increased evaporation rates associated with these wells. When the dose variation was only calculated for the wells used in the experiment (the central rectangle in Figure 8.9) the variation was reduced still further: from 3.6 down to 2.0. Due to the exceptionally low variation in dose that this arrangement produces it was decided that this placement and rotation procedure would be used for all further cell work in this project. CAD files for new shelves for the cell irradiator with markings to ensure correct placement of the cell culture plates were produced and 3D printed with the help of the workshop at the Institute of Cancer Research. These shelves were then included into the standard monthly cell irradiator QA procedure so that the dose rates and corresponding irradiation times could be calculated for a range of commonly used radiation doses.

8.4.3 Dose response curve determination

Cell viability, as measured with CTG-3D assay, at doses ranging from 0 - 8 Gy is shown for PC-3 cells grown as monolayers and spheroids in Figure 8.10 and Figure 8.11 respectively. Figure 8.12 and Figure 8.13 show the results from the same setups (monolayer and spheroid respectively) when MTT was used as the viability assay in place of CTG-3D. Dose response curves based on the experimentally measured data are shown in each case (red dashed line) and show good agreement with the measured data. It is worth briefly noting that the drop in response seen at low doses in these figures is the result of the α value being assigned a slightly negative value in the fits. Whilst there is debate as to whether the linear quadratic model is mechanistic, and whether a negative value of either α or β is biologically realistic, it is nonetheless advised in the literature to not force a non-negativity constraint on these variables during radiobiological analyses[402], and so this is the approach that I have taken here.

The purpose of these experiments was to find the point at which a small, fixed, change in radiation dose would yield the largest change in cellular response, for ease of detection. This condition corresponds to the maximum in the absolute value of the gradient of the dose response curve for these plots (the greatest change in y for a given change in x , regardless of the direction of that change). For this reason, the normalised gradients of the response function were calculated numerically for each experiment and plotted on the figures (black dotted lines). The doses corresponding to the peak in this gradient are compiled in Table 8.3. Before going into implications of these plots for the cell work that measured the *DEE*, it is worth reflecting on some lessons from the lab work done so far.

As noted in the ‘Materials and methods’ section, it was the experience of biologists within our group previously that PC-3 cells produce poor spheroids under normal conditions. It was suggested however that the use of an extracellular matrix material such as Matrigel could alleviate these problems, as it does in some other cell lines. The use of spheroids would be preferable to monolayers as it would better represent the 3D nature of human tissues and allow for factors associated with AuNP penetration into tissue to be included into the analysis. Unfortunately, it was my experience during this work that spheroids produced using PC-3 cells in Matrigel were highly variable in their quality, as can be seen in Figure 8.14, which shows three spheroids imaged on the same day in the same scan from the same plate. Whilst some spheroids formed dense spherical masses that remained dense as they proliferated (left), others formed only loosely assembled amorphous masses with low density (right). Other spheroids existed somewhere on this spectrum, possibly with dense cores and asymmetric, loose outer growths (middle). The variations in density that this produced resulted in variable depths of the spheroids within their wells which made imaging and feeding them difficult.

When imaging, the automated imaging software built into the cell imager could not be used as it tolerates only small changes in focal depth between wells. This meant that images had to be manually focussed, greatly increasing the time required on this busy piece of equipment.

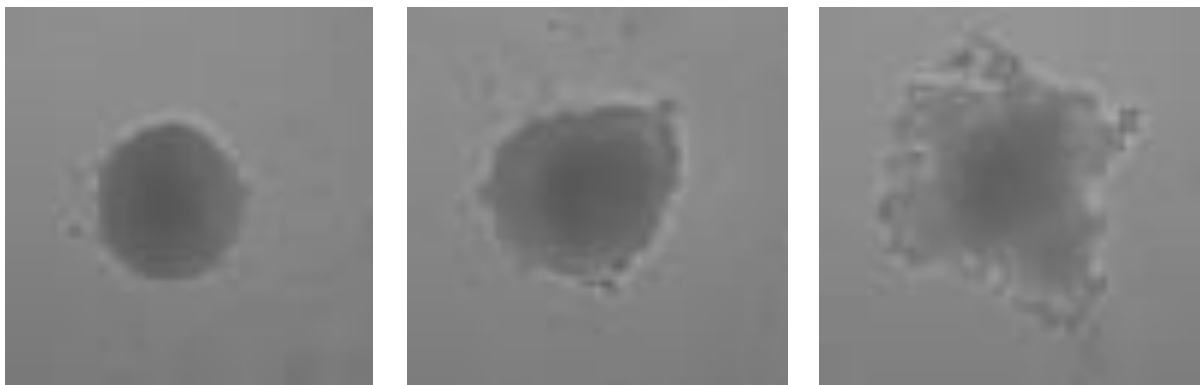


Figure 8.14. A selection of optical light transmission microscope images obtained using the Celigo. Images show spheroids 72 hours after seeding. Despite the use of Matrigel, the spheroids showed varying degrees of compactness and uniformity, from well-defined dense spheroids (LEFT) to a poorly defined loose agglomeration of cells (RIGHT).

Even when feeding spheroids one well at a time (rather than one column at a time as would normally be done) it was not uncommon for spheroids to be accidentally removed with the excess cell medium due to the large variations in their density and higher than expected consequent mobility. Investigations with light microscopes (Figure 8.15) revealed that when replacing spheroids accidentally removed from the tray during feeding their structure could be significantly disrupted, though the disruption was also highly variable, with some spheroids remaining intact after accidental collection and redispersal (top left) whilst others fractured (top right and bottom left) or lost their shape entirely (bottom right). Whilst such disruption could also have occurred during the transfer of spheroids to or from irradiation (they were not imaged after irradiation) this would have had less effect on viability assay results, as in the case of transfer all cell medium was transferred, meaning that there was not an opportunity for some fragments to be removed and others left behind. Feeding, in contrast, involved the removal of only a fraction of the cell medium and consequently the possibility that cells may be accidentally removed from the mixture. To prevent this from affecting the results, when spheroids were accidentally removed from the well during feeding the entire contents of the feeding pipette were deposited back into the well and the well investigated under the light microscope. Where there was any sign of spheroid fragmentation, that spheroid was discounted from further analysis. Where the spheroid was seen to be intact and no loose cells were noted, the feeding was attempted again. Unfortunately, a non-trivial number of spheroids were disqualified by this criterion, reducing the number of repeats for each dose from the planned 10 to as few as 5 in some conditions. This likely contributed to the relatively larger uncertainties associated with the spheroids compared with their monolayer counterparts.

Comparing the dose response curves obtained from spheroids with those obtained from monolayers it can also be seen that the gradient varies more gradually for spheroids than for monolayers. This could result from the cells being linked into a larger structure and so increasing cellular communication, such as bystander effects, which should smooth out the response to radiation when compared with monolayers in which cells respond more in isolation. It could also result from additional shielding for cells lower in the well associated with having an overlying layer of cells to pass through, as well as a thicker matrix material when compared with cellular monolayers. As we are looking to maximise the gradient of the cell's response so as to optimise the dose for *DEE* detection, the steeper

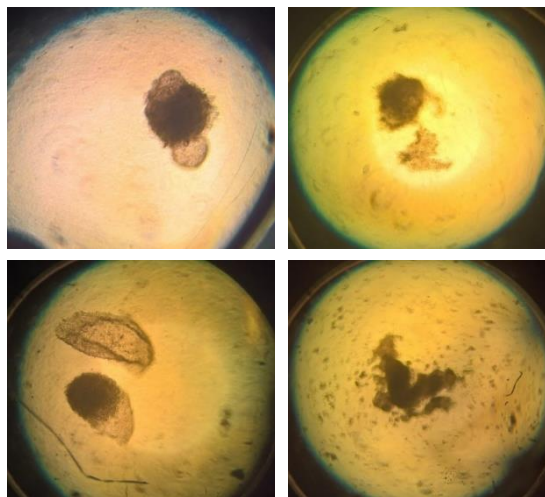


Figure 8.15. Images of spheroids taken down a benchtop optical microscope using a handheld camera. (TOP LEFT) Example of spheroid with loose attachments that could be disrupted during feeding. (REMAINING IMAGES) Examples of spheroids that had become disrupted by accidental transport during feeding.

gradient means that monolayers would have an advantage in this context. As a result of this, and in light of the difficulties noted for PC-3 spheroid work, it was decided that the main *DEE* investigation should use monolayers. The data obtained from the spheroid work was not discounted however, as due to restraints on time and resources it was not possible to repeat the monolayer work a further two times to verify their findings. Instead, the data for spheroids and monolayers with both CTG-3D and MTT were all used as independent estimators of the optimal doses for measuring *DEE*. The average value obtained from these investigations was that 4.6 Gy should produce the greatest sensitivity to DEEs, though this was rounded to 5 Gy for the *DEE* investigation that followed due to this being the nearest dose for which cell irradiator dosimetry was available.

8.4.4 Declaration

As previously noted, due to reasons beyond my control, my access to the lab was severely restricted towards the end of my PhD. As a result, I was unable to perform repeats of the experiments discussed in the next section. Whilst the statistics are sufficiently strong to detect the relatively large DEEs for many of the AuNP types considered, the low number of repeats means that the analysis may lack sufficient statistical power to conclusively establish more subtle effects, such as comparisons between AuNP types. It is standard that a p-value of 0.05 or 0.10 is used as a threshold for “statistical significance”. In order to facilitate as complete a discussion as possible given the low number of repeats, I will also consider results with a p-value < 0.15 (less than a 15% chance the results are coincidental) as possibly significant. Both significant and possibly significant results will be put into the context of the literature and compared with what would be expected based on known RDEE mechanisms. Repeats of the experiment will be necessary to build statistical confidence in the results found, and thus the conclusions of the following section should be taken as tentative at this time.

8.4.5 Determination of AuNP-mediated DEEs

Table 8.4 shows how the various AuNPs affected the proliferation of the PC-3 cells under investigation over the first five days post irradiation. This timeframe was chosen based on observations from the dose response curve studies which showed that without AuNPs, which would be expected to be the fastest proliferating condition, PC-3 monolayers seeded at two thousand cells per well reached 100% confluence after no less than 7 days. As proliferation can slow as the cells approach 100% confluence the timeframe would thus have to be sub 7 days, whilst still allowing enough time for differences in proliferation rate to manifest clearly.

The proliferation in a given condition at 0 Gy can be compared to the control group's proliferation at 0 Gy to get an indication of any toxicity. Comparing the PEG coated AuNPs reveals that the difference in toxicity between AuNRs and AuNSs does not appear to be statistically significant, all else being equal ($p = 0.245$). This is in contradiction to indications in the literature that suggest that AuNRs have a markedly higher toxicity than AuNSs[396]. Whilst it is possible that the low number of repeats means this experiment lacked statistical power to detect this effect, this seems unlikely given the size of the effect reported by others. Another explanation concerns residual traces of CTAB reagent in AuNR synthesis. CTAB is highly toxic[403] and its incomplete removal is widely suspected to be associated with some of the toxicity traditionally assigned to AuNRs. Where it has been concluded in the literature that AuNRs have a higher toxicity than AuNSs, an excess of CTAB was used during the synthesis and only a single washing step was involved prior to recapping and the use of the AuNRs[396]. In contrast, the work presented here involved a triple washing of the CTAB from the AuNRs before capping with PEG and diluting for use, and so residual CTAB is considerably less likely in the mixture. The lack of a significant difference between toxicity in PSS and PEG coated AuNPs ($p = 0.449$) further supports this assertion as PSS was specifically selected due to its ability to detoxify CTAB coated AuNRs[393]. Further, the careful matching of AuNP volumes in the current work have allowed the effect of AuNP shape alone to be isolated, an approach not taken in similar studies which matched total gold concentration or particle number but using shapes of different masses. The results of this chapter thus support the claim that AuNRs are in fact not intrinsically more toxic than AuNSs, as is currently believed.

Similar observations can be made regarding the effect of AuNP coating on toxicity. Comparing the PEGylated and citrate coated AuNS reveals that PEGylation produced a lower toxicity than citrate capping ($p = 0.01$), which is unsurprising given both the known toxicity of citrate coated AuNPs[404] and the widespread use of PEG to reduce AuNP associated uptake and subsequent cytotoxicity[405]. The easy displaceability of citrate compared with PEG also allows for the formation of a smaller, more tightly associated protein corona when citrate capped AuNSs are incubated with cell culture medium, further improving cellular uptake of this particle type. As AuNP associated toxicity is commonly understood to require internalisation of the AuNP, it is therefore unsurprising that the highest levels of toxicity by far were associated with the smaller, more readily taken up citrate capped AuNSs.

Proliferation deficits in the 5-Gy group should result from a combination of AuNP induced toxicity and radiation induced toxicity. By normalising the deficits in proliferation produced in the 5-Gy group with respect to the corresponding 0-Gy group, the deficit produced by the AuNP and radiation combination can be separated from that produced by the AuNPs in isolation. This is represented in Table 8.4 by the term inhibition. If the inhibition associated with 5 Gy of radiation is greater in the presence of a AuNP then the AuNP has a *DEE* greater than one, whereas a *DEE* below one would indicate that the inhibition is reduced in the presence of the AuNP. The first thing to note when looking at the various AuNPs considered here is the relatively large uncertainties (0.05 to 0.07) in the measured DEEs (-0.02 to +0.22) produced by the small number of repeats. Consequently, the results of this experiment should be considered as preliminary, pending confirmation by replication. That said, it is interesting to see what tentative conclusions can be drawn on the basis of the data as it is.

As with toxicity, we can investigate the effect of AuNP shape on *DEE* by comparing the recorded *DEE* values for AuNRs and AuNSs which used the same coating. Though the PEGylated AuNS had a *DEE* of 0.98, indicating a slight radioprotective effect, the difference between them and the controls does not appear significant ($p = 0.47$). The current experiment thus found no *DEE* for this AuNP type. In contrast, the PEGylated AuNRs showed a significant *DEE* (1.22 ± 0.07 , $p < 0.01$). The effect of changing from spherical to rod shape therefore appears to be a marked increase in *DEE*. This could be due to differing uptake and excretion kinetics or due to the dependence of RDEE mechanisms on shape. Given that information in the literature suggests that, in general, AuNRs are taken up to a lesser extent than AuNSs[406][407], it seems unlikely that a higher uptake is the reason that the AuNRs produced a stronger *DEE*, though it cannot be ruled out without an uptake quantification study. On the other hand, several of the mechanisms by which AuNPs deliver RDEEs are dependent on surface area or particle thickness, both of which are affected by the change in shape from a sphere to a rod.

Considering first the chemical mechanisms of RDEE, these depend on the accessible surface area of the AuNP and so would be greater in the AuNRs than AuNSs as the surface area of a sphere is less than a rod with the same volume.

Biological mechanisms of RDEE are not well enough elucidated to comment on with certainty, however it seems likely that surface area plays a more dominant role than volume in these effects, again favouring the rods.

Finally, regarding physical RDEE mechanisms, it should be noted that the smaller radius of the AuNRs means that the maximum distance photoelectrons, Auger electrons and fluorescent x-rays must travel to escape the AuNP, if generated by internal Au atoms, is reduced. This means that AuNRs will self-attenuate less of the radiation they produce, leading to a higher deposition of energy in the cell than AuNS would.

Similarly, the effect of the various coatings on *DEE* can be examined by comparing the AuNSs coated in PEG and citrate, as well as by comparing AuNRs in PEG and PSS. In the case of the AuNSs,

it appears that citrate *may* increase the *DEE* compared with PEG ($p = 0.13$). One potential explanation for this is that the PEG coating reduces cellular uptake, meaning that fewer PEGylated AuNS end up internalised where their DEEs can act most effectively. Alternatively, it is possible that the PEG introduces a steric barrier to the AuNP surface that is not present for the AuNS with the easily displaceable citrate coating. Such a barrier would reduce the chemical and biological RDEE mechanisms which are dependent on surface-substrate interactions. The much higher molecular weight and density of PEG compared with citrate would also help to attenuate photoelectron, Auger electron and fluorescent x-ray emissions from the AuNP, reducing physical RDEE associated with this particle. As with toxicity, an uptake study, or a *DEE* study which matched internalised AuNPs concentration rather than incubated AuNP concentration, would be useful for answering this question. For the present work it was decided against matching intracellular AuNP concentrations however, as extracellular AuNPs can still contribute to *DEE* via physical RDEE mechanisms, meaning the measured *DEE* would not be the result of the same number of AuNPs, even if the same number were internalised, and the resulting DEEs would bias physical mechanisms over chemical and biological ones.

Comparing the PEG and PSS AuNRs, it appears that PSS *may* produce a lower *DEE* than PEG ($p = 0.12$). If confirmed, it seems unlikely to be due to lower PSS AuNP uptake as PSS has been shown to provide superior cellular uptake to PEG[408]. The first difference between PSS and PEG that could be relevant to *DEE* is that PSS is more electron dense. This increased electron density results from both its higher molecular density and the presence of higher z elements such as O and S in addition to the H and C found in PEG. This higher electron density could translate to an increased self-attenuation of photoelectrons, Auger electrons and fluorescent x-rays from the AuNPs, reducing the effect of physical RDEE mechanism mechanisms seen in PSS coated AuNPs.

The second difference of interest between PSS and PEG involves the way in which the coating molecules attach to the AuNP surface. PEG molecules contain a single functional group at one end which attaches to the surface of the AuNR, with the remaining molecule projecting out from the surface as a thin unbranched hydrocarbon chain, reducing in density with increasing distance from the AuNP surface. In contrast, PSS involves a polymer with as many potential attachment functional groups as there are monomers, allowing for a single molecule to wrap round and attach to the AuNP at multiple points. Though the unbound regions of PSS molecules also project out from the AuNP surface, their hydrocarbon chains contain hundreds of bulky benzene residues which produce significant steric hinderance compared with the straight chains of PEG. These benzene derivatives also contain sulfonate groups, which produce electrostatic forces. The combination of these factors is that PSS produces a more tightly bound and more rigid coating than PEG, producing additional barriers to large or negatively charged chemical species trying to access the AuNP surface. This should lead to a reduction in chemical and biological RDEE mechanisms operating in the PSS coated AuNRs compared with their PEGylated counterparts.

Summarising the results of the experiment then, AuNRs produce a greater *DEE* than AuNSs and, for the coatings considered, *DEE* was greatest with citrate, followed by PEG and then finally by

PSS. It is interesting to note that of the two parameters (shape and coating) shape appears to be the dominant factor determining *DEE*, with the best shape and worst coating for *DEE* (PSS coated AuNRs) producing an almost identical *DEE* to the worst shape with best coating (citrate capped AuNSs) (for the claim they differ, $p = 0.49$).

This experiment set out to determine whether there is a conflict between optimising the AuNP parameters of shape and coating for PASI imaging and optimising them for delivering RDEEs. Of the shapes and coatings considered in this work the optimal configuration for PASI imaging would be PSS coated AuNRs, whilst the optimal particle configuration for RDEE generation would be citrate coated AuNRs. It therefore appears that there is no conflict regarding shape but there is regarding coating. Properties that enable good PASI imaging with regards coating involve the separation of the AuNPs from each other using spacer materials to prevent their plasmon resonances from coupling. This usually involves sterically hindering surfaces from different AuNPs from getting close during aggregation, though this leads to an additional hinderance to substrate approach. Though not necessarily true for all coatings, those considered here had high molecular mass, which could lead to increased shielding of the cell from photoelectrons, Auger electrons and fluorescent x-rays emitted by the AuNPs. In combination, this means that the strategy of coating AuNPs to prevent plasmon resonance coupling results in a reduction in RDEEs.

As with all biological investigations, the conclusions of this work should be regarded as preliminary unless and until sufficient repeats of the work are performed to corroborate these findings. Nevertheless, many of the results reported herein do appear to be statistically significant, as indicated by the stated p -values.

The major limitations of this work included the relatively narrow selection of coatings and shapes considered, the lack of uptake quantification and the lack of functionalisation applied to the various coatings. Choice of shapes was constrained to the major ones used in both PASI and RDEE work, however there are other shapes utilised in PASI that have simply never been tested for RDEE activity. It is in fact likely that some of these, such as nanostars, would produce good RDEEs due to their very high surface to volume ratios which could enhance both chemical and biological RDEE pathways. The difficulty of matching volumes for all particles involved made these more extreme geometries less favourable in this study however, especially as a reliable way of producing them with a narrow and tailorable volume distribution was not known to our groups. To justify the time and expense of the syntheses it was therefore decided to focus on AuNP shapes that were known to deliver RDEEs initially. Now that the role of shape in RDEE has been shown, a process of comparing other shapes to optimise for RDEE can begin.

Uptake quantification was not undertaken in this study due to it not being necessary to assess the primary question of this chapter: do AuNP shape or coating affect RDEE? This is because differences in uptake, whatever they are, were considered a function of shape and coating and so just another factor of the effect of those parameters on RDEE. Whilst this argument still holds, it would

have been instructive to see if and how uptake varied between the particle types as this would support a more detailed discussion differentiating between possible mechanisms for any observed *DEE* differences.

In a similar vein to the previous comment, functionalisation of the AuNPs was not undertaken in this study, so as not to bias any particular uptake route and consequently exaggerate/mask differences in measured DEEs. Inclusion of a second experiment in which the particles were functionalised however would allow for some of the limitations regarding AuNP uptake to be mitigated. The ideal comparison for elucidating mechanistic differences in RDEE produced by the changing shape and coating of the various AuNPs would involve all AuNPs in this study being present in the cells at the same AuNP concentration. It is possible that this could be achieved with suitable functionalisation, though this would require a series of uptake and synthesis optimisation studies which would have significantly extended the time required for the current work beyond that which was available.

Further work in this area would involve confirming that the mechanisms suggested are indeed responsible for the observed differences in measured *DEE*. This could be done by first performing an uptake study so that the different levels of AuNP in and outside of the cell could be known. Combined with TEM of some sample cells to determine the spatial distribution of internalised AuNPs, these data could be used in a Monte Carlo study using the Geant4-DNA Physics module to calculate the physical component of RDEE. Any remaining RDEE could then be assigned to chemical or biological mechanisms, which would then need to be differentiated separately. Biological mechanisms could be assessed using quantitative polymerase chain reaction (qPCR) or Northern blotting techniques to look for key DNA repair pathway gene activity, as well as cell cycle analysis to determine changes to cell cycle resulting from AuNP presence. This experiment would not require irradiation. The final component of RDEE, chemical enhancement, could be assessed by comparing the levels of various free radical species produced by irradiation both with and without AuNPs present.

8.5 Conclusion

AuNPs have been widely shown to be of use for increasing the control achieved for a given dose during radiotherapy, however their use *in vivo* would benefit greatly from the ability to quantitatively image their concentration and distribution within the body. The current leading candidate for this type of imaging is PASI, however this technique has some limitations. Whilst parameters needed to optimise AuNPs for PASI detection are known, the effect of this optimisation on the RDEE the AuNPs produce is not known. This work set out to determine what effect on RDEE, if any, is produced by the changes to AuNP shape and coating often associated with PASI.

AuNP types were designed and synthesised such that the same number of AuNPs would produce the same total number of Au atoms, regardless of AuNP type chosen. Groups of cells were then cultured and irradiated with the same concentration of each of the AuNP types. The resulting *DEE* was assessed by normalising the inhibition of cell division over a period of 5 days, as measured using AO/PI staining, optical microscopy and automated cell counting techniques.

The results obtained so far indicate that the choice of AuNP coating and shape do make a difference to the *DEE* produced, with AuNRs producing an increased *DEE* compared with AuNSs with the same coating, and coatings producing *DEEs* in the order citrate > PEG > PSS.

The better performance of AuNRs over AuNSs is consistent with the higher surface area to volume ratio of this geometry, which would improve contact area for chemical and biological enhancement mechanisms and reduce the average pathlength through the AuNP for Auger and photoelectrons, as well as for fluorescence x-rays, reducing AuNP self-attenuation and thus also improving physical enhancement mechanisms.

The order of the coatings is consistent with both their order by coating electron density and their order by size. Two possible mechanisms for this ordering are thus suggested: the higher electron density of the coatings interferes with physical enhancement mechanisms or the higher steric hindrance of the larger coatings reduces access to the AuNP surface, inhibiting chemical and biological enhancements. Insufficient information is available within this study to conclude which mechanism, if either, is dominant, and indeed both may well operate in tandem.

Whilst only preliminary, due to the low number of repeats currently performed, the results in this chapter indicate that shape optimisation for PASI is not in conflict with shape optimisation for RDEE, though coating optimisation is. Fortunately, the size of the effect due to AuNP shape appears to be greater than the effect of coating, such that optimised shapes can produce significant *DEE* even in the presence of a non-ideal coating. The results thus indicate that PASI optimisation of AuNPs does not intrinsically limit their utility as RDEE agents.

Chapter 9.

Overall discussion

This thesis set out to assess the potential of two imaging techniques for quantitatively imaging gold nanoparticle (AuNP) distributions *in vivo*, as part of informing treatment planning where AuNPs were used to deliver a radiotherapy dose enhancing effect (RDEE). The two techniques examined, photoacoustic spectral imaging (PASI) and x-ray photon-counting spectral imaging (x-CSI), were chosen due to their ability to image specific physical properties of the AuNPs that differed markedly from the properties of the tissue they were in. These properties, for PASI and x-CSI respectively, were optical absorption (and to a lesser extent photoacoustic conversion efficiency) and the Z-number of their constituent atoms. Extensive literature reviews, guided by results from simulations and wet-lab work, were conducted to establish the AuNP design parameters affecting delivered RDEE and detection by PASI and x-CSI, and the imaging capabilities of these systems. The results are summarised in Table 9.1, and are discussed in more detail in the following sections. It should be remembered when considering Table 9.1 that PASI technologies are substantially more developed and more widely studied than x-CSI. This is in no small part due to the comparative (to x-CSI) ease and inexpensiveness for research groups to build their own PASI systems, and the availability of commercial PASI systems. It is thus premature to compare x-CSI and PASI in absolute quantitative terms, though general principles can still be determined.

Table 9.1. Summary table showing the performance characteristics of x-CSI and PASI systems currently demonstrated. *Note that the definition of temporal resolution is complicated by the different nature of the two techniques, as discussed in the main body of the text.

Metric	PASI	x-CSI
Spatial resolution	Few 100 μm	$\sim 50 \mu\text{m} - 150 \mu\text{m}$
Temporal resolution*	0.05 s - 0.1 s	0.05 s - 0.5 s
Imaging depth	< 7 cm	Whole body
Radiation type	Non-ionising	Ionising
Lowest AuNP concentration detected	$\sim 10^{-7}$ g/ml	$\sim 10^{-3}$ g/ml
Signal dependent on	AuNP properties (number density, shape, size, and dispersity)	Au concentration
Sensitivity to aggregation	Yes	No

9.1 System resolutions

9.1.1 Spatial resolution

A reference point for the spatial resolution required for the imaging component of AuNP-mediated RDEE delivery will help place the measured resolutions of the techniques into perspective. Radiotherapy treatment planning is usually performed on mono- or dual-energy CT images, though MRI may also be used where improved soft tissue contrast is needed for better target volume delineation. These images have spatial resolutions of the order 500 - 1500 μm , depending on the

modality and spatial axis[409]. To be of maximum use, the AuNP imaging modality should thus at least match this resolution.

The spatial resolution of PASI is affected by the focusing mechanism (acoustic or optical), photoacoustic (PA) signal generation mechanism (linear vs non-linear) and reconstruction technique. For the clinical applications envisaged in this thesis superficial imaging will be inadequate, and so we need to consider imaging at depth (order of cm) and therefore acoustic focussing. Non-linear signal generation mechanisms produce sharper spectral features but are more difficult to quantify. For quantitative imaging therefore, linear mechanisms are thus preferred. Under these constraints, the best spatial resolutions reported in the literature involve voxels of the order of hundreds of micrometres per side[248][249], as noted in Table 9.1.

The spatial resolution of x-CSI systems is primarily affected by the source-object-detector geometry, detector pixel size and the reconstruction algorithm employed. It is likely that the source-object-detector geometries employed on the first clinical x-CSI scanners will be similar to those employed in traditional clinical CT systems. Indeed, the major healthcare manufacturers are constructing their prototypes based on modifications of existing hardware[271][272]. The case of optimising pixel pitch is more complicated, as noted in the literature review in Chapter 4, due to the inherent trade-offs between spectral and spatial resolution produced by increasing charge sharing effects (CSEs) at lower pixel pitches. The reasoning behind this is laid out extensively in Chapters 4 - 7 and is not repeated here for brevity. Suffice it to say that the spatial resolution will vary based on pixel pitch, so the optimal pixel pitch for the task of imaging AuNPs needs to first be known. The results of simulations aiming to optimise sensor thickness and pixel pitch, both when charge sharing correction algorithms (CSCAs) are absent and present, formed the basis of Chapters 6 and 7 respectively. These chapters focussed exclusively on energies around the K-edge of Au and their results were used, in combination with literature values, to produce the spatial resolution estimate listed in Table 9.1. The process of determining these values will now be discussed.

From Chapter 6 it can be seen that absolute detection metrics improve with increasing sensor thickness, however the returns diminish exponentially with increasing thickness. Good absolute photopeak efficiency (*APE*) values are important for maximising the information that can be extracted from a given patient dose, indicating thicker sensors would be preferable. The effect of sensor thickness on binned spectral efficiency (*BSE*) is complicated however, with narrower sensors performing better below 200 μm but worse above 250 μm . Application of a CSCA was shown to remove this complication by making thinner sensor materials consistently perform better than their thicker counterparts, whilst also substantially increasing the peak spectral efficiency achieved ($\sim 68\%$ with CSCA vs $\sim 62\%$ without). Application of a CSCA did not however change the preference of absolute metrics for thicker sensors. However, thicker sensors lower the binned spectral efficiency (*BSE*) and increase the risk of crystal defects (which decrease detector uniformity and degrade spectral resolution) and the cost of manufacture. In summary then, there is a conflict between increasing dose efficiency (thicker sensors) and preserving spectral data and costs (thinner sensors). From the results in Chapter 6 it can be

reasonably concluded that, of the sensor thicknesses considered, 1.5 mm would be most suitable for the application in mind. This is because it offers the most significant improvement in absolute detection efficiency (*ADE*) for a given increase in thickness, and thus the best trade-off between *ADE* and *BSE*. It can also be seen that CSCAs have the potential to offer significant improvements in spectral performance, and so different CSCAs were simulated operating on a 1.5 mm thick sensor in Chapter 7.

From Chapter 7 it can be seen that in addition to improving spectral performance, CSCAs increase the sensitivity of all considered system performance metrics to x-ray flux and pixel pitch (i.e. the per-pixel flux). This produces a clear bias towards lower x-ray fluxes, with optimal performance by all metrics (except RCC) being found at an x-ray flux of $\sim 10^6$ photons $\text{mm}^{-1} \text{s}^{-2}$, a pixel pitch of 300 μm - 350 μm and a dynamic Hybrid or 3x3 CSCA used. The situation is complicated by the intrinsic correlation between x-ray flux and temporal resolution (and thus reduced motion artifacts) however. 10^6 photons $\text{mm}^{-1} \text{s}^{-2}$ is at the extreme low end of x-ray fluxes currently in clinical use, being relevant primarily to some mammographic applications. Conventional CT systems use a flux of 10^8 photons $\text{mm}^{-1} \text{s}^{-2}$, however it is widely expected (based on simulated and early practical results[290][291][292][293]) x-CSI systems will require fewer photons to generate images of comparable quality, with some studies suggesting doses as little as 15% of those currently used being necessary. A flux of 10^7 photons $\text{mm}^{-1} \text{s}^{-2}$ should thus be achievable on conventional CT scanner geometries for a similar temporal resolution, so consequently the optimal pixel pitch at this flux is of interest. At 10^7 photons $\text{mm}^{-1} \text{s}^{-2}$, the optimal pixel pitch for absolute metrics was 200 μm and the optimal pixel pitch for the spectral metric of *BSE* was 250 μm : in both cases in combination with a dynamic Hybrid or 3x3 CSCA.

The results of the optimisation studies in Chapters 6 and 7 thus lead us to the conclusion that a sensor thickness of ~ 1.5 mm and a pixel pitch of 200 - 250 μm running a dynamic Hybrid or 3x3 CSCA would result in the best performance for an x-CSI system designed for imaging AuNPs, but what does this relate to in terms of spatial resolution? This is an impossible question to answer directly because, as noted previously, it will depend on the reconstruction algorithm used and the source-object-detector geometry employed. Upon reviewing the literature, a system employing similar pixel sizes (225 μm) was found to display spatial resolution of approximately 150 μm [410]. However, this system utilised a conventional (which is to say unoptimized) source-object-detector geometry, a static 2x2 CSCA (again sub-optimal) and employed a soft tissue smoothing filter in the reconstruction (reducing the achieved spatial resolution). The resolution of 150 μm should thus be considered a lower limit to the resolution. The first, and only, x-CSI system I am aware of where the source-object-detector geometry was designed specifically for the task of x-CSI imaging produced a spatial resolution of around 34 μm [411]. This system did employ a dynamic 3x3 CSCA, however it also utilises significantly smaller pixels (55 μm pitch) than that predicted to be optimal by the simulations in this thesis. This would therefore represent a reasonable upper limit to the spatial resolution we could expect. It was thus concluded that an x-CSI system properly optimised for AuNP detection would likely display a spatial resolution of roughly 50 - 150 μm , as shown in Table 9.1. This range is approximately consistent with estimates from

review articles considering PC x-ray systems as a whole which suggest spatial resolutions of between 70 and 280 μm [294].

In summary, both PASI and x-CSI provide sufficient spatial resolution for the task of quantitative AuNP imaging, with x-CSI offering a slightly higher resolution (2- to 3-fold improvement).

9.1.2 Temporal resolution

The minimum temporal resolution required for the task of quantitative AuNP imaging is dependent on the location of the tumour being imaged, as this will have an impact on the rate of motion relevant. As a minimum it would be hoped that the chosen imaging modality could match the temporal resolution of a conventional CT scanner, generating an image in the order of a few hundred milliseconds, whilst maintaining the spatial resolutions mentioned above.

The temporal resolution of PASI systems is dependent on a variety of factors which will be specific to the task, such as the number of different probe beam wavelengths used and the number of frames over which images are averaged. It is thus perhaps better to refer to the repeat frequency of a PASI system, which is to say the reciprocal of the time interval between image acquisitions. Repeat frequencies of 10 - 20 Hz (50 - 100 ms between pulses) seem typical from the literature[248][249], and are primarily limited by the time needed to repeat laser pulses and cycle between different wavelengths. It should be noted that the optical pulses require significantly less time than this (a few ns) and there is sufficient time between photoacoustic pulses to allow multiple conventional ultrasound images to be obtained[249]. Consequently, there is room for improvement in temporal resolution with this modality should safe methods for improving laser repetition rates be found, not that this is required for the task considered in this thesis.

At the current time, it is difficult to precisely estimate the temporal resolution of an x-CSI systems designed for AuNP imaging. Some reviewers believe that, as an x-ray CT based modality, “a commercial PC CT scanner would have a temporal resolution no less than that of the state-of-the-art [EI detector] scanners”[294]. Whilst mechanically there is little to prevent x-CSI detectors rotating as fast as their EI counterparts, looking purely at rotation speeds is overly reductive and, I would argue, neglects to account for the primary difference in the way that PC and EI detectors operate. Consider the case where an EI and a PC system both produce an image with some signal-to-noise ratio (SNR), X , in time t . For an EI system, an image with a SNR $>X$ can be produced in a time $t/2$ so long as the photon flux is doubled. This is because the EI system generates a signal based on the total number of photons and the electric noise in the system. Halving the time (and thus also the cumulative noise) and doubling the flux therefore results in an improved SNR. In contrast, PC systems are free from electronic noise in the image (in terms of false counts) but suffer from distortions when photons cause pulse pile-up in the electronics. Halving the time and doubling the flux for a PC system thus results in an image with a SNR $<X$. It is therefore neither obvious nor necessarily true that the temporal resolutions of future x-CSI systems will match those currently achieved in the fastest EI systems. Rather, the temporal resolution of the fastest EI systems should be considered an upper limit on temporal resolution[412]. A likely

lower limit for these systems would be the resolutions achieved by prototype x-CSI systems already in existence that are designed for whole body imaging[294]. This gives a temporal resolution range of 0.05 - 0.5 s, as noted in Table 9.1.

In summary, both PASI and x-CSI are likely to provide sufficient temporal resolution for the task of quantitative AuNP imaging. Comparisons between the two systems would be premature at this time for two reasons. Firstly, and most obviously, due to the different levels of development between the two systems. Neither system has yet reached an inherent limitation and x-CSI is significantly less widely developed than PASI. Secondly, though not immediately obvious, the different way in which the two techniques generate spectral images (simultaneously for x-CSI but sequentially for PASI) will have an as yet unknown impact on their relative temporal resolutions. This is because the temporal resolution of PASI depends on how many wavelengths need to be imaged to generate a single frame in which AuNPs can be differentiated from their surroundings with the desired level of confidence.

9.2 *Other imaging factors*

In addition to the resolution of the system, points to note that intrinsically differentiate PASI and x-CSI from each other include their imaging depths, scalability, and risk.

For most radiotherapy applications the treatment is delivered in a physically targeted fashion to a sub-volume of the patient, either via external beams or implanted fixed sources. In these situations, information regarding AuNP concentrations within the irradiated volume will prove instrumental at the treatment planning stage, however the AuNP concentrations outside the irradiated regions will be of more limited use. It is therefore reasonable to say (to a first approximation) that the required imaging volume should enclose:

- the expected target volume (if the AuNPs are being used to reduce treatment intensity so that less dose is delivered to organs at risk for a given therapeutic effect)
- the expected target volume and the organs at risk (if the AuNPs are being used to increase the therapeutic effect for a fixed treatment intensity).

As previously noted, PASI is able to image at depths of only several cm, whereas x-CSI is capable of whole-body imaging. Due to the targeted nature of radiotherapy, whole-body imaging is not necessary, though whether or not PASI will be able to image the required volume will vary based on the cancer's location and therapeutic decisions. There are many cancers, such as prostate cancer, where a PASI probe can be placed close enough that a several cm penetration depth should allow the region of concern to be imaged, whilst others, such as cancers of the brain, where it will not. The imaging depth of x-CSI is thus not an issue for the applications envisaged by this thesis, whilst for PASI it will likely be useful for treating some cancers, unsuitable for treating some others, and conditionally suitable for treating the rest, dependent on AuNPs being either confined locally or else located in tissues where radiotherapy dose is expected to be nominal.

Scalability in this context refers to the ability of these imaging modalities to increase the spectral information gained without compromising on other system parameters. With PASI, additional spectral channels can be included at a cost to temporal resolution (dividing the available laser pulses over more wavelengths), SNR (averaging each wavelength over fewer images), fluence (dividing light sources across wavelengths) or price (adding additional light sources). In the case of x-CSI there is in principle no such trade-off as all energy bins are acquired simultaneously, however limitations regarding the speed of data readout from the ASICs may lead to reduced count rates, and thus a limitation on system temporal resolution. Another limiting factor for scaling up x-CSI spectral capabilities is the number of comparators that can be incorporated reliably into a single pixel in the ASIC at a given pixel size. Including additional spectral channels in x-CSI may therefore require larger pixel pitches. Additional spectral channels in x-CSI may thus come at the expense of spatial resolution, temporal resolution, or both. Nonetheless, for the task of imaging AuNPs specifically it should be noted that both x-CSI and PASI have been shown to be capable of the task with as few as two spectral data sets (energy bins or optical wavelengths for x-CSI and PASI respectively). Thus both techniques have shown themselves suitable in this regard.

Risks to the patient are different between the two techniques as well, though in both cases are relatively low. x-CSI requires the delivery of a radiation dose to the patient, though significantly lower than doses associated with current planning CTs and likely insignificant compared with the planned radiotherapy doses. x-CSI may therefore actually lower the radiation dose delivered to a patient during radiotherapy planning. PASI produces no additional ionising radiation dose over a standard planning CT, however it does involve non-trivial infrared radiation doses, with the intensity of this radiation being a limiting factor in pushing SNR further in current systems. Additionally, whilst safe, some PASI probe designs (e.g. transrectal and intrauterine) may be intrinsically associated with some level of discomfort. With either technique, where AuNPs are used to reduce the radiation dose delivered outside of the target volume, the overall risk to the patient will thus likely be lower than with conventional CT alone (assuming AuNPs produce a negligible risk, but this is beyond the scope of this thesis).

9.3 AuNP detection and quantification

Any discussion regarding whether x-CSI and PASI are suitable for quantitative imaging of AuNPs in the context of RDEE delivery needs to begin with several important caveats. The use of AuNPs to deliver RDEEs is a concept which bridges several disciplines, with biologists, chemists and physicists often studying the phenomenon of RDEE with different tools and focussing on different mechanisms[96][120][142][152]. Similarly, imaging studies involving PASI and x-CSI often have different applications in mind, resulting in different reporting metrics (number of AuNPs/cells detected vs gold concentration detected). This is not unsurprising as the different studies are designed to examine different physical parameters: whilst a biological study may be concerned with the number of AuNPs internalised per cell, physical studies would be more concerned with total Au concentration and chemical studies more interested in surface area and structure. The situation is further complicated by the slightly different standards for calculating common terms in the different disciplines e.g. measuring

AuNP solution molarity based on AuNP particle number or equivalent gold atom number. The result is that direct comparison of reported concentrations can be misleading. This thesis has attempted to avoid such pitfalls by calculating the equivalent Au concentration directly for all studies considered based on reported AuNP shape and size information, as reported in Chapter 4, though this limited the number of papers which could be compared.

Units and reporting metrics aside, there are fundamental differences in the use of AuNPs for imaging and RDEE studies which complicate the translation of results from one field to the other. As an example, whilst most RDEE work has involved the use of gold nanospheres (AuNS)[96], most PASI studies involve gold nanorods (AuNR) or gold nanostars (AuNSt), and x-CSI studies have even used simple solutions of chloroauric acid[300]. This is a non-trivial difference that needs addressing as a different AuNP shape alters the mean depth of x-ray interaction, available surface area and surface type, all of which can impact on at least one RDEE mechanism. Work presented in Chapter 8 attempted to address this gap by assessing what effect, if any, the transition from RDEE standard AuNPs to PASI standard AuNPs had on RDEE, all else being equal. The results of this chapter, though currently preliminary, indicate reassuringly that AuNP optimisation for PASI is possible whilst still retaining (or even improving) RDEE. This is an important result which will be returned to later. For now, it should simply be noted that drawing together such disparate fields, as this thesis attempts to by its nature, may involve making assumptions based on one discipline which may prove not to hold in the long run. Research has to start somewhere however, and with this noted, I will now discuss the evidence for AuNP detection and quantification using PASI and x-CSI in the literature.

As with spatial and temporal resolutions, a reference point is needed against which a given technique's detection limits can be judged. It was noted in Chapter 4 that RDEE studies have found measurable RDEEs at equivalent Au concentrations ranging from 10^4 - 10^{-4} mg/ml, and no measurable RDEEs at concentrations of 10^{-5} mg/ml. These studies used a range of different AuNP types and coatings, as well as different measures of RDEE and biological models, however this does provide a reference point to begin considering PASI and x-CSI sensitivities.

PASI has shown the ability to detect AuNPs at *in vivo* concentrations as low as 10^{-4} mg/ml, consistent with the lowest concentrations at which AuNP-mediated RDEEs have been detected. It is therefore a useful technique for identifying in which tissues RDEEs would be likely, and for verifying that AuNPs are not present to any significant extent in organs at risk. Quantification with PASI is complicated by a variety of unknown factors of the tissue being imaged through however, such as the wavelength dependent optical attenuation profile which leads to the light fluence at a given imaging depth being unknown. As established in Chapter 3, photoacoustic signal intensity (G) is dependent on the optical properties of the absorber (e_o), the absorber's concentration ($[O]$), the mechanism dependent efficiency of PA signal generation (η) and the fluence of light at the absorber (F_L). The aim of using AuNPs to predict RDEE necessitates the ability to quantify AuNP concentrations, so in this case $[O] = [AuNP]$. To do this accurately the values of e_o , η and F_L are thus needed. e_o can be measured as a function of wavelength for the AuNPs prior to their injection easily, and η can be kept constant

(assuming non-linear effects are avoided) and readily measured *in vitro*. In doing so, calibration curves relating $[AuNP]$ and G can be determined with a high degree of precision *in vitro*[215]. *In vivo* the situation is more complicated however, as the optical properties of the intervening tissue between light source and imaging depth (as well as the level of backscatter from deeper tissues) are not known and will affect F_L in a wavelength dependent fashion.

Semi-quantitative PASI is possible in most situations, with changes in the AuNP concentration over time being assessable by comparing the changing PA signal[224] from a given location. Non-invasive, fully quantitative PASI has been demonstrated with iron oxide nanoparticles[215] at a reasonable accuracy (<10% difference compared with ICP-MS) using a technique that could be generalisable to AuNPs provided some caveats are met. These caveats are that the nanoparticles are not thermally coupled to each other, that they generate PA signals with a linear dependence on F , and that they are in direct contact with a material with known and constant thermoacoustic properties. The latter constraints can be realised by avoiding non-linear signal generation mechanisms and using cell cytoplasm (or a fluid with similar properties) for the *in vitro* calibration phase of the approach, however the first constraint is more difficult. AuNPs do tend to couple readily together, especially upon close contact, so initially this condition could be met by using a dilute mixture of AuNPs, such that individual AuNPs are unlikely to approach closely and so remain uncoupled. This solution is difficult (though not impossible) to achieve with AuNPs that enter cells via endocytosis as endosomal encapsulation results in an increase in AuNP concentration to the point of enforced aggregation. Under these conditions, AuNPs thermally couple due to their close confinement[413]. Whilst plasmon coupling is preventable by using a silica shell to coat the AuNPs[266], this same shell provides for a better thermal match between the AuNP and surrounding media, resulting in a more rapid transfer of heat and a sharper PA signal[392] and therefore is unlikely to result in the thermal isolation criteria required. Conversely, coatings could be designed to prevent thermal coupling between AuNPs and the medium. This would facilitate quantitative imaging, but I would expect this to also reduce thermal stability (with respect to laser heating) and decrease PA signal intensity. To meet this second criteria therefore, it is necessary that the AuNPs be either sufficiently small that they can enter the cells without endocytosis, be transported by some exotic carrier which can bypass endosomal uptake (such as a specifically designed liposomal carrier) or be functionalised with escape proteins to escape endosomal confinement. Of these options, none is without their associated difficulties (smaller particles have reduced targeting ability and liposomes and endosomal escape both involve an intermediary stage at which the quantification assumptions do not hold, meaning confirmation of liposomal/endosomal escape would also be needed) however all are in principle achievable.

The conclusion must therefore be that for the purpose of detection alone, PASI has an exquisite sensitivity that is well suited to the techniques relevant to this thesis, able to detect AuNPs at the lowest concentrations currently associated with RDEEs. Semi-quantitative analysis is trivially possible, as is fully quantitative *in vitro* analysis. Non-invasive, fully quantitative PASI *in vivo* is in principle possible, though it will require specifically designed AuNPs, however the limited work in this area means it

currently needs more work to validate its practical utility. Whatever the AuNP design parameters needed to achieve this imaging, they would represent additional constraints to the AuNP design optimisation for RDEEs, as discussed in Chapter 8. Unfortunately, as no AuNPs have currently been designed specifically to bypass thermal coupling, these parameters could not be included in that chapter, however it is hoped that, much like the parameters that were considered, they will not be directly in conflict with the aim of delivering RDEE with AuNPs.

For x-CSI the situation regarding detection and quantification is largely reversed: with better accuracy and easier quantification of *in vivo* Au concentrations but a higher detection limit than PASI. It needs to be remembered in the following discussion however that x-CSI can increase sensitivity arbitrarily by increasing the radiation dose delivered to the patient, though in practice safety concerns will inform the clinically relevant detection limits. The studies focussed on in this section used systems designed for either pre-clinical animal work or clinical human studies and use doses that would be reasonably acceptable clinically. x-CSI has demonstrated the ability to accurately quantify AuNP concentrations, down to 10^{-3} g/ml, with an associated uncertainty of $\sim \pm 5 \times 10^{-4}$ g/ml *in vitro*[309]. This study also involved a comparison between *in vivo* x-CSI imaging and ICP-OES analysis of *ex vivo* samples based on Au concentration, revealing disagreement of less than 2 mg / ml for 3 of the 4 organs analysed with non-negligible Au concentrations (1 mg/ml - 6 mg/ml). These uncertainties are not insignificant in terms of the concentrations being detected, however it should be noted that other systems have achieved uncertainties an order of magnitude smaller than this, though at minimum detected concentrations twice as large[299]. It is also important to note, as mentioned in Chapter 4, that the detection limits reported on here represent the lowest concentrations the system was tested on, rather than the lowest concentration the systems could detect before they failed to detect AuNP presence. Nevertheless, the relatively large uncertainty implies that these systems are unlikely to be able to quantitatively image AuNPs at Au concentrations much below $\sim 10^{-4}$ mg/ml, though these systems are not specifically optimised for AuNP detection but rather designed for *in vivo* imaging applications in general. This is an important caveat and in truth the detection limits and quantitative accuracy of x-CSI are not yet known. In principle a limit could be established via simulation studies, and this is the primary motivation for the work conducted in Chapters 5, 6 and 7, though the number of variables involved inherently limits the amount of progress towards this goal that can be made in a single, two-modality thesis such as this.

The conclusion regarding the detection and quantification limits for x-CSI must therefore be that x-CSI has so far shown detection and quantification of AuNP down to 10^{-3} g/ml equivalent Au concentration. This represents a level midway between the highest and lowest AuNP concentrations used to demonstrate AuNP-mediated RDEE ($[Au] = 10^1 - 10^{-7}$ g/ml). As RDEE depends on AuNP design, it may be possible to design AuNPs such that they produce only negligible RDEE at concentrations below those detectable by x-CSI, however this would most definitely conflict with the aim of optimising AuNPs for RDEE effect. Nevertheless, it may be a clinically viable option.

Before closing this section, it is worth reflecting on the importance of detection and quantification respectively. Detection plays a primary role in ensuring RDEEs are not occurring in tissues where it is not desired (e.g. organs at risk) whilst quantification is relevant to predicting the RDEE that can be achieved in tissues where it is desired. The excellent detection limits of PASI therefore make it an ideal choice for ensuring the safety of organs at risk, whilst the high quantification accuracy of x-CSI makes it useful for predicting the RDEE expected in the target volumes. There is therefore potential scope for these two techniques to be used in tandem.

9.4 AuNP parameter sensitivities

Whilst both PASI and x-CSI are sensitive to physical properties of AuNPs that allow them to be easily differentiated from the tissues in which they are found, there is an important distinction in which properties these are: PASI utilises properties intrinsic to AuNPs (surface plasmon resonances) whilst x-CSI utilises properties intrinsic to Au atoms themselves (higher *Z*-number). This results in the two having vastly different sensitivities to a range of AuNP design parameters, with x-CSI sensitive only to the total amount of gold present and PASI potentially sensitive to AuNP size, shape, surface coating and inter-particle spacing. These differences provide the two modalities with different advantages and disadvantages when it comes to using AuNPs for *in vivo* applications.

The sensitivity of PASI to changes in inter-AuNP distances means that it can be used to detect AuNP aggregation, allowing smart AuNPs to be designed that can report on cellular pH[242][243] or successful receptor targeting[414], meaning that PASI allows an additional mechanism for verifying accurate targeting of AuNPs to tumour sites. The sensitivity to AuNP geometric parameters additionally adds the ability to multiplex AuNPs, allowing for multiple different cell types to be differentiated using different AuNP populations functionalised to target different cell surface proteins[239]. Combined, these represent a significant advantage in terms of qualitative information that can be obtained to inform the patient's treatment (such as which chemotherapy or antibody agents may be most useful as adjuvant therapies or a map of tumour heterogeneity) that are not available to x-CSI.

In contrast, by being insensitive to AuNP geometry and surface chemistry, x-CSI signals are more consistent, allowing for easier calibration and more accurate [Au] quantification. Further, by tracking [Au] concentration directly, x-CSI is better able to predict the physical mechanisms of RDEE that AuNPs can produce, as well as likely toxicity related to AuNPs (which is normally measured in mg of Au per kg of body mass). This is in contrast to PASI which is sensitive to particle number, making it more suitable for assessing the less predictable biological and chemical effects (which are surface area dependent).

I would suggest that the multiplexing ability of PASI could be extended to x-CSI by using gold nanoshells (AuNSh) as the AuNPs, so long as the shells coated different high *Z*-number cores. The chemical and biological RDEE mechanisms would be largely unaffected (relying on the AuNP surface only) and the physical dose enhancement should still be significant, though may be slightly higher or lower depending on the core element chosen. This would be particularly true as self-attenuation of

fluorescence x-rays could be reduced by using a core material which generates fluorescence x-rays at an energy below the K-edge of Au. Multiplexing with x-CSI is unlikely to be able to match, in the short term, the 7 differentiable agents PASI has been shown to be able to detect[213], though this may improve with time.

9.5 Author's opinions on the contributions of this thesis

This section has been added to convey a more personal expectation as to the place of this thesis within the literature.

It is clear that the constraints of AuNP imaging and RDEE delivery are very different and yet rarely considered side-by-side. As a result, the RDEE literature is replete with studies assessing how non-imaging relevant parameters affect RDEE (e.g. intracellular localisation, irradiation energy and particle type) whilst the PASI based detection of AuNPs is moving rapidly towards silica coated particles, despite the detrimental impact this will likely have on RDEE. Similarly, AuNP quantification studies involving x-CSI only assess concentrations orders of magnitude greater than would be needed for AuNP-mediated RDEE prediction in a clinical context. Without work such as this thesis, which highlight the differences in research trends across the various aspects of this project, it is likely that the three fields would continue to diverge in the AuNP types they use, limiting the research overlap and significantly slowing the development of a suitable AuNP for the task of clinical RDEE delivery.

Therefore, whilst it is too early to conclude which technique would be most suitable for clinical use, and indeed it may eventually be that this answer varies based on tumour location or patient profile, this thesis has highlighted for both PASI and x-CSI where they need to focus their research efforts if they want to eventually be used for clinical AuNP-mediated RDEE prediction. Similarly, information has been provided that will allow AuNP designers to improve the RDEEs produced in the field of RDEE research, as well as providing limits on coatings they should keep in mind if they would like to use PASI as an imaging technique for predicting the achieved RDEEs.

Chapter 10.

Concluding thoughts and future work

Both PASI and x-CSI are techniques capable of detecting AuNPs *in vivo*, though each has limitations which make it unsuitable for clinical use in quantifying AuNP concentrations for predicting RDEEs at the current time. This thesis has identified the limitations relevant to these modalities and lays the groundwork for overcoming them in the future.

PASI has demonstrated an existing capability to detect AuNPs at all concentrations currently shown to produce RDEEs, is relatively safe and is available as both approved clinical scanners and prototype internal probes. Its suitability for AuNP-mediated RDEE applications is however limited by its restricted imaging depth (several cm) and inability to accurately quantify AuNPs concentrations *in vivo*. These restrictions are not insurmountable, rather restricting the cancer types (location, depth, and size) and AuNP types (shapes and surface coatings) that PASI could be used with. Due to the seemingly shallow gradient between AuNP concentration and RDEE found in the literature (8 orders of magnitude different Au concentrations result in RDEEs that vary over only 3 orders of magnitude[96]), even a relatively large quantitative uncertainty may still have clinical utility, so long as PASI could confirm that AuNPs are not present in organs at risk at levels that would produce an RDEE.

Nevertheless, quantitative PASI requires AuNPs to be designed specifically for this task, which may interfere with optimising AuNP design for RDEE, tumour uptake, clearance from the patient post treatment, or other tasks. Indeed, in Chapter 8 of this thesis it was provisionally established that both AuNP shape and surface coating could affect the RDEE delivered. Shapes that favour PASI would reasonably be expected to also favour RDEE (due to the increased surface area when compared with the RDEE research standard of spheres), whilst coating the AuNPs in typical PASI suitable coatings (to detoxify the CTAB used in AuNR synthesis[393][415]) led to a reduction in RDEE (compared with the more RDEE favourable approach of using an easily displaceable capping agent). This work thus highlighted the trade-offs that may be necessary in designing AuNPs that are optimised for both PASI and RDEE. On balance, the effects of the shapes considered were dominant over the effects of coating observed, which is consistent with the prevailing view that at lower energies (keV rather than MeV) it is the physical RDEE mechanisms which dominate. Whether or not this holds at higher energies, and with shapes that generate higher surface-to-volume ratios (such as nanocages) is a matter for further work.

The next piece of work that needs to be done however is an optimisation study involving a wider range of AuNP shapes and coatings than were used here (including silica coating which is becoming increasingly relevant to PASI due to its optical preservation capabilities and commercial availability) to establish an optimised AuNP for RDEE. The work presented in Chapter 8 provides a template for performing this work. By performing a simple PASI study in parallel (using imaging phantoms to assess photoacoustic signal strength, resistance to aggregation and optical window for the various particles being considered), a reasonable trade-off between RDEE and PASI detectability could be established, yielding an RDEE-PASI optimised AuNP.

The next step once an RDEE-PASI optimised AuNP is designed is to repeat the work in Chapter 8, but this time using a serial dilution of the same AuNP in place of a range of different AuNP types, to determine both a relation between AuNP concentration and RDEE and the minimum AuNP concentration for which measurable RDEEs are achieved. If this concentration is within the detection and quantification limits of PASI then the use of AuNPs for RDEE treatment may become clinically advisable. This process will likely need to be repeated for a range of cell types, so that curves relating RDEE and AuNP concentration can be derived for various cancer types (the curves may differ as the different cell types may exhibit different sensitivities to different RDEE mechanisms).

A potentially revolutionary advance with significant implications to this thesis would be the demonstration of a different, non-invasive, *in vivo*, quantitative PASI approach for imaging AuNPs that is independent of AuNP shape and coating. Such an advance appears unlikely in the short term, and so the proposed further work seems reasonable.

x-CSI has demonstrated superior imaging quality, more versatile material decomposition, and lower patient dose than conventional CT, as well as the ability to quantify AuNPs at concentrations relevant to roughly half of the AuNP-mediated RDEE publications considered in this work, with good reproducibility. This leaves the disquieting possibility that, if used clinically, x-CSI would be unable to detect AuNP concentrations which would induce a RDEE in organs at risk or in other off-target tissues. The risk of such off-target effects could be limited by combining the AuNP-mediated RDEE therapy with the ‘tumour tracking’ or ‘normal tissue protective’ approaches mentioned in Chapter 1.

It is possible that the threshold for AuNP detection could be lowered to the required levels by optimising an x-CSI system for AuNP detection, however such a system is not currently available, nor its exact parameters known. The primary obstacle to rapid x-CSI optimisation towards this goal is the sparse availability of physical systems or robust simulation tools. To address this, Chapter 5 of this thesis developed and validated an x-CSI simulation framework (CoGI) which modelled x-ray photon interactions with both phantom and detector, charge deposition, local charge transport (drift and diffusion), long range charge transport (fluorescence x-rays and Auger/photoelectrons), signal generation (both from electrons and holes), signal thresholding (both in isolation or as part of a CSCA) and image reconstruction. This tool was then used in Chapters 6 and 7 to identify the combination of pixel pitch, sensor thickness and CSCA which gave the best spectral performance at the K-edge of gold, on the basis that performance at this energy will be a fundamental hardware factor in determining the ability of an x-CSI system to spectrally distinguish AuNPs from non-gold media.

Intended future work involves using CoGI to establish the effect(s) of x-ray flux on spectral performance and imaging time. An optimised x-CSI system can then be operated within a fully simulated imaging chain to determine the minimum detectable threshold at which AuNPs are detectable *in vivo*, given realistic constraints regarding patient dose, imaging time and patient motion. If the minimum detectable AuNP concentrations are then found to be equal to or below those associated with RDEE then x-CSI could be recommended for use as part of AuNP-mediated RDEE treatment. The work

proposed above regarding using the workflow in Chapter 8 to determine an RDEE optimised AuNP (without the need for PASI detectability) and the relation between that AuNP's concentration and RDEE would then provide the required data to allow this technique to move towards the clinic. Should the minimum concentrations not be detectable with such an optimised x-CSI system, the cell work would need an added constraint which would be that the AuNP selected needs to show no appreciable RDEE at concentrations below those detectable with x-CSI. Such a AuNP design would allow x-CSI to proceed to clinical trials as the sole imaging modality for predicting AuNP-mediated RDEEs.

In the short-term, the most feasible way to progress towards AuNP-mediated RDEE treatments appears to be a hybrid approach, employing a combination of PASI and x-CSI in their current (or near future) forms. Suitable AuNPs for such an approach could involve either systemic introduction of mobile, smartly targeted AuNPs[260] or local introduction of relatively immobile AuNPs (e.g. via intratumoural injection of very large AuNPs). The quantitative capabilities of x-CSI could then be used to measure AuNP concentrations at the radiotherapy target sites, with the high detection sensitivity of PASI used to verify that AuNP concentrations in organs at risk were below the level at which RDEEs would be expected. It may even be possible to use the quantified values from the x-CSI images as points of reference to calibrate PASI so that the concentration below x-CSI detection limits could also be established, though this would need to be demonstrated first. In the case of such dual-modality imaging, the cell work based on Chapter 8 would still be required to provide RDEE-PASI optimised AuNPs and the needed data for AuNP concentration vs RDEE curves, however no other major technological advances would be required.

In conclusion, PASI and x-CSI both show exceptional promise as imaging modalities for predicting AuNP-mediated RDEEs during radiotherapy treatments, however neither can fulfil this role in isolation at the current time. A combination of the two may be suitable, however extensive gaps in knowledge regarding optimal AuNP design for RDEE and the relation between AuNP concentration and RDEE remain.

10.1 Author's view on the broader future of the field

This section was added to convey the personal opinions of the author on the future potential of AuNP-mediated RDEE.

The broadest question for this thesis is whether AuNP-mediated RDEE with PASI/x-CSI in the clinic is feasible in the future. I believe that it is, despite the considerable work still to be done regarding AuNP targeting, safe AuNP clearance from the body, x-CSI sensitivity and PASI quantification.

Whilst, at the time of writing, the only successfully demonstrated approach for solving the problem of AuNP quantification with PASI has constraints which conflict with RDEE, there are many proposed mathematical approaches which do not, though none yet which are generally applicable. I am cautiously optimistic that the problem can be solved, though I suspect the solution will still require specific AuNP parameters. In the short term, assuming the current quantification approach is used, I

would suggest that AuNPs be designed with rigid, narrow projections that can act as spacers to separate AuNPs without excessively impairing surface area access and therefore RDEE. This may be easier said than done, however.

x-CSI has great potential for AuNP quantification clinically, with whole-body imaging capability, excellent spatial resolution and easy inclusion in existing clinical workflows (due to it being able to also produce standard planning CTs). x-CSI is thus the tool I believe will be of most use for the applications envisaged. I suspect much work remains to be done, both in the hardware and software domains, before x-CSI can match the sensitivity of PASI and that required by RDEE applications. My lack of familiarity with all of the aspects of the imaging process mean I must be honest and say I do not know that it will be possible to achieve the needed sensitivities at all, and I suspect much of the low dose advantage may be traded off in improving sensitivity to the required level. Nevertheless, I am cautiously optimistic that this technique will be useable for this application, and I am sure its development will accelerate rapidly as it finds use in a range of other clinical applications as well.

Whilst the cause of biological enhancement is not yet demonstrated, it seems likely to me that it will be found to be surface area dependent, much as chemical enhancement is. My advice to AuNP designers interested in maximising RDEE is to constrain their coating and shape choices to those that allow the surface area of the AuNP to be accessible to small and medium sized biological molecules (such as antioxidants and mRNA strands). Further, considering the considerable constraints placed on AuNP design by RDEE, PASI and targeting requirements, I would suggest to AuNP designers that active targeting of the tumour by functionalising the AuNPs may restrict the solution space too much. Instead, approaches that look to target the AuNPs to the tumour by some bulk mechanism should be considered, such as intratumoural injection, feeding arterial injection or encapsulation of the AuNPs into a larger liposome which can then be functionalised to target the tumour etc. This relieves the tension between tumour targeting and cancer cell targeting and allows more space to optimise for RDEE and PASI imaging simultaneously.

The relation between RDEE and AuNP concentration varies with cell line and tumour type, and the complexity of the interactions between physical, chemical and biological mechanisms make *a priori* prediction difficult at best. The relation between AuNP concentration and clinical outcome may thus require data from clinical studies involving relevant patients. This, to me, is why the quantitative imaging question is the most important point to focus on at the current time. As a physicist I understand the impulse to optimise, quantify and predict, however as a humanist I must accept that while we optimise, patients with terminal disease and no options die, and thousands more suffer debilitating side effects.

Recalling the closing thoughts of Chapter 1, I would like to remind the reader that radiotherapy was in use for decades before its mechanisms of action were understood, and indeed much still remains to be determined, such as the effect it has on the immune system. I would therefore strongly advocate that, as soon as we are able to quantitatively image the distributions *in vivo*, clinical trials are allowed

to assess AuNP-mediated RDEE in informed and consenting patient groups, even if recruitment is limited to patients with a terminal prognosis and no alternative treatment. Data needed to predict RDEE from AuNP concentration can then be collected whilst giving people hope where currently there is none. Just as it is unethical to experiment on patients without their consent, it can be argued that it is unethical to deny patients the ability to consent to an experimental treatment when they exhausted standard treatment options. It is instructive, though deeply terrifying, to think how many lives would have been lost had the early pioneers of radiotherapy refused to allow patients to be treated until we could accurately predict the dose distributions within the patient. As someone with family members who have benefitted from radiotherapy, I am grateful to the patients who took the chances early on, and to the doctors who allowed them that choice.

References

- [1] Lederman, M., (1981), “The early history of radiotherapy: 1895-1939,” *Int. J. Radiat. Oncol. Biol. Phys.*, vol. 7, pp. 639–648.
- [2] Mould, R. F., (1998), “The discovery of radium in 1898 by Maria Sklodowska-Curie (1867-1934) and Pierre Curie (1859-1906) with commentary on their life and times,” *Br. J. Radiol.*, vol. 71, no. 852.
- [3] Mould, R. F., “The early history of x-ray diagnosis with emphasis on the contributions of physics 1895-1915,” *Physics in Medicine and Biology*. pp. 1741–1787, 1995, doi: 10.1088/0031-9155/40/11/001.
- [4] Stevenson, W. C., (1914), “Preliminary clinical report on a new and economical method of radium therapy by means of emanation needles,” *Br. Med. J.*, vol. 2, no. 2792, pp. 9–10.
- [5] Cho, S. H., Jones, B. L. and Krishnan, S., (2009), “The dosimetric feasibility of gold nanoparticle-aided radiation therapy (GNRT) via brachytherapy using low-energy gamma-/x-ray sources,” *Phys. Med. Biol.*, vol. 54, no. 16.
- [6] Ngwa, W., Makrigrigorgos, G. M. and Berbeco, R. I., (2012), “Gold nanoparticle-aided brachytherapy with vascular dose painting: Estimation of dose enhancement to the tumor endothelial cell nucleus,” *Med. Phys.*, vol. 39, no. 1, pp. 392–398.
- [7] Ko, S. Y., Kwon, S. Il, Chun, J., Shin, H. S., Chang, S. K., Im, J. H. and Lee, J. Il, (2019), “Effect of Gold Nanoparticles on Dose Enhancement in Brachytherapy Using a Polymer Gel Dosimeter,” *J. Korean Phys. Soc.*, vol. 75, pp. 415–423.
- [8] Gianfaldoni, S., Gianfaldoni, R., Wollina, U., Lotti, J., Tchernev, G. and Lotti, T., (2017), “An overview on radiotherapy: From its history to its current applications in dermatology,” *Open Access Maced. J. Med. Sci.*, vol. 5, no. 4, pp. 521–525.
- [9] Schreiner, B. F., Reinhard, M. C., Wehr, W. H. and Simpson, B. T., (1935), “Tele-curie-therapy,” *Am. J. Cancer*, vol. 24, no. 2, pp. 386–392.
- [10] Pennington, W. E., (1940), “Radium Bomb to Utilize Various Applicators,” *Radiology*, vol. 35, no. 4.
- [11] Coolidge, W. D., (1913), “A powerful röntgen ray tube with a pure electron discharge,” *Phys. Rev.*, vol. 11, no. 6, pp. 409–430.
- [12] Dresser, R., Rude, J. C. and Cosman, B. J., (1940), “The Differences between 200 Kilovolt and Supervoltage Roentgen Therapy,” *Radiology*, vol. 34, no. 1.
- [13] Lawrence, E. O. and Livingston, M. S., (1932), “The production of high speed light ions without the use of high voltages,” *Phys. Rev.*, vol. 40, no. 19.
- [14] Tuohy, D. I. T. and B, J., (2006), “Back to the future: the history and development of the clinical linear accelerator,” *Phys. Med. Biol.*, vol. 51, pp. R343–R362.
- [15] Robison, R. F., (1995), “The race for megavoltage x-rays versus telegamma,” *Acta Oncol. (Madr)*, vol. 34, no. 8, pp. 1055–1074.
- [16] Ledernan, M. and Greatorex, C. A., (1953), “A cobalt 60 telecurie unit,” *Br. J. Radiol.*, vol. 26, no. 310.
- [17] Phillips, C. E. S., (1907), “The Measurement of Radio-Activity and X-Rays,” *J. Röntgen Soc.*
- [18] Day, M. J. and Rasoul, M., (1969), “Calibration of Farmer-Baldwin dosimeters by chemical dosimetry,” *Phys. Med. Biol.*, vol. 14, no. 2, pp. 283–291.
- [19] Baskar, R., Lee, K. A., Yeo, R. and Yeoh, K. W., (2012), “Cancer and radiation therapy: Current advances and future directions,” *Int. J. Med. Sci.*, vol. 9, no. 3, pp. 193–199.

- [20] Puck, T. T. and Marcus, P. I., (1956), "Action of x-rays on mammalian cells," *J. Exp. Med.*, vol. 103, no. 5, pp. 653–666.
- [21] Almond, P. R., "A Brief History of Dosimetry, Calibration Protocols, and the Need for Accuracy," *2009 AAPM Summer School Clinical Dosimetry for Radiotherapy*, 2009. <https://aapm.org/meetings/09SS/documents/01Almond-HistoryandNeedforAccuracy.pdf> (accessed Oct. 15, 2020).
- [22] Nabavi, M., Nedaie, H. A., Salehi, N. and Naderi, M., (2014), "Stereotactic radiosurgery/radiotherapy: A historical review," *Iran. J. Med. Phys.*, vol. 10, no. 1, pp. 156–167.
- [23] Buzug, T. M., "Computed tomography.," in *Handbook of Medical Technology*, F. Zappoli, A. Lavaroni, and M. Leonardi, Eds. Berlin: Springer.
- [24] Euclid Seeram, RT (R), BSc, MSc, F., *Computed tomography: Physical principles, clinical applications, and quality control*, 3rd ed. .
- [25] Rehman, J. ur, Zahra, Ahmad, N., Khalid, M., Noor ul Huda Khan Asghar, H. M., Gilani, Z. A., Ullah, I., Nasar, G., Akhtar, M. M. and Usmani, M. N., (2018), "Intensity modulated radiation therapy: A review of current practice and future outlooks," *J. Radiat. Res. Appl. Sci.*, vol. 11, no. 4, pp. 361–367.
- [26] Ahmad, S. S., Duke, S., Jena, R., Williams, M. V. and Burnet, N. G., "Advances in radiotherapy," *BMJ (Online)*. pp. 345, e7765, 2012, doi: 10.1136/bmj.e7765.
- [27] "XCOM," *NIST Physical Measurement Laboratory*. <https://www.physics.nist.gov/PhysRefData/Xcom/html/xcom1.html> (accessed Oct. 20, 2020).
- [28] Gilmore, G., *Practical Gamma-ray Spectrometry*, Second. Chichester: John Wiley & Sons, Ltd.
- [29] Meitner, L., (1922), "Uber den Zusammenhang zwischen beta- und gamma-Strahlen," *Zeitschrift fur Phys.*, vol. 9, no. 1, pp. 145–152.
- [30] Singh, A. K., "Experimental Methodologies for the Characterization of Nanoparticles," in *Engineered Nanoparticles*, Elsevier, pp. 125–170.
- [31] Shukla, A. and Kumar, U., (2006), "Positron emission tomography: An overview," *J. Med. Phys.*
- [32] Shibuya, K., Saito, H., Nishikido, F., Takahashi, M. and Yamaya, T., (2020), "Oxygen sensing ability of positronium atom for tumor hypoxia imaging," *Commun. Phys.*, vol. 3, no. 1, p. 173.
- [33] Shalek, R. J. and Bonner, T. W., (1953), "Formation of hydrogen peroxide in water by 1-MeV. Protons," *Nature*, vol. 172, no. 4371, p. 259.
- [34] Shalek, R. J., "The formation of hydrogen peroxide in water by ionizing radiation," Rice University.
- [35] Cantoni, O., Brandi, G., Salvaggio, L. and Cattabeni, F., (1989), "Molecular mechanisms of hydrogen peroxide cytotoxicity.," *Ann. Ist. Super. Sanita*.
- [36] Sheng, Y., Abreu, I. A., Cabelli, D. E., Maroney, M. J., Miller, A. F., Teixeira, M. and Valentine, J. S., (2014), "Superoxide dismutases and superoxide reductases," *Chem. Rev.*
- [37] Brand, M. D., Affourtit, C., Esteves, T. C., Green, K., Lambert, A. J., Miwa, S., Pakay, J. L. and Parker, N., (2004), "Mitochondrial superoxide: Production, biological effects, and activation of uncoupling proteins," *Free Radic. Biol. Med.*
- [38] Henle, E. S. and Linn, S., (1997), "Formation, prevention, and repair of DNA damage by iron/hydrogen peroxide," *J. Biol. Chem.*
- [39] Puig, S., Ramos-Alonso, L., Romero, A. M. and Martínez-Pastor, M. T., (2017), "The elemental role of iron in DNA synthesis and repair," *Metallomics*.
- [40] Bernstein, C. and Bernstein, H., (2015), "Epigenetic reduction of DNA repair in progression to gastrointestinal cancer," *World J. Gastrointest. Oncol.*, vol. 7, no. 5, pp. 30–46.

- [41] Hakem, R., (2008), “DNA-damage repair; the good, the bad, and the ugly,” *EMBO J.*
- [42] Saunders, R., “Book 1 Generating Diversity,” in *Book 1 Generating Diversity*, Second., Milton Keynes: The Open University, pp. 155–162.
- [43] Pawlik, T. M. and Keyomarsi, K., (2004), “Role of cell cycle in mediating sensitivity to radiotherapy,” *Int. J. Radiat. Oncol. Biol. Phys.*
- [44] Asaithamby, A., Hu, B. and Chen, D. J., (2011), “Unrepaired clustered DNA lesions induce chromosome breakage in human cells,” *Proc. Natl. Acad. Sci.*, vol. 108, no. 20, pp. 8293–8298.
- [45] McMillan, T. J., (1992), “Residual DNA damage: What is left over and how does this determine cell fate?,” *Eur. J. Cancer*, vol. 28, no. 1, pp. 267–269.
- [46] Sage, E. and Shikazono, N., (2017), “Radiation-induced clustered DNA lesions: Repair and mutagenesis,” *Free Radic. Biol. Med.*, vol. 107, pp. 125–135.
- [47] Lomax, M. E., Folkes, L. K. and O’Neill, P., (2013), “Biological Consequences of Radiation-induced DNA Damage: Relevance to Radiotherapy,” *Clin. Oncol.*, vol. 25, no. 10, pp. 578–585.
- [48] Kluger, H. M., Chiang, V., Mahajan, A., Zito, C. R., Sznol, M., Tran, T., Weiss, S. A., Cohen, J. V., Yu, J., Hegde, U., Perrotti, E., Anderson, G., Rababate, A., Kluger, Y., Wei, W., Goldberg, S. B. and Jilaveanu, L. B., (2019), “Long-Term Survival of Patients With Melanoma With Active Brain Metastases Treated With Pembrolizumab on a Phase II Trial,” *J. Clin. Oncol.*, vol. 37, no. 1, pp. 52–60.
- [49] Richardson, R. B. and Harper, M.-E., (2016), “Mitochondrial stress controls the radiosensitivity of the oxygen effect: Implications for radiotherapy,” *Oncotarget*, vol. 7, no. 16, pp. 21469–21483.
- [50] Warters, R. L. and Hofer, K. G., (1977), “Radionuclide Toxicity in Cultured Mammalian Cells: Elucidation of the Primary Site for Radiation-Induced Division Delay,” *Radiat. Res.*, vol. 69, no. 2, p. 348.
- [51] Prise, K. M., Schettino, G., Folkard, M. and Held, K. D., (2005), “New insights on cell death from radiation exposure,” *Lancet Oncol.*, vol. 6, no. 7, pp. 520–528.
- [52] Marín, A., Martín, M., Liñán, O., Alvarenga, F., López, M., Fernández, L., Büchser, D. and Cerezo, L., (2015), “Bystander effects and radiotherapy,” *Reports Pract. Oncol. Radiother.*, vol. 20, no. 1, pp. 12–21.
- [53] Icard, P., Ollivier, L., Forgez, P., Otz, J., Alifano, M., Fournel, L., Loi, M. and Thariat, J., (2020), “Perspective: Do Fasting, Caloric Restriction, and Diets Increase Sensitivity to Radiotherapy? A Literature Review,” *Adv. Nutr.*, vol. 11, no. 5, pp. 1089–1101.
- [54] Miyamoto, N., Maeda, K., Abo, D., Morita, R., Takao, S., Matsuura, T., Katoh, N., Umegaki, K., Shimizu, S. and Shirato, H., (2019), “Quantitative evaluation of image recognition performance of fiducial markers in real-time tumor-tracking radiation therapy,” *Phys. Medica*, vol. 65, pp. 33–39.
- [55] Sakata, Y., Hirai, R., Kobuna, K., Tanizawa, A. and Mori, S., (2020), “A machine learning-based real-time tumor tracking system for fluoroscopic gating of lung radiotherapy,” *Phys. Med. Biol.*, vol. 65, no. 8, p. 085014.
- [56] Keall, P., Poulsen, P. and Booth, J. T., (2019), “See, Think, and Act: Real-Time Adaptive Radiotherapy,” *Semin. Radiat. Oncol.*, vol. 29, no. 3, pp. 228–235.
- [57] Imura, M., Yamazaki, K., Shirato, H., Onimaru, R., Fujino, M., Shimizu, S., Harada, T., Ogura, S., Dosaka-Akita, H., Miyasaka, K. and Nishimura, M., (2005), “Insertion and fixation of fiducial markers for setup and tracking of lung tumors in radiotherapy,” *Int. J. Radiat. Oncol. Biol. Phys.*, vol. 63, no. 5, pp. 1442–1447.
- [58] Wiersma, R. D., McCabe, B. P., Belcher, A. H., Jensen, P. J., Smith, B. and Aydogan, B., (2016), “Technical Note: High temporal resolution characterization of gating response time,” *Med. Phys.*, vol. 43, no. 6Part1, pp. 2802–2806.

- [59] Valayer, S., Kim, D., Fogtman, A., Straube, U., Winnard, A., Caplan, N., Green, D. A., van Leeuwen, F. H. P. and Weber, T., (2020), “The Potential of Fasting and Caloric Restriction to Mitigate Radiation Damage—A Systematic Review,” *Front. Nutr.*, vol. 7, p. 584543.
- [60] Heiden, M. G. V., Cantley, L. C. and Thompson, C. B., (2009), “Understanding the warburg effect: The metabolic requirements of cell proliferation,” *Science (80-.)*, vol. 324, no. 5930, pp. 1029–1033.
- [61] Liberti, M. V. and Locasale, J. W., (2016), “The Warburg Effect: How Does it Benefit Cancer Cells?,” *Trends Biochem. Sci.*, vol. 41, no. 3, pp. 211–218.
- [62] Seyfried, B. T. N., Kiebish, M., Marsh, J. and Mukherjee, P., (2009), “Targeting energy metabolism in brain cancer through calorie restriction and the ketogenic diet.,” *J. Cancer Res. Ther.*, vol. 5, no. 9, pp. 7–15.
- [63] Harper, E. and Talbot, C. J., (2019), “Is it Time to Change Radiotherapy: The Dawning of Chronoradiotherapy?,” *Clin. Oncol.*, vol. 31, no. 5, pp. 326–335.
- [64] Van Roemeling, R. and Hrushesky, W. J. M., (1989), “Circadian patterning of continuous floxuridine infusion reduces toxicity and allows higher dose intensity in patients with widespread cancer,” *J. Clin. Oncol.*, vol. 7, no. 11, pp. 1710–1719.
- [65] Sancar, A., Lindsey-Boltz, L. A., Gaddameedhi, S., Selby, C. P., Ye, R., Chiou, Y. Y., Kemp, M. G., Hu, J., Lee, J. H. and Ozturk, N., (2015), “Circadian clock, cancer, and chemotherapy,” *Biochemistry*, vol. 54, no. 2, pp. 110–123.
- [66] Tang, Q., Xie, M., Yu, S., Zhou, X., Xie, Y., Chen, G., Guo, F. and Chen, L., (2019), “Periodic Oxaliplatin Administration in Synergy with PER2-Mediated PCNA Transcription Repression Promotes Chronochemotherapeutic Efficacy of OSCC,” *Adv. Sci.*, vol. 6, no. 21, p. 1900667.
- [67] Guo, P., Wang, H., Jiang, R. and Wang, Z., (2015), “The clinical effect study on malignant tumors with chronoradiotherapy,” *Biol. Rhythm Res.*, vol. 46, no. 2, pp. 249–255.
- [68] Johnke, R. M., Sattler, J. A. and Allison, R. R., (2014), “Radioprotective agents for radiation therapy: Future trends,” *Futur. Oncol.*, vol. 10, no. 15, pp. 2345–2357.
- [69] Hosseinimehr, S. J., (2007), “Trends in the development of radioprotective agents,” *Drug Discov. Today*, vol. 12, no. 19–20, pp. 794–805.
- [70] Mun, G. I., Kim, S., Choi, E., Kim, C. S. and Lee, Y. S., (2018), “Pharmacology of natural radioprotectors,” *Arch. Pharm. Res.*, vol. 41, pp. 1033–1050.
- [71] Newhauser, W. D. and Zhang, R., (2015), “The physics of proton therapy,” *Phys. Med. Biol.*, vol. 60, no. 8, pp. R155–R209.
- [72] Tsujii, H., (2017), “Overview of Carbon-ion Radiotherapy,” *J. Phys. Conf. Ser.*, vol. 777, p. 012032.
- [73] Otero, J., Ardid, M., Felis, I. and Herrero, A., (2018), “Acoustic Location of Bragg Peak for Hadrontherapy Monitoring,” *Proceedings*, vol. 4, no. 1, p. 6.
- [74] Lowe, M., Gosling, A., Nicholas, O., Underwood, T., Miles, E., Chang, Y.-C., Amos, R. A., Burnet, N. G., Clark, C. H., Patel, I., Tsang, Y., Sisson, N. and Gulliford, S., (2020), “Comparing Proton to Photon Radiotherapy Plans: UK Consensus Guidance for Reporting Under Uncertainty for Clinical Trials,” *Clin. Oncol.*, vol. 32, no. 7, pp. 459–466.
- [75] Shehzad, A., Park, J.-W., Lee, J. and Lee, Y. S., (2013), “Curcumin induces radiosensitivity of in vitro and in vivo cancer models by modulating pre-mRNA processing factor 4 (Prp4),” *Chem. Biol. Interact.*, vol. 206, no. 2, pp. 394–402.
- [76] Moeller, B. J., Richardson, R. A. and Dewhirst, M. W., (2007), “Hypoxia and radiotherapy: opportunities for improved outcomes in cancer treatment,” *Cancer Metastasis Rev.*, vol. 26, no. 2, pp. 241–248.
- [77] Boudou, C., Troprès, I., Rousseau, J., Lamalle, L., Adam, J. F., Estève, F. and Elleaume, H.,

- (2007), "Polymer gel dosimetry for synchrotron stereotactic radiotherapy and iodine dose-enhancement measurements," *Phys. Med. Biol.*, vol. 52, no. 16, pp. 4881–4892.
- [78] Zhang, D. G., Feygelman, V., Moros, E. G., Latifi, K. and Zhang, G. G., (2014), "Monte Carlo Study of Radiation Dose Enhancement by Gadolinium in Megavoltage and High Dose Rate Radiotherapy," *PLoS One*, vol. 9, no. 10, p. e109389.
- [79] Sykes, E. A., Dai, Q., Sarsons, C. D., Chen, J., Rocheleau, J. V., Hwang, D. M., Zheng, G., Cramb, D. T., Rinker, K. D. and Chan, W. C. W., (2016), "Tailoring nanoparticle designs to target cancer based on tumor pathophysiology," *Proc. Natl. Acad. Sci.*, vol. 113, no. 9, pp. E1142–E1151.
- [80] Riffle, S. and Hegde, R. S., (2017), "Modeling tumor cell adaptations to hypoxia in multicellular tumor spheroids," *J. Exp. Clin. Cancer Res.*, vol. 36, no. 1, p. 102.
- [81] Jing, X., Yang, F., Shao, C., Wei, K., Xie, M., Shen, H. and Shu, Y., (2019), "Role of hypoxia in cancer therapy by regulating the tumor microenvironment," *Mol. Cancer*, vol. 18, no. 1, p. 157.
- [82] Graham, K. and Unger, E., (2018), "Overcoming tumor hypoxia as a barrier to radiotherapy, chemotherapy and immunotherapy in cancer treatment," *Int. J. Nanomedicine*, vol. Volume 13, pp. 6049–6058.
- [83] Bennett, M. H., Feldmeier, J., Smee, R. and Milross, C., (2018), "Hyperbaric oxygenation for tumour sensitisation to radiotherapy," *Cochrane Database Syst. Rev.*
- [84] Yang, J., Li, W., Luo, L., Jiang, M., Zhu, C., Qin, B., Yin, H., Yuan, X., Yin, X., Zhang, J., Luo, Z., Du, Y. and You, J., (2018), "Hypoxic tumor therapy by hemoglobin-mediated drug delivery and reversal of hypoxia-induced chemoresistance," *Biomaterials*, vol. 182, pp. 145–156.
- [85] Nimalasena, S. *et al.*, (2020), "Intratumoral Hydrogen Peroxide With Radiation Therapy in Locally Advanced Breast Cancer: Results From a Phase 1 Clinical Trial," *Int. J. Radiat. Oncol.*, vol. 108, no. 4, pp. 1019–1029.
- [86] Ho, Y.-J., Chu, S.-W., Liao, E.-C., Fan, C.-H., Chan, H.-L., Wei, K.-C. and Yeh, C.-K., (2019), "Normalization of Tumor Vasculature by Oxygen Microbubbles with Ultrasound," *Theranostics*, vol. 9, no. 24, pp. 7370–7383.
- [87] Khan, M. S., Hwang, J., Seo, Y., Shin, K., Lee, K., Park, C., Choi, Y., Hong, J. W. and Choi, J., (2018), "Engineering oxygen nanobubbles for the effective reversal of hypoxia," *Artif. Cells, Nanomedicine, Biotechnol.*, vol. 46, no. sup3, pp. S318–S327.
- [88] Clarke, R. H., Moosa, S., Anzivino, M., Wang, Y., Floyd, D. H., Purow, B. W. and Lee, K. S., (2014), "Sustained Radiosensitization of Hypoxic Glioma Cells after Oxygen Pretreatment in an Animal Model of Glioblastoma and In Vitro Models of Tumor Hypoxia," *PLoS One*, vol. 9, no. 10, p. e111199.
- [89] Kamlah, F., Eul, B. G., Li, S., Lang, N., Marsh, L. M., Seeger, W., Grimminger, F., Rose, F. and Hänze, J., (2009), "Intravenous injection of siRNA directed against hypoxia-inducible factors prolongs survival in a Lewis lung carcinoma cancer model," *Cancer Gene Ther.*, vol. 16, no. 3, pp. 195–205.
- [90] Chen, Y., Gao, P., Wu, T., Pan, W., Li, N. and Tang, B., (2020), "Organelle-localized radiosensitizers," *Chem. Commun.*, vol. 56, no. 73, pp. 10621–10630.
- [91] Kang, L., Fan, B., Sun, P., Huang, W., Jin, M., Wang, Q. and Gao, Z., (2016), "An effective tumor-targeting strategy utilizing hypoxia-sensitive siRNA delivery system for improved anti-tumor outcome," *Acta Biomater.*, vol. 44, pp. 341–354.
- [92] Shukla, R., Bansal, V., Chaudhary, M., Basu, A., Bhone, R. R. and Sastry, M., (2005), "Biocompatibility of Gold Nanoparticles and Their Endocytotic Fate Inside the Cellular Compartment: A Microscopic Overview," *Langmuir*, vol. 21, no. 23, pp. 10644–10654.
- [93] Pricker, S. P., (1996), "Medical uses of gold compounds: Past, present and future," *Gold Bull.*,

- vol. 29, no. 2, pp. 53–60.
- [94] Herizchi, R., Abbasi, E., Milani, M. and Akbarzadeh, A., (2016), “Current methods for synthesis of gold nanoparticles,” *Artif. Cells, Nanomedicine, Biotechnol.*, vol. 44, no. 2, pp. 596–602.
- [95] Khan, A., Rashid, R., Murtaza, G. and Zahra, A., (2014), “Gold Nanoparticles: Synthesis and Applications in Drug Delivery,” *Trop. J. Pharm. Res.*, vol. 13, no. 7, p. 1169.
- [96] Her, S., Jaffray, D. A. and Allen, C., (2017), “Gold nanoparticles for applications in cancer radiotherapy: Mechanisms and recent advancements,” *Adv. Drug Deliv. Rev.*, vol. 109, pp. 84–101.
- [97] Cobley, C. M., Chen, J., Cho, E. C., Wang, L. V. and Xia, Y., (2011), “Gold nanostructures: a class of multifunctional materials for biomedical applications,” *Chem. Soc. Rev.*, vol. 40, no. 1, pp. 44–56.
- [98] Wu, Y., Ali, M. R. K., Chen, K., Fang, N. and El-Sayed, M. A., (2019), “Gold nanoparticles in biological optical imaging,” *Nano Today*, vol. 24, pp. 120–140.
- [99] Franken, N. A. P., Rodermond, H. M., Stap, J., Haveman, J. and van Bree, C., (2006), “Clonogenic assay of cells in vitro,” *Nat. Protoc.*, vol. 1, no. 5, pp. 2315–2319.
- [100] Berridge, M. V., Herst, P. M. and Tan, A. S., “Tetrazolium dyes as tools in cell biology: New insights into their cellular reduction,” in *Biotechnology Annual Review*, pp. 127–152.
- [101] Mosmann, T., (1983), “Rapid colorimetric assay for cellular growth and survival: Application to proliferation and cytotoxicity assays,” *J. Immunol. Methods*.
- [102] Bergwerf, H. and T. M. P., “MolView,” 2020. <https://molview.org/> (accessed Nov. 13, 2020).
- [103] Sakai, K. and Okada, S., (1984), “Radiation-Induced DNA Damage and Cellular Lethality in Cultured Mammalian Cells,” *Radiat. Res.*, vol. 98, no. 3, p. 479.
- [104] Kurashige, T., Shimamura, M. and Nagayama, Y., (2016), “Differences in quantification of DNA double-strand breaks assessed by 53BP1/γH2AX focus formation assays and the comet assay in mammalian cells treated with irradiation and N-acetyl-L-cysteine,” *J. Radiat. Res.*, vol. 57, no. 3, pp. 312–317.
- [105] Wang, H., Adhikari, S., Butler, B. E., Pandita, T. K., Mitra, S. and Hegde, M. L., “A Perspective on Chromosomal Double Strand Break Markers in Mammalian Cells,” *Jacobs J. Radiat. Oncol.*, vol. 1, no. 1.
- [106] Behrouzki, Z., Zohdiaghdam, R., Khalkhali, H. R. and Mousavi, F., (2019), “Evaluation of Gold Nanoparticle Size Effect on Dose Enhancement Factor in Megavoltage Beam Radiotherapy Using MAGICA Polymer Gel Dosimeter,” *J. Biomed. Phys. Eng.*, vol. 9, no. 1, pp. 89–96.
- [107] Farahani, S., Riyahi Alam, N., Haghgoo, S., Khoobi, M., Geraily, G. and Gorji, E., (2019), “Dosimetry and Radioenhancement Comparison of Gold Nanoparticles in Kilovoltage and Megavoltage Radiotherapy using MAGAT Polymer Gel Dosimeter,” *J. Biomed. Phys. Eng.*, vol. 9, no. 2, pp. 199–210.
- [108] Cho, S. H., (2005), “Estimation of tumour dose enhancement due to gold nanoparticles during typical radiation treatments: a preliminary Monte Carlo study,” *Phys. Med. Biol.*, vol. 50, no. 15, pp. N163–N173.
- [109] Zhang, S. X., Gao, J., Buchholz, T. A., Wang, Z., Salehpour, M. R., Drezek, R. A. and Yu, T.-K., (2009), “Quantifying tumor-selective radiation dose enhancements using gold nanoparticles: a monte carlo simulation study,” *Biomed. Microdevices*, vol. 11, no. 4, pp. 925–933.
- [110] Lechtman, E., Chattopadhyay, N., Cai, Z., Mashouf, S., Reilly, R. and Pignol, J. P., (2011), “Implications on clinical scenario of gold nanoparticle radiosensitization in regards to photon energy, nanoparticle size, concentration and location,” *Phys. Med. Biol.*, vol. 56, no. 15, pp. 4631–4647.

- [111] Gadoue, S. M. and Toomeh, D., (2019), “Enhancement of linear energy transfer in gold nanoparticles mediated radiation therapy,” *Phys. Medica*, vol. 60, pp. 22–29.
- [112] McMahon, S. J., Hyland, W. B., Muir, M. F., Coulter, J. A., Jain, S., Butterworth, K. T., Schettino, G., Dickson, G. R., Hounsell, A. R., O’Sullivan, J. M., Prise, K. M., Hirst, D. G. and Currell, F. J., (2011), “Nanodosimetric effects of gold nanoparticles in megavoltage radiation therapy,” *Radiother. Oncol.*, vol. 100, no. 3, pp. 412–416.
- [113] Jayarathna, S., Manohar, N., Ahmed, M. F., Krishnan, S. and Cho, S. H., (2019), “Evaluation of dose point kernel rescaling methods for nanoscale dose estimation around gold nanoparticles using Geant4 Monte Carlo simulations,” *Sci. Rep.*, vol. 9, no. 1, p. 3583.
- [114] Chow, J. C. L., “Recent progress in Monte Carlo simulation on gold nanoparticle radiosensitization,” *AIMS Biophysics*. 2018, doi: 10.3934/biophy.2018.4.231.
- [115] Sakata, D., Kyriakou, I., Okada, S., Tran, H. N., Lampe, N., Guatelli, S., Bordage, M.-C., Ivanchenko, V., Murakami, K., Sasaki, T., Emfietzoglou, D. and Incerti, S., (2018), “Geant4-DNA track-structure simulations for gold nanoparticles: The importance of electron discrete models in nanometer volumes,” *Med. Phys.*, vol. 45, no. 5, pp. 2230–2242.
- [116] Sung, W., Ye, S.-J., McNamara, A. L., McMahon, S. J., Hainfeld, J., Shin, J., Smilowitz, H. M., Paganetti, H. and Schuemann, J., (2017), “Dependence of gold nanoparticle radiosensitization on cell geometry,” *Nanoscale*, vol. 9, no. 18, pp. 5843–5853.
- [117] Regulla, D. F., Hieber, L. B. and Seidenbusch, M., (1998), “Physical and Biological Interface Dose Effects in Tissue due to X-Ray-Induced Release of Secondary Radiation from Metallic Gold Surfaces,” *Radiat. Res.*, vol. 150, no. 1, p. 92.
- [118] Butterworth, K. T., Coulter, J. A., Jain, S., Forker, J., McMahon, S. J., Schettino, G., Prise, K. M., Currell, F. J. and Hirst, D. G., (2010), “Evaluation of cytotoxicity and radiation enhancement using 1.9 nm gold particles: potential application for cancer therapy,” *Nanotechnology*, vol. 21, no. 29, p. 295101.
- [119] Jain, S., Coulter, J. A., Hounsell, A. R., Butterworth, K. T., McMahon, S. J., Hyland, W. B., Muir, M. F., Dickson, G. R., Prise, K. M., Currell, F. J., O’Sullivan, J. M. and Hirst, D. G., (2011), “Cell-Specific Radiosensitization by Gold Nanoparticles at Megavoltage Radiation Energies,” *Int. J. Radiat. Oncol.*, vol. 79, no. 2, pp. 531–539.
- [120] Lechtman, E., Mashouf, S., Chattopadhyay, N., Keller, B. M., Lai, P., Cai, Z., Reilly, R. M. and Pignol, J.-P., (2013), “A Monte Carlo-based model of gold nanoparticle radiosensitization accounting for increased radiobiological effectiveness,” *Phys. Med. Biol.*, vol. 58, no. 10, pp. 3075–3087.
- [121] Subiel, A., Ashmore, R. and Schettino, G., (2016), “Standards and Methodologies for Characterizing Radiobiological Impact of High-Z Nanoparticles,” *Theranostics*, vol. 6, no. 10, pp. 1651–1671.
- [122] Kellerer, A. M. and Rossi, H. H., (1978), “A generalized formulation of dual radiation action,” *Radiat. Res.*, vol. 75, no. 3, pp. 471–488.
- [123] Rutz, H. P., Coucke, P. A. and Mirimanoff, R., (1991), “A linear-quadratic model of cell survival considering both sublethal and potentially lethal radiation damage,” *Radiother. Oncol.*, vol. 21, no. 4, pp. 273–276.
- [124] McMahon, S. J., (2018), “The linear quadratic model: usage, interpretation and challenges,” *Phys. Med. Biol.*, vol. 64, no. 1, p. 01TR01.
- [125] Rezaei, H., Zabihzadeh, M., Ghorbani, M., Goli Ahmadabad, F. and Mostaghimi, H., (2017), “Evaluation of dose enhancement in presence of gold nanoparticles in eye brachytherapy by 103Pd source,” *Australas. Phys. Eng. Sci. Med.*, vol. 40, no. 3, pp. 545–553.
- [126] Rosa, S., Connolly, C., Schettino, G., Butterworth, K. T. and Prise, K. M., (2017), “Biological mechanisms of gold nanoparticle radiosensitization,” *Cancer Nanotechnol.*, vol. 8, no. 1, p. 2.

- [127] Ajnai, G., Chiu, A., Kan, T., Cheng, C. C., Tsai, T. H. and Chang, J., (2014), “Trends of Gold Nanoparticle-based Drug Delivery System in Cancer Therapy,” *J. Exp. Clin. Med.*, vol. 6, no. 6, pp. 172–178.
- [128] Herold, D. M., Das, I. J., Stobbe, C. C., Iyer, R. V. and Chapman, J. D., (2000), “Gold microspheres: A selective technique for producing biologically effective dose enhancement,” *Int. J. Radiat. Biol.*, vol. 76, no. 10, pp. 1357–1364.
- [129] Butterworth, K. T., McMahon, S. J., Currell, F. J. and Prise, K. M., (2012), “Physical basis and biological mechanisms of gold nanoparticle radiosensitization,” *Nanoscale*, vol. 4, no. 16, p. 4830.
- [130] Kempson, I., (2021), “Mechanisms of nanoparticle radiosensitization,” *WIREs Nanomedicine and Nanobiotechnology*, vol. 13, no. 1.
- [131] Shrestha, S., Cooper, L. N., Andreev, O. A., Reshetnyak, Y. K. and Antosh, M. P., (2016), “Gold Nanoparticles for Radiation Enhancement in Vivo,” *Jacobs J. Radiat. Oncol.*, vol. 3, no. 1.
- [132] Lin, Y., McMahon, S. J., Scarpelli, M., Paganetti, H. and Schuemann, J., (2014), “Comparing gold nano-particle enhanced radiotherapy with protons, megavoltage photons and kilovoltage photons: A Monte Carlo simulation,” *Phys. Med. Biol.*, vol. 59, no. 24, pp. 7675–7689.
- [133] Jain, S., Hirst, D. G. and O’Sullivan, J. M., (2012), “Gold nanoparticles as novel agents for cancer therapy,” *Br. J. Radiol.*, vol. 85, no. 1010, pp. 101–113.
- [134] Khadem Abolfazli, M., Mahdavi, S. R. and Ataei, G., (2015), “Studying Effects of Gold Nanoparticle on Dose Enhancement in Megavoltage Radiation,” *J. Biomed. Phys. Eng.*, vol. 5, no. 4, pp. 185–90.
- [135] McMahon, S. J., Hyland, W. B., Brun, E., Butterworth, K. T., Coulter, J. A., Douki, T., Hirst, D. G., Jain, S., Kavanagh, A. P., Krpetic, Z., Mendenhall, M. H., Muir, M. F., Prise, K. M., Requardt, H., Sanche, L., Schettino, G., Currell, F. J. and Sicard-Roselli, C., (2011), “Energy Dependence of Gold Nanoparticle Radiosensitization in Plasmid DNA,” *J. Phys. Chem. C*, vol. 115, no. 41, pp. 20160–20167.
- [136] Butterworth, K. T., McMahon, S. J., Taggart, L. E. and Prise, K. M., (2013), “Radiosensitization by gold nanoparticles: Effective at megavoltage energies and potential role of oxidative stress,” *Transl. Cancer Res.*
- [137] Xiao, F., Zheng, Y., Cloutier, P., He, Y., Hunting, D. and Sanche, L., (2011), “On the role of low-energy electrons in the radiosensitization of DNA by gold nanoparticles,” *Nanotechnology*, vol. 22, no. 46, p. 465101.
- [138] Sanche, L., (2016), “Interaction of low energy electrons with DNA: Applications to cancer radiation therapy,” *Radiat. Phys. Chem.*, vol. 128, pp. 36–43.
- [139] Taggart, L. E., McMahon, S. J., Currell, F. J., Prise, K. M. and Butterworth, K. T., (2014), “The role of mitochondrial function in gold nanoparticle mediated radiosensitisation,” *Cancer Nanotechnol.*, vol. 5, no. 1, p. 5.
- [140] Howard, D., Sebastian, S., Le, Q. V.-C., Thierry, B. and Kempson, I., (2020), “Chemical Mechanisms of Nanoparticle Radiosensitization and Radioprotection: A Review of Structure-Function Relationships Influencing Reactive Oxygen Species,” *Int. J. Mol. Sci.*, vol. 21, no. 2, p. 579.
- [141] Cheng, N. N., Starkewolf, Z., Davidson, R. A., Sharmah, A., Lee, C., Lien, J. and Guo, T., (2012), “Chemical Enhancement by Nanomaterials under X-ray Irradiation,” *J. Am. Chem. Soc.*, vol. 134, no. 4, pp. 1950–1953.
- [142] Gilles, M., Brun, E. and Sicard-Roselli, C., (2018), “Quantification of hydroxyl radicals and solvated electrons produced by irradiated gold nanoparticles suggests a crucial role of interfacial water,” *J. Colloid Interface Sci.*, vol. 525, pp. 31–38.
- [143] Misawa, M. and Takahashi, J., (2011), “Generation of reactive oxygen species induced by gold

- nanoparticles under x-ray and UV Irradiations,” *Nanomedicine Nanotechnology, Biol. Med.*, vol. 7, no. 5, pp. 604–614.
- [144] Pan, Y., Leifert, A., Ruau, D., Neuss, S., Bornemann, J., Schmid, G., Brandau, W., Simon, U. and Jahnen-Dechent, W., (2009), “Gold nanoparticles of diameter 1.4 nm trigger necrosis by oxidative stress and mitochondrial damage,” *Small*, vol. 5, no. 18, pp. 2067–2076.
- [145] Zheng, Y., Cloutier, P., Hunting, D. J. and Sanche, L., (2008), “Radiosensitization by Gold Nanoparticles: Comparison of DNA Damage Induced by Low and High-Energy Electrons,” *J. Biomed. Nanotechnol.*, vol. 4, no. 4, pp. 469–473.
- [146] Yao, X., Huang, C., Chen, X., Zheng, Y. and Sanche, L., (2015), “Chemical Radiosensitivity of DNA Induced by Gold Nanoparticles,” *J. Biomed. Nanotechnol.*, vol. 11, no. 3, pp. 478–485.
- [147] Liu, Y., Zhang, P., Li, F., Jin, X., Li, J., Chen, W. and Li, Q., (2018), “Metal-based NanoEnhancers for Future Radiotherapy: Radiosensitizing and Synergistic Effects on Tumor Cells,” *Theranostics*, vol. 8, no. 7, pp. 1824–1849.
- [148] Liu, F., Ma, D., Chen, W., Chen, X., Qian, Y., Zhao, Y., Hu, T., Yin, R., Zhu, Y., Zhang, Y., Zhang, Y. and Zhao, W., (2019), “Gold Nanoparticles Suppressed Proliferation, Migration, and Invasion in Papillary Thyroid Carcinoma Cells via Downregulation of CCT3,” *J. Nanomater.*, vol. 2019, pp. 1–12.
- [149] Turnbull, T., Douglass, M., Williamson, N. H., Howard, D., Bhardwaj, R., Lawrence, M., Paterson, D. J., Bezak, E., Thierry, B. and Kempson, I. M., (2019), “Cross-Correlative Single-Cell Analysis Reveals Biological Mechanisms of Nanoparticle Radiosensitization,” *ACS Nano*, vol. 13, no. 5, pp. 5077–5090.
- [150] Roa, W., Zhang, X., Guo, L., Shaw, A., Hu, X., Xiong, Y., Gulavita, S., Patel, S., Sun, X., Chen, J., Moore, R. and Xing, J. Z., (2009), “Gold nanoparticle sensitize radiotherapy of prostate cancer cells by regulation of the cell cycle,” *Nanotechnology*, vol. 20, no. 37, p. 375101.
- [151] Li, Q., Huang, C., Liu, L., Hu, R. and Qu, J., (2018), “Effect of Surface Coating of Gold Nanoparticles on Cytotoxicity and Cell Cycle Progression,” *Nanomaterials*, vol. 8, no. 12, p. 1063.
- [152] Xu, W., Luo, T., Pang, B., Li, P., Zhou, C., Huang, P., Zhang, C., Ren, Q., Hu, W. and Fu, S., (2012), “The radiosensitization of melanoma cells by gold nanorods irradiated with MV X-ray,” *Nano Biomed. Eng.*, vol. 4, no. 1.
- [153] Mackey, M. A. and El-Sayed, M. A., (2014), “Chemosensitization of Cancer Cells via Gold Nanoparticle-Induced Cell Cycle Regulation,” *Photochem. Photobiol.*, vol. 90, no. 2, pp. 306–312.
- [154] Hanžić, N., Horvat, A., Bibić, J., Unfried, K., Jurkin, T., Dražić, G., Marijanović, I., Slade, N. and Gotić, M., (2018), “Syntheses of gold nanoparticles and their impact on the cell cycle in breast cancer cells subjected to megavoltage X-ray irradiation,” *Mater. Sci. Eng. C*, vol. 91, pp. 486–495.
- [155] Mendes, F., Groessel, M., Nazarov, A. A., Tsybin, Y. O., Sava, G., Santos, I., Dyson, P. J. and Casini, A., (2011), “Metal-Based Inhibition of Poly(ADP-ribose) Polymerase – The Guardian Angel of DNA,” *J. Med. Chem.*, vol. 54, no. 7, pp. 2196–2206.
- [156] Balfourier, A., Luciani, N., Wang, G., Lelong, G., Ersen, O., Khelfa, A., Alloyeau, D., Gazeau, F. and Carn, F., (2020), “Unexpected intracellular biodegradation and recrystallization of gold nanoparticles,” *Proc. Natl. Acad. Sci.*, vol. 117, no. 1, pp. 103–113.
- [157] Handel, M. L., Watts, C. K., DeFazio, A., Day, R. O. and Sutherland, R. L., (1995), “Inhibition of AP-1 binding and transcription by gold and selenium involving conserved cysteine residues in Jun and Fos,” *Proc. Natl. Acad. Sci.*, vol. 92, no. 10, pp. 4497–4501.
- [158] Daruich De Souza, C., Ribeiro Nogueira, B. and Rostelato, M. E. C. M., (2019), “Review of the methodologies used in the synthesis gold nanoparticles by chemical reduction,” *J. Alloys Compd.*, vol. 798, pp. 714–740.

- [159] Ashley, M. J., Bourgeois, M. R., Murthy, R. R., Laramy, C. R., Ross, M. B., Naik, R. R., Schatz, G. C. and Mirkin, C. A., (2018), "Shape and Size Control of Substrate-Grown Gold Nanoparticles for Surface-Enhanced Raman Spectroscopy Detection of Chemical Analytes," *J. Phys. Chem. C*, vol. 122, no. 4, pp. 2307–2314.
- [160] Kolb, H. C., Finn, M. G. and Sharpless, K. B., (2001), "Click Chemistry: Diverse Chemical Function from a Few Good Reactions," *Angew. Chemie - Int. Ed.*, vol. 40, no. 11, pp. 2004–2021.
- [161] Chen, Y.-S., Frey, W., Kim, S., Homan, K., Kruizinga, P., Sokolov, K. and Emelianov, S., (2010), "Enhanced thermal stability of silica-coated gold nanorods for photoacoustic imaging and image-guided therapy," *Opt. Express*, vol. 18, no. 9, p. 8867.
- [162] Shim, J. H., Kim, J., Lee, C. and Lee, Y., (2011), "Porous Pd layer-coated au nanoparticles supported on carbon: Synthesis and electrocatalytic activity for oxygen reduction in acid media," *Chem. Mater.*, vol. 23, no. 21, pp. 4694–4700.
- [163] Perry, H. L., Botnar, R. M. and Wilton-Ely, J. D. E. T., (2020), "Gold nanomaterials functionalised with gadolinium chelates and their application in multimodal imaging and therapy," *Chem. Commun.*, vol. 56, no. 29, pp. 4037–4046.
- [164] Su, W., Chen, C., Wang, T., Li, X., Liu, Y., Wang, H., Zhao, S., Zuo, C., Sun, G. and Bu, W., (2020), "Radionuclide-labeled gold nanoparticles for nuclei-targeting internal radio-immunity therapy," *Mater. Horizons*, vol. 7, no. 4, pp. 1115–1125.
- [165] Zhang, L., Chen, H., Wang, L., Liu, T., Yeh, J., Lu, G., Yang, L. and Mao, H., (2010), "Delivery of therapeutic radioisotopes using nanoparticle platforms: Potential benefit in systemic radiation therapy," *Nanotechnol. Sci. Appl.*, vol. 3, no. 1, pp. 159–170.
- [166] Zhang, X.-D., Wu, D., Shen, X., Liu, P.-X., Yang, N., Zhao, B., Zhang, H., Sun, Y. M., Zhang, L.-A. and Fan, F.-Y., (2011), "Size-dependent in vivo toxicity of PEG-coated gold nanoparticles," *Int. J. Nanomedicine*, vol. 6, pp. 2071–2081.
- [167] Chanana, M., Rivera-gil, P., Correa-Duarte, M. A., Liz-Marzán, L. M. and Parak, W. J., (2013), "Physicochemical properties of protein-coated gold nanoparticles in biological fluids and cells before and after proteolytic digestion," *Angew. Chemie - Int. Ed.*, vol. 52, no. 15, pp. 4179–4183.
- [168] McCulloch, A., Bennie, L., Coulter, J. A., McCarthy, H. O., Dromey, B., Grimes, D. R., Quinn, P., Villagomez-Bernabe, B. and Currell, F., (2019), "Nuclear Uptake of Gold Nanoparticles Deduced Using Dual-Angle X-Ray Fluorescence Mapping," *Part. Part. Syst. Charact.*, vol. 36, no. 9.
- [169] Chattopadhyay, N., Cai, Z., Pignol, J. P., Keller, B., Lechtman, E., Bendayan, R. and Reilly, R. M., (2010), "Design and characterization of HER-2-targeted gold nanoparticles for enhanced X-radiation treatment of locally advanced breast cancer," *Mol. Pharm.*, vol. 7, no. 6, pp. 2194–2206.
- [170] Dul, M., Nikolic, T., Stefanidou, M., McAteer, M. A., Williams, P., Mous, J., Roep, B. O., Kochba, E., Levin, Y., Peakman, M., Wong, F. S., Dayan, C. M., Tatovic, D., Coulman, S. A. and Birchall, J. C., (2019), "Conjugation of a peptide autoantigen to gold nanoparticles for intradermally administered antigen specific immunotherapy," *Int. J. Pharm.*, vol. 562, pp. 303–312.
- [171] Mackey, M. A., Saira, F., Mahmoud, M. A. and El-Sayed, M. A., (2013), "Inducing cancer cell death by targeting its nucleus: Solid gold nanospheres versus hollow gold nanocages," *Bioconjug. Chem.*, vol. 24, no. 6, pp. 897–906.
- [172] Smith, S. A., Selby, L. I., Johnston, A. P. R. and Such, G. K., (2019), "The Endosomal Escape of Nanoparticles: Toward More Efficient Cellular Delivery," *Bioconjug. Chem.*, vol. 30, no. 2, pp. 263–272.
- [173] Maeda, H. and Matsumura, Y., (1986), "A New Concept for Macromolecular Therapeutics in Cancer Chemotherapy: Mechanism of Tumoritropic Accumulation of Proteins and the

- Antitumor Agent Smancs,” *Cancer Res.*, vol. 46, no. 8, pp. 6387–6392.
- [174] Chauhan, V. P., Popović, Z., Chen, O., Cui, J., Fukumura, D., Bawendi, M. G. and Jain, R. K., (2011), “Fluorescent nanorods and nanospheres for real-time in vivo probing of nanoparticle shape-dependent tumor penetration,” *Angew. Chemie - Int. Ed.*, vol. 50, no. 48, pp. 11417–11420.
- [175] Stylianopoulos, T., Soteriou, K., Fukumura, D. and Jain, R. K., (2013), “Cationic nanoparticles have superior transvascular flux into solid tumors: Insights from a mathematical model,” *Ann. Biomed. Eng.*, vol. 41, no. 1, pp. 68–77.
- [176] Perry, J. L., Reuter, K. G., Luft, J. C., Pecot, C. V., Zamboni, W. and DeSimone, J. M., (2017), “Mediating Passive Tumor Accumulation through Particle Size, Tumor Type, and Location,” *Nano Lett.*, vol. 17, no. 5, pp. 2879–2886.
- [177] Stylianopoulos, T., (2013), “EPR-effect: Utilizing size-dependent nanoparticle delivery to solid tumors,” *Ther. Deliv.*, vol. 4, no. 4, pp. 421–423.
- [178] Kobayashi, H., Watanabe, R. and Choyke, P. L., (2014), “Improving conventional enhanced permeability and retention (EPR) effects; What is the appropriate target?,” *Theranostics*, vol. 4, no. 1, pp. 81–89.
- [179] Charbgoon, F., Nejabat, M., Abnous, K., Soltani, F., Taghdisi, S. M., Alibolandi, M., Thomas Shier, W., Steele, T. W. J. and Ramezani, M., (2018), “Gold nanoparticle should understand protein corona for being a clinical nanomaterial,” *J. Control. Release*, vol. 272, pp. 39–53.
- [180] Hansen, A. E., Petersen, A. L., Henriksen, J. R., Boerresen, B., Rasmussen, P., Elema, D. R., Rosenschöld, P. M. A., Kristensen, A. T., Kjær, A. and Andresen, T. L., (2015), “Positron Emission Tomography Based Elucidation of the Enhanced Permeability and Retention Effect in Dogs with Cancer Using Copper-64 Liposomes,” *ACS Nano*, vol. 9, no. 7, pp. 6985–6995.
- [181] Wang, A. Z., (2015), “EPR or no EPR? The billion-dollar question,” *Sci. Transl. Med.*, vol. 7, no. 294, pp. 294ec112-294ec112.
- [182] Attia, M. F., Anton, N., Wallyn, J., Omran, Z. and Vandamme, T. F., (2019), “An overview of active and passive targeting strategies to improve the nanocarriers efficiency to tumour sites,” *J. Pharm. Pharmacol.*, vol. 71, no. 8, pp. 1185–1198.
- [183] Wang, C., Bao, C., Liang, S., Fu, H., Wang, K., Deng, M., Liao, Q. and Cui, D., (2014), “RGD-conjugated silica-coated gold nanorods on the surface of carbon nanotubes for targeted photoacoustic imaging of gastric cancer,” *Nanoscale Res. Lett.*, vol. 9, no. 1, pp. 1–10.
- [184] Pirollo, K. F. and Chang, E. H., (2008), “Does a targeting ligand influence nanoparticle tumor localization or uptake?,” *Trends Biotechnol.*, vol. 26, no. 10, pp. 552–558.
- [185] Haute, D. Van and Berlin, J. M., (2017), “Challenges in realizing selectivity for nanoparticle biodistribution and clearance: lessons from gold nanoparticles,” *Ther. Deliv.*, vol. 8, no. 9, pp. 763–774.
- [186] Chithrani, B. D. and Chan, W. C. W., (2007), “Elucidating the mechanism of cellular uptake and removal of protein-coated gold nanoparticles of different sizes and shapes,” *Nano Lett.*, vol. 7, no. 6, pp. 1542–1550.
- [187] Jiao, C. Y., Delaroche, D., Burlina, F., Alves, I. D., Chassaing, G. and Sagan, S., (2009), “Translocation and endocytosis for cell-penetrating peptide internalization,” *J. Biol. Chem.*, vol. 284, no. 49, pp. 33957–33965.
- [188] Cruz, E. and Kayser, V., (2019), “Synthesis and enhanced cellular uptake in vitro of anti-HER2 multifunctional gold nanoparticles,” *Cancers (Basel)*, vol. 11, no. 6, p. 870.
- [189] Shah, A. J., Alles, E. J., Box, C., Eccles, S. A., Robinson, S. P., deSouza, N. and Bamber, J. C., “Non-invasive molecular profiling of cancer using photoacoustic imaging of functionalized gold nanorods,” in *Photons Plus Ultrasound: Imaging and Sensing 2014*, vol. 8943, p. 89435G, doi: 10.1117/12.2038412.

- [190] Patra, A., Ding, T., Engudar, G., Wang, Y., Dykas, M. M., Liedberg, B., Kah, J. C. Y., Venkatesan, T. and Drum, C. L., (2016), “Component-Specific Analysis of Plasma Protein Corona Formation on Gold Nanoparticles Using Multiplexed Surface Plasmon Resonance,” *Small*, vol. 12, no. 9, pp. 1174–1182.
- [191] García-Álvarez, R., Hadjidemetriou, M., Sánchez-Iglesias, A., Liz-Marzán, L. M. and Kostarelos, K., (2018), “In vivo formation of protein corona on gold nanoparticles. the effect of their size and shape,” *Nanoscale*, vol. 10, no. 3, pp. 1256–1264.
- [192] Nativo, P., Prior, I. A. and Brust, M., (2008), “Uptake and intracellular fate of surface-modified gold nanoparticles,” *ACS Nano*, vol. 2, no. 8, pp. 1639–1644.
- [193] Li, Y. and Monteiro-Riviere, N. A., (2016), “Mechanisms of cell uptake, inflammatory potential and protein corona effects with gold nanoparticles,” *Nanomedicine*, vol. 11, no. 24, pp. 3185–3203.
- [194] Selby, L. I., Cortez-Jugo, C. M., Such, G. K. and Johnston, A. P. R., (2017), “Nanoescapology: progress toward understanding the endosomal escape of polymeric nanoparticles,” *Wiley Interdiscip. Rev. Nanomedicine Nanobiotechnology*, vol. 9, no. 5.
- [195] Mahan, M. M. and Doiron, A. L., (2018), “Gold Nanoparticles as X-Ray, CT, and Multimodal Imaging Contrast Agents: Formulation, Targeting, and Methodology,” *J. Nanomater.*, vol. 2018, pp. 1–15.
- [196] Yi, C., Liu, D., Fong, C.-C., Zhang, J. and Yang, M., (2010), “Gold Nanoparticles Promote Osteogenic Differentiation of Mesenchymal Stem Cells through p38 MAPK Pathway,” *ACS Nano*, vol. 4, no. 11, pp. 6439–6448.
- [197] Fallahpoor, M., Abbasi, M., Parach, A. A. and Kalantari, F., (2017), “Internal dosimetry for radioembolization therapy with Yttrium-90 microspheres,” *J. Appl. Clin. Med. Phys.*, vol. 18, no. 2, pp. 176–180.
- [198] Cheheltani, R., Ezzibdeh, R. M., Chhour, P., Pulaparthy, K., Kim, J., Jurcova, M., Hsu, J. C., Blundell, C., Litt, H. I., Ferrari, V. A., Allcock, H. R., Sehgal, C. M. and Cormode, D. P., (2016), “Tunable, biodegradable gold nanoparticles as contrast agents for computed tomography and photoacoustic imaging,” *Biomaterials*, vol. 102, pp. 87–97.
- [199] Eghtedari, M., Oraevsky, A., Copland, J. A., Kotov, N. A., Conjusteau, A. and Motamedi, M., (2007), “High sensitivity of in vivo detection of gold nanorods using a laser optoacoustic imaging system,” *Nano Lett.*, vol. 7, no. 7, pp. 1914–1918.
- [200] Bell, A. G., (1880), “Upon the production and reproduction of sound by light,” *J. Soc. Telegr. Eng.*, vol. 9, no. 34, pp. 404–426.
- [201] Kreuzer, L. B., (1971), “Ultralow gas concentration infrared absorption spectroscopy,” *J. Appl. Phys.*, vol. 42, no. 7, pp. 2934–2943.
- [202] Tam, A. C., (1986), “Applications of photoacoustic sensing techniques,” *Rev. Mod. Phys.*, vol. 58, no. 2, pp. 381–431.
- [203] Park, S., Aglyamov, S. R., Scott, W. G., Emelianov, S. Y., Sethuraman, S., Rubin, J. M., Shah, J., Karpouk, A. B., Mallidi, S. and Smalling, R. W., “Synergy and applications of combined ultrasound, elasticity, and photoacoustic imaging,” in *Proceedings - IEEE Ultrasonics Symposium*, vol. 1, pp. 405–415, doi: 10.1109/ULTSYM.2006.114.
- [204] Sordillo, D. C., Sordillo, L. A., Sordillo, P. P. and Alfano, R. R., “Fourth near-infrared optical window for assessment of bone and other tissues,” in *Photonic Therapeutics and Diagnostics XII*, vol. 9689, p. 96894J, doi: 10.1117/12.2214320.
- [205] Natarajan, S., Foreman, K. M., Soriano, M. I., Rossen, N. S., Shehade, H., Fregoso, D. R., Eggold, J. T., Krishnan, V., Dorigo, O., Krieg, A. J., Heilshorn, S. C., Sinha, S., Fuh, K. C. and Rankin, E. B., (2019), “Collagen remodeling in the hypoxic tumor- mesothelial niche promotes ovarian cancer metastasis,” *Cancer Res.*

- [206] Jolly, L. A., Novitskiy, S., Owens, P., Massoll, N., Cheng, N., Fang, W., Moses, H. L. and Franco, A. T., (2016), “Fibroblast-mediated collagen remodeling within the tumor microenvironment facilitates progression of thyroid cancers driven by brafv600e and pten loss,” *Cancer Res.*
- [207] Anderson, R. R. and Parrish, J. A., (1981), “The optics of human skin,” *J. Invest. Dermatol.*, vol. 77, no. 1, pp. 13–19.
- [208] Smith, A. M., Mancini, M. C. and Nie, S., (2009), “Bioimaging: Second window for in vivo imaging,” *Nat. Nanotechnol.*
- [209] Sordillo, L. A., Pu, Y., Pratavieira, S., Budansky, Y. and Alfano, R. R., (2014), “Deep optical imaging of tissue using the second and third near-infrared spectral windows,” *J. Biomed. Opt.*
- [210] Xu, M. and Wang, L. V., (2006), “Photoacoustic imaging in biomedicine,” *Rev. Sci. Instrum.*, vol. 77, no. 4, p. 041101.
- [211] Link, S., Burda, C., Nikoobakht, B. and El-Sayed, M. A., (2000), “Laser-induced shape changes of colloidal gold nanorods using femtosecond and nanosecond laser pulses,” *J. Phys. Chem. B*, vol. 104, no. 26, pp. 6152–6163.
- [212] Akchurin, G., Khlebtsov, B., Akchurin, G., Tuchin, V., Zharov, V. and Khlebtsov, N., (2008), “Gold nanoshell photomodification under a single-nanosecond laser pulse accompanied by color-shifting and bubble formation phenomena,” *Nanotechnology*, vol. 19, no. 1.
- [213] Zharov, V. P., (2011), “Ultrasharp nonlinear photothermal and photoacoustic resonances and holes beyond the spectral limit,” *Nat. Photonics*, vol. 5, no. 2, pp. 110–116.
- [214] Cox, B., Laufer, J. G., Arridge, S. R. and Beard, P. C., (2012), “Quantitative spectroscopic photoacoustic imaging: a review,” *J. Biomed. Opt.*, vol. 17, no. 6, p. 061202.
- [215] Cook, J. R., Frey, W. and Emelianov, S., (2013), “Quantitative photoacoustic imaging of nanoparticles in cells and tissues,” *ACS Nano*, vol. 7, no. 2, pp. 1272–1280.
- [216] Prael, S., “OMLC.org,” *Optical absorption of Hemoglobin*, 1999. <https://omlc.org/spectra/hemoglobin/summary.html> (accessed Feb. 22, 2021).
- [217] Cao, Q., Zhegalova, N. G., Wang, S. T., Akers, W. J. and Berezin, M. Y., (2013), “Multispectral imaging in the extended near-infrared window based on endogenous chromophores,” *J. Biomed. Opt.*, vol. 18, no. 10, p. 101318.
- [218] Hosseinaee, Z., Tummon Simmons, J. A. and Reza, P. H., (2021), “Dual-Modal Photoacoustic Imaging and Optical Coherence Tomography [Review],” *Front. Phys.*, vol. 8.
- [219] Attia, A. B. E., Balasundaram, G., Moothanchery, M., Dinish, U. S., Bi, R., Ntziachristos, V. and Olivo, M., (2019), “A review of clinical photoacoustic imaging: Current and future trends,” *Photoacoustics*, vol. 16, p. 100144.
- [220] Chen, Z., Yang, S. and Xing, D., (2012), “In vivo detection of hemoglobin oxygen saturation and carboxyhemoglobin saturation with multiwavelength photoacoustic microscopy,” *Opt. Lett.*, vol. 37, no. 16, p. 3414.
- [221] Rockwell, S., Dobrucki, I., Kim, E., Marrison, S. and Vu, V., (2009), “Hypoxia and Radiation Therapy: Past History, Ongoing Research, and Future Promise,” *Curr. Mol. Med.*, vol. 9, no. 4, pp. 442–458.
- [222] Radovanovic, Z., Golubovic, A., Plzak, A., Stojiljkovic, B. and Radovanovic, D., (2004), “Blue dye versus combined blue dye-radioactive tracer technique in detection of sentinel lymph node in breast cancer,” *Eur. J. Surg. Oncol.*, vol. 30, no. 9, pp. 913–917.
- [223] Stoffels, I., Morscher, S., Helfrich, I., Hillen, U., Leyh, J., Burton, N. C., Sardella, T. C. P., Claussen, J., Poeppel, T. D., Bachmann, H. S., Roesch, A., Griewank, K., Schadendorf, D., Gunzer, M. and Klode, J., (2015), “Metastatic status of sentinel lymph nodes in melanoma determined noninvasively with multispectral optoacoustic imaging,” *Sci. Transl. Med.*, vol. 7, no. 317, pp. 317ra199–317ra199.

- [224] Morscher, S., Driessen, W. H. P., Claussen, J. and Burton, N. C., (2014), “Semi-quantitative multispectral optoacoustic tomography (MSOT) for volumetric PK imaging of gastric emptying,” *Photoacoustics*, vol. 2, no. 3, pp. 103–110.
- [225] Jiang, X., Du, B., Tang, S., Hsieh, J.-T. and Zheng, J., (2019), “Photoacoustic Imaging of Nanoparticle Transport in the Kidneys at High Temporal Resolution,” *Angew. Chemie - Int. Ed.*, vol. 58, no. 18, pp. 5994–6000.
- [226] Bhattacharyya, K., Goldschmidt, B. S., Hannink, M., Alexander, S., Jurkevic, A. and Viator, J. A., (2012), “Gold Nanoparticle-Mediated Detection of Circulating Cancer Cells,” *Clin. Lab. Med.*, vol. 32, no. 1, pp. 89–101.
- [227] Chuah, S. Y., Attia, A. B. E., Ho, C. J. H., Li, X., Lee, J. S.-S., Tan, M. W. P., Yong, A. A., Tan, A. W. M., Razansky, D., Olivo, M. and Thng, S. T. G., (2019), “Volumetric Multispectral Optoacoustic Tomography for 3-Dimensional Reconstruction of Skin Tumors: A Further Evaluation with Histopathologic Correlation,” *J. Invest. Dermatol.*, vol. 139, no. 2, pp. 481–485.
- [228] Heijblom, M., Piras, D., van den Engh, F. M., van der Schaaf, M., Klaase, J. M., Steenbergen, W. and Manohar, S., (2016), “The state of the art in breast imaging using the Twente Photoacoustic Mammoscope: results from 31 measurements on malignancies,” *Eur. Radiol.*, vol. 26, no. 11, pp. 3874–3887.
- [229] Manohar, S. and Dantuma, M., (2019), “Current and future trends in photoacoustic breast imaging,” *Photoacoustics*, vol. 16, p. 100134.
- [230] Nyayapathi, N. and Xia, J., (2019), “Photoacoustic imaging of breast cancer: a mini review of system design and image features,” *J. Biomed. Opt.*, vol. 24, no. 12, p. 1.
- [231] Soliman, D., Tserevelakis, G. J., Omar, M. and Ntziachristos, V., (2015), “Combining microscopy with mesoscopy using optical and optoacoustic label-free modes,” *Sci. Rep.*
- [232] Gaponenko, S. V., “Nanoplasmonics I: metal nanoparticles,” in *Introduction to Nanophotonics*, pp. 180–186.
- [233] Amendola, V., Pilot, R., Frasconi, M., Maragò, O. M. and Iati, M. A., (2017), “Surface plasmon resonance in gold nanoparticles: A review,” *J. Phys. Condens. Matter*.
- [234] Petryayeva, E. and Krull, U. J., (2011), “Localized surface plasmon resonance: Nanostructures, bioassays and biosensing—A review,” *Anal. Chim. Acta*, vol. 706, no. 1, pp. 8–24.
- [235] Link, S. and El-Sayed, M. A., (2003), “Optical properties and ultrafast dynamics of metallic nanocrystals,” *Annu. Rev. Phys. Chem.*
- [236] Hu, M. and Hartland, G. V., (2003), “Heat Dissipation for Au Particles in Aqueous Solution: Relaxation Time versus Size,” *J. Phys. Chem. B*, vol. 107, no. 5, pp. 1284–1284.
- [237] Jain, P. K., Lee, K. S., El-Sayed, I. H. and El-Sayed, M. A., (2006), “Calculated absorption and scattering properties of gold nanoparticles of different size, shape, and composition: Applications in biological imaging and biomedicine,” *J. Phys. Chem. B*.
- [238] Goddard, Z. R., Marín, M. J., Russell, D. A. and Searcey, M., (2020), “Active targeting of gold nanoparticles as cancer therapeutics,” *Chem. Soc. Rev.*, vol. 49, no. 23, pp. 8774–8789.
- [239] Bayer, C. L., Chen, Y.-S., Kim, S., Mallidi, S., Sokolov, K. and Emelianov, S., (2011), “Multiplex photoacoustic molecular imaging using targeted silica-coated gold nanorods,” *Biomed. Opt. Express*, vol. 2, no. 7, p. 1828.
- [240] Bayer, C. L., Chen, Y. S., Kim, S., Mallidi, S., Sokolov, K. and Emelianov, S., “Molecular diagnosis of cancer using multiplex photoacoustic imaging with targeted nanorods,” in *Proceedings - IEEE Ultrasonics Symposium*, pp. 503–506, doi: 10.1109/ULTSYM.2010.5935741.
- [241] Li, P. C., Wei, C. W., Liao, C. K., Chen, C. D., Pao, K. C., Wang, C. R. C., Wu, Y. N. and Shieh, D. Bin, (2007), “Photoacoustic imaging of multiple targets using gold nanorods,” *IEEE Trans. Ultrason. Ferroelectr. Freq. Control*, vol. 54, no. 8, pp. 1642–1647.

- [242] Li, S., Lui, K. H., Tsoi, T. H., Lo, W. S., Li, X., Hu, X., Chi-Shing Tai, W., Hiu-Ling Hung, C., Gu, Y. J. and Wong, W. T., (2019), “PH-responsive targeted gold nanoparticles for: In vivo photoacoustic imaging of tumor microenvironments,” *Nanoscale Adv.*
- [243] Song, J., Kim, J., Hwang, S., Jeon, M., Jeong, S., Kim, C. and Kim, S., (2016), “‘smart’ gold nanoparticles for photoacoustic imaging: An imaging contrast agent responsive to the cancer microenvironment and signal amplification via pH-induced aggregation,” *Chem. Commun.*, vol. 52, no. 53, pp. 8287–8290.
- [244] Li, P.-C., Wang, C.-R. C., Shieh, D.-B., Wei, C.-W., Liao, C.-K., Poe, C., Jhan, S., Ding, A.-A. and Wu, Y.-N., (2008), “In vivo photoacoustic molecular imaging with simultaneous multiple selective targeting using antibody-conjugated gold nanorods,” *Opt. Express*, vol. 16, no. 23, p. 18605.
- [245] Maslov, K., Zhang, H. F., Hu, S. and Wang, L. V., (2008), “Optical-resolution photoacoustic microscopy for in vivo imaging of single capillaries,” *Opt. Lett.*, vol. 33, no. 9, p. 929.
- [246] Wang, L. V., (2009), “Multiscale photoacoustic microscopy and computed tomography,” *Nat. Photonics*, vol. 3, no. 9, pp. 503–509.
- [247] Ntziachristos, V. and Razansky, D., (2010), “Molecular imaging by means of multispectral photoacoustic tomography (MSOT),” *Chem. Rev.*, vol. 110, no. 5, pp. 2783–2794.
- [248] Neuschmelting, V., Burton, N. C., Lockau, H., Urich, A., Harmsen, S., Ntziachristos, V. and Kircher, M. F., (2016), “Performance of a Multispectral Optoacoustic Tomography (MSOT) System equipped with 2D vs. 3D Handheld Probes for Potential Clinical Translation,” *Photoacoustics*, vol. 4, no. 1, pp. 1–10.
- [249] Jokerst, J. V., Thangaraj, M., Kempen, P. J., Sinclair, R. and Gambhir, S. S., (2012), “Photoacoustic imaging of mesenchymal stem cells in living mice via silica-coated gold nanorods,” *ACS Nano*, vol. 6, no. 7, pp. 5920–5930.
- [250] Kim, C., Erpelding, T. N., Jankovic, L., Pashley, M. D. and Wang, L. V., (2010), “Deeply penetrating in vivo photoacoustic imaging using a clinical ultrasound array system,” *Biomed. Opt. Express*, vol. 1, no. 1, p. 278.
- [251] Juratli, M. A., Menyae, Y. A., Sarimollaoglu, M., Melerzanov, A. V., Nedosekin, D. A., Culp, W. C., Suen, J. Y., Galanzha, E. I. and Zharov, V. P., (2018), “Noninvasive label-free detection of circulating white and red blood clots in deep vessels with a focused photoacoustic probe,” *Biomed. Opt. Express*, vol. 9, no. 11, p. 5667.
- [252] Kim, J., Kim, J. Y., Jeon, S., Baik, J. W., Cho, S. H. and Kim, C., (2019), “Super-resolution localization photoacoustic microscopy using intrinsic red blood cells as contrast absorbers,” *Light Sci. Appl.*, vol. 8, no. 1, p. 103.
- [253] Luís Dean-Ben, X. and Razansky, D., (2018), “Localization optoacoustic tomography,” *Light Sci. Appl.*, vol. 7, no. 4, p. 18004.
- [254] Galanzha, E. I., Shashkov, E. V., Spring, P. M., Suen, J. Y. and Zharov, V. P., (2009), “In vivo, noninvasive, label-free detection and eradication of circulating metastatic melanoma cells using two-color photoacoustic flow cytometry with a diode laser,” *Cancer Res.*, vol. 69, no. 20, pp. 7926–7934.
- [255] Wang, Y., Xie, X., Wang, X., Ku, G., Gill, K. L., O’Neal, D. P., Stoica, G. and Wang, L. V., (2004), “Photoacoustic tomography of a nanoshell contrast agent in the in vivo rat brain,” *Nano Lett.*, vol. 4, no. 9, pp. 1689–1692.
- [256] Wang, J., Xie, Y., Wang, L., Tang, J., Li, J., Kocafe, D., Kocafe, Y., Zhang, Z., Li, Y. and Chen, C., (2015), “In vivo pharmacokinetic features and biodistribution of star and rod shaped gold nanoparticles by multispectral optoacoustic tomography,” *RSC Adv.*, vol. 5, no. 10, pp. 7529–7538.
- [257] Kim, C., Song, H. M., Cai, X., Yao, J., Wei, A. and Wang, L. V., (2011), “In vivo photoacoustic mapping of lymphatic systems with plasmon-resonant nanostars,” *J. Mater. Chem.*, vol. 21, no.

- 9, pp. 2841–2844.
- [258] Galanzha, E. I., Shashkov, E., Sarimollaoglu, M., Beenken, K. E., Basnakian, A. G., Shirtliff, M. E., Kim, J. W., Smeltzer, M. S. and Zharov, V. P., (2012), “In Vivo Magnetic Enrichment, Photoacoustic Diagnosis, and Photothermal Purging of Infected Blood Using Multifunctional Gold and Magnetic Nanoparticles,” *PLoS One*, vol. 7, no. 9, p. e45557.
- [259] Mulens-Arias, V., Balfourier, A., Nicolás-Boluda, A., Carn, F. and Gazeau, F., (2020), “Endocytosis-driven gold nanoparticle fractal rearrangement in cells and its influence on photothermal conversion,” *Nanoscale*, vol. 12, no. 42, pp. 21832–21849.
- [260] Nam, J. *et al.*, (2013), “PH-responsive assembly of gold nanoparticles and ‘spatiotemporally concerted’ Drug release for synergistic cancer therapy,” *ACS Nano*, vol. 7, no. 4, pp. 3388–3402.
- [261] Galanzha, E. I. and Zharov, V. P., (2012), “Photoacoustic flow cytometry,” *Methods*, vol. 57, no. 3, pp. 280–296.
- [262] Agrawal, S., Johnstonbaugh, K., Clark, J. Y., Raman, J. D., Wang, X. and Kothapalli, S. R., (2020), “Design, development, and multi-characterization of an integrated clinical transrectal ultrasound and photoacoustic device for human prostate imaging,” *Diagnostics*, vol. 10, no. 8, p. 566.
- [263] Jang, J., Kim, J., Lee, H. J. and Chang, J. H., (2021), “Transrectal ultrasound and photoacoustic imaging probe for diagnosis of prostate cancer,” *Sensors (Switzerland)*, vol. 21, no. 4, pp. 1–18.
- [264] Miranda, C., Barkley, J. and Smith, B. S., (2018), “Intrauterine photoacoustic and ultrasound imaging probe,” *J. Biomed. Opt.*
- [265] Jain, P. K., Huang, W. and El-Sayed, M. A., (2007), “On the universal scaling behavior of the distance decay of plasmon coupling in metal nanoparticle pairs: A plasmon ruler equation,” *Nano Lett.*, vol. 7, no. 7, pp. 2080–2088.
- [266] Comenge, J., Fragueiro, O., Sharkey, J., Taylor, A., Held, M., Burton, N. C., Park, B. K., Wilm, B., Murray, P., Brust, M. and Lévy, R., (2016), “Preventing Plasmon Coupling between Gold Nanorods Improves the Sensitivity of Photoacoustic Detection of Labeled Stem Cells in Vivo,” *ACS Nano*, vol. 10, no. 7, pp. 7106–7116.
- [267] Rengan, A. K., Bukhari, A. B., Pradhan, A., Malhotra, R., Banerjee, R., Srivastava, R. and De, A., (2015), “In vivo analysis of biodegradable liposome gold nanoparticles as efficient agents for photothermal therapy of cancer,” *Nano Lett.*, vol. 15, no. 2, pp. 842–848.
- [268] Tan, H., Liu, Y., Xie, J., Gao, Y., Li, Y., Ma, L., Zhang, L., Tang, T. and Zhu, J., (2020), “Light-triggered disassembly of photo-responsive gold nanovesicles for controlled drug release,” *Mater. Chem. Front.*, vol. 4, no. 9, pp. 2805–2811.
- [269] Wang, Y., Hu, X., Weng, J., Li, J., Fan, Q., Zhang, Y. and Ye, D., (2019), “A Photoacoustic Probe for the Imaging of Tumor Apoptosis by Caspase-Mediated Macrocyclization and Self-Assembly,” *Angew. Chemie - Int. Ed.*, vol. 58, no. 15, pp. 4886–4890.
- [270] Lei, P., Wen, X., Wang, L., Zhang, P. and Yang, S., (2019), “Ultrafine intravascular photoacoustic endoscope with a 07 mm diameter probe,” *Opt. Lett.*, vol. 44, no. 22, p. 5406.
- [271] Yu, Z., Leng, S., Jorgensen, S. M., Li, Z., Gutjahr, R., Chen, B., Halaweish, A. F., Kappler, S., Yu, L., Ritman, E. L. and McCollough, C. H., (2016), “Evaluation of conventional imaging performance in a research whole-body CT system with a photon-counting detector array,” *Phys. Med. Biol.*
- [272] Muenzel, D. *et al.*, (2017), “Spectral Photon-counting CT: Initial Experience with Dual-Contrast Agent K-Edge Colonography,” *Radiology*, vol. 283, no. 3, pp. 723–728.
- [273] “XC-Actaeon,” *Direct Conversion*, 2021. <https://directconversion.com/product/xc-actaeon/> (accessed Feb. 24, 2021).
- [274] “MARS for Researchers,” *MARS Bioimaging Limited*, 2020. <https://www.marsbioimaging.com/mars-for-researchers/> (accessed Feb. 24, 2021).

- [275] “MARS for Clinicians,” *MARS Bioimaging Limited*, 2020. <https://www.marsbioimaging.com/clinicians/> (accessed Feb. 24, 2021).
- [276] Otfinowski, P., Deptuch, G. W. and Maj, P., “FRIC - A 50 μm pixel-pitch single photon counting ASIC with Pattern Recognition algorithm in 40 nm CMOS technology,” in *Journal of Instrumentation*, vol. 15, no. 1, doi: 10.1088/1748-0221/15/01/C01016.
- [277] Peizerat, A., Rostaing, J. P., Ouvrier-Buffet, P., Stanchina, S., Radisson, P. and Marche, E., “A 256 energy bin spectrum X-ray photon-counting image sensor providing 8Mcounts/s/pixel and on-chip charge sharing, charge induction and pile-up corrections,” in *IEEE Symposium on VLSI Circuits, Digest of Technical Papers*, pp. C246–C247, doi: 10.23919/VLSIC.2017.8008496.
- [278] Eales, T. D., Marko, I. P., Ikyo, B. A., Adams, A. R., Arafin, S., Sprengel, S., Amann, M. C. and Sweeney, S. J., (2017), “Wavelength Dependence of Efficiency Limiting Mechanisms in Type-I Mid-Infrared GaInAsSb/GaSb Lasers,” *IEEE J. Sel. Top. Quantum Electron.*, vol. 23, no. 6, pp. 1–9.
- [279] Kasap, S., Frey, J. B., Belev, G., Tousignant, O., Mani, H., Greenspan, J., Laperriere, L., Bubon, O., Reznik, A., DeCrescenzo, G., Karim, K. S. and Rowlands, J. A., (2011), “Amorphous and polycrystalline photoconductors for direct conversion flat panel x-ray image sensors,” *Sensors*, vol. 11, no. 5, pp. 5112–5157.
- [280] DenOtter, T. D. and Schubert, J., “Hounsfield Unit,” in *StatPearls*, StatPerals Publishing.
- [281] Rebuffel, V. and Dinten, J. M., (2007), “Dual-energy X-ray imaging: Benefits and limits,” *Insight Non-Destructive Test. Cond. Monit.*, vol. 49, no. 10, pp. 589–594.
- [282] Mendonca, P. R. S., Lamb, P. and Sahani, D. V., (2014), “A flexible method for multi-material decomposition of dual-energy CT images,” *IEEE Trans. Med. Imaging*, vol. 33, no. 1, pp. 99–116.
- [283] Anderson, N. G., Butler, A. P., Scott, N. J. A., Cook, N. J., Butzer, J. S., Schleich, N., Firsching, M., Grasset, R., De Ruiter, N., Campbell, M. and Butler, P. H., (2010), “Spectroscopic (multi-energy) CT distinguishes iodine and barium contrast material in MICE,” *Eur. Radiol.*, vol. 20, no. 9, pp. 2126–2134.
- [284] Cormode, D. P., Si-Mohamed, S., Bar-Ness, D., Sigovan, M., Naha, P. C., Balegamire, J., Lavenne, F., Coulon, P., Roessl, E., Bartels, M., Rokni, M., Blevis, I., Bousset, L. and Douek, P., (2017), “Multicolor spectral photon-counting computed tomography: In vivo dual contrast imaging with a high count rate scanner,” *Sci. Rep.*, vol. 7, no. 1, p. 4784.
- [285] Badea, C. T., Clark, D. P., Holbrook, M., Srivastava, M., Mowery, Y. and Ghaghada, K. B., (2019), “Functional imaging of tumor vasculature using iodine and gadolinium-based nanoparticle contrast agents: A comparison of spectral micro-CT using energy integrating and photon counting detectors,” *Phys. Med. Biol.*, vol. 64, no. 6.
- [286] Martin-Diaconescu, V., Gennari, M., Gerey, B., Tsui, E., Kanady, J., Tran, R., Pécaut, J., Maganas, D., Krewald, V., Gouré, E., Duboc, C., Yano, J., Agapie, T., Collomb, M. N. and Debeer, S., (2015), “Ca K-edge XAS as a probe of calcium centers in complex systems,” *Inorg. Chem.*, vol. 54, no. 4, pp. 1283–1292.
- [287] Piquer, C., Laguna-Marco, M. A., Roca, A. G., Boada, R., Guglieri, C. and Chaboy, J., (2014), “Fe K-edge X-ray absorption spectroscopy study of nanosized nominal magnetite,” *J. Phys. Chem. C*, vol. 118, no. 2, pp. 1332–1346.
- [288] Nasirudin, R. A., Mei, K., Panchev, P., Fehringer, A., Pfeiffer, F., Rummeny, E. J., Fiebich, M. and Noël, P. B., (2015), “Reduction of metal artifact in single photon-counting computed tomography by spectral-driven iterative reconstruction technique,” *PLoS One*, vol. 10, no. 5.
- [289] Rajeswari Amma, M. *et al.*, “Assessment of metal implant induced artefacts using photon counting spectral CT,” p. 46, doi: 10.1117/12.2531003.
- [290] Rajendran, K., Voss, B. A., Zhou, W., Tao, S., DeLone, D. R., Lane, J. I., Weaver, J. M., Carlson, M. L., Fletcher, J. G., McCollough, C. H. and Leng, S., (2020), “Dose Reduction for Sinus and

- Temporal Bone Imaging Using Photon-Counting Detector CT with an Additional Tin Filter,” *Invest. Radiol.*, vol. 55, no. 2, pp. 91–100.
- [291] Pourmorteza, A., Symons, R., Reich, D. S., Bagheri, M., Cork, T. E., Kappler, S., Ulzheimer, S. and Bluemke, D. A., (2017), “Photon-counting CT of the brain: In Vivo human results and image-quality assessment,” *Am. J. Neuroradiol.*, vol. 38, no. 12, pp. 2257–2263.
- [292] Rajagopal, J. R., Farhadi, F., Solomon, J., Sahbaee, P., Saboury, B., Pritchard, W. F., Jones, E. C. and Samei, E., (2020), “Comparison of Low Dose Performance of Photon-Counting and Energy Integrating CT,” *Acad. Radiol.*
- [293] Zhou, W., Lane, J. I., Carlson, M. L., Bruesewitz, M. R., Witte, R. J., Koeller, K. K., Eckel, L. J., Carter, R. E., McCollough, C. H. and Leng, S., (2018), “Comparison of a photon-counting-detector CT with an energy-integrating-detector CT for temporal bone imaging: A cadaveric study,” *Am. J. Neuroradiol.*, vol. 39, no. 9, pp. 1733–1738.
- [294] Willeminck, M. J., Persson, M., Pourmorteza, A., Pelc, N. J. and Fleischmann, D., “Photon-counting CT: Technical principles and clinical prospects,” *Radiology*, vol. 289, no. 2. pp. 293–312, 2018, doi: 10.1148/radiol.2018172656.
- [295] Aamir, R. *et al.*, (2014), “MARS spectral molecular imaging of lamb tissue: data collection and image analysis,” *J. Instrum.*, vol. 9, no. 02, pp. P02005–P02005.
- [296] Balegamire, J., Vandamme, M., Chereul, E., Si-Mohamed, S., Azzouz Maache, S., Almouazen, E., Ettouati, L., Fessi, H., Boussel, L., Douek, P. and Chevalier, Y., (2020), “Iodinated polymer nanoparticles as contrast agent for spectral photon counting computed tomography,” *Biomater. Sci.*, vol. 8, no. 20, pp. 5715–5728.
- [297] Pan, D., Schmieder, A. H., SenPan, A., Yang, X., Wickline, S. A., Roessl, E., Proksa, R., Schirra, C. O. and Lanza, G. M., “Molecular imaging with spectral CT nanoprobe,” in *Design and Applications of Nanoparticles in Biomedical Imaging*, Cham: Springer International Publishing, pp. 385–402.
- [298] Roeder, R. K., Curtis, T. E., Nallathamby, P. D., Irimata, L. E., McGinnity, T. L., Cole, L. E., Vargo-Gogola, T. and Cowden Dahl, K. D., “Nanoparticle imaging probes for molecular imaging with computed tomography and application to cancer imaging,” in *Medical Imaging 2017: Physics of Medical Imaging*, vol. 10132, p. 101320X, doi: 10.1117/12.2255688.
- [299] Moghiseh, M., Lowe, C., Lewis, J. G., Kumar, D., Butler, A., Anderson, N., Raja, A. and Bombonati, A., (2018), “Spectral Photon-Counting Molecular Imaging for Quantification of Monoclonal Antibody-Conjugated Gold Nanoparticles Targeted to Lymphoma and Breast Cancer: An in Vitro Study,” *Contrast Media Mol. Imaging*, vol. 2018.
- [300] Moghiseh, M., Aamir, R., Panta, R. K., de Ruyter, N. J. A., Chernoglazov, A., Healy, J., Butler, A. P. H. and Anderson, N. G., (2016), “Discrimination of Multiple High-Z Materials by Multi-Energy Spectral CT – A Phantom Study,” *JSM Biomed. Imaging Data*, vol. 3, no. 1, p. 1007.
- [301] Symons, R., Krauss, B., Sahbaee, P., Cork, T. E., Lakshmanan, M. N., Bluemke, D. A. and Pourmorteza, A., (2017), “Photon-counting CT for simultaneous imaging of multiple contrast agents in the abdomen: An in vivo study,” *Med. Phys.*, vol. 44, no. 10, pp. 5120–5127.
- [302] Zhang, X. D., Chen, J., Luo, Z., Wu, D., Shen, X., Song, S. S., Sun, Y. M., Liu, P. X., Zhao, J., Huo, S., Fan, S., Fan, F., Liang, X. J. and Xie, J., (2014), “Enhanced tumor accumulation of Sub-2 nm gold nanoclusters for cancer radiation therapy,” *Adv. Healthc. Mater.*, vol. 3, no. 1, pp. 133–141.
- [303] Chattopadhyay, N., Cai, Z., Kwon, Y. L., Lechtman, E., Pignol, J. P. and Reilly, R. M., (2013), “Molecularly targeted gold nanoparticles enhance the radiation response of breast cancer cells and tumor xenografts to X-radiation,” *Breast Cancer Res. Treat.*, vol. 137, no. 1, pp. 81–91.
- [304] Wolfe, T., Chatterjee, D., Lee, J., Grant, J. D., Bhattarai, S., Tailor, R., Goodrich, G., Nicolucci, P. and Krishnan, S., (2015), “Targeted gold nanoparticles enhance sensitization of prostate tumors to megavoltage radiation therapy in vivo,” *Nanomedicine Nanotechnology, Biol. Med.*, vol. 11, no. 5, pp. 1277–1283.

- [305] Joh, D. Y., Sun, L., Stangl, M., Al Zaki, A., Murty, S., Santoiemma, P. P., Davis, J. J., Baumann, B. C., Alonso-Basanta, M., Bhang, D., Kao, G. D., Tsourkas, A. and Dorsey, J. F., (2013), “Selective Targeting of Brain Tumors with Gold Nanoparticle-Induced Radiosensitization,” *PLoS One*, vol. 8, no. 4, p. e62425.
- [306] Hainfeld, J. F., Dilmanian, F. A., Zhong, Z., Slatkin, D. N., Kalef-Ezra, J. A. and Smilowitz, H. M., (2010), “Gold nanoparticles enhance the radiation therapy of a murine squamous cell carcinoma,” *Phys. Med. Biol.*, vol. 55, no. 11, pp. 3045–3059.
- [307] Hainfeld, J. F., O’Connor, M. J., Dilmanian, F. A., Slatkin, D. N., Adams, D. J. and Smilowitz, H. M., (2011), “Micro-CT enables microlocalisation and quantification of Her2-targeted gold nanoparticles within tumour regions,” *Br. J. Radiol.*, vol. 84, no. 1002, pp. 526–533.
- [308] Cole, L. E., Ross, R. D., Tilley, J. M., Vargo-Gogola, T. and Roeder, R. K., (2015), “Gold nanoparticles as contrast agents in x-ray imaging and computed tomography,” *Nanomedicine*, vol. 10, no. 2, pp. 321–341.
- [309] Si-Mohamed, S., Cormode, D. P., Bar-Ness, D., Sigovan, M., Naha, P. C., Langlois, J. B., Chalabreysse, L., Coulon, P., Bleviss, I., Roessler, E., Erhard, K., Boussel, L. and Douek, P., (2017), “Evaluation of spectral photon counting computed tomography K-edge imaging for determination of gold nanoparticle biodistribution: In vivo,” *Nanoscale*, vol. 9, no. 46, pp. 18246–18257.
- [310] Murphy, C., “How can you calculate how many atoms are in a nanoparticle?,” *Sustainable Nano*, 2016. <http://sustainable-nano.com/2016/07/28/how-many-atoms-are-in-a-nanoparticle/> (accessed Feb. 24, 2021).
- [311] Chang, M. Y., Shiau, A. L., Chen, Y. H., Chang, C. J., Chen, H. H. W. and Wu, C. L., (2008), “Increased apoptotic potential and dose-enhancing effect of gold nanoparticles in combination with single-dose clinical electron beams on tumor-bearing mice,” *Cancer Sci.*, vol. 99, no. 7, pp. 1479–1484.
- [312] Chen, N., Yang, W., Bao, Y., Xu, H., Qin, S. and Tu, Y., (2015), “BSA capped Au nanoparticle as an efficient sensitizer for glioblastoma tumor radiation therapy,” *RSC Adv.*, vol. 5, no. 51, pp. 40514–40520.
- [313] Chithrani, D. B., Jelveh, S., Jalali, F., Van Prooijen, M., Allen, C., Bristow, R. G., Hill, R. P. and Jaffray, D. A., (2010), “Gold nanoparticles as radiation sensitizers in cancer therapy,” *Radiat. Res.*
- [314] Coulter, J. A., Jain, S., Butterworth, K. T., Taggart, L. E., Dickson, G. R., McMahon, S. J., Hyland, W. B., Muir, M. F., Trainor, C., Hounsell, A. R., O’Sullivan, J. M., Schettino, G., Currell, F. J., Hirst, D. G. and Prise, K. M., (2012), “Cell type-dependent uptake, localization, and cytotoxicity of 1.9 nm gold nanoparticles,” *Int. J. Nanomedicine*.
- [315] Cui, L., Tse, K., Zahedi, P., Harding, S. M., Zafarana, G., Jaffray, D. A., Bristow, R. G. and Allen, C., (2014), “Hypoxia and cellular localization influence the radiosensitizing effect of gold nanoparticles (AuNPs) in breast cancer cells,” *Radiat. Res.*
- [316] Geng, F., Song, K., Xing, J. Z., Yuan, C., Yan, S., Yang, Q., Chen, J. and Kong, B., (2011), “Thio-glucose bound gold nanoparticles enhance radio-cytotoxic targeting of ovarian cancer,” *Nanotechnology*, vol. 22, no. 28, p. 285101.
- [317] Jain, S., Coulter, J. A., Butterworth, K. T., Hounsell, A. R., McMahon, S. J., Hyland, W. B., Muir, M. F., Dickson, G. R., Prise, K. M., Currell, F. J., Hirst, D. G. and O’Sullivan, J. M., (2014), “Gold nanoparticle cellular uptake, toxicity and radiosensitisation in hypoxic conditions,” *Radiother. Oncol.*, vol. 110, no. 2, pp. 342–347.
- [318] Kaur, H., Pujari, G., Semwal, M. K., Sarma, A. and Avasthi, D. K., (2013), “In vitro studies on radiosensitization effect of glucose capped gold nanoparticles in photon and ion irradiation of HeLa cells,” *Nucl. Instruments Methods Phys. Res. Sect. B Beam Interact. with Mater. Atoms*, vol. 301, pp. 7–11.
- [319] Khoshgard, K., Hashemi, B., Arbabi, A., Rasaei, M. J. and Soleimani, M., (2014),

- “Radiosensitization effect of folate-conjugated gold nanoparticles on HeLa cancer cells under orthovoltage superficial radiotherapy techniques,” *Phys. Med. Biol.*, vol. 59, no. 9, pp. 2249–2263.
- [320] Kong, T., Zeng, J., Wang, X., Yang, X., Yang, J., McQuarrie, S., McEwan, A., Roa, W., Chen, J. and Xing, J. Z., (2008), “Enhancement of radiation cytotoxicity in breast-cancer cells by localized attachment of gold nanoparticles,” *Small*, vol. 4, no. 9, pp. 1537–1543.
- [321] Liu, C.-J., Wang, C.-H., Chen, S.-T., Chen, H.-H., Leng, W.-H., Chien, C.-C., Wang, C.-L., Kempson, I. M., Hwu, Y., Lai, T.-C., Hsiao, M., Yang, C.-S., Chen, Y.-J. and Margaritondo, G., (2010), “Enhancement of cell radiation sensitivity by pegylated gold nanoparticles,” *Phys. Med. Biol.*, vol. 55, no. 4, pp. 931–945.
- [322] Liu, C.-J., Wang, C.-H., Chien, C.-C., Yang, T.-Y., Chen, S.-T., Leng, W.-H., Lee, C.-F., Lee, K.-H., Hwu, Y., Lee, Y.-C., Cheng, C.-L., Yang, C.-S., Chen, Y. J., Je, J. H. and Margaritondo, G., (2008), “Enhanced x-ray irradiation-induced cancer cell damage by gold nanoparticles treated by a new synthesis method of polyethylene glycol modification,” *Nanotechnology*, vol. 19, no. 29, p. 295104.
- [323] Liu, Y., Liu, X., Jin, X., He, P., Zheng, X., Dai, Z., Ye, F., Zhao, T., Chen, W. and Li, Q., (2015), “The dependence of radiation enhancement effect on the concentration of gold nanoparticles exposed to low- and high-LET radiations,” *Phys. Medica*, vol. 31, no. 3, pp. 210–218.
- [324] Rahman, W. N., Bishara, N., Ackerly, T., He, C. F., Jackson, P., Wong, C., Davidson, R. and Geso, M., (2009), “Enhancement of radiation effects by gold nanoparticles for superficial radiation therapy,” *Nanomedicine Nanotechnology, Biol. Med.*, vol. 5, no. 2, pp. 136–142.
- [325] Wang, C., Li, X., Wang, Y., Liu, Z., Fu, L. and Hu, L., (2013), “Enhancement of radiation effect and increase of apoptosis in lung cancer cells by thio-glucose-bound gold nanoparticles at megavoltage radiation energies,” *J. Nanoparticle Res.*, vol. 15, no. 5, p. 1642.
- [326] Wang, C.-H., Zhang, S.-Y., Fang, Q., Shen, Z.-J., Fan, Z.-J., Jin, X.-F., Zeng, Y., Liu, Z.-Y. and Xie, H.-Z., (2015), “Renal dysfunction and hsCRP predict long-term outcomes of percutaneous coronary intervention in acute myocardial infarction,” *Am. J. Med. Sci.*, vol. 349, no. 5, pp. 413–420.
- [327] Zhang, X., Xing, J. Z., Chen, J., Ko, L., Amanie, J., Gulavita, S., Pervez, N., Yee, D., Moore, R. and Roa, W., (2008), “Enhanced radiation sensitivity in prostate cancer by gold-nanoparticles,” *Clin. Investig. Med.*
- [328] Zhang, X. D., Wu, D., Shen, X., Chen, J., Sun, Y. M., Liu, P. X. and Liang, X. J., (2012), “Size-dependent radiosensitization of PEG-coated gold nanoparticles for cancer radiation therapy,” *Biomaterials*, vol. 33, no. 27, pp. 6408–6419.
- [329] Flohr, T., Petersilka, M., Henning, A., Ulzheimer, S., Ferda, J. and Schmidt, B., (2020), “Photon-counting CT review,” *Phys. Medica*, vol. 79, pp. 126–136.
- [330] Krzyzanowska, A., Deptuch, G. W., Maj, P., Grybos, P. and Szczygiel, R., (2017), “Characterization of the Photon Counting CHASE Jr., Chip Built in a 40-nm CMOS Process with a Charge Sharing Correction Algorithm Using a Collimated X-Ray Beam,” *IEEE Trans. Nucl. Sci.*, vol. 64, no. 9, pp. 2561–2568.
- [331] Ballabriga, R., Campbell, M., Heijne, E. H. M., Llopart, X. and Tlustos, L., (2007), “The Medipix3 prototype, a pixel readout chip working in single photon counting mode with improved spectrometric performance,” *IEEE Trans. Nucl. Sci.*, vol. 54, no. 5, pp. 1824–1829.
- [332] Weber, N., Ullberg, C., Eriksson, C., Urech, M. and Stewart, A., “Photon counting dual energy x-ray imaging at CT count rates: measurements and implications of in-pixel charge sharing correction,” in *Medical Imaging 2018: Physics of Medical Imaging*, p. 44, doi: 10.1117/12.2293591.
- [333] Hsieh, S. S. and Sjolín, M., (2018), “Digital count summing vs analog charge summing for photon counting detectors: A performance simulation study,” *Med. Phys.*, vol. 45, no. 9, pp. 4085–4093.

- [334] Hsieh, S. S., (2020), “Coincidence Counters for Charge Sharing Compensation in Spectroscopic Photon Counting Detectors,” *IEEE Trans. Med. Imaging*, vol. 39, no. 3, pp. 678–687.
- [335] Ponchut, C., (2008), “Correction of the charge sharing in photon-counting pixel detector data,” *Nucl. Instruments Methods Phys. Res. Sect. A Accel. Spectrometers, Detect. Assoc. Equip.*, vol. 591, no. 1, pp. 311–313.
- [336] “A Crash Course on Handling DICOM Medical Imaging Data,” *POSTDICOM*, 2021. <https://www.postdicom.com/en/blog/handling-dicom-medical-imaging-data> (accessed Feb. 24, 2021).
- [337] Ackerman, M. J., “The visible human project,” *Proceedings of the IEEE*, 1998. https://www.nlm.nih.gov/research/visible/visible_human.html (accessed Feb. 24, 2021).
- [338] Takahashi, T. and Watanabe, S., “Recent progress in CdTe and CdZnTe detectors,” in *IEEE Transactions on Nuclear Science*, vol. 48, no. 4 I, pp. 950–959, doi: 10.1109/23.958705.
- [339] Ballabriga, R., Campbell, M. and Llopart, X., “Asic developments for radiation imaging applications: The medipix and timepix family,” *Nuclear Instruments and Methods in Physics Research, Section A: Accelerators, Spectrometers, Detectors and Associated Equipment*, vol. 878, pp. 10–23, 2018, doi: 10.1016/j.nima.2017.07.029.
- [340] Shikhaliev, P. M., (2008), “Computed tomography with energy-resolved detection: A feasibility study,” *Phys. Med. Biol.*, vol. 53, no. 5, pp. 1475–1495.
- [341] Roessl, E. and Proksa, R., (2007), “K-edge imaging in x-ray computed tomography using multi-bin photon counting detectors,” *Phys. Med. Biol.*, vol. 52, no. 15, pp. 4679–4696.
- [342] Wang, X., Meier, D., Taguchi, K., Wagenaar, D. J., Patt, B. E. and Frey, E. C., (2011), “Material separation in x-ray CT with energy resolved photon-counting detectors,” *Med. Phys.*, vol. 38, no. 3, pp. 1534–1546.
- [343] Taguchi, K. and Iwanczyk, J. S., “Vision 20/20: Single photon counting x-ray detectors in medical imaging,” *Medical physics*, vol. 40, no. 10, p. 100901, 2013, doi: 10.1118/1.4820371.
- [344] Ballabriga, R., Aloyz, J., Bandi, F. N., Campbell, M., Egidos, N., Fernandez-Tenllado, J. M., Heijne, E. H. M., Kremastiotis, I., Llopart, X., Madsen, B. J., Pennicard, D., Sriskaran, V. and L. Tlustos, (2020), “Photon Counting Detectors for X-ray Imaging with Emphasis on CT,” *IEEE Trans. Radiat. Plasma Med. Sci.*, pp. 1–1.
- [345] Koenig, T., Zuber, M., Hamann, E., Cecilia, A., Ballabriga, R., Campbell, M., Ruat, M., Tlustos, L., Fauler, A., Fiederle, M. and Baumbach, T., (2014), “How spectroscopic x-ray imaging benefits from inter-pixel communication,” *Phys. Med. Biol.*, vol. 59, no. 20, pp. 6195–6213.
- [346] Koenig, T., Hamann, E., Procz, S., Ballabriga, R., Cecilia, A., Zuber, M., Llopart, X., Campbell, M., Fauler, A., Baumbach, T. and Fiederle, M., (2013), “Charge summing in spectroscopic X-ray detectors with high-Z sensors,” *IEEE Trans. Nucl. Sci.*, vol. 60, no. 6, pp. 4713–4718.
- [347] Veale, M. C., Bell, S. J., Duarte, D. D., Schneider, A., Seller, P., Wilson, M. D. and Iniewski, K., (2014), “Measurements of charge sharing in small pixel CdTe detectors,” *Nucl. Instruments Methods Phys. Res. Sect. A Accel. Spectrometers, Detect. Assoc. Equip.*, vol. 767, pp. 218–226.
- [348] Guerra, P., Santos, A. and Darambara, D. G., (2009), “An investigation of performance characteristics of a pixellated room-temperature semiconductor detector for medical imaging,” *J. Phys. D. Appl. Phys.*, vol. 42, no. 17.
- [349] Guerra, P., Santos, A. and Darambara, D. G., (2008), “Development of a simplified simulation model for performance characterization of a pixellated CdZnTe multimodality imaging system,” *Phys. Med. Biol.*, vol. 53, no. 4, pp. 1099–1113.
- [350] Myronakis, M. E. and Darambara, D. G., (2011), “Monte Carlo investigation of charge-transport effects on energy resolution and detection efficiency of pixelated CZT detectors for SPECT/PET applications,” *Med. Phys.*, vol. 38, no. 1, pp. 455–467.
- [351] Yveborg, M., Danielsson, M. and Bornefalk, H., (2015), “Theoretical comparison of a dual

- energy system and photon counting silicon detector used for material quantification in spectral CT,” *IEEE Trans. Med. Imaging*, vol. 34, no. 3, pp. 796–806.
- [352] Roessl, E., Brendel, B., Engel, K. J., Schlomka, J. P., Thran, A. and Proksa, R., (2011), “Sensitivity of photon-counting based K-Edge Imaging in X-ray computed tomography,” *IEEE Trans. Med. Imaging*, vol. 30, no. 9, pp. 1678–1690.
- [353] Jan, S. *et al.*, (2004), “GATE: A simulation toolkit for PET and SPECT,” *Phys. Med. Biol.*, vol. 49, no. 19, pp. 4543–4561.
- [354] Trueb, P., Zamboni, P., And and Broennimann, C., (2017), “Assessment of the spectral performance of hybrid photon counting x-ray detectors,” *Med. Phys.*, vol. 44, no. 9, pp. e207–e214.
- [355] Myronakis, M. E., Zvelebil, M. and Darambara, D. G., (2012), “Computational modelling of pixelated CdZnTe detectors for x- and γ - Ray imaging applications,” *J. Instrum.*, vol. 7, no. 3.
- [356] Ramo, S., (1939), “Currents Induced by Electron Motion,” *Proc. IRE*, vol. 27, no. 9, pp. 584–585.
- [357] Shockley, W., (1938), “Currents to conductors induced by a moving point charge,” *J. Appl. Phys.*, vol. 9, no. 10, pp. 635–636.
- [358] He, Z., (2001), “Review of the Shockley-Ramo theorem and its application in semiconductor gamma-ray detectors,” *Nucl. Instruments Methods Phys. Res. Sect. A Accel. Spectrometers, Detect. Assoc. Equip.*, vol. 463, no. 1–2, pp. 250–267.
- [359] Allison, J. *et al.*, (2006), “Geant4 developments and applications,” *IEEE Trans. Nucl. Sci.*, vol. 53, no. 1, pp. 270–278.
- [360] COMSOL, “Multiphysics Software Product Suite,” 2014. <https://www.comsol.com/> (accessed Mar. 04, 2021).
- [361] Prettyman, T. H., (1999), “Method for mapping charge pulses in semiconductor radiation detectors,” *Nucl. Instruments Methods Phys. Res. Sect. A Accel. Spectrometers, Detect. Assoc. Equip.*, vol. 422, no. 1–3, pp. 232–237.
- [362] Prettyman, T. H., (1999), “Theoretical framework for mapping pulse shapes in semiconductor radiation detectors,” *Nucl. Instruments Methods Phys. Res. Sect. A Accel. Spectrometers, Detect. Assoc. Equip.*
- [363] “GR1,” *Kromek*, 2021. <https://www.kromek.com/product/gr1/> (accessed Feb. 26, 2021).
- [364] “Beryllium ‘Window’ EDS Detector,” *Practical Electron Microscopy and Database*, 2018. <https://www.globalsino.com/EM/page3924.html> (accessed Feb. 26, 2021).
- [365] Scienti, O. L. P. P., Bamber, J. C. and Darambara, D., (2020), “Inclusion of a Charge Sharing Correction Algorithm into an x-ray Photon Counting Spectral Detector Simulation Framework,” *IEEE Trans. Radiat. Plasma Med. Sci.*, pp. 1–1.
- [366] Primak, A. N., Ramirez Giraldo, J. C., Liu, X., Yu, L. and McCollough, C. H., (2009), “Improved dual-energy material discrimination for dual-source CT by means of additional spectral filtration,” *Med. Phys.*, vol. 36, no. 4, pp. 1359–1369.
- [367] Katsura, M., Sato, J., Akahane, M., Kunitatsu, A. and Abe, O., (2018), “Current and novel techniques for metal artifact reduction at CT: Practical guide for radiologists,” *Radiographics*, vol. 38, no. 2, pp. 450–461.
- [368] Mori, I., Machida, Y., Osanai, M. and Inuma, K., (2013), “Photon starvation artifacts of X-ray CT: Their true cause and a solution,” *Radiol. Phys. Technol.*, vol. 6, no. 1, pp. 130–141.
- [369] Boas, F. E. and Fleischmann, D., (2011), “Evaluation of two iterative techniques for reducing metal artifacts in computed tomography,” *Radiology*, vol. 259, no. 3, pp. 894–902.
- [370] Poikela, T., Plosila, J., Westerlund, T., Campbell, M., Gaspari, M. De, Llopart, X., Gromov, V.,

- Kluit, R., Beuzekom, M. van, Zappon, F., Zivkovic, V., Brezina, C., Desch, K., Fu, Y. and Kruth, A., (2014), "Timepix3: a 65K channel hybrid pixel readout chip with simultaneous ToA/ToT and sparse readout," *J. Instrum.*, vol. 9, no. 05, pp. C05013–C05013.
- [371] Ballabriga, R., Alozy, J., Blaj, G., Campbell, M., Fiederle, M., Frojdh, E., Heijne, E. H. M., Llopart, X., Pichotka, M., Procz, S., Tlustos, L. and Wong, W., (2013), "The Medipix3RX: A high resolution, zero dead-time pixel detector readout chip allowing spectroscopic imaging," *J. Instrum.*, vol. 8, no. 2, pp. C02016–C02016.
- [372] Stamp, L. K., Anderson, N. G., Becce, F., Rajeswari, M., Polson, M., Guyen, O., Viry, A., Choi, C., Kirkbride, T. E. and Raja, A. Y., (2019), "Clinical Utility of Multi-Energy Spectral Photon-Counting Computed Tomography in Crystal Arthritis," *Arthritis Rheumatol.*, vol. 71, no. 7, pp. 1158–1162.
- [373] Si-Mohamed, S., Bar-Ness, D., Sigovan, M., Cormode, D. P., Coulon, P., Coche, E., Vlassenbroek, A., Normand, G., Bousset, L. and Douek, P., (2017), "Review of an initial experience with an experimental spectral photon-counting computed tomography system," *Nucl. Instruments Methods Phys. Res. Sect. A Accel. Spectrometers, Detect. Assoc. Equip.*, vol. 873, pp. 27–35.
- [374] Genocchi, B., Pickford Scienti, O. and Darambara, D. G., (2017), "Optimal configuration of a low-dose breast-specific gamma camera based on semiconductor CdZnTe pixelated detectors," *J. Phys. Conf. Ser.*, vol. 841, no. 1, p. 012012.
- [375] Scienti, O. L. P. P., Bamber, J. C. and Darambara, D. G., (2020), "The Effects of Spectral X-Ray Photon Counting Detector Parameters on Detector Performance: Thickness and Pitch," *IEEE Access*, vol. 8, pp. 196541–196552.
- [376] Tao, S., Marsh, J. F., Tao, A., Michalak, G. J., Rajendran, K., McCollough, C. H. and Leng, S., (2020), "Multi-energy CT imaging for large patients using dual-source photon-counting detector CT," *Phys. Med. Biol.*, vol. 65, no. 17, p. 17NT01.
- [377] Symons, R., Pourmorteza, A., Sandfort, V., Ahlman, M. A., Cropper, T., Mallek, M., Kappler, S., Ulzheimer, S., Mahesh, M., Jones, E. C., Malayeri, A. A., Folio, L. R. and Bluemke, D. A., (2017), "Feasibility of dose-reduced chest CT with photon-counting detectors: Initial results in humans," *Radiology*, vol. 285, no. 3, pp. 980–989.
- [378] Koenig, T., Schulze, J., Zuber, M., Rink, K., Butzer, J., Hamann, E., Cecilia, A., Zwerger, A., Fauler, A., Fiederle, M. and Oelfke, U., (2012), "Imaging properties of small-pixel spectroscopic x-ray detectors based on cadmium telluride sensors," *Phys. Med. Biol.*, vol. 57, no. 21, pp. 6743–6759.
- [379] Simard, M., Panta, R. K., Bell, S. T., Butler, A. P. H. and Bouchard, H., (2020), "Quantitative imaging performance of MARS spectral photon-counting CT for radiotherapy," *Med. Phys.*, vol. 47, no. 8, pp. 3423–3434.
- [380] Thomas, B., Veale, M. C., Wilson, M. D., Seller, P., Schneider, A. and Iniewski, K., (2017), "Characterisation of Redlen high-flux CdZnTe," *J. Instrum.*, vol. 12, no. 12, pp. C12045–C12045.
- [381] Gimenez, E. N., Ballabriga, R., Campbell, M., Horswell, I., Llopart, X., Marchal, J., Sawhney, K. J. S., Tartoni, N. and Turecek, D., (2011), "Characterization of Medipix3 with synchrotron radiation," *IEEE Trans. Nucl. Sci.*, vol. 58, no. 1 PART 2, pp. 323–332.
- [382] Lee, O., Kappler, S., Polster, C. and Taguchi, K., (2017), "Estimation of Basis Line-Integrals in a Spectral Distortion-Modeled Photon Counting Detector Using Low-Order Polynomial Approximation of X-ray Transmittance," *IEEE Trans. Med. Imaging*, vol. 36, no. 2, pp. 560–573.
- [383] Di Trapani, V., Bravin, A., Brun, F., Dreossi, D., Longo, R., Mittone, A., Rigon, L. and Delogu, P., (2020), "Characterization of the acquisition modes implemented in Pixirad-1/Pixie-III X-ray Detector: Effects of charge sharing correction on spectral resolution and image quality," *Nucl. Instruments Methods Phys. Res. Sect. A Accel. Spectrometers, Detect. Assoc. Equip.*, vol. 955,

p. 163220.

- [384] Taguchi, K., (2020), “Multi-energy inter-pixel coincidence counters for charge sharing correction and compensation in photon counting detectors,” *Med. Phys.*, vol. 47, no. 5, pp. 2085–2098.
- [385] Ullberg, C., Urech, M., Weber, N., Engman, A., Redz, A. and Henckel, F., “Measurements of a dual-energy fast photon counting CdTe detector with integrated charge sharing correction,” in *Medical Imaging 2013: Physics of Medical Imaging*, vol. 8668, p. 86680P, doi: 10.1117/12.2007892.
- [386] Persson, M., Wang, A. and Pelc, N. J., (2020), “Detective quantum efficiency of photon-counting CdTe and Si detectors for computed tomography: a simulation study,” *J. Med. Imaging*, vol. 7, no. 04, p. 1.
- [387] Hsieh, S. S., Rajbhandary, P. L. and Pelc, N. J., (2018), “Spectral resolution and high-flux capability tradeoffs in CdTe detectors for clinical CT,” *Med. Phys.*, vol. 45, no. 4, pp. 1433–1443.
- [388] Trueb P., Zambon P., B. C., “Spectral performance of photon-counting detectors: How well can we capture the rainbow?,” in *Spectral, Photon Counting Computed Tomography: Technology and Applications.*, I. K. Taguchi K., Bleviss I., Ed. CRC Press, pp. 191–216.
- [389] Hubbell, J. H. and Seltzer, S. M., “NIST: X-Ray Mass Attenuation Coefficients,” *Physical Reference Data*, 1996. <http://www.nist.gov/pml/data/xraycoef/> (accessed Feb. 26, 2021).
- [390] Pickford Scienti, O. L. P., Bamber, J. C. and Darambara, D. G., (2020), “Cdte based energy resolving, x-ray photon counting detector performance assessment: The effects of charge sharing correction algorithm choice,” *Sensors (Switzerland)*, vol. 20, no. 21, pp. 1–24.
- [391] Hainfeld, J. F., Slatkin, D. N. and Smilowitz, H. M., (2004), “The use of gold nanoparticles to enhance radiotherapy in mice,” *Phys. Med. Biol.*
- [392] Chen, Y. S., Frey, W., Kim, S., Kruizinga, P., Homan, K. and Emelianov, S., (2011), “Silica-coated gold nanorods as photoacoustic signal nanoamplifiers,” *Nano Lett.*, vol. 11, no. 2, pp. 348–354.
- [393] Leonov, A. P., Zheng, J., Clogston, J. D., Stern, S. T., Patri, A. K. and Wei, A., (2008), “Detoxification of gold nanorods by treatment with polystyrenesulfonate,” *ACS Nano*, vol. 2, no. 12, pp. 2481–2488.
- [394] Roach, L., Ye, S., Moorcroft, S. C. T., Critchley, K., Coletta, P. L. and Evans, S. D., (2018), “Morphological control of seedlessly-synthesized gold nanorods using binary surfactants,” *Nanotechnology*, vol. 29, no. 13, p. 135601.
- [395] Corning, “Corning® Matrigel® Matrix,” *Technical Sheet*, 2016. <https://www.corning.com/worldwide/en/products/life-sciences/products/surfaces/matrigel-matrix.html> (accessed Feb. 25, 2021).
- [396] Lee, Y. J., Ahn, E. Y. and Park, Y., (2019), “Shape-dependent cytotoxicity and cellular uptake of gold nanoparticles synthesized using green tea extract,” *Nanoscale Res. Lett.*, vol. 14, no. 1, p. 129.
- [397] Hendel, T., Wuithschick, M., Kettemann, F., Birnbaum, A., Rademann, K. and Polte, J., (2014), “In Situ Determination of Colloidal Gold Concentrations with UV–Vis Spectroscopy: Limitations and Perspectives,” *Anal. Chem.*, vol. 86, no. 22, pp. 11115–11124.
- [398] Promega, “CellTiter-Glo ® 3D Cell Viability Assay,” *Technical manual*, 2015. https://www.promega.co.uk/products/cell-health-assays/cell-viability-and-cytotoxicity-assays/celltiter_glo-3d-cell-viability-assay/?catNum=G9681#protocols (accessed Feb. 25, 2021).
- [399] “Celigo Image Cytometer,” *Nexcelom*, 2021. <http://www.nexcelom.com/Celigo/celigo-features.php#feature1> (accessed Feb. 25, 2021).

- [400] Murphy, C. J., Thompson, L. B., Chernak, D. J., Yang, J. A., Sivapalan, S. T., Boulos, S. P., Huang, J., Alkilany, A. M. and Sisco, P. N., (2011), “Gold nanorod crystal growth: From seed-mediated synthesis to nanoscale sculpting,” *Curr. Opin. Colloid Interface Sci.*, vol. 16, no. 2, pp. 128–134.
- [401] Tong, W., Walsh, M. J., Mulvaney, P., Etheridge, J. and Funston, A. M., (2017), “Control of Symmetry Breaking Size and Aspect Ratio in Gold Nanorods: Underlying Role of Silver Nitrate,” *J. Phys. Chem. C*, vol. 121, no. 6, pp. 3549–3559.
- [402] van Leeuwen, C. M., Oei, A. L., Crezee, J., Bel, A., Franken, N. A. P., Stalpers, L. J. A. and Kok, H. P., (2018), “The alfa and beta of tumours: a review of parameters of the linear-quadratic model, derived from clinical radiotherapy studies,” *Radiat. Oncol.*, vol. 13, no. 1, p. 96.
- [403] He, J., Unser, S., Bruzas, I., Cary, R., Shi, Z., Mehra, R., Aron, K. and Sagle, L., (2018), “The facile removal of CTAB from the surface of gold nanorods,” *Colloids Surfaces B Biointerfaces*, vol. 163, pp. 140–145.
- [404] Freese, C., Uboldi, C., Gibson, M. I., Unger, R. E., Weksler, B. B., Romero, I. A., Couraud, P. O. and Kirkpatrick, C. J., (2012), “Uptake and cytotoxicity of citrate-coated gold nanospheres: Comparative studies on human endothelial and epithelial cells,” *Part. Fibre Toxicol.*, vol. 9, no. 1, p. 23.
- [405] Soenen, S. J., Manshian, B. B., Abdelmonem, A. M., Montenegro, J. M., Tan, S., Balcaen, L., Vanhaecke, F., Brisson, A. R., Parak, W. J., De Smedt, S. C. and Braeckmans, K., (2014), “The cellular interactions of PEGylated gold nanoparticles: Effect of PEGylation on cellular uptake and cytotoxicity,” *Part. Part. Syst. Charact.*, vol. 31, no. 7, pp. 794–800.
- [406] Arnida, Janát-Amsbury, M. M., Ray, A., Peterson, C. M. and Ghandehari, H., (2011), “Geometry and surface characteristics of gold nanoparticles influence their biodistribution and uptake by macrophages,” *Eur. J. Pharm. Biopharm.*, vol. 77, no. 3, pp. 417–423.
- [407] Chithrani, B. D., Ghazani, A. A. and Chan, W. C. W., (2006), “Determining the size and shape dependence of gold nanoparticle uptake into mammalian cells,” *Nano Lett.*, vol. 6, no. 4, pp. 662–668.
- [408] Rayavarapu, R. G., Petersen, W., Hartsuiker, L., Chin, P., Janssen, H., Van Leeuwen, F. W. B., Otto, C., Manohar, S. and Van Leeuwen, T. G., (2010), “In vitro toxicity studies of polymer-coated gold nanorods,” *Nanotechnology*, vol. 21, no. 14, p. 145101.
- [409] Kazemifar, S., McGuire, S., Timmerman, R., Wardak, Z., Nguyen, D., Park, Y., Jiang, S. and Owringi, A., (2019), “MRI-only brain radiotherapy: Assessing the dosimetric accuracy of synthetic CT images generated using a deep learning approach,” *Radiother. Oncol.*, vol. 136, pp. 56–63.
- [410] Leng, S., Rajendran, K., Gong, H., Zhou, W., Halaweish, A. F., Henning, A., Kappler, S., Baer, M., Fletcher, J. G. and McCollough, C. H., (2018), “150- μm Spatial Resolution Using Photon-Counting Detector Computed Tomography Technology: Technical Performance and First Patient Images,” *Invest. Radiol.*, vol. 53, no. 11, pp. 655–662.
- [411] Gongadze, A., Zhemchugov, A., Chelkov, G., Kozhevnikov, D., Potrap, I., Demichev, M., Smolyanskiy, P., Abramishvili, R., Kotov, S., Butler, A. P., Butler, P. H. and Bell, S. T., (2015), “Alignment and resolution studies of a MARS CT scanner,” *Phys. Part. Nucl. Lett.*, vol. 12, no. 5, pp. 725–735.
- [412] Toia, P., La Grutta, L., Sollami, G., Clemente, A., Gagliardo, C., Galia, M., Maffei, E., Midiri, M. and Cademartiri, F., (2020), “Technical development in cardiac CT: Current standards and future improvements—a narrative review,” *Cardiovasc. Diagn. Ther.*, vol. 10, no. 6, pp. 2018–2035.
- [413] Nam, S. Y., Ricles, L. M., Suggs, L. J. and Emelianov, S. Y., (2012), “Nonlinear photoacoustic signal increase from endocytosis of gold nanoparticles,” *Opt. Lett.*, vol. 37, no. 22, p. 4708.
- [414] Mallidi, S., Larson, T., Aaron, J., Sokolov, K. and Emelianov, S., (2007), “Molecular specific optoacoustic imaging with plasmonic nanoparticles,” *Opt. Express*, vol. 15, no. 11, p. 6583.

- [415] Ye, S., Marston, G., Markham, A. F., Louise Coletta, P. and Evans, S. D., (2019), “Developing gold nanotubes as photoacoustic contrast agents,” *J. Phys. Conf. Ser.*, vol. 1151, no. 1, p. 012018.

Appendix 1: Publications, Presentations and Awards

Publications:

- 1) Pickford Scienti, O. L. P., Bamber, J. C. and Darambara, D. G., (2020), “CdTe based energy resolving, x-ray photon counting detector performance assessment: The effects of charge sharing correction algorithm choice,” *Sensors (Switzerland)*, vol. 20, no. 21, pp. 1-24.
- 2) Scienti, O. L. P. P., Bamber, J. C. and Darambara, D. G., (2020), “The Effects of Spectral X-Ray Photon Counting Detector Parameters on Detector Performance: Thickness and Pitch,” *IEEE Access*, vol. 8, pp. 196541-196552.
- 3) Scienti, O. L. P. P., Bamber, J. C. and Darambara, D., (2020), “Inclusion of a Charge Sharing Correction Algorithm into an x-ray Photon Counting Spectral Detector Simulation Framework,” *IEEE Trans. Radiat. Plasma Med. Sci.*, pp. 1-1.
- 4) Genocchi, B., Pickford Scienti, O. and Darambara, D. G., (2017), “Optimal configuration of a low-dose breast-specific gamma camera based on semiconductor CdZnTe pixelated detectors,” *J. Phys. Conf. Ser.*, vol. 841, no. 1, p. 012012.
- 5) Scienti, O. P., Shah, A., Bamber, J. and Darambara, D., (2016) “An assessment of photoacoustic and photon counting multispectral X-ray imaging techniques for imaging gold nanorods in vivo as part of predicting dose enhancing effects,” in 2016 IEEE Nuclear Science Symposium, Medical Imaging Conference and Room-Temperature Semiconductor Detector Workshop, NSS/MIC/RTSD 2016, vol. 2017-January, pp. 1-2

Presentations:

1. Pickford Scienti, O., Bamber, J. and Darambara, D. “Development of an x-ray photon counting multispectral imaging detector for predicting dose enhancing effects produced by *in vivo* AuNPs.”, *IEEE Nuclear Science Symposium and Medical Imaging Conference (IEEE NSS/MIC)*, 2019 [Oral presentation]
2. Pickford Scienti, O., Bamber, J. and Darambara, D. “Comparison of charge sharing correction algorithms and their effect on optimal pixel geometry for Au k-edge imaging applications.”, *Spectral x-ray Workshop, CERN*, 2019 [Oral presentation]

3. Pickford Scienti, O., Bamber, J. and Darambara, D. “Analysis of the effects of silica coating of gold nanoparticles on dose enhancement and particle quantification using x-ray photon counting multispectral imaging (x-CSI) and photoacoustic spectral imaging (PASI).”, *IEEE Nuclear Science Symposium and Medical Imaging Conference (IEEE NSS/MIC)*, 2018 [Poster presentation]
4. Pickford Scienti, O., Bamber, J. and Darambara, D. “Analysis of the effects of Si-coating AuNP with respect to dose enhancement, photoacoustic spectral imaging (PASI) and x-ray imaging (x-CSI).”, *IEEE Nuclear Science Symposium and Medical Imaging Conference (IEEE NSS/MIC)*, 20 [Oral presentation]
5. Pickford Scienti, O., Shah, A., Bamber, J. and Darambara, D. “Developing x-ray photon counting and photoacoustic multispectral imaging techniques for in vivo AuNP imaging to predict dose enhancing effects.”, *Spectral x-ray Workshop, CERN*, 2017 [Oral presentation]
6. Pickford Scienti, O., Shah, A., Bamber, J. and Darambara, D. “An Assessment of Photoacoustic and Photon Counting Multispectral X-Ray Imaging Techniques for Imaging GNPs *in vivo* with a view to Predicting Dose Enhancing Effects”, *IEEE Nuclear Science Symposium and Medical Imaging Conference (IEEE NSS/MIC)*, 2016 [Oral presentation]

Awards:

1. Christopher J Thomson Best Student Paper Award (IEEE Medical Imaging Conference, 2019)

Appendix 2: AuNR synthesis protocol

Note that to eliminate the risk of additional nucleation sites in the reaction mixture, glassware should be new or else thoroughly cleaned (with aqua regia if heavy metals have been used in it before, otherwise with soap and water and then rinsed with double distilled H₂O at least 5 times and left to drip dry upside down).

1. Label an Eppendorf tube containing ~200 μl of NaBH₄ with 'A' and place into the freezer. When frozen, proceed to Step 2.
2. Place 32.5 ml of CTAB into a 50-ml vial and melt using a water bath set to 72°C for approximately 20 min or until clear.
3. Reduce temperature of water bath to 30°C and add a small beaker to the bath to preheat until it reaches the same temperature as the CTAB.
4. Place the small beaker into a water bath at 28°C on a hotplate with magnetic stirrer bar. Transfer to it 5 ml CTAB, stirring lightly (~350 rpm). At this point place an Eppendorf tube, labelled 'B', containing ~900 μl of double distilled H₂O into the freezer to chill (but not freeze).
5. Add 5 ml of 0.5 mM HAuCl₄ and allow to stir for ~7 min. During this time, remove 'A' from the freezer and allow to air melt.
6. Just before, or as, 'A' has melted fully, transfer 100 μl of chilled NaBH₄ from 'A' to tube 'B' and shake for 30 s to mix. Increase the stirring of the CTAB mixture to a vigorous speed (~750 rpm; it should not be very frothy) and immediately transfer 600 μl of the 'A'-'B' mixture to the CTAB on the hotplate. Start a timer for 25 minutes. This is now the 'seed mixture'.
7. When ten minutes is left on the timer, transfer 5 ml of CTAB from the 50-ml vial into a small (~10 ml) sample container and place into water bath at 28°C.
8. When four minutes are left on the timer, add 200 μl of 4 μM AgNO₃ to the CTAB sample container, followed by 5 ml of 1 mM HAuCl₄ and then 80 μl of 0.1 M L-ascorbic acid. Place lid on container and shake until colourless. Leave to settle for at least 10 s. This is now the 'growth mixture'.
9. When timer goes off, add 20 μl of the 'seed mixture' to the 'growth mixture', seal tightly with a lid, swirl **once** only and then place in a stable position in a water bath at 28°C. Leave for the AuNP seeds to grow for 3 hr.
10. Divide the solution into centrifuge tubes and centrifuge at 12000 x g for 12 min (with centrifuge set to 25°C). After centrifuging, quickly remove supernatant (before redispersion can occur) and top back up to the original volume with double distilled H₂O to redisperse. Repeat the centrifugation, and the supernatant removal, leaving the particles in concentrated form until required for use.

Appendix 3: Protocol for determining dose response curves

1. Approximately 1 million PC-3 cells were thawed from cold storage and plated into Corning T-75 conical flasks with 13 ml of cell culture medium (ten parts RPMI to one part low endotoxin BSA). These flasks were incubated at 37°C in a CO₂ enriched atmosphere (5%)
2. Three days after thawing (80% - 90% confluence), the cells were passaged, using 5 ml of TrypLE and a ten-minute incubation to facilitate cell detachment. The cells collected were divided across three new flasks and returned to the incubator.
3. Two days after incubating these cells, a bottle of Matrigel was removed from the freezer and placed in the fridge to thaw, along with a bag of 200 µl pipette tips.
4. Three days after incubating (80% - 90% confluence), these cells were passaged, using 5 ml of TrypLE and a ten-minute incubation to facilitate cell detachment. All cells were pooled together and counted using a haemocytometer.
5. A 96-well round bottom plate was prepared on ice in a tissue hood, along with the chilled pipette tips (which were used for Steps 7 and 8) and Matrigel (also on ice).
6. One thousand PC-3 cells, suspended in 100 µl of cell culture medium, were placed into each of the wells indicated in the left-hand layout in Figure 0.1.
7. 8 ml of a 5% Matrigel solution was made by mixing 400 µl of refrigerated Matrigel to 7.6 ml of cell culture medium.
8. 100 µl of this 5% Matrigel solution was added to each of these wells, making a final concentration of 2.5% Matrigel.
9. The plate was then centrifuged for four minutes at 4 °C and 1000 rpm.
10. The surrounding wells were all filled with phosphate buffered saline (PBS) to prevent evaporation from the edge-most spheroid containing wells (a problem and solution known to our group through previous experience).
11. The 96-well plate was then placed into an incubator at 37 °C and 5% [CO₂].
12. Steps 5 - 10 were repeated to produce a total of two such plates of spheroids.
13. The two plates of spheroids were then left in the incubator for 72 hr, to allow time for the spheroids to form (time chosen based on pilot studies).
14. One plate was removed from the incubator and placed into a tissue culture hood. Each row of spheroids in this plate was transferred to the second row of a new plate according to the

right-hand layout in Figure 0.1. This produced a total of five new plates, which were labelled with 0, 2, 4, 6 and 8 respectively.

15. These five plates were then taken to the cell irradiator room and irradiated individually with a dose corresponding to their plate number in Gy (0, 2, 4, 6 or 8 Gy). The 0-Gy single row plate was placed into the irradiator and left for 2 min without the x-ray beam switched on, to match the handling of the other plates. Plates were left on the side for the duration of the irradiation, so that the total time outside of the incubator was the same for all conditions.
16. When these plates had all been irradiated, they were returned to the incubator. Steps 14 and 15 were then repeated for the other multi-row plate of spheroids.
17. All plates were then returned to the incubator and allowed to recover for 24 hr.
18. The plates were then removed from the incubator. For each dose, one plate was assayed using MTT (as detailed in Section 2.1.1.2) and the other with Cell Titre Glo 3D (as detailed in the associated references).

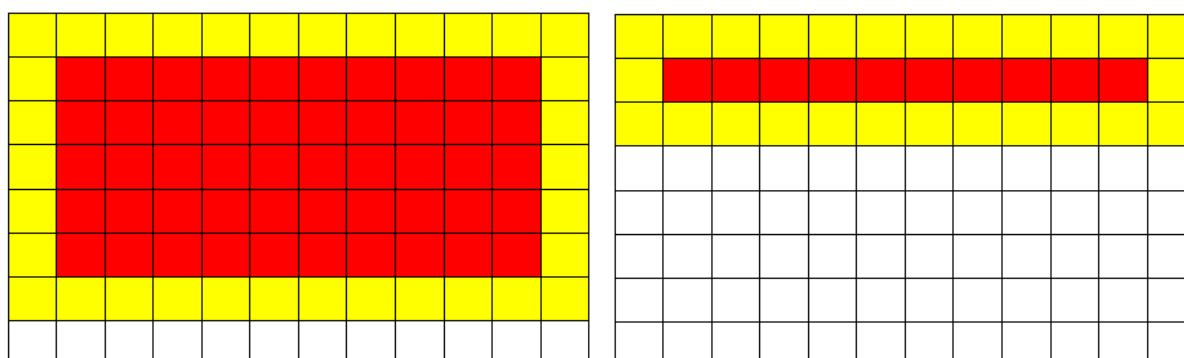


Figure 0.1. Schematic of a 96-well plate showing the two arrangements of wells used in this work. Wells indicated in red contained spheroids or monolayers of cells whilst yellow wells indicate wells that were filled with 200 μ l of PBS.

For the PC-3 monolayers, the above procedure was used, except that flat bottom plates were used in place of the round bottom plates, Step 2 was skipped, and Steps 3-15 were replaced with the following steps.

- Two thousand PC-3 cells, suspended in 200 μ l of cell culture medium, were placed into each of the wells according to the right-hand layout in Figure 0.1. The surrounding wells were all filled with PBS, as explained in the spheroid experiment.
- The 96-well plate was then placed into an incubator at 37 °C and 5% [CO₂].
- The previous two steps were repeated to produce a total of ten such plates of adherent PC-3 cell monolayers.
- After 24 hr, the ten plates were split into two groups, with each group containing five plates labelled sequentially as “0”, “2”, “4”, “6” and “8”. One group was returned to the incubator and the other taken to the cell irradiator room.

- The plates were then irradiated individually with a dose corresponding to their plate number in Gy (0, 2, 4, 6 or 8 Gy). The 0-Gy plate was placed into the irradiator and left for two minutes without the x-ray beam switched on, to match the handling of the other plates. Plates were left outside of the incubator for the duration of the irradiation, so that the total time outside of the incubator was the same for all conditions.
- The group of plates was then returned to the incubator and the previous step repeated for the other group of five plates.

Appendix 4: Protocol for measuring RDEE

1. Approximately one million PC-3 cells were thawed from cold storage and plated into Corning T-75 conical flasks with 13 ml of cell culture medium (composed of ten parts RPMI to one part low endotoxin BSA). These flasks were incubated at 37°C in a CO₂ enriched atmosphere (5%)
2. Three days after thawing (80% - 90% confluence), the cells were passaged, using 5 ml of TrypLE and a ten-minute incubation to facilitate cell detachment. The cells collected were divided across three new flasks and returned to the incubator.
3. Three days after Step 2 had been completed, 12 ml of 2-µg/ml solution of AuNP, for each AuNP type, was prepared. As the AuNPs were suspended in ethanol, this first needed to be removed so that it would not affect the results. This was done by diluting the stock AuNP solutions in Eppendorf tubes (24 µg Au into 1.5 ml of PBS), centrifuging the tubes for five minutes at 18000 x g, removing the supernatant and then redispersing the AuNPs in 1 ml of cell medium. The contents of the tube were then thoroughly mixed before being added to 11 ml of medium, to make up the final concentration mentioned above. These were then left for 24 hours to allow time for any BSA-protein based coronas to form.
4. On the same day, the cells were passaged (80% - 90% confluence), using 5 ml of TrypLE and a ten-minute incubation to facilitate cell detachment. Collected cells were pooled together and counted using a haemocytometer.
5. The fifty wells of a 96-well flat bottom plate indicated in Figure 0.2 were each seeded with two thousand cells in 100 µl of cell medium. The surrounding wells were each filled with 100 µl of PBS to prevent evaporation from the edge most wells which had been noticed in previous experiments using these plates within our labs. The exclusion of these wells also allowed for a more uniform plate irradiation (see 'Discussion' section). This was done for two such plates. These cells were then left overnight to adhere.
6. After 24 hr in solution, 100 µl of AuNPs from Step 3 were added to the wells of each plate according to the scheme laid out in Figure 0.2 to make up a final AuNP concentration of 1 µg/ml. The cells were then left to incubate with the AuNPs for a further 24 hr. To avoid biasing for a particular enhancement/uptake mechanism, the AuNPs were introduced to the cells at the same concentration and left in place throughout the experiment, regardless of the AuNP type used. It should be noted that this is in contrast to most similar experiments in which the AuNPs are washed off prior to irradiating. Washing prior to irradiation means that only AuNPs that are taken up by the cells can contribute to measured RDEE. The method employed in this current work should better reflect realistic clinical situations where AuNPs would be distributed both intracellularly and extracellularly, for example if delivered via an intratumoural injection of AuNPs.

7. After the 24 hr had elapsed the plates were removed from the incubator at the same time and taken to the cell irradiator. One plate (the 0-Gy plate) was placed in the cell irradiator for the time it would take to deliver 5 Gy of irradiation (158 s), but the radiation source was not activated. The second plate was then put in for the same amount of time, however this time the 5 Gy irradiation was delivered.
8. Both plates were then returned to the incubator and the damage allowed to fix for 24 hours (see Section 1.2.3, page 19).
9. After 24 hr, 8 ml of PBS was mixed with AO (8 μ l, 37.7 mM) and PI (40 μ l, 15 mM) and labelled as mixture A. These dyes are used for staining live and dead cells respectively, as discussed in Step 12. Separately, 8 ml of PBS was mixed with AO (28 μ l, 37.7 mM) and PI (40 μ l, 15 mM) and labelled as mixture B.
10. 50 μ l of either mixture A or B were added to each of the wells of the two plates (one irradiated and one unirradiated) as indicated in Figure 0.2. The use of two different AO concentrations was a result of different levels being recommended (and discouraged) by literature sources and group members with relevant experience. Due to the limited number of repeats that would be performed, both concentrations were tried so that some useful data would be ensured to result.
11. These plates were then imaged using the “Live and Dead” data acquisition settings on a Celigo Image Cytometer. The Celigo’s image analysis software was used to count the number of live and dead cells in each well, by counting the number of discrete fluorescent foci in the image at the emission wavelengths of AO and PI respectively. After imaging the plates were returned to the incubator.

Imaging and analysis were repeated after 5 days, so that the effect on cell proliferation for the various conditions could be calculated.

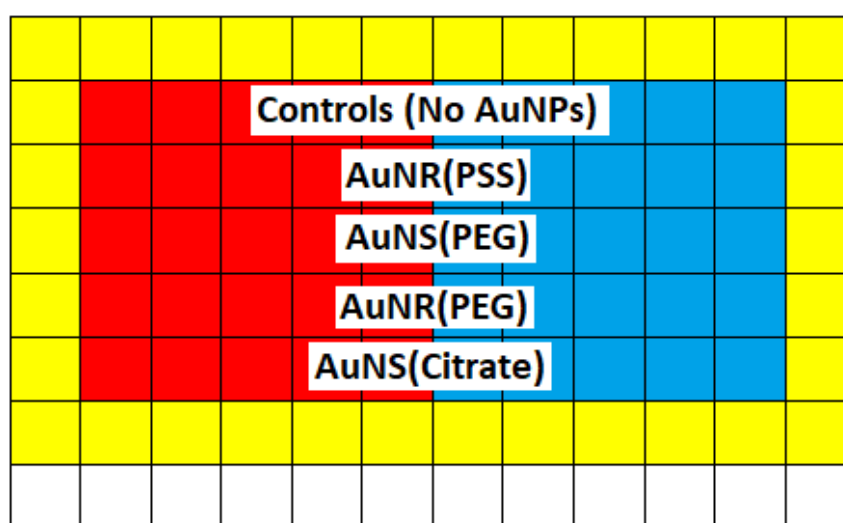


Figure 0.2. Schematic of a 96-well plate showing the division of AuNP conditions and AO/PI mixtures. Wells marked in red or blue were plated with two thousand PC-3 cells to form monolayers. Wells marked in yellow contained 200 μ l of PBS. AuNPs of the types listed were added to each well as described in the text. Mixture A was added to the red well whilst mixture B was added to the blue wells (see text for the composition of the mixtures).

Appendix 5: List of Tables

Table 2.1. Fictional data resulting from a series of hypothetical cell irradiations and controls, with and without Au, to assist in explaining how various RDEE metrics are calculated.....	36
Table 2.2. Parameters that can affect the RDEE delivered by AuNPs, and the major components of each to be considered.....	41
Table 2.3. List of the most common elements in the human body (those comprising >1% of body mass) and their Z-number. Au is included at the end of the list for comparison.....	42
Table 2.4. Common ligands considered in AuNP designs intended for therapeutic use.	49
Table 3.1. List of optical windows proposed in the literature and their corresponding wavelength ranges. Note that the first and second windows were originally proposed as a single window, before later being reclassified based on the increasing contribution of water to absorption above 950 nm.	59
Table 4.1. Summary of energy-integrating based dual energy approaches and the complications in generalising them to multispectral systems.	87
Table 4.2. A summary of RDEE studies in the literature. AuNP concentrations reported are given, as well as the calculated standardised density.....	103
Table 5.1. List of physical properties at 298.15K for common semiconductor radiation sensors. Data obtained from Ballabriga et al[344]. Z-numbers for compounds are listed in order of appearance in the material's name.	109
Table 5.2. List of the physical effects and electronic processes modelled in CoGI to represent an x-CSI scanner.	112
Table 5.3. Summary of advances in CoGI over previous work in the group.	133
Table 5.4. List of material properties used by CoGI in modelling the GRI photospectrometer.	134
Table 5.5. List of material properties used by CoGI in modelling the GRI photospectrometer.	136
Table 5.6. Comparison of photopeak metrics found in simulation (CoGI) and experiment (GRI).	139
Table 5.7. Comparison of the counts assigned to the photopeak energy bin in experiment (Actaeon) and simulations (CoGI). Differences between CoGI and CoGI(Long) are explained in the text.	140
Table 7.1. A list of the different CSCAs used in this work along with their NS, NL, and CM categorisations...	170
Table 7.2. The ratios of maximum count rates for dynamic and static 2x2 and 3x3 CSCAs.	186
Table 8.1. Summary of the physical parameters of the AuNPs provided by collaborators at Liverpool University. Particle sizes were assumed to be normally distributed and the uncertainties shown represent σ for that	

distribution. Zeta potentials were measured in triplicate and the standard error in the mean presented in the table. UV-Vis data was not obtained for the largest AuNS batch as it was not deemed necessary given that the large uncertainty in size made this batch unsuitable for this project anyway..... 203

Table 8.2. The variation in dose experienced across the plate is listed for the various configurations considered in Figure 8.7, Figure 8.8 and Figure 8.9. The values reported are the maximum deviations from the MidDose for the plate, as defined in Equation 8.10..... 207

Table 8.3. Summary of the doses corresponding to the steepest gradient in the fitted dose response curves for the various metrics assessed..... 209

Table 8.4. Summary of the changes in proliferation associated with 5 Gy irradiation for the various experimental conditions. The DEE was calculated for each condition. Standard errors in the mean (SEM) were calculated for the raw data at each time point and added in quadrature to determine the associated uncertainties in proliferation (presented here in bracket notation, where the figure in brackets represents the uncertainty in the final reported digit). Uncertainties in inhibition and DEE were calculated by adding, in quadrature, the uncertainties in proliferation for the different doses. No uncertainty is associated with the DEE value for the control group as it is 1.00 by definition. 210

Table 9.1. Summary table showing the performance characteristics of x-CSI and PASI systems currently demonstrated. *Note that the definition of temporal resolution is complicated by the different nature of the two techniques, as discussed in the main body of the text. 224

Appendix 6: List of Figures

Figure 1.1. Interaction cross-section diagram for photons with Cd. The lines represent the cross-sections for the photon to interact with the atom via the various physical processes. It can be seen that photoelectric absorption is favoured at lower energies whilst pair production dominates at higher energies. At energies relevant to internal organ radiotherapy (MeV) Compton scattering can be seen to dominate. As photons are Compton scattered however, they will lose energy and thus become increasingly likely to be photoelectrically absorbed. Figure plotted using data from NIST[27]. 12

Figure 1.2. Diagram showing the alternative deexcitation pathways of x-ray fluorescence and Auger electron production. On the left is an atom with a vacancy in its inner most electron shell (green circle) which has two possible routes to deexcite (dotted arrows). In fluorescence x-ray production (upper path) an electron from a higher orbital falls directly into the lower energy vacancy, emitting the difference in energy between its starting and final orbitals as a photon of set energy (purple wave). In Auger electron production the transition of the outer electron to the inner orbital is coupled (purple line) to the promotion of an electron outwards to infinity (ionisation). The result of this process is an Auger electron of set energy. If, after Auger electron emission, the ion is not in its lowest energy state then further x-ray/Auger electron deexcitations may occur. 13

Figure 1.3. Diagrammatic model of Compton scattering. An incident photon (purple arrow) interacts with an atomically bound electron, transferring to it enough energy to liberate it from the atom, leaving a vacant orbital (green circle). The photon is scattered through an angle θ and is shifted into a lower energy photon (red arrow). The electron (yellow ball) is ejected at an angle of ϕ from the path of the original photon (black dashed line). The angles θ and ϕ , as well as the kinetic energy of the ejected electron and the final wavelength of the scattered photon, are derived from the laws of conservation of momentum and energy. 14

Figure 1.4. A plot showing the distribution of energies with which an 80 keV photon could scatter during Compton scattering. The angular distribution was calculated as described in the text. Figure based on information from 'Practical Gamma-ray Spectrometry'[28]..... 15

Figure 1.5. Schematic representation of alternative pathways for DNA double strand break repairs. Enzymes responsible for the various stages have been omitted for clarity. A double strand break (DSB) results in the two strands of a DNA helix being completely separated from each other, with trailing ends (red and green highlighted regions) that are prone to rapid deterioration (left). In non-homologous end joining (NHEJ) repair (upper path), the trailing ends of the two strands are cut back to leave a level end (upper middle), which can then be joined together to reproduce a double stranded structure (upper right). In homologous end joining (HEJ) repair (lower path), a sister length of DNA is available, either from a sister chromosome or an identical strand present after DNA replication. This sister helix of DNA (purple strands) is used as a template to ensure accurate DNA replication (lower middle). In this

process, the 3' ends in the DSB region associate with their complimentary sequences in the sister strands, allowing the replication of replacement DNA (yellow highlighted regions). The end result (lower right) is that the repaired double strand of DNA contains a complete copy of the information that had been destroyed by the DSB originally. This is in contrast with the final strand from the NHEJ process, which is shortened as a result of the missing bases and may now contain a range of mutations from frame shifts to sequence deletions. 20

Figure 1.6. Illustration for explaining the various approaches to tumour tracking discussed in the text. For the first two columns (A, B, D, E, G, H) the larger ellipsoid in each image represents the patient body and the lighter, smaller circle represents the tumour. The tumour rises and falls during the treatment, and the images in the first and second columns represent the lowest and highest it moves to respectively. In these columns, the dashed white lines represent the limits of the irradiating beam at that moment in time. The third column represents the radiation dose deposited by the beam, with brighter regions corresponding to a higher dose. Outlines of the extreme tumour locations and the simulated patient body are included for reference. The sizes of the tumours and their motions are exaggerated for visibility. This illustration is considering the case of a single beam. Modern radiotherapy usually involves a range of different beams at different angles and intensities, so the dose to the tumour will be much higher than that to the healthy tissue overall. This diagram considers a single beam for illustrative purposes only. 23

Figure 1.7. A sketch (based on fictional data) showing how ions and x-ray photons differ in their energy deposition profiles as a function of depth. Doses are normalised to the same maximum for both particle types. The target of the irradiation is at a normalised depth of 1. x-rays deposit their energy in a way that drops off exponentially with depth (after an initial build-up region which is usually very small but varies with energy), with considerable dose deposited both before and after the target depth. In contrast, ions deposit most of their energy at a defined depth (the Bragg peak), with a low level of dose deposition per unit length prior to this point and almost no dose deposition at deeper sites. 26

Figure 2.1. The chemical structure of MTT (left) and the molecule that results from its reduction (right). MTT is usually provided in the form of a bromine salt, however the Br⁻ ion is omitted for clarity. The molecular structures were drawn using the online software MolView, which is open source and provided by The MolView Project[102]. 33

Figure 2.2. Plot of surviving cell fractions found at various radiation doses for both control (without AuNPs) and AuNP incubated cells. The DEE that would be calculated for each dose is also shown on the plot, to illustrate that this metric varies depending on the dose selected in its calculation. Data is fictional, for illustrative purposes only. 37

Figure 2.3. Visual summary of the advantages of AuNPs for delivering RDEE therapeutically. **Synthesis:** There are multiple shapes which can be synthesised readily and with rudimentary lab supplies. **Functionalisation:** A range of ligands can be readily attached in combination using click

chemistry. **Tumour localisation:** AuNPs administered intravenously can accumulate preferentially at the site of a tumour. **Controllable uptake:** AuNPs can be functionalised to enter cancerous cells (darker blue) preferentially, and even targeted to organelles such as the nucleus (red spheres) once internalised. **RDEE:** Radiotherapy dose enhancement effects can be delivered by physical (secondary electron generation), chemical (catalytic ROS generation) and biological (DNA repair inhibition) mechanisms. 40

Figure 2.4. Figure comparing the measured RDEE based on cell work (triangles) with that predicted based on physical dose enhancement alone (dashed line). It should be noted that the x-axis measures increase in physical dose whilst the y-axis measures a ratio. An increase in physical dose of 1 is thus equal to a sensitizer enhancement ratio of 2. Figure reproduced, unedited, from Butterworth et al's 2017 review paper[126] under the terms of the Creative Commons Attribution 4.0 International License (<http://creativecommons.org/licenses/by/4.0/>)..... 43

Figure 2.5. Mechanisms of AuNP uptake into a cell (grey circle). Translocation (right side of cell) involves AuNPs (gold balls) interacting with protein channels or transporter proteins (red ovals) to move directly from outside of the cell to the inside. Translocation is rapid and the transporter is not depleted in the process. In contrast, endocytosis (left side of cell) is a complex process which begins when the AuNP binds an external receptor protein (purple cylinder). This binding leads to invagination of the membrane around the receptor. This invagination then pinches and buds off into the cytosol to produce an endosome. This process is slower and more energy intensive than translocation as the external receptors must be regenerated. N.B. the receptors normally attach not to the AuNP surface but rather to ligands attached to it. These ligands have been omitted in this diagram for clarity. 50

Figure 3.1. Steps involved in acquiring a photoacoustic image. For simplicity, the case of a single optically absorbing structure is shown (blue sphere), and the light source and ultrasound transducer are not shown. The light source is assumed to be placed on the mouse's back, at the top of the figure. 58

Figure 3.2. Flow diagram of possible energy dissipation mechanisms for optical absorbers relevant to photoacoustic imaging, based on work by A.C. Tam[202]. Ovals represent the form of the excitation energy at each stage whilst arrows indicate the processes which result in the energy changing form. Luminescence (green), photoelectric (purple) and photochemical (light blue) mechanisms may all lead to heat as a product, however their transition through intermediary stages results in a delay to heat production when compared with direct thermal deexcitation (red). Which mechanism dominates will depend on the absorber type and energies involved. For the purposes of this thesis, direct thermal deexcitation is the primary mechanism of interest..... 60

Figure 3.3. Plot of the optical attenuation coefficient versus wavelength for deoxy-haemoglobin (Hb) and oxy-haemoglobin (HbO₂). Whilst attenuation is shown, these complexes are almost non-scattering

at these wavelengths and so these curves also represent absorption. Data for the plots was obtained from OMLC.com[216]. 63

Figure 3.4. (A) Without an external electric field, the electron displacement relative to atomic centres is random and there is no net displacement. (B) In the presence of an external electric field the electrons on the AuNP surface undergo a net displacement to produce an opposing field across the AuNP. A restoring force on the electrons is thus produced to pull them back to equilibrium (as they can be modelled as a mass on a spring). Since the electric field associated with an electromagnetic wave oscillates with time, the surface electron displacement is also driven in a cyclical manner. When the frequency of the driving wave matches the natural frequency of the surface electron system, resonance is achieved and the restoring force can draw energy from the passing wave most efficiently. Note that the electromagnetic wave and AuNPs are not shown to the same scale as AuNP size has been exaggerated for clarity. For the above mechanism to hold, AuNPs need to be much smaller than the wavelength of the driving electromagnetic wave. 67

Figure 4.1. The basic principle behind all electromagnetic (EM) transmission imaging techniques. A beam of EM radiation (lime cone) is projected towards an object of interest (central blue square and circle). A pixelated detector (grey rectangle) placed behind the object of interest records the intensity of received EM radiation. Variations in intensity result from variations in beam attenuation, reflecting changes in a material property of the object (such as density or optical transparency). An image of the object is thus formed on the detector. Ideally each pixel in the image is related to the straight line integral between the EM radiation source (grey projector in bottom left) and that pixel. In this case the denser blue circle in the object of interest results in a darker circle in the detected image, corresponding to a lower EM flux at those locations. 78

Figure 4.2. The process of CT scanning an object involves the acquisition of multiple projections through the object, taken at different angles. (LEFT) A cylindrical test object (blue) containing two cylindrical inserts (red and yellow) and a jacket (purple) is imaged using a similar setup to that shown in Figure 4.1. The x-ray beams are not shown here for clarity. (RIGHT) The object of interest is then rotated 90 degrees around a central axis (shown in black) and imaged again. This process is repeated for a number of angles ranging from 0 - 180°. In clinical settings it is more common to rotate the source-detector combination rather than the patient. 80

Figure 4.3. Demonstration of how increasing numbers of projections lead to improved image reconstruction. (TOP LINE) A slice through the object being imaged in Figure 4.2. The remaining images show the results of reconstructions based on n equally spaced projection images, where n is, from left to right, (MIDDLE LINE) 1, 2, 4, (BOTTOM LINE) 16, 64 and 128. There is clearly a rapid improvement in image reconstruction as n increases at low values of n , though the benefits show diminishing returns as n increases to larger values. 81

Figure 4.4. The semiconductor material (grey), anode (blue rectangle) and cathode (red rectangle) of a semiconductor-based radiation detector are shown. (LEFT) Initially no significant free charge is present within the semiconductor. An incident photon (yellow bolt) interacts with the semiconductor, producing a highly excited electron. (MIDDLE) The excited electron rapidly deexcites through Auger recombination, producing a cloud (purple) of conduction band electrons and corresponding valence band holes. (RIGHT) Under the influence of an applied electric field, the electron cloud (red oval) and hole cloud (blue oval) drift towards the anode and cathode respectively. The clouds also expand laterally due to diffusion and electrostatic repulsion during this motion. Holes typically have a lower mobility and so will both drift and diffuse at lower rates than the electrons..... 84

Figure 4.5. Current dual energy approaches can be broadly classified into three categories. In all figures the object being imaged is the pink circle, the x-ray source is in black, the detector is in grey, the high energy x-ray beam is shown in blue and the low energy beam is shown in red. (LEFT) Voltage switching approaches involve imaging the object twice for each projection angle, once at a lower tube voltage and once at a higher tube voltage. This switching can be performed rapidly so that the resulting images are temporally offset, but spatially approximately coincident. (MIDDLE) Dual source approaches involve the simultaneous acquisition of the images using two different x-ray beam-detector pairs. The acquired images are thus temporally synced but spatially offset. (RIGHT) Dual detector approaches involve the use of multiple detectors behind each other. The x-ray beam is attenuated in an energy dependent way as it passes through the first detector such that a beam with a higher average energy spectrum is incident on the second detector. The resulting images are spatially and temporally coincident but show a higher correlation. 86

Figure 4.6. Basic principles behind PC approaches. (LEFT) some physical feature of the system such as voltage or current is sampled constantly (blue line). Some level of noise is always present in these measurements, however when a photon interacts with the detector material it causes a sharp and significant change in the measured quantity. A threshold is set (orange line) sufficiently above the noise floor such that any signal rises above this level indicate a photon interaction. Once a signal crosses the threshold, the total signal over some short time interval, dt , is integrated to produce a value, S . In this figure, the signal rose above threshold on three occasions, and so three counts will be recorded. (RIGHT) For each event detected, S is compared with a series of pre-set thresholds, each associated with a counter. If S is greater than a given threshold then the corresponding counter is incremented by 1. In this example the red counter would be incremented three times, the green counter incremented twice, and the purple counter not incremented at all. The number of events between given thresholds is then determined by subtraction of adjacent counters. 90

Figure 4.7. Electrons in an atom can be subdivided into a range of shells based on their principal quantum number, n . The inner shell is the K shell, corresponding to $n=1$, and it can hold 2 electrons. The next shell is the L shell, corresponding to $n=2$, and it can hold 8 electrons. The next shell is the M shell, corresponding to $n=3$, and it can hold 18 electrons. Further shells corresponding to $n < 3$ exist

but are not shown here for convenience. For a given atom, lower values of n correspond to more tightly bound electrons. Shells greater than $n=1$ show a fine structure, but exploration of this is beyond the scope of this thesis. 94

Figure 4.8. Interaction cross-section diagrams for Au and a 'Human Body' representative material across energies relevant to medical imaging (1 - 140 keV). The 'Human Body' material is composed of elements in the same proportions as they make up the human body. This material would not be suitable for imaging simulations due to the gross averaging that is employed, however it is sufficient for illustrating the different physical mechanisms which dominate for Au and human body tissues in general. Photon-Au interactions in this energy range are most likely to be photoelectric in nature, whilst above 20 keV the dominant photon- 'Human Body' interactions are Compton scatterings. Figure plotted using data from NIST[27]. 97

Figure 4.9. Comparisons of attenuation cross-sections for Au and the previously mentioned 'Human Body' representative material (see Figure 4.8) across energies relevant to medical imaging (1 - 140 keV). Monoenergetic imaging systems are only sensitive to differences in total attenuation (TOP), though may still be able to differentiate between these two material types based on their density. In contrast, dual energy systems can decompose images into photoelectric (BOTTOM LEFT) and Compton (BOTTOM RIGHT) interactions. This will allow for better material separation as photoelectric interactions are predominantly associated with photon-Au interactions whilst Compton interactions are predominantly associated with photon-'Human Body' interactions. Figure plotted using data from NIST[27]. 98

Figure 4.10. Total attenuation cross-section diagram for three contrast agents: Au, I and Gd. K-edges are clearly visible for all three elements, and the L-Edge for Au can also be seen towards the left of the figure. Figure plotted using data from NIST[27]. 98

Figure 4.11. The unit cell of Au is face centred cubic, with 8 Au atoms present at the corners of the unit cell (gold spheres on blue frame) and 6 Au atoms present at the faces of the unit cell (orange spheres on red frame). Note that Au atom colours in the diagram are different simply for visualisation clarity, but no unit cell location is materially different from any other. 101

Figure 5.1. Schematic representation of the process of radioactive nuclear decay. This diagram is designed to illustrate the general principles of nuclear decay and is not designed to be reflective of a particular isotope or atomic decay. Energy levels are shown separately for the protons (red) and neutrons (blue). (TOP) In the initial configuration shown here the most energetic protons occupy a significantly higher energy level than the most energetic neutrons. (SECOND LINE) A proton can spontaneously transition into a neutron, with the emission of an electron (purple) to conserve charge. (THIRD LINE) The new neutron occupies an energy level with vacant levels beneath it. This neutron thus spontaneously deexcites via emission of a gamma ray (orange wave) to fill this vacancy. (BOTTOM) The resulting configuration is in a lower total energy state than it was previously, resulting

in a consequent increase in atomic stability. The change in Z-number means that the final atom is now a different element to the one it was before it decayed. Note that there may be a significant delay between the second and third lines of this diagram, and the deexcitation may proceed via a variety of routes if more than one lower energy level vacancy is available to it. 113

Figure 5.2. A fictional energy spectrum was sampled at two different resolutions: 2 keV or 4 keV. The spectrum was then reconstructed using the process of linear interpolation described in the text. Over most of the spectrum the difference in sampling is small, however around the K-edge of the target (sharp spike at ~100 keV) the 2 keV step size leads to a much narrower peak, more consistent with the K-edge which should ideally be modelled with a δ function. 115

Figure 5.3.(LEFT) The situation within a semiconductor in which an electron (yellow ball) is moving with respect to four fixed electrodes (A-D). Calculation of the induced charge on electrode A by the movement of this electron as a function of time is a time consuming and computationally intensive process to solve directly. The problem can be greatly simplified by approaches such as the one detailed in this section. (RIGHT) These approaches all require the calculation of the weighting potential, which is the electric field that is present within the volume of interest (the semiconductor in this case) when the electrode of interest (A) is set to unit voltage, and all other electrodes are set to zero Volts..... 118

Figure 5.4. Flow chart illustrating how information is fed into and passed between the various components of CoGI. With reference to Table 5.2, C1 handles the Photon-matter interactions, C2 models the effect of semiconductor charge transport. C3 then takes the output from C1 and C2 and implements signal processing to generate the detector output. 122

Figure 5.5. 3x3 grids of pixels like the one pictured above were used in calculating the CIE maps in COMSOL. Each pixel is defined as the central collecting anode (smallest squares) plus half of the distance between it and its neighbouring anodes (medium sized squares). 3 different pixel types were simulated in turn: 'central' pixels surrounded by 8 others (purple), 'edge' pixels surrounded on all but one side (green) and 'corner' pixels surrounded on all but 2 sides (red). 125

Figure 5.6. Summary of the steps involved in CoGI. The descriptions for each step in this summary are given in terms of the aims the step intends to achieve. In contrast, the step descriptions in the text focus on the operations performed to achieve these results. This summary table thus provides a higher-level overview of the motivations and actions of the various steps in CoGI. 127

Figure 5.7. The process of trilinear interpolation. (LEFT) The point at which the value is desired (gold ball) is surrounded by 8 points with a known value (red and blue balls), with the 8 points forming the vertices of a cube. (MIDDLE) Interpolation along one spatial axis collapses the 3D cube into a 2D square, with the point of interest imbedded within its surface. (RIGHT) Interpolation along a second spatial axis collapses the 2D square into a 1D line that intersects with the point of interest. The value at this point can now be determined by interpolation along the third spatial dimension. 129

Figure 5.8. Setup for simulation of ^{57}Co on the Actaeon pixelated detector. The ^{57}Co source (small pink square) is placed in contact with the carbon fibre window (blue rectangle) and directly over the gap between the two CdTe crystals (yellow rectangles). The ASICs on which the CdTe crystals are mounted are not simulated, though the cathode and pixelated anodes are..... 137

Figure 5.9. Comparison of the main ^{241}Am photopeak as recorded by a GRI spectrometer (Exp) and predicted by CoGI (Sim). The data recorded/simulated are shown (circles), along with the Gaussian fits (coloured lines). The widths of the two peaks and areas underneath them are in good agreement. 138

Figure 5.10. Simulated ^{57}Co energy spectrum produced by CoGI with (solid blue line) and without (black dashed line) a CSCA applied. The spectral features corresponding to x-ray fluorescence (A), escape peak (B) and full-energy photopeak (C) from the raw spectrum were used to calibrate the simulated detector using a linear calibration technique..... 139

Figure 5.11. Example of how a coplanar arrangement can be implemented in an anode. The anode is divided into two interlaced strips (red and blue). Both anode strips are of a negative voltage with respect to the cathode, but there is an additional voltage difference between the red and blue strips. This results in a steep gradient in field strength in proximity to the anodes, similar to the small pixel effect in a pixelated anode. 141

Figure 6.1. Simulation setup (not to scale). The CdTe sensor was modelled by a solid rectangular block (grey) measuring 2.1 cm x 2.1 cm at its face and with a thickness that varied based on the geometric template chosen between 1 mm and 3 mm (see text). A rectangular radiation source was defined (yellow) that was slightly larger than the CdTe in the y- and z-axes and parallel to one of the larger sensor faces. Both radiation source and CdTe sensor were centred with respect to the x-axis. Radiation was emitted from the radiation source from a random location (rectangular distribution) propagating initially with zero y and z components so that it was perpendicularly incident on the sensor (emitted parallel to the x-axis)..... 150

Figure 6.2. Plot of absolute detection efficiency (ADE) as a function of pixel pitch and pixel thickness. ADE is defined as the counts recorded divided by the number of photons incident on the sensor. The data shown concerns a flux of $\sim 10^7$ photons $\text{mm}^{-2} \text{s}^{-1}$ 155

Figure 6.3. Plot of absolute photopeak bin efficiency (APE) as a function of pitch and thickness. APE is defined as the counts recorded in the photopeak bin divided by the number of photons of 80 keV incident on the sensor. The data shown concerns a flux of $\sim 10^7$ photons $\text{mm}^{-2} \text{s}^{-1}$ 155

Figure 6.4. Plot of absolute photopeak bin efficiency (APE) as a function of pitch and thickness. APE is defined as the counts recorded in the photopeak bin divided by the number of photons of 80 keV incident on the sensor. In this case, a CSCA (3x3Dy) has been applied. The data shown concerns a flux of $\sim 10^7$ photons $\text{mm}^{-2} \text{s}^{-1}$ 156

Figure 6.5. Plot of relative coincidence counts (RCC) as a function of pixel pitch and pixel thickness. RCC are defined as the counts recorded in the coincidence bin divided by the sum of counts in all bins. The data shown concerns a flux of $\sim 10^6$ photons $\text{mm}^{-2} \text{s}^{-1}$ 156

Figure 6.6. Plot of relative coincidence counts (RCC) as a function of pixel pitch and pixel thickness. RCC are defined as the counts recorded in the coincidence bin divided by the sum of counts in all bins. The data shown concerns a flux of $\sim 10^7$ photons $\text{mm}^{-2} \text{s}^{-1}$ 157

Figure 6.7. Plot of relative coincidence counts (RCC) as a function of pixel pitch and pixel thickness. RCC are defined as the counts recorded in the coincidence bin divided by the sum of counts in all bins. The data shown concerns a flux of $\sim 10^8$ photons $\text{mm}^{-2} \text{s}^{-1}$ 157

Figure 6.8. Plot of binned spectral efficiency (BSE) as a function of pixel pitch and thickness. BSE is defined as the counts in the photopeak bin divided by the sum of counts in all bins. The relation between efficiency and thickness is reversed between small (left inset) and large (right inset) pixel pitches. The data shown concerns a flux of $\sim 10^7$ photons $\text{mm}^{-2} \text{s}^{-1}$ 158

Figure 6.9. Plot of binned spectral efficiency (BSE) as a function of pixel pitch and thickness. BSE is defined as the counts in the photopeak bin divided by the sum of counts in all bins. In this case, a CSCA (3x3Dy) has been applied. The data shown concerns a flux of $\sim 10^7$ photons $\text{mm}^{-2} \text{s}^{-1}$ 158

Figure 6.10. When a fluorescence photon is produced (yellow circle) the direction of its emission is random. In thinner pixels (solid lined box) there are more possible angles of escape from the sensor (red angle) than there are angles in a thicker pixel (purple angle and dashed line respectively)..... 163

Figure 7.1. Hybrid CSCAs first define a 3x3 neighbourhood based on their neighbourhood locality rules. Secondly 4 overlapping 2x2 neighbourhoods are constructed to cover the 3x3 neighbourhood, as shown. The charge (stars) in each 2x2 neighbourhood is summed and compared, with the winner selected based on the CM of the CSCA. In this example, assuming all stars represent equal amounts of charge, the four neighbourhoods would have charge of: red (top left) = 3, green (top right) = 4, blue (bottom left) = 2 and yellow (bottom right) = 3. The output signal for this pattern of events would thus be 4 (the highest sum) for an additive CSCA or 2 (the lowest sum) for a subtractive CSCA. All pixels would then be reset and any charge not used for the signal generation process discarded. 169

Figure 7.2. A 4-pixel by 4-pixel array of pixels in which three events (stars) are detected within the search time of the CSCA. The red star indicates the first event detected which triggers the CSCA. (LEFT) A static CSCA uses predefined neighbourhoods (grey shaded regions) which remain the same throughout the irradiation. In this example, the bottom left neighbourhood (dark grey) could sum the energy from the 2 events within its neighbourhood, and the top left neighbourhood (light grey) would sum the energy from the upper event into a separate count. (CENTRE) A 2x2 dynamic CSCAs defines a 2x2 neighbourhood such that the pixel with the first detected event is located in the bottom left. In this example, two of the events could be summed and the third would cause a different neighbourhood to be

formed. (RIGHT) 3x3 and Hybrid dynamic CSCAs define a 3x3 neighbourhood such that the pixel with the first detected event is located at the centre. In this example, all three events could be summed together to a single count, fully reconstructing the energy of the original photon if all three events were triggered by charge sharing from a single photon..... 170

Figure 7.3. A plot of ADE versus pixel pitch at an incident photon flux of $\sim 10^6$ photons $\text{mm}^{-2} \text{s}^{-1}$. The Hybrid and 3x3 CSCAs perform indistinguishably according to this metric, resulting in significant overlap. Similarly, the 2x2 dynamic and static CSCAs overlap almost entirely at this flux level. The case where no CSCA is applied is also shown, along with the Theoretical ADE value proposed earlier, for reference. 175

Figure 7.4. A plot of ADE versus pixel pitch at an incident photon flux of $\sim 10^7$ photons $\text{mm}^{-2} \text{s}^{-1}$. The Hybrid and 3x3 CSCAs perform indistinguishably according to this metric, resulting in significant overlap. Figure inset shows that the dynamic and static CSCAs swap order at the highest pitches considered in this figure. The case where no CSCA is applied is also shown, along with the Theoretical ADE value proposed earlier, for reference..... 175

Figure 7.5. A plot of ADE versus pixel pitch at an incident photon flux of $\sim 10^8$ photons $\text{mm}^{-2} \text{s}^{-1}$. The Hybrid and 3x3 CSCAs perform indistinguishably according to this metric, resulting in significant overlap. The case where no CSCA is applied is also shown, along with the Theoretical ADE value proposed earlier, for reference. 176

Figure 7.6. A plot of the difference between each CSCA and the Theoretical ADE proposed earlier at an incident photon flux of $\sim 10^6$ photons $\text{mm}^{-2} \text{s}^{-1}$. The difference is taken directly from the data for Figure 7.3 and so is expressed in percentage points. Again, the case where no CSCA is applied is presented for comparison. 176

Figure 7.7. A plot of the difference between each CSCA and the Theoretical ADE proposed earlier at an incident photon flux of $\sim 10^7$ photons $\text{mm}^{-2} \text{s}^{-1}$. The difference is taken directly from the data for Figure 7.4 and so is expressed in percentage points. Again, the case where no CSCA is applied is presented for comparison. 177

Figure 7.8. A plot of APE versus pixel pitch at an incident photon flux of $\sim 10^6$ photons $\text{mm}^{-2} \text{s}^{-1}$. The dynamic Hybrid and dynamic 3x3 CSCAs perform indistinguishably according to this metric, resulting in significant overlap. Similarly, the 2x2 dynamic and static CSCAs overlap almost entirely at this flux level. The case where no CSCA is applied is also shown as a reference..... 178

Figure 7.9. A plot of APE versus pixel pitch at an incident photon flux of $\sim 10^7$ photons $\text{mm}^{-2} \text{s}^{-1}$. The dynamic Hybrid and dynamic 3x3 CSCAs perform indistinguishably according to this metric, resulting in significant overlap. Similarly, the 2x2 dynamic and static CSCAs overlap at low pitches (below $\sim 350 \mu\text{m}$) but begin to become distinguishable at the higher pitches considered here. The case where no CSCA is applied is also shown as a reference. 178

Figure 7.10. A plot of RCC versus pixel pitch at an incident photon flux of $\sim 10^7$ photons $\text{mm}^{-2} \text{s}^{-1}$. The dynamic Hybrid and dynamic 3x3 CSCAs overlap significantly with each other at all pitches, and with the static 3x3 CSCA at pitches below $\sim 300 \mu\text{m}$. Similarly, the 2x2 dynamic and static CSCAs overlap at low pitches (below $\sim 300 \mu\text{m}$) but begin to become distinguishable at the higher pitches considered here. The case where no CSCA is applied is also shown, for reference. 179

Figure 7.11. A plot of BSE versus pixel pitch at an incident photon flux of $\sim 10^6$ photons $\text{mm}^{-2} \text{s}^{-1}$. The dynamic Hybrid and dynamic 3x3 CSCAs perform indistinguishably according to this metric, resulting in significant overlap. The same is true for the dynamic 2x2 and static 2x2 CSCAs. Similarly, the static Hybrid and static 3x3 CSCAs overlap significantly at lower fluxes but diverge from about $\sim 300 \mu\text{m}$. The case where no CSCA is applied is also shown, for reference. 180

Figure 7.12. A plot of BSE versus pixel pitch at an incident photon flux of $\sim 10^7$ photons $\text{mm}^{-2} \text{s}^{-1}$. The dynamic Hybrid and dynamic 3x3 CSCAs perform exceptionally closely according to this metric (see inset), resulting in significant overlap. The same is true for the dynamic 2x2 and static 2x2 CSCAs. The case where no CSCA is applied is also shown, for reference. 181

Figure 7.13. A plot of BSE versus pixel pitch at an incident photon flux of $\sim 10^8$ photons $\text{mm}^{-2} \text{s}^{-1}$. The dynamic Hybrid and dynamic 3x3 CSCAs perform exceptionally closely according to this metric, resulting in significant overlap. The case where no CSCA is applied is also shown, for reference... 181

Figure 7.14. (a) Heat map representing CIE across a single pixel as generated and viewed in COMSOL. The plot represents a cut through taken perpendicular to the incident photon flux and at a depth below the anode equal to 10% of the pixel's length. The edges of the anode are marked by the white square superimposed on the image. (b) A plot of CIE vs distance along a path taken across the centre of the pixel (the horizontal black line in a). Other black lines are spatial markers from COMSOL and can be ignored here. 182

Figure 7.15. A 4x4 pixel array can produce a range of different counts depending on its segmentation. The numbers in pixels refer to the order in which they are triggered. Pixels with the same number can be triggered in any order, so long as they are all triggered before higher numbered pixels. For the case where no CSCA is applied (a) the maximum count rate is equal to the number of pixels: 16. For a static 2x2 CSCA (b) the maximum count rate is equal to the number of neighbourhoods defined: 4. For a dynamic 2x2 CSCA however the maximum count rate depends on the order in which the pixels are triggered and can range from 4 (c) up to 16 (d). The more highly ordered state of the triggering required to produce 16 counts makes it less likely however, so the measured count rate will likely lie somewhere in between 4 and 16. 185

Figure 8.1. A AuNR of length L and diameter $2R$ can be considered as being comprised of two hemispheres of radius R and a connecting cylinder of length $(L - 2R)$ and radius R 197

Figure 8.2. (LEFT) The plate is irradiated for 1/2 of the irradiation time in one orientation and then (RIGHT) rotated before being irradiated for the second 1/2 of the time required. 200

Figure 8.3. Schematic of a 96-well plate showing the division of AuNP conditions and AO/PI mixtures. Wells marked in red or blue were plated with two thousand PC-3 cells to form monolayers. Wells marked in yellow contained 200 µl of PBS. AuNPs of the types listed were added to each well as described in the text. Mixture A was added to the red well whilst mixture B was added to the blue wells (see Appendix 4 for the composition of the mixtures). 202

Figure 8.4. Optical absorption spectra for AuNRs produced from the first (blue) and second (red) syntheses. Absorption spectra have been normalised at 400 nm as this wavelength should represent intraband transitions and not plasmon resonances, and so can be used to determine the quantity of Au atoms present. 203

Figure 8.5. Map of relative dose within the cell irradiator, recorded by digitising the dosimetry film and applying a median filter to remove grain noise but preserve the dose gradient. The reported values are normalised to the reference dose delivered (5 Gy). 204

Figure 8.6. Shows the same normalised map of relative dose from Figure 8.5, however with a region of pixels removed (set to 0) in the middle of the high dose region (the blue rectangular shape within the yellow oval). This region represents the area in which a 96-well cell culture plate can be placed so that the maximum variation in dose across the plate is less than 5% from the MidDose. Note that due to the removal of the highest dose regions in this process, the colour scaling of dose has been shifted slightly compared to Figure 8.5. This map was not used in further calculations but is a useful visual aid for checking the tolerance to plate placement. 205

Figure 8.7. Enlarged subsection of Figure 8.5 showing only the cell-culture-plate-sized area identified as having the lowest variation in dose. This map represents the doses that would be produced across the plate if it were left in a single orientation for the full irradiation time. 205

Figure 8.8. Enlarged subsection of Figure 8.5 showing only the cell-culture-plate-sized area identified as having the lowest variation in dose. This map represents the doses that would be produced across the plate if it were rotated by 180° halfway through its irradiation. Repeats of each experimental condition will run in the direction labelled “Into irradiator”, and the different experimental conditions will run in the direction labelled as “Across irradiator”. 206

Figure 8.9. Reproduction of Figure 8.8 with lines added to separate the area in which the experimental cells would sit (central region) from those that will be filled with PBS (outer regions). As a result of this arrangement, the dose distribution across experimental conditions will be reduced. 206

Figure 8.10. Cell viability as measured by the luminescence produced by a monolayer of PC-3 cells irradiated at different doses when assayed with Cell Titre Glo-3D. Experimental data (signal) are

plotted as blue circles with error bars representing 2σ derived from a sample size of $n=10$ wells. The dose response curve extrapolated from these points is plotted as a red dashed line. These data sets are plotted against left axis. The absolute gradient for this curve, normalised to its peak, is plotted as a black dotted line, against the right axis. 207

Figure 8.11. Cell viability as measured by the luminescence produced by PC-3 spheroids irradiated at different doses when assayed with Cell Titre Glo-3D. Experimental data (signal) are plotted as blue circles with error bars representing 2σ derived from sample sizes ranging from $n = 5 - 10$ spheroids, depending on dose. The dose response curve extrapolated from these points is plotted as a red dashed line. These data sets are plotted against the left axis. The absolute gradient for this curve, normalised to its peak, is plotted as a black dotted line, against the right axis. 208

Figure 8.12. Cell viability as measured by the absorption produced by a monolayer of cells irradiated at different doses when assayed with MTT. Experimental data (signal) are plotted as blue circles with error bars representing 2σ as derived from a sample size of $n=10$ wells. The dose response curve extrapolated from these points is plotted as a red dashed line. These data sets are plotted against the left axis. The absolute value of gradient for this curve, normalised to the peak, is plotted as a black dotted line, against the right axis. 208

Figure 8.13. Cell viability as measured by the absorption produced by PC-3 spheroids irradiated at different doses when assayed with MTT. Experimental data (signal) are plotted as blue circles with error bars representing 2σ as derived from samples sizes ranging from $n = 7 - 9$ spheroids, depending on dose. The dose response curve extrapolated from these points is plotted as a red dashed line. These data sets are plotted against the left axis. The absolute value of gradient for this curve, normalised to the peak, is plotted as a black dotted line, against the right axis. 209

Figure 8.14. A selection of optical light transmission microscope images obtained using the Celigo. Images show spheroids 72 hours after seeding. Despite the use of Matrigel, the spheroids showed varying degrees of compactness and uniformity, from well-defined dense spheroids (LEFT) to a poorly defined loose agglomeration of cells (RIGHT). 215

Figure 8.15. Images of spheroids taken down a benchtop optical microscope using a handheld camera. (TOP LEFT) Example of spheroid with loose attachments that could be disrupted during feeding. (REMAINING IMAGES) Examples of spheroids that had become disrupted by accidental transport during feeding. 216

Figure 0.1. Schematic of a 96-well plate showing the two arrangements of wells used in this work. Wells indicated in red contained spheroids or monolayers of cells whilst yellow wells indicate wells that were filled with 200 μ l of PBS. 271

Figure 0.2. Schematic of a 96-well plate showing the division of AuNP conditions and AO/PI mixtures. Wells marked in red or blue were plated with two thousand PC-3 cells to form monolayers. Wells

marked in yellow contained 200 µl of PBS. AuNPs of the types listed were added to each well as described in the text. Mixture A was added to the red well whilst mixture B was added to the blue wells (see text for the composition of the mixtures).....274